TOWARDS THE CONTROL OF THERMAL EXPANSION: FROM 1996 TO TODAY

EDITED BY: Andrea Sanson and Jun Chen
PUBLISHED IN: Frontiers in Chemistry

frontiers Research Topics

ISSN 1664-8714
ISBN 978-2-88945-934-6
DOI 10.3389/978-2-88945-934-6

About Frontiers

Frontiers is more than just an open-access publisher of scholarly articles: it is a pioneering approach to the world of academia, radically improving the way scholarly research is managed. The grand vision of Frontiers is a world where all people have an equal opportunity to seek, share and generate knowledge. Frontiers provides immediate and permanent online open access to all its publications, but this alone is not enough to realize our grand goals.

Frontiers Journal Series

The Frontiers Journal Series is a multi-tier and interdisciplinary set of open-access, online journals, promising a paradigm shift from the current review, selection and dissemination processes in academic publishing. All Frontiers journals are driven by researchers for researchers; therefore, they constitute a service to the scholarly community. At the same time, the Frontiers Journal Series operates on a revolutionary invention, the tiered publishing system, initially addressing specific communities of scholars, and gradually climbing up to broader public understanding, thus serving the interests of the lay society, too.

Dedication to Quality

Each Frontiers article is a landmark of the highest quality, thanks to genuinely collaborative interactions between authors and review editors, who include some of the world's best academicians. Research must be certified by peers before entering a stream of knowledge that may eventually reach the public - and shape society; therefore, Frontiers only applies the most rigorous and unbiased reviews.
Frontiers revolutionizes research publishing by freely delivering the most outstanding research, evaluated with no bias from both the academic and social point of view. By applying the most advanced information technologies, Frontiers is catapulting scholarly publishing into a new generation.

What are Frontiers Research Topics?

Frontiers Research Topics are very popular trademarks of the Frontiers Journals Series: they are collections of at least ten articles, all centered on a particular subject. With their unique mix of varied contributions from Original Research to Review Articles, Frontiers Research Topics unify the most influential researchers, the latest key findings and historical advances in a hot research area! Find out more on how to host your own Frontiers Research Topic or contribute to one as an author by contacting the Frontiers Editorial Office: researchtopics@frontiersin.org

TOWARDS THE CONTROL OF THERMAL EXPANSION: FROM 1996 TO TODAY

Topic Editors:
Andrea Sanson, University of Padua, Italy
Jun Chen, University of Science and Technology Beijing, China

Citation: Sanson, A., Chen, J., eds. (2019). Towards the Control of Thermal Expansion: From 1996 to Today. Lausanne: Frontiers Media.
doi: 10.3389/978-2-88945-934-6

Table of Contents

frontiers in Chemistry

EDITORIAL
published: 08 May 2019
doi: 10.3389/fchem.2019.00284

Editorial: Towards the Control of Thermal Expansion: From 1996 to Today

Andrea Sanson[1]* *and Jun Chen*[2]

[1] Department of Physics and Astronomy, University of Padua, Padua, Italy, [2] School of Mathematics and Physics, University of Science and Technology Beijing, Beijing, China

Keywords: thermal expansion control, negative thermal expansion (NTE), materials physics and chemistry, materials science, solid state physics

Editorial on the Research Topic

Towards the Control of Thermal Expansion: From 1996 to Today

Most materials expand on heating, known as positive thermal expansion (PTE). Thermal expansion is critical in many technological applications, like precise instruments, glazes and coating materials, optical and electronic devices, high-temperature materials design. As a matter of fact, different materials in contact with each other can have different thermal expansion, giving rise to thermal shock breakage. For this reason, controlling thermal expansion represents a challenge for materials design.

Negative thermal expansion (NTE), that is material contraction on heating over a certain temperature range, is relatively rare but has important technological applications. Since the large isotropic NTE was discovered in zirconium tungstate over a wide temperature range in 1996, the interest in NTE has rapidly grown to become the most promising route to achieve the control of thermal expansion. Since then, many NTE materials have been discovered.

NTE phenomenon is known to arise from a range of different physical mechanisms, such as low-energy vibrational modes, ferroelectricity, magnetic, and valence transitions. However, this does not lead to straightforward control of thermal expansion. Moreover, composites of negative and positive thermal expansion materials may fail after repeated cycling, so direct control of thermal expansion within a single homogenous phase is desirable and yet difficult to achieve. To date, different methods are under investigation to achieve the control of thermal expansion.

The present Research Topic includes a collection of original research and review (mini review) articles dedicated to the physical-chemical phenomena connected to NTE and to the state-of-the-art for control thermal expansion. The collection begins with a review by Takenaka on phase-transition type NTE materials, presenting some recent works related to how giant NTE materials are used as practical thermal expansion compensators. Hu et al. present a second review on the NTE behavior in materials with giant magnetocaloric effects (MCE), including some representative examples of MCE materials. An article perspective is presented by Attfield, where NTE is classified in terms of intrinsic structural and electronic mechanisms, and morphological NTE due to the specific morphology of the sample.

Many articles of the collection are dedicated to developing new materials with zero or adjustable thermal expansion. Liu et al. fabricated $Zr_2MoP_2O_{12}/ZrO_2$ composites with a variable coefficient of thermal expansion (CTE) from -5.7×10^{-6} K^{-1} to $+5.6\times10^{-6}$ K^{-1} by changing the $Zr_2MoP_2O_{12}$ content, reaching a near zero CTE from 25 to 700°C for the composition ratio $Zr_2MoP_2O_{12}/ZrO_2$ of 2:1. Similarly, Zhang et al. synthetized $Zr_2WP_2O_{12}/ZrO_2$ composites and adjusted the CTE

Edited and reviewed by:
Bretislav Friedrich,
Fritz-Haber-Institut, Germany

***Correspondence:**
Andrea Sanson
andrea.sanson@unipd.it

Specialty section:
This article was submitted to Physical Chemistry and Chemical Physics, a section of the journal Frontiers in Chemistry

Received: *29 March 2019*
Accepted: *08 April 2019*
Published: *08 May 2019*

Citation:
Sanson A and Chen J (2019) Editorial: Towards the Control of Thermal Expansion: From 1996 to Today. Front. Chem. 7:284. doi: 10.3389/fchem.2019.00284

from -3.3×10^{-6} K^{-1} to $+4.1\times10^{-6}$ K^{-1} by varying the mass ratio $Zr_2WP_2O_{12}/ZrO_2$, obtaining again a zero CTE for the ratio 2:1. Near-zero thermal expansion behavior over a wide temperature range was also found out by Li et al. in $HfMg_{1-x}Zn_xMo_3O_{12}$ solid solutions, whose phase transition temperature from monoclinic to orthorhombic structure increases with the content of Zn^{2+}. Giant NTE properties were observed in Fe-doped MnNiGe compounds by Zhao et al. with CTE values of about -285×10^{-6} K^{-1} and -1167×10^{-6} K^{-1} in $Mn_{0.90}Fe_{0.10}NiGe$ and $MnNi_{0.90}Fe_{0.10}Ge$, respectively. Furthermore, these materials were combined with Cu in order to control their NTE properties. Guo et al. investigated NTE and magnetic properties of anti-perovskite $Ga_{1-x}Cr_xN_{0.83}Mn_3$ compounds. They observed that Cr doping introduces ferromagnetic order thus giving rise to the broadening of NTE temperature window. Finally, Zhou et al. obtained huge PTE and NTE in fence-like metal organic frameworks obtained with a series of transition metal ions.

Part of the published works have a computational character. By using an efficient approach for obtaining the variation of the dynamical matrix as a function of the lattice constant, Vila et al. obtained that the large NTE of ZrW_2O_8 arises almost exclusively from the transverse contributions of the O-atoms. A second study was performed by Vila et al. on ZrW_2O_8, combining theoretical calculations of the structure and vibrational properties with the experimental results from extended x-ray absorption fine structure spectroscopy. *Ab initio* lattice dynamics calculations were combined with inelastic neutron scattering by Singh et al. to study the NTE dynamics in the metal organic framework compound AgC_4N_3. Ablitt et al. performed density functional theory simulations in Ruddlesden–Popper layered perovskite series, showing that by changing the fraction of layer interface in the structure one may control the anisotropic compliance necessary for the pronounced uniaxial NTE observed in these systems. Occhialini et al. discussed the broad issue of structural NTE with particular attention on perovskite-structured materials, providing a model treatment beyond mean field theory to identify the key elements that move toward control of NTE. First-principles calculations were performed in NiSi and isostructural compound NiGe by Goel et al. with the aim of studying the phonon modes which give the major contribution to the NTE behavior in NiSi, and reasons for negligible NTE in NiGe.

Lastly, high-pressure synchrotron powder X-ray diffraction studies of $Cr_2Mo_3O_{12}$ and $Y_2Mo_3O_{12}$ were conducted by Young et al. revealing that the monoclinic polymorphs of these materials do not undergo phase transitions within the studied pressure range, making them unique among the $A_2M_3O_{12}$ family of NTE materials. Jiang et al. investigated the thermal expansion properties of the ultraviolet non-linear optical crystal $BaAlBO_3F_2$ and the practical implications were discussed. Wang et al. proposed the new strain gauge method to measure the thermal expansion and magnetostriction of solid materials at low temperatures, opening up an interesting way for exploring potential magnetostrictive and NTE materials.

In summary, the present papers taken together give an overview of research on NTE and on the tuning of thermal expansion. We hope that the different perspectives here reported will inspire new studies and findings toward the design of materials with controlled thermal expansion.

AUTHOR CONTRIBUTIONS

All authors listed have made a substantial, direct and intellectual contribution to the work, and approved it for publication.

Conflict of Interest Statement: The authors declare that the research was conducted in the absence of any commercial or financial relationships that could be construed as a potential conflict of interest.

frontiers in Chemistry

REVIEW
published: 02 July 2018
doi: 10.3389/fchem.2018.00267

Progress of Research in Negative Thermal Expansion Materials: Paradigm Shift in the Control of Thermal Expansion

*Koshi Takenaka**

Department of Applied Physics, Nagoya University, Nagoya, Japan

To meet strong demands for the control of thermal expansion necessary because of the advanced development of industrial technology, widely various giant negative thermal expansion (NTE) materials have been developed during the last decade. Discovery of large isotropic NTE in ZrW_2O_8 has greatly advanced research on NTE deriving from its characteristic crystal structure, which is now classified as *conventional* NTE. Materials classified in this category have increased rapidly. In addition to development of conventional NTE materials, remarkable progress has been made in *phase-transition-type* NTE materials using a phase transition accompanied by volume contraction upon heating. These giant NTE materials have brought a paradigm shift in the control of thermal expansion. This report classifies and reviews mechanisms and materials of NTE to suggest means of improving their functionality and of developing new materials. A subsequent summary presents some recent activities related to how these giant NTE materials are used as practical thermal expansion compensators, with some examples of composites containing these NTE materials.

Keywords: negative thermal expansion, phase transition, thermal expansion control, composites, microstructural effects

OPEN ACCESS

Edited by:
Jun Chen,
University of Science and Technology Beijing, China

Reviewed by:
Ren Zhang,
Intel (United States), United States
Oh-Hoon Kwon,
Ulsan National Institute of Science and Technology, South Korea
Cora Lind,
University of Toledo, United States

***Correspondence:**
Koshi Takenaka
takenaka@nuap.nagoya-u.ac.jp

Specialty section:
This article was submitted to Physical Chemistry and Chemical Physics, a section of the journal Frontiers in Chemistry

Received: *22 March 2018*
Accepted: *12 June 2018*
Published: *02 July 2018*

Citation:
Takenaka K (2018) Progress of Research in Negative Thermal Expansion Materials: Paradigm Shift in the Control of Thermal Expansion. Front. Chem. 6:267. doi: 10.3389/fchem.2018.00267

INTRODUCTION

Control of thermal expansion, an urgent demand in modern industrial technology, is making remarkable progress. Even a minute change of 10^{-5} in linear distortion fatally degrades the performance of high-precision devices and instruments. Furthermore, for a device comprising multiple materials, mismatched thermal expansion between the constituents themselves can cause severe damage such as exfoliation of interfaces and breakage of wires. In addition to work in fields that have traditionally avoided the adverse influence of thermal expansion such as optical instruments and precise machining equipment, control of thermal expansion has been strongly sought in recent years for advanced electronics such as power semiconductor devices, thermoelectric conversion systems, and fuel cells. Difficulties attributable to thermal expansion control are universal and are difficult to resolve.

The core technology of thermal expansion control is *negative* thermal expansion (NTE) materials: substances that contract when heated (Chu et al., 1987; Sleight, 1998; Evans, 1999; Barrera et al., 2005; Lind, 2012; Takenaka, 2012; Chen et al., 2015). After discovery of the large isotropic NTE of ZrW_2O_8 in 1996, for which the coefficient of linear thermal expansion α_L (subscript L signifying "linear") reaches -9×10^{-6} K^{-1} (Mary et al., 1996), the successive discovery of giant

NTE materials has encouraged remarkable progress of research in this field, particularly during the last decade. Such development has brought a paradigm shift for the control of thermal expansion. For further improvement of the NTE functions and for the development of new materials, the achievements of the last two decades in this field are summarized briefly, particularly addressing recently discovered giant NTE materials (**Figure 1**).

POSITIVE AND NEGATIVE THERMAL EXPANSION

Thermal Expansion of Solids

The origin of thermal expansion of solids can be summarized briefly (Cochran, 1973). One might consider atoms connected together by springs as a model of solids, but these springs are *anharmonic* and do not exactly and simply obey Hooke's law. The atoms are prevented from becoming extremely close to one another because of Pauli's exclusion principle. As a result, excursions to longer interatomic distances occur more readily than those to shorter interatomic distances. Consequently, the average interatomic distance increases concomitantly with increasing temperature *T*. More intuitively, one can generally infer from Pauli's exclusion principle that as the temperature rises and the thermal vibration of an atom increases, it tries to maintain its distance from other atoms to avoid mutual collision. This increasing distance with vibration explains thermal expansion.

Conventional NTE Materials

In stark contrast to ordinary materials, some materials contract upon heating. Some examples are those of a silicon oxide family including β-eucryptite ($LiAlSiO_4$) and cordierite ($Mg_2Al_2Si_5O_{18}$), which were reported in the 1950s (Gillery and Bush, 1959). These silicates have strong covalent bonds such as Al–O and Si–O bonds, and not so strong ionic bonds such as Li–O and Mg–O bonds. The ionic bonds expand on heating, resulting in the expansion of two-dimensional sheets in β-eucryptite, for example. Thermal expansion of these ionic bonds pulls the two-dimensional sheets closer together because these two-dimensional sheets are joined by strong covalent bonds that do not expand when heated (**Figure 2**). For β-eucryptite with a hexagonal crystal lattice, on warming from 293 K to 1073 K, the in-plane (*a* axis) direction in which the Li–O bond is dominant expands 0.62%, whereas the out-of-plane (*c* axis) direction, in which the Si–O bond is dominant, contracts 1.39%. This thermal distortion causes unit-cell volume contraction of 0.15%. From another viewpoint, open spaces are filled by the thermal distortion of strong covalent bonds. This concept is exemplified more clearly in the open-framework or flexible-network materials described next. Readers might doubt that the NTE of β-eucryptite is much larger. Details of the discrepancy between the unit-cell volumetric NTE and the bulk NTE are discussed in Chapter 4.

Flexible-network materials are a well-known family of NTE materials that includes ZrW_2O_8 and vanadates and phosphates of certain kinds (Mary et al., 1996; Pryde et al., 1996; Evans et al., 1997). This network consists of rigid units connected by soft

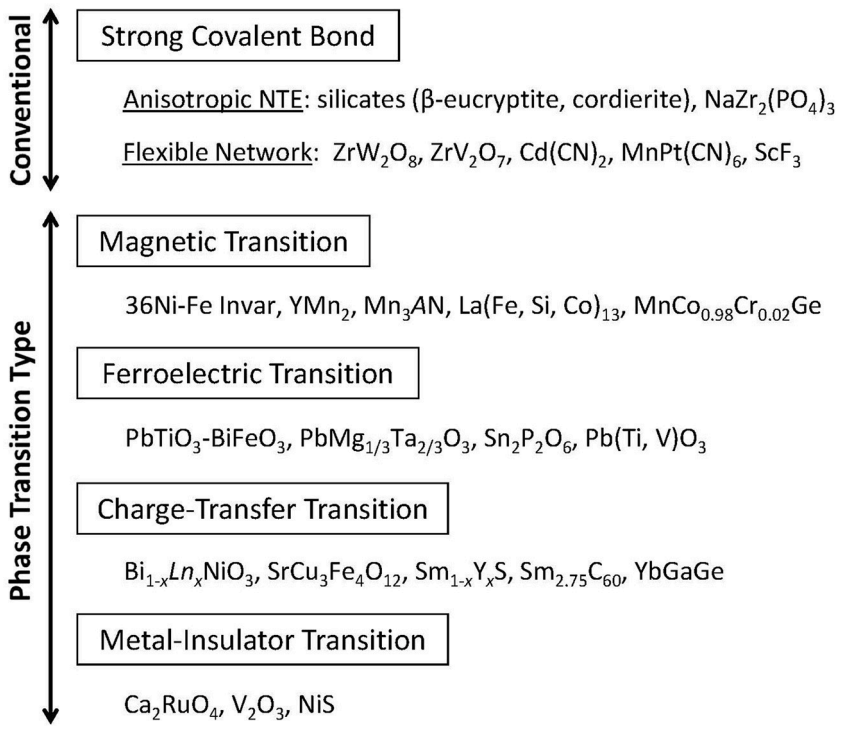

FIGURE 1 | Classification of negative thermal expansion materials. Materials are divisible into two categories: *conventional* and *phase-transition-type* materials.

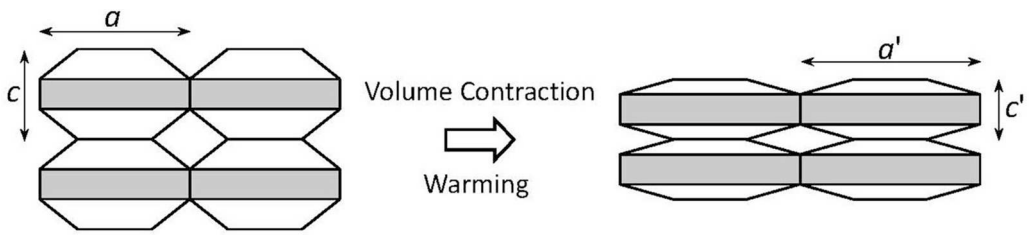

FIGURE 2 | Schematic of anisotropic thermal expansion in the silicates. As the shaded layers undergo thermal expansion, they are pulled closer together in the direction perpendicular to the layer, which causes significant thermal contraction in this direction and yields slight net volumetric thermal contraction.

linkages. The rigid units are formed by strong covalent bonds. For ZrW_2O_8, W–O covalent bonds are strong. Therefore WO_4 units are rigid. They do not expand on heating. By contrast, although the W–O and Zr–O bond distances are not changed, the Zr–O–W linkages are soft. Transverse oxygen displacement is induced easily on heating. These displacements consume open spaces in the crystal structure, resulting in volumetric NTE (**Figure 3**). Different from the silicates, anisotropic lattice thermal expansion is unimportant. The volume change related to NTE is much greater. In fact, ZrW_2O_8 has attracted great attention because of its large and isotropic NTE of $\alpha_L = -9 \times 10^{-6}$ K^{-1} (Mary et al., 1996). NTE appears at the whole T range below 1443 K. The total volume change related to NTE, $\Delta V/V$, reaches 2.7% (Evans, 1999).

Negative thermal expansion that is explainable from the concept that strong atomic bonds and thermally induced deformation fill open spaces in the crystal lattice explains *conventional* NTE materials (**Figure 1**), which include widely diverse materials. In addition to cyanides (Chapman et al., 2006; Phillips et al., 2008), the fluoride group (Greve et al., 2010; Attfield, 2011; Chatterji et al., 2011; Chen et al., 2017), such as ScF_3 and ZnF_2, has attracted attention recently. Particularly, $Cd(CN)_2{\cdot}xCCl_4$ shows large NTE of $\alpha_L = -34 \times 10^{-6}$ K^{-1} and $\Delta V/V = 2.1\%$ at T =175–375 K (Phillips et al., 2008).

At present, most industrial thermal-expansion compensators, including β-eucryptite, belong to the group of conventional type oxides. This type of NTE has a structural origin for its phenomena. Therefore, NTE appears in almost the entire T range, which is extremely important industrially. However, when discussing practically used materials, their NTE magnitude, at most $\alpha_L = -7 \times 10^{-6}$ K^{-1}, is not large from today's perspective. Because the coexistence of strong and not strong chemical bonds is fundamentally important for conventional NTE, low thermal conductivity and low stiffness are unavoidable in these materials. Low thermal conductivity and low stiffness are weak points even for some *phase-transition-type* NTE materials described in the next chapter. Diligent efforts are continuing toward overcoming them. For example, high thermal conductivity is indispensable for rapid heat dissipation of devices. Development of NTE materials with high thermal conductivity is desired.

PHASE-TRANSITION TYPE NTE MATERIALS

Various attempts have been made to overcome the shortcomings of the conventional NTE materials presented in the preceding chapter. The current trend of NTE material development is to use the phase transition accompanied by volume contraction upon heating. The effectiveness of this approach was recognized widely by discovery of the giant NTE of $\alpha_L = -25 \times 10^{-6}$ K^{-1} in antiferromagnetic antiperovskite $Mn_3Zn_{1-x}Ge_xN$, which uses magnetovolume effects (Takenaka and Takagi, 2005). The giant NTE of manganese nitride strongly influenced subsequent NTE research, leading to the discovery of many NTE materials using magnetic, ferroelectric, charge-transfer, and metal–insulator phase transitions. The phase-transition type NTE concept became dominant in the field (**Figure 1**). The relation between phase transition and NTE might not be a modern concept because NTE accompanying the magnetic transition (Fe-Pt Invar alloy, Wasserman, 1990) and the ferroelectric transition ($PbTiO_3$, Shirane and Hoshino, 1951) has been known for a long time. The novelty of the present method is the modification of the properties of "mother" materials showing a phase transition (in many cases, first-order phase transition), intentionally using chemical approaches such as element substitution (**Figure 4**).

Specifications of the recently discovered giant NTE materials are presented in **Table 1**. Phase-transition type materials have an operating temperature that is limited to several tens to 100 K around the phase transition, but they have a negative α_L that is several times to 10 times larger than those of conventional type materials. Although a wide operating temperature window ΔT is generally suitable for practical applications, limited ΔT presents no difficulty in many cases, such as precision equipment that is expected to operate at room temperatures. $Bi_{0.95}La_{0.05}NiO_3$ exhibits large negative α_L of -82×10^{-6} K^{-1} (Azuma et al., 2015), which is comparable to the magnitude of positive α_L of epoxy resin, although the operating-temperature window ΔT is not so wide (60 K). Despite that operating temperature window limitation, it is of great importance that it suppresses the thermal expansion of plastics, which has heretofore been difficult.

For phase-transition-type NTE materials, a certain mechanism causes excessive shrinkage that can overcome positive lattice thermal expansion. The mechanisms of prototypical phase-transition-type NTE are described in

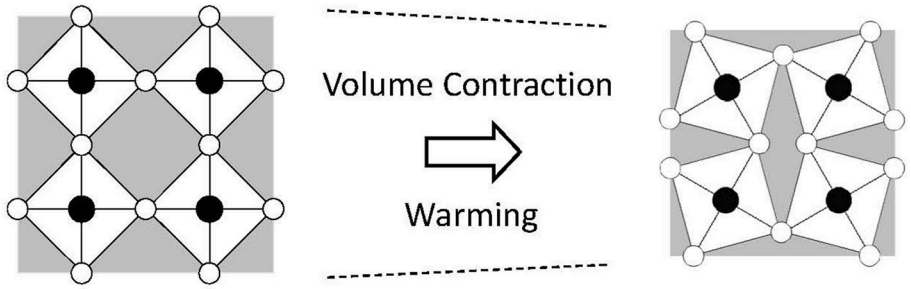

FIGURE 3 | Schematic of negative thermal expansion in a flexible network. A vibrational mode consuming an open space in a crystal lattice is thermally excited, which yields net volumetric thermal contraction.

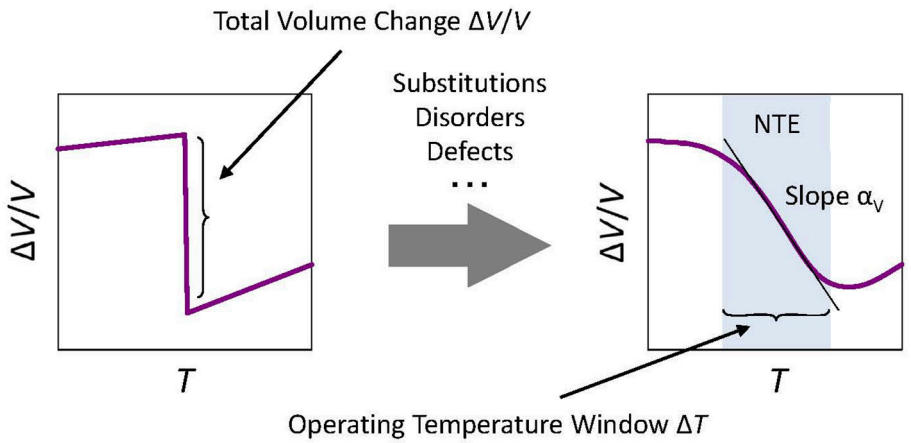

FIGURE 4 | Concept of total volume change $\Delta V/V$ related to negative thermal expansion (NTE). In the case of phase-transition-type NTE materials, "slope" α_V (coefficient of *volumetric* thermal expansion) shares a tradeoff relation with the width of the operating-temperature window ΔT, roughly described as $\Delta V/V \sim |\alpha_V| \Delta T$. As an isotropic material, a coefficient of *linear* thermal expansion α_L is related to α_V as $\alpha_V = 3\alpha_L$. Therefore, coefficients α_V and α_L are not intrinsic for such phase-transition-type materials. Instead, the total volume change $\Delta V/V$ is the intrinsic index indicating the potential of NTE.

TABLE 1 | Parameters related to *crystallographic* negative thermal expansion for prototypical materials.

Materials	$\Delta V/V$ [%]	T_{NTE} [K]	ΔT [K]	α_L[ppm/K][a]	Structure[b]	Category[c]	Method[d]
β-eucryptite (Gillery and Bush, 1959)	0.15	293–1,073	780	−0.6	Hexagonal	CV	X
ZrW_2O_8 (Evans, 1999)	2.7	2–1,443	1,441	−6 ∼ −9	Cubic	CV	D/N
$Cd(CN)_2 \cdot xCCl_4$ (Phillips et al., 2008)	2.1	170–375	205	−34	Cubic	CV	X
$Mn_3Ga_{0.7}Ge_{0.3}N_{0.88}C_{0.12}$ (Takenaka and Takagi, 2005)	0.5	197–319	122	−18	Cubic	MG	D
$LaFe_{10.5}Co_{1.0}Si_{1.5}$ (Huang et al., 2013)	1.1	240–350	110	−26	Cubic	MG	D
$MnCo_{0.98}Cr_{0.02}Ge$ (Zhao et al., 2015)	3.2	122–332	210	−52	Orthorhombic	MG	D
$0.4PbTiO_3$-$0.6BiFeO_3$ (Chen et al., 2006)	2.7	298–923	625	−13	Tetragonal	FE	X
$SrCu_3Fe_4O_{12}$ (Yamada et al., 2011)	0.4	180–250	70	−20	Cubic	CT	X
$Bi_{0.95}La_{0.05}NiO_3$ (Azuma et al., 2011)	2.0	320–380	60	−82	Triclinic	CT	D
$Sm_{2.75}C_{60}$ (Arvanitidis et al., 2003)	0.8	4–30	26	−100	Orthorhombic	CT	X
$Ca_2Ru_{0.9}Mn_{0.1}O_4$ (Qi et al., 2012)	0.8	150–400	250	−10	Orthorhombic	MI	X
AgI (Lawn, 1964)	6.0	430	–	–	Hexagonal	Others	X

Microstructural effects are not considered. Parameters of materials with phase transition accompanied by large volume contraction upon cooling, not broadened, are also listed for comparison.

[a] *Averaged value when the material is anisotropic.*

[b] *For NTE region or lower-temperature, larger-volume phase.*

[c] *CV, conventional; MG, magnetic transition; FE, ferroelectric transition; CT, charge-transfer transition; MI, metal–insulator transition.*

[d] *D, dilatometry; N, neutron diffraction; X, X-ray diffraction.*

this chapter. It is noteworthy that the mode of classification, including the conventional type, is not absolute. For example, ferroelectric transition and charge-transfer transition have a common point of charge disproportionation. Other phase transitions such as structural phase transition are often coupled with the magnetic transition.

It is noteworthy that slope α_L presents a tradeoff relation with the width of operating-temperature window ΔT in the case of phase-transition-type NTE materials (**Figure 4**). The total volume change $\Delta V/V$ is a value that is peculiar to the substance. It is difficult to increase it artificially. As a result, the wider the operating-temperature window ΔT becomes, the smaller the negative slope α_L becomes. For isotropic materials, we obtain the simple relation of $\Delta V/V = 3\alpha_L \Delta T$. Therefore, slope α_L is not intrinsic for such phase-transition-type materials. Instead, $\Delta V/V$ is the intrinsic and the most important index indicating the potential of NTE. The word "giant" is customarily used in the field, but no clear definition exists. One important turning point was the discovery of ZrW_2O_8 in 1996, and a material that surpasses it by the negative coefficient of linear thermal expansion and/or the total volume change related to NTE: a so-called giant NTE material.

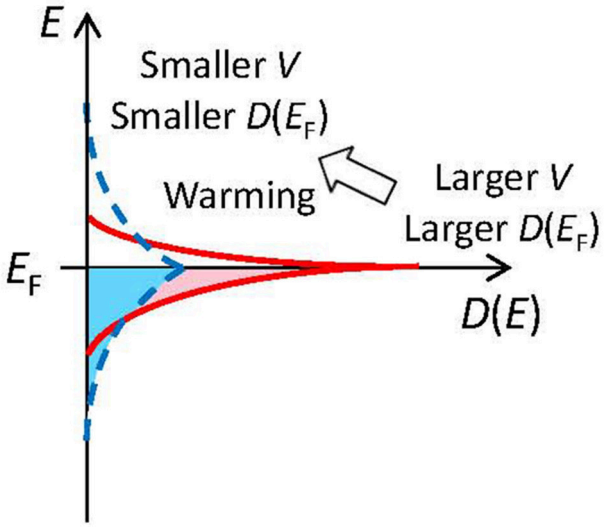

FIGURE 5 | Relation between volume and density of states at the Fermi level $D(E_F)$ (schematic). Volume expansion shrinks the electronic band width and therefore enhances $D(E_F)$, which is favorable for the magnetic state. It also strengthens the electronic repulsion effects.

Magnetic Transition

The magnetovolume effect is a phenomenon by which the volume changes according to the amplitude of the magnetic moment in itinerant systems. The relative volume change attributable to magnetism is known as the spontaneous volume magnetostriction ω_s. Generally speaking, less-itinerant electrons are necessary for magnetism. Electronic spins are aligned via the exchange interaction. That exchange interaction does not work well when electrons are itinerant. Volume expansion decreases the overlap of electronic orbitals and makes electrons less itinerant. This effect is explainable by the electronic theory of solids as follows: volume expansion suppresses the bandwidth and condenses the density of states near the Fermi level E_F, which is helpful for magnetism (**Figure 5**). Therefore, if possible, the system expands the volume to assist magnetism when the magnetic order sets in. This expansion is the magnetovolume effect, which is intimately related with the origin of magnetism in metals. Therefore, it has persisted as a central topic in the field of condensed-matter physics.

The materials classified into this category include 36Ni-Fe alloy (Invar alloy, which has low thermal expansion rather than negative thermal expansion) (Wasserman, 1990), Fe_3Pt (Sumiyama et al., 1979), YMn_2 (Nakamura et al., 1988) in the past, and Mn_3AN (where A is a transition metal or semiconducting elements, Takenaka and Takagi, 2005; Hamada and Takenaka, 2011; Wang et al., 2012; Takenaka et al., 2014), $La(Fe, Si, Co)_{13}$ (Fujita et al., 2001; Huang et al., 2013), and $MnCo_{0.98}Cr_{0.02}Ge$ (Zhao et al., 2015) in recent years. Mass production technology developed in 2012 for manganese nitrides has made them commercially available (Smartec®; Kojundo Chemical Lab. Co. Ltd., Japan, Kawahara et al., 2017).

The low thermal expansion of 36Ni-Fe Invar alloy was reportedly explained by the difference in atomic radius in the early stages of research. The concept of the 2γ model (Weiss, 1963) is that upon heating, the spin configuration of Fe changes gradually from a high-spin state with a larger radius to a low-spin state with a smaller radius. A controversy has long persisted (van Schilfgaarde et al., 1999) between this atomic picture and the itinerant-electron picture described in earlier paragraphs, which emphasizes the contribution from electronic density anomaly near E_F (Wohlfarth, 1977; Moriya and Usami, 1980). Although details are not included herein, metallic electronic images are regarded as superior in the sense that they can universally explain the magnetovolume effect of various materials, not merely Invar alloys. Nevertheless, differences in atomic radius between high-spin and low-spin states can play an important role in volume change in real materials such as cobalt oxides (Burley et al., 2004). The 2γ model, which still holds importance as a possible mechanism of NTE, is closely related to NTE caused by charge transfer in the sense that NTE is induced by a change in the atomic radius.

Negative thermal expansion is reported also for localized-moment magnets of certain kinds. Actually, NTE is known to appear in the T range of several tens of degrees on the high T side of the magnetic transition with a compound having a certain spinel or breathing pyrochlore structure (Hemberger et al., 2007; Okamoto et al., 2018; Pokharel et al., 2018). In these materials, NTE disappears below the critical temperature at which the magnetic long-range order is formed. From the localized-moment picture, the magnetovolume effect is attributed to the peculiar volume dependence of the magnetic exchange interaction J, $\partial J/\partial\omega$ ($\omega = \Delta V/V$) (Hausch, 1973). The generalized framework extended to the strain derivative of J is also discussed (Filippetti and Hill, 2000). The argument based on the Bethe–Slater curve of single J discussed previously is too naive to explain the diverse phenomena of real materials. However, if

there exist multiple (e.g., ferromagnetic and antiferromagnetic) J and competition between them, then the once discarded localized-moment picture might be revived as worthy of consideration.

Ferroelectric Transition

Actually, NTE is widely known to appear in ferroelectric materials with charge disproportionation such as $PbTiO_3$ (Shirane and Hoshino, 1951), $0.4PbTiO_3$-$0.6BiFeO_3$ (Chen et al., 2006), $Sn_2P_2S_6$ (Rong et al., 2016), and $Pb(Ti,V)O_3$ (Pan et al., 2017). From general consideration of the relation between valence and bond length, the averaged bond length in the charge disproportionate case is greater than the bond length in the charge uniform case (Evans, 1999, **Figure 6**). Atomic bonds are readily expanded, but they are difficult to shrink. We can regard that fact as representing a kind of anharmonicity of atomic bonds. It is noteworthy that anisotropy is fundamentally important for NTE materials of this type. Phenomenologically, dielectric polarization corresponds to volume change (Chen et al., 2015), similar to magnetic NTE materials in which magnetic moments are intimately related to the volume change, but their physical origin differs greatly.

Charge-Transfer Transition

When charge transfer occurs between the constituent elements, atoms with an increasing number of valence electrons become larger. On the other hand, those with a decreasing number of valence electrons become smaller. However, the change in the atomic radius varies according to the atomic species, electronic configuration, etc. In addition, the effect of the atomic radius on the crystal size depends on the atom's position in the crystal structure. If the contribution from atoms with a decreasing number of valence electrons upon heating is greater, then one can expect net NTE.

A famous example of charge-transfer-type NTE materials, bismuth-nickel oxides (Azuma et al., 2011, 2015), is discussed next. When these oxides are warmed, charges are transferred from Ni to Bi. Therefore, the atomic radius of Ni contracts and that of bismuth expands on warming, but the atomic radius of nickel dominates the lattice volume because the Ni–O octahedron dominates the lattice volume. For that reason, the net volumetric NTE occurs in the bismuth-nickel oxide. A similar mechanism functions for NTE of $LaCu_3Fe_4O_{12}$ (Yamada et al., 2011).

Negative thermal expansion is also induced by intra-atomic charge transfer that increases the 4*f* electron number with decreasing temperature. For example, $Sm_{1-x}Y_xS$ (Jayaraman et al., 1975; Alekseev et al., 2006), $Sm_{2.75}C_{60}$ (Arvanitidis et al., 2003), and YbGaGe (Salvador et al., 2003; Sleight, 2003) are known for negative or low thermal expansion by such a mechanism. In the case of Sm, two electronic configurations of $(4f)^5(5d)^1$ and $(4f)^6$ compete energetically, but the atomic radius is determined mainly by the 4*f* electron number. Therefore, NTE appears if the electrons are transferred from the 5*d* to the 4*f* orbitals with decreasing temperature.

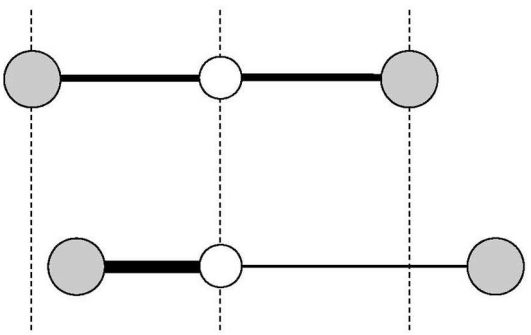

FIGURE 6 | Schematic of negative thermal expansion in a ferroelectric material with charge disproportionation**.** When charge disproportionation occurs, because the higher-valence interatomic bond length does not shrink as much as the lower-valence one expands **(Bottom)**, the bond length becomes longer than that of the averaged case **(Upper)**.

Metal–Insulator Transition

An example in which the effect of electronic repulsion manifests as an apparent physical property is a Mott insulator (Mott, 1990). In transition metal compounds of a certain kind, the metallic state is often lost because of electronic correlations at low temperatures and the system becomes an insulating state. This transition is called a Mott transition. Generally, a Mott insulating state appears at the lower-T side. The volume of the low-T insulating phase is known to expand upon Mott transition for V_2O_3 (1.5%) (McWhan and Remeika, 1970) and NiS (1.8%) (Matoba et al., 1991). The mechanism of volume expansion in the insulating state might resemble a magnetovolume effect in the itinerant-electron magnets (**Figure 5**). It can be understood that volume expansion suppresses the bandwidth and that it therefore enhances electronic-correlation effects, which stabilizes the low-T Mott insulating state. Furthermore, Ca_2RuO_4 (Takenaka et al., 2017a) is classified into this category, as explained in the next chapter.

Other Factors

Some materials are also known to have volume of the low-T phase which becomes greater than that of the high-T phase with the phase transition because of mechanisms other than the four explained above. They are not understood so systematically as the four above, but they are suggestive for the development of new materials. They are therefore explained here. Silver iodide, AgI (Lawn, 1964; Kumar et al., 2006), which is known as a superionic conductor, undergoes a structural phase transition from β and γ phases with larger volume at low temperatures to α phase and smaller volume at high temperatures near 400 K. The volume change is known to reach 5%. The fact that the relation between NTE and ionic conductivity is discussed (Sleight, 1998) also for the famous NTE material β-eucryptite is suggestive of its importance for future development.

Related to a structural phase transition, certain martensitic transformations accompany volume expansion on cooling. For example, MnCoGe is known to expand by 3.9% in the martensitic transformation from high-T hexagonal phase to low-T orthorhombic phase at around 370 K (Johnson, 1975). Actually,

$MnCo_{0.98}Cr_{0.02}Ge$, with one of the largest total volume change related to NTE found to date, belongs to the same family and shows the same martensitic transformation simultaneously with the magnetic transition (Zhao et al., 2015). Correlation between magnetism and structure in these materials is an interesting subject that has yet to be explored (Kanomata et al., 1995).

Although the relation between NTE and superconductivity is not well understood, $Ca_{0.85}La_{0.15}Fe_2As_2$ with the superconducting transition temperature of 43 K exhibits a marked NTE of $\alpha_L = -16 \times 10^{-6}$ K^{-1} and $\Delta V/V = 1.4\%$ at almost all temperatures below 300 K (Robello et al., 2012). Orbital ordering is regarded as involving the Mott transition in Ca_2RuO_4 (Mizokawa et al., 2001; Qi et al., 2010) and, although weak, NTE appears just above the Verwey transition (ca. 110 K) in Fe_3O_4 (Wright et al., 2000). These results suggest that an orbital-ordering transition might be a universal mechanism of NTE.

Mechanism of Broadening Volume Change

From the viewpoint of the mechanism of how the sharp volume change accompanying the first-order phase transition becomes a gradual change with temperature, the phase-transition-type NTE materials are broadly divisible into two categories: "phase-separation" type and "second-order-transition" type. In the former category, which includes bismuth-nickel oxides (Azuma et al., 2011, 2015), the system separates into the larger-unit-cell L phase and the smaller-unit-cell S phase, while preserving the first-order phase transition. NTE is induced because the volume fraction of the L phase increases concomitantly with decreasing *T*. In the latter category, which includes magnetic NTE materials such as antiperovskite manganese nitrides (Takenaka and Takagi, 2005; Hamada and Takenaka, 2011; Wang et al., 2012; Takenaka et al., 2014), the phase transition changes from first-order-like to second-order-like. Negative thermal expansion of these materials is characterized by a gradual increase in the unit-cell volume of a single phase with decreasing *T* *without* phase separation. For manganese nitrides, a detailed neutron diffraction study (Iikubo et al., 2008) demonstrated that the evolution of the amplitude of the magnetic moment is in one-to-one correspondence with the volume increase due to NTE. For the phase-transition-type materials, the mechanism of broadening the volume change is a key issue dominating the operating-temperatures of NTE. To elucidate the broadening mechanism, a certain kind of diffraction study and microscopic observations are required in addition to dilatometry.

ANISOTROPIC THERMAL EXPANSION AND MICROSTRUCTURAL EFFECTS

Negative thermal expansion discussed in the former chapters is associated with NTE of the crystallographic unit cell. For these materials, NTE of the unit cell found using a crystallographic technique such as x-ray diffraction and NTE of the bulk measured using a dilatometric technique are fundamentally equal. However, in some cases, the crystallographic NTE and the dilatometric NTE do not coincide. Actually, β-eucryptite, which is a representative practical thermal-expansion compensator, is one example. The colossal NTE measured in the sintered body of layered ruthenium oxide Ca_2RuO_4 (Takenaka et al., 2017a) reaffirmed this discrepancy as an important subject in NTE research (**Figure 7**). The total volume change $\Delta V/V$ related to NTE reaches a maximum of 6.7%, exceeding twice the former maximum (3.2%) obtained with $MnCo_{0.98}Cr_{0.02}Ge$ (Zhao et al., 2015). Despite the wide operating-temperature window of 135–345 K ($\Delta T = 210$ K), α_L shows a remarkable size of -115×10^{-6} K^{-1} because of this large total volume change.

Originally, Ca_2RuO_4 was known for unit-cell volume expansion of about 1% at the onset of high-*T* metallic to low-*T* insulating phase transition at 360 K (Friedt et al., 2001; Qi et al., 2012). Therefore, Ca_2RuO_4 is classified as the metal–insulator transition category of NTE described in the preceding chapter. Even in our sample showing a huge bulk NTE, during warming from 150 to 340 K, the *c* axis expands by 4.6%, whereas the *a* axis and the *b* axis shrink respectively by 0.6 and 5.0%. As a result, the unit cell shrinks by 1%. The anisotropic thermal expansion of this unit cell and the fairly large NTE with volume change of $\Delta V/V = 1\%$ are regarded as attributable to the Mott transition coupled with electronic orbital ordering, although the details remain to be explored.

The colossal NTE of Ca_2RuO_4 ceramics is proposed as explainable by anisotropic thermal deformation of the crystal grain which fills in the volume of pores that are contained in the sintered body (**Figure 8**). Such deformation is trivial in the

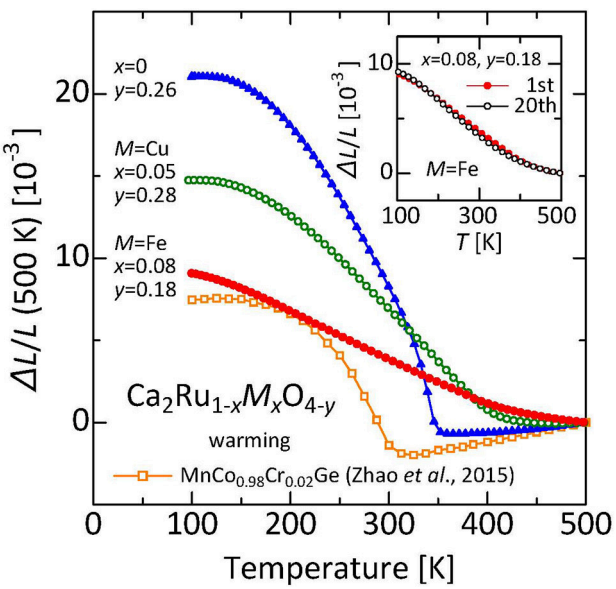

FIGURE 7 | Linear thermal expansion of $Ca_2Ru_{1-x}M_xO_{4-y}$ (M = Fe, Cu). Reference temperature: 500 K. Inset: Linear thermal expansion $\Delta L/L$ of $Ca_2Ru_{0.92}Fe_{0.08}O_{3.82}$ before and after 20 iterations of thermal cycling (reference temperature: 500 K). Data related to the warming process were collected using a laser interference dilatometer. Referred from earlier reports (Takenaka et al., 2017a,b). For comparison, data of $MnCo_{0.98}Cr_{0.02}Ge$ (Zhao et al., 2015) are also shown.

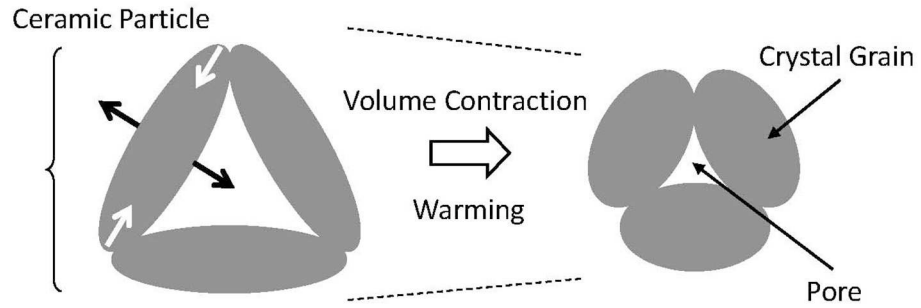

FIGURE 8 | Schematic explanation $\Delta L/L$ of microstructural effect for bulk negative thermal expansion. The ceramic body consists of crystal grains with anisotropic thermal expansion and pores. When the temperature increases, the crystal grain expands in one direction and contracts in a perpendicular direction. If there exists open space in the direction in which the crystal grain expands, then this ceramic body contracts.

field of ceramics. Moreover, it is not limited to β-eucryptite, for example, also known as $MgTi_2O_5$ (Kuszyk and Bradt, 1973; Ohya et al., 1987; Yamai and Ota, 1993). In most cases, however, it is a "one-time" phenomenon that induces microcracks, which is useless as a practical thermal-expansion compensator. One well-known exception is β-eucryptite, the practical use of which was achieved by overcoming the difficulty of advanced control of microcracks (Pelletant et al., 2012; Benavente et al., 2016). Although the NTE characteristics of β-eucryptite vary according to fabrication conditions, the total volume change of the bulk specimen (1.7%) reaches 10 times that of the unit cell (0.15%); also, α_L is -7×10^{-6} K^{-1}.

The ruthenium oxides are characterized by rather low onset temperatures of anisotropic thermal expansion of the unit cell, which is about 500 K. For many other materials including β-eucryptite and $MgTi_2O_5$, the onset temperature is close to the sintering temperature, typically over 1,300 K. Therefore, the inner stress accumulates greatly during cooling to room temperature. Compared with those, the accumulated inner stresses are expected to be much smaller for the ruthenates. Indeed, the linear thermal expansion $\Delta L(T)/L$ of $Ca_2Ru_{0.92}Fe_{0.08}O_{3.82}$ is reproducible after 20 repetitions of thermal cycling of 300 K → 500 K → 300 K (inset of **Figure 7**), which suggests that possible degradation of the characteristics because of the thermal history is avoidable. Recently reported theoretical calculations indicate that the microstructural effects *without* cracks can reproduce the gigantic NTE observed in the ruthenate sintered body (Takezawa et al., 2018). Enhancement of NTE in the ruthenates occurs at a scale of 10 times that of β-eucryptite. Examples for which the material structure is deeply involved in the bulk function of NTE do not exist among recently discovered NTE materials. The concept of microstructural effects provides a strategy for realizing giant NTE. Control of thermal expansion using specific characteristics of materials, particularly in a negative α region, are highly limited in an operating temperature and/or a magnitude of α because of the severe constraints of available materials. To overcome these difficulties, designated structures consisting of two materials having different (positive) thermal expansions and voids are proposed as an artificial materials showing NTE (Takezawa et al., 2015; Wang et al., 2016). The present result is expected to stimulate those activities as a "natural" counterpart of the artificial structures. Structures composed of Structures composed of crystal grains exhibiting anisotropic thermal expansion and voids are expected to be important subjects of future NTE research.

COMPOSITES CONTAINING GIANT NTE MATERIALS

Forming a composite using a NTE material as a thermal-expansion compensator is an effective method of controlling the thermal expansion of a material. Many commercial materials exist such as zero-expansion glass used for precision optical equipment and a zero-expansion ceramic material used for semiconductor device manufacturing. Many earlier studies have examined composites containing NTE materials, particularly β-eucryptite (Xue et al., 2010; Borrell et al., 2012) and ZrW_2O_8 (Holzer and Dunand, 1999; Matsumoto et al., 2003; Sullivan and Lukehart, 2005; Lind et al., 2011), as thermal expansion compensating fillers. Regarding phase-transition-type giant NTE materials, composites containing Mn_3AN (Ding et al., 2011; Takenaka et al., 2012, 2015; Takenaka and Ichigo, 2014; Lin et al., 2017), $BiNi_{1-x}Fe_xO_3$ (Nabetani et al., 2015), $La(Fe, Si, Co)_{13}$ (Shan et al., 2015), and $Ca_2Ru_{0.92}Fe_{0.08}O_{3.82}$ (Takenaka et al., 2017b) have been reported. Because their chemical reactivity is higher at high temperatures than those of conventional NTE materials, phase-transition-type NTE materials are difficult to use as thermal expansion compensating filler, particularly in cases of metal matrix composites (MMCs). However, powder metallurgy, which enables us to form MMCs at lower temperatures and in a shorter time than when using the conventional method, produced MMCs containing manganese nitrides (Ding et al., 2011; Takenaka et al., 2012, 2015). Some concern arose about difficulties arising from a large thermal expansion difference at the interface between the matrix and the gigantic NTE material. Additional research on the interfaces is expected to be indispensable for the development of industrial materials with high reliability, although this difficulty has not arisen for some composites at present (Takenaka and Ichigo, 2014). Here, plastic

matrix composites (PMCs) containing manganese nitrides and ruthenium oxides are discussed.

Generally, the operating temperatures of phase-transition-type NTE materials are not high (ca. 600 K at highest). Therefore, plastics for which the operating temperature range and composite processing temperature are low are indeed the most compatible matrices. In electronic devices, plastics are used in various components such as printed circuit boards, sealing materials, and substrate-chip bonding films. As miniaturization and high integration of integrated circuits progress, problems originating from thermal expansion mismatch between these plastics and inorganic materials such as semiconductors have become more severe. To suppress the large thermal expansion of plastics, conventional thermal expansion compensators such as silica are insufficient. The use of large NTE of phase-transition-type NTE materials is indispensable. Furthermore, control of thermal expansion at a local region at the micrometer level in an integrated circuit, such as underfill of a three-dimensional integrated circuit (3DIC) is strongly demanded (Kino et al., 2017). It is technically important to miniaturize the particle diameter of a giant NTE material to submicrometer size, or less (Lin et al., 2016; Yang et al., 2016).

Before presenting scientific arguments, to summarize briefly how to evaluate the thermal expansion of composites, the author presents discussion of a simple case in which particles of an isotropic reinforcement are dispersed uniformly in an isotropic matrix for analyzing PMCs containing thermal expansion compensating particles. In that case, thermal expansion of the composite falls between the two bounds: The rule of mixture (ROM) and Turner's model (Takenaka, 2012). A bound, ROM, is given, assuming that thermally induced *stress* is uniform throughout a composite, which is equivalent to saying that the matrix and the filler exhibit their own thermal expansion independently. Consequently, the thermal expansion of a composite is given as the volume-weighted sum of contributions from the matrix and the dispersed filler.

$$\alpha_c = v_m\alpha_m + v_t\alpha_t \quad (1)$$

Another bound, that of Turner's model, is given as the approximation that *strain* is uniform throughout a composite as a result of elastic interactions between the matrix and the filler at the interfaces. It gives the following estimation.

$$\alpha_c = (v_m E_m\alpha_m + v_t E_t\alpha_t)/(v_m E_m + v_t E_t) \quad (2)$$

In the equations above, subscripts c, m, and t respectively denote a composite, matrix, and thermal-expansion compensator. Also, v_m and v_t respectively represent the volume fractions of the matrix and thermal-expansion compensator; $v_m + v_t = 1$. E represents Young's modulus. In Equation (2), the constituent with the larger elastic modulus contributes more to α_c beyond the volume fraction. In the case of PMCs containing NTE filler, the relations $\alpha_m > \alpha_t$ and $E_m < E_t$ are always fulfilled. Therefore, Equation (1), ROM, gives the upper bound; Equation (2), Turner's model, gives the lower bound for α_c.

Figure 9 displays a plot of the $\Delta L(T)/L$ experimental values along with curves calculated assuming ROM and Turner's moles

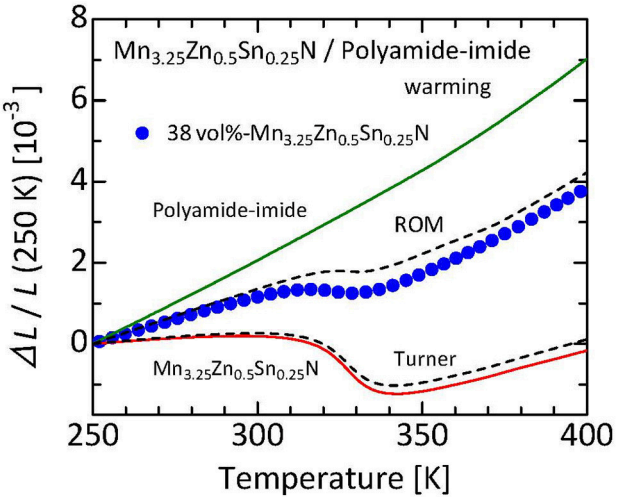

FIGURE 9 | Linear thermal expansion $\Delta L/L$ of 38 vol%-$Mn_{3.25}Zn_{0.5}Sn_{0.25}N$/polyamide-imide composite. Reference temperature: 250 K. Data were collected on a warming process using a laser interference dilatometer. Curves calculated by assuming the ROM and Turner's model are also displayed for comparison. Referred from an earlier report (Takenaka and Ichigo, 2014).

for 38 vol%-$Mn_{3.25}Zn_{0.5}Sn_{0.25}N$/polyamide-imide composite (Takenaka and Ichigo, 2014). The typical grain size of the nitride filler is 30–50 μm. This nitride thermal expansion compensating filler shows a huge NTE of $\alpha_L = -45 \times 10^{-6}$ K^{-1} at T = 305–340 K, resulting in NTE ($\alpha_L = -3 \times 10^{-6}$ K^{-1} at T = 315–327 K) for the composite. Displacement in $\Delta L/L$ is less than 160 ppm at T = 303–333 K, equivalent to the averaged α_L of 5.3×10^{-6} K^{-1}. The obtained $\Delta L(T)/L$ of the composite is between the ROM and Turner's estimates. This result reflects much larger E of the nitride filler (200 GPa, Nakamura et al., 2009) than the matrix (5 GPa, Reinecke et al., 1996), demonstrating the excellent thermal expansion compensating capability of the manganese nitride.

The results of bis-phenol epoxy resin matrix composite in which the ruthenium oxide particles are dispersed (Takenaka et al., 2017b) can be discussed next. The filler is $Ca_2Ru_{0.92}Fe_{0.08}O_{3.82}$. Although Fe doping somewhat suppresses negative α_L to -28×10^{-6} K^{-1}, the operating temperature window is expanded to 100–500 K. Furthermore, T-linearity of $\Delta L(T)/L$ is improved. Thermal expansion exhibits almost T-linear behavior, even near the lowest temperature used for the present dilatometry measurements. Therefore, NTE apparently continues down to the lower temperature. In that case, the total volume change $\Delta V/V$ might become greater than the present estimate of 2.8% (T = 100–500 K). Unfortunately, thermal expansion below 100 K was not measured successfully because of exfoliation of the strain gage. Nevertheless, the composite exhibits low thermal expansion down to 4 K, suggesting NTE of the ruthenate below 100 K.

Figure 10A presents a plot of the $\Delta L(T)/L$ experimental values for the 56 vol%- $Ca_2Ru_{0.92}Fe_{0.08}O_{3.82}$/bis-phenol epoxy resin composite (Takenaka et al., 2017b). For the epoxy resin and the composite, $\Delta L(T)/L$ was measured down to 5 K using a strain

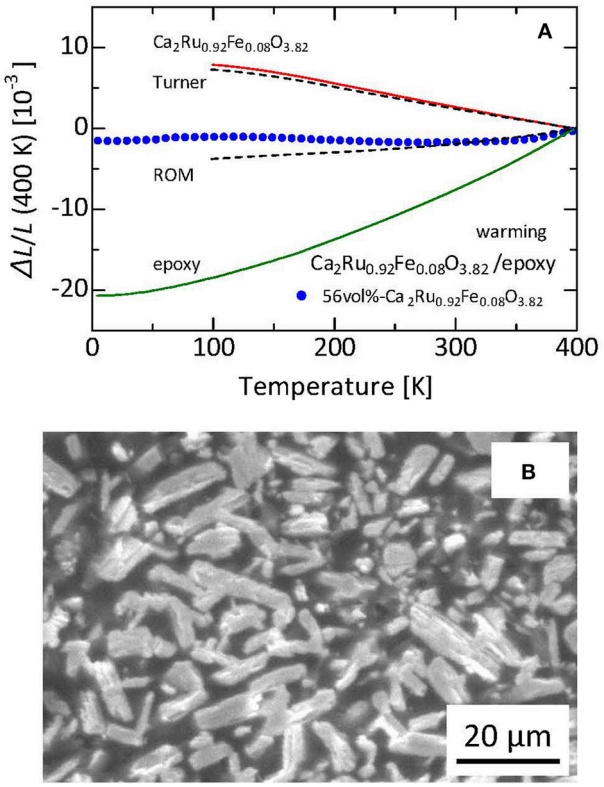

FIGURE 10 | (A) Linear thermal expansion (a) and microscopic image **(B)** of 56 vol%-$Ca_2Ru_{0.92}Fe_{0.08}O_{3.82}$/epoxy composite. Reference temperature: 400 K. Curves calculated by assuming the ROM and Turner's model are also displayed for comparison. Reproduced from an earlier report (Takenaka et al., 2017b). Copyright (2017) The Japan Society of Applied Physics.

gage. **Figure 10B** depicts an SEM image of the composite. Dark-gray and light-gray regions respectively represent the epoxy-resin matrix and the ruthenate filler. The ruthenate filler particles, with average size of 20–30 μm, are dispersed uniformly. Each particle is regarded as consisting of smaller crystal grains (ca. 80vol%) and pores (ca. 20vol%). Here, Young's modulus of the epoxy resin is 3.2 GPa (Nabetani et al., 2015). Young's modulus of the ruthenate ceramics particle is estimated as 100 GPa considering the Young's modulus of the related substance Sr_2RuO_4 of 160 GPa (Hao et al., 2014) and sample porosity of 0.2 (Wagh et al., 1991). The obtained linear thermal expansion of the composite falls between Equations (1, 2), similar to reports of many earlier studies (Sullivan and Lukehart, 2005; Takenaka and Ichigo, 2014; Nabetani et al., 2015). Therefore, the ruthenium oxide particles dispersed in the composite have sufficient stiffness and negative α_L. They suppress thermal expansion of the matrix effectively via elastic interactions at the interfaces.

CONCLUDING REMARKS

Because of the phase transition accompanied by large volume contraction on heating, giant NTE beyond that of conventional materials has been realized. That achievement has enabled us to compensate the large thermal expansion of plastics, which has been difficult to date, although the operating temperature ranges of the accomplishments have remained limited. The conventional wisdom of materials science, which has held that "negative CTE cannot be so large," has been rejected. Concepts and technologies related to thermal expansion control are about to change dramatically. One remarkable achievement in recent years is the huge NTE observed for ruthenium oxide sintered bodies. A structure comprising crystal grains exhibiting anisotropic thermal expansion and pores presents fertile ground for the development of new NTE materials. Today, thermal expansion adjustable composites are being fabricated using recently discovered giant NTE materials including the ruthenates.

AUTHOR CONTRIBUTIONS

The author confirms being the sole contributor of this work and approved it for publication.

ACKNOWLEDGMENTS

The author is grateful to M. Azuma, Y. Okamoto, N, Katayama, A. Takezawa, and S. Mori for many fruitful discussions and to his students for their enthusiastic conduct of experiments. This work was partly supported by Grants-in-Aid for Scientific Research (Nos. 17H02763 and 18H01351) from MEXT, Japan and by Adaptable and Seamless Technology Transfer Program (A-STEP; No. AS2911907T) from JST, Japan.

REFERENCES

Alekseev, P. A., Mignot, J.-M., Nefeodova, E. V., Nemkovski, K. S., Lazukov, V. N., Tiden, N. N., et al. (2006). Magnetic spectral response and lattice properties in mixed-valence $Sm_{1-x}Y_xS$ solid solutions studied with X-ray diffraction, X-ray absorption spectroscopy, and inelastic neutron scattering. *Phys. Rev. B* 74:035114. doi: 10.1103/PhysRevB.74.035114

Arvanitidis, J., Papagelis, K., Margadonna, S., Prassides, K., and Fitch, A. N. (2003). Temperature-induced valence transition and associated lattice collapse in samarium fulleride. *Nature* 425, 599–602. doi: 10.1038/nature01994

Attfield, J. P. (2011). A fresh twist on shrinking materials. *Nature* 480, 465–466. doi: 10.1038/480465a

Azuma, M., Chen, W.-T., Seki, H., Czapski, M., Olga, S., Oka, K., et al. (2011). Colossal negative thermal expansion in $BiNiO_3$ induced by intermetallic charge transfer. *Nat. Commun.* 2, 347. doi: 10.1038/ncomms1361

Azuma, M., Oka, K., and Nabetani, K. (2015). Negative thermal expansion induced by intermetallic charge transfer. *Sci. Technol. Adv. Mater.* 16:034904. doi: 10.1088/1468-6996/16/3/034904

Barrera, G. D., Bruno, J. A. O., Barron, T. H. K., and Allan, N. L. (2005). Negative thermal expansion. *J. Phys.* 17, R217–R252. doi: 10.1088/0953-8984/17/4/R03

Benavente, R., Salvador, M. D., Martinez-Amesti, A., Fernandez, A., and Borrell, A. (2016). Effect of sintering technology in β-eucryptite ceramics: influence on fatigue life and effect of microcracks. *Mater. Sci. Eng. A* 651, 668–674. doi: 10.1016/j.msea.2015.11.013

Borrell, A., Garcia-Moreno, O., Torrecillas, R., Garcia-Rocha, V., and Fernandez, A. (2012). Lithium aluminosilicate reinforced with carbon nanofiber and alumina for controlled-thermal-expansion materials. *Sci. Technol. Adv. Mater.* 13:015007. doi: 10.1088/1468-6996/13/1/015007

Burley, J. C., Mitchell, J. F., and Short, S. (2004). Competing electronic ground states in $La_{1-x}Sr_xCoO_3$. *Phys. Rev. B* 69:054401. doi: 10.1103/PhysRevB.69.054401

Chapman, K. W., Chupas, P. J., and Kepart, C. J. (2006). Compositional dependence of negative thermal expansion in the Prussian blue analogues $M^{II}Pt^{IV}(CN)_6$ (M = Mn, Fe, Co, Ni, Cu, Zn, Cd). *J. Am. Chem. Soc.* 128, 7009–7014. doi: 10.1021/ja060916r

Chatterji, T., Zbiri, M., and Hansen, T. C. (2011). Negative thermal expansion in ZnF_2. *Appl. Phys. Lett.* 98:181911. doi: 10.1063/1.3588414

Chen, J., Gao, Q., Sanson, A., Jiang, X., Huang, Q., Carnera, A., et al. (2017). Tunable thermal expansion in framework materials through redox intercalation. *Nat. Commun.* 8:14441. doi: 10.1038/ncomms14441

Chen, J., Hu, L., Deng, J. X., and Xing, X. R. (2015). Negative thermal expansion in functional materials: controllable thermal expansion by chemical modifications. *Chem. Soc. Rev.* 44, 3522–3567. doi: 10.1039/C4CS00461B

Chen, J., Xing, X. R., Liu, G. R., Li, J. H., and Liu, Y. T. (2006). Structure and negative thermal expansion in the $PbTiO_3$-$BiFeO_3$ system. *Appl. Phys. Lett.* 89:101914. doi: 10.1063/1.2347279

Chu, C. N., Saka, N., and Suh, N. P. (1987). Negative thermal expansion ceramics: a review. *Mater. Sci. Eng.* 95, 303–308. doi: 10.1016/0025-5416(87)90523-4

Cochran, W. (1973). *The Dynamics of Atoms in Crystals (Edward Arnold)*. London.

Ding, L., Wang, C., Na, Y. Y., Chu, L. H., and Yan, J., Yan, J. (2011). Preparation and near zero thermal expansion property of $Mn_3Cu_{0.5}A_{05}N$/Cu (A=Ni, Sn) composites. *Scripta Mater.* 65, 687–690. doi: 10.1016/j.scriptamat.2011.07.008

Evans, J. S. O. (1999). Negative thermal expansion materials. *J. Chem. Dalton Trans.* 3317–3326. doi: 10.1039/a904297k

Evans, J. S. O., Mary, T. A., and Sleight, A. W. (1997). Negative thermal expansion in a large molybdate and tungstate family. *J. Solid State Chem.* 13, 580–583. doi: 10.1006/jssc.1997.7605

Filippetti, A., and Hill, N. A. (2000). Magnetic stress as a driving force of structural disorders: the case of CrN. *Phys. Rev. Lett.* 85, 5166–5169. doi: 10.1103/PhysRevLett.85.5166

Friedt, O., Braden, M., Andre, G., Adelmann, P., Nahatsuji, S., and Maeno, Y. (2001). Structural and magnetic aspects of the metal–insulator transition in $Ca_{2-x}Sr_xRuO_4$. *Phys. Rev. B* 63:174432. doi: 10.1103/PhysRevB.63.174432

Fujita, A., Fujieda, S., Fukamichi, K., Mitamura, H., and Goto, T. (2001). Itinerant-electron metamagnetic transition and large magnetovolume effects in $La(Fe_xSi_{1-x})_{13}$ compounds. *Phys. Rev. B* 65:014410. doi: 10.1103/PhysRevB.65.014410

Gillery, F. H., and Bush, E. A. (1959). Thermal contraction of β-eucryptite ($Li_2O{\cdot}Al_2O_3{\cdot}2SiO_2$) by X-ray and Dilatometer Methods. *J. Am. Ceram. Soc.* 42, 175–177. doi: 10.1111/j.1151-2916.1959.tb12942.x

Greve, B. K., Martin, K. L., Lee, P. L., Chupas, P. J., Chapman, K. W., and Wilkinson, A. P. (2010). Pronounced negative thermal expansion from a simple structure: cubic ScF_3. *J. Am. Chem. Soc.* 132, 15496–15498. doi: 10.1021/ja106711v

Hamada, T., and Takenaka, K. (2011). Giant negative thermal expansion in antiperovskite manganese nitrides. *J. Appl. Phys.* 109:07E309. doi: 10.1063/1.3540604

Hao, X. P., Cui, H. L., Lv, Z. L., and Ji, G. F. (2014). Electronic and elastic properties of Sr_2RuO_4 with pressure effects by first principles calculation. *Phys. B* 441, 62–67. doi: 10.1016/j.physb.2014.02.009

Hausch, G. (1973). Magnetovolume effects in invar alloys: spontaneous and forced volume magnetostriction. *Phys. Stat. Sol.* 18, 735–740. doi: 10.1002/pssa.2210180236

Hemberger, J., Krug von Nidda, H. A., Tsurkan, V., and Loidl, A. (2007). Large magnetostriction and negative thermal expansion in the frustrated antiferromagnet $ZnCr_2Se_4$. *Phys. Rev. Lett.* 98:147203. doi: 10.1103/PhysRevLett.98.147203

Holzer, H., and Dunand, D. C. (1999). Phase transformation and thermal expansion of Cu/ZrW_2O_8 metal matrix composites. *J. Mater. Res.* 14, 780–789. doi: 10.1557/JMR.1999.0104

Huang, R. J., Liu, Y. Y., Fan, W., Tan, J., Xiao, F. R., Qian, L. H., et al. (2013). Giant negative thermal expansion in $NaZn_{13}$-type $La(Fe, Si, Co)_{13}$ compounds. *J. Am. Chem. Soc.* 135, 11469–11472. doi: 10.1021/ja405161z

Iikubo, S., Kodama, K., Takenaka, K., Takagi, H., and Shamoto, S. (2008). Magnetovolume effect in $Mn_3Cu_{1-x}Ge_xN$ related to the magnetic structure: neutron powder diffraction measurements. *Phys. Rev. B* 77:020409. doi: 10.1103/PhysRevB.77.020409

Jayaraman, A., Dernier, P., and Longinotti, L. D. (1975). Study of valence transition in SmS induced by alloying, temperature, and pressure. *Phys. Rev. B* 11:2783–2794. doi: 10.1103/PhysRevB.11.2783

Johnson, V. (1975). Diffusionless orthorhombic to hexagonal transitions in ternary silicides and germanides. *Inorg. Chem.* 14, 1117–1120. doi: 10.1021/ic50147a032

Kanomata, T., Ishigaki, H., Suzuki, T., Yoshida, H., Abe, S., and Kaneko, T. (1995). Magneto-volume effects of $MnCo_{1-x}Ge$ ($0 \leq x \leq 0.2$). *J. Magn. Magn. Mater.* 140–144, 131–132. doi: 10.1016/0304-8853(94)00833-7

Kawahara, M., Matsumoto, H., and Takenaka, K. (2017). "Performance of plastic composites by antiperovskite manganese nitrides with giant negative thermal expansion," in *Proceedings of the Second Internastional Symposium on Negative Thermal Expansion and Related Materials (ISNTE-II)*, Vol. 61, (Yokohama).

Kino, H., Fukushima, T., and Tanaka, T. (2017). "Remarkable suppression of local stress in 3D IC by manganese nitride-based filler with large negative CTE," in *Proceedings of 2017 IEEE 67th Electronic Components and Technology Conference* (Lake Buena Vista, FL), 1523–1528.

Kumar, P. S., Kini, N. S., Umarji, A. M., and Sunandana, C. S. (2006). Search for a novel zero thermal expansion material: dilatometry of the AgI-CuI system. *J. Mater. Sci.* 41, 3861–3865. doi: 10.1007/s10853-006-6657-x

Kuszyk, J. A., and Bradt, R. C. (1973). Influence of grain size effects of thermal expansion anisotropy in $MgTi_2O_5$. *J. Am. Ceram. Soc.* 56, 420–423. doi: 10.1111/j.1151-2916.1973.tb12714.x

Lawn, B. R. (1964). The thermal expansion of silver iodide and the cuprous halides. *Acta Cryst.* 17, 1341- 1347. doi: 10.1107/S0365110X64003401

Lin, J. C., Tong, P., Zhang, K., Ma, X., Tong, H., Guo, X., et al. (2017). The $GaNMn_3$-epoxy composites with tunable coefficient of thermal expansion and good dielectric performance. *Compos. Sci. Technol.* 146, 177–182. doi: 10.1016/j.compscitech.2017.04.028

Lin, J. C., Tong, P., Zhang, K., Tong, H., Guo, X., Yang, C., et al. (2016). Colossal negative thermal expansion with an extended temperature interval covering room temperature in fine-powdered $Mn_{0.98}CoGe$. *Appl. Phys. Lett.* 109:241903. doi: 10.1063/1.4972234

Lind, C. (2012). Two decades of negative thermal expansion research: where do we stand? *Materials (Basel)* 5, 1125–1154. doi: 10.3390/ma5061125

Lind, C., Coleman, M. R., Kozy, L. C., and Sharma, G. R. (2011). Zirconium tungstate/polymer nanocomposites: challenges and opportunities. *Phys. Status Solid B* 248, 123–129. doi: 10.1002/pssb.201083967

Mary, T. A., Evans, J. S. O., Vogt, T., and Sleight, A. W. (1996). Negative thermal expansion from 0.3 to 1050 Kelvin in ZrW_2O_8. *Science* 272, 90–92. doi: 10.1126/science.272.5258.90

Matoba, M., Anzai, S., and Fujimori, A. (1991). Thermal expansion, thermoelectric power, and XPS study of the nonmetal-metal transition in $Ni_{1-x}S_{1-y}Sey$. *J. Phys. Soc. Jpn.* 60, 4230–4244. doi: 10.1143/JPSJ.60.4230

Matsumoto, A., Kobayashi, K., Nishio, T., and Ozaki, K. (2003). Fabrication and thermal expansion of Al-ZrW_2O_8 composites by pulse current sintering process. *Mater. Sci. Forum* 426–432, 2279–2284. doi: 10.4028/www.scientific.net/MSF.426-432.2279

McWhan, D. B., and Remeika, J. P. (1970). Metal-insulator transition in $(V_{1-x}Cr_x)_2O_3$. *Phys. Rev. B* 2, 3734–3750. doi: 10.1103/PhysRevB.2.3734

Mizokawa, T., Tjeng, L. H., Sawatzky, G. A., Ghiringhelli, G., Tjernberg, O., Brookes, N. B., et al. (2001). Spin–Orbit coupling in the Mott insulator Ca_2RuO_4. *Phys. Rev. Lett.* 87:077202. doi: 10.1103/PhysRevLett.87.077202

Moriya, T., and Usami, K. (1980). Magneto-volume effect and Invar phenomena in ferromagnetic metals. *Solid State Commun.* 34, 95–99. doi: 10.1016/0038-1098(80)91241-7

Mott, N. F. (1990). *Metal–Insulator Transitions, 2nd Edn.* London: Taylor and Francis.

Nabetani, K., Muramatsu, Y., Oka, K., Nakano, K., Hojo, H., Mizumaki, M., et al. (2015). Suppression of temperature hysteresis in negative thermal expansion

compound $BiNi_{1-x}Fe_xO_3$ and zero-thermal expansion composite. *Appl. Phys. Lett*. 106:061912. doi: 10.1063/1.4908258

Nakamura, H., Wada, H., Yoshimura, K., Shiga, M., Nakamura, Y., Sakurai, J., et al. (1988). Effect of chemical pressure on the magnetism of YMn_2: magnetic properties of $Y_{1-x}Sc_xMn_2$ and $Y_{1-x}La_xMn_2$. *J. Phys. F Metal Phys*. 18, 981–991. doi: 10.1088/0305-4608/18/5/015

Nakamura, Y., Takenaka, K., Kishimoto, A., and Takagi, H. (2009). Mechanical properties of metallic perovskite $Mn_3Cu_{0.5}Ge_{0.5}N$: high-stiffness isotropic negative thermal expansion material. *J. Am. Ceram. Soc*. 92, 2999–3003. doi: 10.1111/j.1551-2916.2009.03297.x

Ohya, Y., Nakagawa, Z., and Hamano, K. (1987). Grain-boundary microcracking due to thermal expansion anisotropy in aluminum titanate ceramics. *J. Am. Ceram. Soc*. 70, C184–C186. doi: 10.1111/j.1151-2916.1987.tb05720.x

Okamoto, Y., Mori, M., Katayama, N., Miyake, A., Tokunaga, M., Matsuo, A., et al. (2018). Magnetic and structural properties of A-site ordered chromium spinel sulfides: alternating antiferromagnetic and ferromagnetic interactions in the breathing pyrochlore lattice. *J. Phys. Soc. Jpn*. 87:034709. doi: 10.7566/JPSJ.87.034709

Pan, Z., Chen, J., Jiang, X., Hu, L., Yu, R., Yamamoto, H., et al. (2017). Colossal volume contraction in strong polar perovskites of $Pb(Ti, V)O_3$. *J. Am. Chem. Soc*. 139, 14865–14868. doi: 10.1021/jacs.7b08625

Pelletant, A., Reveron, H., Chevalier, J., Fantozzi, G., Blanchard, L., Guinot, F., et al. (2012). Grain size dependence of pure β-eucryptite thermal expansion coefficient. *Mater. Lett*. 66, 68–71. doi: 10.1016/j.matlet.2011.07.107

Phillips, A. E., Goodwin, A. L., Halder, G. J., Southon, P. D., and Kepert, C. J. (2008). Nanoporosity and exceptional negative thermal expansion in single-network cadmium cyanide. *Angew. Chem. Int. Ed*. 47, 1396–1399. doi: 10.1002/anie.200704421

Pokharel, G., May, A. F., Parker, D. S., Calder, S., Ehlers, G., Huq, A., et al. (2018). Negative thermal expansion and magnetoelastic coupling in the breathing pyrochlore lattice material $LiGaCr_4S_8$. *Phys. Rev. B* 97:134117 doi: 10.1103/PhysRevB.97.134117

Pryde, A. K. A., Hammonds, K. D., Dove, M. T., Heine, V., Gale, J. D., and Warren, M. C. (1996). Origin of the negative thermal expansion in ZrW_2O_8 and ZrV_2O_7. *J. Phys.* 8, 10973–10982. doi: 10.1088/0953-8984/8/50/023

Qi, T. F., Korneta, O. B., Parkin, S., De Long, L. E., Schlottmann, P., and Cao, G. (2010). Negative volume thermal expansion via orbital and magnetic orders in $Ca_2Ru_{1-x}Cr_xO_4$ ($0 < x < 0.13$). *Phys. Rev. Lett*. 105:177203. doi: 10.1103/PhysRevLett.105.177203

Qi, T. F., Korneta, O. B., Parkin, S., Hu, J. P., and Cao, G. (2012). Magnetic and orbital orders coupled to negative thermal expansion in Mott insulators $Ca_2M_{1-x}Cr_xO_4$ (M = Mn and Fe). *Phys. Rev. B* 85:165143. doi: 10.1103/PhysRevB.85.165143

Reinecke, H., DelaCampa, J. G., and DeAbajo, J. (1996). Synthesis and characterization of novel poly(amide imide)s. *J. Appl. Polym. Sci*. 61, 923–928. doi: 10.1002/(SICI)1097-4628(19960808)61:6<923::AID-APP5>3.0.CO;2-J

Robello, A., Neumeier, J. J., Gao, Z. S., Qi, Y. P., and Ma, Y. W. (2012). Giant negative thermal expansion in La-doped $CaFe_2As_2$. *Phys. Rev. B* 86:104303. doi: 10.1103/PhysRevB.86.104303

Rong, Y. C., Li, M. L., Chen, J., Zhou, M., Lin, K., Hu, L., et al. (2016). Large negative thermal expansion in non-perovskite lead-free ferroelectric $Sn_2P_2S_6$. *Phys. Chem. Chem. Phys*. 18, 6247–6251. doi: 10.1039/C6CP00011H

Salvador, J. R., Guo, F., Hogan, T., and Kantzidis, M. G. (2003). Zero thermal expansion in YbGaGe due to an electronic valence transition. *Nature* 425, 702–705. doi: 10.1038/nature02011

Shan, X. R., Huang, R. J., Han, Y. M., Huang, C. J., and Li, L. F. (2015). Preparation and property study of $La(Fe, Si, Co)_{13}$/Cu composite with nearly zero thermal expansion behavior. *J. Alloy. Compd*. 648, 463–466. doi: 10.1016/j.jallcom.2015.06.139

Shirane, G., and Hoshino, S. (1951). On the phase transition in lead titanate. *J. Phys. Soc. Jpn*. 6, 265–270. doi: 10.1143/JPSJ.6.265

Sleight, A. (2003). Zero-expansion plan. *Nature* 425, 674–676. doi: 10.1038/425674a

Sleight, A. W. (1998). Compounds that contract on heating. *Inorg. Chem*. 37, 2854–2860. doi: 10.1021/ic980253h

Sullivan, L. M., and Lukehart, C. M. (2005). Zirconium tungstate (ZrW_2O_8)/polyimide nanocomposites exhibiting reduced coefficient of thermal expansion. *Chem. Mater*. 17, 2136–2141. doi: 10.1021/cm0482737

Sumiyama, K., Shiga, M., Morioka, M., and Nakamura, Y. (1979). Characteristic magnetovolume effects in Invar type Fe-Pt alloys. *J. Phys. F Metal Phys*. 9, 1665–1677. doi: 10.1088/0305-4608/9/8/017

Takenaka, K. (2012). Negative thermal expansion materials: technological key for control of thermal expansion. *Sci. Technol. Adv. Mater*. 13:013001. doi: 10.1088/1468-6996/13/1/013001

Takenaka, K., and Ichigo, M. (2014). Thermal expansion adjustable polymer matrix composites with giant negative thermal expansion. *Compos. Sci. Technol*. 104, 47–51. doi: 10.1016/j.compscitech.2014.08.029

Takenaka, K., and Takagi, H. (2005). Giant negative thermal expansion in Ge-doped antiperovskite manganese nitrides. *Appl. Phys. Lett*. 87:261902. doi: 10.1063/1.2147726

Takenaka, K., Hamada, T., Kasugai, D., and Sugimoto, N. (2012). Tailoring thermal expansion in metal matrix composites blended by antiperovskite manganese nitrides exhibiting giant negative thermal expansion. *J. Appl. Phys*. 112:083517. doi: 10.1063/1.4759121

Takenaka, K., Ichigo, M., Hamada, T., Ozawa, A., Shibayama, T., Inagaki, T., et al. (2014). Magnetovolume effects in manganese nitrides with antiperovskite structure. *Sci. Technol. Adv. Mater*. 15:015009. doi: 10.1088/1468-6996/15/1/015009

Takenaka, K., Kuzuoka, K., and Sugimoto, N. (2015). Matrix-filler interfaces and physical properties of metal matrix composites with negative thermal expansion manganese nitride. *J. Appl. Phys*. 118:084902. doi: 10.1063/1.4929363

Takenaka, K., Okamoto, Y., Shinoda, T., Katayama, N., and Sakai, Y. (2017a). Colossal negative thermal expansion in reduced layered ruthenate. *Nat. Commun*. 8:14102. doi: 10.1038/ncomms14102

Takenaka, K., Shinoda, T., Inoue, N., Okamoto, Y., Katayama, N., Sakai, Y., et al. (2017b). Giant negative thermal expansion in Fe-doped layered-ruthenate ceramics. *Appl. Phys. Express* 10:115501. doi: 10.7567/APEX.10.115501

Takezawa, A., Kobashi, M., and Kitamura, M. (2015). Porous composite with negative thermal expansion obtained by photopolymer additive manufacturing. *APL Mater*. 3:076103. doi: 10.1063/1.4926759

Takezawa, A., Takenaka, K., and Zhang, X. P. (2018). Inverse analysis of giant macroscopic negative thermal expansion of Ca_2RuO_{y-4} ceramics based on elastic mechanics and structural topology optimization. *Appl. Phys. Expr*. 11:055801. doi: 10.7567/APEX.11.055801

van Schilfgaarde, M., Abrikosov, I. A., and Johansson, B. (1999). Origin of the Invar effect in iron-nickel alloys. *Nature* 400, 46–49. doi: 10.1038/21848

Wagh, A. S., Poeppel, R. B., and Singh, J. P. (1991). Open pore description of mechanical properties of ceramics. *J. Mater. Sci*. 26, 3862–3868.

Wang, C., Chu, L., Yao, Q., Sun, Y., Wu, M., Ding, L., et al. (2012). Tuning the range, magnitude, and sign of the thermal expansion in intermetallic $Mn_3(Zn, M)_xN$ (M = Ag, Ge). *Phys. Rev. B* 85:220103R. doi: 10.1103/PhysRevB.85.220103

Wang, Q. M., Jackson, J. A., Ge, Q., Hopkin, J. B., Spadaccini, C. M., and Fang, N. X. (2016). Lightweight mechanical metamaterials with tunable negative thermal expansion. *Phys. Rev. Lett*. 117:175901. doi: 10.1103/PhysRevLett.117.175901

Wasserman, E. F. (1990). Invar: moment-volume instabilities in transition metals and alloys. *Ferromagn. Mater*. 5, 237–322. doi: 10.1016/S1574-9304(05)80063-X

Weiss, R. J. (1963). The origin of the 'Invar' effect. *Proc. Phys. Soc*. 82, 281–288.

Wohlfarth, E. P. (1977). Thermodynamic aspects of itinerant electron magnetism. *Physica* 91B, 305–314. doi: 10.1016/0378-4363(77)90199-1

Wright, J. P., Bell, A. M. T., and Attfield, J. P. (2000). Variable temperature powder neutron diffraction study of the Verwey transition in magnetite Fe_3O_4. *Solid State Sci*. 2, 747–753. doi: 10.1016/S1293-2558(00)01107-9

Xue, Z. W., Wang, L. D., Liu, Z., and Fei, W. D. (2010). Effect of interfacial state on thermal expansion behaviors of β-eucryptite particle-reinforced Cu compounds. *Scripta Mater*. 62, 867–870. doi: 10.1016/j.scriptamat.2010.02.022

Yamada, I., Tsuchida, K., Ohgushi, K., Hayashi, N., Kim, J., Tsuji, N., et al. (2011). Giant negative thermal expansion in the iron perovskite $SrCu_3Fe_4O_{12}$. *Angew. Chem. Int. Ed*. 50, 6579–6582. doi: 10.1002/anie.201102228

Yamai, I., and Ota, T. (1993). Grain size-microcracking relation for $NaZr_2(PO_4)_3$ family ceramics. *J. Am. Ceram. Soc.* 76, 487–491. doi: 10.1111/j.1151-2916.1993.tb03811.x

Yang, C., Tong, P., Lin, J. C., Guo, X. G., Zhang, K., Wang, M., et al. (2016). Size effects on negative thermal expansion in cubic ScF_3. *Appl. Phys. Lett.* 109:023110. doi: 10.1063/1.4959083

Zhao, Y. Y., Hu, F.-X., Bao, L.-F., Wang, J., Wu, H., Huang, Q.-Z., et al. (2015). Giant negative thermal expansion in bonded MnCoGe-based compounds with Ni_2In-type hexagonal structure. *J. Am. Chem. Soc.* 137, 1746–1749. doi: 10.1021/ja510693a

Conflict of Interest Statement: The author declares that the research was conducted in the absence of any commercial or financial relationships that could be construed as a potential conflict of interest.

frontiers in Chemistry

REVIEW
published: 25 September 2018
doi: 10.3389/fchem.2018.00438

Negative Thermal Expansion in the Materials With Giant Magnetocaloric Effect

Fengxia Hu[1,2]*, *Feiran Shen*[1,2], *Jiazheng Hao*[1], *Yao Liu*[1,2], *Jing Wang*[1,2], *Jirong Sun*[1,2] and *Baogen Shen*[1,2]

[1] Beijing National Laboratory for Condensed Matter Physics and State Key Laboratory of Magnetism, Institute of Physics, Chinese Academy of Sciences, Beijing, China, [2] School of Physical Sciences, University of Chinese Academy of Sciences, Beijing, China

Negative thermal expansion (NTE) behaviors in the materials with giant magnetocaloric effects (MCE) have been reviewed. Attentions are mainly focused on the hexagonal Ni_2In-type MM'X compounds. Other MCE materials, such as $La(Fe,Si)_{13}$, RCo_2, and antiperovskite compounds are also simply introduced. The novel MCE and phase-transition-type NTE materials have similar physics origin though the applications are distinct. Spin-lattice coupling plays a key role for the both effect of NTE and giant MCE. Most of the giant MCE materials show abnormal lattice expansion owing to magnetic interactions, which provides a natural platform for exploring NTE materials. We anticipate that the present review can help finding more ways to regulate phase transition and dig novel NTE materials.

Keywords: negative thermal expansion, thermal compensation, giant magnetocaloric effect, spin-lattice coupling, magnetostructural transition

OPEN ACCESS

Edited by:
Jun Chen,
University of Science and Technology Beijing, China

Reviewed by:
Jianchao Lin,
Institute of Solid State Physics, Chinese Academy of Sciences, China
Cong Wang,
Beihang University, China

***Correspondence:**
Fengxia Hu
fxhu@iphy.ac.cn

Specialty section:
This article was submitted to Physical Chemistry and Chemical Physics, a section of the journal Frontiers in Chemistry

Received: *02 July 2018*
Accepted: *03 September 2018*
Published: *25 September 2018*

Citation:
Hu F, Shen F, Hao J, Liu Y, Wang J, Sun J and Shen B (2018) Negative Thermal Expansion in the Materials With Giant Magnetocaloric Effect. Front. Chem. 6:438. doi: 10.3389/fchem.2018.00438

INTRODUCTION

Magnetic cooling technique based on magnetocaloric effect (MCE) has attracted an increasing attention for its environmental-friendly and energy-saving superiority compared to conventional vapor compression technique (Annaorazov et al., 1996; Pecharsky and Gschneidner, 1997; Hu et al., 2000a, 2001; Wada and Tanabe, 2001; Tegus et al., 2002; Fujita et al., 2003; Gschneidner et al., 2005; Krenke et al., 2005; Shen et al., 2009; Liu E. K. et al., 2012; Liu J. et al., 2012; Wu et al., 2015). The discovery of giant MCE materials, such as FeRh (Annaorazov et al., 1996), $Gd_5Si_2Ge_2$ (Pecharsky and Gschneidner, 1997; Gschneidner et al., 2005), $La(Fe,Si)_{13}$ (Hu et al., 2001; Fujita et al., 2003; Shen et al., 2009), MnFeP(As,Ge) (Tegus et al., 2002), MnAs (Wada and Tanabe, 2001), NiMn-based Heusler alloys (Hu et al., 2000a; Krenke et al., 2005; Liu J. et al., 2012), Ni_2In-type MM'X compounds (Liu E. K. et al., 2012; Wu et al., 2015), has promoted the developing of solid-state magnetic refrigeration technique. A common feature of these materials is the strong spin-lattice coupling. In other words, magnetic and structural transition concurrently takes place, and the change of lattice during the transition does contribute to the giant MCE. Note that a number of MCE materials show abnormal lattice expansion owing to magnetic interactions, which provides a natural platform for exploring negative thermal expansion materials. However, not all the giant MCE materials show negative thermal expansion (NTE), some of them still show positive thermal expansion (PTE), depending entirely on the characteristics of the magnetostructural/magnetoelastic transition and the specific physical origin in different systems.

For example, FeRh alloy shows giant MCE. It crystallizes in the CsCl-type cubic structure and experiences PTE with volume change of $\Delta V/V \sim +0.9\%$ along with the AFM-FM (antiferromagnetic-ferromagnetic) transition without the change of space group. $Gd_5Si_2Ge_2$ also exhibits giant MCE (Pecharsky and Gschneidner, 1997), which originates from a coupled magnetostructural transition in which slabs of a well defined arrangement of R and T atoms shift ~0.5Å with respect to one another along the *a*-axis when the transition occurs under the influence of temperature (Gschneidner et al., 1997; Morellon et al., 2000). Such a shift gives rise to a PTE with volume change of $\Delta V/V \sim +$ (0.4–1)% depending on the compositions. $MnFeP_{1-x}As_x$ ($0.15 < x < 0.66$) alloys with giant MCE crystallize in hexagonal Fe_2P-type structure and undergo a first-order FM-PM (paramganetic) magnetic transition around room temperature (Tegus et al., 2002). The space group ($P\bar{6}\,2m$) keeps unchanged upon the magnetic transition, but the lattice shows an anomaly expansion in the direction of the *a* and *b* axes and a contraction of the *c* axis as the FM phase is formed, which originates from an increase in the intralayer metal-metal bond distance (Liu et al., 2009). As a result, a PTE with $\Delta V/V \sim +0.06\%$ was observed with increasing temperature. The FM Heusler alloy Ni_2MnGa with $L2_1$ structure shows a giant MCE owing to the martensitic magnetostructural transformation from FM austenitic to FM martensitic phase (Wada and Tanabe, 2001). On heating, the alloy displays a PTE with $\Delta V/V \sim +1\%$.

However, the $La(Fe_{1-x}Si_x)_{13}$-based materials with giant MCE show NTE with $\Delta V/V \sim -$ (1.0–1.6)% around T_C, depending on compositions, due to the itinerant ferromagnetic nature of the materials (Shen et al., 2009). The space group ($Fm\bar{3}\,c$) keeps unchanged across the magnetic transition. Moreover, the hexagonal MnCoGe/MnNiGe-based compounds also show giant MCE and NTE. The optimal compositions undergo a magnetostructural transition from a Ni_2In-type hexagonal PM phase (space group $P6_3/mmc$) to a TiNiSi-type orthorhombic FM phase (space group *Pnma*). The c axis of hexagonal phase expands while the a-axis contracts upon the martensitic structural transition. As a result, NTE as large as $\Delta V/V = -(2.68–3.9)\%$ occurs depending on compositions (Liu E. K. et al., 2012; Wu et al., 2015; Zhao et al., 2015).

Materials with precise thermal expansion or zero thermal expansion (ZTE) are in urgent demand in modern industry (Rathmann et al., 1968; Namba et al., 2001; Du et al., 2016), such as engineered components, optical mirrors, and printed circuit boards. Generally, ZTE can be reached by combining the materials with PTE and NTE coefficients. To meet various demands, lots of efforts have been made to search for NTE materials, and a number of materials have been discovered showing giant NTE, e.g., ZrW_2O_8 (Mary et al., 1996), CuO nanoparticles (Zheng et al., 2008), $(Bi,La)NiO_3$ (Azuma et al., 2011), $PbTiO_3$-based compounds (Chen et al., 2011), antiperovskite manganese nitrides (Takenaka and Takagi, 2005; Iikubo et al., 2008; Sun et al., 2010a; Song et al., 2011; Wang et al., 2012; Lin et al., 2015), $La(Fe,Co,Si)_{13}$ (Huang et al., 2013), MnCoGe-based materials (Zhao et al., 2015), and reduced Ca_2RuO_4 (Takenaka et al., 2017). Among these NTE materials, the phase-transition-type materials (Takenaka and Takagi, 2005; Iikubo et al., 2008; Sun et al., 2010a; Song et al., 2011; Huang et al., 2013; Zhao et al., 2015) have attracted specific attention.

In this paper, we mainly review the negative thermal expansion behaviors based on magnetostructural or magnetoelastic transition in the materials showing giant magnetocaloric effect. Here, the magnetostructural transition refers to the concurrent magnetic and structural transition where the lattice structure (space group) changes during the transition, while the magnetoelastic transition refers to the concurrent magnetic and elastic transition where the lattice structure (space group) remains unchanged but lattice parameter changes elastically.

$LA(FE,SI)_{13}$-BASED COMPOUNDS

Crystal Structure

$LaFe_{13}$ does not exist due to the positive formation enthalpy between La and Fe. To get $LaFe_{13}$-based alloys, a third element is needed. The first stable $LaFe_{13-x}M_x$ compounds were made by Krypiakewytsch et al. (1968) in 1968 when Fe was partially replaced by Si or Al. The compounds show cubic $NaZn_{13}$-type structure with space-group of $Fm\bar{3}c$. In the structure, La atoms occupy the 8a site, while Fe atoms occupy the 8b and 96i sites. Fe atoms at these two sites are denoted as Fe^{I} and Fe^{II}, respectively. Al or Si randomly substitute for Fe^{II} site. Fe atoms at Fe^{I} site and La form a CsCl structure. The Fe^{I} are surrounded by an icosahedron of 12 Fe^{II}, and the Fe^{II} are surrounded by nine nearest Fe^{II} and one Fe^{I}, as shown in **Figure 1**.

Magnetocaloric Effect

By analyzing phase formation rule of $NaZn_{13}$-type compounds, $LaFe_{13-x}Si_x$ compounds with Si content ranging from $x = 1.2$ to 2.4 were successfully synthesized (Hu, 2002; Shen et al., 2009). In 2001, we firstly reported the large MCE in $LaFe_{11.4}Si_{1.6}$, originating from a negative lattice expansion and a field-induced itinerant-electron metamagnetic transition (Hu et al., 2001). The maximal magnetic entropy change, $-\Delta S$, reaches

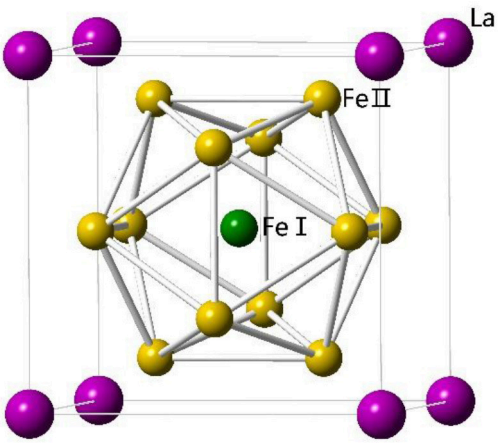

FIGURE 1 | Crystal structure of $NaZn_{13}$-type $La(Fe,X)_{13}$ compounds.

19.4 J $kg^{-1}K^{-1}$ around 213 K under a magnetic field change of 0-5T, largely exceeding that of $LaFe_{10.4}Si_{2.6}$ with typical second-order transition, as shown in **Figure 2A**. The differential curves given in the inset of **Figure 2A** clearly illustrates the asymmetrical broadening of $-\Delta S$ peak caused by the field-induced itinerant-electron metamagnetic transition. **Figure 2B** displays the comparison of lattice change around phase transition between $LaFe_{11.4}Si_{1.6}$ and $LaFe_{10.4}Si_{2.6}$. One can notice, for $LaFe_{11.4}Si_{1.6}$, the negative expansion of lattice parameter can be as much as −0.4%.

Introducing the substitution of Co for Fe or interstitial atoms C/H can both impact the exchange coupling between the magnetic elements. This fact can adjust the temperature of phase transition in a wide temperature range covering room temperature while a large MCE is maintained. The maximal room temperature $-\Delta S$ can reach 12 J $kg^{-1}K^{-1}$ and 20 J $kg^{-1}K^{-1}$ under 2 T and 5 T magnetic fields, respectively, for the typical $La(Fe,Si)_{13}$-based compounds (Hu et al., 2002; Shen et al., 2009). The large MCE make the $La(Fe,Si)_{13}$-based compounds attractive to be as room temperature refrigerants. For $La(Fe_{1-x}Co_x)_{11.9}Si_{1.1}$ (Hu et al., 2002, 2005), the $-\Delta S$ is one times larger than the conventional refrigerant Gd, and is comparable or even exceeds that of $Gd_5Si_2Ge_2$, the milestone MCE material discovered in 1997 (Pecharsky and Gschneidner, 1997). The large MCE is closely related to negative lattice expansion across phase transition, which can be identified in the temperature dependence of lattice parameter for $La(Fe_{1-x}Co_x)_{11.9}Si_{1.1}$ (x = 0.04, 0.06, 0.08) compounds (**Figure 3**).

Negative Thermal Expansion Behaviors

Although the large MCE of $La(Fe,Si)_{13}$-based compounds owing to the significant negative lattice expansion was discovered in the early 2000 (Hu et al., 2000b; Shen et al., 2009), these materials have never been considered as negative thermal expansion (NTE) materials till 2013. As NTE materials, Huang et al. firstly reported the giant NTE in $La(Fe,Si,Co)_{13}$ compounds (Huang et al., 2013).

For $LaFe_{13-x}Si_x$, the NTE properties were found to be strongly dependent on the Si contents. A sharp volume change from 170 to 240 K was observed in $LaFe_{11.5}Si_{1.5}$ with a NTE temperature window (ΔT) about 70 K. The estimated $\Delta L/L$ is 3.5×10^{-3}, which is comparable to those of Mn_3ZnN (4.6×10^{-3}) (Takenaka and Takagi, 2005) and Mn_3GaN (3.8×10^{-3}) (Takenaka et al., 2008). With increasing Si content from x=1.5 to 2.4, the linear expansion becomes broader gradually, leading to a large negative slope in a wider temperature range. This result illustrates that the replacement of Fe by Si can broaden the temperature window of NTE. However, the numerical values of NTE coefficient rapidly drop with the increase of Si content, which is an unfavorable character for practical applications.

To improve the performance of NTE behavior, the substitution of Co for Fe was introduced. **Figure 4** displays linear thermal expansion as a function of temperature and

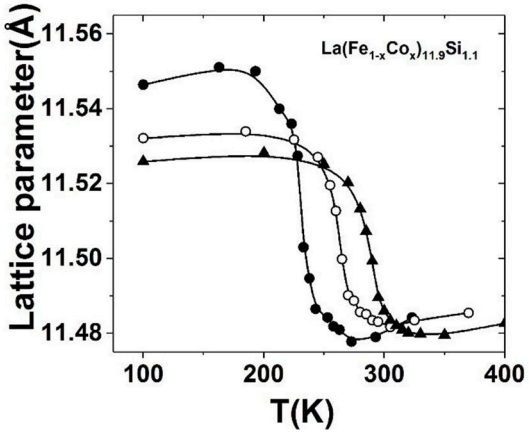

FIGURE 3 | The temperature dependence of lattice parameter for $La(Fe_{1-x}Co_x)_{11.9}Si_{1.1}$ (x = 0.04, 0.06, 0.08) compounds. Reprinted with permission from Hu et al. (2005).

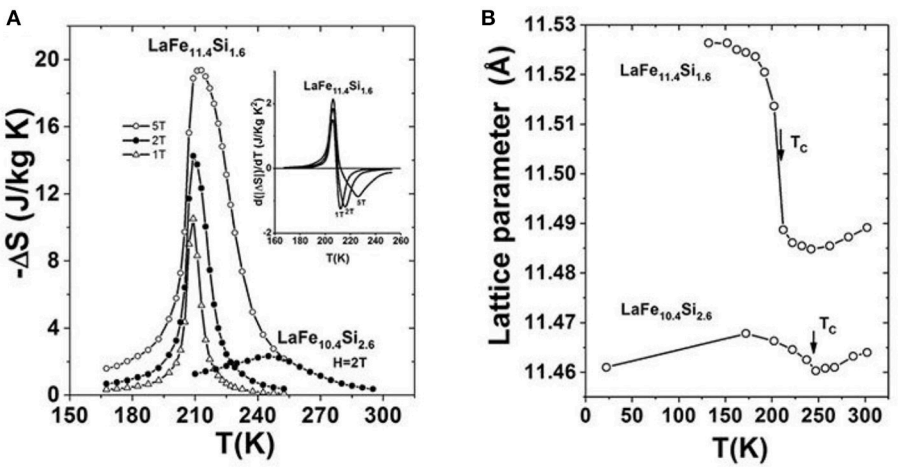

FIGURE 2 | (A) Magnetic entropy change $-\Delta S$ of $LaFe_{11.4}Si_{1.6}$ compared with $LaFe_{10.4}Si_{2.6}$. The differential curves of $-\Delta S$ for the former is given in the inset. **(B)** Temperature dependence of lattice parameter of $LaFe_{11.4}Si_{1.6}$ compared to that of $LaFe_{10.4}Si_{2.6}$. Reprinted with permission from Hu et al. (2001).

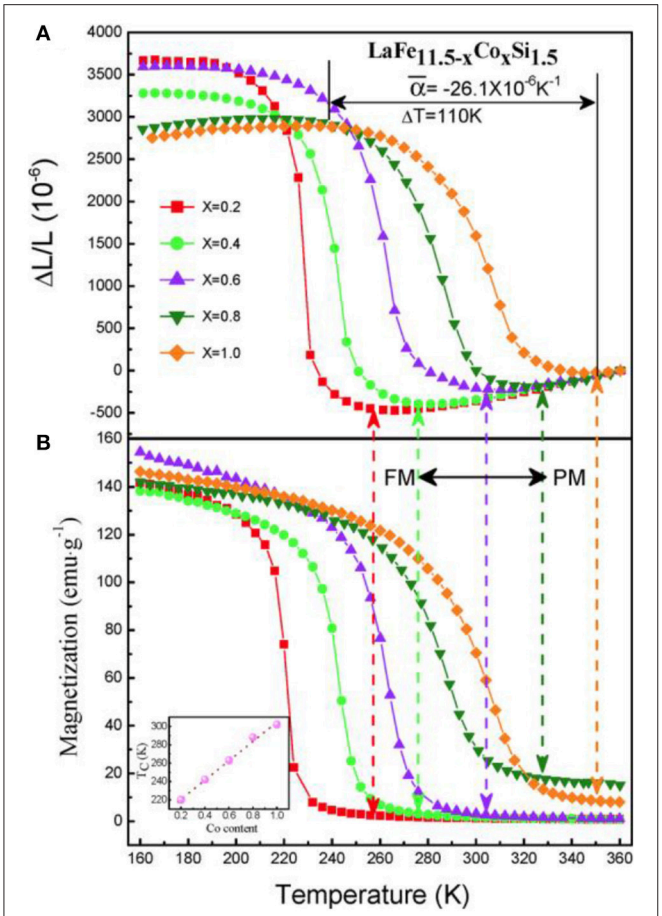

FIGURE 4 | Temperature dependence of **(A)** linear thermal expansions ΔL/L (reference temperature: 360 K) compared to **(B)** the magnetization for $LaFe_{11.5-x}Co_xSi_{1.5}$ (x = 0.2, 0.4, 0.6, 0.8, and 1.0). Reprinted with permission from Huang et al. (2013).

its comparison with magnetization for $LaFe_{11.5-x}Co_xSi_{1.5}$. Increasing Co content broadens the temperature window, ΔT, of NTE, and drives it to a higher temperature. The ΔT width of NTE is 74 K, 90 K, and 110 K for x = 0.2, 0.4, and 1.0, respectively. More importantly, the change of ΔL/L within the NTE window reduces less rapidly with Co compared to the case with Si. The composition with x = 0.10 produces an average coefficient of thermal expansion (CTE) of $\bar{\alpha} = -26.1 \times 10^{-6}$ K^{-1} from 240 K to 350 K, covering room temperature. This numerical value of $\bar{\alpha}$ is about 3 times larger than that of the commercial NTE materials ZrW_2O_8 with $\alpha = -9 \times 10^{-6}$ K^{-1}. Moreover, the absolute value of the negative CTE reaches those of high-expansion metals such as Al ($\alpha = 23 \times 10^{-6}$ K^{-1} at room temperature). These findings suggest the potential application of $La(Fe,Si)_{13}$-based compounds as NTE materials.

More interestingly, zero thermal expansion (ZTE) has been recently reported in $La(Fe,Si)_{13}$-based compounds in a wide temperature range away from phase transition (Li et al., 2017), which is a fascinating phenomenon in these compounds.

Ni_2In-TYPE MM'X COMPOUNDS

Crystal Structure

Hexagonal Ni_2In-type MM'X (M, M' = transitional element, X = main element) compounds have attracted lots of attention owing to the rich magnetic and structural behaviors. Ferromagnetic or antiferromagnetic coupling occurs depending on the compositions and atomic local environments (Niziol et al., 1981; Caron et al., 2011; Gercsi et al., 2011; Liu E. K. et al., 2012). As a member of family, the stoichiometric MnCoGe alloy undergoes diffusionless martensitic structural transition, T_{stru}, from Ni_2In-type hexagonal (space group: $P6_3/mmc$) to TiNiSi-type orthorhombic (space group: Pnma) structure at T_{stru} ~420 K and a transition of ferromagnetic ordering at T_c~345 K (Niziol et al., 1981). Both the martensitic and austenitic phases display ferromagnetic nature, and the orthorhombic phase shows a higher magnetic moment M_s ~4.13 μ_B than the hexagonal phase (M_s ~2.76 μ_B) (Niziol et al., 1981). On the other hand, the stoichiometric MnNiGe undergoes a similar martensitic structural transformation at T_{stru}~470 K, and a magnetic transition at T_N^M ~346 K. The martensitic and austenitic phases have distinct magnetic structure. The former shows spiral antiferromagnetic (AFM) coupling with Neel temperature T_N^M at 346 K while the latter exhibits ferromagnetic (FM) nature with intrinsic Curie temperature T_C^A at 205 K (Niziol et al., 1981).

Figure 5 shows the sketches of orthorhombic martensitic and hexagonal austenitic structures for MnCoGe (Wu et al., 2015).

Magnetocaloric and Barocaloric Effects

For the MM'X compounds, austenitic phase has a smaller volume than martensitic phase. This fact prompts one to think that the introduction of smaller atoms or vacancies may stabilize the austenitic phase and shift T_{stru} to a lower temperature. Following this way, magnetostructural transition has been indeed realized by introducing smaller atoms or vacancies, such as $MnCo_{1-x}Ge$ (Wang et al., 2006), $Mn_{1-x}CoGe$ (Liu et al., 2010), $Mn_{1-x}Cr_xCoGe$ (Caron et al., 2011). Moreover, It has demonstrated that valence electron concentration (e/a) can also affect T_{stru}. By introducing Indium (In) atom (2.00 Å, $5s^25p^1$) with a larger radius but fewer e/a to replace Mn (1.79 Å, $3d^54s^2$), Co (1.67 Å, $3d^74s^2$), or Ge (1.52 Å, $4s^24p^2$), magnetostructural transition is also created in (Liu E. K. et al., 2012). As a result, large MCE has been observed in these MnCoGe-based materials.

On the other hand, it has been found that, for MnNiGe, the AFM coupling in the martensitic structure is not robust. The replacements of Mn or Ni by Fe atom can convert the AFM into FM coupling and stabilize the austenitic phase (Liu E. K. et al., 2012). As a result, the T_{stru} shifts to low temperature, and magnetostructural transition is realized and hence large MCE appears in an extended temperature window from 350 K down to 70 K in MnFeNiGe alloys.

Moreover, giant barocaloric effect has been demonstrated in $MnCoGe_{0.99}In_{0.01}$ compound (Wu et al., 2015). Neutron powder diffraction (NPD) studies indicated that the lattice of hexagonal phase expands significantly along the c-axis (c_H) by 11.3% while contracts along the a-axis (a_H) by −6.8% during the magnetostructural transformation, T_{mstru}. As a result, negative

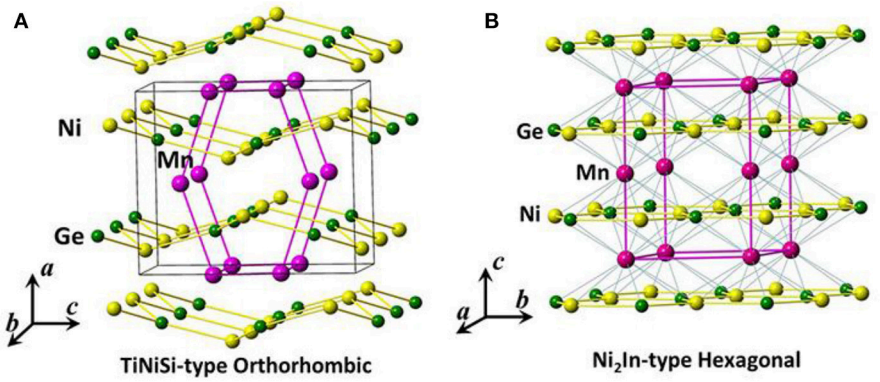

FIGURE 5 | The sketches of **(A)** orthorhombic martensitic and **(B)** hexagonal austenitic structures. The black lines in **(A)** enclose one unit cell of TiNiSi-type orthorhombic structure while the purple lines in **(B)** enclose the one of Ni_2In-type hexagonal structure. The unit cell of hexagonal phase transforms into the zigzag-type structure in the orthorhombic phase, as indicated by purple lines in **(A)**.

lattice expansion as large as $\Delta V/V = (V_{ortho}/2\text{-}V_{hex})/V_{hex} \sim -3.9\%$ occurs for $MnCoGe_{0.99}In_{0.01}$, as shown in **Figure 6**. Note that the unit cell volume and lattice constants of hexagonal and orthorhombic phases have relations as $a_o{=}c_H$, $b_o{=}a_H$, $c_o{=}\sqrt{3}a_H$ and $V_O{=}2V_H$.

The calorimetric measurements using a differential scanning calorimeter (DSC) revealed that the total change of transition entropy can be as large as 55 J $kg^{-1}K^{-1}$ contributed by the large difference of internal energy across the transition for $MnCoGe_{0.99}In_{0.01}$. High resolution NPD studies under hydrostatic pressure revealed that pressure can shift the T_{mstr} to lower temperature at a rate of 7.7 K/kbar. The large latent heat and high sensitivity of the magnetostructural transition to pressure result in giant inverse barocaloric effect (Wu et al., 2015). The entropy change, ΔS, and adiabatic temperature change, ΔT_{ad}, under a pressure of 3 kbar reaches 52 J $kg^{-1}K^{-1}$ and −18 K, which exceed those of most materials, including the giant magnetocaloric effect driven by a magnetic field of 5 T (Gschneidner et al., 2005) that can be only available by superconducting magnets. The refrigeration cooling power (RCP) reaches 1190 J kg^{-1}.

Negative Thermal Expansion Behavior

Similar to the case of $La(Fe,Si)_{13}$-based compounds, the Ni_2In-type MM'X compounds have rarely been considered as negative thermal expansion (NTE) materials because of the limited temperature region of phase transition, though they surely have significant negative lattice expansion and large MCE and barocaloric effect owing to the magnetostructural transition.

Giant Negative Thermal Expansion in MnCoGe-Based Materials

In 2015, Zhao et al. firstly reported giant NTE in bonded MnCoGe-based materials (Zhao et al., 2015). The as-prepared compounds are very brittle and even collapse into powders during preparation. Through introducing a few amounts (3–4 wt%) of epoxy to bond the powders, residual stress was introduced, hence the structural transition was broadened due to the lattice softening enforced by the stress. Hence, giant NTE has been achieved in a wide temperature region. Moreover, excellent mechanical properties and tunable electrical conductivity has been demonstrated for the bonded powders.

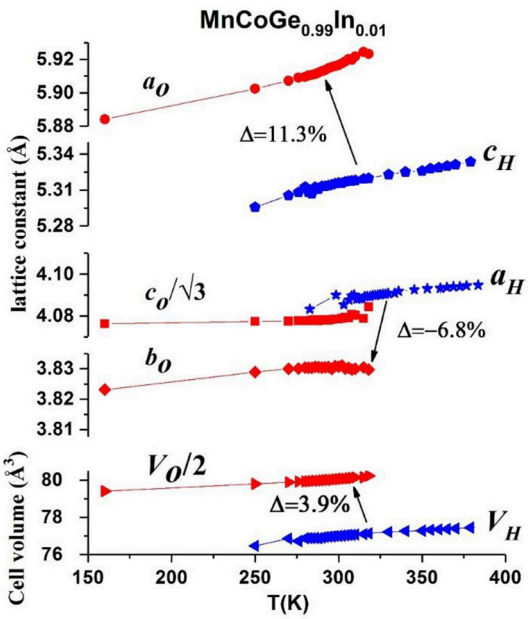

FIGURE 6 | Lattice constants and unit-cell volume of hex. and orth. structure as a function of temperature for $MnCoGe_{0.99}In_{0.01}$. The blue and red symbols correspond to the hex. and orth. structure, respectively. The red circle, red square and red rhombus stand for a_o, $c_o/\sqrt{3}$ and b_o, respectively. The blue pentagon and blue star represent the c_h and a_h, respectively. The unit-cell volume of hex. and half of unit-cell volume of orth. structure are symbolized as blue and red triangle, respectively. Reproduced under a Creative Commons Attribution 4.0 International License from Wu et al. (2015).

Neutron powder diffraction (NPD) studies indicate that the change of lattice volume during the magnetic transition can be as much as 3.9, 3.9, and 3.8% for $MnCoGe_{1-x}In_x$ ($x = 0.01, 0.02$), and $MnCoGe_{0.97}Sb_{0.03}$, respectively. Accordingly, the evaluated linear expansion is equal to $\Delta L/L \sim 10{,}995 \times 10^{-6}$ and the

average NTE coefficient is about $\bar{\alpha} \sim -183.3 \times 10^{-6}$/K if the polycrystalline powder is supposed to expand isotropically for $MnCoGe_{0.99}In_{0.01}$.

Linear expansion, ΔL/L, was measured using high resolution strain gauge for the bonded plates. It was found that the ΔL/L behaves isotropically, independent of the in-plane measured axis. **Figure 7** shows the ΔL/L as a function of temperature for some typical compositions. The maximal ΔL/L keeps above 10,231 $\times 10^{-6}$, while the average linear NTE coefficient ranges from −51.5 $\times 10^{-6}$/K to −94.7 $\times 10^{-6}$/K in the tunable temperature region from ∼60 to 330 K covering room temperature for the bonded MnCoGe-based materials with different compositions. Because of the significant broadening of phase transition caused by residual stress and the possibly porosities introduced, the ΔL/L and $\bar{\alpha}$ are somewhat smaller than those estimated from the X-ray diffraction (XRD) or NPD measurements. However, the maximal ΔL/L measured has reached 93% of the crystallographic value. These novel NTE properties are over the performance of most other reported materials previously. For example, the average $\bar{\alpha} \sim -51.5 \times 10^{-6}$/K with operation temperature window as wide as 210 K was observed in $MnCo_{0.98}Cr_{0.02}Ge$, which is more than 5 times larger than that of the commercial NTE materials ZrW_2O_8 with $\bar{\alpha} = -9 \times 10^{-6}$/K.[1] More interestingly, in the temperature region from 250 to 305 K covering room temperature, the CET α (−119 $\times 10^{-6}$/K) remains nearly independent of temperature (see **Figure 7A**), and this value is about 40% larger than the that (−82 $\times 10^{-6}$ /K) of $Bi_{0.95}La_{0.05}NiO_3$ (320–380 K) (Azuma et al., 2011), and more than four times larger than the α (−25 $\times 10^{-6}$ /K) of an antiperovskite manganese nitride (316–386 K) (Takenaka and Takagi, 2005).

Figures 8A,B presents the temperature dependence of magnetization (M-T curves) measured under a 0.3 T magnetic field for the bonded and as-prepared compositions with and without magnetostructural coupling. From **Figure 8** and the dM/dT plots in the insets, one can distinguish that the structural/magnetostructural transformation (T_{stru}/T_{mstru}) was significantly broadened while the pure magnetic transition keeps unchanged around T_C for the bonded samples. For the bonded $MnCoGe_{0.99}$ with magnetostructural transition, the T_{mstru} shifts by 10 K to low temperature, while for the $Mn_{0.97}In_{0.03}CoGe$ with decoupled T_{stru} and T_C, the T_{stru} shifts by 7 K to low temperature while T_C keeps unchanged (261 K). The significant broadening of the structural/magnetostructural transformation enforced by the residual stress governs the NTE behavior in the bonded samples.

From viewpoint of industry, electrical conductivity is a critical parameter for practical applications. For the bonded MnCoGe-based materials, the electrical conductivity can be adjusted through choosing distinct binders. It has been experimentally demonstrated that the electrical resistivity for the materials with Ag-epoxy as binder is lower than the one with epoxy as binder by 3 orders of magnitude. Moreover, the mechanical properties have been largely improved. All these suggest the high potential of MnCoGe-based compounds as NTE materials, which can be used to compensate the materials with high PTE, such as the popularly-used organic or plastic materials.

Ultra-Low Thermal Expansion Realized in $MnCoGe_{0.99}In_{0.01}$ Through Self-Compensation

The martensitic structural transition in Ni_2In-type MM'X compounds behaves extremely sensitive to pressure compared to magnetic field (Wu et al., 2015). The introduced residual strain and defects during pulverization (Wu et al., 2016) or cold pressing (Liu et al., 2015) can also affect the magnetostructural coupling besides hydrostatic pressure. It has been reported that

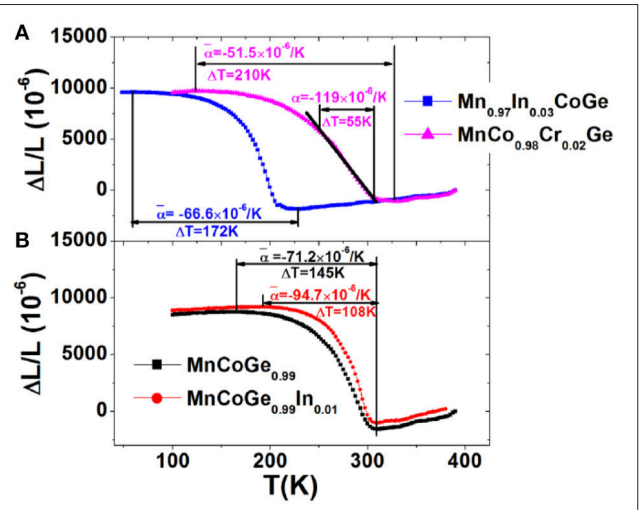

FIGURE 7 | Temperature dependent linear thermal expansions ΔL/L (the reference temperature is 390 K) for bonded samples with various compositions **(A)** $Mn_{0.97}In_{0.03}CoGe$, $MnCo_{0.98}Cr_{0.02}Ge$, and **(B)** $MnCoGe_{0.99}$, $MnCoGe_{0.99}In_{0.01}$. Reprinted with permission from Zhao et al. (2015).

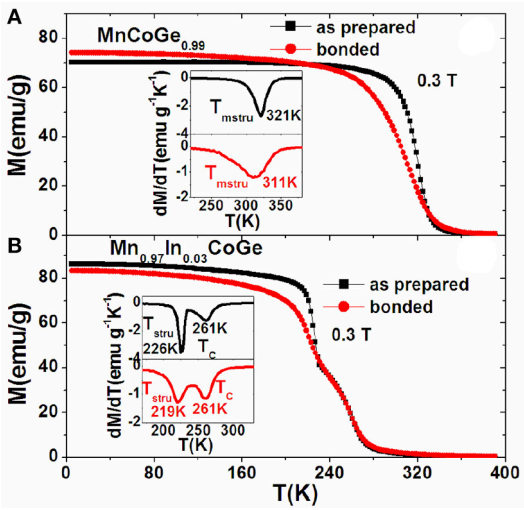

FIGURE 8 | The comparison of temperature dependent magnetization under 0.3T for the bonded and as-prepared compositions **(A)** $MnCoGe_{0.99}$ with magnetostructural coupling and **(B)** $Mn_{0.97}In_{0.03}CoGe$ with decoupled T_{stru} and T_C. The insets show corresponding dM/dT plots. Reprinted with permission from Zhao et al. (2015).

the introduced residual strain in the $MnCoGe_{1-x}In_x$ thin slices prepared by cold pressing can stabilize the austenite phase, as a result, the temperature window of martensitic transformation is broadened, the magnetic and structural transition becomes decoupling (Liu et al., 2015). Similarly, with reducing particle size, austenitic phase becomes stable and a high fraction of austenitic phase loses the martensitic transformation, and retains the hexagonal FM structure in the entire temperature range. Considering the large difference of volume between austenitic and martensitic phases, one may prompt to think that adjusting phase fraction and magnetostructural transition through residual strain can lead to controllable NTE or even ZTE.

Indeed, ultra-low thermal expansion has been realized in the giant NTE material $MnCoGe_{0.99}In_{0.01}$ by controlling the crystallinity degree and phase transition (Shen et al., 2017). A high fraction of sample can be converted into amorphous structure by ball milling, which turns to show PTE while the remained crystallites exhibit decreased NTE in an extended temperature window. Ultra-low thermal expansion can be reached and the NTE can be totally adjusted through self-compensation effect.

Samples with different particle sizes were made through energetic ball milling. For small particles, high-resolution TEM (transmission electron microscopy) images indicate the mixture of a high fraction of amorphous structures and nanocrystallites full of atomic defects. The amounts of the amorphous structure were estimated by high-resolution neutron powder diffraction (NPD).

Figure 9 shows ΔL/L vs. temperature for the bonded particles compared to the bulk, which was measured by using high-resolution strain gauge. One can notice that the maximal ΔL/L declines while the operating ΔT significantly broadens with reducing particle size. For small particles P3 (2–5 μm) and P4 (1–2 μm), NTE dominates in the entirely measured temperature range from 310 K to 100 K.

For the smallest particles with size P5 (0.3–1 μm), the NTE disappears and turns out to be ultra-low PTE, and the CTE α is as small as $+ 0.68 \times 10^{-6}$/K from 200 to 310 K. This result suggests that the material can be also useful as a ZTE material, in addition to be used as compensators for PTE material. Moreover, one can notice that the low NTE for P4 (1–2 μm) and the ultra-low PTE for P5 (0.3–1 μm) is nearly independent of temperature in the corresponding temperature region (see the pink lines in **Figure 9**), which is appreciable for practical applications.

The tunable CTE with particle size originates from the coexistence of crystalline phases and amorphous structure, particularly for the small particles. Variable temperature XRD and neutron NPD studies revealed that the phase ratio changes remarkably with crystallite size. About 7, 14.5, 38.5, 44.8, and 55.2% austenitic phase lost the martensitic transformation and remains the hexagonal structure down to low temperature for the particles P1 (10–20 μm), P2 (5–10 μm), P3 (2–5 μm), P4 (1–2 μm), and P5 (0.3–1 μm), respectively.

Figure 10 shows the unit cell volume as a function of temperature (*V-T* curve) for the orthorhombic structure (red dot), hexagonal structure (blue dot), and the weighted average volume $\bar{V}$ (black dot) calculated based on the refined phase fraction. Moreover, the temperature dependence of lattice volume was fit based on the Grüneisen law, and the results agree well with the refined results for either orthorhombic or hexagonal phase.

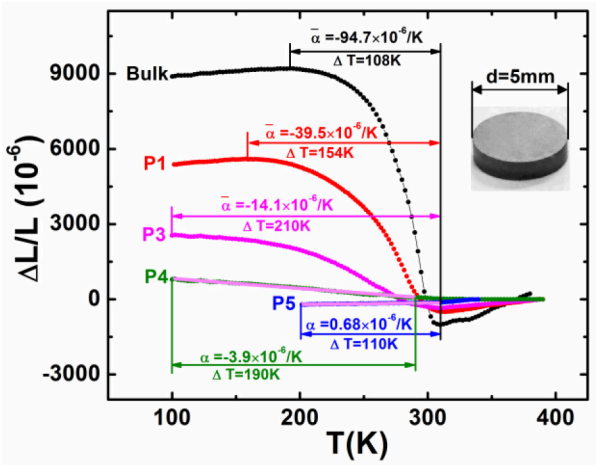

FIGURE 9 | Linear thermal expansion ΔL/L as a function of temperature for the bonded $MnCoGe_{0.99}In_{0.01}$ samples with different particle size in comparison to the bulk (the reference temperature is 390 K). Particle size: P1 (10–20 μm), P3 (2–5 μm), P4 (1–2 μm), and P5 (0.3–1 μm). The morphology of the bonded sample is shown in the inset. Adapted from Shen et al. (2017). APL Materials, Vol. 5, Article ID 106102, (2017); licensed under a Creative Commons Attribution (CC BY) license.

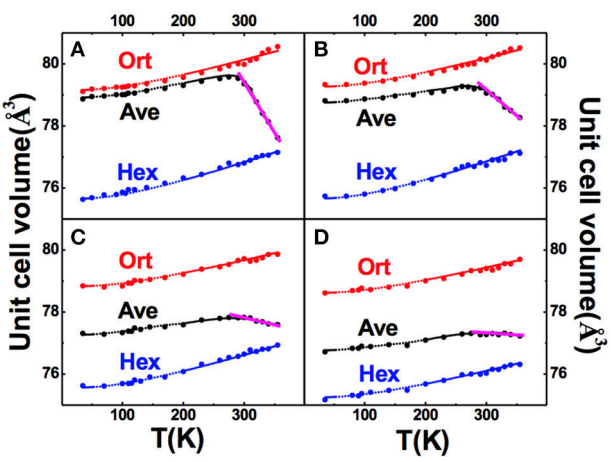

FIGURE 10 | Refined unit cell volumes of martensitic structure (red dot), austenitic structure (blue dot), and the weighted average (black dot), as a function of temperature for the overall crystalline phases of various particles of $MnCoGe_{0.99}In_{0.01}$: **(A)** P_1(10~20 μm), **(B)** P_2(5~10 μm), **(C)** P_4(1~2 μm), **(D)** P_5(0.3~1 μm). The fitting curves according to Grüneisen law are represented by the small dots. Adapted from Shen et al. (2017). APL Materials, Vol. 5, Article ID 106102, (2017); licensed under a Creative Commons Attribution (CC BY) license.

From **Figure 10** (black curve), one can notice that PTE occurs below 290 K and turns to be NTE above this point. TEM studies indicated that crystallite size reduces with particle size, and the average crystallite sizes are about 15 nm and 8 nm for P4 (1–2 μm) and P5 (0.3–1 μm), respectively. With reducing the crystallite size, the both PTE and NTE coefficients decline, which are mainly caused by the instability of magnetostructural transformation due to residual stress and defects.

On the other hand, the contribution from amorphous structure cannot be ignored, noting the amount reaches 40% for the smallest particles P5(0.3∼1 μm). Detailed analysis indicated that the amorphous structure shows positive thermal expansion (PTE), and its compensation effect plays an essential role in the realization of ultra-low expansion even if the possible contribution from the small fraction of epoxy was considered. Details were given in the Supplementary Material in Shen et al. (2017).

Colossal Negative Thermal Expansion in Fine-Powdered $Mn_{0.98}CoGe$

In 2016, Lin et al. prepared fine-powdered $Mn_{0.98}CoGe$ by two ways of high energy ball milling (BM) and repeated thermal cycling (TC) across the martensitic transformation, and compared the NTE behaviors (Lin et al., 2016). It was found that the both ways can make the temperature window (ΔT) of NTE broadening. For the powders experienced TC for ten times, the ΔT broadens to 90 K (309–399 K), and the CTE is about $\alpha_L \sim -141 \times 10^{-6}$/K.

The SEM result showed that the average particle size for the powder of $Mn_{0.98}CoGe$ alloy through 10 times of TC treatments is 8.2 μm, and for the powder through 0.5, 5, and 12 h of BM process are 7.4, 3.9, and 2.2 μm, respectively.

Figures 11A–D display the refined phase fractions for both orthorhombic and hexagonal phases based on the variable temperature XRD patterns for typical samples. For the powders experienced TC for 10 times, the transition of two phases is ∼98%. For the powders prepared by BM for 0.5 h, the martensite transformation is broadened, and the transition ratio decreased to ∼93%. With increasing BM time to 5 and 12 h, the martensite transformation window was further broadened, and the transition ratio reduced to ∼60 and 36%, respectively.

Figures 11E–H show the corresponding volumetric thermal expansion coefficient (α_V) calculated based on the refined phase volume and fraction. For the powders experienced TC for 10 times, NTE effect appears between 309 and 399 K (ΔT = 90 K), and the corresponding α_V is about -423×10^{-6}/K. For the powders prepared by BM for 0.5 h, ΔT extends to 135 K (from 258 to 393 K), and α_V value becomes -238×10^{-6}/K. Further increasing BM time to 5 and 12 h results in the decreases of both ΔT and α_V, and the α_V values are about -135×10^{-6}/K (236–366 K, ΔT = 130 K) and -93×10^{-6}/K (264–303 K, ΔT = 39 K), respectively. The corresponding linear α_L values are about -141×10^{-6}/K (ΔT = 90 K), -79.6×10^{-6}/K (ΔT = 135 K), -45×10^{-6}/K (ΔT = 130 K), and -31×10^{-6}/K (ΔT = 39 K) for the samples experienced TC for 10 times, BM for 0.5 h, BM for 5 h, and BM for 12 h, respectively.

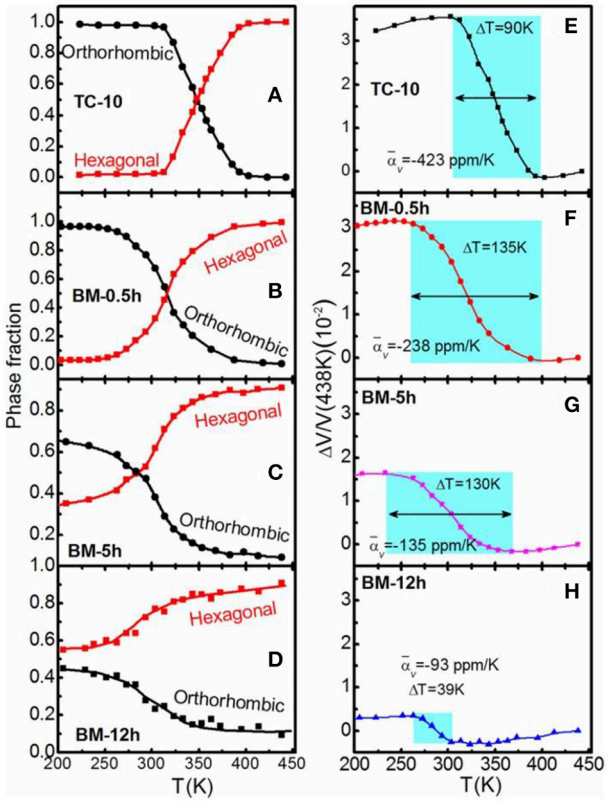

FIGURE 11 | The temperature dependent phase fraction for the $Mn_{0.98}CoGe$ samples prepared by **(A)** TC for 10 times, **(B)** BM for 0.5 h, **(C)** BM for 5 h, and **(D)** BM for12 h; The temperature dependent volumetric thermal expansions $\Delta V/V$ (the reference temperature is 438 K) for the corresponding samples is shown in **(E–H)**, respectively. The NTE temperature region is highlighted for all samples. Reprinted with permission from Lin et al. (2016).

For the samples experienced TC for 10 times, the both temperature window of NTE and the α_L magnitude are larger than those of typical NTE material $Bi_{0.95}La_{0.05}NiO_3$ ($\alpha_L = -137 \times 10^{-6}$/K, 320–380 K) (Azuma et al., 2011). This α_L magnitude for the samples experienced TC for 10 times is several times larger than that of common metals (Takenaka et al., 2012) and even larger than that of most polymers (Sullivan and Lukehart, 2005; Chu et al., 2012; Takenaka and Ichigo, 2014).

The NTE behavior has different origins for the samples prepared by the two ways. For the powder prepared by BM, the broadening of temperature window of martensitic transformation originates from the accumulated residual strain. With increasing the BM time, the overall NTE window first expands and then shrinks. For the powder prepared by TC, the sample does not suffer any external pressure, and the introduced strain is thus weaker than the case by BM, hence leading to the completely different evolution of phase transition with temperature.

All these results suggest the TC or slightly BM treatments can both extend temperature interval and optimize the NTE properties, which have high potential applications as the PTE compensators by forming composites.

Negative Thermal Expansion in Mn-Co-Ge-In Thin Films

In recent years, many materials with magnetostructural transition, such as $Gd_5Si_2Ge_2$ (Pires et al., 2015), FeRh (Zhou et al., 2013), metamagnetic NiMn-based Heusler alloys (Akkera et al., 2015), and MnAs (Mosca et al., 2008), have been explored in nanostructured thin films, aiming to activate novel properties and explore applications in micro-scale of these materials. Recently, Liu et al. firstly explored the fabrication of MnCoGe-based alloy films, and studied the magnetocaloric effect and thermal expansion behaviors of the films obtained (Liu et al., 2018).

$MnCoGe_{0.995}In_{0.005}$ films with thickness of 45 nm were successfully grown on (001)–$LaAlO_3$, (001)–$SrTiO_3$, and (0001)–Al_2O_3 substrates by using pulsed laser deposition (PLD) technique. It was found that the obtained films exhibit three dimensional growth mode, and the island size varies for thin films grown on different substrates. Room temperature XRD patterns imply that the films crystallize in mixed hexagonal and orthorhombic structures, which are textured along the out of plane (00*l*) direction for the hexagonal structure and (*h*00) orientations for the orthorhombic structure. For all the films, there exists obvious thermal hysteresis between the heating and cooling process in a wide temperature range, indicating that first-order magnetostructural transformation was retained. Moreover, the temperature window of the transformation for the films significantly broadened compared to that of the bulk alloy.

The broadened magnetostructural transformation of Mn-Co-Ge-In films can be ascribed to the stress effect and crystalline defects. Besides, the commercially supplied Al_2O_3, $SrTiO_3$, and $LaAlO_3$ substrates have positive linear thermal expansion coefficients $+ 7.5 \times 10^{-6}$/K, $+ 9.4 \times 10^{-6}$/K, and $+ 1 \times 10^{-5}$/K, respectively. Consequently, the different films denote tunable negative thermal expansion due to different island size and strain state of the films along with the compensating effect from substrates. As can be seen from **Figure 12**, for Mn-Co-Ge-In/Al_2O_3 and Mn-Co-Ge-In/$SrTiO_3$, the NTE coefficients are -6.56×10^{-6}/K (from 270 K to 390 K) and -4.82×10^{-6}/K (from 290 K to 390 K), respectively. These values are a bit smaller in comparison to those of the well-known commercial NTE materials ZrW_2O_8 (-9×10^{-6}/K). Otherwise, the Mn-Co-Ge-In/LAO with the smallest island size denotes near-zero CTE of -2×10^{-6}/K in the temperature range from 290 to 390 K.

The deposition of films completely overcomes the brittleness nature of Mn-Co-Ge-In alloy and much more durable. Repeated experiments demonstrated that the NTE behavior is completely repeatable between different cycles for the all films (**Figure 12**). All the results denotes that durable thin films with different CTE can be designed through choosing appropriate substrates or introducing a buffer layer, which would be quite useful for practical applications.

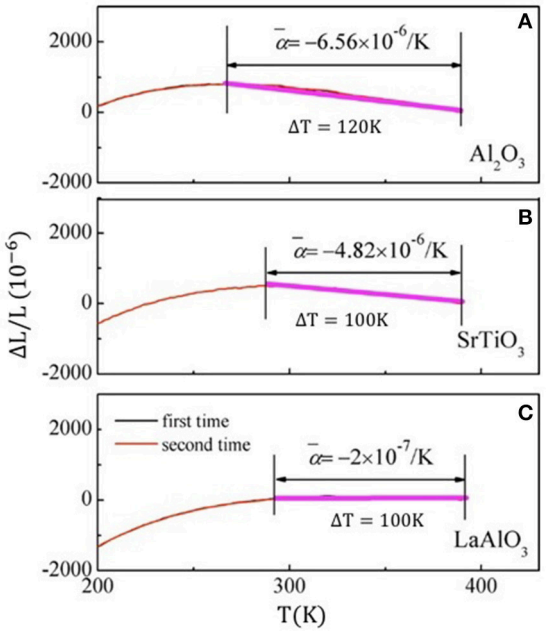

FIGURE 12 | Temperature dependent linear thermal expansion ΔL/L for the Mn-Co-Ge-In thin films grown on Al_2O_3 **(A)**, $SrTiO_3$ **(B)**, $LaAlO_3$ **(C)**. Each has been repeated at least two times. Reprinted with permission from Liu et al. (2018).

Negative Thermal Expansion in Fe-Doped MnNiGe Composites

Similar to MnCoGe-based alloys, MnNiGe-based alloys also denote NTE due to the martensitic transition from Ni_2In-type hexagonal to TiNiSi-type orthorhombic structure. Still, Fe-doped MnNiGe alloys naturally crack into small pieces after annealing. Recently, by preparing the alloy through solid state interaction, Zhao et al. (2018) reported the NTE of MnNiGe-based alloy. The average CTE of $Mn_{0.9}Fe_{0.1}NiGe$ alloy with Fe replacing Mn reaches a giant value of $\alpha_L \sim -285.23 \times 10^{-6}$ K in a temperature window from 192 to 305 K ($\Delta T = 113$ K), while the α_L of $MnNi_{0.9}Fe_{0.1}Ge$ alloy with Fe replacing Ni reaches $-1{,}167 \times 10^{-6}$/K in a narrow temperature window (246–305 K, $\Delta T = 59$ K). The introduction of Fe changes the magnetic state of martensitic phase from the spiral AFM structure into FM state.

Furthermore, commercial Cu powders with positive thermal expansion has been chosen as the matrix metal, both acting as the compensators to control CTE and bonder to increase the mechanical properties of the alloy. The study (Zhao et al., 2018) revealed that the introduced Cu powers rarely react with the Fe-doped MnNiGe alloy. The cracks and holes can be filled by Cu particles, and the resulted MnNiGe/*x*%Cu composites is more compact with increasing Cu contents. The CTE of both $Mn_{0.9}Fe_{0.1}NiGe$ and $MnNi_{0.9}Fe_{0.1}Ge$ alloy decreases by introducing 35% Cu, as shown in **Figure 13A**. The linear thermal expansion behavior of $Mn_{0.92}Fe_{0.08}NiGe$/*x*% Cu and $Mn_{0.84}Fe_{0.16}NiGe$/*x*% Cu are presented in **Figures 13B,C**. The absolute CTE values of the two serials of composites decrease and the NTE temperature windows become narrow with increasing the Cu ratio. Increasing the Cu content to 70%, the composites display near-ZTE behaviors due to the compensation effect between the PTE properties of Cu matrix and the NTE properties of Fe-doped MnNiGe alloys. A low thermal expansion behavior with a CTE $\alpha_L \sim -4.73 \times 10^{-6}$/K was observed in a temperature

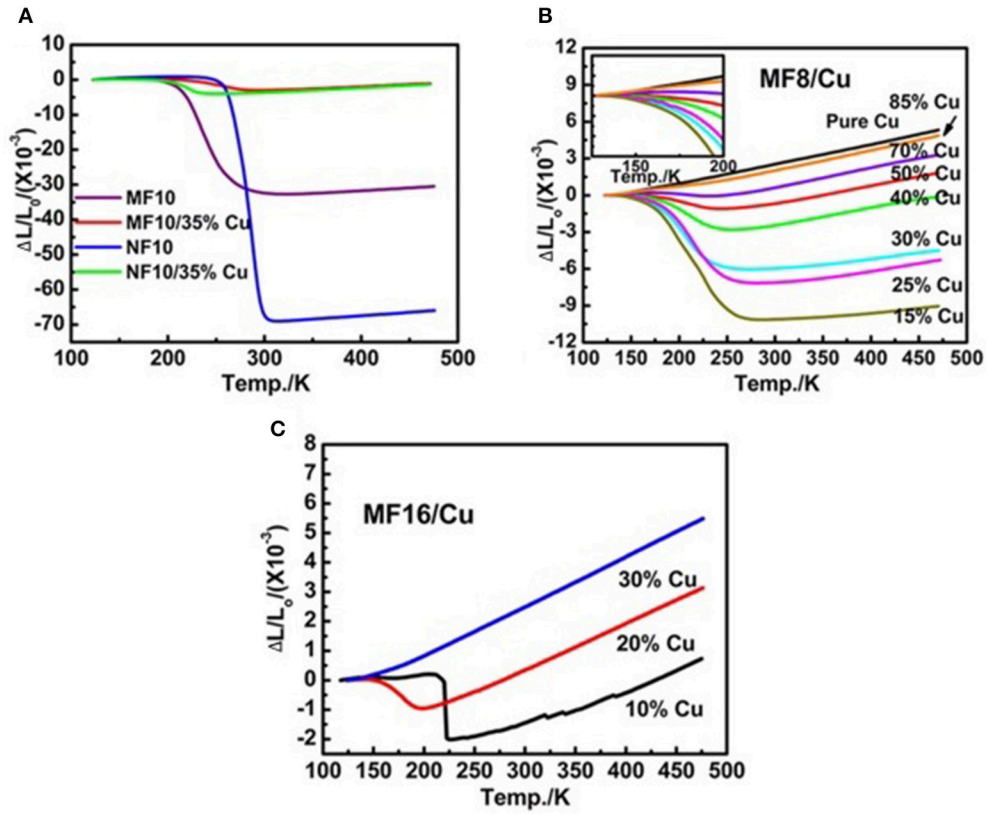

FIGURE 13 | The temperature dependence of $\Delta L/L_0$ curves of **(A)** $Mn_{0.9}Fe_{0.1}NiGe$, $MnNi_{0.9}Fe_{0.1}Ge$, $Mn_{0.9}Fe_{0.1}NiGe$/35%Cu and $MnNi_{0.9}Fe_{0.1}Ge$/35%Cu, **(B)** $MnNi_{0.92}Fe_{0.08}Ge$/*x*%Cu (*x* = 15, 25, 30, 40, 50, 70, 85, 100), and **(C)** $MnNi_{0.94}Fe_{0.16}Ge$ /*x*%Cu (*x* = 10, 20, 30), where the L_0 is the length of the sample at 123 K. Reproduced under a Creative Commons Attribution 4.0 International License from (Zhao et al., 2018).

range from 173 to 229 K ($\Delta T = 56$ K). In $MnNi_{0.92}Fe_{0.08}$/10%Cu composite, a low $\alpha_L \sim 1.16 \times 10^{-6}$ /K is also achieved in a wide temperature range from 125 to 215 K ($\Delta T = 90$ K).

In addition, the mechanical performance can be enhanced for the Fe-doped MnNiGe compounds with Cu as binders. All these suggest the high potential of the composites as NTE materials.

RCo_2 COMPOUNDS

Crystal Structure

The cubic Laves phases RCo_2 (R = rare earth elements) have intensively been studied for the rich magnetic properties, which arise from the highly localized 4f electrons of rare earth elements and the interactions with the itinerant 3d electrons of the transition elements. For the RCo_2 with R = Nd, Pr, Sm, Gd, Tb, Tm, the magnetic transition is of second-order in nature, while for R = Dy, Ho, and Er, the magnetic transition becomes of first-order (Khmelevskyi and Mohn, 2000). RCo_2 compounds have a cubic Laves C15 structure with space group $Fd\bar{3}m$ around room temperature. In the cubic C15 structure, rare atoms locate at sites 8(a) (0.125, 0.125, 0.125) and Co atoms at sites 16(d) (0.5, 0.5, 0.5) (**Figure 14A**; Ouyang et al., 2005a). With temperature decreasing, $ErCo_2$ and $TbCo_2$ exhibit a rhombohedral distortion (space group $R\bar{3}m$) below Curie temperature T_C (Ouyang et al., 2005a; Kozlenko et al., 2015). At low temperature, Er (Tb), Co1, and Co2 atoms occupy Wyckoff sites 6c (0, 0, z), 3b (0, 0, 0.5) and 9e (0.5, 0, 0), respectively. **Figure 14B** shows the crystal and magnetic structure of the $TbCo_{1.9}Fe_{0.1}$ compound at 10 K, the moments of Tb and Co atoms are antiparallel alignment along the c axis, which is similar to that of $ErCo_2$ and $TbCo_2$. However, $NdCo_2$ and $HoCo_2$ (Ouyang et al., 2005b; Mudryk et al., 2016) undergo two crystallographic transitions: the room temperature cubic lattice (space group $Fd\bar{3}m$) transforms into the tetragonal one ($I4_1/amd$) at T_C, and then becomes orthorhombic (space group: Fddd) below spin orientation T_{SR}.

Magnetocaloric Effect

Numerous studies have been carried out on phase transition and magnetocaloric effect (MCE) for RCo_2 compounds (Wada et al., 1999, 2001; Duc et al., 2002; Gomes et al., 2002; Wang et al., 2002a,b, 2003; Liu and Altounian, 2005). Experimental and theoretical investigations show that the compounds with R = Er, Ho, and Dy show giant MCE owing to the first-order nature of magnetic transition. In 2001, Wada et al. reported the MCE of single crystal $ErCo_2$. The maximum magnetic entropy change, $-\Delta S$, is as high as 10.6 J mol^{-1} K^{-1} (37.2 J kg^{-1} K^{-1}) and the maximal adiabatic temperature change, ΔT_{ad}, reaches ~9.2 K under a magnetic field change of 0–5 T (Wada et al., 1999). Owing

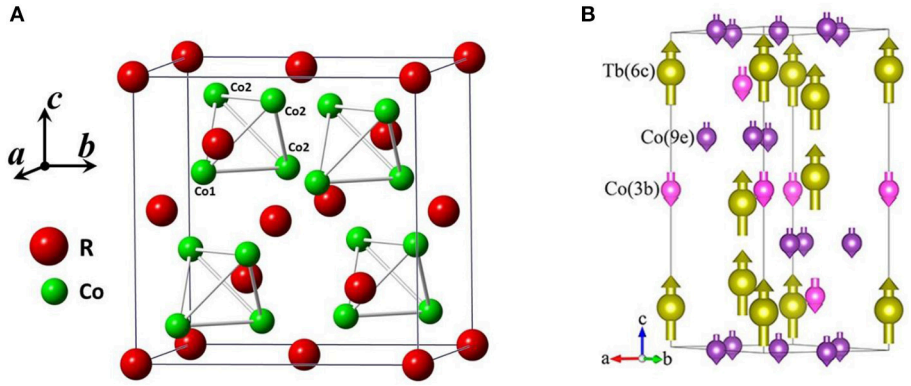

FIGURE 14 | (A) Schematic of crystal structure for RCo_2 cubic Laves phase(space group $Fd\bar{3}m$). **(B)** Crystal and magnetic structure of $TbCo_{1.9}Fe_{0.1}$ compound with rhombohedral distortion (space group $R\bar{3}m$) at 10 K. **(B)** reprinted with permission from (Song et al., 2018). Copyright 2018, ACS Publishing Limited.

to the large MCE, $ErCo_2$ is usually considered to be a standard material for comparison in the low temperature region around 30 K. Furthermore, the maximum entropy change of $DyCo_2$ and $HoCo_2$ is 11 and 20 J kg^{-1} K^{-1} (Duc et al., 2002) under 0–5 T, respectively. The large MCE of RCo_2 compounds is relevant to the large magnetic moment of R atoms, and more importantly, the crystallographic transition with negative volume expansion of different amplitudes also plays a key role for the various MCE. A small magnetic moment is induced in Co atoms, which is usually antiparallel to R atoms, resulting in the ferrimagnetic nature of the compounds.

In addition, some studies indicated that the replacement of R atoms by other Lanthanide elements can regulate the phase transition and MCE. Liu et al. (Liu and Altounian, 2005) reported that the Curie temperature of $(Er_{1-x}Gd_x)Co_2$ increases from 32 to 403 K with the substitution of Er by Gd. However, the maximum value of -ΔS under 0–5 T decreases from 15.3 J kg^{-1} K^{-1} at $x = 0.1$ to 3.2 J kg^{-1} K^{-1} at $x = 0.6$. Furthermore, it has been found that the substitution of Dy by Gd will rapidly reduce the MCE in $DyCo_2$ (Wang et al., 2002b), but replacing Tb with Er increases the MCE of $TbCo_2$ (Gomes et al., 2002). On the other hand, Wang et al. (2002a) reported that using 7% of Si to replace Co can increase the Curie temperature of $DyCo_2$ up to 168 K, but weakens the first-order phase transition properties and causes a significant reduction in the magnetocaloric effect. It is worth mentioning that the replacement of Co by Ni lowers T_C of $Ho(Co_{1-x}Ni_x)_2$, while the large MCE is retained up to $x = 0.1$ though the phase transition changed from first-order to the second-order in nature (Wada et al., 2001).

Negative Thermal Expansion Behaviors

In RCo_2 compounds with R = Dy, Ho, and Er, the magnetic ordering around T_C is accompanied by negative thermal expansion of lattice. Recently, Song et al. reported a wide temperature ZTE in the $Tb(Co, Fe)_2$ and found a negligible thermal expansion coefficient, α_L, in $TbCo_{1.9}Fe_{0.1}$, which is nearly two orders smaller than that of the common alloys (Song et al., 2018).

Figure 15A displays the temperature dependent linear thermal expansion ($\Delta L/L_0$) for $Tb(Co_{2-x}Fe_x)$ compounds. It is found that the NTE and PTE can be obtained by adjusting the Fe concentration in $Tb(Co_{2-x}Fe_x)$. Remarkably, the $TbCo_{1.9}Fe_{0.1}$ compound exhibits a ZTE property over a wide temperature range from 123 to 307 K. The average linear CTE of $Tb(Co_{1.9}Fe_{0.1})$ is $\alpha_L = 0.48 \times 10^{-6}$ K^{-1} and intrinsic unit cell also confirmed the reliability of ZTE which was determined by SXRD (synchrotron X-ray diffraction), as shown in **Figure 15B**. This CTE of $Tb(Co_{1.9}Fe_{0.1})$ is about two orders of magnitude smaller than that of the Al ($\alpha_L = 23.1 \times 10^{-6}$ K^{-1}) and Cu ($\alpha_L = 17.7 \times 10^{-6}K^{-1}$). Furthermore, this value is also smaller than the CTE of Invar alloys with composition $Fe_{0.65}Ni_{0.35}$ ($\alpha_L = 1.5 \times 10^{-6}$ K^{-1}, 193–373 K) (Guillaume, 1897).

The magnetic moment of Tb atoms, M_{Tb}, plays a dominationg role in the ferrimagnetic nature of the $Tb(Co_{2-x}Fe_x)$ compounds. The spontaneous volume magnetostriction (ω_s) was used to quantitatively describe the contribution of magentovolume effect to the abnormal change of lattice. For $TbCo_{1.9}Fe_{0.1}$, and the ω_s is denoted by $\omega_s = \omega_{exp}$-ω_{nm},where ω_{exp} is the unit cell volume obtained by NPD, and ω_{nm} is calculated based on the Debye-Grüneisen relationship. A strong correlation between M_{Tb}^2 and ω_s was denoted by the equation $\omega_s(T) = k\ C\ M(T)^2$, where k and C represent compressibility and magnetovolume coupling constant, and M(T) the amplitudes of magnetization (Gruneisen and Goens, 1926; Sayetat et al., 1998). That is to say, the spontaneous magnetostriction is closely related to the magnetization. The decrease of magnetization with temperature is responsible for the negative contribution to volume expansion, which neutralizes the normal lattice expansion, and hence produces the ZTE.

A BRIEF INTRODUCTION ON ANTIPEROVSKITE COMPOUNDS

Antiperovskite compounds A_3BC (A = Fe, Mn; B = Ga, Sn, Cu, Zr, Fe, Co; C = C, N, H) are well-known (Takenaka and Takagi, 2005; Iikubo et al., 2008; Sun et al., 2010a,b, 2012; Song

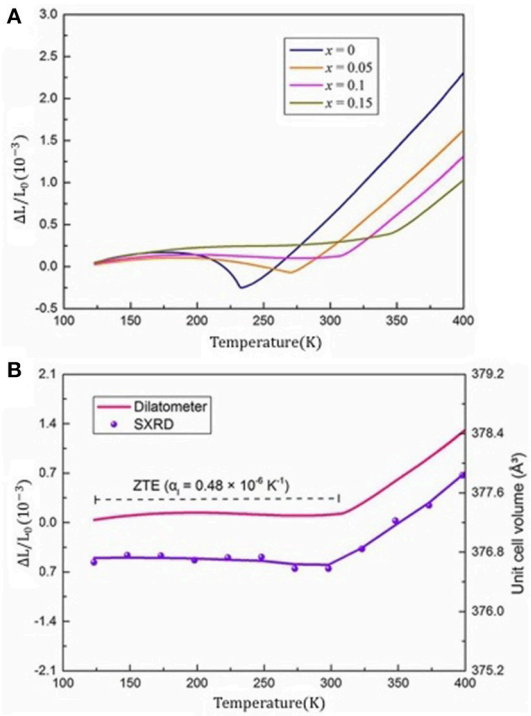

FIGURE 15 | (A) Temperature dependent linear thermal expansion ($\Delta L/L_0$) of $Tb(Co_{2-x}Fe_x)$. **(B)** The ZTE in the $TbCo_{1.9}Fe_{0.1}$ measured by both dilatometer and SXRD. Reprinted with permission from (Song et al., 2018). Copyright 2018, ACS Publishing Limited.

et al., 2011; Wang et al., 2012; Lin et al., 2015; Shi et al., 2016, 2018; Guo et al., 2018) for the rich characteristics of NTE and ZTE, as well as the baromagnetic, and barocaloric properties, though the comprehensive performance of MCE is not as good as the conventional material Gd around room temperature. This material has a very large family, which shows rich magnetic and lattice structure depending on compositions and atomic occupations. Experts, such as C. Wang's group and Y.P. Sun's group, have done a lot of excellent studies in the antiperovskite compounds, particularly on the NTE properties. Moreover, fascinating properties were also reported in some compositions, such as baromagnetic (Shi et al., 2016), barocaloric effect caused by spin frustration (Matsunami et al., 2015), and large magnetocaloric effect (Sun et al., 2012). Specifically, C. Wang' group have reported a large amount of research work on NTE and MCE in antiperovskite compounds and also thought that lattice entropy is important to be excited due to large negative thermal expansion behavior driven by magnetic effects in the antiperovskite compounds so as to improve the magnetocaloric effect. A specific review article focusing on the antiperovskite compounds should be summarized separately, and we do not address more here.

CONCLUSION

In summary, negative thermal expansion (NTE) behaviors in the materials with giant magnetocaloric effects (MCE) have been reviewed. Representative materials including $La(Fe,Si)_{13}$, MM'X, and RCo_2 have been included. Antiperovskite compounds are also briefly introduced. MCE materials are used for magnetic refrigeration while NTE materials for thermal compensation. Although the materials have distinct applications, the physical sources are similar particularly for the novel MCE and phase-transition-type NTE materials, both originating from the strong spin-lattice coupling. A number of MCE materials show abnormal lattice expansion owing to magnetic interactions, which provides a natural platform for exploring negative thermal expansion materials. The magnetostructural transformation in the giant MCE materials can be adjusted by utilizing its sensitivity to chemical/physical pressure, hence abnormal lattice expansion in an extended temperature range can be achieved. The present review provides implications for developing novel NTE materials and multifunctional devices.

AUTHOR CONTRIBUTIONS

FH wrote the article in cooperation with FS, JH, and YL. All authors reviewed the manuscript.

FUNDING

This work was supported by the National Key Research and Development Program of China (Grant Nos. 2017YFB0702702, 2018YFA0305704, 2014CB643700, and 2017YFA0303601), the National Natural Sciences Foundation of China (Grant Nos. 51531008, U1832219, 51771223, 51590880, and 11474341), and the Key Program and Strategic Priority Research Program (B) of the Chinese Academy of Sciences.

REFERENCES

Akkera, H. S., Singh, I., and Kaur, D. (2015). Martensitic phase transformation of magnetron sputtered nanostructured Ni–Mn–In ferromagnetic shape memory alloy thin films. *J. Alloys Compd.* 642, 53–62. doi: 10.1016/j.jallcom.2015.03.261

Annaorazov, M. P., Nikitin, S. A., Tyurin, A. L., Asatryan, K. A., and Dovletov, A. (1996). Anomalously high entropy change in FeRh alloy. *J. Appl. Phys.* 79, 1689–1695. doi: 10.1063/1.360955

Azuma, M., Chen, W. T., Seki, H., Czapski, M., Olga, S., Oka, K., et al. (2011). Colossal negative thermal expansion in $BiNiO_3$ induced by intermetallic charge transfer. *Nat. Commun.* 2:347. doi: 10.1038/ncomms1361

Caron, L., Trung, N. T., and Bruck, E. (2011). Pressure-tuned magnetocaloric effect in $Mn_{0.93}Cr_{0.07}CoGe$. *Phys. Rev. B* 84, 020414– 020417. doi: 10.1103/PhysRevB.84.020414

Chen, J., Nittala, K., Forrester, J. S., Jones, J. L., Deng, J. X., Yu, R. B., et al. (2011). The Role of Spontaneous Polarization in the Negative Thermal Expansion of Tetragonal $PbTiO_3$-Based Compounds. *J. Am. Chem. Soc.* 133, 11114–11117. doi: 10.1021/ja2046292

Chu, X. X., Wu, Z. X., Huang, C. J., Huang, R. J., Zhou, Y., and Li, L. F. (2012). ZrW_2O_8-doped epoxy as low thermal expansion insulating materials for superconducting feeder system. *Cryogenics* 52, 638–641. doi: 10.1016/j.cryogenics.2012.04.016

Du, Z. C., Zhu, M. R., Wang, Z. G., and Yang, J. G. (2016). Design and application of composite platform with extreme low thermal deformation for satellite. *Compos. Struct.* 152, 693–703. doi: 10.1016/j.compstruct.2016.05.073

Duc, N. H., Anh, D. T. K., and Brommer, P. E. (2002). Metamagnetism, giant magnetoresistance and magnetocaloric effects in RCo_2-based compounds in the vicinity of the Curie temperature. *Phys. B* 319, 1–8. doi: 10.1016/S0921-4526(02)01099-2

Fujita, A., Fujieda, S., Hasegawa, S., and Fukamichi, K. (2003). Itinerant-electron metamagnetic transition and large magnetocaloric effects in $La(Fe_xSi_{1-x})_{13}$ compounds and their hydrides. *Phys. Rev. B* 67:104416. doi: 10.1103/PhysRevB.67.104416

Gercsi, Z., Hono, K., and Sandeman, K. G. (2011). Designed metamagnetism in $CoMnGe_{1-x}P_x$. *Phys. Rev. B* 83:174403. doi: 10.1103/PhysRevB.83.174403

Gomes, A. M., Reis, M. S., Oliveira, I. S., Guimar, A. P., and Takeuchi, A. Y. (2002). Magnetocaloric effect in (Er, Tb)Co_2. *J. Magn. Magn. Mater.* 242. 870–872. doi: 10.1016/S0304-8853(01)01327-0

Gruneisen, E., and Goens, E. (1926). Tests on metal crystals IV thermo electrical characteristics of zinc and cadmium. *Z. Phys.* 37, 278–291. doi: 10.1007/BF01397101

Gschneidner, K. A., Pecharsky, A., and Dennis, K. W. (1997). Some observations on the Gd-rich side of the Gd-C system. *J. Alloys Compd.* 260, 107–110. doi: 10.1016/S0925-8388(97)00146-1

Gschneidner, K. A. Jr., Pecharsky, V. K., and Tsokol, A. O. (2005). Recent developments in magnetocaloric materials. *Rep. Prog. Phys.* 68, 1479–1539. doi: 10.1088/0034-4885/68/6/R04

Guillaume, C. É. (1897). Investigations on Nickel and its alloys. *CR. Acad. Sci.* 125:18.

Guo, X. G., Tong, P., Lin, J. C., Yang, C., Zhang, K., Lin, S., et al. (2018). Effects of Cr substitution on negative thermal expansion and magnetic properties of antiperovskite Ga1–xCrxN0.83Mn3 compounds. *Front. Chem.* 6:75. doi: 10.3389/fchem.2018.00075

Hu, F. X. (2002). *Magnetic Properties and Magnetic Entropy Change of Fe-Based La(Fe,M)13 Compounds and Ni-Mn-Ga Alloys*. Ph. D thesis, Institute of Physics, Chinese academy of Sciences.

Hu, F. X., Gao, J., Qian, X. L., Ilyn, M., Tishin, A. M., Sun, J. R., et al. (2005). Magnetocaloric effect in itinerant electron metamagnetic systems $La(Fe_{1-x}Cox)_{11.9}Si_{1.1}$. *J. Appl. Phys.* 97:10M303. doi: 10.1063/1.1847071

Hu, F. X., Shen, B. G., and Sun, J. R. (2000a). Magnetic entropy change in $Ni_{51.5}Mn_{22.7}Ga_{25.8}$ alloy. *Appl. Phys. Lett.* 76, 3460–3462. doi: 10.1063/1.126677

Hu, F. X., Shen, B. G., Sun, J. R., Cheng, Z. H., Rao, G. H., and Zhang, X. X. (2001). Influence of negative lattice expansion and metamagnetic transition on magnetic entropy change in the compound $LaFe_{11.4}Si_{1.6}$. *Appl. Phys. Lett.* 78, 3675–3677. doi: 10.1063/1.1375836

Hu, F. X., Shen, B. G., Sun, J. R., Wang, G. J., and Cheng, Z. H. (2002). Very large magnetic entropy change near room temperature in $LaFe_{11.2}Co_{0.7}Si_{1.1}$. *Appl. Phy. Lett.* 80, 826–828. doi: 10.1063/1.1447592

Hu, F. X., Shen, B. G., Sun, J. R., and Zhang, X. X. (2000b). Great magnetic entropy change in La (Fe, $M)_{13}$ (M = Si, Al) with Co doping. *Chin. Phys.* 9, 550–553. doi: 10.1088/1009-1963/9/7/016

Huang, R. J., Liu, Y. Y., Fan, W., Tan, J., Xiao, F. R., Qian, L. H., et al. (2013). Giant negative thermal expansion in $NaZn_{13}$-Type La(Fe, Si, $Co)_{13}$ compounds. *J. Am. Chem. Soc.* 135, 11469–11472. doi: 10.1021/ja405161z

Iikubo, S., Kodama, K., Takenaka, K., Takagi, H., Takigawa, M., and Shamoto, S. (2008). Local lattice distortion in the giant negative thermal expansion material $Mn_3Cu_{1-x}Ge_xN$. *Phys. Rev. Lett.* 101:205901. doi: 10.1103/PhysRevLett.101.205901

Khmelevskyi, S., and Mohn, P. (2000). Order of the magnetic phase transitions in RCo_2 (R = rare earth) intermetallic compounds. *J. Phys. Condens. Matter.* 12, 9453–9464. doi: 10.1088/0953-8984/12/45/308

Kozlenko, D. P., Burzo, E., Vlaic, P., Kichanov, S. E., Rutkauskas, A. V., and Savenko, B. N. (2015). Sequential cobalt magnetization collapse in $ErCo_2$: beyond the limits of itinerant electron metamagnetism. *Sci. Rep.* 5:8620. doi: 10.1038/srep08620

Krenke, T., Duman, E., Acet, M., Wassermann, E. F., Moya, X., Manosa, L., et al. (2005). Inverse magnetocaloric effect in ferromagnetic Ni-Mn-Sn alloys. *Nature Mater.* 4, 450–454. doi: 10.1038/nmat1395

Krypiakewytsch, P. I., Zaretsch, O. S., Hladysch, E. I., and Bodak, O. I. (1968). Ternary compounds of $NaZn_{13}$ type. *Z. Anorg. Allg. Chem.* 358:90. doi: 10.1002/zaac.19683580110

Li, S. P., Huang, R. J., Zhao, Y. Q., Wang, W., Han, Y. M., and Li, L. F. (2017). Zero thermal expansion achieved by an electrolytic hydriding method in $La(Fe, Si)_{13}$ compounds. *Adv. Func. Mater.* 27:1604195. doi: 10.1002/adfm.201604195

Lin, J. C., Tong, P., Tong, W., Lin, S., Wang, B. S., Song, W. H., et al. (2015). Tunable negative thermal expansion related with the gradual evolution of antiferromagnetic ordering in antiperovskite manganese nitrides Ag1-xNMn3+x ($0 \leq x \leq 0.6$). *Appl. Phys. Lett.* 106:082405. doi: 10.1063/1.4913663

Lin, J. C., Tong, P., Zhang, K., Tong, H. Y., Guo, X. G., Yang, C., et al. (2016). Colossal negative thermal expansion with an extended temperature interval covering room temperature in fine-powdered $Mn_{0.98}CoGe$. *Appl. Phy. Lett.* 109:241903. doi: 10.1063/1.4972234

Liu, D. M., Huang, Q. Z., Yue, M., Lynn, J. W., Liu, L. J., Chen, Y., et al. (2009). Temperature, magnetic field, and pressure dependence of the crystal and magnetic structures of the magnetocaloric compound Mn1.1Fe0.9(P0.8Ge0.2). *Phys. Rev. B* 80, 174415. doi: 10.1103/PhysRevB.80.174415

Liu, E. K., Wang, W. H., Feng, L., Zhu, W., Li, G. J., Chen, J. L., et al. (2012). Stable magnetostructural coupling with tunable magnetoresponsive effects in hexagonal ferromagnets. *Nat. Commun.* 3:873. doi: 10.1038/ncomms1868

Liu, E. K., Zhu, W., Feng, L., Chen, J. L., Wang, W. H., Wu, G. H., et al. (2010). Vacancy-tuned paramagnetic/ferromagnetic martensitic transformation in Mn-poor $Mn_{1-x}CoGe$ alloys, *Europhys. Lett.* 91:17003. doi: 10.1209/0295-5075/91/17003

Liu, J., Gottschall, T., Skokov, K. P., Moore, J. D., and Gutfleisch, O. (2012). Giant magnetocaloric effect driven by structural transitions. *Nat. Mater.* 11, 620–626. doi: 10.1038/NMAT3334

Liu, X. B., and Altounian, Z. (2005). Magnetocaloric effect in $(Er_{1-x}Gd_x)Co_2$ pseudobinary compounds. *J. Magn. Magn. Mater.* 292, 83–88. doi: 10.1016/j.jmmm.2004.10.100

Liu, Y., Qiao, K. M., Zuo, S. L., Zhang, H. R., Kuang, H., Wang, J., et al. (2018). Negative thermal expansion and magnetocaloric effect in Mn-Co-Ge-In thin films. *Appl. Phys. Lett.* 112:012401. doi: 10.1063/1.5009985

Liu, Y., Shen, F. R., Zhang, M., Bao, L. F., Wu, R. R., Zhao, Y. Y., et al. (2015). Stress modulated martensitic transition and magnetocaloric effect in hexagonal Ni_2In-type $MnCoGe_{1--x}In_x$ alloys. *J. Alloys Compd.* 649, 1048–1052. doi: 10.1016/j.jallcom.2015.07.234

Mary, T. A., Evans, J. S. O., Vogt, T., and Sleight, A. W. (1996). Negative thermal expansion from 0.3 to 1050 Kelvin in ZrW_2O_8. *Science* 272, 90–92. doi: 10.1126/science.272.5258.90

Matsunami, D., Fujita, A., Takenaka, K., and Kano, M. (2015). Giant barocaloric effect enhanced by the frustration of the antiferromagnetic phase in Mn3GaN. *Nature Mater.* 14, 73–78. doi: 10.1038/NMAT4117

Morellon, L., Blasco, J., Algarabel, P. A., and Ibarra, M. R. (2000). Nature of the first-order antiferromagnetic-ferromagnetic transition in the Ge-rich magnetocaloric compounds Gd-5(SixGe1-x)(4). *Phys. Rev. B* 62, 1022–1026. doi: 10.1103/PhysRevB.62.1022

Mosca, D. H., Vidal, F., and Etgens, V. H. (2008). Strain engineering of the magnetocaloric effect in MnAs epilayers. *Phys. Rev. Lett.* 101:125503. doi: 10.1103/PhysRevLett.101.125503

Mudryk, Y., Paudyal, D., Pathak, A. K., Pecharsky, V. K., and Gschneidner, K. A. (2016). Balancing structural distortions via competing 4f and itinerant interactions: a case of polymorphism in magnetocaloric $HoCo_2$. *J. Mater. Chem. C* 4, 4521–4531. doi: 10.1039/c6tc00867d

Namba, Y., Takehara, H., and Nagano, Y. (2001). Fracture strength of zero-thermal-expansion glass-ceramics for ultra-precision components. *CIRP Ann. Manuf. Technol.* 50, 239–242. doi: 10.1016/S0007-8506(07)62113-1

Niziol, S., Weselucha, A., Bazela, W., and Szytula, A. (1981). Magnetic properties of the $Co_xNi_{1--x}MnGe$ system. *Solid State Commun.* 39, 1081–1085. doi: 10.1016/0038-1098(81)90213-1

Ouyang, Z. W., Wang, F. W., Hang, Q., Liu, W. F., Liu, G. Y., Lynn, J. W., et al. (2005a). Temperature dependent neutron powder diffraction study of the Laves phase compound $TbCo_2$. *J. Alloys Compd.* 390, 21–25. doi: 10.1016/j.jallcom.2004.08.028

Ouyang, Z. W., Wang, F. W., Huang, Q., Liu, W. F., Xiao, Y. G., Lynn, J. W., et al. (2005b). Magnetic structure, magnetostriction, and magnetic

transitions of the Laves-phase compound $NdCo_2$. *Phys. Rev. B* 71:064405. doi: 10.1103/PhysRevB.71.064405

Pecharsky, V. K., and Gschneidner, K. A. Jr. (1997). The giant magnetocaloric effect in $Gd_5(Si_2Ge_2)$. *Phys. Rev. Lett.* 78, 4494–4497. doi: 10.1103/PhysRevLett.78.4494

Pires, A. L., Belo, J. H., Gomes, L., Hadimani, R. L., Jiles, D. C., Fernandes, L., et al. (2015). Annealing influence on the magnetostructural transition in $Gd_5Si_{1.3}Ge_{2.7}$ thin films. *Mater. Lett.* 159, 301–304. doi: 10.1016/j.matlet.2015.05.029

Rathmann, C. L., Mann, G. H., and Nordberg, M. E. (1968). A new ultralow-expansion, modified fused-silica glass. *Appl. Opt.* 7:819. doi: 10.1364/AO.7.000819

Sayetat, F., Fertey, P., and Kessler, M. (1998). An easy method for the determination of debye temperature from thermal expansion analyses. *J. Appl. Crystallogr.* 31, 121–127. doi: 10.1107/S0021889897006936

Shen, B. G., Sun, J. R., Hu, F. X., Zhang, H. W., and Cheng, Z. H. (2009). Recent progress in exploring magnetocaloric materials. *Adv. Mater.* 21, 4545–4564. doi: 10.1002/adma.200901072

Shen, F. R., Kuang, H., Hu, F. X., Wu, H., Huang, Q. Z., Liang, F. X., et al. (2017). Ultra-low thermal expansion realized in giant negative thermal expansion materials through self-compensation. *APL Mater.* 5:106102. doi: 10.1063/1.4990481

Shi, K. W., Sun, Y., Colin, C. V., Wang, L., Yan, J., Deng, S. H., et al. (2018). Investigation of the spin-lattice coupling in Mn3Ga1-xSnxN antiperovskites. *Phys. Rev. B* 97:054110. doi: 10.1103/PhysRevB.97.054110

Shi, K. W., Sun, Y., Yan, J., Deng, S. H., Wang, L., Wu, H., et al. (2016). Baromagnetic effect in antiperovskite Mn3Ga0.95N0.94 by neutron powder diffraction analysis. *Adv. Mater.* 28, 3761–3767. doi: 10.1002/adma.201600310

Song, X. Y., Sun, Z. H., Huang, Q. Z., Rettenmayr, M., Liu, X. M., Seyring, M., et al. (2011). Adjustable zero thermal expansion in antiperovskite manganese nitride. *Adv. Mater.* 23:4690. doi: 10.1002/adma.201102552

Song, Y. Z., Chen, J., Liu, X. Z., Wang, C. W., Zhang, J., Liu, H., et al. (2018). Zero thermal expansion in magnetic and metallic $Tb(Co, Fe)_2$ intermetallic compounds. *J. Am. Chem. Soc.* 140, 602–605. doi: 10.1021/jacs.7b12235

Sullivan, L. M., and Lukehart, C. M. (2005). Zirconium tungstate (ZrW_2O_8)/polyimide nanocomposites exhibiting reduced coefficient of thermal expansion. *Chem. Mater.* 17, 2136–2141. doi: 10.1021/cm0482737

Sun, Y., Wang, C., Huang, Q. Z., Guo, Y. F., Chu, L. H., Arai, M., et al. (2012). Neutron diffraction study of unusual phase separation in the antiperovskite nitride Mn3ZnN. *Inorg. Chem.* 51, 7232–7236. doi: 10.1021/ic300978x

Sun, Y., Wang, C., Wen, Y. C., Chu, L. H., and Man, N. (2010a). Negative thermal expansion and correlated magnetic and electrical properties of Si-Doped Mn3GaN compounds. *J. Am. Ceram. Soc.* 93, 650–653. doi: 10.1111/j.1551-2916.2009.03482.x

Sun, Y., Wang, C., Wen, Y. C., Chu, L. H., Pan, H., and Niez, M. (2010b). Negative thermal expansion and magnetic transition in anti-perovskite structured Mn3Zn1-xSnxN compounds. *J. Am. Ceram. Soc.* 93, 2178–2181. doi: 10.1111/j.1551-2916.2010.03711.x

Takenaka, K., Asano, K., Misawa, M., and Takagi, H. (2008). Negative thermal expansion in Ge-free antiperovskite manganese nitrides: Tin-doping effect. *Appl. Phys. Lett.* 92:011927. doi: 10.1063/1.2831715

Takenaka, K., Hamada, T., Kasugai, D., and Sugimoto, N. (2012). Tailoring thermal expansion in metal matrix composites blended by antiperovskite manganese nitrides exhibiting giant negative thermal expansion. *J. Appl. Phys.* 112:083517. doi: 10.1063/1.4759121

Takenaka, K., and Ichigo, M. (2014). Thermal expansion adjustable polymer matrix composites with giant negative thermal expansion filler. *Compos. Sci. Technol.* 104, 47–51. doi: 10.1016/j.compscitech.2014.08.029

Takenaka, K., Okamoto, Y., Shinoda, T., Katayama, N., and Sakai, Y. (2017). Colossal negative thermal expansion in reduced layered ruthenate. *Nat. Commun.* 8:14102. doi: 10.1038/ncomms14102

Takenaka, K., and Takagi, H. (2005). Giant negative thermal expansion in Ge-doped anti-perovskite manganese nitrides. *Appl. Phys. Lett.* 87:261902. doi: 10.1063/1.2147726

Tegus, O., Brück, E., Buschow, K. H. J., and de Boer, F. R. (2002). Transition-metal-based magnetic refrigerants for room-temperature applications. *Nature* 415, 150–152. doi: 10.1038/415150a

Wada, H., and Tanabe, Y. (2001). Giant magnetocaloric effect of $MnAs_{1-x}Sb_x$. *Appl. Phys. Lett.* 79, 3302–3304. doi: 10.1063/1.1419048

Wada, H., Tanabe, Y., Shiga, M., Sugawara, H., and Sato, H. (2001). Magnetocaloric effects of Laves phase $Er(Co_{1-x}Ni_x)_2$ compounds. *J. Alloys Compd.* 316, 245–249. doi: 10.1016/S0925-8388(00)01305-0

Wada, H., Tomekawa, S., and Shiga, M. (1999). Magnetocaloric properties of a first-order magnetic transition system $ErCo_2$. *Cryogenics* 39, 915–919. doi: 10.1016/S0011-2275(99)00121-6

Wang, C., Chu, L. H., Yao, Q. R., Sun, Y., Wu, M. M., Ding, L., et al. (2012). Tuning the range, magnitude, and sign of the thermal expansion in intermetallic Mn3(Zn, M)x N(M = Ag, Ge). *Phys. Rev. B* 85:220103. doi: 10.1103/PhysRevB.85.220103

Wang, D. H., Liu, H. D., Tang, S. L., Tang, T., Wen, J. F., and Du, Y. W. (2002a). Low-field magnetic entropy change in $Dy(Co_{1-x}Si_x)_2$. *Solid State Commun.* 121, 199–202. doi: 10.1016/S0038-1098(01)00486-0

Wang, D. H., Liu, H. D., Tang, S. L., Yang, S., Huang, S. L., and Du, Y. W. (2002b). Magnetic properties and magnetocaloric effects in $(Gd_xDy_{1-x})Co_2$ compounds. *Phys. Lett. A* 297, 247–252. doi: 10.1016/S0375-9601(02)00159-7

Wang, D. H., Tang, S. L., Huang, S. L., Su, Z. H., Han, Z. D., and Du, Y. W. (2003). The origin of the large magnetocaloric effect in RCo_2 (R=Er, Ho and Dy). *J. Alloy. Compd.* 360, 11–13. doi: 10.1016/S0925-8388(03)00324-4

Wang, J. T., Wang, D. S., Chen, C. F., Nashima, O., Kanomata, T., Mizuseki, H., et al. (2006). Vacancy induced structural and magnetic transition in $MnCo_{1-x}Ge$. *Appl. phys. Lett.* 89, 262504–262506. doi: 10.1063/1.2424273

Wu, R. R., Bao, L. F., Hu, F. X., Wu, H., Huang, Q. Z., Wang, J., et al. (2015). Giant barocaloric effect in hexagonal Ni_2In-type Mn-Co-Ge-In compounds around room temperature. *Sci. Rep.* 5:18027. doi: 10.1038/srep18027

Wu, R. R., Shen, F. R., Hu, F. X., Wang, J., Bao, L. F., Zhang, L., et al. (2016). Critical dependence of magnetostructural coupling and magnetocaloric effect on particle size in Mn-Fe-Ni-Ge compounds. *Sci. Rep.* 6:20993. doi: 10.1038/srep20993

Zhao, W. J., Sun, Y., Liu, Y. F., Shi, K. W., Lu, H. Q., Song, P., et al. (2018). Negative thermal expansion over a wide temperature range in Fe-doped MnNiGe composites. *Front. Chem.* 6:15. doi: 10.3389/fchem.2018.00015

Zhao, Y. Y., Hu, F. X., Bao, L. F., Wang, J., Wu, H., Huang, Q. Z., et al. (2015). Giant negative thermal expansion in bonded MnCoGe-based compounds with Ni_2In-type hexagonal structure. *J. Am. Chem. Soc.* 137, 1746–1749. doi: 10.1021/ja510693a

Zheng, X. G., Kubozono, H., Yamada, H., Kato, K., Ishiwata, Y., and Xu, C. N. (2008). Giant negative thermal expansion in magnetic nanocrystals. *Nat. Nanotechnol.* 3, 724–726. doi: 10.1038/nnano.2008.309

Zhou, T. J., Cher, M. K., Shen, L., Hu, J. F., and Yuan, Z. M. (2013). On the origin of giant magnetocaloric effect and thermal hysteresis in multifunctional alpha-FeRh thin films. *Phys. Lett. A* 377, 3052–3059. doi: 10.1016/j.physleta.2013.09.027

Conflict of Interest Statement: The authors declare that the research was conducted in the absence of any commercial or financial relationships that could be construed as a potential conflict of interest.

frontiers in Chemistry

PERSPECTIVE
published: 22 August 2018
doi: 10.3389/fchem.2018.00371

Mechanisms and Materials for NTE

*J. Paul Attfield**

Centre for Science at Extreme Conditions and School of Chemistry, University of Edinburgh, Edinburgh, United Kingdom

Negative thermal expansion (NTE) upon heating is an unusual property but is observed in many materials over varying ranges of temperature. A brief review of mechanisms for NTE and prominent materials will be presented here. Broadly there are two basic mechanisms for intrinsic NTE within a homogenous solid; structural and electronic. Structural NTE is driven by transverse vibrational motion in insulating framework–type materials e.g., ZrW_2O_8 and ScF_3. Electronic NTE results from thermal changes in electronic structure or magnetism and is often associated with phase transitions. A classic example is the Invar alloy, $Fe_{0.64}Ni_{0.36}$, but many exotic mechanisms have been discovered more recently such as colossal NTE driven by Bi–Ni charge transfer in the perovskite $BiNiO_3$. In addition there are several types of NTE that result from specific sample morphologies. Several simple materials, e.g., Au, CuO, are reported to show NTE as nanoparticles but not in the bulk. Microstructural enhancements of NTE can be achieved in ceramics of materials with anisotropic thermal expansion such as beta–eucryptite and Ca_2RuO_4, and artificial NTE metamaterials can be fabricated from engineered structures of normal (positive) thermal expansion substances.

Keywords: thermal expansion, negative thermal expansion, thermal expansion coefficient, structural NTE, electronic NTE, morphological NTE

OPEN ACCESS

Edited by:
Andrea Sanson,
Università degli Studi di Padova, Italy

Reviewed by:
Angus Wilkinson,
Georgia Institute of Technology, United States
Ranjan Mittal,
Bhabha Atomic Research Centre, India
Xianran Xing,
University of Science and Technology Beijing, China

***Correspondence:**
J. Paul Attfield
j.p.attfield@ed.ac.uk

Specialty section:
This article was submitted to Physical Chemistry and Chemical Physics, a section of the journal Frontiers in Chemistry

Received: *21 June 2018*
Accepted: *02 August 2018*
Published: *22 August 2018*

Citation:
Attfield JP (2018) Mechanisms and Materials for NTE. Front. Chem. 6:371. doi: 10.3389/fchem.2018.00371

INTRODUCTION

NTE (negative thermal expansion) refers to the unusual phenomenon of volume contraction upon heating. Although most materials display positive thermal expansion (PTE) on heating, NTE is found in a wide variety of substances over varying ranges of temperature. This brief review is an attempt to summarize the mechanisms and prominent materials that show NTE. Further details may be found in more substantial reviews published by other authors in recent years (Lind, 2012; Takenaka, 2012; Chen et al., 2015; Dove and Fang, 2016; Liu et al., 2018; Mittal et al., 2018) and in the other papers in this special issue.

Control of thermal expansion is important for many applications from ceramic cooker hobs to housings for optical devices, with zero thermal expansion (ZTE) materials or composites of PTE and NTE components being particularly useful. Thermal expansion is quantified through the linear or volume (bulk) thermal expansion coefficients (TECs), $\alpha_L = (1/L)(dL/dT)$, and $\alpha_V = (1/V)(dV/dT)$, which respectively measure the change in length L or volume V of an object with temperature T. α_L and α_V are typically quoted in 10^{-6} K^{-1} units, equivalent to ppm (parts per million) K^{-1} or MK^{-1}. Isotropic substances such as simple liquids, glasses, polycrystalline ceramics, and cubic crystals, have the same α_L in all directions with $\alpha_V = 3\alpha_L$. ZrW_2O_8 is a famous example of a cubic NTE material (Mary et al., 1996). However uniaxial (tetragonal, hexagonal, or trigonal) crystals may have different linear TECs $\alpha_{||}$ and $\alpha_{\perp}$ parallel and perpendicular to the unique symmetry axis, respectively, and crystals with orthorhombic or lower symmetry have three different values α_1, α_2, and α_3 in mutually perpendicular directions. The volume TEC is given by

$\alpha_V = \alpha_{||} + 2\alpha_\perp$ or $\alpha_V = \alpha_1 + \alpha_2 + \alpha_3$ and when the linear TECs are very different, such as a mix of negative and positive values, then highly anisotropic thermal expansion may be obtained. TECs of crystalline materials are usually measured by determining how unit cell lengths change with temperature from diffraction measurements. Direct strain gauge (dilatometry) measurements of crystals can also be used, and are particularly useful for ceramics and amorphous materials such as glasses. Diffraction and dilatometry expansion measurements can give different results due to the effects of microstructure, as discussed in section Microstructural NTE.

NTE materials have negative α_V over some temperature range. Reported α_V values vary from -1 to $-1{,}000 \times 10^{-6}$ K^{-1}, but it is also important to consider the temperature range to which the quoted α_V refers as very large negative α_V's may result from modest volume decreases over very narrow temperature ranges at a phase transition. For this reason it is often more useful to consider the overall volume decrease; materials with $-\Delta L/L >$ 1% and so $-\Delta V/V > 3\%$ have notably large NTE.

The thermodynamic origin of thermal expansion in solids is expressed through the relation $\alpha_V = \gamma C_V/BV$ where C_V is heat capacity at constant V, $B = -V(\mathrm{d}p/\mathrm{d}V)$ is the bulk modulus with p being pressure, and γ is the weighted or macroscopic Grüneisen parameter summed over values for the active phonon frequencies ω_i as $\gamma_i = -\mathrm{d}(\ln\ \omega_i)/\mathrm{d}(\ln\ V)$. C_V and B always take positive values, hence variations in the sign of α_V arise from corresponding variations in the sign of γ. NTE is often associated with other unusual lattice properties such as negative linear compressibility under applied pressure (Mittal et al., 2018) and pressure-induced softening where $\mathrm{d}B/\mathrm{d}p$ becomes negative (Dove and Fang, 2016).

Conventional PTE arises because γ is usually positive as a consequence of the shape of the interatomic potential for bonding between two atoms, as shown in **Figure 1**. Anharmonicity in the shape of the potential leads to an increase in the average interatomic distance as higher vibrational states become more populated as temperature rises. As this pairwise potential shape applies qualitatively to all type of chemical bonding, it might appear that PTE should be a universal behavior, but NTE can arise from two "escapes" that circumvent the latter argument.

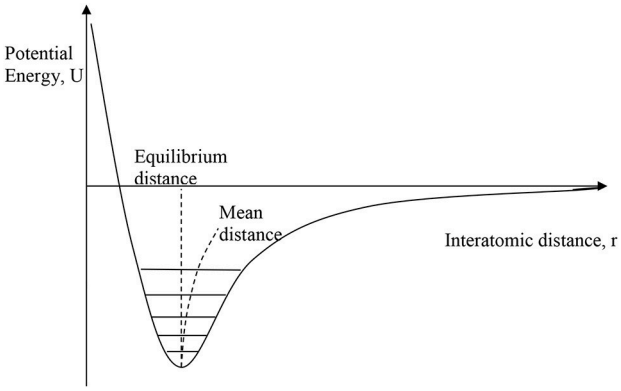

FIGURE 1 | The interatomic bonding potential, showing the variation of potential energy with interatomic distance for a pair of bonded atoms. Vibrational energy levels are quantised and with increasing temperature the occupation of higher levels leads to a slight increase in the mean interatomic distance relative to the minimum–energy equilibrium distance as shown.

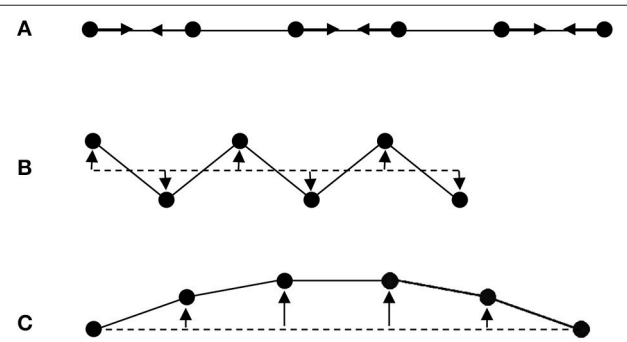

FIGURE 2 | Schematic illustrations of lattice modes for a chain of atoms. **(A)** Longitudinal optic (LO) mode leading to PTE through asymmetry of the pairwise bonding potential shown in **Figure 1**. **(B)** High energy transverse optic (TO) mode that greatly shortens the chain giving large NTE as the vibrational amplitude increases with temperature. **(C)** Low energy transverse acoustic (TA) mode leading to more modest NTE as temperature increases.

INTRINSIC NTE MECHANISMS

Structural NTE

The first "escape" from the universal PTE behavior expected from the interatomic potential in **Figure 1** arises from the more complex vibrational properties of large arrays of atoms. **Figure 2** shows some of the possible motions for a chain of atoms. Longitudinal (L) vibrations in the direction of the bonds (**Figure 2A**) tend to lengthen the chain as temperature increases through thermal expansion of the individual bonds via the anharmonicity of the interatomic potential (**Figure 1**). However, transverse (T) motions perpendicular to the direction of the chain tend to shorten the chain–length as the amplitude of vibration increases with temperature (**Figures 2B,C**) and so can lead to NTE. This is sometimes known as the tension or "guitar string" effect. Lattice vibrations, also known as phonons, are usefully classified as optic (O) with short wavelengths and high frequencies and energies, or acoustic (A) with long wavelengths and low frequencies and energies. Transverse optic (TO) phonons like that shown in **Figure 2B** lead to large chain shortening (NTE) but may only be excited at high temperatures in view of their high energies, whereas transverse acoustic (TA) modes that lead to more modest NTE are excited at lower temperatures. Detailed theoretical and experimental analyses of phonon spectra are needed to assess the contributions of TO and TA vibrations to the NTE of real materials (Dove and Fang, 2016; Mittal et al., 2018).

Structural NTE results when the shortening effects of the transverse phonon amplitudes due to bending or torsional motions outweigh the expansion effects of the longitudinal modes. Low atomic connectivity so that atoms have free space to move into during transverse motions leading to large amplitudes

is a necessary feature for NTE to prevail. Planar 3-coordination is the maximum connectivity known to lead to negative expansion, as exemplified by graphene sheets of carbon atoms (Yoon et al., 2011). However when these sheets are stacked in the three-dimensional lattice of graphite, conventional PTE arising from soft van der Waals bonding potentials in the stacking (high symmetry) direction gives a large $\alpha_{||} = 23.1 \times 10^{-6}$ K^{-1} that outweighs the NTE in the perpendicular directions ($\alpha_{\perp} = -0.6 \times 10^{-6}$ K^{-1}) leading to bulk PTE ($\alpha_V = \alpha_{||} + 2\alpha_{\perp} = 21.9 \times 10^{-6}$ K^{-1}) (Morgan, 1972).

Bulk structural NTE requires a large proportion of 2-coordinate linker groups, connecting more highly-coordinated atoms into a three-dimensional structure. Some representative examples of structural NTE material types, with 2-connected linkers underlined, are Sc$\underline{F}_3$, $\underline{Ag}_2O$, $ZrW_2\underline{O}_8$, $ZrV_2\underline{O}_7$, $LiAlSi\underline{O}_4$ (the mineral β-eucryptite), zeolitic forms of $Si\underline{O}_2$ (e.g., ITQ-4) and related $AlP\underline{O}_4$ (e.g., $AlPO_4$-17) frameworks, $Cd(\underline{CN})_2$, $Co_3[Co(\underline{CN})_6]_2$, and metal organic frameworks such as IRMOF-1 ($Zn_4O(\underline{bdc})_3$, where bdc is 1,4-benzodicarboxylate). These have α_V values of magnitude -20 to -120×10^{-6} K^{-1} over typical temperature ranges of a few hundred K; details and citations are shown in Dove and Fang (2016). All of these materials have the majority of their atoms in the 2-connected linkers. The metal fluoride and oxide examples have 2-coordinate atoms linking tetrahedral or octahedral units together. These polyhedra tend to be rigid so the transverse vibrations of the lattice may be described in the rigid unit mode (RUM) picture (Dove and Fang, 2016).

The importance of the transverse motions of the linker atoms or groups to NTE is further demonstrated by changes observed when additional molecules or ions are inserted into NTE materials. The inserted species within cavities in the structure are adjacent to the linkers and so reduce the amplitudes of their transverse vibrations. Redox insertion of only 6% Li into Fe-doped ScF_3 switches the TEC from negative to positive (Chen et al., 2017), and the same change is found when K^+ or H_2O is inserted into the channels of the cyanide framework material $YFe(CN)_6$ (Gao et al., 2017).

Electronic NTE

A disparate group of materials, usually dense metal alloys or ceramics, display NTE that is not driven by the structural (transverse vibration) mechanism. Although they have a wide variety of physical properties, and so are sometimes described as having different NTE mechanisms, they have the common feature that NTE results from thermal changes in the interatomic bonding potential, as illustrated in **Figure 3**. Changes in bonding with temperature such that the interatomic potential becomes more strongly bonding can shift the curve to a smaller equilibrium distance at higher temperature. This may occur through a relatively sharp first order phase transition between two distinct states, or the potential may gradually evolve with changing temperature through a second or higher order transition. When the effect of this "escape" outweighs the usual PTE from the anharmonicity of the potentials then NTE may be observed over temperature range of the crossover.

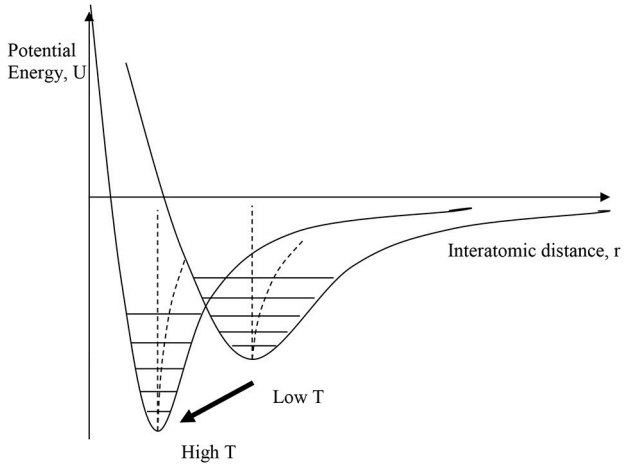

FIGURE 3 | Illustration of electronic mechanisms for NTE, where the interatomic bonding potential changes with temperature, moving to a more strongly bonding curve with smaller equilibrium distance at higher temperature. This may occur through a relatively sharp first order phase transition between two distinct states, or the potential may gradually evolve with changing temperature.

Figure 4 illustrates the schematic changes in lattice volume with temperature for a material displaying electronic NTE. Both the larger-volume low-T and the smaller-volume high-T states shown in **Figure 3** display conventional PTE behavior, but the change between them in the crossover region with lower and upper temperatures T_l and T_u leads to NTE. T_u often marks an ordering temperature such as a magnetic or ferroelectric Curie transition, and the lower limit T_l is reached where the order parameter (magnetization or electric polarization) is fully saturated. In other cases such as charge transfer materials, T_l and T_u mark the lower and upper limits of the two-phase region where the low-T and high-T phases coexist. The electronically-induced excess volume ΔV_{ex} relative to the extrapolated volume of the high-T state, V_{HT}, may be used to calculate the spontaneous volume striction $\Delta V_{ex}/V_{HT}$. Variations in the magnitude of ΔV_{ex} and in the separation between T_l and T_u may be used to tune electronic materials from reduced PTE, through ZTE to NTE behavior. A famous material that launched the study of unusual thermal expansion properties is the Invar alloy $Fe_{0.64}Ni_{0.36}$ named for an *invariant* length with a very small $\alpha_L = 1 \times 10^{-6}$ K^{-1} (effectively ZTE) below magnetic $T_C = 500$ K.

The transitions or changes that give rise to electronic NTE are usually associated with an increase in electron delocalization on passing from the low-T to the high-T phase. The low-T phase is more electron localized or correlated (e.g., magnetically ordered), due to electron-electron repulsions that may be described by the Hubbard U energy, while the more electron delocalized or disordered high-T phase is stabilized by entropy. Electrons near the Fermi level are often in d- or f-states that are non-bonding or weakly antibonding, so their delocalization allows the bonding potential to become more negative and shift to shorter distance as shown in **Figure 3**.

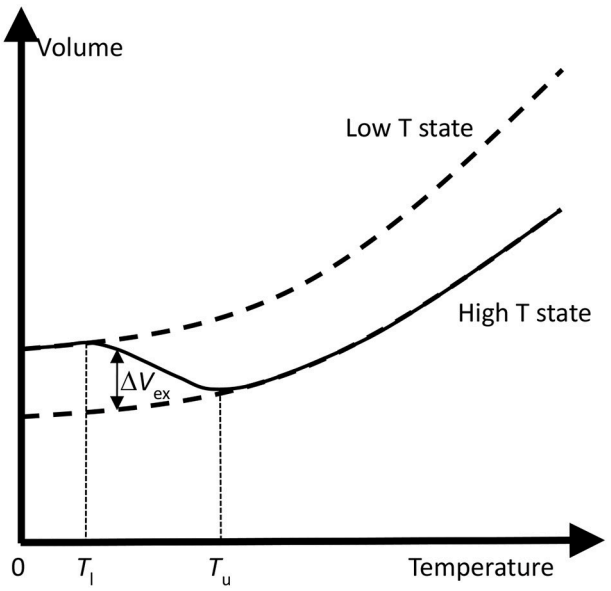

FIGURE 4 | Schematic changes in lattice volume with temperature for a material displaying electronic NTE. The change from the larger-volume low-*T* to the smaller-volume high-*T* states (as shown in **Figure 3**) leads to NTE in the crossover region with lower and upper temperatures T_l and T_u. T_u often marks an ordering temperature such as a magnetic or ferroelectric Curie transition. The electronically-induced excess volume ΔV_{ex} relative to the extrapolated volume of the high-*T* state is shown.

Classes of materials where electronic NTE is found are;

- Metallic magnets, notably the Invar alloy above, also R_2Fe_{17} (R = rare earth) and related intermetallics, the permanent magnet family $R_2Fe_{14}B$, the $Mn_3(Cu,Ge)N$ antiperovskites, and metallic perovskite oxides $SrRuO_3$ and manganites such as $La_{0.8}Ba_{0.2}MnO_3$. NTE is usually observed over a wide temperature range below the magnetic Curie transition.
- Insulating magnets—these generally do not show NTE but some examples are found for frustrated spinels e.g., $CdCr_2O_4$ and $CdCr_2S_4$, the multiferroic $Pb(Fe_{0.5}Nb_{0.5})O_3$, and orbitally ordered MnF_3, below their Curie or Néel temperatures.
- Charge transfer materials, e.g., $Bi_{0.95}La_{0.05}NiO_3$, $LaCu_3Fe_4O_{12}$, $Sm_{0.67}Y_{0.33}S$, $Sm_{2.75}C_{60}$, and $Yb_8Ge_3Sb_5$, can show very large NTE resulting from volume collapses at metal to insulator charge transfer transitions. $Bi_{0.95}La_{0.05}NiO_3$ has $\alpha_V = -410 \times 10^{-6}$ K^{-1} between 300 and 370 K, termed colossal NTE (CNTE). The oxides have intermetallic Bi/Ni or Cu/Fe charge transfer transitions, whereas electrons released through the ionization process $R^{2+} \rightarrow R^{3+} + e^-$ in the R = Sm, Yb materials are delocalized in the conduction band at high temperatures. NTE in V_2OPO_4 where charge ordering occurs without a metal-insulator transition was recently reported (Pachoud et al., 2018).
- Orbital ordering transitions usually associated with first-order Jahn-Teller distortions give rise to NTE in several materials. Ca_2RuO_4 has orbital order associated with a metal-insulator transition, while insulating $LaMnO_3$ which is much studied as the parent phase of the perovskite manganites undergoes a 0.4% cell volume decrease at 750 K where the orbital order-disorder transition occurs.
- Ferroelectrics associated with off-center displacements of cations to give a net polarization sometimes show NTE below their Curie transitions. Prominent examples are perovskite oxides of lead with transition metal cations showing a second-order Jahn-Teller effect such as $PbTiO_3$, $Pb(Mg_{0.33}Ta_{0.67})O_3$, and $Pb(Fe_{0.5}Nb_{0.5})O_3$. Cooling below T_C leads to a change from symmetric O–M–O–M–O to asymmetric O·····M-O·····M-O chains of atoms leading to polarity in the chain direction. The lengthening of O·····M bonds where electrons are localized in antibonding states outweighs the shortening of the M-O bonds, leading to a net expansion in the polar chain direction on cooling and hence the excess volume associated with NTE below T_C. This can lead to very large volume collapses on warming, for example, $Pb_{0.8}Bi_{0.2}VO_3$ shows $\Delta V/V = -7.9\%$ around $T_C \approx 600$ K (Yamamoto et al., 2018).
- Superconductors sometimes show an excess volume and NTE below their critical temperatures T_c, for example in MgB_2, $La_{1.85}Sr_{0.15}CuO_4$, and $NdFeAsO_{0.89}F_{0.11}$. Electron-phonon coupling is directly implicated in the superconducting mechanism for BCS-type MgB_2, whereas the latter two materials are unconventional superconductors where a magnetic pairing mechanism may be important. Loss of bonding electron density at the Fermi level due to electron-pairing below T_c is the general cause of NTE in superconductors.

Further details and citations when not shown above are given in the comprehensive review of NTE in functional materials by Chen et al. (2015).

MORPHOLOGICAL NTE

The structural and electronic mechanisms for NTE described above apply to chemically homogenous materials such as a single crystal. However, there are further instances where NTE can arise or differ from the normal bulk behavior due to the specific morphology of the sample.

Nanoparticle NTE

A variety of materials that show bulk PTE have been found to display NTE when prepared as small particles, usually in the nanoscale regime. For example, the magnetic insulators CuO and MnF_2 show PTE in the bulk but as 5 nm particles they display NTE below their Néel temperatures. CuO has a giant NTE of $\alpha_V = -110 \times 10^{-6}$ K^{-1} between 20 and 170 K (Zheng et al., 2008). Nanoparticles of Au (Li et al., 2002) and TiO_2 (Zhu et al., 2016) are also reported to display NTE.

The origin of nanoparticle NTE is usually electronic as, for example, the excess volume of CuO particles above follows the general behavior shown in **Figure 4**. Localization of ordered or correlated states tends to be enhanced at and near surfaces so the associated lattice expansion on cooling can dominate the overall behavior in small particles with a large proportion of surface atoms. The structural NTE mechanism could also play a

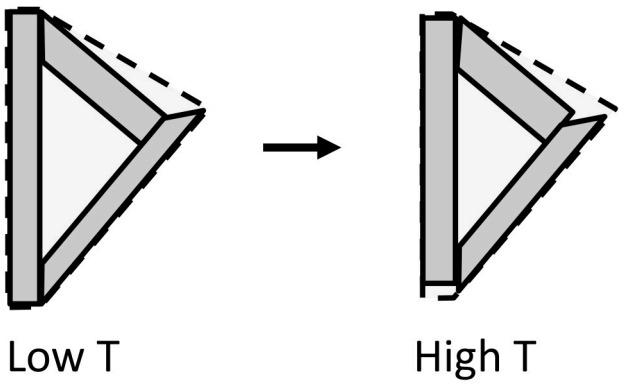

FIGURE 5 | Illustrative two-dimensional model for the microstructural NTE effect, showing three crystallites enclosing a void. The crystallites shown have contracted by 10% along their long axis and expanded by 10% in the perpendicular direction on changing from low *T* to high *T*, so their total area has not changed. However, the enclosing area for the ensemble shown by broken lines undergoes an overall decrease of 8%, illustrating how anisotropic thermal expansion may lead to overall NTE.

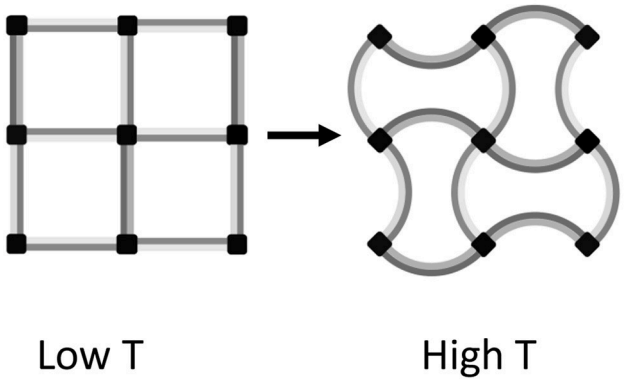

FIGURE 6 | Illustrative two-dimensional example of an NTE metamaterial consisting of a square lattice of bimaterial strips acting as struts between 4-connected nodes. On heating from the low *T* to the high *T* state, the light and dark gray materials respectively expand in length by 6 and 17%, but the separation between nodes decreases by 4% corresponding to an 8% area contraction. Hence the metamaterial consisting of only PTE substances shows bulk NTE.

part as surface atoms have a lower connectivity than the bulk so transverse vibrational amplitudes may be enhanced.

Microstructural NTE

Direct measurement of α_V for ceramic samples sometimes gives a more negative value than that expected from crystallographic measurement of the linear TECs. The excess negative expansion is achieved by reducing the volumes of microcracks or voids within the ceramic on heating, as illustrated schematically in **Figure 5**. Microstructural NTE was reported in an early study of β-eucryptite ($LiAlSiO_4$) (Gillery and Bush, 1959) and very large effects have recently been discovered in Ca_2RuO_4 (Takenaka et al., 2017a). These ceramic materials both have anisotropic thermal expansion with one strongly negative coefficient that dominates the expansion of their ceramics. For example, on heating from 150 to 340 K, the orthorhombic *a*, *b*, and *c* axes of Ca_2RuO_4 show length changes of −0.6, −5.0, and +4.5% respectively, so an overall $\Delta V/V = -1.1\%$ is expected. However an 80% dense ceramic sample gave $\Delta V/V = -6.7\%$ revealing a substantial microstructural NTE effect.

Anisotropic thermal expansion leads to stresses at grain boundaries that result in microcracking in β-eucryptite ceramics on cooling to room temperature after sintering. Reduction of the microcrack volumes on subsequent heating results in bulk NTE and an enhancement of the excess NTE with increasing grain size (and hence internal microcrack volume) has been established (Pelletant et al., 2012). However, this is less problematic for Ca_2RuO_4-based ceramics, which have been combined with epoxy resin to generate ZTE materials that are stable to microcracking on thermal cycling (Takenaka et al., 2017b).

Metamaterials NTE

Artificial structures consisting of two or more materials with different TECs (which may all be positive) can be engineered to contract when heating. A simple example based on bonded strips of two materials with different positive TECs is shown in **Figure 6**. The structure contracts on heating through reduction of the volume of internal voids, which outweighs the increase in volume of the materials themselves. Designs for three-dimensional cellular metamaterials with varying TECs based on the use of such bimaterial connectors were proposed by Lakes (2007).

Recent developments in additive manufacturing through three-dimensional printing technologies have enabled metamaterials with bulk NTE to be generated. In a recent example, a two-component polymer metamaterial showed bulk negative expansion with $\alpha_L = -50 \times 10^{-6}$ K^{-1} although the individual components had PTE with an average $\alpha_L = 40 \times 10^{-6}$ K^{-1} (Qu et al., 2017).

SUMMARY

Although many diverse examples of NTE materials are reported, they may be classified according to two types of intrinsic mechanism. Electronic NTE arises from reduction in first-neighbor distances upon heating due to changes in the interatomic potential. These changes may arise from a variety of physical property transitions such as magnetism, charge transfer, ferroelectricity, and superconductivity that alter the distribution of electron density. Structural NTE occurs through reduction in second- or higher- neighbor distances upon heating due to dominant effects of transverse vibrations such as bending or torsional modes, and is found in many framework-type materials with a high proportion of 2-connected linkers.

The intrinsic NTE mechanisms may be enhanced in nanoparticles, most likely through electronic effects from localization of ordered or correlated states near surfaces. Further

morphological mechanisms for NTE of bulk artifacts result from reducing the volume of internal voids upon heating. Microstructural NTE is found for ceramics of materials having anisotropic thermal expansion coefficients. Artificial structures of substances with different expansion coefficients may be used to generate metamaterials with NTE even when the individual components have PTE behavior.

AUTHOR CONTRIBUTIONS

The author confirms being the sole contributor of this work and approved it for publication.

FUNDING

The author acknowledges financial support from EPSRC.

ACKNOWLEDGMENTS

This paper is based upon a talk presented at the 2nd International Symposium on Negative Thermal Expansion and Related Materials (ISNTE-II) at Tokyo Institute of Technology, Yokohama, Japan in December 2017. The author thanks the organizers and participants for their contributions that helped to shape the ideas presented in this paper.

REFERENCES

Chen, J., Gao, Q., Sanson, A., Jiang, X., Huang, Q., Carnera, A., et al. (2017). Tunable thermal expansion in framework materials through redox intercalation. *Nat. Commun*. 8:14441. doi: 10.1038/ncomms14441

Chen, J., Hu, L., Deng, J., and Xing, X. (2015). Negative thermal expansion in functional materials: controllable thermal expansion by chemical modifications. *Chem. Soc. Rev*. 44, 3522–3567. doi: 10.1039/C4CS00461B

Dove, M. T., and Fang, H. (2016). Negative thermal expansion and associated anomalous physical properties: review of the lattice dynamics theoretical foundation. *Rep. Prog. Phys*. 79:066503. doi: 10.1088/0034-4885/79/6/066503

Gao, Q.,Chen, J., Sun, Q., Chang, D., Huang, Q., Wu, H., et al. (2017). Switching between giant positive and negative thermal expansions of a YFe(CN)6-based Prussian blue analogue induced by guest species. *Angew. Chem. Int. Ed*. 56, 9023–9028. doi: 10.1002/anie.201702955

Gillery, F. H., and Bush, E. A. (1959). Thermal contraction of β-eucryptite-. (Li2O.Al2O3.2SiO2) by X-ray and dilatometer methods. *J. Am. Cer. Soc*. 42, 175–177. doi: 10.1111/j.1151-2916.1959.tb12942.x

Lakes, R. (2007). Cellular solids with tunable positive or negative thermal expansion of unbounded magnitude. *Appl. Phys. Lett*. 90:221905. doi: 10.1063/1.2743951

Li, W. H., Wu, S. Y., Yang, C. C., Lai, S. K., Lee, K. C., Huang, H. L., et al. (2002). Thermal contraction of Au nanoparticles. *Phys. Rev. Lett*. 89:135504. doi: 10.1103/PhysRevLett.89.135504

Lind, C. (2012). Two decades of negative thermal expansion research: where do we stand? *Materials* 5, 1125–1154. doi: 10.3390/ma5061125

Liu, Z., Gao, Q., Chen, J., Deng, J., Lin, K., and Xing, X. R. (2018). Negative thermal expansion in molecular materials. *Chem. Commun*. 54, 5164–5176. doi: 10.1039/C8CC03219J

Mary, T. A., Evans, J. S. O., Vogt, T., and Sleight, A. W. (1996). Negative thermal expansion from 0.3 to 1050 Kelvin in ZrW2O8. *Science* 272, 90–92. doi: 10.1126/science.272.5258.90

Mittal, R., Gupta, M. K., and Chaplot, S. L. (2018). Phonons and anomalous thermal expansion behavior in crystalline solids. *Prog. Materials Sci*. 92, 360–445. doi: 10.1016/j.pmatsci.2017.10.002

Morgan, W. C. (1972). Thermal expansion coefficients of graphite crystals. *Carbon* 10, 73–79. doi: 10.1016/0008-6223(72)90011-5

Pachoud, E., Cumby, J., Lithgow, C. T., and Attfield, J. P. (2018). Charge order and negative thermal expansion in V2OPO4. *J. Am. Chem. Soc*. 140, 636–641. doi: 10.1021/jacs.7b09441

Pelletant, A., Reveron, H., Chêvalier, J., Fantozzi, G., Blanchard, L., Guinot, F., et al. (2012). Grain size dependence of pure β-eucryptite thermal expansion coefficient. *Mater. Lett*. 66, 68–71. doi: 10.1016/j.matlet.2011.07.107

Qu, J., Kadic, M., Naber, A., and Wegener, M. (2017). Micro-structured two-component 3D metamaterials with negative thermal-expansion coefficient from positive constituents. *Sci. Rep*. 7:40643. doi: 10.1038/srep40643

Takenaka, K. (2012). Negative thermal expansion materials: technological key for control of thermal expansion. *Sci. Technol. Adv. Mater*. 13:013001. doi: 10.1088/1468-6996/13/1/013001

Takenaka, K., Okamoto, Y., Shinoda, T., Katayama, N., and Sakai, Y. (2017a). Colossal negative thermal expansion in reduced layered ruthenate. *Nature Comm*. 8:14102. doi: 10.1038/ncomms14102

Takenaka, K., Shinoda, T., Inoue, N., Okamoto, Y., Katayama, N., and Sakai, Y., et al. (2017b). Giant negative thermal expansion in Fe-doped layered ruthenate ceramics. *Appl. Phys. Express* 10:115501. doi: 10.7567/APEX.10.115501

Yamamoto, H., Imai, T., Sakai, Y., and Azuma, M. (2018). Colossal negative thermal expansion in electron-doped PbVO3 perovskites. *Angew. Chem. Int. Ed*. 57, 1–5. doi: 10.1002/anie.201804082

Yoon, D., Son, Y. W., and Cheong, H. (2011). Negative thermal expansion coefficient of graphene measured by Raman spectroscopy. *Nano Lett*. 11, 3227–3231. doi: 10.1021/nl201488g

Zheng, X. G., Kubozono, H., Yamada, H., Kato, K., Ishiwata, Y., and Xu, C. N. (2008). Giant negative thermal expansion in magnetic nanocrystals. *Nature Nat. Nanotechnol*. 3, 724–726. doi: 10.1038/nnano.2008.309

Zhu, H., Li, Q., Ren, Y., Fan, L., Chen, J., Deng, J., et al. (2016). Hydration and thermal expansion in anatase nanoparticles. *Adv Mater*. 28, 6894–6899. doi: 10.1002/adma.201600973

Conflict of Interest Statement: The author declares that the research was conducted in the absence of any commercial or financial relationships that could be construed as a potential conflict of interest.

frontiers in Chemistry

ORIGINAL RESEARCH
published: 14 August 2018
doi: 10.3389/fchem.2018.00347

Adjustable Thermal Expansion Properties in $Zr_2MoP_2O_{12}/ZrO_2$ Ceramic Composites

Hongfei Liu[1], Weikang Sun[1], Xiang Xie[1], Lu Yang[1], Zhiping Zhang[2], Min Zhou[1], Xianghua Zeng[1] and Xiaobing Chen[2]*

[1] Department of Microelectronics, School of Physical Science and Technology, Yangzhou University, Yangzhou, China,
[2] Department of Electrical and Mechanical Engineering, Guangling College, Yangzhou University, Yangzhou, China

OPEN ACCESS

Edited by:
Jun Chen,
University of Science and Technology Beijing, China

Reviewed by:
Kewen Shi,
Beihang University, China
Sihao Deng,
Southwest University of Science and Technology, China
Cristina Artini,
Università di Genova, Italy

***Correspondence:**
Zhiping Zhang
zp-hf@163.com

Specialty section:
This article was submitted to Physical Chemistry and Chemical Physics, a section of the journal Frontiers in Chemistry

Received: 02 May 2018
Accepted: 24 July 2018
Published: 14 August 2018

Citation:
Liu H, Sun W, Xie X, Yang L, Zhang Z, Zhou M, Zeng X and Chen X (2018) Adjustable Thermal Expansion Properties in $Zr_2MoP_2O_{12}/ZrO_2$ Ceramic Composites. Front. Chem. 6:347. doi: 10.3389/fchem.2018.00347

$Zr_2MoP_2O_{12}/ZrO_2$ composites were successfully synthesized by the solid state method in attempt to fabricate the near-zero thermal expansion ceramics. The phase composition, micromorphology and thermal expansion behavior of the $Zr_2MoP_2O_{12}/ZrO_2$ composites with different mass ratios were investigated using X-ray diffraction, scanning electron microscopy and thermal mechanical analysis. Results indicate that $Zr_2MoP_2O_{12}/ZrO_2$ composites can be prepared by pre-sintering at 500°C for 3 h and then sintering at 1050°C for 6 h. The resulting $Zr_2MoP_2O_{12}/ZrO_2$ composites consisted of orthorhombic $Zr_2MoP_2O_{12}$ and monoclinic ZrO_2. With increasing content of $Zr_2MoP_2O_{12}$, the $Zr_2MoP_2O_{12}/ZrO_2$ ceramics became more compact and the coefficient of thermal expansion decreased gradually. $Zr_2MoP_2O_{12}/ZrO_2$ composites show an adjustable coefficient of thermal expansion (CTE) from 5.57×10^{-6} K^{-1} to -5.73×10^{-6} K^{-1} by changing the mass ratio of $Zr_2MoP_2O_{12}$ and ZrO_2. The $Zr_2MoP_2O_{12}/ZrO_2$ composite with a mass ratio of 2:1 showed near zero thermal expansion, and the average linear thermal expansion coefficient is measured to be 0.0065×10^{-6} K^{-1} in the temperature range from 25 to 700°C.

Keywords: ceramics, $Zr_2MoP_2O_{12}$, ZrO_2, composites, thermal expansion control

INTRODUCTION

It is well known that the vast majority of materials expand on heating. However, some materials shrink as the temperature rises and display negative thermal expansion (NTE). NTE materials have attracted considerable attention due to the anomalous phenomenon and their potential application in controlled thermal expansion composites and other areas (Chen et al., 2015). Control of thermal expansion is crucial to many applications. Mismatch of thermal expansion in component materials of high-precision device may result in serious problems, such as mechanical destruction and positional deviation. An easy method to prepare the material with near-zero or low thermal expansion is combining NTE materials with positive thermal expansion materials (Liu et al.2012; 2012a; Gao et al., 2016; Zhang et al., 2017). Materials displaying zero or low thermal expansion are both dimensionally stable and highly resistant to thermal shock.

The longtime leading NTE exemplar was ZrW_2O_8. Cubic ZrW_2O_8 exhibits strong isotropic NTE over a wide temperature range (Mary et al., 1996; Nishiiyama et al., 2006; Kanamori et al., 2008; Banek et al., 2010; Liu et al., 2011, 2012b). With the goal of thermal expansion control, several studies of the composites containing ZrW_2O_8 have been reported, such as ZrW_2O_8/ZrO_2 (Lommens et al., 2005; Yang et al., 2007), ZrW_2O_8/Cu (Yilmaz, 2002), ZrW_2O_8/Al (Wu et al., 2013), ZrW_2O_8/cement (Kofteros et al., 2001), ZrW_2O_8/PI, and ZrW_2O_8/epoxy (Sullivan and Lukehart, 2005; Yang et al., 2010). The thermal expansion coefficient of composites can be effectively controlled by using ZrW_2O_8 as NTE filler, however, the cubic ZrW_2O_8 is metastable at room temperature and needs to be quenched after sintering at 1200°C. Meanwhile, ZrW_2O_8 undergoes a structural phase transition from α -ZrW_2O_8 to β -ZrW_2O_8 at around 160°C and the coefficient of thermal expansion will decrease from about -8.8×10^{-6} K^{-1} to -4.9×10^{-6} K^{-1}. In addition, when ZrW_2O_8 was heated to about 740°C in air, it will decompose into ZrO_2 and WO_3 (Mary et al., 1996; Nishiiyama et al., 2006; Kanamori et al., 2008; Banek et al., 2010; Liu et al., 2011, 2012b). Quenching, thermal decomposition and the abrupt change of thermal expansion are disadvantageous for composite design.

Orthorhombic $Zr_2MoP_2O_{12}$, a member of $A_2M_3O_{12}$ family, has received widespread attention in recent years. It shows stable NTE and its average linear expansion coefficient is -4.5×10^{-6} K^{-1} over a broad temperature range from −264 to 1050°C. What's more, it overcomes all the limitations of ZrW_2O_8 discussed above, suggesting its potential use for fabricating near-zero or low thermal expansion materials (Cetinkol et al., 2009; Isobe et al., 2016). ZrO_2 ceramics has been widely used in optical, electrical and high temperature fields. The average linear thermal expansion coefficient of ZrO_2 is about 10×10^{-6} K^{-1}(Lommens et al., 2005; Yang et al., 2007). The absolute values of thermal expansion coefficient of ZrO_2 and $Zr_2MoP_2O_{12}$ are thus similar but have opposite signs, suggesting that these materials are good candidates for the preparation of ceramic composites with tunable CTEs. In this work, a new series of $Zr_2MoP_2O_{12}/ZrO_2$ composites were synthesized by solid state method with the goal of tailoring the thermal expansion. The effects of mass ratio between $Zr_2MoP_2O_{12}$ and ZrO_2 on the phase composition, microstructure, and thermal expansion coefficient of the $Zr_2MoP_2O_{12}/ZrO_2$ ceramic composites were also investigated.

EXPERIMENTAL

Sample Preparation

$Zr_2MoP_2O_{12}$, ZrO_2, and $Zr_2MoP_2O_{12}/ZrO_2$ composites (mass ratios: 1:2, 1:1, 2:1) were prepared using stoichiometric amounts of ZrO_2 (purity ≥99.95%, metals basis), MoO_3 (purity ≥99.99%, metals basis), and $NH_4H_2PO_4$ (purity ≥99.5%, metals basis). A summary of samples prepared can be found in **Table 1**. The starting compounds were mixed in ethanol using ball milling for 6 h to form a uniform mixture and dried at 80°C, then the mixtures were pre-heated at 500°C for 3 h. The mixtures, under 50 MPa, were cold pressed into pellets which were 7 mm in diameter and about 2 mm in thickness. Finally, the pellets were calcined at 1050°C in air for 6 h and cooled down in the furnace. In the solid-state synthesis, the following reactions may take place:

TABLE 1 | Synthesis conditions for ZrO_2, $Zr_2MoP_2O_{12}$, and $Zr_2MoP_2O_{12}/ZrO_2$ ceramics.

Mass ratios of $Zr_2MoP_2O_{12}$:ZrO_2	m(ZrO_2)/g	m(MoO_3)/g	m($NH_4H_2PO_4$)/g
0:1	10	0	0
1:2	9.8523	1.0824	1.7290
1:1	8.7776	1.6227	2.5930
2:1	7.7038	2.1635	3.4576
1:0	4.1655	2.4330	3.8895

$$ZrO_2 + MoO_3 + 2NH_4H_2PO_4 \rightarrow ZrP_2O_7 + 2NH_3\uparrow + 3H_2O + MoO_3(500^\circ C) \quad (1)$$

$$ZrO_2 + MoO_3 + ZrP_2O_7 \rightarrow Zr_2MoP_2O_{12}(1050^\circ C) \quad (2)$$

$$Or: (1 + x)ZrO_2 + MoO_3 + ZrP_2O_7 \rightarrow Zr_2MoP_2O_{12} + xZrO_2(1050^\circ C) \quad (3)$$

In this work, the 2:1 $Zr_2MoP_2O_{12}/ZrO_2$ composite was also prepared using the pure $Zr_2MoP_2O_{12}$ and ZrO_2 as raw materials, and the synthetic process is the same as that of the above process.

Experimental Techniques

Identification of the different phases presented in the samples was performed using powder X-ray diffraction (PXRD) on a Shimadzu XRD 7000 with Cu Ka radiation. Data were collected at 40 kV and 35 mA, with a scanning speed of 5°/min over an angular range of 10–60°. The micromorphologies of the samples were observed using a scanning electron microscopy (SEM, TESCAN VEGA3). The elemental composition of the samples were analyzed using energy-dispersive X-ray spectrometry (EDX, Bruker XFlash 6160) as well.The CTEs of the samples were measured by thermal mechanical analyzer (TMA/SS, Seiko 6300) using a heating rate of 5°C/min from room temperature to 700°C in air.

RESULTS AND DISCUSSION

XRD Analysis

Figure 1 shows typical XRD patterns of the $Zr_2MoP_2O_{12}/ZrO_2$ (mass ratios 1:2, 1:1, and 2:1) composites in addition to those of the pure $Zr_2MoP_2O_{12}$ and ZrO_2 ceramics obtained under the same preparation condition. **Figure 1a** shows typical powder XRD pattern of pure ZrO_2 ceramics sintered at 1050°C for 6 h, all the observed reflections could be well indexed and attributed to monoclinic ZrO_2 in agreement with JCPDS card number 65–1,023. The typical powder XRD pattern of pure $Zr_2MoP_2O_{12}$ specimen sintered at 1050°C for 6 h is shown in **Figure 1e**, all diffraction peaks match those expected for orthorhombic $Zr_2MoP_2O_{12}$, which agrees with literature reports (Cetinkol et al., 2009; Isobe et al., 2016). No impurity phases were detected, confirming the purity of the two products. The

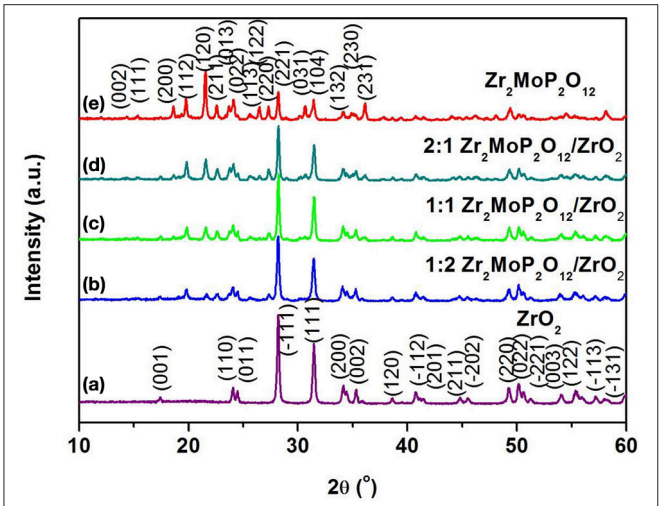

FIGURE 1 | XRD patterns of the obtained ZrO_2 ceramics, $Zr_2MoP_2O_{12}$ ceramics and $Zr_2MoP_2O_{12}/ZrO_2$ composites with different mass ratios sintered at 1050°C for 6 h.

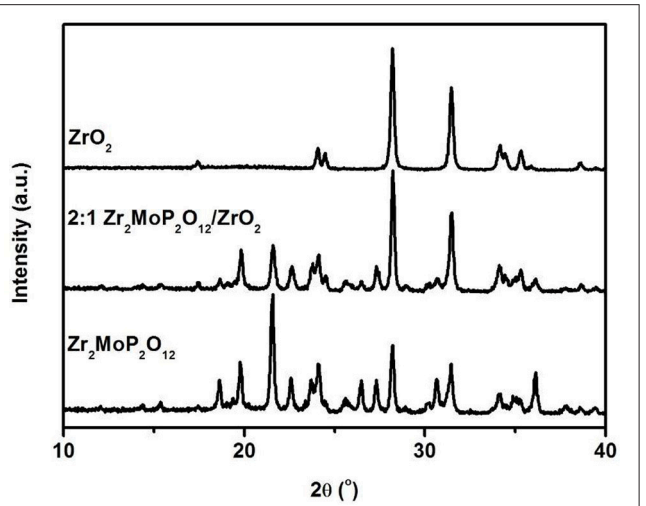

FIGURE 2 | XRD patterns of the obtained 2:1 $Zr_2MoP_2O_{12}/ZrO_2$ composites sintered at 1050°C for 6 h using the $Zr_2MoP_2O_{12}$ and ZrO_2 as raw materials, and the XRD patterns of pure $Zr_2MoP_2O_{12}$ and ZrO_2 were also given for reference.

PXRD patterns of the $Zr_2MoP_2O_{12}/ZrO_2$ (mass ratio: 1:2, 1:1, and 2:1) composites were shown in **Figures 1b–d**, it can be seen that all the diffraction peaks of the specimens could be indexed as both monoclinic ZrO_2 and orthorhombic $Zr_2MoP_2O_{12}$. With increasing mass ratio of $Zr_2MoP_2O_{12}$, the intensity of diffraction peaks of $Zr_2MoP_2O_{12}$ become much stronger. The diffraction peaks of both ZrO_2 and $Zr_2MoP_2O_{12}$ were sharp and intense, indicating their highly crystalline nature.

To investigate whether a chemical reaction occurred between ZrO_2 and $Zr_2MoP_2O_{12}$ during sintering at 1050°C. The 2:1 $Zr_2MoP_2O_{12}/ZrO_2$ composite was also prepared using the pure $Zr_2MoP_2O_{12}$ and ZrO_2 as raw materials. The $Zr_2MoP_2O_{12}$ was mixed with ZrO_2 at a mass ratio of 2:1 and finally calcined at 1050°C in air for 6 h. The XRD patterns of the ZrO_2, $Zr_2MoP_2O_{12}$, and 2:1 $Zr_2MoP_2O_{12}/ZrO_2$ were shown in **Figure 2**. Except for monoclinic ZrO_2 and orthorhombic $Zr_2MoP_2O_{12}$, no new peaks were detected, confirming that no chemical reaction occurred between ZrO_2 and $Zr_2MoP_2O_{12}$ during sintering at 1050°C.

SEM Images and Density Analysis

Further study was carried out by the SEM analysis to identify microstructures of as-prepared $Zr_2MoP_2O_{12}$, ZrO_2, and $Zr_2MoP_2O_{12}/ZrO_2$ composites. **Figure 3** shows SEM images of fracture surfaces of the pure ZrO_2, pure $Zr_2MoP_2O_{12}$ sintered bodies, and the $Zr_2MoP_2O_{12}/ZrO_2$ composites fabricated with different mass ratio of 1:2, 1:1, and 2:1. As shown in **Figure 3a**, as-prepared ZrO_2 ceramics sintered at 1050°C is not compact and the ZrO_2 grain growth is not observed obviously due to the insufficient sintering. The SEM images of the $Zr_2MoP_2O_{12}/ZrO_2$ composites fabricated at different mass ratio of 1:2, 1:1, and 2:1 are shown in **Figures 3b–d**. It can be seen that the $Zr_2MoP_2O_{12}/ZrO_2$ composites show nearly the same SEM images of fracture surfaces, which consist of irregular grains and some pores. With increasing content of $Zr_2MoP_2O_{12}$, $Zr_2MoP_2O_{12}/ZrO_2$ ceramics became denser and displayed larger particle sizes and less porosity, suggesting that the increase of $Zr_2MoP_2O_{12}$ slightly promoted the particle growth and increased the density of the $Zr_2MoP_2O_{12}/ZrO_2$ ceramics. **Figure 3e** shows the SEM images of fracture surfaces of the obtained pure $Zr_2MoP_2O_{12}$ ceramics. The $Zr_2MoP_2O_{12}$ sintered body was denser compared with the ZrO_2 ceramics fabricated at same sintering temperature. It is compact, which is in agreement with the results reported earlier (Cetinkol et al., 2009; Isobe et al., 2016). The elemental composition and distribution of 2:1 $Zr_2MoP_2O_{12}/ZrO_2$ composite was also investigated using the EDX. The distribution of zirconium, oxygen, phosphorus, molybdenum is shown in **Figures 3f–j**.

Thermal Expansion Properties

For a better analysis of the thermal expansion behaviors of the composites, **Figure 4A** shows the thermal expansion curves of the $Zr_2MoP_2O_{12}/ZrO_2$ composites with different mass ratio calcined at 1050°C for 6 h. The thermal expansion curves of the pure $Zr_2MoP_2O_{12}$ and pure ZrO_2 ceramics are also given for reference. As shown in **Figures 4A-a**, Pure ZrO_2 specimen shows positive thermal expansion in the testing temperature from 25 to 700°C with an average linear thermal expansion coefficient of 5.57×10^{-6} K^{-1}, which agrees with literature reports (Lommens et al., 2005; Yang et al., 2007). In **Figures 4A-e**, it can be seen that pure $Zr_2MoP_2O_{12}$ ceramics showed strong negative thermal expansion. Its average linear thermal expansion coefficient was measured to be -5.73×10^{-6} K^{-1} in the testing temperature range of 25–700°C. It can be found that the thermal expansion curves of the obtained samples except pure $Zr_2MoP_2O_{12}$ ceramics overlap below 200°C, this abnormal behavior in the beginning of thermal expansion curves may be caused by the instrument. Above 200°C, all the samples show stable and almost linear change in the curves

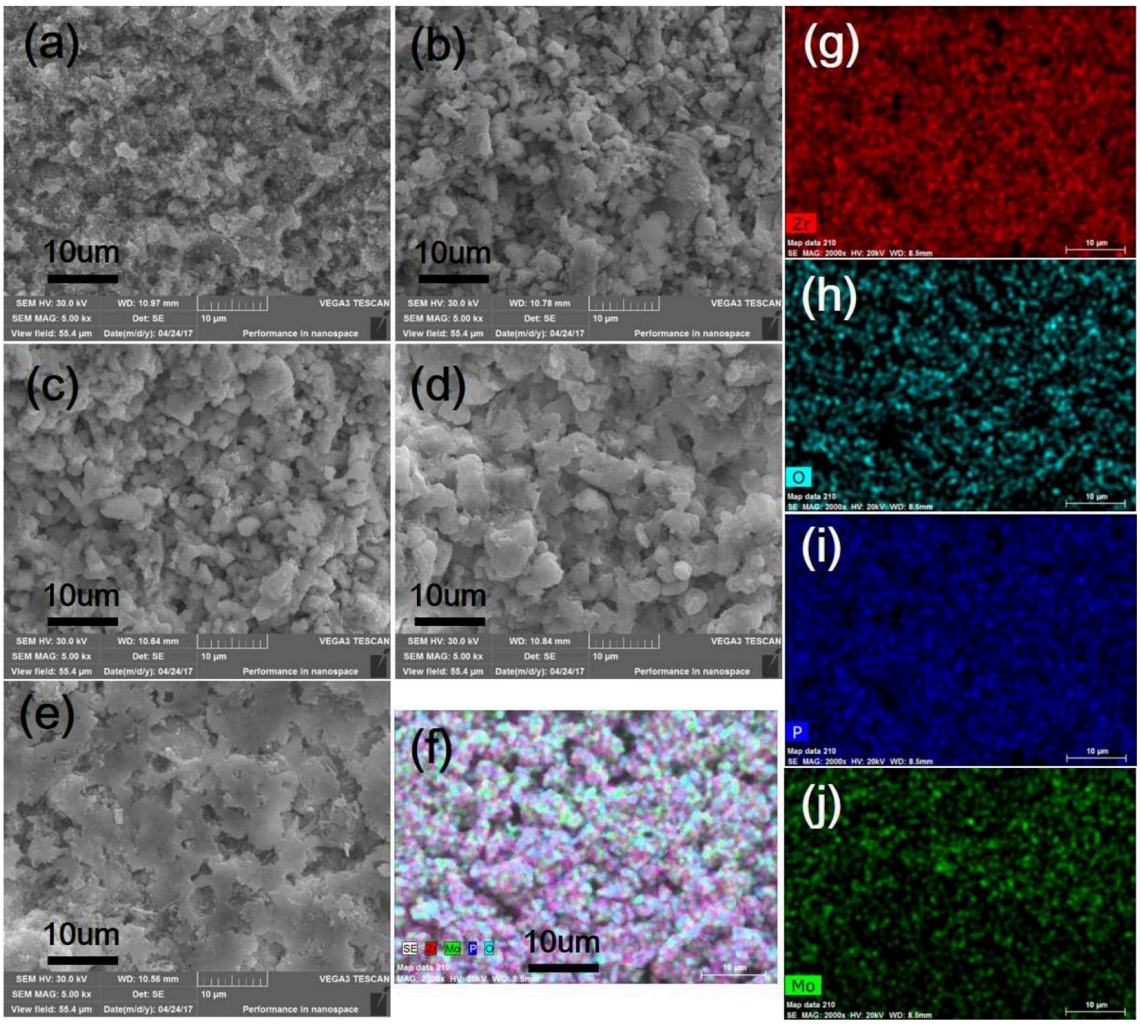

FIGURE 3 | SEM images of the obtained ZrO_2 ceramics, $Zr_2MoP_2O_{12}$ ceramics and $Zr_2MoP_2O_{12}/ZrO_2$ composites with different mass ratios sintered at 1050°C for 6 h. **(a)** ZrO_2 **(b)** $Zr_2MoP_2O_{12}$:ZrO_2 = 1:2 **(c)** $Zr_2MoP_2O_{12}$:ZrO_2 = 1:1 **(d)** $Zr_2MoP_2O_{12}$:ZrO_2 = 2:1 **(e)** $Zr_2MoP_2O_{12}$ **(f)** overlaid with elemental analysis results of 2:1 $Zr_2MoP_2O_{12}/ZrO_2$ composite using EDX **(g–j)** distribution of zirconium, oxygen, phosphorus, molybdenum elements in the selected area.

of thermal expansion with the increased temperature. Based on the above SEM analysis, the compact microstructure of the composites will promotes the stability of thermal expansion performance. Average linear thermal expansion coefficients of the obtained pure ZrO_2, pure $Zr_2MoP_2O_{12}$, and $Zr_2MoP_2O_{12}/ZrO_2$ composites with different mass ratios are summarized in **Table 2**. With increasing content of $Zr_2MoP_2O_{12}$, the thermal expansion coefficient of $Zr_2MoP_2O_{12}/ZrO_2$ composite decreased gradually. The 1:2 $Zr_2MoP_2O_{12}/ZrO_2$ composite showed positive thermal expansion with a thermal expansion coefficient of 2.30×10^{-6} K^{-1}. When the mass ratio of $Zr_2MoP_2O_{12}/ZrO_2$ decreased to 1:1, the composite also exhibited positive thermal expansion, but the CTE value decreased to 1.14×10^{-6} K^{-1}. The 2:1 $Zr_2MoP_2O_{12}/ZrO_2$ composite showed very low thermal expansion with an average linear thermal expansion coefficient of 0.0082×10^{-6} K^{-1} in the temperature range of 25–700°C. **Figure 4B** shows the cyclic thermal expansion curves of the $Zr_2MoP_2O_{12}/ZrO_2$ composites. The two thermal expansion curves are almost the same, and the second average linear thermal expansion coefficient was test to be 0.0049×10^{-6} K^{-1} in the same temperature range, indicating the 2:1 $Zr_2MoP_2O_{12}/ZrO_2$ composite shows a stable thermal expansion property and the mass ratio of 2:1 ($Zr_2MoP_2O_{12}/ZrO_2$) is appropriate one. With the increase of the temperature, the volume shrinkage of the NTE $Zr_2MoP_2O_{12}$ just can accommodate the volume expansion of ZrO_2, which will keep a little change of the volume value of the 2:1 $Zr_2MoP_2O_{12}/ZrO_2$ composite. This near-zero expansion ceramic composite can withstand thermal stresses arising during sintering and subsequent quenching, which is an important criterion for a number of potential application in many fields. The results suggest that the thermal expansion coefficients of $Zr_2MoP_2O_{12}/ZrO_2$ composites can be tailored from 5.57×10^{-6} K^{-1} to -5.73×10^{-6} K^{-1} by adjusting the weight fraction of $Zr_2MoP_2O_{12}$. **Figure 5** shows the relation between coefficients of

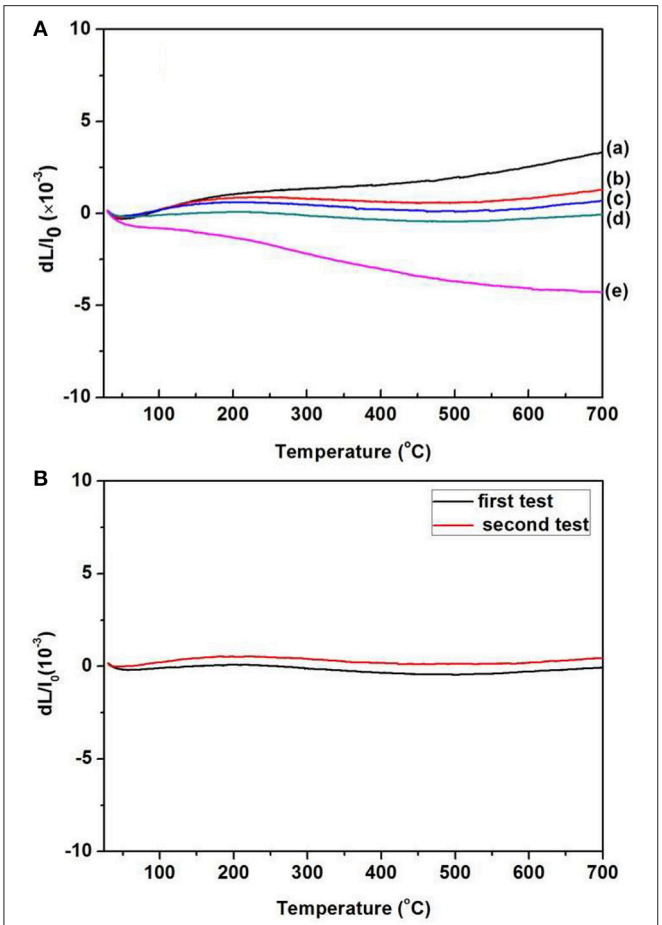

FIGURE 4 | (A) Thermal expansion curves of the obtained ZrO_2 ceramics, $Zr_2MoP_2O_{12}$ ceramics and $Zr_2MoP_2O_{12}/ZrO_2$ composites with different mass rati006Fs sintered at 1050°C for 6 h. **(a)** ZrO_2 **(b)** $Zr_2MoP_2O_{12}$:ZrO_2 = 1:2 **(c)** $Zr_2MoP_2O_{12}$:ZrO_2 = 1:1 **(d)** $Zr_2MoP_2O_{12}$:ZrO_2 = 2:1 **(e)** $Zr_2MoP_2O_{12}$. **(B)** Cyclic thermal expansion curves of the 2:1 $Zr_2MoP_2O_{12}/ZrO_2$ composite.

thermal expansion and the mass ratio of the $Zr_2MoP_2O_{12}/ZrO_2$ composites sintered at 1050°C for 6 h. The points is the data measured in the work. There is no linear relationship between the coefficients of thermal expansion and the mass ratio of the $Zr_2MoP_2O_{12}/ZrO_2$ composites. The red line is the best-fit line. According to the fitting equation, when the mass ration of $Zr_2MoP_2O_{12}/ZrO_2$ is 0.57, the $Zr_2MoP_2O_{12}/ZrO_2$ composite show zero thermal expansion. This fitting result deviates from the data obtained in the experiment. When the mass ration of $Zr_2MoP_2O_{12}/ZrO_2$ is 0.67, the near-zero thermal expansion $Zr_2MoP_2O_{12}/ZrO_2$ composite was obtained. This deviation mainly caused by the defects in the composites, such as pores and microcracks.

CONCLUSIONS

With the goal of thermal expansion control, NTE $Zr_2MoP_2O_{12}$ was combined with the positive thermal expansion ZrO_2 to fabricate the composites with a tailorable thermal expansion. The obtained $Zr_2MoP_2O_{12}/ZrO_2$ composites synthesized at 1050°C for 6 h were composed of orthorhombic $Zr_2MoP_2O_{12}$ and monoclinic ZrO_2, no intermediate phase was observed. With increasing content of $Zr_2MoP_2O_{12}$, the thermal expansion coefficient of $Zr_2MoP_2O_{12}/ZrO_2$ composite decreased while the density of the composite increased gradually. The thermal expansion coefficients of the $Zr_2MoP_2O_{12}/ZrO_2$ composites can be tailored from 5.57×10^{-6} K^{-1} to -5.73×10^{-6} K^{-1} by changing the weight fraction of $Zr_2MoP_2O_{12}$. In addition, the 2:1 $Zr_2MoP_2O_{12}/ZrO_2$ composite displayed near-zero thermal expansion with an average linear thermal expansion coefficient of 0.0065×10^{-6} K^{-1} in the testing temperature range of 25–700°C. This near-zero thermal expansion material will have a number of potential application in many fields due to its dimensional stability and high resistance to thermal shock.

TABLE 2 | Average linear thermal expansion coefficients of ZrO_2 ceramics, $Zr_2MoP_2O_{12}$ ceramics, and $Zr_2MoP_2O_{12}/ZrO_2$ composites with different mass ratios in corresponding testing temperature range from 25 to 700°C.

Samples (mass ratio)	Coefficient of thermal expansion
ZrO_2	5.57×10^{-6} K^{-1}
$Zr_2MoP_2O_{12}/ZrO_2$ = 1:2	2.30×10^{-6} K^{-1}
$Zr_2MoP_2O_{12}/ZrO_2$ = 1:1	1.14×10^{-6} K^{-1}
$Zr_2MoP_2O_{12}/ZrO_2$ = 2:1	0.0065×10^{-6} K^{-1}(mean value)
$Zr_2MoP_2O_{12}$	-5.73×10^{-6} K^{-1}

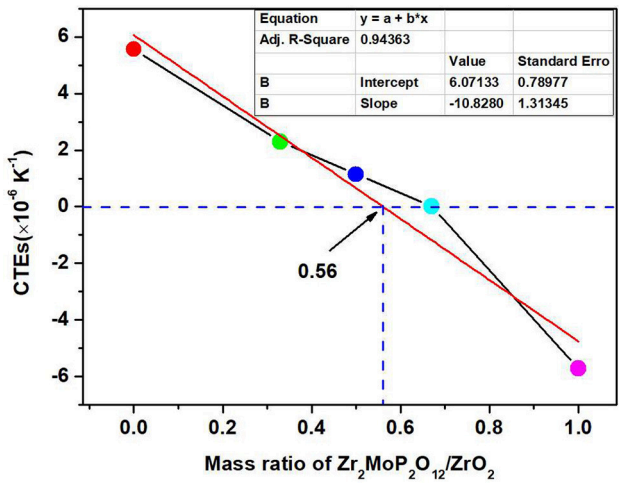

FIGURE 5 | Relation between coefficients of thermal expansion and the mass ratio of the $Zr_2MoP_2O_{12}/ZrO_2$ composites sintered at 1050°C for 6 h.

AUTHOR CONTRIBUTIONS

HL and ZZ designed experiments. WS, XX, and LY carried out experiments. HL, ZZ, XZ, MZ, and XC analyzed experimental results. HL and ZZ wrote the manuscript.

ACKNOWLEDGMENTS

The authors thank the National Natural Science Foundation of China (No.51602280 and No.51102207), Qing Lan Project of Jiangsu Province, Guangling College of Yangzhou University Natural Science Research Foundation (ZKZD17001). Yangzhou University Science and Technique Innovation Foundation (No.2015CJX007).

REFERENCES

Banek, N. A., Baiz, H. I., Latigo, A., and Lind, C. (2010). Autohydration of nanosized cubic zirconium tungstate. *J. Am. Chem. Soc*. 132, 8278–8279. doi: 10.1021/ja101475f

Cetinkol, M., Wilkinson, A. P., and Lee, P. (2009). Structural changes accompanying negative thermal expansion in $Zr_2(MoO_4)(PO_4)_2$. *J. Solid State Chem*. 182, 1304–1311. doi: 10.1016/j.jssc.2009.02.029

Chen, J., Hu, L., Deng, J., and Xing, X. (2015). Negative thermal expansion in functional materials: controllable thermal expansion by chemical modifications. *Chem. Soc. Rev*. 44, 3522–3567. doi: 10.1039/C4CS00461B

Gao, X. D., Coleman, M. R., and Lind, C. (2016). Surface modification of ZrW_2O_8 and $ZrW_2O_7(OH)_2\times2H_2O$ filler particles for controlled thermal expansion polycarbonate composites. *Pol. Comp*. 37, 1359–1368. doi: 10.1002/pc.23304

Isobe, T., Houtsuki, N., Hayakawa, Y., Yoshida, K., Matsushita, S., and Nakajima, A. (2016). Preparation and properties of $Zr_2MoP_2O_{12}$ ceramics with negative thermal expansion. *Mater. Design*. 112, 11–16. doi: 10.1016/j.matdes.2016.09.048

Kanamori, K., Kineri, T., Fukuda, R., Nishio, K., and Yasumori, A. (2008). Preparation and formation mechanism of ZrW_2O_8 by Sol–Gel process. *J. Am. Ceram. Soc*. 90, 3542–3545. doi: 10.1111/j.1551-2916.2008.02726.x

Kofteros, M., Rodriguez, S., and Tandon, V. (2001). A preliminary study of thermal expansion compensation in cement by ZrW_2O_8 additions. *Scripta Mater*. 45, 369–374. doi: 10.1016/S1359-6462(01)01009-0

Liu, H. F., Zhang, W., Zhang, Z. P., and Chen, X. B. (2012a). Synthesis and negative thermal expansion properties of solid solutions $Yb_{2-x}La_xW_3O_{12}$ ($0 \leq x \leq 2$). *Ceram. Int*. 38, 2951–2956. doi: 10.1016/j.ceramint.2011.11.072

Liu, H. F., Zhang, Z. P., Zhang, W., and Chen, X. B. (2011). Negative thermal expansion ZrW_2O_8 thin films prepared by pulsed laser deposition. *Surf. Coat. Technol*. 205, 5073–5076. doi: 10.1016/j.surfcoat.2011.05.010

Liu, H. F., Zhang, Z. P., Zhang, W., and Chen, X. B. (2012b). Effects of HCl concentration on the growth and negative thermal expansion property of the ZrW_2O_8 nanorods. *Ceram. Int*. 38, 1341–1345. doi: 10.1016/j.ceramint.2011.09.010

Liu, Q. Q., Yang, J., Cheng, X. N., Liang, G. S., and Sun, X. J. (2012). Preparation and characterization of negative thermal expansion $Sc_2W_3O_{12}$/Cu core–shell composite. *Ceram. Int*. 38, 541–545. doi: 10.1016/j.ceramint.2011.07.041

Lommens, P., Meyer, C. D., Bruneel, E., Buysser, K. D., Driessche, I. V., and Hoste, S. (2005). Synthesis and thermal expansion of ZrO_2/ZrW_2O_8 composites. *J. Europ. Ceram. Soc*. 25, 3605–3610. doi: 10.1016/j.jeurceramsoc.2004.09.015

Mary, T. A., Evans, J. S. O., Vogt, T., and Sleight, A. W. (1996). Negative thermal expansion from 0.3 K to 1050 K in ZrW_2O_8. *Science* 272, 90–92.

Nishiiyama, S., Hayashi, T., and Hattori, T. (2006). Synthesis of ZrW_2O_8 by quick cooling and measurement of negative thermal expansion of the sintered bodies. *J. Alloys Compd*. 417, 187–189. doi: 10.1016/j.jallcom.2005.07.075

Sullivan, L. M., and Lukehart, C. M. (2005). Zirconium tungstate (ZrW2O8)/polyimide nanocomposites exhibiting reduced coefficient of thermal expansion. *Chem. Mater*. 17, 2136–2141. doi: 10.1021/cm0482737

Wu, Y., Wang, M. L., Chen, Z., Ma, N. H., and Wang, H. W. (2013). The effect of phase transformation on the thermal expansion property in Al/ZrW_2O_8 composites. *J. Mater. Sci*. 48, 2928–2933. doi: 10.1007/s10853-012-6933-x

Yang, J., Yang, Y. S., Liu, Q. Q., Xu, G. F., and Cheng, X. N. (2010). Preparation of negative thermal expansion ZrW_2O_8 powders and its application in polyimide/ZrW_2O_8 composites. *J. Mater. Sci. Technol*. 26, 665–668. doi: 10.1016/S1005-0302(10)60103-X

Yang, X. B., Cheng, X. N., Yan, X. H., Yang, J., Fu, T. B., and Qiu, J. (2007). Synthesis of ZrO_2/ZrW_2O_8 composites with low thermal expansion. *Compos. Sci. Technol*. 67, 1167–1171. doi: 10.1016/j.compscitech.2006.05.012

Yilmaz, S. (2002). Thermal mismatch stress development in Cu-ZrW_2O_8 composite investigated by synchrotron X-ray diffraction. *Comp. Sci. Technol*. 62, 1835–1839. doi: 10.1016/S0266-3538(02)00104-5

Zhang, Z., Sun, W., Liu, H., Xie, G., Chen, X., and Zeng, X. (2017). Synthesis of $Zr_2WP_2O_{12}/ZrO_2$ composites with adjustable thermal expansion. *Front. Chem*. 5:105. doi: 10.3389/fchem.2017.00105

Conflict of Interest Statement: The authors declare that the research was conducted in the absence of any commercial or financial relationships that could be construed as a potential conflict of interest.

frontiers in Chemistry

ORIGINAL RESEARCH
published: 21 November 2017
doi: 10.3389/fchem.2017.00105

Synthesis of $Zr_2WP_2O_{12}/ZrO_2$ Composites with Adjustable Thermal Expansion

Zhiping Zhang[1,2], Weikang Sun[1], Hongfei Liu[1], Guanhua Xie[2], Xiaobing Chen[1,2] and Xianghua Zeng[1]*

[1] Department of Electrical and Mechanical Engineering, Guangling College, Yangzhou University, Yangzhou, China, [2] School of Physiccal Science and Technology, Yangzhou University, Yangzhou, China

$Zr_2WP_2O_{12}/ZrO_2$ composites were fabricated by solid state reaction with the goal of tailoring the thermal expansion coefficient. XRD, SEM and TMA were used to investigate the composition, microstructure, and thermal expansion behavior of $Zr_2WP_2O_{12}/ZrO_2$ composites with different mass ratio. Relative densities of all the resulting $Zr_2WP_2O_{12}/ZrO_2$ samples were also tested by Archimedes' methods. The obtained $Zr_2WP_2O_{12}/ZrO_2$ composites were comprised of orthorhombic $Zr_2WP_2O_{12}$ and monoclinic ZrO_2. As the increase of the $Zr_2WP_2O_{12}$, the relative densities of $Zr_2WP_2O_{12}/ZrO_2$ ceramic composites increased gradually. The coefficient of thermal expansion of the $Zr_2WP_2O_{12}/ZrO_2$ composites can be tailored from 4.1×10^{-6} K^{-1} to -3.3×10^{-6} K^{-1} by changing the content of $Zr_2WP_2O_{12}$. The 2:1 $Zr_2WP_2O_{12}/ZrO_2$ specimen shows close to zero thermal expansion from 25 to 700°C with an average linear thermal expansion coefficient of -0.09×10^{-6} K^{-1}. These adjustable and near zero expansion ceramic composites will have great potential application in many fields.

Keywords: $Zr_2WP_2O_{12}$, ZrO_2, composites, thermal expansion, ceramics

OPEN ACCESS

Edited by:
Jun Chen,
University of Science and Technology Beijing, China

Reviewed by:
Peng Tong,
Institute of Solid State Physics, Hefei Institutes of Physical Science (CAS), China
Rongjin Huang,
Technical Institute of Physics and Chemistry (CAS), China

****Correspondence:***
Hongfei Liu
liuhf@yzu.edu.cn

Specialty section:
This article was submitted to Physical Chemistry and Chemical Physics, a section of the journal Frontiers in Chemistry

Received: *27 September 2017*
Accepted: *03 November 2017*
Published: *21 November 2017*

Citation:
Zhang Z, Sun W, Liu H, Xie G, Chen X and Zeng X (2017) Synthesis of $Zr_2WP_2O_{12}/ZrO_2$ Composites with Adjustable Thermal Expansion. Front. Chem. 5:105. doi: 10.3389/fchem.2017.00105

INTRODUCTION

Lots of materials known to show positive thermal expansion as temperature increase. In contrast, some materials show completely different thermal expansion properties and contract upon heating. This negative thermal expansion (NTE) phenomena has been found in some $A_2(MO_4)_3$ compounds, where the A cation can be a trivalent main group metal, transition metal, or rare earth element ranging from Lu to Ho, while M corresponds to W or Mo (Sumithra and Umarji, 2004, 2006; Liu H. F. et al., 2012; Liu Q. Q. et al., 2012; Liu et al., 2015). In addition, compounds with aliovalent cations on the A and M site have been reported. For example, $Zr_2WP_2O_{12}$ has been reported to exhibit strong and stable NTE over a wide temperature range. $Zr_2WP_2O_{12}$ adopts the orthorhombic $Sc_2W_3O_{12}$ structure, which consists of ZrO_6 octahedra that share corners with two WO_4 tetrahedra and four PO_4 tetrahedra. Zr-O-W (P) linkages in this structure will lead to the volume contraction due to transverse vibration of bridging oxygen atoms as temperature increase (Isobe et al., 2008, 2009; Cetinkol and Wilkinson, 2009; Tani et al., 2010).

Thermal expansion is an important property of materials, and mismatch in thermal expansion often induces unstable performance or failure of devices in the field of microelectronics, optics and micromachines. To avoid the above problems, control of thermal expansion of materials can be necessary. An easy approach is to mix the NTE material with the positive thermal expansion material in the right proportion.

Most studies describing attempts to synthesize controllable thermal expansion composites mainly focus on ZrW_2O_8 based composites, such as ZrW_2O_8/ZrO_2 (De Buysser et al., 2004; Lommens et al., 2005; Yang et al., 2007; Khazeni et al., 2011; Romao et al., 2015), ZrW_2O_8/Cu and ZrW_2O_8/polyimide (Yilmaz, 2002; Sullivan and Lukehart, 2005; Yang et al., 2010; Hu et al., 2014). The coefficient of thermal expansion (CTE) of the composites drops with the increase of the ZrW_2O_8 filler. However, the cubic NTE phase of ZrW_2O_8 is metastable at room temperature, and has to be prepared by rapid quenching after sintering at 1,200°C. Cubic ZrW_2O_8 show a isotropic NTE over a wide temperature range, but a phase transition from α -ZrW_2O_8 to β -ZrW_2O_8 occurs around 160°C, which leads to the decrease of CTE. This change in thermal expansion may be disadvantageous for composite design. Moreover, when heated to 740°C, ZrW_2O_8 decomposes into ZrO_2 and WO_3 (Mary et al., 1996; Banek et al., 2010; Gao et al., 2016). In addition, cubic ZrW_2O_8 undergoes a pressure induced phase transition to an orthorhombic phase with a positive CTE. This transformation has been observed in composites during thermal cycling, and leads to irreproducible thermal expansion behavior (Perottoni and Jornada, 1998; Miao et al., 2004; Varga et al., 2007; Liu et al., 2014).

$Zr_2WP_2O_{12}$ is a new NTE material for use as a filler to adjust the CTE of ceramics, glasses, metals, and polymers. It exhibits a strong NTE over the broadest temperature range (room temperature to its sublimation point of about 1,600°C). Moreover, it does not suffer from the same limitations as ZrW_2O_8, as it is thermodynamically stable and does not undergo any phase transformations.

The synthesis and NTE behavior of $Zr_2WP_2O_{12}$ ceramics have been reported previously (Isobe et al., 2008, 2009; Cetinkol and Wilkinson, 2009; Tani et al., 2010). $Zr_2WP_2O_{12}$ ceramics show stable NTE with an average linear CET of about -5×10^{-6} K^{-1}. In addition, the $Zr_2WP_2O_{12}$ ceramics display excellent mechanical properties (Isobe et al., 2008, 2009; Cetinkol and Wilkinson, 2009). ZrO_2 ceramics and fibers has been widely used in optics, electronics and high temperature fields (Lommens et al., 2005; Yang et al., 2007). In some special occasions, ZrO_2 need to keep precision dimensional stability with the change in temperature, because a mismatch in size among different precision devices can cause some problems. The average linear CTE of ZrO_2 is about 10×10^{-6} K^{-1} from room temperature to 1,000°C. The absolute values of the CTE of ZrO_2 and $Zr_2WP_2O_{12}$ are thus similar but have opposite signs, suggesting that these materials are good candidates for the preparation of ceramic composites with tunable CTEs. It is beneficial that ZrO_2 does not react with $Zr_2WP_2O_{12}$ at high temperatures, as it is a starting material in the solid state synthesis of $Zr_2WP_2O_{12}$.

A new series of $Zr_2WP_2O_{12}/ZrO_2$ ceramic composites that are expected to show an adjustable CTE were synthesized by a solid state reaction method. This work is devoted to exploring the effects of mass ratio of $Zr_2WP_2O_{12}$ and ZrO_2 on the microstructure, density, and CTE values of the $Zr_2WP_2O_{12}/ZrO_2$ ceramic composites.

TABLE 1 | Synthesis conditions for $ZrO_2/Zr_2WP_2O_{12}$ ceramics.

Mass ratio of $Zr_2WP_2O_{12}$:ZrO_2	m(ZrO_2)/g	m(WO_3)/g	m($NH_4H_2PO_4$)/g
0:1	10	0	0
1:1	6.99	1.87	1.86
2:1	7.18	2.99	2.97
3:1	6.58	3.36	3.34
4:1	5.18	2.99	2.97
1:0	3.97	3.74	3.71

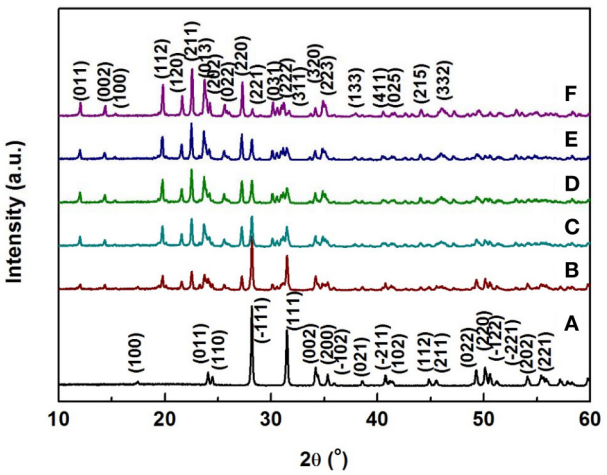

FIGURE 1 | XRD patterns of ZrO_2, $Zr_2WP_2O_{12}$, and $Zr_2WP_2O_{12}$-ZrO_2 composites with different mass ratios sintered at 1,200°C for 6 h. **(A)** ZrO_2, **(B)** 1:1 $Zr_2WP_2O_{12}$:ZrO_2, **(C)** 2:1 $Zr_2WP_2O_{12}$:ZrO_2, **(D)** 3:1 $Zr_2WP_2O_{12}$:ZrO_2, **(E)** 4:1 $Zr_2WP_2O_{12}$-ZrO_2, **(F)** $Zr_2WP_2O_{12}$.

EXPERIMENTAL DETAILS

All $Zr_2WP_2O_{12}$, ZrO_2, and $Zr_2WP_2O_{12}/ZrO_2$ ceramics (mass ratios: 1:1, 2:1, 3:1, 4:1) were synthesized through a conventional solid state route. The raw materials were ZrO_2 (Aladdin, purity ≥99.95%), WO_3 (Aladdin, purity ≥99.95%), and $NH_4H_2PO_4$ powders (Aladdin, purity ≥99.5%). A summary of samples prepared can be found in **Table 1**. Reactant mixtures were milled for 6 h to form a homogeneous powder and dried at 80°C, followed by heating at 500°C for 3 h. After this pre-sintering step, the mixtures were uni-axially cold pressed into pellets of 7 mm in diameter and about 2 mm in thickness. Pellets were calcined at 1,200°C in air for 6 h and cooled down in the furnace.

Powder X-ray diffraction experiments were performed on a Shimadzu XRD 7000 using CuKα radiation. Data were collected at 40 kV and 30 mA over the 10° to 60° 2θ range with a scanning speed of 5°/min. The fractured surface morphologies of the samples were observed using a TESCAN VEGA3 scanning electron microscope (SEM). The relative densities of the resulting samples were measured using Archimedes' method. The CTEs of the samples were measured with a Seiko 6300 TMA/SS thermal mechanical analyzer at a heating rate of 5°C/min in air between 25 and 700°C.

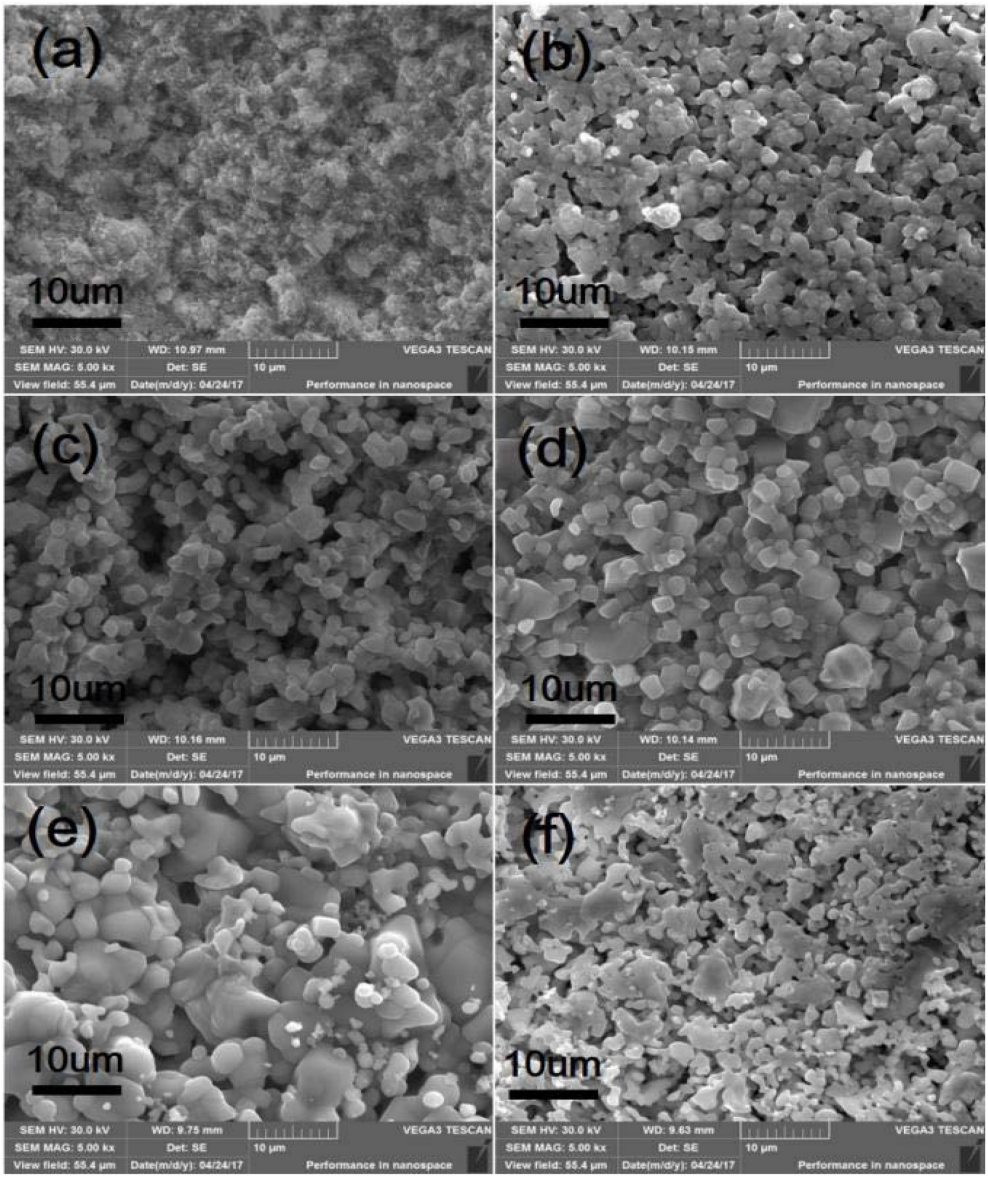

FIGURE 2 | SEM images of ZrO_2, $Zr_2WP_2O_{12}$, and $Zr_2WP_2O_{12}$-ZrO_2 composites with different mass ratios sintered at 1,200°C for 6 h, **(a)** ZrO_2, **(b)** 1:1 $Zr_2WP_2O_{12}$:ZrO_2, **(c)** 2:1 $Zr_2WP_2O_{12}$:ZrO_2, **(d)** 3:1 $Zr_2WP_2O_{12}$:ZrO_2, **(e)** 4:1 $Zr_2WP_2O_{12}$-ZrO_2, **(f)** $Zr_2WP_2O_{12}$.

RESULTS AND DISCUSSION

XRD Analysis

Figure 1 shows typical room temperature XRD patterns of $Zr_2WP_2O_{12}/ZrO_2$ composites with different mass ratios synthesized at 1,200°C for 6 h. The XRD patterns of pure ZrO_2 and pure $Zr_2WP_2O_{12}$ ceramics are also displayed for reference. For pure ZrO_2 ceramics (**Figure 1A**), all observed reflections could be well indexed and attributed to monoclinic ZrO_2 in agreement with JCPDS card number 65–1,023. For pure $Zr_2WP_2O_{12}$ ceramics (**Figure 1F**), all diffraction peaks matched those expected for orthorhombic $Zr_2WP_2O_{12}$ (JCPDS 43-0258). No impurity phases were detected. XRD patterns of $Zr_2WP_2O_{12}/ZrO_2$ composites with mass ratios of 1:1, 2:1, 3:1, and 4:1 (**Figures 1B–E**) displayed diffraction peaks belonging to both monoclinic ZrO_2 and orthorhombic $Zr_2WP_2O_{12}$. As no intermediate phase exists between ZrO_2 and $Zr_2WP_2O_{12}$, no reaction can occur between excess ZrO_2 and $Zr_2WP_2O_{12}$. As expected, the diffraction peaks of $Zr_2WP_2O_{12}$ became more intense with increasing mass ratio of $Zr_2WP_2O_{12}$.

SEM and Density Analysis

SEM micrographs of different weight ratio $Zr_2WP_2O_{12}/ZrO_2$ ceramic composites, ZrO_2 and $Zr_2WP_2O_{12}$ ceramics after sintering at 1,200°C for 6 h are shown in **Figure 2**. The SEM

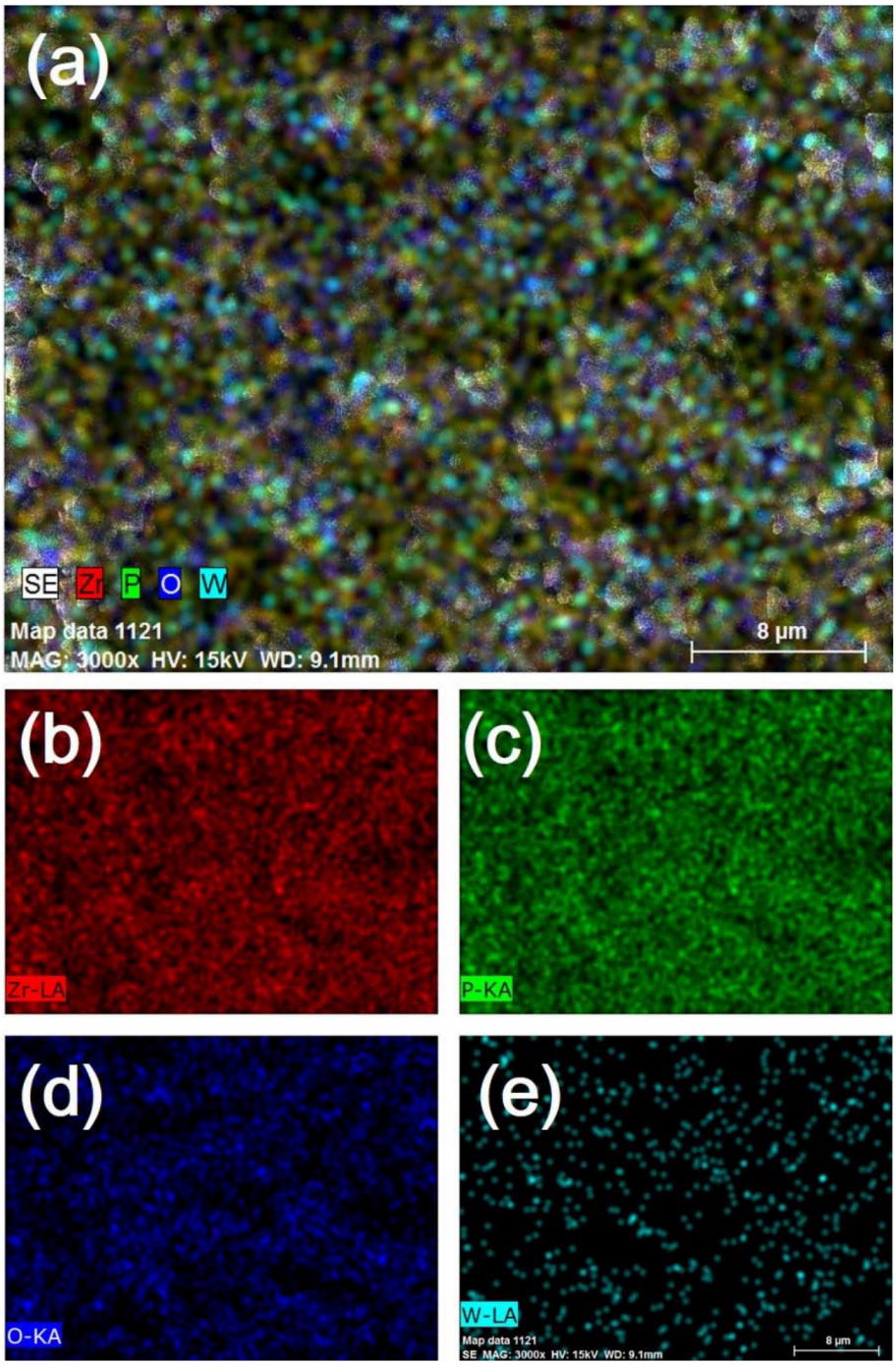

FIGURE 3 | EDX composition maps **(a)** Zr, P, W and O, **(b)** Zr, **(c)** P, **(d)** O, and **(e)** W analysis for 2:1 $Zr_2WP_2O_{12}$:ZrO_2 composite.

image of the ZrO_2 ceramics (**Figure 2a** revealed significant porosity, which is likely due to insufficient sintering. It is known that the sintering temperature required to fabricate dense and tough ZrO_2 ceramics is higher than 1,400°C (Varga et al., 2007). **Figures 2b–e** show SEM images of sintered $Zr_2WP_2O_{12}/ZrO_2$ ceramic composites as a function of different mass ratios. With increasing amount of $Zr_2WP_2O_{12}$, $Zr_2WP_2O_{12}/ZrO_2$ ceramic composites sintered for the same time at the same temperature became denser and displayed larger grain sizes and less porosity. The average grain size of 1:1 $Zr_2WP_2O_{12}/ZrO_2$ composites was about 2–3 µm, but increased to about 6–8 µm when the mass ratio of $Zr_2WP_2O_{12}/ZrO_2$ was increased to 4:1. Pure $Zr_2WP_2O_{12}$

TABLE 2 | Relative densities of ZrO_2, $Zr_2WP_2O_{12}$, and $Zr_2WP_2O_{12}$-ZrO_2 composites with different mass ratios.

Sample	Relative density (%)
ZrO_2	74.5
1:1 $Zr_2WP_2O_{12}$-ZrO_2	84.1
2:1 $Zr_2WP_2O_{12}$-ZrO_2	85.5
3:1 $Zr_2WP_2O_{12}$-ZrO_2	89.8
4:1 $Zr_2WP_2O_{12}$-ZrO_2	91.5
$Zr_2WP_2O_{12}$	79.7

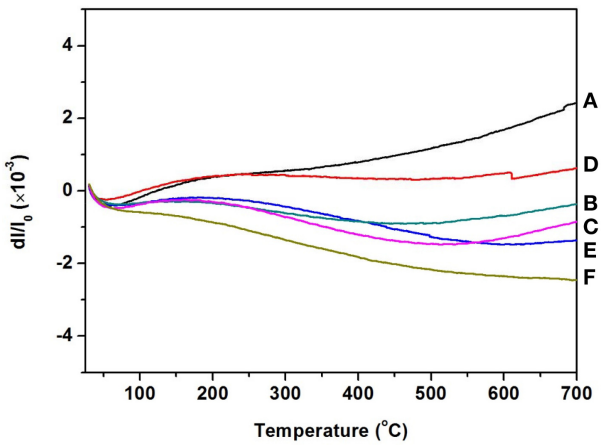

FIGURE 4 | Thermal expansion curves of ZrO_2, $Zr_2WP_2O_{12}$, and $Zr_2WP_2O_{12}$-ZrO_2 composites. **(A)** ZrO_2, **(B)** 1:1 $Zr_2WP_2O_{12}$:ZrO_2, **(C)** 2:1 $Zr_2WP_2O_{12}$:ZrO_2, **(D)** 3:1 $Zr_2WP_2O_{12}$:ZrO_2, **(E)** 4:1 $Zr_2WP_2O_{12}$-ZrO_2, **(F)** $Zr_2WP_2O_{12}$.

TABLE 3 | Average linear thermal expansion coefficients of ZrO_2, $Zr_2WP_2O_{12}$, and $Zr_2WP_2O_{12}$-ZrO_2 composites in corresponding testing temperature range from 25 to 700°C.

Samples	Coefficient of thermal expansion
ZrO_2	4.10×10^{-6} K^{-1}
1:1 $Zr_2WP_2O_{12}$-ZrO_2	1.32×10^{-6} K^{-1}
2:1 $Zr_2WP_2O_{12}$-ZrO_2	-0.09×10^{-6} K^{-1}
3:1 $Zr_2WP_2O_{12}$-ZrO_2	-0.88×10^{-6} K^{-1}
4:1 $Zr_2WP_2O_{12}$-ZrO_2	-1.50×10^{-6} K^{-1}
$Zr_2WP_2O_{12}$	-3.30×10^{-6} K^{-1}

(**Figure 2f**) showed a wide size distribution of spherical grains with some residual porosity, which is in agreement with results reported earlier (Isobe et al., 2008, 2009; Cetinkol and Wilkinson, 2009). **Figure 3** shows the composition maps analysis of the 2:1 $Zr_2WP_2O_{12}$:ZrO_2 composite. Homogeneous spatial distributions of Zr, P, W, and O elements were observed. These results indicates that $Zr_2WP_2O_{12}$ and ZrO_2 phase uniformly distributed as expected.

In this work, the densities of the resulting $Zr_2WP_2O_{12}$, ZrO_2, and $Zr_2WP_2O_{12}/ZrO_2$ (mass ratio: 1:1, 2:1, 3:1, 4:1) ceramics were also measured using Archimedes' technique. The relative densities were calculated from theoretical values for $Zr_2WP_2O_{12}$ (3.63 g/cm^3) and ZrO_2 (5.817 g/cm^3). As shown in **Table 2**, the results are consistent with the SEM analysis above. The relative densities of pure $Zr_2WP_2O_{12}$ and ZrO_2 were low, however, the densities of $Zr_2WP_2O_{12}/ZrO_2$ (mass ratio: 1:1, 2:1, 3:1, 4:1) ceramics increased with increasing content of $Zr_2WP_2O_{12}$. For a 4:1 mass ratio $Zr_2WP_2O_{12}/ZrO_2$ composite, the relative density of the sample reached 91.5% of the theoretical density values. The sintering temperature of $Zr_2WP_2O_{12}$ is lower than that of ZrO_2, which results in a decreased sintering temperature and better densification of $Zr_2WP_2O_{12}/ZrO_2$ ceramics with increasing content of $Zr_2WP_2O_{12}$.

Thermal Expansion Analysis

Figure 4 gives the information about the thermal expansion of all the $Zr_2WP_2O_{12}/ZrO_2$ ceramic composites synthesized at 1,200°C for 6 h. For purposes of comparison, the thermal expansion curves of pure ZrO_2 and pure $Zr_2WP_2O_{12}$ ceramics are also given in **Figure 4**. Average linear CTEs of the obtained ZrO_2, $Zr_2WP_2O_{12}$, and $Zr_2WP_2O_{12}/ZrO_2$ ceramics with different mass ratios are summarized in **Table 3**. Pure ZrO_2 ceramics (**Figure 4A**) showed positive thermal expansion between 25 and 700°C, and the average linear CTE was measured to be 4.1×10^{-6} K^{-1}, which is lower than the value reported in the literature (Lommens et al., 2005; Yang et al., 2007). This is likely due to insufficient sintering of the ZrO_2 ceramics, as some of the expansion can be absorbed by the empty pore space. Pure $Zr_2WP_2O_{12}$ ceramics (**Figure 4F**) showed NTE in the testing temperature range. The average linear CTE of the $Zr_2WP_2O_{12}$ ceramics was measured to be -3.3×10^{-6} K^{-1} in the temperature range of 25–700°C, which is consistent with literature reports (Cetinkol and Wilkinson, 2009; Isobe et al., 2009). As can be expected, the CTEs of the $Zr_2WP_2O_{12}/ZrO_2$ composites decreased from 4.1×10^{-6} K^{-1} to -3.3×10^{-6} K^{-1} as the weight fraction of $Zr_2WP_2O_{12}$ was increased. As shown in **Figure 4C**, the 2:1 $Zr_2WP_2O_{12}/ZrO_2$ specimen showed close to zero thermal expansion with an average linear CTE of -0.09×10^{-6} K^{-1} in the temperature range of 25–700°C. This near zero expansion ceramic composite will have a number of potential applications in many fields. These results suggest that the CTE of the $Zr_2WP_2O_{12}$-ZrO_2 composites can be modified in the range from 4.1×10^{-6} K^{-1} to -3.3×10^{-6} K^{-1}, and that it is even possible to achieve zero thermal expansion by adjusting the mass ratios of $Zr_2WP_2O_{12}$ and ZrO_2.

CONCLUSIONS

$Zr_2WP_2O_{12}/ZrO_2$ ceramic composites with adjustable thermal expansion coefficients were successfully fabricated by a solid state reaction method. The composites consisted of orthorhombic $Zr_2WP_2O_{12}$ and monoclinic ZrO_2 with no intermediate phases observed. With increasing amount of $Zr_2WP_2O_{12}$, the relative densities of the $Zr_2WP_2O_{12}/ZrO_2$ ceramic composites increased gradually. The CTE of the $Zr_2WP_2O_{12}/ZrO_2$ composites can be tailored from 4.1×10^{-6} K^{-1} to -3.3×10^{-6} K^{-1} by changing the weight fraction of $Zr_2WP_2O_{12}$. For a mass ratio of $Zr_2WP_2O_{12}/ZrO_2$ of 2:1, the $Zr_2WP_2O_{12}/ZrO_2$ ceramic

composite showed close to zero thermal expansion with an average linear CTE of -0.09×10^{-6} K^{-1} between 25 and 700°C.

AUTHOR CONTRIBUTIONS

HL, XC, and ZZ designed experiments; WS and GX carried out experiments; HL, ZZ, and XZ analyzed experimental results and wrote the manuscript.

ACKNOWLEDGMENTS

The authors thank the National Natural Science Foundation of China (No.51602280 and No.51102207). Qing Lan Project of Jiangsu Province. Guang ling College of Yangzhou University Natural Science Research Foundation (No. ZKZD17001). The authors are grateful to Dr. Cora Lind-Kovacs for revising the paper.

REFERENCES

Banek, N. A., Baiz, H. I., Latigo, A., and Lind, C. (2010). Autohydration of nanosized cubic zirconium tungstate. *J. Am. Chem. Soc.* 132, 8278–8279. doi: 10.1021/ja101475f

Cetinkol, M., and Wilkinson, A. P. (2009). Pressure dependence of negative thermal expansion in $Zr_2(WO_4)(PO_4)_2$. *Solid State Commun.* 149, 421–424. doi: 10.1016/j.ssc.2009.01.002

De Buysser, K., Lommens, P., De Meyer, C., Bruneel, E., Hoste, S., and Driessche, I. V. (2004). ZrO_2-ZrW_2O_8 composites with tailor-made thermal expansion. *Ceram. Silikaty* 48, 139–144.

Gao, X., Coleman, M. R., and Lind, C. (2016). Surface modification of ZrW_2O_8 and $ZrW_2O_7(OH)_2{\cdot}2H_2O$ filler particles for controlled thermal expansion polycarbonate composites. *Pol. Comp.* 37, 1359–1368. doi: 10.1002/pc.23304

Hu, L., Chen, J., Fan, L. L., Ren, Y., Rong, Y. C., Pan, Z., et al. (2014). Zero thermal expansion and ferromagnetism in cubic $Sc_{1-x}M_xF_3$ (M= Ga, Fe) over a wide temperature range. *J. Am. Chem. Soc.* 136, 13566–13569. doi: 10.1021/ja5077487

Isobe, T., Kato, Y., Mizutani, M., Ota, T., and Daimon, K. (2008). Pressureless sintering of negative thermal expansion $ZrW_2O_8/Zr_2WP_2O_{12}$ composites. *Mater. Lett.* 62, 3913–3915. doi: 10.1016/j.matlet.2008.05.046

Isobe, T., Umezome, T., Kameshima, Y., Nakajima, A., and Okada, K. (2009). Preparation and properties of negative thermal expansion $Zr_2WP_2O_{12}$ ceramics. *Mater. Res. Bull.* 44, 2045–2049. doi: 10.1016/j.materresbull.2009.07.020

Khazeni, N., Mavis, B., Gunduz, G., and Colak, U. (2011). Synthesis of zirconium tungstate-zirconia core-shell composite particles. *Mater. Res. Bull.* 46, 2025–2031. doi: 10.1016/j.materresbull.2011.07.006

Liu, H. F., Pan, K. M., Jin, Q., Zhang, Z. P., Wang, G., and Zeng, X. H. (2014). Negative thermal expansion and shift in phase transition temperature in Mo-substituted ZrW_2O_8 thin films prepared by pulsed laser deposition. *Ceram. Int.* 40, 3873–3878. doi: 10.1016/j.ceramint.2013.08.028

Liu, H. F., Zhang, W., Zhang, Z. P., and Chen, X. B. (2012). Synthesis and negative thermal expansion properties of solid solutions $Yb_{2-x}La_xW_3O_{12}$ ($0 \leq x \leq 2$). *Ceram. Int.* 38, 2951–2956. doi: 10.1016/j.ceramint.2011.11.072

Liu, H. F., Zhang, Z. P., Ma, J., Zhu, J., and Zeng, X. H. (2015). Effect of isovalent substitution on phase transition and negative thermal expansion of $In_{2-x}Sc_xW_3O_{12}$ ceramics. *Ceram. Int.* 41, 9873–9877. doi: 10.1016/j.ceramint.2015.04.062

Liu, Q. Q., Yang, J., Cheng, X. N., Liang, G. S., and Sun, X. J. (2012). Preparation and characterization of negative thermal expansion $Sc_2W_3O_{12}$/Cu core–shell composite. *Ceram. Int.* 38, 541–545. doi: 10.1016/j.ceramint.2011.07.041

Lommens, P., Meyer, C. D., Bruneel, E., Buysser, K. D., Driessche, I. V., and Hoste, S. (2005). Synthesis and thermal expansion of ZrO_2/ZrW_2O_8 composites. *J. Eur. Ceram. Soc.* 25, 3605–3610. doi: 10.1016/j.jeurceramsoc.2004.09.015

Mary, T. A., Evans, J. S. O., Vogt, T., and Sleight, A. W. (1996). Negative thermal expansion from 0.3 K to 1050 K in ZrW_2O_8. *Science* 272, 90–92. doi: 10.1126/science.272.5258.90

Miao, X. G., Sun, D., Hoo, P. W., Liu, J. L., Hu, Y. F., and Chen, Y. M. (2004). Effect of titania addition on yttria-stabilised tetragonal zirconia ceramics sintered at high temperatures. *Ceram. Int.* 30, 1041–1047. doi: 10.1016/j.ceramint.2003.10.025

Perottoni, C. A., and Jornada, J. A. H. (1998). Pressure-induced amorphization and negative thermal expansion in ZrW_2O_8. *Science* 280, 886–888. doi: 10.1126/science.280.5365.886

Romao, C. P., Marinkovic, B. A., Werner-Zwanzige, U., and White, M. A. (2015). Thermal expansion reduction in alumina-toughened zirconia by incorporation of zirconium tungstate and aluminum tungstate. *J. Am. Chem. Soc.* 98, 2858–2865. doi: 10.1111/jace.13675

Sullivan, L. M., and Lukehart, C. M. (2005). Zirconium tungstate (ZrW_2O_8)/polyimide nanocomposites exhibiting reduced coefficient of thermal expansion. *Chem. Mater.* 17, 2136–2141. doi: 10.1021/cm0482737

Sumithra, S., and Umarji, A. M. (2004). Role of crystal structure on the thermal expansion of $Ln_2W_3O_{12}$ (Ln =La, Nd, Dy, Y., Er and Yb). *Solid State Sci.* 6, 1313–1319. doi: 10.1016/j.solidstatesciences.2004.07.023

Sumithra, S., and Umarji, A. M. (2006). Negative thermal expansion in rare earth molybdates. *Solid State Sci.* 8, 1453–1458. doi: 10.1016/j.solidstatesciences.2006.03.010

Tani, J., Takahashi, M., and Kido, H. (2010). Fabrication and thermal expansion properties of $ZrW_2O_8/Zr_2WP_2O_{12}$ composites. *J. Eur. Ceram. Soc.* 30, 1483–1488. doi: 10.1016/j.jeurceramsoc.2009.11.010

Varga, T., Lind, C., Wilkinson, A. P., Xu, H., Lesher, C. E., and Navrotsky, A. (2007). Heats of formation for several crystalline polymorphs and pressure-induced amorphous forms of AMo_2O_8 (A=Zr, Hf) and ZrW_2O_8. *Chem. Mater.* 19, 468–476. doi: 10.1021/cm0617743

Yang, J., Yang, Y. S., Liu, Q. Q., Xu, G. F., and Cheng, X. N. (2010). Preparation of negative thermal expansion ZrW_2O_8 powders and its application in polyimide/ZrW_2O_8 composites. *J. Mater. Sci. Technol.* 26, 665–668. doi: 10.1016/S1005-0302(10)60103-X

Yang, X. B., Cheng, X. N., Yan, X. H., Yang, J., Fu, T. B., and Qiu, J. (2007). Synthesis of ZrO_2/ZrW_2O_8 composites with low thermal expansion. *Compos. Sci. Technol.* 67, 1167–1171. doi: 10.1016/j.compscitech.2006.05.012

Yilmaz, S. (2002). Thermal mismatch stress development in Cu-ZrW_2O_8 composite investigated by synchrotron X-ray diffraction. *Comp. Sci. Technol.* 62, 1835–1839. doi: 10.1016/S0266-3538(02)00104-5

Conflict of Interest Statement: The authors declare that the research was conducted in the absence of any commercial or financial relationships that could be construed as a potential conflict of interest.

frontiers in Chemistry

ORIGINAL RESEARCH
published: 17 April 2018
doi: 10.3389/fchem.2018.00115

Near-Zero Thermal Expansion and Phase Transitions in $HfMg_{1-x}Zn_xMo_3O_{12}$

Sailei Li[1], *Xianghong Ge*[1,2], *Huanli Yuan*[1,3], *Dongxia Chen*[1], *Juan Guo*[1], *Ruofan Shen*[1], *Mingju Chao*[1] *and Erjun Liang*[1]*

[1] School of Physical Science & Engineering and Key Laboratory of Materials Physics of Ministry of Education, Zhengzhou University, Zhengzhou, China, [2] College of Science, Zhongyuan University of Technology, Zhengzhou, China, [3] Department of Physics and Electronic Engineering, Zhoukou Normal University, Zhoukou, China

The effects of Zn^{2+} incorporation on the phase formation, thermal expansion, phase transition, and vibrational properties of $HfMg_{1-x}Zn_xMo_3O_{12}$ are investigated by XRD, dilatometry, and Raman spectroscopy. The results show that (i) single phase formation is only possible for $x \leq 0.5$, otherwise, additional phases of $HfMo_2O_8$ and $ZnMoO_4$ appear; (ii) The phase transition temperature from monoclinic to orthorhombic structure of the single phase $HfMg_{1-x}Zn_xMo_3O_{12}$ can be well-tailored, which increases with the content of Zn^{2+}; (iii) The incorporation of Zn^{2+} leads to an pronounced reduction in the positive expansion of the *b*-axis and an enhanced negative thermal expansion (NTE) in the *c*-axes, leading to a near-zero thermal expansion (ZTE) property with lower anisotropy over a wide temperature range; (iv) Replacement of Mg^{2+} by Zn^{2+} weakens the Mo–O bonds as revealed by obvious red shifts of all the Mo–O stretching modes with increasing the content of Zn^{2+} and improves the sintering performance of the samples which is observed by SEM. The mechanisms of the negative and near-ZTE are discussed.

Keywords: thermal expansion, near-zero thermal expansion, phase transition, X-ray diffraction (XRD), Raman spectrum

OPEN ACCESS

Edited by:
Jun Chen,
University of Science and Technology Beijing, China

Reviewed by:
Xuehua Yan,
Jiangsu University, China
Ying Sun,
Beihang University, China

***Correspondence:**
Erjun Liang
ejliang@zzu.edu.cn

Specialty section:
This article was submitted to Physical Chemistry and Chemical Physics, a section of the journal Frontiers in Chemistry

Received: *15 January 2018*
Accepted: *29 March 2018*
Published: *17 April 2018*

Citation:
Li S, Ge X, Yuan H, Chen D, Guo J, Shen R, Chao M and Liang E (2018) Near-Zero Thermal Expansion and Phase Transitions in $HfMg_{1-x}Zn_xMo_3O_{12}$. Front. Chem. 6:115. doi: 10.3389/fchem.2018.00115

INTRODUCTION

Large difference in coefficients of thermal expansion (CTE) of materials could lead to performance deterioration and even failure of devices due to thermal stress when temperature changes abruptly or frequently. Since most materials expand on heating and contract on cooling, materials with opposite property, namely negative thermal expansion (NTE), are particularly desired for tailoring CTEs. The rediscovery of NTE in ZrW_2O_8 in a wide temperature range (Evans et al., 1996, 1997a) triggered continuous efforts on understanding the NTE phenomenon and searching for more NTE materials (Yang et al., 2007; Chen et al., 2013, 2015; Tallentire et al., 2013; Lama et al., 2014; Liu et al., 2014; Peng et al., 2014; Xiao et al., 2014; Hu et al., 2015). To date, different families of NTE materials based on various mechanisms, such as the phonon effect (Pryde et al., 1996; Wang et al., 2011; Bridges et al., 2014; Cheng et al., 2016a; Ge et al., 2016a), magnetovolume effect (Takenaka and Takagi, 2005; Qu et al., 2012; Yan et al., 2014), spontaneous ferroelectric polarization (Chen et al., 2013; Peng et al., 2016), and charge transfer (Long et al., 2009; Azuma et al., 2011; Yamada et al., 2016) have been reported. Among the materials, the family of $A_2M_3O_{12}$ (A = transition metal or a mixture of tetravalent and bivalent cations, M = W, Mo) have been particularly attractive, because whose NTEs go over a wide temperature range and can be tuned

from low positive to large negative values due to chemical flexibility (Evans et al., 1997b; Suzuki and Omote, 2006; Wu et al., 2009, 2012, 2014; Li et al., 2011; Das et al., 2013; Miller et al., 2013; Song et al., 2014a; Liu et al., 2015; Chen et al., 2016; Cheng et al., 2016a).

In recent years, a number of novel NTE materials have been designed based on the basic structure of $A_2M_3O_{12}$ family, including those with a general formula ABM_3O_{12} where A is tetravalent Hf^{4+} or Zr^{4+} and B is bivalent cation Mg^{2+} or Mn^{2+}, and M is W or Mo or a combination of them (Suzuki and Omote, 2004; Baiz et al., 2008; Gindhart et al., 2008; Marinkovic et al., 2008; Song et al., 2013; Li et al., 2014, 2016, 2017; Ge et al., 2016a; Liu et al., 2018) and those with a formula ABM_2XO_{12} where A and M are the same as in ABM_3O_{12}, B is a trivalent cation and X is P^{5+} or V^{5+} (Chen et al., 2016; Cheng et al., 2016b, 2017; Ge et al., 2016b,c). The most distinct characteristics of the materials with formula ABM_2XO_{12} are that they exhibit NTE over a wide temperature range and intense photoluminescence in the visible range. Nearly an order higher ionic conductivity was observed for $HfMgW_3O_{12}$ with respect to the family $A_2M_3O_{12}$ (Omote et al., 2011). $HfMgMo_3O_{12}$ with a linear CTE of 1.02×10^{-6} K^{-1} from 298 to 1013 K was reported by Marinkovic et al. (2008). It crystallizes in orthorhombic symmetry with space group *Pnma*(62) or $Pna2_1$ (33) and transforms to monoclinic structure at 175 K (Miller et al., 2012).

In this paper, we investigate the effects of Zn^{2+} incorporation on the structure, phase transition, thermal expansion, and vibrational properties of $HfMgMo_3O_{12}$. It is shown that single phase solid solution of $HfMg_{1-x}Zn_xMo_3O_{12}$ can be achieved only for the compositions of $x \leq 0.5$, otherwise, additional phases of $HfMo_2O_8$ and $ZnMoO_4$ appear. The monoclinic to orthorhombic phase transition temperature increases with the content of Zn^{2+} for $x \leq 0.5$ so that $HfMg_{0.5}Zn_{0.5}Mo_3O_{12}$ crystallizes in monoclinic phase and all other samples ($x \leq 0.4$) adopt orthorhombic structure at room temperature (RT). The incorporation of Zn^{2+} alters the axial CTE differently for each axis and finally results in near-zero thermal expansion (ZTE) property over wide temperature ranges with smaller thermal expansion anisotropy with respect to $HfMgMo_3O_{12}$. The mechanisms of Zn^{2+} incorporation on the phase transition, thermal expansion and vibrational properties are discussed.

EXPERIMENTAL

Analytic grade reagents of HfO_2, MgO, ZnO, and MoO_3 were mixed with stoichiometric ratios for $HfMg_{1-x}Zn_xMo_3O_{12}$ with $x = 0.0$, 0.1, 0.2, 0.3, 0.4, 0.5, 0.6, 0.7, 0.8, and 1.0. The mixtures were ground in an agate mortar for 2 h, then, pressed under 325 MPa into cylinders with diameter of 10 mm and height of 6 mm using a uniaxial tablet machine. The cylinders were sintered at 1,073 K for 5 h in a muffle furnace in air and cooled down to 300 K naturally.

The as-prepared samples were analyzed by XRD with a PANalytical X'Pert PRO X-ray Diffractometer to identify the crystalline phase. Variable-temperature X-ray powder data were collected on a Rigaku (Japan, SmartLab 3KW) diffractometer with Cu Kα ($\lambda = 0.15405$ nm) radiation. Diffraction data were collected with a step size of 0.01° in the 2θ range of 10°–120°. The sample was heated at a rate of 10 K/min and remained at each measurement temperature for 5 min before measurement. Unit cell dimensions above the phase transition temperature were determined with software of PowderX. Variable-temperature/RT Raman spectra were recorded with A LabRAM HR Evolution Raman spectrometer (France HORIBA JobinYvon S.A.A.) equipped with a Linkam THMS600 Heating and Freezing Stage (Japan Hightech) (an accuracy of ±0.1 K). The excitation wavelength is 633 nm and low excitation laser power is necessary to avoid local heating by the laser. The microstructures and energy dispersive spectra of the samples were examined with a scanning electron microscope (SEM, Model Quanta 250). The relative length changes were measured with LINSEIS DIL L75 dilatometer at the heating and cooling rates of 5 K/min.

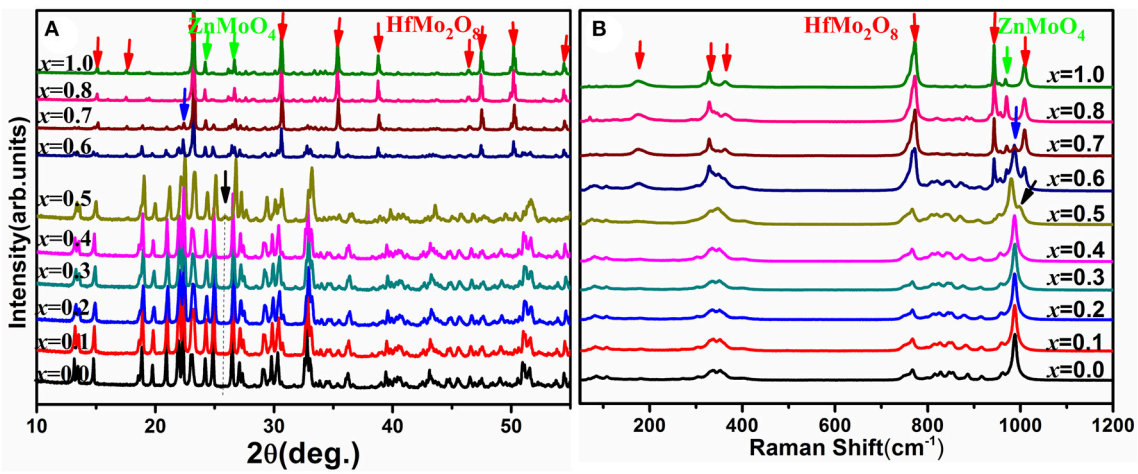

FIGURE 1 | (A) X-ray diffraction patterns of the solid solutions of $HfMg_{1-x}Zn_xMo_3O_{12}$; **(B)** Raman spectra of the solid solutions of $HfMg_{1-x}Zn_xMo_3O_{12}$.

RESULTS AND DISCUSSION

Figure 1A shows the XRD patterns of the solid solutions of $HfMg_{1-x}Zn_xMo_3O_{12}$. When $x = 0.0$, the diffraction peaks are corresponding to $HfMgMo_3O_{12}$, which adopts an orthorhombic structure with space group *Pnma* or *Pna*2_1 (Marinkovic et al., 2008). No obvious changes in the XRD patterns could be observed with increasing the content of Zn^{2+} till $x = 0.4$. It is reasonable to conclude that $HfMg_{1-x}Zn_xMo_3O_{12}$ for $x \leq 0.4$ crystallized in an orthorhombic structure. Nevertheless, some subtle changes are observed for $x = 0.5$, such as the weak peak appearing at about 25.6° which is characteristic for a monoclinic structure (Song et al., 2014b; Ge et al., 2016a) of $ABMo_3O_{12}$. $HfMg_{0.5}Zn_{0.5}Mo_3O_{12}$ at RT is thus identified as a monoclinic structure. The XRD patterns change obviously with further increasing content of Zn^{2+}. Detailed analyses show that the newly appeared peaks correspond well to $HfMo_2O_8$ and $ZnMoO_4$ (Reichelt et al., 2000; Allen et al., 2004), respectively.

The above analysis is supported by Raman spectroscopic analysis (**Figure 1B**). The Raman spectra are consistent with each other for $x \leq 0.4$ while the Raman band at 988 cm^{-1} splits into two bands at 980 and 998 cm^{-1} for $x = 0.5$ (as indicated by the black arrowhead), which is characteristic for a phase transition from higher orthorhombic symmetry to lower monoclinic symmetry (Li et al., 2011; Ge et al., 2016a) for the $ABMo_3O_{12}$ family. Distinct changes of the Raman spectra occur for higher content of Zn^{2+}. The new Raman bands at about 175, 328, 362, 772, 943, and 1,008 cm^{-1} correspond well to $HfMo_2O_8$ (Liang et al., 2008b) and that around 968 cm^{-1} arises from $ZnMoO_4$ (Ahsaine et al., 2016). Both XRD and Raman analyses demonstrate that a single phase solid solution of $HfMg_{1-x}Zn_xMo_3O_{12}$ is only possible for $x \leq 0.5$ and additional phases of $HfMo_2O_8$ and $ZnMoO_4$ form for $x \geq 0.6$. At RT, $HfMg_{1-x}Zn_xMo_3O_{12}$ for $x \leq 0.4$ adopt an orthorhombic structure while $HfMg_{0.5}Zn_{0.5}Mo_3O_{12}$ crystallizes in a monoclinic structure.

Raman spectroscopy is very sensitive to the monoclinic-to-orthorhombic phase transition (Li et al., 2011, 2016; Ge et al., 2016a). In order to get some insights into the influence of Zn^{2+} on the phase transition, we carried out temperature-dependent

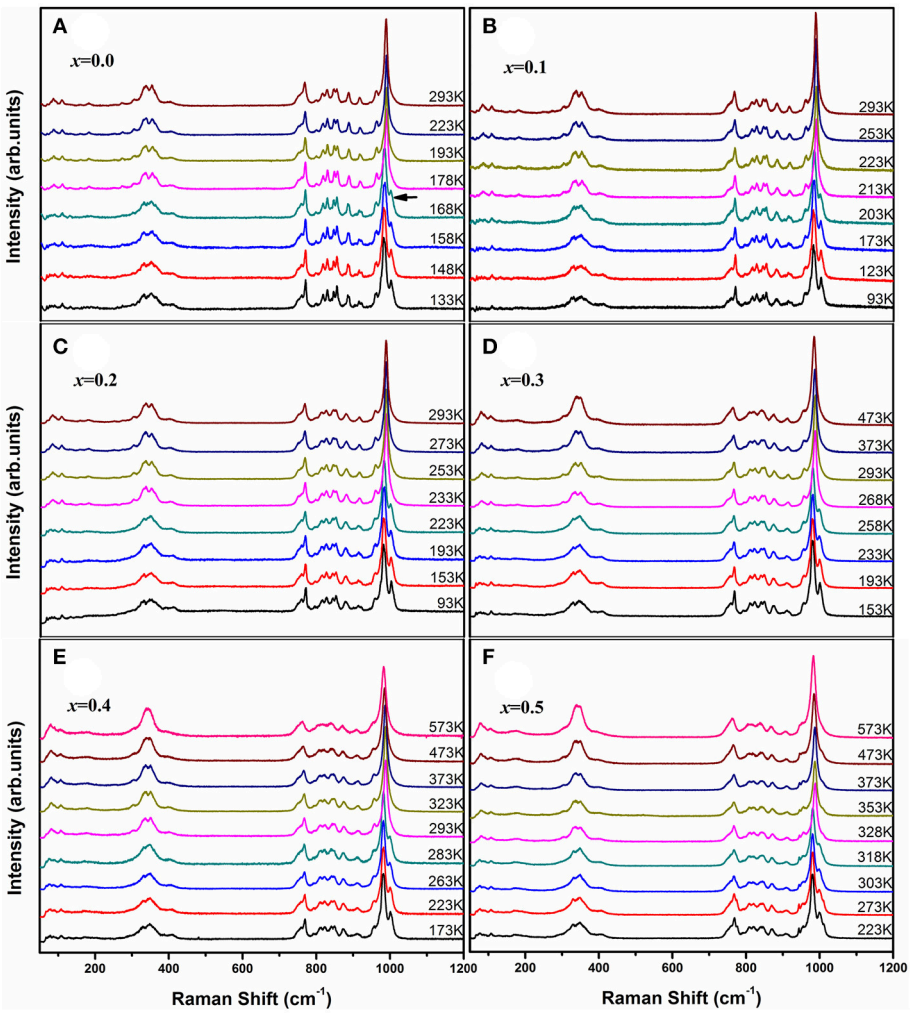

FIGURE 2 | Temperature-dependent Raman spectra of $HfMg_{1-x}Zn_xMo_3O_{12}$ with $x = 0.0$ **(A)**, 0.1 **(B)**, 0.2 **(C)**, 0.3 **(D)**, 0.4 **(E)**, and 0.5 **(F)**.

Raman spectral observation of $HfMg_{1-x}Zn_xMo_3O_{12}$ ($x \leq 0.5$) as shown in **Figure 2**. The XRD analyses suggest that $HfMg_{1-x}Zn_xMo_3O_{12}$ ($x \leq 0.5$) have similar open framework structure as $HfMgMo_3O_{12}$. In the orthorhombic phase, there are four molecular formulas in a unit cell, in which each MoO_4 tetrahedron sharing its four vortexes with HfO_6/MgO_6 octahedra and each HfO_6/MgO_6 octahedron shares its corners with six MoO_4 tetrahedra. Hf and Mg are alternatively aligned in the [010] direction forming a quasi-layered structure (Omote et al., 2011). The Raman modes from 1,050 to 900 cm^{-1}, from 900 to 750 cm^{-1}, from 400 to 320 cm^{-1}, and from 320 to 280 cm^{-1} are identified as symmetric stretching (ν_1), asymmetric stretching (ν_3), asymmetric bending (ν_4), and symmetric bending (ν_2) modes in the MoO_4 tetrahedra, respectively (Liang et al., 2008a; Li et al., 2011). **Figure 2A** shows the temperature dependent Raman spectra of $HfMgMo_3O_{12}$. The most distinctive change of the Raman spectra is the disappearance of the band at about 1,001 cm^{-1} with temperature increase from 168 to 178 K, which can be regarded as characteristic of the phase transition from low temperature monoclinic to high temperature orthorhombic structure (Li et al., 2011; Ge et al., 2016a). The phase transition temperature agrees well with the result derived from XRD analysis (Miller et al., 2012). In **Figures 2B–F** we present the temperature dependent Raman spectra for Zn^{2+}-containing samples. It is shown that the vanishing of the characteristic Raman band for the monoclinic structure occurs in the ranges of 168–178, 203–213, 223–233, 258–268, 283–293, and 318–328 K for $x = 0.0$, 0.1, 0.2, 0.3, 0.4, and 0.5, respectively, demonstrating that the phase transition temperature increases with the content of Zn^{2+}.

In the orthorhombic structure of $HfMg_{1-x}Zn_xMo_3O_{12}$ ($x \leq 0.5$), the four vortexes of each MoO_4 tetrahedron are shared with two HfO_6 and two MgO_6/ZnO_6 octahedra while each $HfO_6/MgO_6/ZnO_6$ octahedron shares its corners with six MoO_4 tetrahedra. Statistically, each MoO_4 tetrahedron links to 0.0, 0.2, 0.4, 0.8, and 1.0 ZnO_6 octahedron for $x = 0.0$, 0.1, 0.2, 0.3, 0.4, and 0.5. Since the ionic radius of Zn^{2+} is 74 pm which is slightly larger than that of Mg^{2+} (72 pm), large lattice distortion and increase in phase transition temperature is not expected if only the ionic radius is considered. The experimentally observed obvious increase in phase transition temperature is therefore attributed to the difference in electronegativity between Zn^{2+} (1.65 Pauling) and Mg^{2+} (1.31 Pauling). Replacement of Mg^{2+} by Zn^{2+} causes an increase in electronegativity at theZn^{2+}-cation side and a decrease in the effective negative charge on oxygen, and hence a decrease in the oxygen-oxygen repulsion. With increasing the content of Zn^{2+}, oxygen-oxygen attractive forces increase, causing the network collapse transition to occur at higher temperatures (Evans et al., 1997b).

Figure 3 shows the relative length changes of sintered cylinders with increasing temperature measured by dilatometry. All the samples for $x \leq 0.6$ exhibit abrupt length increase around the temperature of monoclinic to orthorhombic phase transition. The phase transition temperature increases with increasing the content of Zn^{2+} except the one for $x = 0.6$ whose phase transition temperature is lower than that of $x \leq 0.5$ due to the generation of $HfMo_2O_8$ and $ZnMoO_4$. In this case, it can be deduced that the real content of Zn^{2+} in $HfMg_{1-x}Zn_xMo_3O_{12}$ is lower than $HfMg_{0.5}Zn_{0.5}Mo_3O_{12}$. These results comply well with the above Raman spectroscopic analyses. The CTEs are calculated from the relative length change and shown in the **Table 1**. It indicates that all the single phase samples present excellent near-ZTE property above the phase transition temperature. It is interesting to notice that even for the multi-phase samples for $x = 0.8$ and 1.0, a near-ZTE property in a wide temperature range are realized. However, in this paper we focus on the effect of Zn^{2+} incorporation on the structure and properties of the single phase $HfMg_{1-x}Zn_xMo_3O_{12}$.

In order to get insight into the axial thermal expansion property, we carried out temperature-dependent powder XRD measurements for the samples of $x = 0.2$ and 0.3. For comparison, variable-temperature XRD data of $HfMgMo_3O_{12}$ were also collected. **Figure 4A** shows the selected temperature-dependent XRD patterns for $HfMg_{0.7}Zn_{0.3}Mo_3O_{12}$ at different temperatures. It is obvious that its XRD pattern changes distinctively around 225 K, which is attributed to the phase transformation from lower temperature monoclinic to higher temperature orthorhombic structure. Lattice constants and cell volume at each temperature are calculated and given in **Figure 4B**. It is evident that the *a*- and *c*-axes contract while the *b*-axis expands with increasing temperature. The CTEs for the *a*-, *b*-, and *c*-axes and

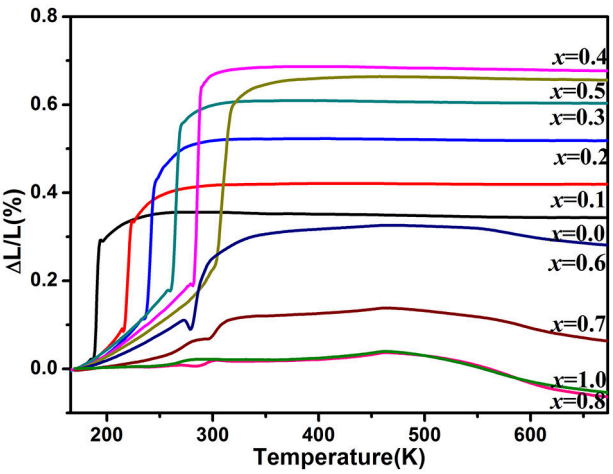

FIGURE 3 | Variations of relative length of the solid solutions of $HfMg_{1-x}Zn_xMo_3O_{12}$ with increasing temperature from 170 to 673 K.

TABLE 1 | Values of CTEs of $HfMg_{1-x}Zn_xMo_3O_{12}$.

Samples (*x*)	CTEs (10^{-6} K^{-1})	Fit range (K)
0.0	−0.21	248–673
0.1	0.05	303–673
0.2	−0.05	308–673
0.3	−0.09	323–673
0.4	−0.11	343–673
0.5	−0.11	373–673

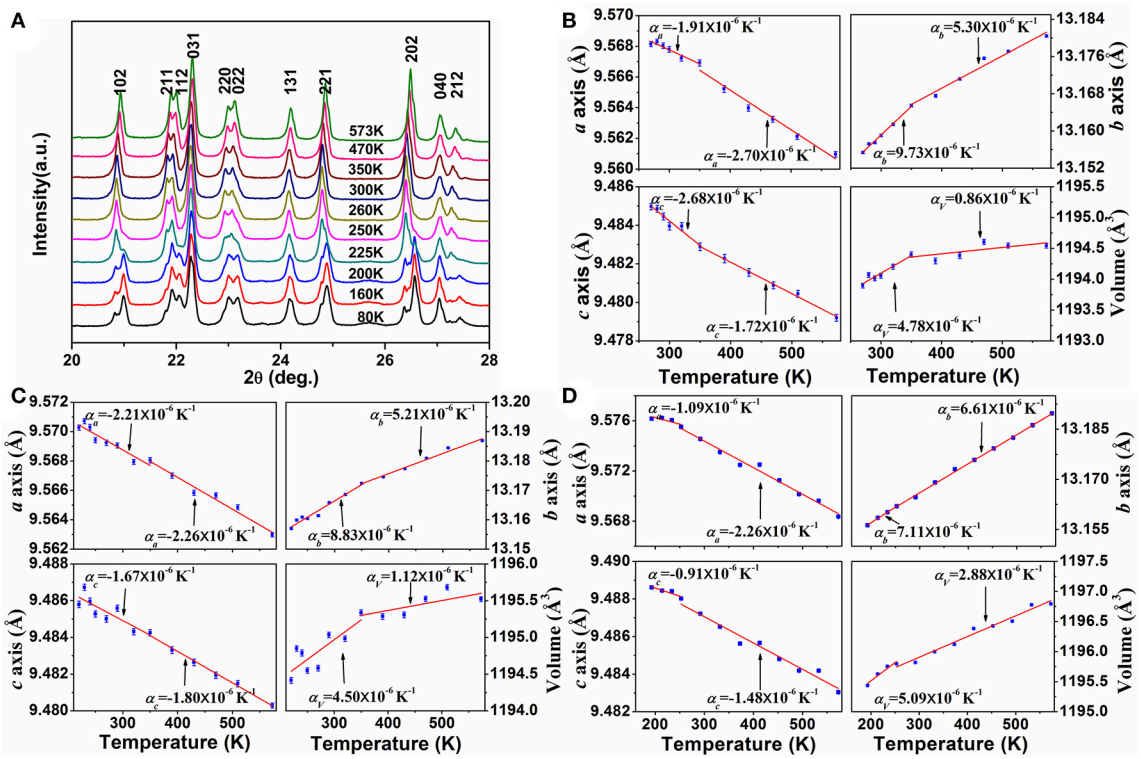

FIGURE 4 | (A) Variable-temperature XRD patterns of $HfMg_{0.7}Zn_{0.3}Mo_3O_{12}$ (The XRD patterns were measured for $2\theta = 10°$-$120°$, here only a small range is shown for clarity); Changes of lattice constants and volume of $HfMg_{1-x}Zn_xMo_3O_{12}$ with temperature: **(B)** for $x = 0.3$, **(C)** for $x = 0.2$, **(D)** for $HfMgMo_3O_{12}$.

volume are calculated to be $\alpha_a = -2.70 \times 10^{-6}\ K^{-1}$, $\alpha_b = 5.30 \times 10^{-6}\ K^{-1}$, $\alpha_c = -1.72 \times 10^{-6}\ K^{-1}$, $\alpha_V = 0.86 \times 10^{-6}\ K^{-1}(350 - 573\ K)$, respectively. This gives rise to a linear CTE $\alpha_l = 0.29 \times 10^{-6}\ K^{-1}$. Similar axial thermal expansion behaviors are obtained for $HfMg_{0.8}Zn_{0.2}Mo_3O_{12}$ from temperature dependent XRD measurements (not shown here). The changes of its lattice constants and volume with temperature are given in **Figure 4C**. The CTEs for the *a*-, *b*-, and *c*-axes and volume are calculated to be $\alpha_a = -2.26 \times 10^{-6}\ K^{-1}$, $\alpha_b = 5.21 \times 10^{-6}\ K^{-1}$, $\alpha_c = -1.80 \times 10^{-6}\ K^{-1}$, $\alpha_V = 1.12 \times 10^{-6}\ K^{-1}$, respectively, corresponding to a linear CTE $\alpha_l = 0.37 \times 10^{-6}\ K^{-1}$ $(350 - 573\ K)$. These results are consistent with the values measured by dilatometry, confirming $HfMg_{0.7}Zn_{0.3}Mo_3O_{12}$ and $HfMg_{0.8}Zn_{0.2}Mo_3O_{12}$ being intrinsically ZTE materials. **Figure 4D** shows the changes of lattice constants and volume of $HfMgMo_3O_{12}$ with temperature.

Considering the fact that the intrinsic linear CTE of $HfMgMo_3O_{12}$ is $1.02 \times 10^{-6}\ K^{-1}$ (Marinkovic et al., 2008), it is reasonable to conclude that the incorporation of Zn^{2+} reduces the linear CTE and results in near ZTE of $HfMg_{1-x}Zn_xMo_3O_{12}$. A comparison of the axial CTEs for $HfMgMo_3O_{12}$, $HfMg_{0.8}Zn_{0.2}Mo_3O_{12}$, and $HfMg_{0.7}Zn_{0.3}Mo_3O_{12}$ are given in **Table 2**. It is found that partial substitution of Mg^{2+} by Zn^{2+} leads to a significant reduction of the CTE in the *b*-axis and an increase of the NTE in the *c*-axis, resulting in a near ZTE and lower anisotropy of thermal expansion in the Zn-containing compounds with respect to $HfMgMo_3O_{12}$ (see **Table 2**). The anisotropy of thermal expansion is defined as the maximum difference in the axial thermal expansion coefficients (Srikanth et al., 1992; Miller et al., 2013). The near zero linear thermal expansion and lower anisotropy property of the Zn-containing compounds suggest that they could withstand higher thermal shock resistance.

The difference in the linear CTEs measured by XRD and dilatometry could be understood by the microstructural effects. In contrast to XRD measurement which gives the thermal expansion property of cell lattice, dilatometry reveals the bulk thermal expansion property, including both intrinsic (thermal expansion of a material arising from the lattice dynamics) and extrinsic (thermal expansion related to microstructures such as texture, grain size, grain boundaries, poses, and microcracks) effects. The difference measured by the two methods reflects the extrinsic effect in the sintered bulk, which, on heating, can add a small negative component to the intrinsic linear expansion coefficients. Generally speaking, a smaller difference suggests a better sintered quality of the bulk material which is desired for most applications. The absolute differences for the Zn-containing compounds ($\Delta\alpha_l = 0.42 \times 10^{-6}\ K^{-1}$ for $x = 0.2$ and $\Delta\alpha_l = 0.38 \times 10^{-6}\ K^{-1}$ for $x = 0.3$) are obviously smaller than that for $HfMgMo_3O_{12}$ ($\Delta\alpha_l = 1.17 \times 10^{-6}\ K^{-1}$). It means that partial substitution of Mg^{2+} by Zn^{2+} in $HfMgMo_3O_{12}$ could

TABLE 2 | Intrinsic thermal expansion coefficients (α) for $HfMg_{0.7}Zn_{0.3}Mo_3O_{12}$ and $HfMg_{0.8}Zn_{0.2}Mo_3O_{12}$ as obtained from variable-temperature XRD and literature and experimental values for $HfMgMo_3O_{12}$.

Sample (Structure)	Fit range (K)	α_a (10^{-6} K^{-1})	α_b (10^{-6} K^{-1})	α_c (10^{-6} K^{-1})	α_l (10^{-6} K^{-1})	$\Delta\alpha_{max}$ (10^{-6} K^{-1})	References
$HfMgMo_3O_{12}$ (Orthorhombic)	298–1,013	−3.44	8.0	−1.49	1.02	11.44	Marinkovic et al., 2008
$HfMgMo_3O_{12}$ (Orthorhombic)	253–573	−2.26	6.61	−1.48	0.96	8.87	This work
$HfMg_{0.8}Zn_{0.2}Mo_3O_{12}$ (Orthorhombic)	350–573	−2.26	5.21	−1.80	0.37	7.47	This work
$HfMg_{0.7}Zn_{0.3}Mo_3O_{12}$ (Orthorhombic)	350–573	−2.70	5.30	−1.72	0.29	8	This work

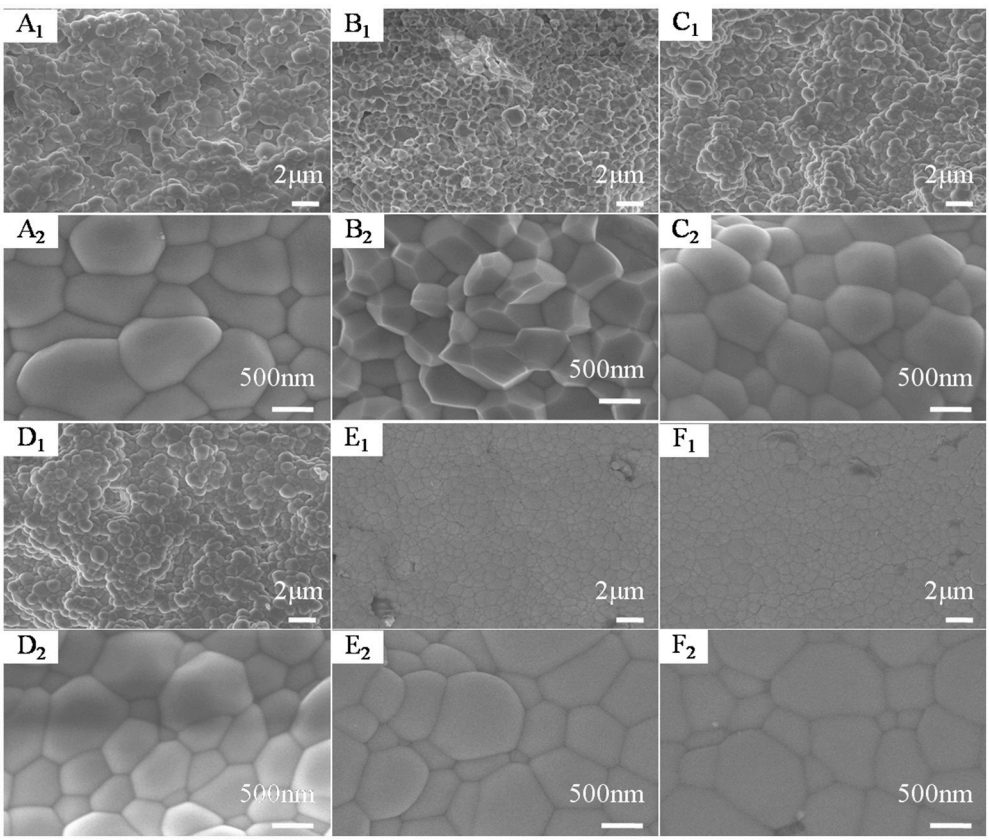

FIGURE 5 | SEM images of $HfMg_{1-x}Zn_xMo_3O_{12}$ with $x = 0.0$ **(A)**, 0.1 **(B)**, 0.2 **(C)**, 0.3 **(D)**, 0.4 **(E)**, and 0.5 **(F)**.

improve the sintering performance of the material and minimize the possible contributions of extrinsic effects. The analysis is supported by microstructural observation.

Figure 5 shows the SEM images of $HfMg_{1-x}Zn_xMo_3O_{12}$ ceramics with $x = 0.0$ (**Figure 5A**), 0.1 (**Figure 5B**), 0.2 (**Figure 5C**), 0.3 (**Figure 5D**), 0.4 (**Figure 5E**), and 0.5 (**Figure 5F**). The micro morphology of the sample for $x = 0.1$ is dominated by well crystallized polyhdra or truncated polyhedra and the average particle size is obviously smaller than that of $HfMgMo_3O_{12}$. With increasing the content of Zn^{2+}, the polyhedra become more rounded. Compared to $HfMgMo_3O_{12}$, the incorporation of Zn^{2+} seems to lead to less pores in the ceramic bodies and pores can hardly be found in the solid solutions for $x = 0.1$–0.3. It illustrates that proper amount incorporation of Zn^{2+} favors the formation of uniform distribution of particles and efficient reduction of porosity in the sintered body.

The schematic diagram of $HfMgMo_3O_{12}$ is given in **Figure 6A** to help us understand the mechanism of the phenomenons. In $HfMg_{1-x}Zn_xMo_3O_{12}$ ($x \leq 0.5$), Zn^{2+} is expected to substitute for Mg^{2+} due to the same valence and similar cation radius and each ZnO_6 octahedron shares all its corners with six

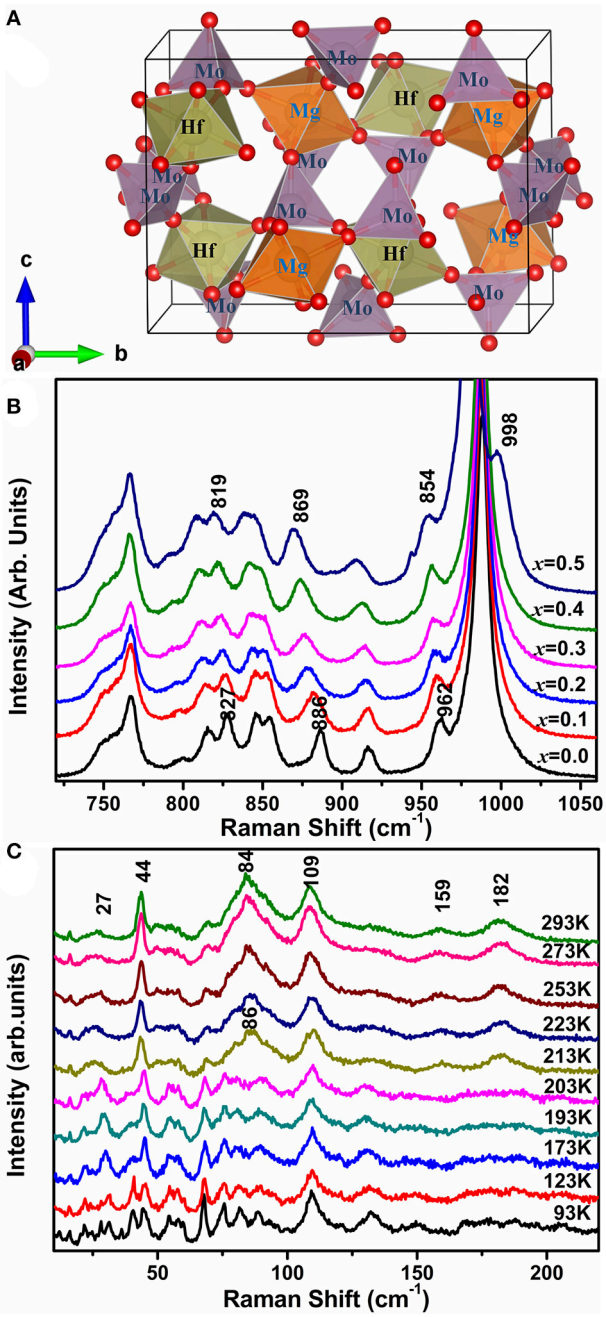

FIGURE 6 | (A) Schematic diagram of $HfMgMo_3O_{12}$ building block (red sphere indicates oxygen atom); **(B)** Raman spectra of $HfMg_{1-x}Zn_xMo_3O_{12}$ in the high wavenumber regions; **(C)** Temperature-dependent Raman spectra of $HfMg_{0.9}Zn_{0.1}Mo_3O_{12}$ in the low wavenumber region.

MoO_4 tetrahedra. In order to see the bond strength changes induced by local electronic environment upon substitution of $Zn^{2+}$for Mg^{2+}, we show in **Figure 6B** the Raman spectra of the stretching region for $x = 0.0$, 0.1, 0.2, 0.3, 0.4, and 0.5. It is obvious that all the stretching modes shift successively to lower wavenumbers with increasing the content of Zn^{2+}, indicating a softening of the Mo-O bonds upon incorporation of Zn^{2+}. Once an Mg^{2+} is replaced by Zn^{2+}, the local electronic equilibrium around the MoO_4 tetrahedron is broken. Zn^{2+} has obviously a higher electronegativity and ability to drag electrons to the ZnO_6 octahedron from its connected six MoO_4 tetrahedra than Mg^{2+}, resulting in the weakening of the Mo–O bonds. The differences in ionic radius and electronegativity could cause a slight rotation of the connected polyhedra and hence the M-O-M linkages. This is probably the reason that the positive expansion of the *b*-axis is pronouncedly reduced and the NTE in the *c*-axes become more negative, resulting hence in a lower anisotropy in thermal expansion and near-zero CTEs of the Zn-containing compounds. Due to the large difference in electronegativity between Zn^{2+} (1.65 Pauling) and Mg^{2+} (1.31 Pauling), the more of Zn^{2+} is incorporated, the more of the MoO_4 tetrahedra get distorted as revealed by Raman spectroscopy, resulting in larger distortion and instability of the lattice. When the forming energy for the single phase exceeds that for the multi-phases, then the multi-phases form.

Figure 6C shows the temperature-dependent Raman spectra of $HfMg_{0.9}Zn_{0.1}Mo_3O_{12}$ in the low wavenumber region. Obvious change of the Raman spectra occur between 203 and 213 K, corresponding to the monoclinic to orthorhombic phase transition, such as the appearance of new Raman modes at about 27,44, 86, 159, and 182 cm^{-1}. The modes at about 44 and 86 cm^{-1} are split into two or three modes in the low temperature phase and become degenerated in the high temperature phase. The low wavenumber modes arise from the external librational and translational vibrations of the connected octahedra–tetrahedra, or the librational and translational motions of metal ions in the Hf(Mg/Zn)–O–Mo linkages, which can also be regarded as the transverse vibrations of the bridging oxygen from the point of view of relative movement. Such an harmonic vibrations along with the distortion of the polyhedra are believed to be the origin of the NTE in the open frame work structure since they bring the two end atoms closer upon heating (Evans, 1999; Ding et al., 2008; Marinkovic et al., 2009; Wang et al., 2013).

CONCLUSION

Solid solutions of $HfMg_{1-x}Zn_xMo_3O_{12}$ with near-ZTE are successfully synthesized by solid state reaction and the effects of Zn^{2+} incorporation on the phase formation, thermal expansion, phase transition, and vibrational properties and micro-morphologies are investigated by XRD, dilatometry, Raman spectroscopy, and SEM. It is shown that (i) single phase formation is only possible for $x \leq 0.5$, otherwise, additional phases of $HfMo_2O_8$ and $ZnMoO_4$ generate; (ii) $HfMg_{1-x}Zn_xMo_3O_{12}$ crystallize in an orthorhombic structure for $x \leq 0.4$ and in a monoclinic structure for $x = 0.5$ at RT; (iii) The phase transition temperature from monoclinic to orthorhombic structure increases with the content of Zn^{2+}, which occurs within 168–178, 203–213, 223–233, 258–268, 283–293, and 318–328 K for $x = 0.0$, 0.1, 0.2, 0.3, 0.4, and 0.5, respectively; (iv) The incorporation of Zn^{2+} leads to an

pronounced reduction in the positive expansion of the *b*-axis and an enhanced NTE in *c*-axes, making the Zn-containing materials exhibit near-ZTE over a wide temperature range and lower anisotropy in thermal expansion in the orthorhombic phase; (v) Replacement of Mg^{2+} by Zn^{2+} breaks the local electronic equilibrium around the MoO_4 tetrahedron and weakens the Mo–O bonds, leading to obvious red shifts of all the Mo–O stretching modes with increasing the content of Zn^{2+} due to obviously higher electronegativity of Zn^{2+} than Mg^{2+}; (vi) The incorporation of Zn^{2+} improves sintering property of samples, minimizing the possible contributions of extrinsic effects such as pores, which is preferred for most applications.

AUTHOR CONTRIBUTIONS

EL conceived the idea and supervised the research. SL and RS are in charge of the synthesis and part measurements of the materials. XG, HY, and DC are in charge of the thermal expansion and Raman characterization. JG and MC are in charge of the XRD characterization and structural analyses. SL, XG, and EL are in charge of the manuscript preparation.

ACKNOWLEDGMENTS

This work was supported by the National Natural Science Foundation of China (No. 11574276; No. 51302249).

REFERENCES

Ahsaine, H. A., Zbair, M., Ezahri, M., Benlhachemi, A., Bakiz, B., Guinneton, F., et al. (2016). Structural and temperature-dependent vibrational analyses of the non-centrosymmetric $ZnMoO_4$ molybdate. *J. Mater. Environ. Sci.* 7, 907–915.

Allen, S., Ward, R. J., Hampson, M. R., Gover, R. K., and Evans, J. S. (2004). Structures and phase transitions of trigonal $ZrMo_2O_8$ and $HfMo_2O_8$. *Acta Crystallogr. B.* 60, 32–40. doi: 10.1107/S01087681030 25138

Azuma, M., Chen, W., Seki, H., Czapski, M., Olga, S., Oka, K., et al. (2011). Colossal negative thermal expansion in $BiNiO_3$ induced by intermetallic charge transfer. *Nat. Commun.* 2:347. doi: 10.1038/ncomms1361

Baiz, T. I., Gindhart, A. M., Kraemer, S. K., and Lind, C. (2008). Synthesis of $MgHf(WO_4)_3$and $MgZr(WO_4)_3$ using a non-hydrolytic sol-gel method. *J. Solgel Sci. Technol.* 47, 128–130. doi: 10.1007/s10971-008-1 765-5

Bridges, F., Keiber, T., Juhas, P., Billinge, S. J. L., Sutton, L., Wilde, J., et al. (2014). Local vibrations and negative thermal expansion in ZrW_2O_8. *Phys. Rev. Lett.* 112:045505. doi: 10.1103/PhysRevLett.112.045505

Chen, D. X., Yuan, B. H., Cheng, Y. G., Ge, X. H., Jia, Y., Liang, E. J., et al. (2016). Phase transition and near-zero thermal expansion in $ZrFeMo_2VO_{12}$. *Phys. Lett. A* 380, 4070–4074. doi: 10.1016/j.physleta.2016.10.009

Chen, J., Hu, L., Deng, J., and Xing, X. (2015). Negative thermal expansion in functional materials: controllable thermal expansion by chemical modifications. *Chem. Soc. Rev.* 44, 3522–3567. doi: 10.1039/C4CS00461B

Chen, J., Wang, F. F., Huang, Q. Z., Hu, L., Song, X. P., Deng, J. X., et al. (2013). Effectively control negative thermal expansion of single-phase ferroelectrics of $PbTiO_3$-(Bi,La)FeO_3 over a giant range. *Sci. Rep.* 3:2458. doi: 10.1038/srep02458

Cheng, Y. G., Liang, Y., Ge, X. H., Liu, X. S., Yuan, B. H., Guo, J., et al. (2016a). A novel material of $HfScMo_2VO_{12}$ with negative thermal expansion and intense white-light emission. *RSC Adv.* 6, 53657–53661. doi: 10.1039/C6RA09666B

Cheng, Y. G., Liang, Y., Mao, Y. C., Ge, X. H., Yuan, B. H., Guo, J., et al. (2017). A novel material of $HfScW_2PO_{12}$ with negative thermal expansion from 140 K to 1469 K and intense blue photoluminescence. *Mater. Res. Bull.* 85, 176–180. doi: 10.1016/j.materresbull.2016.09.008

Cheng, Y. G., Mao, Y. C., Liu, X. S., Yuan, B. H., Chao, M. J., and Liang, E. J. (2016b). Near-zero thermal expansion of $In_{2(1-x)}(HfMg)_xMo_3O_{12}$ with tailored phase transition. *Chin. Phys. B* 25:86501. doi: 10.1088/1674-1056/25/8/086501

Das, S., Das, S., and Das, K. (2013). Low temperature synthesis of negative thermal expansion $Y_2W_3O_{12}$. *J. Mater. Eng. Perf.* 22, 3357–3363. doi: 10.1007/s11665-013-0652-6

Ding, P., Liang, E. J., Jia, Y., and Du, Z. Y. (2008). Electronic structure, bonding and phonon modes in the negative thermal expansion materials of $Cd(CN)_2$ and $Zn(CN)_2$. *J. Phys. Condens. Matter* 20:275224. doi: 10.1088/0953-8984/20/27/275224

Evans, J. S. O. (1999). Negative thermal expansion materials. *J. Chem. Soc. Dalton Trans.* 1999, 3317–3326. doi: 10.1039/a904297k

Evans, J. S. O., Hu, Z., Jorgensen, J. D., Argyriou, D. N., Short, S., and Sleight, A. W. (1997a). Compressibility, phase transitions, and oxygen migration in zirconium tungstate, ZrW_2O_8. *Science* 275, 61–65. doi: 10.1126/science.275.5296.61

Evans, J. S. O., Mary, T. A., and Sleight, A. W. (1997b). Negative thermal expansion in a large molybdate and tungstate family. *J. Solid State Chem.* 133, 580–583. doi: 10.1006/jssc.1997.7605

Evans, J. S. O., Mary,T. A., Vogt, T., Subramanian, M. A., and Sleight, A. W. (1996). Negative thermal expansion in ZrW_2O_8 and HfW_2O_8. *Chem. Mater.* 8, 2809–2823. doi: 10.1021/cm9602959

Ge, X., Liu, X., Cheng, Y., Yuan, B., Chen, D., Chao, M., et al. (2016c). Negative thermal expansion and photoluminescence properties in a novel material $ZrScW_2PO_{12}$. *J. Appl. Phys.* 120:205101. doi: 10.1063/1.4968546

Ge, X. H., Mao, Y. C., Li, L., Li, L. P., Yuan, N., Cheng, Y. G., et al. (2016a). Phase transition and negative thermal expansion property of $ZrMnMo_3O_{12}$. *Chin. Phys. Lett.* 33:046503. doi: 10.1088/0256-307X/33/4/046503

Ge, X. H., Mao, Y. C., Liu, X. S., Cheng, Y. G., Yuan, B. H., Chao, M. J., et al. (2016b). Negative thermal expansion and broad band photoluminescence in a novel material of $ZrScMo_2VO_{12}$. *Sci. Rep.* 6:24832. doi: 10.1038/srep24832

Gindhart, A. M., Lind, C., and Green, M. (2008). Polymorphism in the negative thermal expansion material magnesium hafnium tungstate. *J. Mater. Res.* 23, 210–213. doi: 10.1557/JMR.2008.0013

Hu, L., Chen, J., Fan, L. L., Ren, Y., Rong, Y. C., Pan, Z., et al. (2015). ChemInform abstract: zero thermal expansion and ferromagnetism in cubic $Sc_{1-x}M_xF_3$ (M: Ga, Fe) over a wide temperature range. *Cheminform* 46:13566. doi: 10.1002/chin.201507003

Lama, P., Das, R. K., Smith, V. J., and Barbour, L. J. (2014). A combined stretching-tilting mechanism produces negative, zero and positive linear thermal expansion in a semi-flexible Cd(II)-MOF. *Chem. Commun.* 50, 6464–6467. doi: 10.1039/C4CC02634A

Li, F., Liu, X. S., Song, W. B., Yuan, B. H., Cheng, Y. G., Yuan, H. L., et al. (2014). Phase transition, crystal water and low thermal expansion behavior of $Al_{2-2x}(ZrMg)_xW_3O_{12}\cdot n(H_2O)$. *J. Solid State Chem.* 218, 15–22. doi: 10.1016/j.jssc.2014.06.009

Li, T., Ge, X. H., Liu, X. S., Cheng, Y. G., Liu, Y. Y., Yuan, H. L., et al. (2016). Enhanced negative thermal expansion by solid solution of $HfMgMo_{1.5}W_{1.5}O_{12}$. *Mater. Expr.* 6, 515–520. doi: 10.1166/mex.2016.1337

Li, T., Liu, X. S., Cheng, Y. G., Ge, X. H., Zhang, M. D., Lian, H., et al. (2017). Zero and controllable thermal expansion in $HfMgMo_{3-x}W_xO_{12}$. *Chin. Phys. B* 26:348. doi: 10.1088/1674-1056/26/1/016501

Li, Z. Y., Song, W. B., and Liang, E. J. (2011). Structures, phase transition, and crystal water of $Fe_{2-x}Y_xMo_3O_{12}$. *J. Phys. Chem. C* 115, 17806–17811. doi: 10.1021/jp201962b

Liang, E. J., Huo, H. L., Wang, J. P., and Chao, M. J. (2008a). Effect of water species on the phonon modes in orthorhombic $Y_2(MoO_4)_3$ revealed by Raman spectroscopy. *J. Phys. Chem. C* 112, 6577–6581. doi: 10.1021/jp8013332

Liang, E. J., Liang, Y., Zhao, Y., Liu, J., and Jiang, Y. (2008b). Low-frequency phonon modes and negative thermal expansion in $A(MO_4)_2$ (A = Zr, Hf and M = W, Mo) by Raman and Terahertz time-domain spectroscopy. *J. Phys. Chem. A* 112, 12582–12587. doi: 10.1021/jp805256d

Liu, X. S., Cheng, Y. G., Liang, E. J., and Chao, M. J. (2014). Interaction of crystal water with the building block in $Y_2Mo_3O_{12}$ and the effect of Ce^{3+} doping. *Phys. Chem. Chem. Phys.* 16, 12848–12857. doi: 10.1039/c4cp00144c

Liu, X. S., Wang, J. Q., Fan, C. Z., Shang, R., Cheng, F. X., Yuan, B. H., et al. (2015). Control of reaction pathways for rapid synthesis of negative thermal expansion ceramic $Zr_2P_2WO_{12}$ with uniform microstructure. *Int. J. Appl. Ceram. Technol.* 12, E28–E33. doi: 10.1111/ijac.12201

Liu, Y. Y., Yuan, B. H., Cheng, Y. G., Liang, E. J., Ge, X. H., Yuan, H. L., et al. (2018). Phase transition and negative thermal expansion of $HfMnMo_3O_{12}$. *Mater. Res. Bull.* 99, 255–259. doi: 10.1016/j.materresbull.2017.11.009

Long, Y. W., Hayashi, N., Saito, T., Azuma, M., Muranaka, S., and Shimakawa, Y. (2009). Temperature-induced A-B intersite charge transfer in an A-site-ordered $LaCu_3Fe_4O_{12}$ perovskite. *Cheminform* 40, 60–63. doi: 10.1002/chin.200947022

Marinkovic, B. A., Ari, M., Avillez, R. R. D., Rizzo, F., Ferreira, F. F., Miller, K. J., et al. (2009). Correlation between AO_6 polyhedral distortion and negative thermal expansion in orthorhombic $Y_2Mo_3O_{12}$ and related materials. *Chem. Mater.* 21, 2886–2894. doi: 10.1021/cm900650c

Marinkovic, B. A., Jardim, P. M., Ari, M., Avillez, R. R. D., Rizzo, F., and Ferreira, F. F. (2008). Low positive thermal expansion in $HfMgMo_3O_{12}$. *Phys. Status Solidi* 245, 2514–2519. doi: 10.1002/pssb.200880262

Miller, K. J., Johnson, M. B., White, M. A., and Marinkovic, B. A. (2012). Low-temperature investigations of the open-framework material $HfMgMo_3O_{12}$. *Solid State Commun.* 152, 1748–1752. doi: 10.1016/j.ssc.2012.06.022

Miller, K. J., Romao, C. P., Bieringer, M., Marinkovic, B. A., Prisco, L., and White, M. A. (2013). Near-zero thermal expansion in $In(HfMg)_{0.5}Mo_3O_{12}$. *J. Am. Ceram. Soc.* 96, 561-566. doi: 10.1111/jace.12085

Omote, A., Yotsuhashi, S., Zenitani, Y., and Yamada, Y. (2011). High ion conductivity in $MgHf(WO_4)_3$ solids with ordered structure: 1-D alignments of $Mg^{2+}$and Hf $^{4+}$ ions. *J. Am. Ceram. Soc.* 94, 2285–2288. doi: 10.1111/j.1551-2916.2011.04644.x

Peng, X., Chen, J., Lin, K., Fan, L. L., Rong, Y. C., Deng, J. X., et al. (2016). Structure and control of negative thermal expansion of Nd/Sm substituted $0.5PbTiO_3$-$0.5BiFeO_3$ ferroelectrics. *RSC Adv.* 6, 32979–32982. doi: 10.1039/C6RA03774G

Peng, Z., Sun, Y. Z., and Peng, L. M. (2014). Hydrothermal synthesis of ZrW_2O_8 nanorods and its application in ZrW_2O_8/Cu composites with controllable thermal expansion coefficients. *Mater. Des.* 54, 989–994. doi: 10.1016/j.matdes.2013.09.012

Pryde, A. K. A., Hammonds, K. D., Dove, M. T., Heine, V., Gale, J. D., and Warren, M. C. (1996). Origin of the negative thermal expansion in ZrW_2O_8 and ZrV_2O_7. *J. Phys. Condens. Matter* 8:10973. doi: 10.1088/0953-8984/8/50/023

Qu, B. Y., He, H. Y., and Pan, B. C. (2012).Origin of the giant negative thermal expansion in $Mn_3(Cu_{0.5}Ge_{0.5})N$. *Adv. Conden. Matter Phys.* 2012, 275–281. doi: 10.1155/2012/913168

Reichelt, W., Weber, T., Söhnel, T., and Däbritz, S. (2000). Mischkristallbildung im system $CuMoO_4/ZnMoO_4$. *Z. Anorgan. Allgem. Chem.* 626, 2020–2027. doi: 10.1002/1521-3749(200009)626:9<2020::AID-ZAAC2020>3.0.CO;2-K

Song, W. B., Liang, E. J., Liu, X. S., Li, Z. Y., Yuan, B. H., and Wang, J. Q. (2013). A negative thermal expansion material of $ZrMgMo_3O_{12}$. *Chin. Phys. Lett.* 30:126502. doi: 10.1088/0256-307X/30/12/126502

Song, W. B., Wang, J. Q., Li, Z. Y., Liu, X. S., Yuan, B. H., and Liang, E. J. (2014a). Phase transition and thermal expansion property of $Cr_{2-x}Zr_{0.5x}Mg_{0.5x}Mo_3O_{12}$ solid solution. *Chin. Phys. B* 23:433. doi: 10.1088/1674-1056/23/6/066501

Song, W. B., Yuan, B. H., Liu, X. S., Li, Z. Y., Wang, J. Q., and Liang, E. J. (2014b). Tuning the monoclinic-to-orthorhombic phase transition temperature of $Fe_2Mo_3O_{12}$ by substitutional co-incorporation of Zr^{4+} and Mg^{2+}. *J. Mater. Res.* 29, 849–855. doi: 10.1557/jmr.2014.63

Srikanth, V., Subbarao, E. C., and Rao, G. V. (1992). Thermal expansion anisotropy, microcracking and acoustic emission of Nb_2O_5 ceramics.*Ceram. Int.* 18, 251-261. doi: 10.1016/0272-8842(92)90103-K

Suzuki, T., and Omote, A. (2004). Negative thermal expansion in $(HfMg)(WO_4)_3$. *J. Am. Ceram. Soc.* 87, 1365–1367. doi: 10.1111/j.1151-2916.2004.tb07737.x

Suzuki, T., and Omote, A. (2006). Zero thermal expansion in $(Al_{2x}(HfMg)_{1-x})(WO_4)_3$. *J. Am. Ceram. Soc.* 89, 691–693. doi: 10.1111/j.1551-2916.2005.00729.x

Takenaka, K., and Takagi, H. (2005). Giant negative thermal expansion in Ge-doped anti-perovskite manganese nitrides. *Appl. Phys. Lett.* 87:261902. doi: 10.1063/1.2147726

Tallentire, S. E., Child, F., Fall, I., Vella-Zarb, L., Evans, I. R., Tucker, M. G., et al. (2013). Systematic and controllable negative, zero, and positive thermal expansion in cubic $Zr_{1-x}Sn_xMo_2O_8$. *J. Am. Chem. Soc.* 135, 12849–12856. doi: 10.1021/ja4060564

Wang, L., Wang, F., Yuan, P. F., Sun, Q., Liang, E. J., Jia, Y., et al. (2013). Negative thermal expansion correlated with polyhedral movements and distortions in orthorhombic $Y_2Mo_3O_{12}$. *Mater. Res. Bull.* 48, 2724–2729. doi: 10.1016/j.materresbull.2013.04.001

Wang, X., Huang, Q. , Deng, J., Yu, R., Chen, J., and Xing, X. (2011). Phase transformation and negative thermal expansion in $TaVO_5$. *Inorg. Chem.* 50, 2685–2690. doi: 10.1021/ic200003n

Wu, M, Liu, X., Chen, D. , Huang, Q., Wu, H., and Liu, Y. (2014). Structure, phase transition, and controllable thermal expansion behaviors of $Sc_{2-x}Fe_xMo_3O_{12}$. *Inorg. Chem.* 53, 9206–9212. doi: 10.1021/ic501271t

Wu, M. M., Peng, J., Han, S. B., Hu, Z. B., Liu, Y. T., and Chen, D. F. (2012). Phase transition and negative thermal expansion properties of $Sc_{2-x}Cr_xMo_3O_{12}$. *Ceram. Int.* 38, 6525–6529. doi: 10.1016/j.ceramint.2012.05.033

Wu, M. M., Xiao, X. L., Hu, Z. B., Liu, Y. T., and Chen, D. F. (2009). Controllable thermal expansion and phase transition in $Yb_{2-x}Cr_xMo_3O_{12}$. *Solid State Sci.* 11, 325–329. doi: 10.1016/j.solidstatesciences.2008.08.002

Xiao, X., Zhou, W. J., Liu, X. S., Chao, M. J., Li, Y. C., Zhang, N., et al.,(2014). Electrical properties of Al-$ZrMgMo_3O_{12}$ with controllable thermal expansion. *Ceram. Int.* 41, 2361–2366. doi: 10.1016/j.ceramint.2014.10.048

Yamada, I., Shiro, K., Etani, H., Marukawa, S., Hayashi, N., Mizumaki, M., et al. (2016). Valence transitions in negative thermal expansion material $SrCu_3Fe_4O_{12}$. *Inorg. Chem.* 53, 10563–10569. doi: 10.1021/ic501665c

Yan, J., Sun, Y., Wang, C., Chu, L. H., Shi, Z. X., Deng, S. H., et al. (2014). Study of structure of $Mn_3Cu_{0.5}Ge_{0.5}N$/Cu composite with nearly zero thermal expansion behavior around room temperature. *Scr. Mater.* 84–85, 19–22. doi: 10.1016/j.scriptamat.2014.04.010

Yang, X. B., Cheng, X. N., Yan, X. H., Yang, J., Fu, T. B., and Qiu, J. (2007). Synthesis of ZrO_2/ZrW_2O_8 composites with low thermal expansion. *Compos. Sci. Technol.* 67, 1167–1171. doi: 10.1016/j.compscitech.2006.05.012

Conflict of Interest Statement: The authors declare that the research was conducted in the absence of any commercial or financial relationships that could be construed as a potential conflict of interest.

frontiers in Chemistry

ORIGINAL RESEARCH
published: 06 February 2018
doi: 10.3389/fchem.2018.00015

Negative Thermal Expansion over a Wide Temperature Range in Fe-Doped MnNiGe Composites

Wenjun Zhao[1], Ying Sun[1], Yufei Liu[2], Kewen Shi[1], Huiqing Lu[1], Ping Song[1], Lei Wang[1], Huimin Han[1], Xiuliang Yuan[1] and Cong Wang[1]*

[1] Department of Physics, Center for Condensed Matter and Materials Physics, Beihang University, Beijing, China, [2] Capital Normal University High School, Beijing, China

Fe-doped MnNiGe alloys were successfully synthesized by solid-state reaction. Giant negative thermal expansion (NTE) behaviors with the coefficients of thermal expansion (CTE) of -285.23×10^{-6} K^{-1} (192–305 K) and -1167.09×10^{-6} K^{-1} (246–305 K) have been obtained in $Mn_{0.90}Fe_{0.10}NiGe$ and $MnNi_{0.90}Fe_{0.10}Ge$, respectively. Furthermore, these materials were combined with Cu in order to control the NTE properties. The results indicate that the absolute value of CTE gradually decreases with increasing Cu contents. In $Mn_{0.92}Fe_{0.08}NiGe/x\%Cu$, the CTE gradually changes from -64.92×10^{-6} K^{-1} (125–274 K) to -4.73×10^{-6} K^{-1} (173–229 K) with increasing value of x from 15 to 70. The magnetic measurements reveal that the NTE behaviors in this work are strongly correlated with the process of the magnetic phase transition and the introduction of Fe atoms could also change the spiral anti-ferromagnetic (s-AFM) state into ferromagnetic (FM) state at low temperature. Our study launches a new candidate for controlling thermal expansion properties of metal matrix materials which could have potential application in variable temperature environment.

Keywords: Fe-Doped MnNiGe, Heusler alloys, negative thermal expansion, magnetic transition, composites

OPEN ACCESS

Edited by:
Jun Chen,
University of Science and Technology Beijing, China

Reviewed by:
Fengxia Hu,
Institute of Physics (CAS), China
Hongfei Liu,
Yangzhou University, China

***Correspondence:**
Ying Sun
sunying@buaa.edu.cn

Specialty section:
This article was submitted to Physical Chemistry and Chemical Physics, a section of the journal Frontiers in Chemistry

Received: *09 December 2017*
Accepted: *18 January 2018*
Published: *06 February 2018*

Citation:
Zhao W, Sun Y, Liu Y, Shi K, Lu H, Song P, Wang L, Han H, Yuan X and Wang C (2018) Negative Thermal Expansion over a Wide Temperature Range in Fe-Doped MnNiGe Composites. Front. Chem. 6:15. doi: 10.3389/fchem.2018.00015

INTRODUCTION

Solid materials usually expand during heating while contract during cooling, i.e., positive thermal expansion (PTE). When functional materials are used in variable temperature environment, PTE will reduce the structural stability and safety reliability of precision parts, or even destroy the functional properties of materials (Chen et al., 2015). Thus, zero thermal expansion (ZTE) or controllable thermal expansion materials are highly required and also wildly applied (Wang et al., 2012) in areas such as aerospace, optical instruments, high-precision machining and processing, microelectronic devices, electro-optical sensor, electronic packaging, and so on. It is important to explore new NTE materials, which could be used to combine with PTE materials as thermal-expansion compensators to obtain near-ZTE materials by adjusting their mass ratio. Until now, there are some kinds of material systems with NTE property have been reported, such as ZrW_2O_8 (Sun X. J. et al., 2013; Ge et al., 2016), $PbTiO_3$-based compounds (Chen et al., 2011), $(Bi,La)NiO_3$ (Azuma et al., 2011), antiperovskite manganese nitrides (Sun et al., 2012b; Yan et al., 2012), ScF_3-based compounds (Greve et al., 2010), $La(Fe,Co,Si)_{13}$ (Huang et al., 2013), MnCoGe-based materials (Zhao et al., 2015), Ca_2RuO_4 (Takenaka et al., 2017), and so on. The previous studies have revealed different mechanisms which lead to the NTE behaviors, including phonon model (Li et al., 2002), rigid unit modes (Dove et al., 1995), phase transition mechanism (Xing et al., 2003),

electronic valence transfer mechanism (Arvanitidis et al., 2003), magnetic transition mechanism (Sun et al., 2012a), and so on.

Recently, MnM'X (M': Co, Ni, Fe, et al, X: Si, Ge, Sn, et al) Heusler alloys have attracted a lot of attention due to the abundant structural and magnetic properties. In 2013, researchers found that the volume of polycrystalline MnCoSi alloy contracted about 0.2% at 300 K (Barcza et al., 2013). Especially, Zhao et al. (2015) found that $MnCo_{0.98}Cr_{0.02}Ge$, bonded with 3–4 wt.% epoxy, undergoes a giant NTE with a linear thermal coefficient of -119×10^{-6} K^{-1} from 250 to 305 K during the martensitic structural transition. Furthermore, the result from Lin et al. (2016) indicates that fine-powder $Mn_{0.98}CoGe$ can broaden the NTE temperature window to ∼135 K (258–393 K) with CTE -79.6×10^{-6} K^{-1}.

As a typical MnM'X Heusler alloy, MnNiGe undergoes a martensitic structural transition from the hexagonal Ni_2In-type structure (space group P63/mmc, 194) to orthorhombic TiNiSi-type structure (space group Pnma, 62) at ∼470 K during cooling process (Ma et al., 2015), which means that there is a potentially good negative thermal expansion effect in this system. Otherwise, the previous study indicates that the introduction of Fe in MnNiGe alloy can change the magnetic competing relationship in parent phases (Liu et al., 2012). And researchers do have observed NTE property in MnNiGe-based compounds after combining with epoxy resin, i.e., a giant CTE of -60.7×10^{-6} K^{-1} over 231–338 K ($\Delta T = 107$ K) and a near-ZTE of 0.6×10^{-6} K^{-1} over 175–231 K ($\Delta T = 56$ K) for the sample of $Mn_{0.94}Fe_{0.06}NiGe$ after mixing with 20 wt.% of epoxy resin (Xu et al., 2017). Unfortunately, the NTE properties of pure MnNiGe-based compounds have not been reported due to the brittle of MnNiGe-based compounds, to our knowledge. Thus, we prepared Fe-doped MnNiGe compounds successfully by solid-state reaction, and observed the giant NTE properties near room temperature (RT) in pure parent alloys. Moreover, the NTE properties were further controlled by combining with commercial Cu. The obtained results in this work broaden the application of Fe-doped MnNiGe alloys.

EXPERIMENTAL DETAILS

Polycrystalline samples of $Mn_{1-x}Fe_xNiGe$ ($x = 0.08, 0.10, 0.16$) and $MnNi_{0.90}Fe_{0.10}Ge$, $Mn_{1-x}Fe_xNiGe$/Cu ($x = 0.08, 0.10, 0.16$) and $MnNi_{0.90}Fe_{0.10}Ge$/Cu composites (hereafter referred as MFx (x = 8, 10, 16) and NF10, MFx/Cu (x = 8, 10, 16) and NF10/Cu, respectively) were prepared by solid-state reaction, using Mn, Fe, Ni, Ge, and Cu (4N) powders as raw materials (Deng et al., 2015). Firstly, the stoichiometric amounts of the starting materials (Mn, Ni, Fe, Ge powders) were mixed, then ground about 2 h in a mortar and pressed into pellets by tablet machine. The pellets were sealed in a quartz tube under vacuum (10^{-5} Pa). The quartz tube was sintered in a box furnace at 900°C for 80 h and cooled down to RT. Then, the composites of $Mn_{1-x}Fe_xNiGe$/Cu ($x = 0.08, 0.10, 0.16$), $MnNi_{0.90}Fe_{0.10}Ge$/Cu were prepared by mixing $Mn_{1-x}Fe_xNiGe$ ($x = 0.08, 0.10, 0.16$), $MnNi_{0.90}Fe_{0.10}Ge$ and commercial Cu powder with different mass ratio, respectively. After grounding the mixture in an agate mortar for 1 h, the mixture was pressed into rectangular blocks and sealed into quartz tubes in vacuum. Finally, the quartz tubes were sintered in a box furnace at 500°C for 10 h, and then cooled down to RT naturally.

X-ray diffraction (XRD) patterns were obtained from an X' Pert PRO powder diffractometer using Cu K_α radiation at (RT), and the XRD data were handled with a software MDI jade 6.0. The linear thermal expansion coefficients of samples were measured from 125 to 475 K by using a Netzsch DIL 402C dilatometer. The instantaneous linear coefficient of thermal expansion α_l over certain temperature range for every sample was calculated based on the as-measured thermal strain. The α_l is defined as:

$$\alpha_l = (1/L_0)^*(dL/dT) \quad (1)$$

where dL and dT are the variations in length and temperature respectively, L_0 is the initial length at 125 K, dL/L_0 is the thermal expansion strain (Chen et al., 2015).

The temperature dependence of magnetization curves were measured between 10 and 450 K under zero field-cooling condition (ZFC) in an applied magnetic field of 1,000 Oe using a Physical Property Measurement System (PPMS). A scanning electron microscopy (SEM, NanoSEM430, FEI) was used to characterize the microstructure of composites.

RESULTS AND DISCUSSION

Phase Purity and Crystal Structure

First, the room temperature XRD patterns of MF8, MF10, MF16, and NF10 are collected to inspect the effect of Fe doping on the crystal structure of MnNiGe alloy. As shown in **Figure 1**, the mainly diffraction patterns of samples can be indexed using hexagonal Ni_2In-type structure. Based on XRD data, the lattice parameters (a_h and c_h) of MF8, MF10, MF16, and NF10 are calculated by Rietveld refinement as shown in **Figure 1**. The results indicate that both a_h and c_h decrease with increasing Fe doping content at Mn sites because the atom radius of the Mn is larger than Fe. From the enlarged view of XRD patterns in the inset of **Figure 1**, it is clear that residual orthorhombic TiNiSi-type structure appeared in the main matrix of hexagonal Ni_2In-type structure for all four samples, the residual mass fractions of orthorhombic phase are calculated to be 14, 4, 4, and 3 wt.%, respectively.

Thermal Expansion Properties

Linear thermal expansion curves of samples have been recorded from 125 to 475 K in **Figure 2**. **Table 1** lists the thermal expansion values and the related temperature ranges. As shown in **Figure 2A**, obvious NTE behaviors are observed in MF10 and NF10 near RT, respectively. The average CTE of MF10 reaches to a giant value of -285.23×10^{-6} K^{-1} with a wide operation-temperature range of 192–305 K ($\Delta T = 113$ K), while the CTE of NF10 is as large as -1167.09×10^{-6} K^{-1} with a temperature range of 246–305 K ($\Delta T = 59$ K). The results indicate that Fe-doped at Ni sites in MnNiGe has a broader temperature range while a larger CTE value can be obtained by Fe doping at Mn sites. Unfortunately, the dL/L_0 curves of pure MF8 and MF16

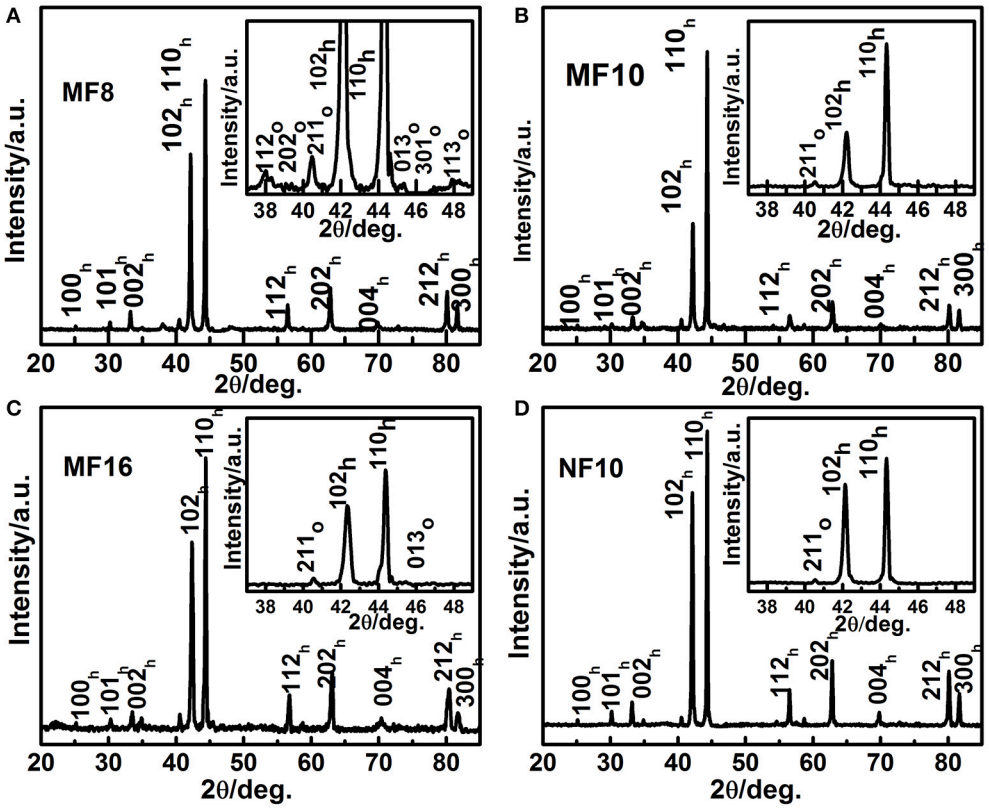

FIGURE 1 | Room temperature X-ray diffraction patterns of **(A)** MF8, **(B)** MF10, **(C)** MF16, and **(D)** NF10.

have not been obtained due to the brittle of the two samples. By comparison, the CTE of Fe-doping MnNiGe is obviously larger than the reported systems such as ZrW_2O_8 (-9.1×10^{-6} K^{-1}) (Mary et al., 1996), MnCoGe-based compound (-141×10^{-6} K^{-1}) (Zhao et al., 2015; Lin et al., 2016), and Mn-Co-Ge-In compound (-51.5×10^{-6} K^{-1}) (Shen et al., 2017).

One of the typical applications for NTE materials is to control thermal expansion behaviors in the form of PTE/NTE composites. In this work, commercial Cu has been selected as matrix metal because of its excellent electronic and mechanic properties and wide usage in the electronic industrial area. Otherwise, in our materials, Fe-doped MnNiGe alloys always collapsed during naturally cooling or the measurement process of CTE, the combination with Cu can also increase the mechanical property of Fe-doped MnNiGe alloys. Therefore, variable mass ratio of MF8/*x*%Cu (x = 15, 25, 30, 40, 50, 70, 85, 100), MF16/*x*%Cu (x = 10, 20, 30), MF10/35%Cu and NF10/35%Cu compounds were prepared. **Figure 2D** displays the XRD patterns of the MF8/*x*%Cu composites. All of the diffraction peaks can be indexed as characteristic peaks of either MF8 or Cu and no additional peaks were observed, indicating that no chemical reaction generated between MF8 and Cu during heating treatment in furnace.

The measurements for linear thermal expansion behaviors have been carried out as shown in **Figure 2**. The amplitudes of the NTE behaviors ($\Delta L/L_0$) in MF10 and NF10 obviously decrease from 3.18 to 0.40% and 6.95 to 0.32% by introducing 35%Cu, and the CTEs (listed in **Table 1**) gradually decrease from -285.23×10^{-6} K^{-1} (192–305 K) and -1167.09×10^{-6} K^{-1} (246–305 K) to -26.15×10^{-6} K^{-1} (167–290 K) and -56.73×10^{-6} K^{-1} (176–247 K), respectively, as shown in **Figure 2A**. The linear thermal expansion behaviors of MF8/*x*%Cu and MF16/*x*%Cu are presented in **Figures 2B,C**).With the increasing of Cu mass ratio x for both of the two serials composites, the NTE temperature ranges become narrow, i.e., the decreasing of the ΔT, and the absolute CTE values increase. Obviously, in MF8/*x*%Cu serials composites, a low thermal expansion behavior with a CTE of -4.73×10^{-6} K^{-1} in a wide temperature range 173–229 K ($\Delta T = 56$ K) is observed in MF8/70%Cu composite. When the mass ratio of Cu is 30% (sample No. 7 in **Table 1**), the CTE is -41.99×10^{-6} K^{-1} between 126 K to 270 K. The NTE behavior is observed in the temperature range 119–274 K ($\Delta T = 155$ K) for sample MF8/15%Cu, and the corresponding CTE is -64.92×10^{-6} K^{-1}. In MF16/10%Cu composite, there is a low CTE of 1.16×10^{-6} K^{-1} in a wide temperature range 125–215 K ($\Delta T = 90$ K). With further increasing temperature, a sharp decreasing in NTE curve is observed and the corresponding CTE is -174.58×10^{-6} K^{-1} (216–228 K). However, the negative thermal expansion disappeared when the mass ratio of Cu increases to 30% in MF16/*x*%Cu composites, this may be due

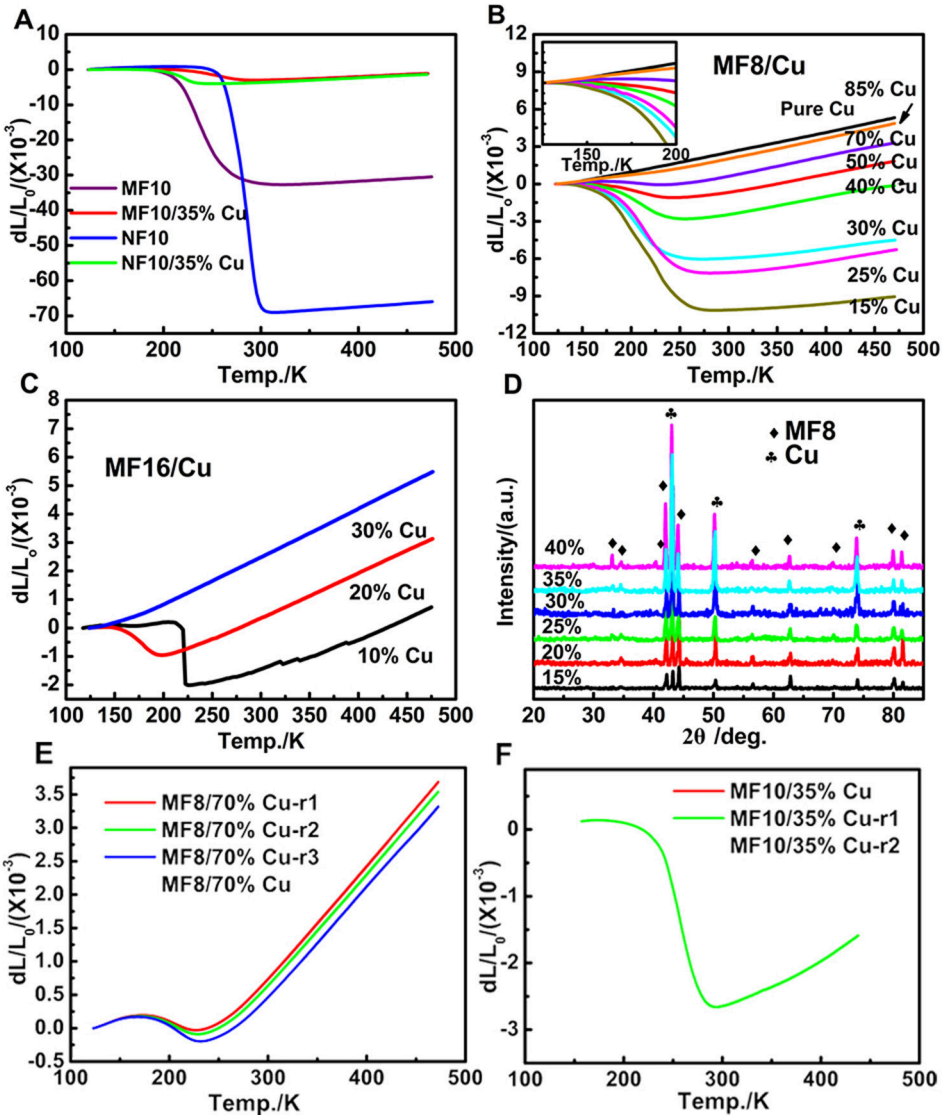

FIGURE 2 | The temperature dependence of dL/L_0 curves of **(A)** MF10, NF10, MF10/35%Cu and NF10/35%Cu, **(B)** MF8/*x*%Cu ($x = 15, 25, 30, 40, 50, 70, 85, 100$) and **(C)** MF16/*x*%Cu ($x = 10, 20, 30$), where the L_0 is the length of the sample at 123 K; **(D)** X-Ray patterns of MF8/*x*%Cu composites at RT; the repeated measurement temperature dependence of dL/L_0 curves of **(E)** MF8/70%Cu and **(F)** MF10/35%Cu.

to the NTE temperature region decreases to below 125 K which is the minimum measuring temperature limit. In order to confirm the stability of the NTE behavior in our samples, we measured the thermal expansion properties of MF10/35%Cu and MF8/70%Cu again and the results are very close to the first measurement result, as shown in **Figures 2E,F**. Therefore, our studies suggest this could be a new alternative for metal matrix composites to achieve near-ZTE materials.

Magnetic Properties

To well understand the thermal expansion property of samples, magnetic properties are further investigated. Temperature dependence of magnetization (M-T) curves of the Fe-doped MnNiGe alloys are first carried out as shown in **Figure 3A** (the inset presents the breaking part of MF16), and the related dM/dT-T curves are shown in **Figure 3B**. The M-T curves of MF8, MF10, and NF10 increase slowly first and then drop sharply with temperature increasing, indicating that a magnetic transition occurred. With further increasing temperature, the M-T curves undergo another sharp drop and hence enter into paramagnetic phases (PM). There are two transition points of magnetic properties, which indicates two different ordered magnetic phases exist in MF8, MF10, and NF10. The magnetic transition temperature points (the low transition temperature T_t and Néel temperature T_N) are defined in **Figure 3B** (Azuma et al., 2011) to be $T_t = 158$ K, 146 K and 112 K, $T_N = 272$, 224, and 218 K for MF8, MF10, and NF10, respectively.

In order to clarify the types of magnetic phases, the isothermal magnetization M(H) curves at 10 K of MF10 and NF10 are carried out in **Figure 3C**. The M-H curves of MF10 and NF10 tend to be linear behavior with no hysteresis behaviors and near zero macroscopic saturation magnetization in the low magnetic field, indicating typical AFM characters (Song et al., 2008; Sun Y. et al., 2013). The slightly bending of the M-H curves may be caused by a potential magnetic phase transition under external magnetic field. Depending on the previous studies, this AFM phase in low temperature is the typical spiral AFM (s-AFM) (Johnson and Frederick, 1973). In MF10 and NF10, with temperature increasing to T_t, s-AFM phase transforms to another AFM phase, of which the magnetization is lower than that of s-AFM, as shown in **Figure 3A**. With further increasing temperature, all of the three samples transit to PM phase at T_N, successively. However, only one magnetic phase transition is observed in MF16, and the M-H curve shows typical FM characteristics which indicates the magnetic transition of MF16 is a FM-PM transition at Currie temperature $T_C = 128$ K as shown in **Figure 3B**. In addition, in MFx ($x = 8, 10, 16$), with Fe content increasing, the magnetization increased (**Figure 3A**) and T_t or T_N/T_C decreased regularly (**Figure 3B**), signifying that the introduction of Fe has changed the s-AFM structure into an FM state. Moreover, **Figure 3D** shows the relationship of dL/dL_0 and M(T) curves in MF10 and NF10. The black real line and the black dot real line are dL/dL_0 curve and M(T) curve for MF10, while the temperature range related NTE property has been defined by the perpendicular black dot dash line with a double arrow. Similarly, the red ones are corresponding to NF10. It is clear that the large temperature windows of observed NTE behaviors are in consistent with the magnetization decreasing slowly during the AFM-PM transformation in MF10 and NF10, which indicates a strong relationship between magnetism and thermal expansion properties in these serials compounds, as well the composites.

TABLE 1 | CTEs and ΔT of the composites with different Cu mass ratio.

No.	Samples	Mass ratio of MFx/NF10 (%)	CTE($\times 10^{-6}$ K^{-1})	Temperature range (ΔT) /K
1	MF10	100	−285.23	192–305 (113)
2	MF10/35%Cu	65	−26.15	167–290 (123)
3	NF10	100	−1167.09	246–305 (59)
4	NF10/35%Cu	65	−56.73	176–247 (71)
5	MF8/15%Cu	85	−64.92	125–274 (149)
6	MF8/25%Cu	75	−50.23	125–264 (140)
7	MF8/30%Cu	70	−41.99	126–270 (144)
8	MF8/40%Cu	60	−22.53	130–255 (125)
9	MF8/50%Cu	50	−11.32	141–241 (100)
10	MF8/70%Cu	30	−4.73	173–229 (56)
11	MF16/10%Cu	90	1.16	125–215 (90)
			−174.58	216–228 (112)
12	MF16/20%Cu	80	−13.26	125–195 (71)

Microstructural Properties

The microstructures of pure MF10 and NF10, composites MF8/70%Cu and MF10/35%Cu are carried out and shown in

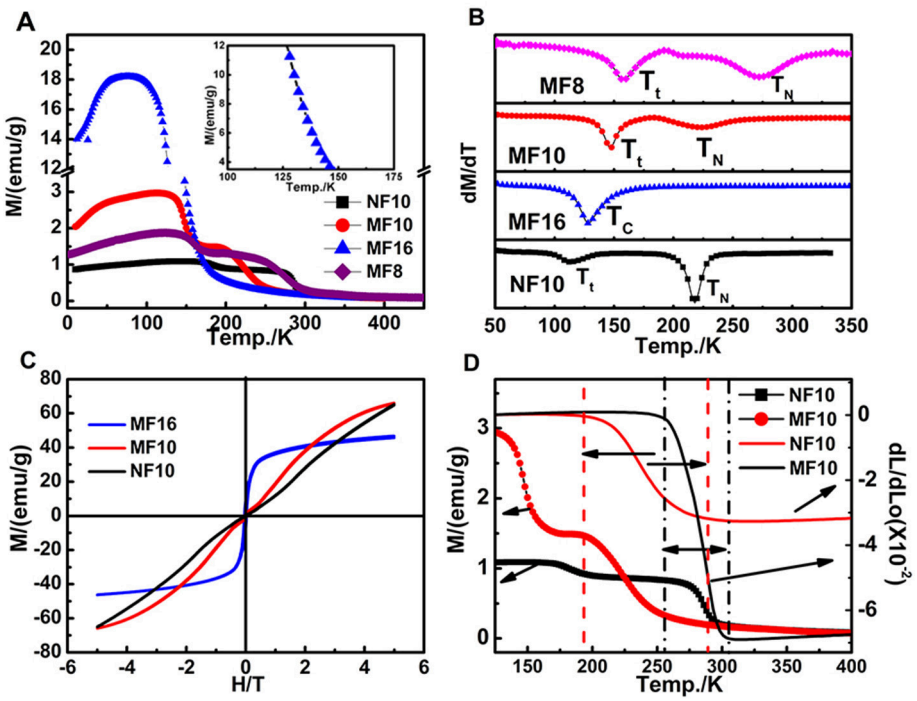

FIGURE 3 | (A) M-T curves (ZFC) of MF8, MF10, MF16, and NF10 with external magnetic field of 1000 Oe; **(B)** the related dM/dT-T curves of four samples; **(C)** the isothermal M(H) curves of MF10, MF16, and NF10 at 10 K; **(D)** M(T) curves and dL/L_0 curves of pure MF10 and NF10 over 125–400 K.

Figure 4. Firstly, in both of MF10 and NF10 samples have massive cavities, and the size of cavities in MF10 is smaller (∼28 μm) than that in NF10 in which the size of cavities is as large as 60 μm. Compared with the results of NTE in **Figure 2A**, large size of cavities sample (NF10) has a larger NTE behavior which indicated that the porosity in pure Fe-doped MnNiGe has positive contribution to the large NTE behaviors. Otherwise, it is clear that two kinds of aggregations and a few holes and cracks can be seen in composites samples. One aggregation consists of small flaky particles with a size ∼5 μm, and the other one consists of irregular and granular particles with a larger size (more than 20 μm). Meanwhile, the chemical compositions of these areas are also analyzed by the energy dispersive X-Ray spectroscopy (EDS). We labeled the locations containing different species in **Figures 5A,D** as areas 1 and 2, areas 3 and 4, respectively. The related EDS of areas 1–2 and areas 3–4 are shown in **Figures 5B,C** and **Figures 5E,F**, respectively. As shown in **Figure 5**, Mn, Ni, Fe, Ge, and Cu peaks are observed in all of the spectra. In MF8/70%Cu, the composition analysis demonstrates that the atomic ratio of area 1 is Mn: Fe: Ni: Ge: Cu = 24.36: 3.77: 35.70: 32.95: 3.22. Combined with **Figure 2D**, the main component of area 1 is MF8, the small amount of Cu is mainly originating from the adherence during mixed grinding and isothermal heat treatment. The atomic ratio of the area 2 is Mn: Fe: Ni: Ge: Cu = 2.01: 0.22: 0.83: 1.30: 95.62, which indicates the major component of the particles in area 2 is Cu metal. Using the same analysis method, the main component of area 3 is MF10, while the component of area 4 is mainly Cu, as shown in **Figures 5E,F**. It can be found that the cracks and holes are filled with Cu particles and the composites have a more compact structure with increasing Cu content, i.e., the MF8 is well dispersed in Cu matrix in MF8/70%Cu, where the stability of the composites is guaranteed (Yan et al., 2014). The composites

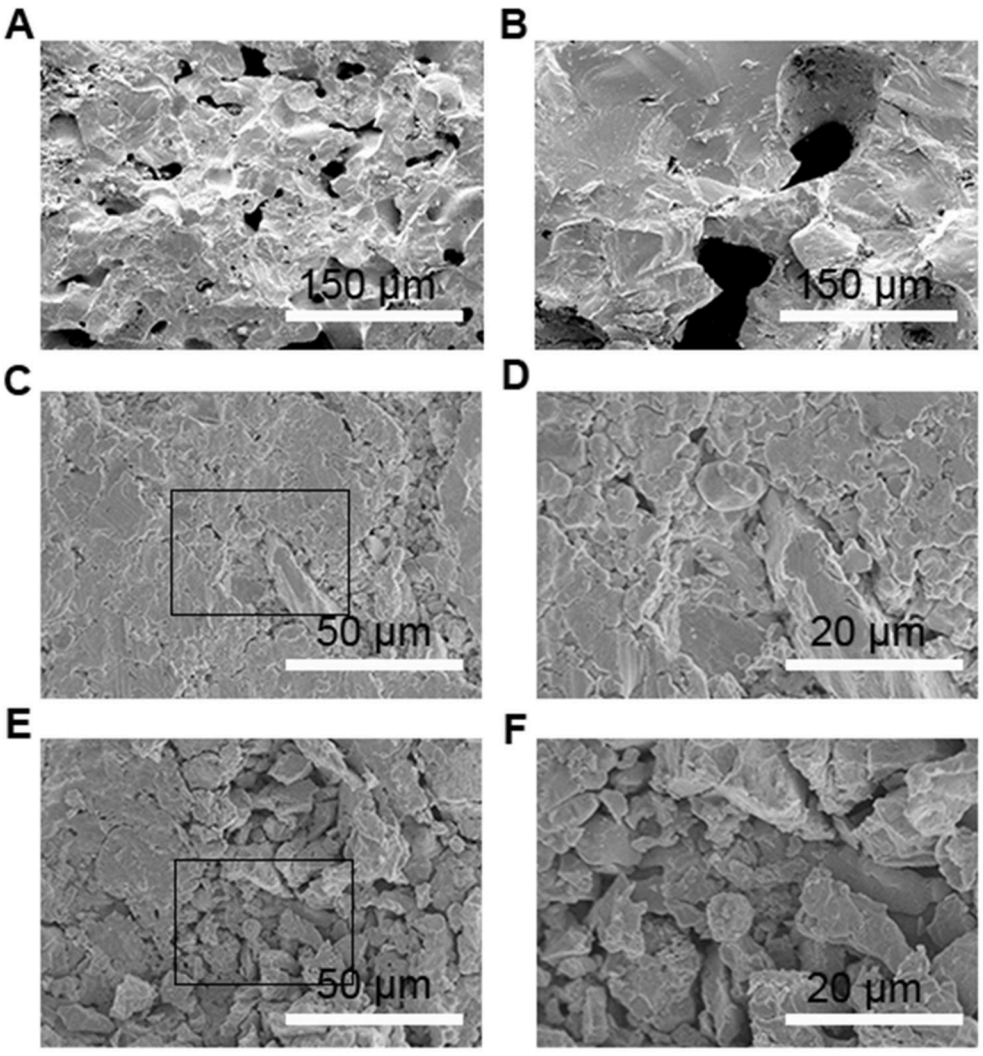

FIGURE 4 | SEM images of **(A)** MF10 and **(B)** NF10, **(C,D)** MF8/70%Cu, **(E,F)** MF10/35%Cu.

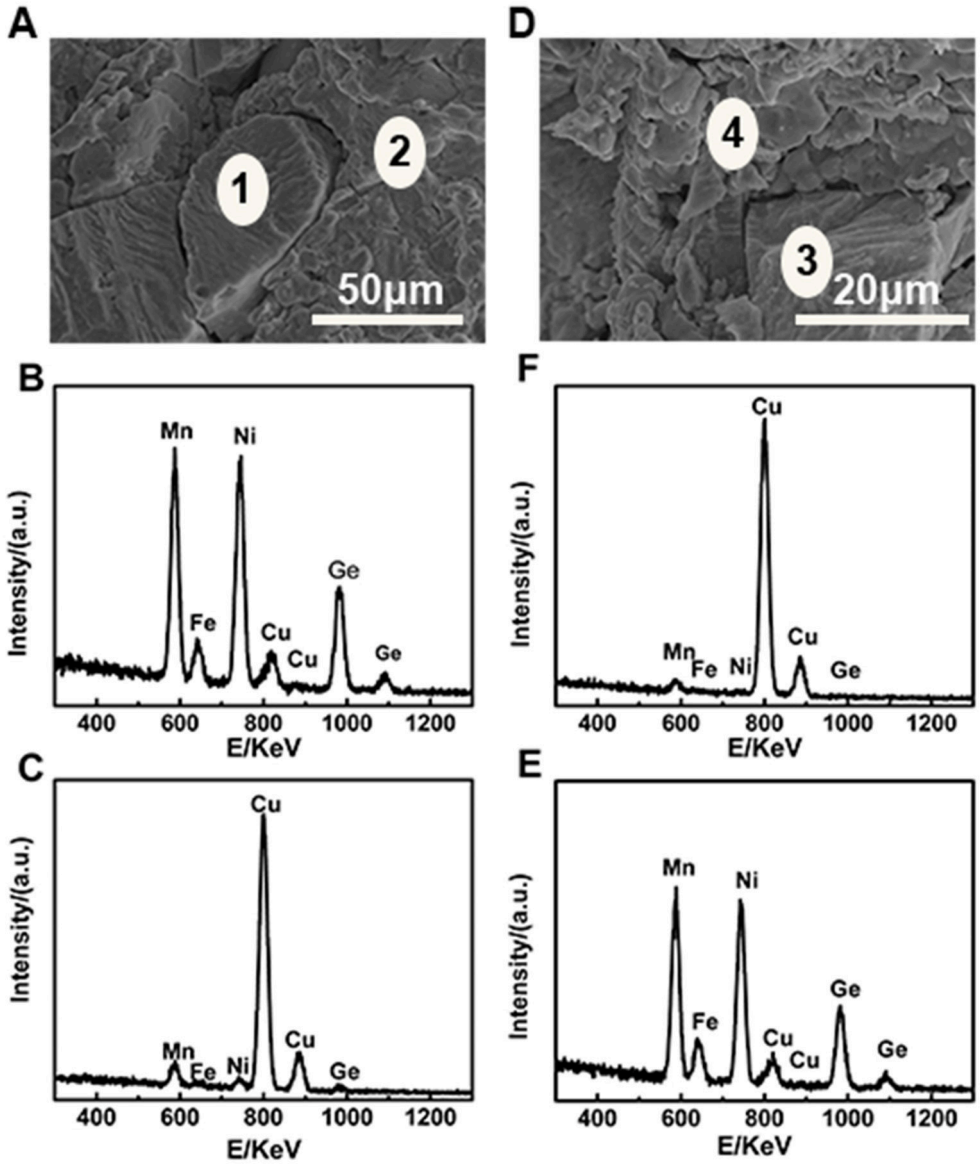

FIGURE 5 | SEM images of **(A)** MF8/70%Cu and **(D)** MF10/35%Cu, respectively and related EDS spectra of **(B,C)** in **(A)** and **(E,F)** in **(D)**, respectively.

display low thermal expansion or near-ZTE properties due to the competition between the positive expansion property of Cu matrix and the negative thermal expansion properties of Fe-doped MnNiGe alloys when placed in a variable temperature environment.

CONCLUSION

In summary, polycrystalline samples of $Mn_{1-x}Fe_xNiGe$ ($x = 0.08, 0.10, 0.16$) and $MnNi_{0.90}Fe_{0.10}Ge$ were prepared by solid-state reaction. Giant negative thermal expansion properties were observed over a wide temperature region in Fe-doped MnNiGe compounds. Especially, the average coefficient of thermal expansion (CTE) for NF10 reaches as large as -1167.09×10^{-6} K^{-1} between 246 and 305 K ($\Delta T = 59$ K). The scanning electron microscopy results show that the porosity has positive contribution to the NTE behavior of MF10 and NF10. AFM-PM phase transition, which is correlated with negative thermal expansion (NTE) of the samples, has been characterized by the magnetic measurements. The $Mn_{1-x}Fe_xNiGe/Cu$ ($x = 8$, 16) composites with controllable thermal expansion have been successfully prepared by adjusting the mass ratio of Cu. In MF8/x%Cu composites, the absolute value of average CTE gradually decreases with increasing matrix Cu content and the CTE reaches to -4.73×10^{-6} K^{-1} (173–229 K) with 70%Cu. In addition, the combining with metal Cu also modifies the mechanical performance of Fe-doped MnNiGe

compounds. This can be a new candidate for controlling thermal expansion properties of metal matrix materials which may have potential applications in variable temperature environment.

AUTHOR CONTRIBUTIONS

YS, CW, WZ conceived the idea and designed experiments; WZ, YL, XY, and HH carried out experiments; and KS, HL, PS, and LW analyzed experimental results. All authors wrote and reviewed the manuscript.

ACKNOWLEDGMENTS

This work is financially supported by the National Natural Science Foundation of China (NSFC) (Nos. 51472017, 51732001, 51572010), the Fundamental Research Funds for the Central Universities, Aeronautical Science Foundation of China, and the Project-sponsored by SRF for ROCS, SEM. The authors also thanks Professor Lai fengLi, Professor Rong jin Huang, and Doctor Wei Wang in theTechnical Institute of Physics and Chemistry, CAS, for the help at this work.

REFERENCES

Arvanitidis, J., Papagelis, K., Margadonna, S., Prassides, K., and Fitch, A. N. (2003). Temperature-induced valence transition and associated lattice collapse in samarium fulleride. *Nature* 425, 599–602. doi: 10.1038/nature01994

Azuma, M., Chen, W. T., Seki, H., Czapski, M., Olga, S., Oka, K., et al. (2011). Colossal negative thermal expansion in $BiNiO_3$ induced by intermetallic charge transfer. *Nat. Commun.* 2:347. doi: 10.1038/ncomms1361

Barcza, A., Gercsi, Z., Michor, H., Suzuki, K., Kockelmann, W., Knight, K. S., et al. (2013). Magnetoelastic coupling and competing entropy changes in substituted CoMnSi metamagnets. *Phys. Rev. B* 87:064410. doi: 10.1103/PhysRevB.87.064410

Chen, J., Hu, L., Deng, J., and Xing, X. (2015). Negative thermal expansion in functional materials: controllable thermal expansion by chemical modifications. *Chem. Soc. Rev.* 44, 3522–3567. doi: 10.1039/c4cs00461b

Chen, J., Nittala, K., Forrester, J. S., Jones, J. L., Deng, J. X., Yu, R. B., et al. (2011). The role of spontaneous polarization in the negative thermal expansion of tetragonal $PbTiO_3$-based compounds. *J. Am. Chem. Soc.* 133, 11114–11117. doi: 10.1021/ja2046292

Deng, S. H., Sun, Y., Wu, H., Huang, Q. Z., Yan, J., Shi, K. W., et al. (2015). Invar-like behavior of antiperovskite $Mn_{3+x}Ni_{1-x}N$ compounds. *Chem. Mater.* 27, 2495–2501. doi: 10.1021/cm504702m

Dove, M. T., Heine, V., and Hammonds, K. D. (1995). Rigid unit modes in framework silicates. *Mineral. Mag.* 59, 629–639. doi: 10.1180/minmag.1995.059.397.07

Ge, X. H., Liu, X. S., Cheng, Y. G., Yuan, B. H., Chen, D. X., Chao, M. J., et al. (2016). Negative thermal expansion and photoluminescence properties in a novel material $ZrScW_2PO_{12}$. *J. Appl. Phys.* 120:205101. doi: 10.1063/1.4968546

Greve, B. K., Martin, K. L., Lee, P. L., Chupas, P. J., Chapman, K. W., and Wilkinson, A. P. (2010). Pronounced negative thermal expansion from a simple structure: cubic ScF_3. *J. Am. Chem. Soc.* 132, 15496–15498. doi: 10.1021/ja106711v

Huang, R. J., Liu, Y. Y., Fan, W., Tan, J., Xiao, F. R., Qian, L. H., et al. (2013). Giant negative thermal expansion in $NaZn_{13}$-type $La(Fe,Si,Co)_{13}$ compounds. *J. Am. Chem. Soc.* 135, 11469–11472. doi: 10.1021/ja405161z

Johnson, V., and Frederick, C. G. (1973). Magnetic and crystallographic properties of ternary manganese silicides with ordered Co2P structure. *Phys. Status Solidi A* 20, 331–335. doi: 10.1002/pssa.2210200133

Li, J., Yokochi, A., Amos, T. G., and Sleight, A. W. (2002). Strong negative thermal expansion along the O–Cu–O linkage in $CuScO_2$. *Chem. Mater.* 14, 2602–2606. doi: 10.1021/cm011633v

Lin, J. C., Tong, P., Zhang, K., Tong, H. Y., Guo, X. G., Yang, C., et al. (2016). Colossal negative thermal expansion with an extended temperature interval covering room temperature in fine-powdered $Mn_{0.98}CoGe$. *Appl. Phys. Lett.* 109, 241903. doi: 10.1063/1.4972234

Liu, E., Wang, W., Feng, L., Zhu, W., Li, G., Chen, J., et al. (2012). Stable magnetostructural coupling with tunable magnetoresponsive effects in hexagonal ferromagnets. *Nat. Commun.* 3:873. doi: 10.1038/ncomms1868

Ma, S. C., Su, Y., Yang, M., Yang, F., Huang, Y. L., Liu, K., et al. (2015). Magnetic phase transition and magnetocaloric effect in Mn-Fe-Ni-Ge ribbons. *J. Alloys Compd.* 629, 322–325. doi: 10.1016/j.jallcom.2014.12.250

Mary, T. A., Evans, J. S. O., Vogt, T., and Sleight, A. W. (1996). Negative thermal expansion from 0.3 to 1050 kelvin in ZrW_2O_8. *Science* 272, 90–92. doi: 10.1126/science.272.5258.90

Shen, F. R., Kuang, H., Hu, F. X., Wu, H., Huang, Q. Z., Liang, F. X., et al. (2017). Ultra-low thermal expansion realized in giant negative thermal expansion materials through self-compensation. *APL Mater.* 5:106102. doi: 10.1063/1.4990481

Song, B., Jian, J. K., Bao, H. Q., Lei, M., Li, H., Wang, G., et al. (2008). Observation of spin-glass behavior in antiperovskite Mn_3GaN. *Appl. Phys. Lett.* 92:192511. doi: 10.1063/1.293105

Sun, X. J., Cheng, X. N., and Yang, J. (2013). Effect of acids on the morphology and negative thermal expansion analysis of ZrW_2O_8 powders prepared by the hydrothermal method. *Ceram. Int.* 39, 165–170. doi: 10.1016/j.ceramint.2012.06.005

Sun, Y., Guo, Y., Tsujimoto, Y., Yang, J., Shen, B., Yi, W., et al. (2013). Carbon-induced ferromagnetism in the antiferromagnetic metallic host material Mn_3ZnN. *Inorg. Chem.* 52, 800–806. doi: 10.1021/ic3019265

Sun, Y., Guo, Y. F., Wang, X. X., Tsujimoto, Y., Matsushita, Y., and Shi, Y. G. (2012a). Resistive switching phenomenon driven by antiferromagnetic phase separation in an antiperovskite nitride Mn_3ZnN. *Appl. Phys. Lett.* 100:161907. doi: 10.1063/1.4704664

Sun, Y., Wang, C., Huang, Q., Guo, Y., Chu, L., Arai, M., et al. (2012b). Neutron diffraction study of unusual phase separation in the antiperovskite nitride Mn_3ZnN. *Inorg. Chem.* 51, 7232–7236. doi: 10.1021/ic300978x

Takenaka, K., Okamoto, Y., Shinoda, T., Katayama, N., and Sakai, Y. (2017). Colossal negative thermal expansion in reduced layered ruthenate. *Nat. Commun.* 8:14102. doi: 10.1038/ncomms14102

Wang, C., Chu, L. H., Yao, Q. R., Sun, Y., Wu, M. M., Ding, L., et al. (2012). Tuning the range, magnitude, and sign of the thermal expansion in intermetallic $Mn_3(Zn, M)_xN$(M = Ag, Ge). *Phys. Rev. B* 85:220103(R). doi: 10.1103/PhysRevB.85.220103

Xing, X. R., Deng, J. X., Chen, J., and Liu, G. R. (2003). Novel thermal expansion of lead titanate. *Rare Met.* 22, 294–297. doi: 10.1016/S1001-0521(08)60123-0

Xu, K., Li, Z., Liu, E., Zhou, H., Zhang, Y., and Jing, C. (2017). Magnetocaloric effect and negative thermal expansion in hexagonal Fe doped MnNiGe compounds with a magnetoelastic AFM-FM-like transition. *Sci. Rep.* 7:41675. doi: 10.1038/srep41675

Yan, J., Sun, Y., Wang, C., Chu, L. H., Shi, Z. X., Deng, S. H., et al. (2014). Study of structure of $Mn_3Cu_{0.5}Ge_{0.5}N$/Cu composite with

nearly zero thermal expansion behavior around room temperature. *Scripta Mater.* 84–85, 19–22. doi: 10.1016/j.scriptamat.2014.04.010

Yan, X. H., Liu, J. Q., Hu, Z. Y., Li, B. Y., and Cheng, X. N. (2012). Thermal expansion of anti-perovskite $Mn_3Zn_{1-x}Sn_xN$ compounds. *Key Eng. Mater.* 512–515, 890–893. doi: 10.4028/www.scientific.net/KEM.512-515.890

Zhao, Y. Y., Hu, F. X., Bao, L. F., Wang, J., Wu, H., Huang, Q. Z., et al. (2015). giant negative thermal expansion in bonded MnCoGe-based compounds with Ni_2 in-type hexagonal structure. *J. Am. Chem. Soc.* 137, 1746–1749. doi: 10.1021/ja510693a

Conflict of Interest Statement: The authors declare that the research was conducted in the absence of any commercial or financial relationships that could be construed as a potential conflict of interest.

frontiers in Chemistry

ORIGINAL RESEARCH
published: 21 March 2018
doi: 10.3389/fchem.2018.00075

Effects of Cr Substitution on Negative Thermal Expansion and Magnetic Properties of Antiperovskite $Ga_{1-x}Cr_xN_{0.83}Mn_3$ Compounds

Xinge Guo[1,2], *Peng Tong*[2]*, *Jianchao Lin*[2], *Cheng Yang*[2], *Kui Zhang*[2], *Shuai Lin*[2], *Wenhai Song*[2] *and Yuping Sun*[2,3,4]

[1] School of Science, Hebei University of Science and Technology, Shijiazhuang, China, [2] Key Laboratory of Materials Physics, Institute of Solid State Physics, Chinese Academy of Sciences, Hefei, China, [3] High Magnetic Field Laboratory, Chinese Academy of Sciences, Hefei, China, [4] Collaborative Innovation Center of Advanced Microstructures, Nanjing University, Nanjing, China

Negative thermal expansion (NTE) and magnetic properties were investigated for antiperovskite $Ga_{1-x}Cr_xN_{0.83}Mn_3$ compounds. As x increases, the temperature span (ΔT) of NTE related with Γ^{5g} antiferromagnetic (AFM) order is expanded and shifted to lower temperatures. At $x = 0.1$, NTE happens between 256 and 318 K ($\Delta T =$ 62 K) with an average linear coefficient of thermal expansion, $\alpha_L = -46$ ppm/K. The ΔT is expanded to 81 K (151–232 K) in $x = 0.2$ with $\alpha_L = -22.6$ ppm/K. Finally, NTE is no longer visible for $x \geq 0.3$. Ferromagnetic order is introduced by Cr doping and continuously strengthened with increasing x, which may impede the AFM ordering and thus account for the broadening of NTE temperature window. Moreover, our specific heat measurement suggests the electronic density of states at the Fermi level is enhanced upon Cr doping, which favors the FM order rather than the AFM one.

Keywords: negative thermal expansion, antiferromagnetic order, specific heat, antiperovskite compounds, Cr substitution

OPEN ACCESS

Edited by:
Andrea Sanson, Dipartimento di Fisica e Astronomia, Università degli Studi di Padova, Italy

Reviewed by:
Lars Gundlach, University of Delaware, United States
Titus Sebastiaan Van Erp, Norwegian University of Science and Technology, Norway

***Correspondence:**
Peng Tong
tongpeng@issp.ac.cn

Specialty section:
This article was submitted to Physical Chemistry and Chemical Physics, a section of the journal Frontiers in Chemistry

Received: *11 January 2018*
Accepted: *06 March 2018*
Published: *21 March 2018*

Citation:
Guo X, Tong P, Lin J, Yang C, Zhang K, Lin S, Song W and Sun Y (2018) Effects of Cr Substitution on Negative Thermal Expansion and Magnetic Properties of Antiperovskite $Ga_{1-x}Cr_xN_{0.83}Mn_3$ Compounds. Front. Chem. 6:75. doi: 10.3389/fchem.2018.00075

INTRODUCTION

Negative thermal expansion (NTE) materials, which contract upon heating, have received great attentions recently (Mary et al., 1996; Takenaka and Takagi, 2005; Goodwin et al., 2008; Long et al., 2009; Greve et al., 2010; Azuma et al., 2011; Yamada et al., 2011; Huang et al., 2013; Panda et al., 2014; Zhao et al., 2015). From the view point of applications, NTE materials can be used as fillers for compensating and controlling the positive thermal expansion (PTE) of normal materials by forming composites (Romao et al., 2003; Chen et al., 2015). NTE has been observed in many materials due to different mechanisms, including flexible framework in crystal structure (Mary et al., 1996; Goodwin et al., 2008; Greve et al., 2010; Ge et al., 2016; Hu et al., 2016; Jiang et al., 2016), ferroelectricity (Xing et al., 2003; Chen et al., 2013), charge transformation (Long et al., 2009; Azuma et al., 2011; Yamada et al., 2011), magnetovolume effect (MVE) (Takenaka and Takagi, 2005; Huang et al., 2013; Li et al., 2015, 2016), and martensitic transformation (Zhao et al., 2015; Lin et al., 2016). Among them, the NTE related with MVE in antiperovskite manganese nitrides $ANMn_3$ (A: transition metal or semiconducting elements) has been extensively studied because of the large and isotropic

NTE with tunable linear coefficient of thermal expansion (α_L), good mechanical properties (large Young's modulus and hardness) and thermal/electrical conductivities (Takenaka and Takagi, 2005; Sun et al., 2007; Huang et al., 2008; Song et al., 2011; Tong et al., 2013a,b; Tan et al., 2014).

Large lattice volume contraction of a few percent at the antiferromagnetic (AFM) to paramagnetic (PM) phase transition due to MVE has been reported in antiperovskite manganese nitrides decades ago (Fruchart and Bertaut, 1978). However, due to the limited temperature window (a few K) of MVE, these materials cannot be practically used as PTE compensators. In 2005, Takenaka firstly reported the broadening of MVE window in $Cu_{1-x}Ge_xNMn_3$ (Takenaka and Takagi, 2005). From then on, many studies reported the NTE properties in $ANMn_3$ (A = Zn, Ga, Ag, and Cu) by substituting A with non-magnetic elements, such as Ge, Sn, Si (Sun et al., 2007, 2010a,b; Huang et al., 2008; Takenaka et al., 2008; Dai et al., 2014). Neutron diffraction studies indicated that the pronounced MVE occurs due to the ordering of the non-collinear triangular Γ^{5g} AFM spin configuration, and the non-magnetic element doping slows down the ordering of Γ^{5g} AFM phase (Iikubo et al., 2008a; Song et al., 2011; Deng et al., 2015a,b). Local structure measured via the neutron pair distribution function (PDF) (Iikubo et al., 2008b; Tong et al., 2013a) and x-ray absorption fine structure measurements (Matsuno et al., 2009) suggested a strong relation between the broadening of AFM transition and the local lattice distortions, though a detailed mechanism is still under debate (Tong et al., 2013a). Very recently, we found that by partially replacing A in $ANMn_3$ (i.e., $GaN_{0.8}Mn_3$, $AgNMn_3$) with Mn, the MVE window was expanded as well (Guo et al., 2015; Lin et al., 2015), while local structural distortion was not observed (Guo et al., 2015). For example, in $Ga_{1-x}Mn_xN_{0.8}Mn_3$ the ΔT of NTE reaches 54 K (between 255 and 309 K, $\alpha_L = -42$ ppm/K) and 73 K (between 206 and 279 K, $\alpha_L = -25$ ppm/K) for $x = 0.25$ and 0.3, respectively (Guo et al., 2015). Large NTE with $\alpha_L \sim -20$ ppm/K at cryogenic temperatures (below 120 K) was achieved in $(Ga_{0.7}Cu_{0.3})_{1-x}Mn_xNMn_3$ with $x = 0.25$ and 0.3 (Guo et al., 2017). In those Mn-doped compounds, in addition to the AFM order that gives rise to the large volume change, the coexisting FM order was demonstrated to impede the growth of the AFM order and thus cause the broadened ΔT of lattice contraction (Guo et al., 2015, 2017; Lin et al., 2015). It is interesting to check whether other 3d elements can tune the NTE of $ANMn_3$ as the Mn does.

Here, we report influences of Cr substitution for Ga on thermal expansion and magnetic properties of MVE-compound $GaN_{0.83}Mn_3$. $GaN_{0.83}Mn_3$ is AFM below $T_N \sim 360$ K (Kasugai et al., 2012). Upon substituting Cr for Ga, the AFM ground is quickly suppressed. Meanwhile, FM order is introduced and increasingly enhanced with increasing Cr doping level. Accompanying with the suppression of AFM state, the sharp MVE of the parent compound is quickly moved to lower temperatures and the related temperature range is widened. A quite large NTE temperature window of 81 K (151–232 K) with a considerably large average $\alpha_L \sim -22.6$ ppm/K was observed in $x = 0.2$. The emergence of FM order can be attributed to the increasing electronic density of states (DOS) at the Fermi energy (E_F) as indicated by the increased electronic contribution to the specific heat at low temperatures.

EXPERIMENTAL

Polycrystalline samples $Ga_{1-x}Cr_xN_{0.83}Mn_3$ ($x = 0$, 0.1, 0.2, 0.3, 0.4) were prepared by direct solid state reaction with Ga ingot (4N), Cr (3N), Mn (4N), and self-made Mn_2N powders. The starting materials were mixed in the desired proportions, sealed in evacuated quartz tubes (10^{-3} Pa) and then annealed at 873–973 K for 5 days. After quenching the tubes to room temperature, the products were pulverized, mixed, pressed into pellets, and annealed again at 1,073–1,173 K for extra 8 days. The final samples were checked by X-ray diffraction (XRD) on a Bruker X-ray diffractometer (D8 Advance) with Cu Kα radiations at room temperature. The magnetization measurements were performed on a Superconducting Quantum Interference Device Magnetometer (SQUID, Quantum Design). By using a strain gauge, linear thermal expansion $\Delta L/L$ was measured on a Physical Property Measurement System (PPMS, Quantum Design; Lin et al., 2015). On the same PPMS system, specific heat was measured for $x = 0$ and 0.2 compounds.

RESULTS AND DISCUSSION

Figure 1 shows the room-temperature XRD patterns for $Ga_{1-x}Cr_xN_{0.83}Mn_3$ ($x = 0$, 0.1, 0.2, 0.3, 0.4) samples. All the samples are single-phase with a typical cubic antiperovskite structure (space group: Pm-3m), except for a very small amount of CrN detected in $x = 0.4$. The (111) peak shifts toward higher angles as x increases, which indicates the decrease of lattice constant with the increase of Cr content. **Figure 2A** presents the temperature dependent magnetization $M(T)$ of $Ga_{1-x}Cr_xN_{0.83}Mn_3$ ($0 \leq x \leq 0.3$) measured at $H = 100$ Oe under both zero-field-cooling (ZFC) and field-cooling (FC) modes. As shown in **Figure 2B**, there is a kink at 358 K for $x = 0$, indicating an AFM to PM transition as often observed in antiperovskite manganese nitrides. This value agrees well with the Neel temperature (T_N) of $GaN_{0.83}Mn_3$ reported previously (Kasugai et al., 2012). When $x = 0.1$, T_N is decreased to 318 K. In slightly Mn-doped $Ga_{1-x}Mn_xN_{0.8}Mn_3$ (Guo et al., 2015), $(Ga_{0.7}Cu_{0.3})_{1-x}Mn_xN_{0.8}Mn_3$ (Guo et al., 2017), and $Ag_{1-x}Mn_xNMn_3$ (Lin et al., 2015), the $M(T)$s are featured by a clear peak in the ZFC curves, while the related FC $M(T)$s show a FM-like transition. This behavior was verified as a glassy transition (Guo et al., 2015, 2017; Lin et al., 2015). In contrast, for $x = 0.1$ Cr doped sample, FM-like transition was observed at around 120 K in both ZFC and FC $M(T)$ curves with an obvious divergence between them at lower temperatures. The absence of peak in ZFC $M(T)$ curve is indicative of the emergence of long range FM order below 120 K. For $x = 0.2$, the FM-like transition is increased to 230 K. The kink on ZFC $M(T)$ referring to T_N is no longer visible. Instead, a drop of magnetization happens at 210 K in both ZFC and FC $M(T)$ curves, similar to that observed in $Ga_{1-x}Mn_xN_{0.8}Mn_3$ with $x = 0.3$ (Guo et al., 2015). The $M(T)$ curves for $x = 0.3$ display a FM transition at 322 K, though the FC

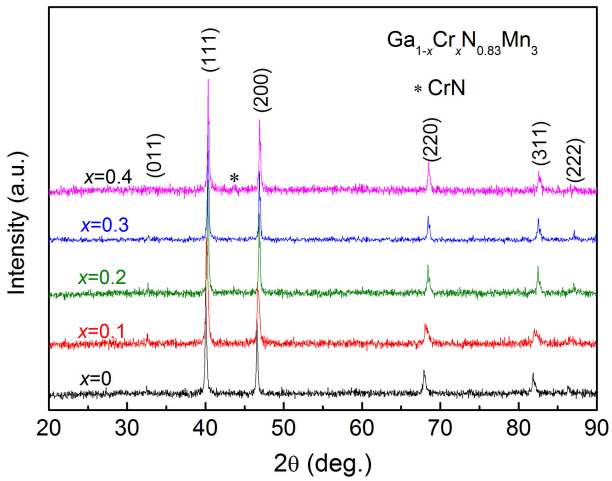

FIGURE 1 | X-ray diffractions at room temperature for $Ga_{1-x}Cr_xN_{0.83}Mn_3$ ($x = 0$, 0.1, 0.2, 0.3, 0.4). The asterisk marks the diffractions from CrN.

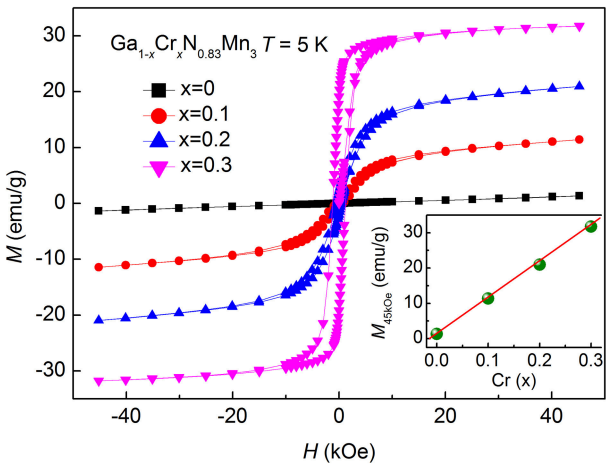

FIGURE 3 | The isothermal magnetization $M(H)$ loops at 5K for $Ga_{1-x}Cr_xN_{0.83}Mn_3$ ($x = 0$, 0.1, 0.2, 0.3) measured between −45 and 45 kOe. Inset shows the magnetization at 45 kOe, M_{45kOe}, as a function of Cr content (x).

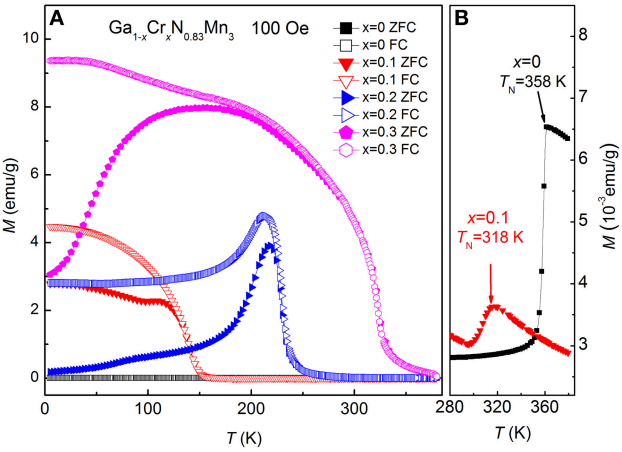

FIGURE 2 | (A) The magnetization $M(T)$ measured at both zero-field-cooling (ZFC) and field-cooling (FC) modes for $Ga_{1-x}Cr_xN_{0.83}Mn_3$ ($x = 0$, 0.1, 0.2, 0.3). **(B)** shows an enlargement of the high-temperature ZFC data for $x = 0$ and 0.1, where the antiferromagnetic to paramagnetic transition at T_N is marked in each curve.

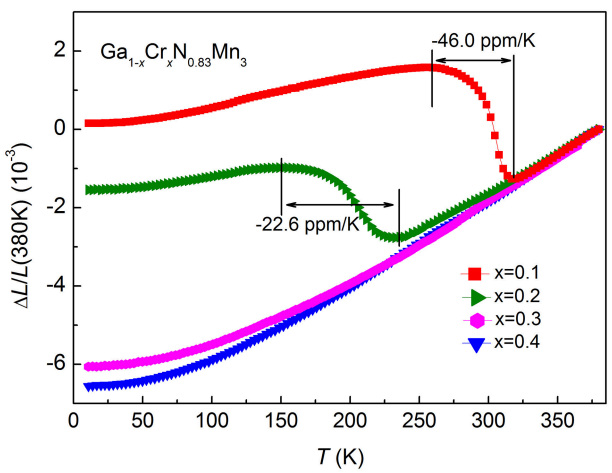

FIGURE 4 | Linear thermal expansion $\Delta L/L$ (380 K) for $Ga_{1-x}Cr_xN_{0.83}Mn_3$ ($x = 0.1$, 0.2, 0.3 and 0.4). The temperature range of negative thermal expansion and the related average linear coefficient of thermal expansion are marked for $x = 0.1$ and 0.2.

curve deviates from the ZFC one at low temperatures. **Figure 3** shows the isothermal hysteresis loop $M(H)$s at 5 K for $x = 0$–0.3 samples. The magnetization at 45 kOe (M_{45kOe}) increases quickly and linearly with increasing x (inset of **Figure 3**). At the same time the slopes of $M(H)$ curves at high magnetic fields become smaller as x increases, indicating the FM component is enhanced at the expense of AFM component. For $x = 0.3$, a FM ground state is established.

Figure 4 shows the linear thermal expansion $\Delta L/L$ (380 K) for $Ga_{1-x}Cr_xN_{0.83}Mn_3$ ($0.1 \leq x \leq 0.4$). Because of the large volume change at T_N which is above room temperature, the as-prepared $GaN_{0.83}Mn_3$ sample was brittle and thus not subjected to the strain gauge measurement. As shown in **Figure 4**, at $x = 0.1$, the lattice undergoes a continuous shrinkage upon heating between 256 and 318 K ($\Delta T = 62$ K) with an average $\alpha_L = -46$ ppm/K. The onset temperature of NTE region is consistent with the broad AFM transition shown in **Figure 2B**. For $x = 0.2$, The NTE temperature window shifts to 151–232 K ($\Delta T = 81$ K), and the corresponding average α_L is about ~ -22.6 ppm/K. The lattice contraction coincides well with the drop of magnetization displayed in both ZFC and FC $M(T)$s as shown in **Figure 2A**. When x is further increased ($\geq$0.3), no NTE was observed down to 5 K.

Among the many ordered spin configurations, the Γ^{5g}-type AFM one is special because it adopts a larger lattice volume relative to the PM or FM state, which is considered as the

prerequisite for the showing up of NTE (Takenaka et al., 2014). The Γ^{5g}-type AFM order is the ground state below T_N for the $x < 0.2$ compounds (Kasugai et al., 2012). Most likely, this particular AFM order is involved below 210 K in $x = 0.2$ sample, as manifested by the drop of the magnetization shown in **Figure 2A**. Upon doping with Cr, the FM order emergences and becomes increasingly strong with x, as revealed by enhanced T_C and the low-temperature magnetization. The strengthened FM phase would impede the growth and propagation of AFM order upon cooling probably via the magnetically coupled AFM/FM interfaces (Guo et al., 2015). When x is increased to 0.3, the FM phase is overwhelmingly strong so that the MVE associated with the AFM ordering is no longer able to influence the overall thermal expansion. As a result, the $x = 0.3$ compound displays a normal PTE.

The parent compound of $Ga_{1-x}Mn_xN_{0.8}Mn_3$ is very close to that of the current solid solutions in terms of the chemical composition and the value of T_N. However, Cr doping is more effective in disturbing the AFM order and consequently in expanding the temperature range of lattice contraction relative to Mn doping. For example, with 20% Cr doping the ΔT of NTE is about 80 K, which is even larger than that of 30% Mn doped sample ($\Delta T = 73$ K; Guo et al., 2015). As shown in the inset of **Figure 3**, M_{45kOe} at 5 K increases linearly with Cr doping level and reaches 31.8 emu/g for $x = 0.3$. But, for $Ga_{1-x}Mn_xN_{0.8}Mn_3$ the value of M_{45kOe} at 5 K shows a tendency toward saturation with increasing x, and the related value for $x = 0.3$ is only 22.3 emu/g (Guo et al., 2015). Such a difference indicates the more rapid strengthening of FM order in Cr-doped compounds than in Mn-doped ones. So the AFM phase in Cr-doped sample experienced a stronger impendence from the more rapidly developing FM order, leading to a wider NTE window relative to Mn-doped compounds at the same doping level.

Figure 5 shows the specific heat $C_p(T)$ for $GaN_{0.83}Mn_3$ and $Ga_{0.8}Cr_{0.2}N_{0.83}Mn_3$ between 6 and 245 K. A broad peak was observed at 220 K for $x = 0.2$ compound, which is resulted from the structural transition (i.e., the NTE) observed in **Figure 4**. As shown in the inset of **Figure 5**, the low-temperature specific heat data for each compound plotted as $C_p(T)/T$ vs. T^2 can be well-fitted linearly by using the expression, $C_p(T)/T = \gamma + \beta T^2$, where γ (i.e., the Sommerfeld constant) represents for the electronic contribution, the second term is the lattice contribution based on the Debye approximation (Wang et al., 2010). The fitted values of γ are equal to 24.3(3) and 30.2(1) mJ/(mol K^2) for $GaN_{0.83}Mn_3$ and $Ga_{0.8}Cr_{0.2}N_{0.83}Mn_3$, respectively. The value of γ corresponds to the density of the electronic DOS at E_F in the ground state. The enhanced γ in the Cr-doped compound indicates an enhancement of DOS at E_F. According the Stoner criterion, FM interactions are enhanced in Cr-doped compound compared with the parent compound (Wang et al., 2010). This may explain why Cr doping suppresses the AFM ground state and finally changes the background to FM in $x = 0.3$ compound. According to the result reported by Garica, the γ is remarkably suppressed when the PM state transforms to AFM phase in $GaNMn_3$ (Garcia et al., 1980), which suggests again that the increased DOS at E_F is not beneficial to the stabilization of AFM ground state of $GaN_{0.83}Mn_3$.

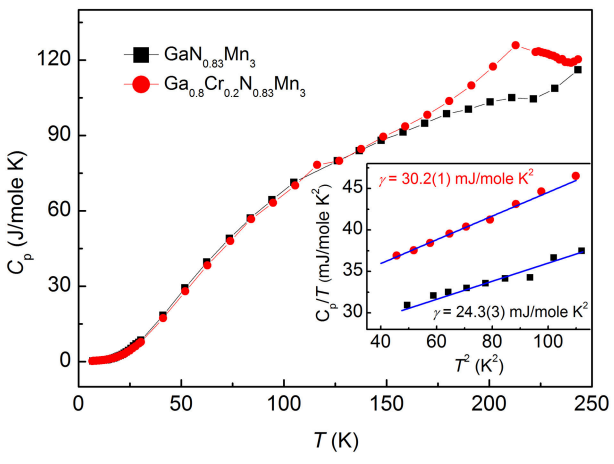

FIGURE 5 | Specific heat $C_p(T)$ for $Ga_{1-x}Cr_xN_{0.83}Mn_3$ with $x = 0$ and 0.2. Inset shows a linear fit to the $C_p(T)/T$ vs. T^2 curves at low temperatures. The fitted electronic coefficients of specific heat (γ, the Sommerfeld constant) are shown for both compounds.

Although there are no theoretical reports on the electronic structure of Cr-doped $GaNMn_3$, studies on $GaNMn_3$ and Mn_4N may give some hints of understanding the magnetism of current compounds. In $GaNMn_3$, all Mn atoms locate at the face centers of the cubic lattice. The hybridized Mn 3d states with N 2p orbitals contribute mainly to the DOS at E_F (Miao et al., 2005). But Ga contributes little to the overall DOS at E_F (Miao et al., 2005). However, as to Mn_4N, the corner Mn atoms (MnI) contribute a lot to the DOS at E_F, while contribution from the face-center Mn atoms (MnII) is very similar to that in $GaNMn_3$ (Miao et al., 2005). In Mn_4N the magnetic moments at MnI (3.5 μB) are antiparallel to those at MnII (0.9 μB), leading to a ferrimagnetic ground state below 756 K (Takei et al., 1962). So MnI atoms play a dominant role in determining the magnetic properties of Mn_4N. Analogously, when Cr elements occupy the corner sites (i.e., Ga sites) of the $GaN_{0.83}Mn_3$, their 3d orbitals will contribute to the DOS at E_F. So the substitution of Cr for Ga introduces extra d electrons to the system, and thus increases the DOS at E_F, leading to the enhanced FM interactions. A thorough theoretical study on the electronic band structures is needed in order to shed lights on the differences of magnetism and thermal expansion between Cr and Mn doped compounds.

CONCLUSIONS

In summary, we report large NTE at low temperatures in antiperovskite compounds $Ga_{1-x}Cr_xN_{0.83}Mn_3$ ($0 \leq x \leq 0.3$). With increasing x, the NTE window was expanded and moved to lower temperatures quickly. For $x = 0.1$ and $x = 0.2$, the NTE occurs at 256–318 K ($\Delta T = 62$ K) and 151–232 K ($\Delta T = 81$ K) with an average α_L of −46 and −22.6 ppm/K, respectively. Finally, for $x \geq 0.3$, NTE was not observed down to 5 K. As revealed by the specific heat measurement, Cr doping increases the DOS at E_F, which favors the emergence of FM order against

the AFM background. The competing FM order was suggested to suppress the original AFM order and hinder its propagation upon cooling, leading to the NTE with wide ΔT.

AUTHOR CONTRIBUTIONS

XG and PT designed the synthetic work; XG carried out the synthesis and characterization of all the compounds; JL, CY, KZ, and SL participated in characterization of structure and magnetism; WS and XG carried out the heat capacity; XG and PT analyzed the data and wrote the manuscript; PT revised the paper; YS did discussion for this work. All authors listed, have made substantial, direct, and intellectual contribution to the work, and approved it for publication.

ACKNOWLEDGMENTS

This work was supported by the National Natural Science Foundation of China under contract Nos. U1632158 and 51322105, the Key Research Program of Frontier Sciences, CAS (QYZDB-SSW-SLH015), the Doctoral Initial Funding of Hebei University of Science and Technology (Grant No. 1181297), and the Natural Science Foundation of Hebei Province (Grant No. A2018208071).

REFERENCES

Azuma, M., Chen, W. T., Seki, H., Czapski, M., Olga, S., Oka, K., et al. (2011). Colossal negative thermal expansion in $BiNiO_3$ induced by intermetallic charge transfer. *Nat. Commun.* 2:347. doi: 10.1038/ncomms1361

Chen, J., Fan, L. L., Ren, Y., Pan, Z., Deng, J. X., Yu, R. B., et al. (2013). Unusual transformation from strong negative to positive thermal expansion in $PbTiO_3$-$BiFeO_3$ perovskite. *Phys. Rev. Lett.* 110:115901. doi: 10.1103/PhysRevLett.110.115901

Chen, J., Hu, L., Deng, J., and Xing, X. (2015). Negative thermal expansion in functional materials: controllable thermal expansion by chemical modifications. *Chem. Soc. Rev.* 44, 3522–3567. doi: 10.1039/C4CS00461B

Dai, Y. J., Song, X. Y., Huang, R. J., Li, L. F., and Sun, Z. H. (2014). Effect of Si doping on structure, thermal expansion and magnetism of antiperovskite manganese nitrides $Mn_3Cu_{1-x}Si_xN$. *Mater. Lett.* 139, 409–413. doi: 10.1016/j.matlet.2014.10.136

Deng, S. H., Sun, Y., Wang, L., Shi, Z. X., Wu, H., Huang, Q. Z., et al. (2015a). Frustrated triangular magnetic structures of Mn_3ZnN: applications in thermal expansion. *J. Phys. Chem. C* 119, 24983–24990. doi: 10.1021/acs.jpcc.5b07225

Deng, S. H., Sun, Y., Wu, H., Huang, Q. Z., Yan, J., Shi, K. W., et al. (2015b). Invar-like behavior of antiperovskite $Mn_{3+x}Ni_{1-x}N$ compounds. *Chem. Mater.* 27, 2495–2501. doi: 10.1021/cm504702m

Fruchart, D., and Bertaut, E. F. (1978). Magnetic studies of the metallic perovskite-type compounds of manganese. *J. Phys. Soc. Jpn.* 44, 781–791. doi: 10.1143/JPSJ.44.781

Garcia, J., Navarro, R., Bartolome, J., Burriel, R., Gonzalez, D., and Fruchart, D. (1980). Specific heat of the cubic metallic perovskites Mn_3ZnN and Mn_3GaN. *J. Magn. Magn. Mater.* 15-8, 1155–1156. doi: 10.1016/0304-8853(80)90231-0

Ge, X., Mao, Y., Liu, X., Cheng, Y., Yuan, B., Chao, M., et al. (2016). Negative thermal expansion and broad band photoluminescence in a novel material of $ZrScMo_2VO_{12}$. *Sci. Rep.* 6:24832. doi: 10.1038/srep24832

Goodwin, A. L., Calleja, M., Conterio, M. J., Dove, M. T., Evans, J. S. O., Keen, D. A., et al. (2008). Colossal positive and negative thermal expansion in the framework material $Ag_3[Co(CN)_6]$. *Science* 319, 794–797. doi: 10.1126/science.1151442

Greve, B. K., Martin, K. L., Lee, P. L., Chupas, P. J., Chapman, K. W., and Wilkinson, A. P. (2010). Pronounced negative thermal expansion from a simple structure: cubic ScF_3. *J. Am. Chem. Soc.* 132, 15496–15498. doi: 10.1021/ja106711v

Guo, X. G., Lin, J. C., Tong, P., Wang, M., Wu, Y., Yang, C., et al. (2015). Magnetically driven negative thermal expansion in antiperovskite $Ga_{1-x}Mn_xN_{0.8}Mn_3$ ($0.1 \leq x \leq 0.3$). *Appl. Phys. Lett.* 107:202406. doi: 10.1063/1.4936239

Guo, X. G., Tong, P., Lin, J. C., Yang, C., Zhang, K., Wang, M., et al. (2017). Large negative thermal expansion in $(Ga_{0.7}Cu_{0.3})_{1-x}Mn_xNMn_3$ ($x \leq 0.4$), compensating for the thermal expansion of cryogenic materials. *Scr. Mater.* 128, 74–77. doi: 10.1016/j.scriptamat.2016.10.002

Hu, L., Chen, J., Xu, J. , Wang, N., Han, F., Ren, Y., et al. (2016). Atomic linkage flexibility tuned isotropic negative, zero, and positive thermal expansion in $MZrF_6$ (M = Ca, Mn, Fe, Co, Ni, and Zn). *J. Am. Chem. Soc.* 138, 14530–14533. doi: 10.1021/jacs.6b08746

Huang, R. J., Li, L. F., Cai, F. S., Xu, X. D., and Qian, L. H. (2008). Low-temperature negative thermal expansion of the antiperovskite manganese nitride Mn_3CuN codoped with Ge and Si. *Appl. Phys. Lett.* 93:081902. doi: 10.1063/1.2970998

Huang, R. J., Liu, Y. Y., Fan, W., Tan, J., Xiao, F. R., Qian, L. H., et al. (2013). Giant negative thermal expansion in $NaZn_{13}$-Type $La(Fe, Si, Co)_{13}$ Compounds. *J. Am. Chem. Soc.* 135, 11469–11472. doi: 10.1021/ja405161z

Iikubo, S., Kodama, K., Takenaka, K., Takagi, H., and Shamoto, S. (2008a). Magnetovolume effect in $Mn_3Cu_{1-x}Ge_xN$ related to the magnetic structure: neutron powder diffraction measurements. *Phys. Rev. B* 77:020409. doi: 10.1103/PhysRevB.77.020409

Iikubo, S., Kodama, K., Takenaka, K., Takagi, H., Takigawa, M., and Shamoto, S. (2008b). Local lattice distortion in the giant negative thermal expansion material $Mn_3Cu_{1-x}Ge_xN$. *Phys. Rev. Lett.* 101:205901. doi: 10.1103/PhysRevLett.101.205901

Jiang, X., Molokeev, M. S., Gong, P., Yang, Y., Wang, W., Wang, S., et al. (2016). Near-zero thermal expansion and high ultraviolet transparency in a borate crystal of $Zn_4B_6O_{13}$. *Adv. Mater.* 28, 7936–7940. doi: 10.1002/adma.201601816

Kasugai, D., Ozawa, A., Inagaki, T., and Takenaka, K. (2012). Effects of nitrogen deficiency on the magnetostructural properties of antiperovskite manganese nitrides. *J. Appl. Phys.* 111:07E314. doi: 10.1063/1.3672243

Li, B., Luo, X. H., Wang, H., Ren, W. J., Yano, S., Wang, C. W., et al. (2016). Colossal negative thermal expansion induced by magnetic phase competition on frustrated lattices in Laves phase compound $(Hf,Ta)Fe_2$. *Phys. Rev. B* 93:224405. Doi:10.1103/PhysRevB.93.224405

Li, S. P., Huang, R. J., Li, W., Wang, W., Zhao, Y. Q., and Li, L. F. (2015). Low-temperature negative thermal expansion behavior of $LaFe_{11.2}Al_{1.8-x}Si_x$ compounds. *J. Alloys Compd.* 646, 119–123. doi: 10.1016/j.jallcom.2015.05.274

Lin, J. C., Tong, P., Tong, W., Lin, S., Wang, B. S., Song, W. H., et al. (2015). Tunable negative thermal expansion related with the gradual evolution of antiferromagnetic ordering in antiperovskite manganese nitrides $Ag_{1-x}NMn_{3+x}$ ($0 \leq x \leq 0.6$). *Appl. Phys. Lett.* 106:082405. doi: 10.1063/1.4913663

Lin, J. C., Tong, P., Zhang, K., Tong, H. Y., Guo, X. G., Yang, C., et al. (2016). Colossal negative thermal expansion with an extended temperature interval covering room temperature in fine-powdered $Mn_{0.98}CoGe$. *Appl. Phys. Lett.* 109:241903. doi: 10.1063/1.4972234

Long, Y. W., Hayashi, N., Saito, T., Azuma, M., Muranaka, S., and Shimakawa, Y. (2009). Temperature-induced A-B intersite charge transfer in an A-site-ordered $LaCu_3Fe_4O_{12}$ perovskite. *Nature* 458, 60–63. doi: 10.1038/nature07816

Mary, T. A., Evans, J. S. O., Vogt, T., and Sleight, A. W. (1996). Negative thermal expansion from 0.3 to 1050 Kelvin in ZrW_2O_8. *Science* 272, 90–92. doi: 10.1126/science.272.5258.90

Matsuno, J., Takenaka, K., Takagi, H., Matsumura, D., Nishihata, Y., and Mizuki, J. (2009). Local structure anomaly around Ge dopants in $Mn_3Cu_{0.7}Ge_{0.3}N$ with negative thermal expansion. *Appl. Phys. Lett.* 94:181904. doi: 10.1063/1.3129169

Miao, M., Herwadkar, A., and Lambrecht, W. (2005). Electronic structure and magnetic properties of Mn_3GaN precipitates in $Ga_{1-x}Mn_xN$. *Phys. Rev. B* 72:033204. doi: 10.1103/PhysRevB.72.033204

Panda, M. K., Runcevski, T., Sahoo, S. C., Belik, A. A., Nath, N. K., Dinnebier, R. E., et al. (2014). Colossal positive and negative thermal expansion

and thermosalient effect in a pentamorphic organometallic martensite. *Nat. Commun.* 5:4811. doi: 10.1038/ncomms5811

Romao, C. P., Miller, K. J., Whitman, C. A., White, M. A., and Marinkovic, B. A. (2003). "Negative thermal expansion (thermomiotic) materials," in *Comprehensive Inorganic Chemistry, II,* eds J. Reedijk and K. Poeppelmeier (Amsterdam: Elsevier), 127–151.

Song, X., Sun, Z., Huang, Q., Rettenmayr, M., Liu, X., Seyring, M., et al. (2011). Adjustable zero thermal expansion in antiperovskite manganese nitride. *Adv. Mater.* 23:4690. doi: 10.1002/adma.201102552

Sun, Y., Wang, C., Wen, Y. C., Chu, L. H., Nie, M., and Liu, F. S. (2010a). Negative thermal expansion and correlated magnetic and electrical properties of Si-doped Mn_3GaN compounds. *J. Am. Ceram. Soc.* 93, 650–653. doi: 10.1111/j.1551-2916.2009.03482.x

Sun, Y., Wang, C., Wen, Y. C., Chu, L. H., Pan, H., and Nie, M. (2010b). Negative thermal expansion and magnetic transition in anti-perovskite structured $Mn_3Zn_{1-x}Sn_xN$ Compounds. *J. Am. Ceram. Soc.* 93, 2178–2181. doi: 10.1111/j.1551-2916.2010.03711.x

Sun, Y., Wang, C., Wen, Y. C., Zhu, K. G., and Zhao, J. T. (2007). Lattice contraction and magnetic and electronic transport properties of $Mn_3Zn_{1-x}Ge_xN$. *Appl. Phys. Lett.* 91:231913. doi: 10.1063/1.2822813

Takei, W. J., Heikes, R. R., and Shirane, G. (1962). Magnetic structure of Mn_4N-type compounds. *Phys. Rev.* 125:1893. doi: 10.1103/PhysRev.125.1893

Takenaka, K., Asano, K., Misawa, M., and Takagi, H. (2008). Negative thermal expansion in Ge-free antiperovskite manganese nitrides: tin-doping effect. *Appl. Phys. Lett.* 92:011927. doi: 10.1063/1.2831715

Takenaka, K., Ichigo, M., Hamada, T., Ozawa, A., Shibayama, T., Inagaki, T., et al. (2014). Magnetovolume effects in manganese nitrides with antiperovskite structure. *Sci. Technol. Adv. Mater.* 15:015009. doi: 10.1088/1468-6996/15/1/015009

Takenaka, K., and Takagi, K. (2005). Giant negative thermal expansion in Ge-doped anti-perovskite manganese nitrides. *Appl. Phys. Lett.* 87:261902. doi: 10.1063/1.2147726

Tan, J., Huang, R. J., Li, W., Han, Y. M., and Li, L. F. (2014). Broadened negative thermal expansion operation-temperature window in antiperovskite $Mn_3Zn_{0.6}Ge_{0.4}N$ prepared by spark plasma sintering. *J. Alloys Compd.* 593, 103–105. doi: 10.1016/j.jallcom.2014.01.027

Tong, P., Louca, D., King, G., Llobet, A., Lin, J. C., and Sun, Y. P. (2013a). Magnetic transition broadening and local lattice distortion in the negative thermal expansion antiperovskite $Cu_{1-x}Sn_xNMn_3$. *Appl. Phys. Lett.* 102:041908. doi: 10.1063/1.4790151

Tong, P., Wang, B. S., and Sun, Y. P. (2013b). Mn-based antiperovskite functional materials: review of research. *Chin. Phys. B* 22:067501. doi: 10.1088/1674-1056/22/6/067501

Wang, B. S., Li, C. C., Lin, J. C., Lin, S., Tong, P., Zhu, X. B., et al. (2010). Metastability across the antiferromagnetic-ferromagnetic intermediate phase transition and enhanced giant magnetoresistance in Zn-doped antiperovskite compounds $Ga_{1-x}Zn_xCMn_3$. *Appl. Phys. Lett.* 97:142505. doi: 10.1063/1.3499216

Xing, X. R., Chen, J., Deng, J. X., and Liu, G. R. (2003). Solid solution $Pb_{1-x}Sr_xTiO_3$ and its thermal expansion. *J. Alloys Compd.* 360, 286–289. doi: 10.1016/S0925-8388(03)00345-1

Yamada, I., Tsuchida, K., Ohgushi, K., Hayashi, N., Kim, J., Tsuji, N., et al (2011). Giant negative thermal expansion in the iron perovskite $SrCu_3Fe_4O_{12}$. *Angew Chem. Int. Ed. Engl.* 50, 6579–6582. doi: 10.1002/anie.201102228

Zhao, Y. Y., Hu, F. X., Bao, L. F., Wang, J., Wu, H., Huang, Q. Z., et al. (2015). Giant negative thermal expansion in bonded MnCoGe-Based compounds with Ni_2In-Type hexagonal structure. *J. Am. Chem. Soc.* 137, 1746–1749. doi: 10.1021/ja510693a

Conflict of Interest Statement: The authors declare that the research was conducted in the absence of any commercial or financial relationships that could be construed as a potential conflict of interest.

frontiers in Chemistry

ORIGINAL RESEARCH
published: 24 July 2018
doi: 10.3389/fchem.2018.00306

Controlling Thermal Expansion Behaviors of Fence-Like Metal-Organic Frameworks by Varying/Mixing Metal Ions

Hao-Long Zhou[1], *Jie-Peng Zhang*[1]* *and Xiao-Ming Chen*[1,2]

[1] MOE Key Laboratory of Bioinorganic and Synthetic Chemistry, School of Chemistry, Sun Yat-Sen University, Guangzhou, China, [2] Department of Chemistry and Key Laboratory for Preparation and Application of Ordered Structural Materials of Guangdong Province, Shantou University, Shantou, China

Solvothermal reactions of 3-(4-pyridyl)-benzoic acid (Hpba) with a series of transition metal ions yielded isostructral metal-organic frameworks $[M(pba)_2]\cdot 2DMA$ (MCF-52; M = Ni^{2+}, Co^{2+}, Zn^{2+}, Cd^{2+}, or mixed Zn^{2+}/Cd^{2+}; DMA = *N*,*N*-dimethylacetamide) possessing two-dimensional fence-like coordination networks based on mononuclear 4-connected metal nodes and 2-connected organic ligands. Variable-temperature single-crystal X-ray diffraction studies of these materials revealed huge positive and negative thermal expansions with $|\alpha| > 150 \times 10^{-6}$ K^{-1}, in which the larger metal ions give the larger thermal expansion coefficients, because the increased space not only enhance the ligand vibrational motion and hinged-fence effect, but also allow larger changes of steric hindrance between the layers. In addition, the solid-solution crystal with mixed metal ions further validates the abundant thermal expansion mechanisms of these metal-organic layers.

Keywords: thermal expansion, porous coordination polymers, metal-organic framework, flexibility, pyridyl-carboxylate, structure-property relationship, metal ion radius, solid solution

OPEN ACCESS

Edited by:
Jun Chen,
University of Science and Technology Beijing, China

Reviewed by:
Xingxing Jiang,
Technical Institute of Physics and Chemistry (CAS), China
Jianchao Lin,
Institute of Solid State Physics (CAS), China

***Correspondence:**
Jie-Peng Zhang
zhangjp7@mail.sysu.edu.cn

Specialty section:
This article was submitted to Physical Chemistry and Chemical Physics, a section of the journal Frontiers in Chemistry

Received: *28 May 2018*
Accepted: *05 July 2018*
Published: *24 July 2018*

Citation:
Zhou H-L, Zhang J-P and Chen X-M (2018) Controlling Thermal Expansion Behaviors of Fence-Like Metal-Organic Frameworks by Varying/Mixing Metal Ions. Front. Chem. 6:306. doi: 10.3389/fchem.2018.00306

INTRODUCTION

Most solids expand slightly as temperature increases ($0 < \alpha < 20 \times 10^{-6}$ K^{-1}, α for axial thermal expansion coefficients, $\alpha = \partial l/\partial T \times 1/l$), which is known as thermal expansion or positive thermal expansion (PTE). Though the structure changes of PTE materials are very small, thermal expansion can often affect other material properties, for example, lead to the loss of precision and function for optical instruments, microelectronic devices so on (Evans, 1999; Liu et al., 2018). In contrast, materials with abnormal thermal expansion behaviors, such as zero thermal expansion (ZTE, $|\alpha| \approx 0 \times 10^{-6}$ K^{-1}), negative thermal expansion (NTE, $\alpha < 0 \times 10^{-6}$ K^{-1}), or very large thermal expansion ($|\alpha| > 100 \times 10^{-6}$ K^{-1}), are scarce (Mary et al., 1996; Chapman et al., 2005; Goodwin et al., 2008; Das et al., 2010; Zhou et al., 2015). NTE compounds may be applied to compensate the thermal expansion of a "normal" PTE material, so that it can remain functional in extremely high or low temperatures without degradation (Mary et al., 1996; Chapman et al., 2005; Rowsell et al., 2005; Wu et al., 2008; Zhou et al., 2016). On the other hand, materials with exceptionally large PTE and NTE can be useful to design sensitive thermomechanical actuators (Das et al., 2010; Zhou et al., 2013, 2015). However, designing and controlling thermal expansion behaviors of materials are still great challenges.

By virtue of their notable porosities and framework flexibilities, porous coordination polymers (PCPs), also known as metal-organic frameworks (MOFs), can show large structural responses toward the change of various environmental parameters, such as temperature, pressure, and magnetic/electric fields (Férey and Serre, 2009; Horike et al., 2009; Nagarkar et al., 2014; Schneemann et al., 2014; Chang et al., 2015; Kanoo et al., 2017; Zhang et al., 2017). Researches on the abnormal thermal expansion behaviors of MOFs have received more and more attentions in recent years (Rowsell et al., 2005; Yang et al., 2009; DeVries et al., 2011; Grobler et al., 2013; Wei et al., 2013; Zhou et al., 2013, 2015; Cai and Katrusiak, 2014; Li et al., 2017). Due to the unique host-guest interactions, the thermal expansion of MOFs can be effectively tuned by the type and amount of guest molecules (Phillips et al., 2008; Yang et al., 2009; Grobler et al., 2013). Besides the steric hindrance and supramolecular interactions caused by the guest molecule (Goodwin et al., 2005; Grobler et al., 2013), the motion of a guest molecule and the thermal expansion of a guest aggregation can also modulate the thermal expansion properties of framework materials (Zhou et al., 2013, 2015). However, the thermal expansion coefficients of MOFs are difficult to tune finely and on demand by using the host-guest mechanism, because guest changing can induce much larger structural transformation and guest loading can be easily disturbed in the open environment. From the view point of framework/material design, it is more direct and predictable to tune the thermal expansion of the framework by changing the metal nodes and/or the organic linkers while maintaining the connection of the framework (Chapman et al., 2006; Korcok et al., 2009). Actually, the variation of metal nodes often affects the flexibility and dynamic responsive behaviors of the framework materials (Millange et al., 2008; Choi et al., 2010; Wang et al., 2011; He et al., 2017), but it has been rarely utilized to regulate the thermal expansion behaviors of MOFs, since the structural variations in such systems are always very small and difficult to quantitatively visualized.

Herein, we report a series of isostructral fence-like MOFs $[M(pba)_2]\cdot 2DMA$ (**1**; MCF-52; M = Ni^{2+}, Co^{2+}, Zn^{2+}, Cd^{2+}, or mixed Zn^{2+}/Cd^{2+}; Hpba = (3-pyridin-4-yl)benzoic acid; DMA = *N*,*N*-dimethylacetamide) exhibiting huge and controllable PTE and NTE ($\alpha_a = 154\sim228 \times 10^{-6}$ K^{-1}, $\alpha_b = 41\sim164\times10^{-6}$ K^{-1} and $\alpha_c = -37\sim-152 \times 10^{-6}$ K^{-1}) dependent on the metal-ion radius. The thermal expansion mechanisms were systematically studied by comparing their single-crystal structures at different temperatures.

MATERIALS AND METHODS

Materials and Instruments

All commercially available reagents and solvents were used as received without further purification. The ligand Hpba was synthesized according to the reported procedure (Zhou et al., 2013). Elemental (C, H, N) analyses (EA) were performed with a Vario EL elemental analyzer. Infrared (IR) spectra were recorded with a Bruker TENSOR 27 Fourier transform FT-IR spectrophotometer on KBr pellets in the range of 4,000–400 cm^{-1}. Inductively coupled plasma-atomic emission spectroscopy (ICP-AES) results were collected by an Optima8300 coupled plasma-atomic emission spectrophotometer. Powder X-ray diffraction (PXRD) patterns were collected on a Bruker D8 ADVANCE X-ray powder diffractometer (Cu Kα, λ = 1.5418 Å). Scanning electron microscopy (SEM) and energy dispersive spectroscopy (EDS) images were recorded on a Quanta 400 field-emitted SEM device. Thermogravimetry (TG) analyses were performed on a TA Q50 instrument with a ramp rate of 10°C min^{-1} under a nitrogen flow. The high-pressure CO_2 adsorption isotherm was measured on an automatic volumetric BELSORP-HP sorption apparatus in the range of 0–40 bar at 298 K. Prior to the sorption measurement, the as-synthesized sample was placed in the sample tube and dried under high vacuum at 230°C for 6 h to remove the solvent guests.

Synthesis

Hpba (0.80 g, 4.0 mmol) was dissolved in DMA (60 mL) using a 250-mL vial, to which a DMA solution of $Cd(NO_3)_2\cdot 6H_2O$ (0.1 mol/L, 20 mL) and methanol (40 mL) were sequentially added. The mixture was then sealed with a screw cap, and heated to 90°C for 72 h. Colorless block-like crystals of $[Cd(pba)_2]\cdot 2DMA$ (MCF-52-Cd) were filtered and washed by DMA (yielded 1090 mg, ca. 80%). EA calcd (%) for $[Cd(pba)_2]\cdot 2DMA$ ($C_{32}H_{34}N_4O_6Cd$): C 56.27, H 5.02, N 8.20; Found: C 56.04, H 4.97, N 8.37. IR: 432(m), 472(w), 548(s), 589(m), 626(s), 682(s), 694(m), 769(s), 825(w), 845(m), 924(w), 1016(m), 1064(w), 1185(w), 1223(w), 1270(w), 1296(w), 1391(s), 1436(m), 1504(w), 1542(s), 1612(s),1637(m), 2938(w), 3071(w).

Crystallography

Single-crystal X-ray diffraction (SCXRD) data were recorded on an Agilent SuperNova CCD diffractometer using mirror-monochromated Cu Kα radiation. The single crystals of $[M(pba)_2]\cdot 2DMA$ were mounted on the top of a glass fiber. The test temperature was controlled by dry N_2 open flow using a Cryostream Plus cooler system, and corrected by a thermal couple at the crystal position. The variable-temperature unit-cell parameters (Tables S1–S5) were obtained by indexing the diffraction spots obtained with 30 diffraction images. Absorption corrections were applied by using the multi-scan program *CrysAlisPro*. The crystal structures were solved through the direct method and developed by the difference Fourier technique using the *SHELXTL* software package. Anisotropic thermal parameters were used to refine all non-hydrogen atoms of the frameworks. Hydrogen atoms were generated geometrically and the positions were refined in the riding mode. Crystallographic data are provided in Datasheet 1 and structural refinement details are summarized in Tables S6–S10. CCDC 1844211–1844220 for $[M(pba)_2]\cdot 2DMA$ contain the supplementary crystallographic data.

RESULTS AND DISCUSSION

Synthesis, Structure, Stability, and Porosity

High-quality single-crystal samples of $[Cd(pba)_2]\cdot 2DMA$ can be obtained through solvothermal reaction of $Cd(NO_3)_2$ and Hpba in mixed solvent DMA/methanol at 90°C. SCXRD revealed that

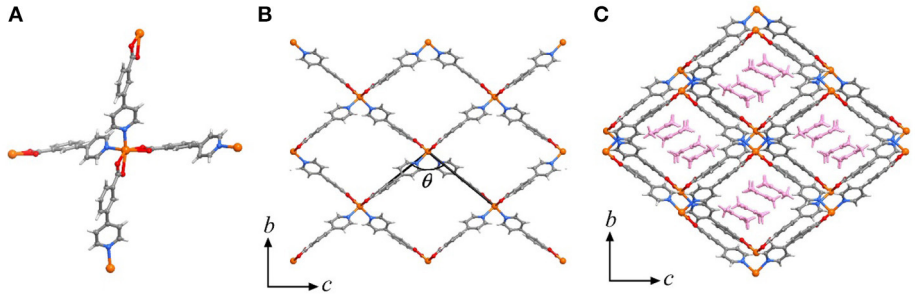

FIGURE 1 | Perspective views of the crystal structure of $[M(pba)_2]\cdot 2DMA$. **(A)** Coordination environment of the metal node. **(B)** The metal-organic fence, and the definition of its interior angle. **(C)** The stacking structure of metal-organic fences with DMA as guests, which are highlighted in pink. Metal ion: orange, C: dark gray, H: light gray, N: blue, O: red.

$[Cd(pba)_2]\cdot 2DMA$ crystallizes in the orthogonal space group $P2_12_12_1$, containing one Cd^{2+} ion with pseudo-octahedron coordination configuration, two bent pba^- ligands and two DMA guest molecules in its asymmetric unit. Each Cd^{2+} ion is coordinated by two carboxylate groups and two pyridyl groups from four pba^- ligands with a tetrahedral configuration, in which the carboxylate group exhibits the bidentate chelating mode. Each pba^- ligand coordinates with two Cd^{2+} ions by using its carboxylate and pyridyl ends. Considering Cd^{2+} ions as 4-connected nodes and pba^- ligands as linkers, the coordination network can be simplified as a two-dimensional (2D) rhombus grid or a typical hinged fence with the 4-connected **sql** topology parallel to the *bc*-plane (**Figure 1**). Such 2D grids stack in a zigzag-offset fashion via C–H···O hydrogen bonds and C–H···π interactions to form the 3D supramolecular structure (**Figure 2**). Thanks to the long ligands, after layers stacking, 1D rhombus nano-channels with a cross-sectional area up to 8.5 × 11.3 $Å^2$ are formed along the *a*-axis direction and the solvent accessible void reaches 46%. The DMA guests are packed closely in a "face to face" way in the channels (**Figure 1C**).

Comparison between the measured PXRD pattern and the simulated one shows the high purity of the $[Cd(pba)_2]\cdot 2DMA$ samples (Figure S1). Then we also studied the stability and porosity of $[Cd(pba)_2]\cdot 2DMA$. The TG curve (Figure S2) showed no weight loss below 80°C. Although the pore diameter is large, the relatively high boiling point and closely packing of DMA guest can effectively limit the guest escape. Then a steady plateau starts up from 230°C until decomposition above 350°C, and the weight loss of 26.4%, according with the theoretical value of 25.6%, meaning that the guests can be removed completely. Thus, the as-synthesized samples of $[Cd(pba)_2]\cdot 2DMA$ were activated by heating at 230°C under vacuum. The PXRD pattern shows the crystallinity can't maintain well after activation, which may be attributed to that the entire framework is formed by stacking 2D layers through the relatively weak van der Waals force. Interestingly, activated $[Cd(pba)_2]$ can revert to its original crystallinity after exposed to the DMA vapor. In addition, high pressure sorption experiment showed that activated $[Cd(pba)_2]$ can adsorb considerable amount of CO_2 at 298 K and 40 bar (Figure S3), giving a pore volume of 0.16 cm^3/g and a BET surface area of 347 m^2/g. These results indicated that the desolvation-induced amorphism arises from local distortions of the coordination framework rather than destroying the framework connections.

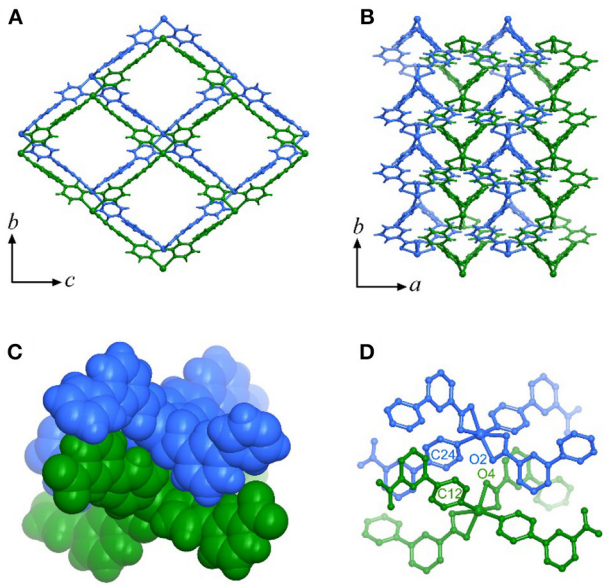

FIGURE 2 | The stacking mode of the metal-organic fences. **(A)** Top view of the stacking layers. **(B)** Side view of the stacking layers. **(C)** Stacking of the tetrahedral building units of adjacent layers (highlighted in the space-filling mode). **(D)** The key atoms of adjacent tetrahedral building units.

Thermal Expansion Properties

The hinged-fence structural models may bring notable thermal expansion behaviors (DeVries et al., 2011; Zhou et al., 2013, 2015). In situ variable-temperature SCXRD measurements in the range of 112–300 K were used to characterize the thermal expansion properties of $[Cd(pba)_2]\cdot 2DMA$ (**Figure 3** and **Table 1**). Encouragingly, $[Cd(pba)_2]\cdot 2DMA$ possesses the exceptionally large thermal expansion coefficients. From 112 to 300 K, the *a*-, *b*-, and *c*-axes of $[Cd(pba)_2]\cdot 2DMA$ change +4.2, +3.1, and −2.9%, respectively, giving linear thermal expansion

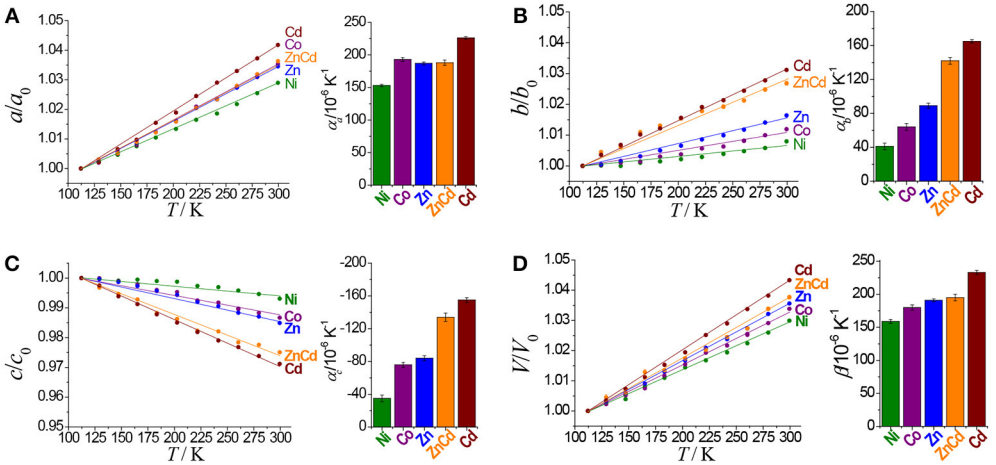

FIGURE 3 | Thermal expansion behaviors of $[M(pba)_2]\cdot 2DMA$.

TABLE 1 | Thermal expansion coefficients of this series of isostructral metal-organic fences based on different metal ions.

	r_{ion} / Å	$\alpha_a/10^{-6}$ K^{-1}	$\alpha_b/10^{-6}$ K^{-1}	$\alpha_c/10^{-6}$ K^{-1}	$\beta_V/10^{-6}$ K^{-1}
$[Ni(pba)_2]\cdot 2DMA$	0.69	153(2)	41(4)	−35(4)	159(3)
$[Co(pba)_2]\cdot 2DMA$	0.72	193(3)	64(4)	−76(3)	180(4)
$[Zn(pba)_2]\cdot 2DMA$	0.74	187(2)	89(3)	−84(3)	191(2)
$[Zn_{0.77}Cd_{0.23}(pba)_2]\cdot 2DMA$	0.74∼0.96	188(4)	142(4)	−134(5)	195(5)
$[Cd(pba)_2]\cdot 2DMA$	0.96	226(2)	165(2)	−155(3)	233(3)

TABLE 2 | Temperature induced variation of the interior angle θ (°) for the metal-organic fences.

	$[Ni(pba)_2]\cdot 2DMA$	$[Co(pba)_2]\cdot 2DMA$	$[Zn(pba)_2]\cdot 2DMA$	$[Zn_{0.77}Cd_{0.23}(pba)_2]\cdot 2DMA$	$[Cd(pba)_2]\cdot 2DMA$
112 K	95.271(3)	96.625(5)	96.342(3)	98.809(4)	101.844(4)
300 K	94.428(3)	95.223(4)	94.602(3)	95.912(3)	98.499(4)
Δ	−0.843	−1.402	−1.740	−2.897	−3.345

coefficients $\alpha_a = +226 \times 10^{-6}$ K^{-1}, $\alpha_b = +165 \times 10^{-6}$ K^{-1} and $\alpha_c = -155 \times 10^{-6}$ K^{-1}. As a combined result, the volume increased by 4.3%, corresponding to a thermal expansion coefficient of $+233 \times 10^{-6}$ K^{-1}. It is worth noting that this is the first solid material exhibiting such huge thermal expansion with all axial thermal expansion coefficients $|\alpha| > 150 \times 10^{-6}$ K^{-1} (Goodwin et al., 2008; Das et al., 2010; Zhou et al., 2015).

To clarify the structural origin of such huge expansion behaviors of these isostructural compounds, their single-crystal structures were determined at 112 K and 300 K. Structural analyses revealed that the interlayer interactions are mainly C–H···π interactions between the aromatic rings. From 112 to 300 K, the two shortest C–H···π separations, C6–H6···C22 and C18–H18···C10, increased from 3.036(5) and 3.115(5) Å to 3.128(5) and 3.285(5) Å, respectively, resulting in an increase of the interlayer distance from 5.750(1) to 5.978(1) Å and the huge PTE of the *a*-axis. The temperature change also causes the hinged-fence effect of the 2D rhombus grids parallel to the *bc*-plane, resulting in the reverse thermal expansion behavior of the *b*- and *c*-axes. The angle between adjacent pyridyl groups of the grid is defined as θ (**Figure 1B**). As the temperature rises from 112 to 300 K, θ decreases from 101.8° to 98.5°, causing the deformation of the entire metal-organic fence with the PTE of the *b*-axis and the NTE of the *c*-axis (**Table 2**). The comparison of structural detail between 112 and 300 K shows that the changes are very small in coordination bond lengths ($\Delta_{max} < 0.02$ Å, Table S11) but very large in the coordination bond angles ($\Delta_{max} > 4°$, Tables S12–S16). In other words, the distortion of the metallic coordination octahedron is the main source of such a huge thermal expansion.

Replacing $Cd(NO_3)_2\cdot 6H_2O$ by $Ni(NO_3)_2\cdot 6H_2O$, $Co(NO_3)_2\cdot 6H_2O$, or $Zn(NO_3)_2\cdot 6H_2O$ in the synthesis gave isostructural crystals of $[Ni(pba)_2]\cdot 2DMA$, $[Co(pba)_2]\cdot 2DMA$, and $[Zn(pba)_2]\cdot 2DMA$, respectively (Figure S4). SCXRD from 112 to 300 K showed that the thermal expansion magnitude of these compounds is in the same order of their metal ion radii, i.e., Ni (0.69 Å) < Co (0.72 Å) < Zn (0.74 Å) < Cd (0.92 Å). Specifically, as the radii of the metal ions increases from 0.69 Å to 0.92 Å, the thermal expansion coefficient of the *a*-axis increases by 48%, while the thermal expansion coefficients of the *b*- and *c*-axes increase by more than 300% (**Figure 3** and **Table 1**). In other words, the metal ion has a significant impact for the thermal expansion of the *bc*-plane showing the hinged-fence effect. Analyzing the crystal-structure details showed that, from 112 to 300 K, the maximal variation of coordination bond angles is less than 1.5° in $[Ni(pba)_2]\cdot 2DMA$ but more than 4.0° in $[Cd(pba)_2]\cdot 2DMA$ (Tables S12–S16), meanwhile the fence angle θ decreases by only 0.8° in $[Ni(pba)_2]\cdot 2DMA$ but decreases by 3.3° in $[Cd(pba)_2]\cdot 2DMA$ (**Table 2**). Thus, it can be seen that the increase of metal ion radius can effectively enlarge the distortion

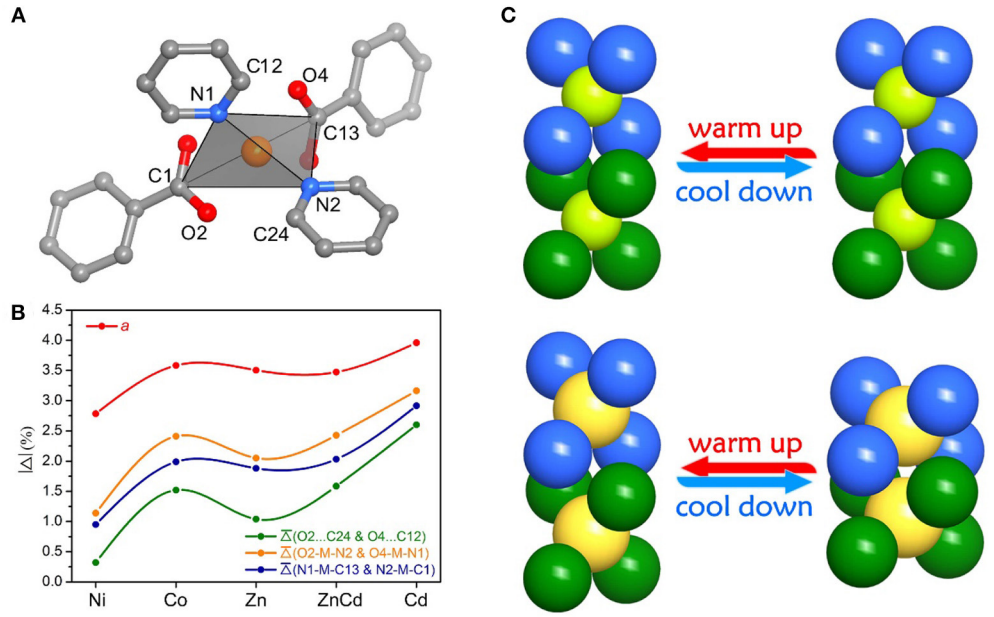

FIGURE 4 | Elucidation of the thermal expansion mechanism for the fence stacking. **(A)** The tetrahedral building unit. **(B)** The selected parameters and variations for the geometry of the tetrahedral building unit and the interlayer separation/interaction. **(C)** Schematic views of thermal expansion upon the change of steric hindrance and metal ions.

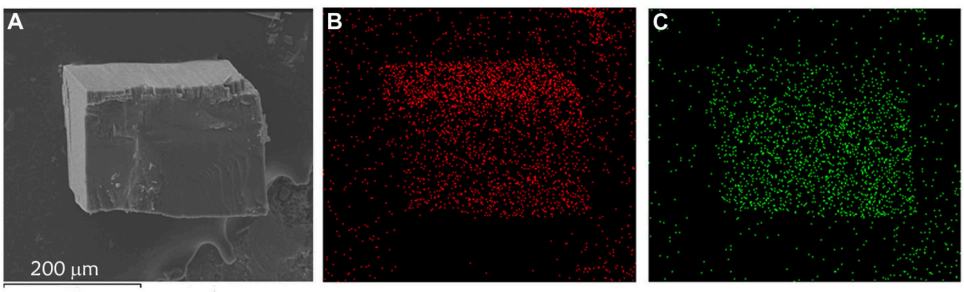

FIGURE 5 | SEM and EDS images of $[Zn_{0.77}Cd_{0.23}(pba)_2]\cdot 2DMA$. **(A)** SEM image of $[Zn_{0.77}Cd_{0.23}(pba)_2]\cdot 2DMA$. **(B)** EDS image of zinc. **(C)** EDS image of cadmium.

of the coordination octahedron and enhance the hinged-fence effect.

The relationship between the PTE of the *a*-axis and the metal ion radius can be explained by the change of steric hindrance. Each metal ion coordinates with two carboxyl groups and two pyridyl groups arranged in a tetrahedral configuration. The tetrahedral building units in adjacent layers intercalate into each other. The shapes of the tetrahedral units, defined by the locations of the pyridyl groups and carboxyl groups, control the steric hindrance between the interlayer tetrahedra. Detailed analyses of crystal structures with different metal ions showed that the larger metal ions correspond to the more open tetrahedra (O2···C24 and O4···C12 between the pyridyl groups and carboxyl groups), smaller steric hindrance, and shorter interlayer separation (i.e., the *a*-axis length). Further, the larger the metal ions allow the coordination tetrahedra to be more flexible, leading to the greater changes of the interlayer separations and the larger PTE of the *a*-axis (**Figure 4** and Table S17).

Solid-solution-type MOFs have been successfully used to achieve adsorption properties between those of two corresponding parent phases (Deng et al., 2010; Horike et al., 2012; Chen et al., 2015; Inukai et al., 2015), but this strategy has not been applied to control thermal expansion behaviors. Preliminary trial showed that using a 1:1 mixture of $Cd(NO_3)_2\cdot 6H_2O$ and $Zn(NO_3)_2\cdot 6H_2O$ as starting material can give solid-solution crystals $[Zn_{0.77}Cd_{0.23}(pba)_2]\cdot 2DMA$, in which the Zn/Cd ratio was determined by ICP-AES measurement of the acid-digested samples. SEM and EDS images revealed that Zn^{2+} and Cd^{2+} ions were uniformly distributed in the crystal (**Figure 5**). Variable-temperature SCXRD showed that the unit-cell parameters of $[Zn_{0.77}Cd_{0.23}(pba)_2]\cdot 2DMA$ are in between those of $[Zn(pba)_2]\cdot 2DMA$ and $[Cd(pba)_2]\cdot 2DMA$

(**Figure 3** and **Table 1**). Free refinements of the single-crystal structures of $[Zn_{0.77}Cd_{0.23}(pba)_2]\cdot 2DMA$ at 112 and 300 K gave the Zn^{2+}/Cd^{2+} occupancy of 0.75/0.25 (Table S10), in agreement with the results of ICP-AES. As expected, the thermal expansion magnitude of its *bc*-plane is between that of $[Zn(pba)_2]\cdot 2DMA$ and $[Cd(pba)_2]\cdot 2DMA$**.** The structural details show that, from 112 to 300 K, the temperature-induced variation of the fence angle θ is 2.9° between 1.7° of $[Zn(pba)_2]\cdot 2DMA$ and 3.3° of $[Cd(pba)_2]\cdot 2DMA$ (**Table 2**). Unexpectedly, the thermal expansion of the *a*-axis of $[Zn_{0.77}Cd_{0.23}(pba)_2]\cdot 2DMA$ approximates to that of $[Zn(pba)_2]\cdot 2DMA$, rather than in between those of $[Zn(pba)_2]\cdot 2DMA$ and $[Cd(pba)_2]\cdot 2DMA$. As mentioned above, the thermal expansion behavior of the *a*-axis depends on the distance between the vertices of the tetrahedral units and the corresponding steric hindrance. In $[Zn_{0.77}Cd_{0.23}(pba)_2]\cdot 2DMA$, the smaller ion Zn(II) with the larger steric hindrance may restrain the proximity of the adjacent layers, so that its thermal expansion behavior of *a*-axis is mainly dependent on Zn(II).

CONCLUSIONS

In summary, a series of isostructral metal-organic fences were obtained using the bent organic ligand with Ni(II), Co(II), Zn(II), and Cd(II). Due to the van der Waals interactions between these stacking 2D metal organic layers, the interlayer distance is particularly sensitive to temperature change, resulting in extraordinarily large PTE. On the other hand, the hinged-fence effect occurs across the metal-organic fence, causing cooperative large PTE and NTE behaviors. Interestingly, the larger ions possessing more flexible coordination geometries can not only induce larger fencing actions but also control the inter-layer steric hindrance, leading to larger thermal expansion magnitudes. Overall, this series of compounds exhibit abundant thermal expansion mechanisms and represent the first solid material with all axial thermal expansion coefficients $|\alpha| > 150 \times 10^{-6}\ K^{-1}$.

AUTHOR CONTRIBUTIONS

J-PZ planned the research and supervised the project. H-LZ carried out the syntheses, characterization, and crystal structure determination. H-LZ, J-PZ, and X-MC analyzed the data and co-wrote the manuscript.

FUNDING

This work was financially supported by the National Basic Research Program of China (973 Project, 2014CB845602) and the National Natural Science Foundation of China (21731007, 91622109, and 21473260).

SUPPLEMENTARY MATERIAL

The Supplementary Material for this article can be found online at: https://www.frontiersin.org/articles/10.3389/fchem.2018.00306/full#supplementary-material

REFERENCES

Cai, W. Z., and Katrusiak, A. (2014). Giant negative linear compression positively coupled to massive thermal expansion in a metal-organic framework. *Nat. Commun.* 5:4337. doi: 10.1038/ncomms5337

Chang, Z., Yang, D. H., Xu, J., Hu, T. L., and Bu, X. H. (2015). Flexible metal-organic frameworks: recent advances and potential applications. *Adv. Mater.* 27, 5432–5441. doi: 10.1002/adma.201501523

Chapman, K. W., Chupas, P. J., and Kepert, C. J. (2005). Direct observation of a transverse vibrational mechanism for negative thermal expansion in Zn(CN)2: an atomic pair distribution function analysis. *J. Am. Chem. Soc.* 127, 15630–15636. doi: 10.1021/ja055197f

Chapman, K. W., Chupas, P. J., and Kepert, C. J. (2006). Compositional dependence of negative thermal expansion in the Prussian blue analogues MPtIVPtII(CN)6 (M = Mn, Fe, Co, Ni, Cu, Zn, Cd). *J. Am. Chem. Soc.* 128, 7009–7014. doi: 10.1021/ja060916r

Chen, S., Shang, R., Wang, B. W., Wang, Z. M., and Gao, S. (2015). An a-site mixed-ammonium solid solution perovskite series of [(NH2NH3)x(CH3NH3)1-x][Mn(HCOO)3] (x=1.00-0.67). *Angew. Chem. Int. Ed.* 54, 11093–11096. doi: 10.1002/anie.201504396

Choi, H. J., Dinca, M., Dailly, A., and Long, J. R. (2010). Hydrogen storage in water-stable metal-organic frameworks incorporating 1,3-and 1,4-benzenedipyrazolate. *Energ. Environ. Sci.* 3, 117–123. doi: 10.1039/B917512A

Das, D., Jacobs, T., and Barbour, L. J. (2010). Exceptionally large positive and negative anisotropic thermal expansion of an organic crystalline material. *Nat. Mater.* 9, 36–39. doi: 10.1038/nmat2583

Deng, H. X., Doonan, C. J., Furukawa, H., Ferreira, R. B., Towne, J., Knobler, C. B., et al. (2010). Multiple functional groups of varying ratios in metal-organic frameworks. *Science* 327, 846–850. doi: 10.1126/science.1181761

DeVries, L. D., Barron, P. M., Hurley, E. P., Hu, C. H., and Choe, W. (2011). "Nanoscale lattice fence" in a metal-organic framework: interplay between hinged topology and highly an isotropic thermal response. *J. Am. Chem. Soc.* 133, 14848–14851. doi: 10.1021/ja2032822

Evans, J. S. O. (1999). Negative thermal expansion materials. *J. Chem. Soc. Dalton Trans.* 3317–3326. doi: 10.1039/a904297k

Férey, G., and Serre, C. (2009). Large breathing effects in three-dimensional porous hybrid matter: facts, analyses, rules and consequences. *Chem. Soc. Rev.* 38, 1380–1399. doi: 10.1039/b804302g

Goodwin, A. L., Calleja, M., Conterio, M. J., Dove, M. T., Evans, J. S. O., Keen, D. A., et al. (2008). Colossal positive and negative thermal expansion in the framework material Ag3[Co(CN)6]. *Science* 319, 794–797. doi: 10.1126/science.1151442

Goodwin, A. L., Chapman, K. W., and Kepert, C. J. (2005). Guest-dependent negative thermal expansion in nanoporous Prussian Blue analogues MPtIVPtII(CN)6•x(H2O) ($0 \leq x \leq 2$; M = Zn, Cd). *J. Am. Chem. Soc.* 127, 17980–17981. doi: 10.1021/ja056460f

Grobler, I., Smith, V. J., Bhatt, P. M., Herbert, S. A., and Barbour, L. J. (2013). Tunable anisotropic thermal expansion of a porous zinc(II) metal-organic framework. *J. Am. Chem. Soc.* 135, 6411–6414. doi: 10.1021/ja401671p

He, C. T., Ye, Z. M., Xu, Y. T., Zhou, D. D., Zhou, H. L., Chen, D., et al. (2017). Hyperfine adjustment of flexible pore-surface pockets enables smart recognition of gas size and quadrupole moment. *Chem. Sci.* 8, 7560–7565. doi: 10.1039/C7SC03067C

Horike, S., Inubushi, Y., Hori, T., Fukushima, T., and Kitagawa, S. (2012). A solid solution approach to 2D coordination polymers for CH4/CO2 and CH4/C2H6 gas separation: equilibrium and kinetic studies. *Chem. Sci.* 3, 116–120. doi: 10.1039/C1SC00591J

Horike, S., Shimomura, S., and Kitagawa, S. (2009). Soft porous crystals. *Nat. Chem.* 1, 695–704. doi: 10.1038/nchem.444

Inukai, M., Fukushima, T., Hijikata, Y., Ogiwara, N., Horike, S., and Kitagawa, S. (2015). Control of molecular rotor rotational frequencies in porous

coordination polymers using a solid-solution approach. *J. Am. Chem. Soc.* 137, 12183–12186. doi: 10.1021/jacs.5b05413

Kanoo, P., Haldar, R., Sutar, P., Chakraborty, A., and Maji, T. K. (2017). "Gated and stepwise sorption processes in functional metal-organic frameworks," in *Functional Supramolecular Materials: From Surfaces to MOFs*, ed R. Banerjee (London: The Royal Society of Chemistry), 412–453. doi: 10.1039/9781788010276-00412

Korcok, J. L., Katz, M. J., and Leznoff, D. B. (2009). Impact of metallophilicity on "colossal" positive and negative thermal expansion in a series of isostructural dicyanometallate coordination polymers. *J. Am. Chem. Soc.* 131, 4866–4871. doi: 10.1021/ja809631r

Li, W., Wang, Z. M., Deschler, F., Gao, S., Friend, R. H., and Cheetham, A. K. (2017). Chemically diverse and multifunctional hybrid organic-inorganic perovskites. *Nat. Rev. Mater.* 2:16099. doi: 10.1038/natrevmats.2016.99

Liu, Z., Gao, Q., Chen, J., Deng, J., Lin, K., and Xing, X. (2018). Negative thermal expansion in molecular materials. *Chem. Commun.* 54, 5164–5176. doi: 10.1039/C8CC01153B

Mary, T. A., Evans, J. S. O., Vogt, T., and Sleight, A. W. (1996). Negative thermal expansion from 0.3 to 1050 Kelvin in ZrW2O8. *Science* 272, 90–92. doi: 10.1126/science.272.5258.90

Millange, F., Guillou, N., Walton, R. I., Greneche, J. M., Margiolaki, I., and Férey, G. (2008). Effect of the nature of the metal on the breathing steps in MOFs with dynamic frameworks. *Chem. Commun.* 4732–4734. doi: 10.1039/b809419e

Nagarkar, S. S., Desai, A. V., and Ghosh, S. K. (2014). Stimulus-responsive metal-organic frameworks. *Chem. Asian J.* 9, 2358–2376. doi: 10.1002/asia.201402004

Phillips, A. E., Goodwin, A. L., Halder, G. J., Southon, P. D., and Kepert, C. J. (2008). Nanoporosity and exceptional negative thermal expansion in single-network cadmium cyanide. *Angew. Chem. Int. Ed.* 47, 1396–1399. doi: 10.1002/anie.200704421

Rowsell, J. L. C., Spencer, E. C., Eckert, J., Howard, J. A. K., and Yaghi, O. M. (2005). Gas adsorption sites in a large-pore metal-organic framework. *Science* 309, 1350–1354. doi: 10.1126/science.1113247

Schneemann, A., Bon, V., Schwedler, I., Senkovska, I., Kaskel, S., and Fischer, R. A. (2014). Flexible metal-organic frameworks. *Chem. Soc. Rev.* 43, 6062–6096. doi: 10.1039/C4CS00101J

Wang, F., Liu, Z. S., Yang, H., Tan, Y. X., and Zhang, J. (2011). Hybrid zeolitic imidazolate frameworks with catalytically active TO_4 building blocks. *Angew. Chem. Int. Ed.* 50, 450–453. doi: 10.1002/anie.201005917

Wei, Y. S., Chen, K. J., Liao, P. Q., Zhu, B. Y., Lin, R. B., Zhou, H. L., et al. (2013). Turning on the flexibility of isoreticular porous coordination frameworks for drastically tunable framework breathing and thermal expansion. *Chem. Sci.* 4, 1539–1546. doi: 10.1039/c3sc22222e

Wu, Y., Kobayashi, A., Halder, G. J., Peterson, V. K., Chapman, K. W., Lock, N., et al. (2008). Negative thermal expansion in the metal-organic framework material Cu_3(1,3,5-benzenetricarboxylate)$_2$. *Angew. Chem. Int. Ed.* 47, 8929–8932. doi: 10.1002/anie.200803925

Yang, C., Wang, X. P., and Omary, M. A. (2009). Crystallographic observation of dynamic gas adsorption sites and thermal expansion in a breathable fluorous metal-organic framework. *Angew. Chem. Int. Ed.* 48, 2500–2505. doi: 10.1002/anie.200804739

Zhang, J. P., Zhou, H. L., Zhou, D. D., Liao, P. Q., and Chen, X. M. (2017). Controlling flexibility of metal–organic frameworks. *Natl. Sci. Rev.* nwx127. doi: 10.1093/nsr/nwx127

Zhou, H. L., Bai, J., Ye, J. W., Mo, Z. W., Zhang, W. X., Zhang, J. P., et al. (2016). Thermal and gas dual-responsive behaviors of an expanded UiO-66-type porous coordination polymer. *ChemPlusChem* 81, 817–821. doi: 10.1002/cplu.201600145

Zhou, H. L., Lin, R. B., He, C. T., Zhang, Y. B., Feng, N. D., Wang, Q., et al. (2013). Direct visualization of a guest-triggered crystal deformation based on a flexible ultramicroporous framework. *Nat. Commun.* 4:2534. doi: 10.1038/ncomms3534

Zhou, H. L., Zhang, Y. B., Zhang, J. P., and Chen, X. M. (2015). Supramolecular-jack-like guest in ultramicroporous crystal for exceptional thermal expansion behaviour. *Nat. Commun.* 6:6917. doi: 10.1038/ncomms7917

Conflict of Interest Statement: The authors declare that the research was conducted in the absence of any commercial or financial relationships that could be construed as a potential conflict of interest.

frontiers in Chemistry

ORIGINAL RESEARCH
published: 30 July 2018
doi: 10.3389/fchem.2018.00296

Efficient Calculation of the Negative Thermal Expansion in ZrW_2O_8

Fernando D. Vila, Scott T. Hayashi and John J. Rehr*

Department of Physics, University of Washington, Seattle, WA, United States

We present a study of the origin of the negative thermal expansion (NTE) on ZrW_2O_8 by combining an efficient approach for computing the dynamical matrix with the Lanczos algorithm for generating the phonon density of states in the quasi-harmonic approximation. The simulations show that the NTE arises primarily from the motion of the O-sublattice, and in particular, from the transverse motion of the O atoms in the W–O and W–O–Zr bonds. In the low frequency range these combine to keep the WO_4 tetrahedra rigid and induce internal distortions in the ZrO_6 octahedra. The force constants associated with these distortions become stronger with expansion, resulting in negative Grüneisen parameters and NTE from the low frequency modes that dominate the positive contributions from the high frequency modes. This leads us to propose an anharmonic, two-frequency Einstein model that quantitatively captures the NTE behavior.

Keywords: zirconium tungstate, NTE, DFT, quasi-harmonic approximation, phonon density of states

OPEN ACCESS

Edited by:
Andrea Sanson,
Università Degli Studi di Padova, Italy

Reviewed by:
Simone Sanna,
Justus Liebig Universität Gießen, Germany
Alessandro Erba,
Università degli Studi di Torino, Italy

****Correspondence:***
Fernando D. Vila
fdv@uw.edu

Specialty section:
This article was submitted to Physical Chemistry and Chemical Physics, a section of the journal Frontiers in Chemistry

Received: *27 April 2018*
Accepted: *26 June 2018*
Published: *30 July 2018*

Citation:
Vila FD, Hayashi ST and Rehr JJ (2018) Efficient Calculation of the Negative Thermal Expansion in ZrW_2O_8. Front. Chem. 6:296. doi: 10.3389/fchem.2018.00296

1. INTRODUCTION

There has been considerable interest in recent years in developing materials with electronic and structural properties tuned toward specific applications. Likewise, there is broad interest in pre-screening potential materials using theoretical simulations in an effort to minimize their complexity and simplify their synthesis. Although great progress has been made in the prediction of many properties (Jain et al., 2013) such as band gaps, electronic properties, equilibrium structures, and spectra, thermal properties depend on additional calculations of vibrational properties and often remain difficult for first principles computational methods. This is typically due to the complexity of the materials under consideration. For example, complex ceramics like ZrW_2O_8 with large unit cells have heretofore been too demanding for routine screening using first principles calculations of both electronic and vibrational properties with conventional electronic structure codes. On the other hand, efficient calculations of many vibrational properties are now possible. For example, we have previously shown (Poiarkova and Rehr, 2001; Krappe and Rossner, 2002; Vila et al., 2007) that an efficient Lanczos algorithm for the projected phonon density of states (PDOS) obtained from standard density functional theory (DFT) calculations (Lee and Gonze, 1995; Rignanese et al., 1996; Baroni et al., 2001) of the dynamical matrix (DM) and the quasi-harmonic approximation (Allen and De Wette, 1969; Boyer, 1979) can produce accurate Debye-Waller factors for EXAFS and x-ray crystallography. Here we develop an extension of this approach for efficient calculations of the thermal properties of ZrW_2O_8, a quintessential example of negative thermal expansion (NTE) ceramics, in which the NTE is large over a broad range of temperatures.

The origin of the NTE in ZrW_2O_8 is controversial, having been previously attributed to a variety of mechanisms. For instance, the Rigid Unit Mode (RUM) model (Hammonds et al., 1996; Pryde et al., 1996, 1997; Hancock et al., 2004; Tucker et al., 2005, 2007) suggests that the tetrahedra and octahedra that make up the structure are mostly unaffected by the active modes. In contrast, other works (Cao et al., 2002, 2003; Bridges et al., 2014) have suggested that these units are distorted

while the Zr-W distance remains more or less unchanged. Yet another alternative (Mary et al., 1996; Gupta et al., 2013; Sanson, 2014) suggests that the Zr–O–W bonds bend, pulling the Zr and W atoms closer and thus causing the NTE. In this paper we take advantage of the local nature of the PDOS to study the origin of the NTE. This procedure allows us to partition the contributions to the Helmholtz free energy from different atomic sites and deduce the origin of NTE from the shifts in the local free energy minima. In a second study in this collection (Vila et al., under review) we apply these methods to study the effects of the NTE on the EXAFS properties of the system, such as the EXAFS mean square relative displacements for relevant single- and multiple-scattering paths (Cao et al., 2003), as well as the anisotropic behavior of the crystallographic mean square atomic displacements. The following sections present a brief summary of the Lanczos algorithm for the PDOS, show how we compute the dynamical matrix efficiently, give a detailed discussion of the volume and temperature effects on the force constants, potentials and PDOS, and present a simple two-frequency model that reproduces the observed NTE quite accurately.

2. METHODS

2.1. Helmholtz Free Energy

The quasi-harmonic approximation (QHA) (Allen and De Wette, 1969; Boyer, 1979) has been widely used to study thermal effects on the structural properties of both crystalline (Erba et al., 2015) and molecular solids (Erba et al., 2016; Brandenburg et al., 2017). QHA simulations usually rely on the full diagonalization of the force constant matrix obtained with density functional perturbation theory (DFPT) or other analytic derivative approaches (Baroni et al., 2010; Erba, 2014). We have previously shown (Vila et al., 2007) that it can also be combined with the Lanczos algorithm in order to avoid the full diagonalization and efficiently compute many thermal properties of materials. Briefly, the lattice thermal expansion $a(T)$ can be obtained by minimizing the Helmholtz free energy $A(a,T)$ at a given T,

$$\left.\frac{\partial A(a,T)}{\partial a}\right|_{a=a(T)} = 0. \tag{1}$$

Within the quasi-harmonic approximation $A(a,T)$ is given by

$$A(a,T) = U(a) + F(a,T), \tag{2}$$

where $U(a)$ is the internal energy of the electronic system in its ground state, and $F(a,T)$ is the total vibrational free energy (VFE) of the system in the Born-Oppenheimer approximation. For convenience we define $F(a,T) = F_0(a) + F_T(a,T)$. Here $F_0(a)$ and $F_T(a,T)$ are the zero-point and temperature-dependent components, respectively. They can be calculated in terms of the density of vibrational modes of the lattice $\rho(a,\omega)$ at a given a,

$$F_0(a) = \frac{\hbar}{2}\int_0^\infty \omega\,\rho(a,\omega)d\omega, \tag{3a}$$

$$F_T(a,T) = k_B T\int_0^\infty \ln[1-e^{-\hbar\omega/k_B T}]\,\rho(a,\omega)\,d\omega, \tag{3b}$$

where

$$\rho(a,\omega) = \sum_{i\alpha}\rho_{i\alpha}(a,\omega) \tag{4}$$

is the total PDOS, and $\rho_{i\alpha}(a,\omega)$ is the PDOS projected onto the $\alpha = \{x,y,z\}$ coordinate of atom i. For simplicity we assume in this work that the system contracts isotropically with a cubic unit cell of lattice constant a and ignore equilibrium distortions.

2.2. Projected Phonon Density of States

Although highly simplified phenomenological approaches like the Einstein and Debye models based on empirical data can be quite useful, they are generally inadequate to treat complex materials (Dimakis and Bunker, 1998; Poiarkova and Rehr, 1999). As an alternative which overcomes many of these limitations Poiarkova and Rehr (1999, 2001) introduced a method for EXAFS calculations in which the unit-normalized PDOS, projected onto a simple bond or arbitrary multiple-scattering path, is calculated from the imaginary part of the lattice dynamical Green's function. Vila et al. (2007) introduced an extension of the method to compute the PDOS projected onto atomic displacements $\rho_{i\alpha}(a,\omega)$,

$$\rho_{i\alpha}(a,\omega) = -\frac{2\omega}{\pi}\mathrm{Im}\left\langle i\alpha\left|\frac{1}{\omega^2 - \mathbf{D}(a) + i\epsilon}\right|i\alpha\right\rangle. \tag{5}$$

Here $|i\alpha\rangle$ is a Lanczos seed vector representing a normalized, mass-weighted displacement of atom i along the Cartesian direction α such that the position of the center of mass of the cell is not changed, and $\mathbf{D}(a)$ is the *dynamical matrix* (DM) of force constants computed at lattice constant a,

$$D_{jl\alpha,j'l'\beta}(a) = \left(M_j M_{j'}\right)^{-1/2}\frac{\partial^2 U(a)}{\partial u_{jl\alpha}\partial u_{j'l'\beta}}, \tag{6}$$

where $u_{jl\alpha}$ is the displacement of atom j in unit cell l along the direction α, and M_j is the mass of atom j. As described below, $\mathbf{D}(a(T))$ can be interpolated from $\mathbf{D}(a)$, which makes the force constants depend parametrically on the temperature and thus includes the dominant effects of anharmonicity. Efficient calculations of the lattice dynamical Green's function can be accomplished using a continued fraction representation, with parameters obtained with the iterative Lanczos algorithm (Deuflhard and Hohmann, 1995). This approach yields an efficient many-pole representation for the PDOS; since the pole locations can be interpreted as Gaussian quadrature points (Haydock, 1980), the method is well suited for accurate spectral integrations, as needed for example in the calculation of the VFE. The first iteration of the Lanczos algorithm corresponds to a *correlated Einstein* model for the $|i\alpha\rangle$ displacement such that $\rho_{i\alpha}(a,\omega) = \delta(\omega-\omega_E)$ with an Einstein frequency $\omega_E^2 = \langle i\alpha|\mathbf{D}(a)|i\alpha\rangle$. Poiarkova et al. showed that a second tier continued fraction gave about 10% errors for EXAFS Debye-Waller factors, while Krappe and Rossner (2002) later showed that six iterations are needed to achieve convergence to within 1%. We have found (Vila et al., 2007) that 16 or more iterations may be needed to achieve the same precision for $\rho_{i\alpha}(a,\omega)$. Nevertheless, this

algorithm avoids the explicit calculations of phonon-spectra and hence permits highly efficient calculations.

2.3. Dynamical Matrix

The main computational bottleneck to using this approach for many complex materials of industrial or technological interest then lies in obtaining sufficiently accurate DMs. Although empirical or model potential estimates of the interatomic force constants are sometimes available, they are not useful in screening a broad range of potential new materials. Moreover, their temperature dependence usually limits their accuracy and generality. Nevertheless, we have previously shown (Vila et al., 2007) that *ab initio* DMs obtained from density functional theory (DFT) calculations provide accurate force constants that can be used to compute both EXAFS Debye-Waller factors and thermal expansion. In that study we restricted our attention to simple periodic systems using the methodology implemented in ABINIT (Gonze et al., 2002), described in detail in Gonze and Lee (1997). This method computes $\tilde{D}_{j\alpha j'\beta}\left(a,\mathbf{q}\right)$, the dynamical matrix in reciprocal space:

$$\tilde{D}_{j\alpha j'\beta}\left(a,\mathbf{q}\right)=\sum_{l'}D_{j0\alpha,j'l'\beta}(a)e^{i\mathbf{q}\cdot\left(\mathbf{R}_{j'l'}-\mathbf{R}_{j0}\right)}, \tag{7}$$

and then Fourier transforms it back into real space. This approach is efficient for systems with simple unit cells of just a few atoms and high symmetry. In this paper we extend this method by using our recently developed parallelization scheme (Vila et al., Submitted) for the efficient computation of the DM in more complex unit cells based on first principles DFT calculations. This method computes the real space DM in Equation (6) directly using finite differences in supercells, taking advantage of the real space efficiency of codes like VASP (Kresse and Hafner, 1993, 1994; Kresse and Furthmüller, 1996a,b; Kresse and Joubert, 1999). This real space approach is particularly well suited for large unit cells with low symmetry such as those in supercell simulations of supported nanoparticles. In such cases the use of analytic methods such as DFPT results in very demanding calculations both in computing time and memory. A similar approach has recently been described for molecular systems (Liu et al., 2017) that suggest that the high availability of commodity processors can be used to take advantage of the parallelization of the finite differences. Similarly, our approach also relies on the parallel computation of complete rows of the DM, directly from the analytical DFT forces in VASP as a function of the lattice constant:

$$\frac{\partial^2 U(a)}{\partial u_{jl\alpha}\partial u_{j'l'\beta}}=\frac{\partial F_{jl\alpha}(a)}{\partial u_{j'l'\beta}}, \tag{8}$$

where $F_{jl\alpha}$ is the force on atom j in unit cell l along the direction α. For the case of ZrW_2O_8 treated here we use centered finite differences with displacements of 0.015 Å, which provide sufficiently accurate force constants. The most efficient row partition of the DM depends on the configuration of the computing system used. Details for the partition used here are presented in section 2.5.

2.4. Other Considerations

As discussed in section 2.1, the temperature-dependence of the lattice constant $a(T)$ is obtained by minimizing the free energy $A(a,T)$ in Equation (2) with respect to a at a given temperature T. The temperature dependence can be obtained quite efficiently since it only requires the recomputation of the integral in Equation (3) given a PDOS $\rho_{i\alpha}(a,\omega)$ at a certain lattice constant. The variation with lattice constant, however, requires the recomputation of $\rho_{i\alpha}(a,\omega)$, and thus of $\mathbf{D}(a)$, which is the most computationally demanding step. In previous work (Vila et al., 2007) we solved this issue for simple materials by computing $A(a,T)$ in a lattice constant grid that can be fitted or interpolated to find the minimum lattice constant as a function of temperature. To improve efficiency we took advantage of two properties of these simple systems: (i) we assumed that the shape of $A(a,T)$ can be accurately described using a Morse potential form as a function of lattice constant; and (ii) we reduced the number of calculations of $\mathbf{D}(a)$ by taking advantage of the nearly linear behavior of $\mathbf{D}(a)$ as a function of lattice constant near equilibrium,

$$\mathbf{D}(a)=\mathbf{D}_2+\mathbf{D}_3(a-a_0) \tag{9}$$

where $\mathbf{D}_2$ is the constant harmonic DM at a_0, the lattice constant of minimum internal energy, and $\mathbf{D}_3$ is the constant matrix of anharmonic constants. This parametrization assumes that anharmonic contributions of order higher than cubic are small, and allows us to compute the DM for only two lattice constants that can be used to determine $\mathbf{D}_2$ and $\mathbf{D}_3$. This approach typically cuts the computational time by a factor of about 2/3 or more. Given the complexity of some of the systems in the present study and the importance of having reliable efficiency enhancements for computational screening of materials, here we have opted to verify that this approximation is still valid by computing the DMs over a more complete grid of lattice constants. We have also changed the form used to fit $A(a,T)$ to a simple polynomial.

2.5. Computational Details

All structural optimizations and DM calculations were performed with VASP (Kresse and Hafner, 1993, 1994; Kresse and Furthmüller, 1996a,b; Kresse and Joubert, 1999) using PAW potentials (Kresse and Joubert, 1999) and the PBEsol exchange-correlation functional (Perdew et al., 2008). An $8\times8\times8$ k-point grid was used in all calculations, which was sufficient to achieve converged results. To reduce the effect of Pulay stress, the planewave energy cutoff was set at 350 eV. The finite difference force calculations used a three point centered stencil with 0.015 Å displacements. To obtain the variation of the DM with respect to lattice constant, we start by optimizing the size of unit cell and the reduced positions of the atoms in it while preserving its symmetry. This produces an optimized unit cell expanded by 1% from the experimental value. Given that the reduced positions do not change with volume until the phase transition at about 430 K (Evans et al., 1999), we freeze them and expand/contract around the optimal lattice size. We compute the DM at expansions of 0.0, 0.5, 1.0, 1.5, and 2.0% with respect to the experimental lattice constant, which correspond to contractions of 0.5 and 1.0%, and expansions of 0.5 and 1.0% with respect to the optimal lattice

contant. This procedure provides an adequate number of points for the interpolation of both the energies and components of the DM. For this material and taking into consideration the computing system being used, we partitioned the DM into 44 independent blocks, one per atom in the simulation cell, each using 512 processors for a total of 22,528. This procedure reduced the computing time from 33 h/core to 0.8 h/core. Equivalent simulations using DFPT in ABINIT would require on the order of 30–40 h/core, with a maximum number of processors of about 200–300.

3. RESULTS AND DISCUSSION

3.1. Structure

Figure 1 shows the structure of the unit cell of ZrW_2O_8 used here. The cell is composed of four ZrO_6 octahedra linked to eight WO_4 tetrahedra. The ZrO_6 units are all equivalent, with three short and three long Zr–O bonds, each connecting to a WO_4 unit (**Figure 2A**). The WO_4 units have three long W–O bonds, connecting to the ZrO_6 units, and a short one that is essentially free (**Figure 2B**). Unlike the ZrO_6 units, there are two types of WO_4 units depending on the direction of the free W–O bond: Four of them point toward a ZrO_6 unit and have a truly free W–O bond, while the other four point to another WO_4 unit and have a more restricted W–O bond. These two types of tetrahedra are paired (**Figure 2B**). Here we label the different types of atoms in the cell as follows: O_{SL} and O_{LS} are O atoms bridging WO_4 and ZrO_6 units, with short W–O and long Zr–O bonds, and vice versa. They correspond, respectively, to the O_2 and O_1 atoms in the more traditional notation (Mary et al., 1996). The O_{FF} and O_{FR} are O atoms in truly free and somewhat restricted W–O bonds, respectively. They correspond to the O_4 and O_3 atoms in the traditional notation (Mary et al., 1996). Finally, the W atoms bonded to O_{FF} and O_{FR} center are similarly labeled W_{FF} and W_{FR}, and correspond to the W_1 and W_2 atoms in the traditional notation (Mary et al., 1996), respectively. **Table 1** presents a comparison between the experimental (Auray et al., 1995) and optimized structural parameters obtained in the PBEsol optimization. The changes in internal structure are minimal except for the overall expansion of the cell of 1% predicted by PBEsol.

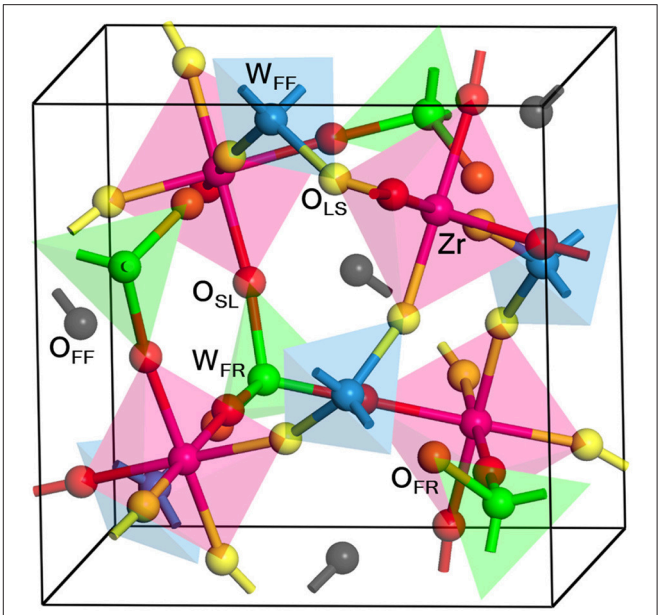

FIGURE 1 | Structure of the ZrW_2O_8 cell. The cell is composed of four equivalent Zr atoms (magenta), eight W atoms, of type W_{FF} (blue) and W_{FR} (green), and 32 O atoms of type O_{LS} (yellow), O_{SL} (red), O_{FR} (orange) and O_{FF} (black). Examples of the different types of O and W atoms are highlighted, and the coordination tetrahedra and octahedra are also included for clarity. The W_{FF}, W_{FR}, O_{LS}, O_{SL}, O_{FR}, and O_{FF} atoms correspond, respectively, to the W_1, W_2, O_1, O_2, O_3, and O_4 in the traditional notation (Mary et al., 1996).

3.2. Bond Force Constants

Figure 3 shows the lattice constant dependence of the mean force constants for the parallel stretch and perpendicular scissoring displacements for the different bond types in ZrW_2O_8 (The numerical data for this and all other plots in this work can be found in **Supplementary Data Sheet 1**). The parallel force constants were obtained by rotating the 6×6 $(jl, j'l')_{\alpha,\beta}$ blocks of the DM formed by jl and $j'l'$ near-neighbor atoms into a local coordinate system along the bond. The scissors force constants were obtained similarly by rotating the 3×3 $(jl, jl)_{\alpha,\beta}$ block for O atom jl into coordinates parallel and perpendicular to the W–O bond. For the W_{FF}–O_{FF} and W_{FR}–O_{FR} bonds, motion of the O atoms orthogonal to the bonds is nearly equivalent in all directions. For the W_{FF}–O_{LS} and W_{FR}–O_{SL} bonds, we average over the in-plane and out-of-plane directions defined by the W–O–Zr plane. These directions are also nearly equivalent, with anisotropies of at most 20%.

We find that of all the elements of the DM, only those associated with the O atoms exhibit the positive anharmonicity essential to observe NTE. Indeed, only the deviations perpendicular to the bonds have positive slope (**Figure 3**, bottom). The force constants associated with the perpendicular O distortions are also much weaker than the parallel ones, and are therefore activated at much lower temperature. The strength of the parallel bond distortions follows closely the trends in the bond distances shown in **Table 1**, with the shorter W_{FF}–O_{FF} and W_{FR}–O_{FR} bonds having the largest force constants, followed by the slightly longer W_{FF}–O_{LS} and W_{FR}–O_{SL} bonds. As discussed in section 2.4, the components of the dynamical matrix should vary mostly linearly with cell expansion in simple systems. Given the large NTE observed for ZrW_2O_8, which implies the existence of significant anharmonicity, it is worth examining the accuracy of the linear approximation. **Figure 3** shows that the linearity of the bond-parallel force constants is excellent for small displacements, while the transverse ones show a slight curvature. The mean absolute errors from a linear approximation are $\pm$ 3 N/m for the strong parallel displacements and only $\pm$ 0.4 N/m for the transverse ones. Consequently, the linear approximation can be used to estimate the the lattice dependence of the dynamical matrix to high accuracy.

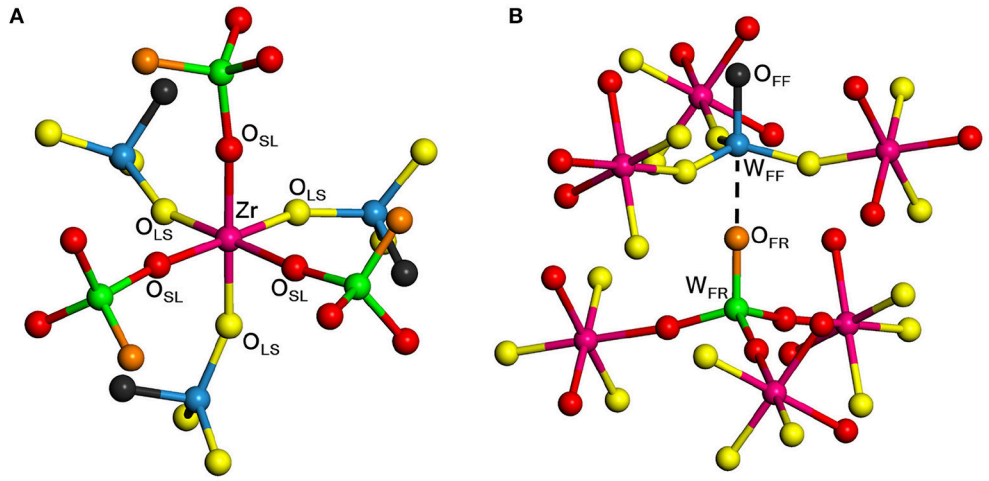

FIGURE 2 | Local structure of ZrW_2O_8 around the Zr octahedra **(A)** and W tetrahedra **(B)**. The color key is the same as in **Figure 1**. Examples of the different types of O and W atoms are highlighted. The bottom figure shows the pairing of the two types of W atoms. The W_{FF}, W_{FR}, O_{LS}, O_{SL}, O_{FR}, and O_{FF} atoms correspond, respectively, to the W_1, W_2, O_1, O_2, O_3, and O_4 in the traditional notation (Mary et al., 1996).

TABLE 1 | Experimental and theoretical structural parameters for the ZrW_2O_8 cell used in this work.

Parameter		Expt.	PBEsol
Lattice		9.155	9.246
Bonds	W_{FR}–O_{FR}	1.736	1.751
	W_{FR}–O_{SL}	1.785	1.797
	W_{FF}–O_{FF}	1.712	1.728
	W_{FF}–O_{LS}	1.799	1.826
	Zr–O_{SL}	2.092	2.119
	Zr–O_{LS}	2.051	2.062
	Zr–W_{FR}	3.867	3.909
	Zr–W_{FF}	3.751	3.795
Angles	Zr-O_{SL}–W_{FR}	171.5	173.2
	Zr-O_{LS}–W_{FF}	153.9	155.0

All distances in Å and angles in deg. The experimental values are taken from Auray et al. (1995). See text and ***Figure 1*** *for an explanation on the labels.*

3.3. Helmholtz and Vibrational Free Energies

Figure 4 (top) shows the variation with lattice constant and temperature of the internal energy $U(a)$, total vibrational free energy $F(a, T)$, and Helmholtz free energy $A(a, T)$, together with the optimal lattice constant as a function of temperature obtained by fitting $A(a, T)$ to a 5th-order polynomial and minimizing numerically. The NTE clearly arises from the lower relative VFE at smaller lattice constants. To help understand the origin of this behavior, the bottom of **Figure 4** also shows a decomposition of the VFE at low and high temperature, obtained by partitioning the sum over atoms in Equation (3) into its O, W, and Zr components. This decomposition reveals that the W and Zr contributions to the VFE are virtually constant with variations in lattice constant; consequently the variation of total VFE closely follows the variation of only the O component. This further substantiates our finding that the perpendicular O distortions are the primary origin of NTE in ZrW_2O_8.

3.4. Negative Thermal Expansion

The relative thermal expansion obtained by minimizing $A(a, T)$ with respect to lattice constant is shown in **Figure 5**. The agreement with experiment is clearly very good except at very low temperatures, where the theoretical curve shows the expected flattening due to zero-point effects, which does not appear to be pronounced in the experiment (Evans et al., 1996). **Figure 5** also shows the NTE that would be obtained by only considering the components of the VFE arising from the O, W, and Zr lattices. As expected from the previous discussion, the NTE arises exclusively from the O component. The Zr and W contributions have a minimal effect on the system, in contrast with the hypothesis (Mary et al., 1996; Gupta et al., 2013; Sanson, 2014) that the bending of the Zr–O–W bonds causes the NTE by pulling the Zr and W atoms together.

3.5. Total and Projected Phonon Densities of States

Figure 6 shows a comparison between the theoretical total density of states at 0 K and experiment (Ernst et al., 1998) obtained from inelastic neutron scattering at 300 K. The PDOS can be roughly divided into three regions: high frequency range (above 20 THz), associated with bond stretching modes, middle range (between 5 and 13 THz), corresponding mostly to bond bending modes, and low frequency range (below 5 THz), which are thought to correspond to librational and translational modes (Chaplot, 2005). The overall agreement is excellent; the small discrepancy at the lowest frequencies around 1 THz, where the Lanczos approach yields a single peak, is likely due to the size of the 44-atom unit cell used in the calculations.

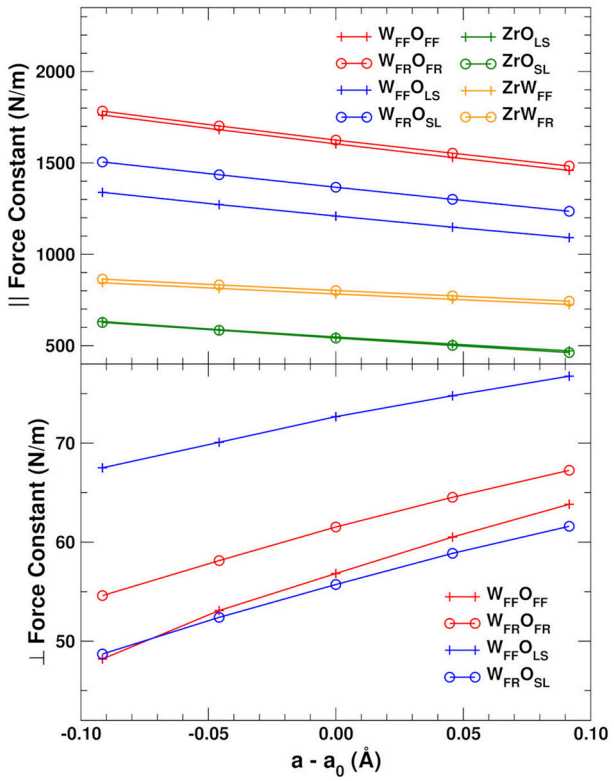

FIGURE 3 | Mean force constants for the parallel OW and OZr stretch **(Top)** and perpendicular OW scissoring **(Bottom)** displacements in ZrW_2O_8. The perpendicular force constants are averaged over two directions in the plane orthogonal to the W–O bond for the W_{FF}–O_{FF} and W_{FR}–O_{FR} bonds, and over the in-plane and out-of-plane directions for the W_{FF}–O_{LS} and W_{FR}–O_{SL} bonds. See text for further details.

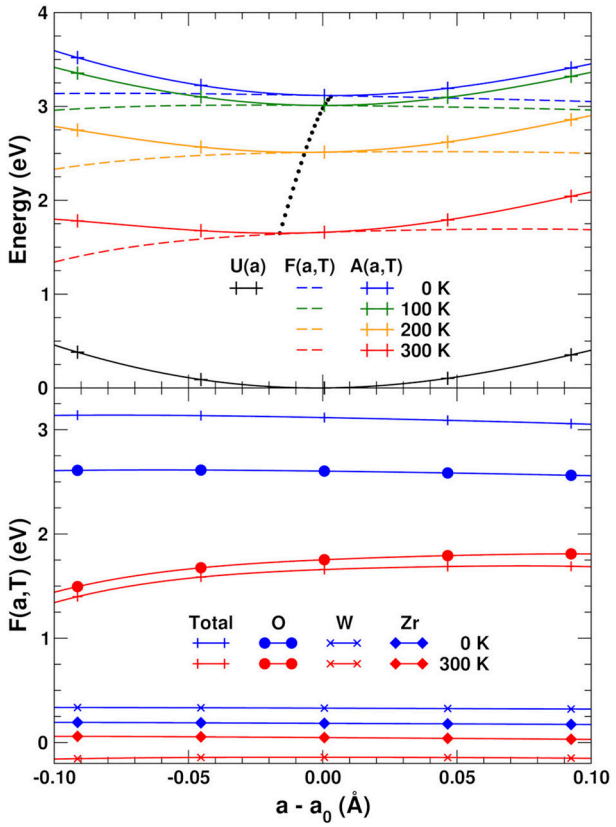

FIGURE 4 | (Top) Internal energy $U(a)$, total vibrational free energy $F(a, T)$ and Helmholtz free energy $A(a, T)$ as a function of lattice constant and temperature. The potentials are interpolated using a 5th-order polynomial. The black dots indicate the optimal lattice constant as a function of temperature. **(Bottom)** Total $F(a, T)$ and contributions from the O, W, and Zr sites.

To understand the physical origin of the NTE more completely, we consider the behavior of the projected phonon density of states, or PDOS. **Figure 7** shows the PDOS projected onto the O, W, and Zr sites. The high frequency PDOS only has significant weight on the O sites. The W and Zr sites have most of their weight in the low and medium regions, respectively. The variation of the PDOS with lattice constant depends greatly on the projection site as shown by the Grüneisen parameters $\gamma = d \ln \omega / d \ln V$ of the different sites and frequency ranges: The middle range is essentially independent of lattice constant with a $\gamma = -0.3 \pm 0.3$, except for the Zr sites which show a very small decrease of the frequencies with expansion and $\gamma = 2.0$. This positive γ results in the very small tendency to normal behavior seen in the Zr component of the thermal expansion shown in **Figure 5**. The high frequency range, found only on the O sites, also contributes to positive thermal expansion with a $\gamma = 1.9 \pm 0.2$. These high frequencies result from the strong parallel force constants discussed in section 3.2, as demonstrated in **Figure 8**, which shows that the DOS projected onto the longitudinal (i.e., along the O–W or Zr–O–W direction) motion of the O atoms only has weight in the high frequency range. These stretch modes become weaker as the system expands, and would result in net positive thermal expansion if not countered by the low frequency region. In fact, if the high frequency range is neglected, the relative NTE at 0 K is overestimated by about 30%. The low frequency region exhibits a large negative $\gamma = -11 \pm 2$ for the O sites, and about $\gamma = -3 \pm 1$ for the W sites, in agreement with our finding that the W sites have a small contribution to the NTE, while the O sites account for most of it. For the overall low frequency range we estimate the same γ of -8 ± 4, as in previous theoretical estimates, (Gupta et al., 2013) which is in reasonable agreement with experimental estimates ranging from -7 to -20 (Hancock et al., 2004). **Figure 8** also shows the projection onto the transverse motion of the O atoms, which is localized in the medium and low frequency ranges, as expected for bending and librational modes, respectively.

To explore the role of the rigid WO_4 units on the NTE, we have also projected the PDOS onto rotational linear combinations of the transverse in-plane and out-of-plane distortions described above, with axes along the different W–O bonds (**Figures 9**, **10**). These projections eliminate all the internal O–W–O bending contributions seen in the 5–12 THz range of **Figure 8**, with only features associated with O–Zr–O bending remaining in that range. All these PDOS features show the expected negative Grüneisen parameters γ, and point to the need

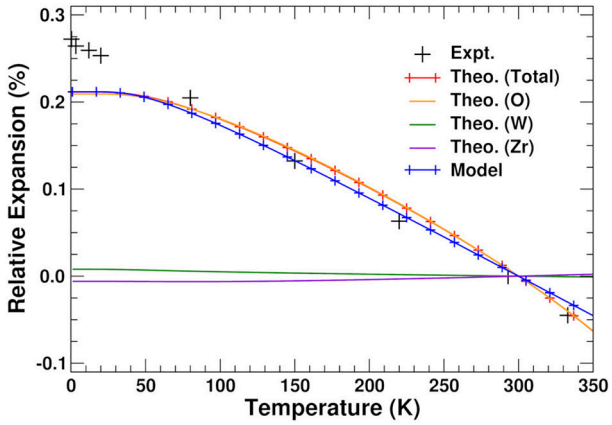

FIGURE 5 | Total, O, W, and Zr components, and results from our two-pole model (see text) of relative thermal expansion in ZrW_2O_8 as a function of temperature. The experimental results are taken from Evans et al. (1996).

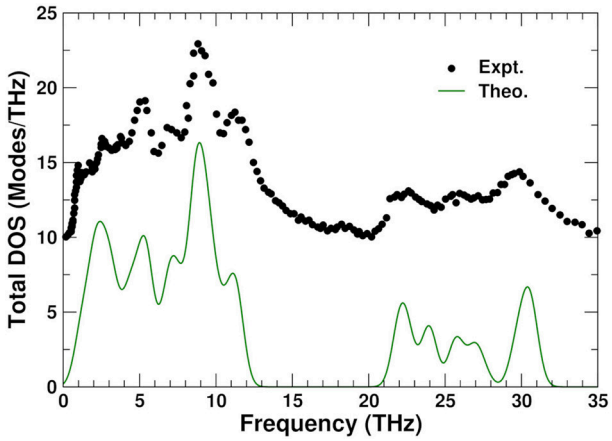

FIGURE 6 | Comparison of the theoretical (0 K) and experimental (Ernst et al., 1998) (300 K) total phonon density of states (DOS) in ZrW_2O_8. The experimental result has been vertically shifted for clarity.

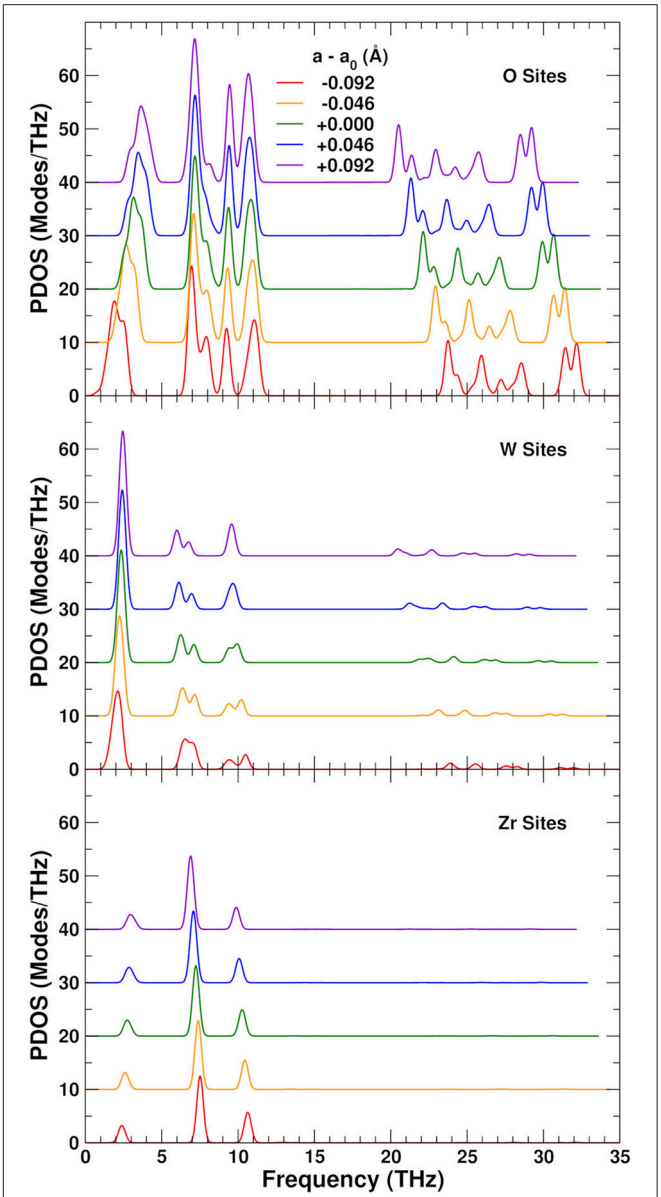

FIGURE 7 | Variation of the projected phonon density of states (PDOS) as a function of lattice constant in ZrW_2O_8. The partial PDOS projected onto O , W, and Zr sites are shown in the top, middle and lower panels, respectively. The curves for different lattice constants have been vertically shifted for clarity.

for a mixed model that is neither purely rigid (Hammonds et al., 1996; Pryde et al., 1996, 1997; Hancock et al., 2004; Tucker et al., 2005, 2007) nor fully distorted (Cao et al., 2002, 2003; Bridges et al., 2014) but one in which the NTE arises from the rigid motion of WO_4 units and the internal distortion of the ZrO_6 ones.

3.6. Simple NTE Model

Based on the results discussed in the previous sections, we are led to formulate a simple anharmonic two-frequency Einstein model to describe the NTE. This model is based on approximations to the different contributions to $A(a, T)$ and $F(a, T)$ in Equations (2) and (3). Near equilibrium the internal energy $U(a)$ can be approximated accurately with a harmonic potential $U(a) = (1/2)K_U(\Delta a)^2$, and $\Delta a \equiv a - a_0$. The VFE $F(a, T)$ can be simplified by analyzing the different contributions arising from the PDOS of **Figure 7**: We have found that the total O-PDOS can be reduced to a very good approximation to just two constant weight poles representing the active regions of the O-PDOS: one for the low frequency (L) region below 5.4 THz with a negative Grüneisen coefficient, and a second high frequency (H) pole for the modes above 20 THz with a positive Grüneisen coefficient. The intermediate region of the O, Zr, and W PDOS do not contribute to the NTE since they are nearly constant with Δa. The contribution from the H pole can be further simplified by noticing that the H modes only contribute to $F_0(a)$ since at the temperatures relevant here the H modes are inactive. We can also

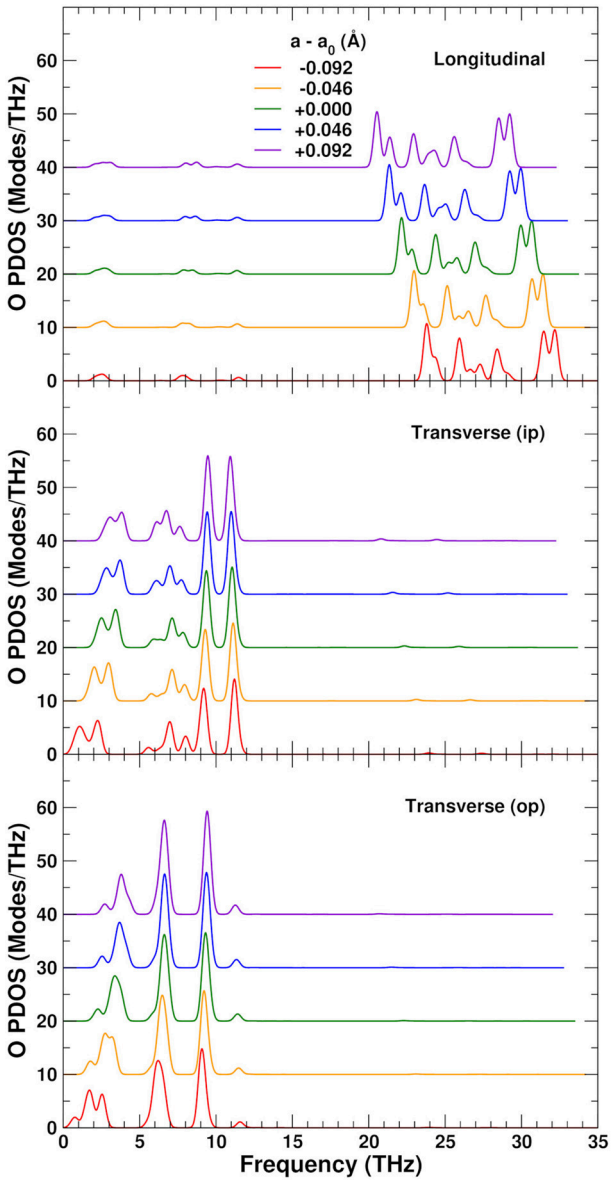

FIGURE 8 | Variation of the O-sites phonon density of states (PDOS) as a function of lattice constant in ZrW_2O_8, projected onto longitudinal (along the O–W or Zr–O–W direction), and transverse in-plane (ip) and out of plane (op) displacements. The curves for different lattice constants have been vertically shifted for clarity.

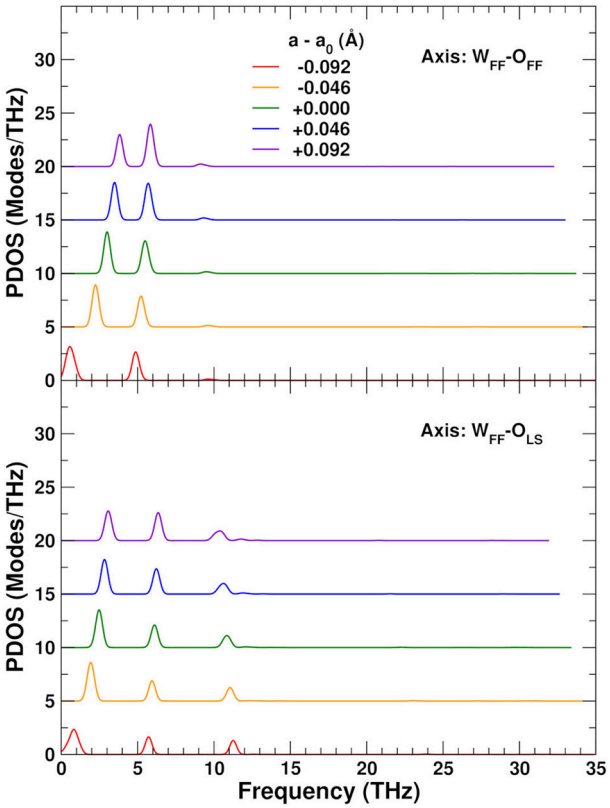

FIGURE 9 | Variation of the ZrW_2O_8 phonon density of states (PDOS) projected onto rotational coordinates around the W_{FF}–O_{FF} and W_{FF}–O_{LS} axes, as a function of the lattice constant. The curves for different lattice constants have been vertically shifted for clarity.

take advantage of the linear behavior of the force constants as a function of Δa as discussed in section 2.4: For a given pole ν with effective force constant k_ν, we can write $k_\nu = k_{2\nu} + 6k_{3\nu}\Delta a$ (Frenkel and Rehr, 1993; Vila et al., 2007), where $k_{2\nu}$ and $k_{3\nu}$ are, respectively, the effective quasi-harmonic and anharmonic force constants. Thus, the frequency ω_ν associated with this pole can be approximated as

$$\omega_\nu = \sqrt{\frac{k_\nu}{\mu_\nu}} = \sqrt{\frac{k_{2\nu} + 6k_{3\nu}\Delta a}{\mu_\nu}} \simeq \omega_\nu^0 + \omega_\nu' \Delta a, \qquad (10)$$

where we define $\omega_\nu^0 = \sqrt{k_{2\nu}/\mu_\nu}$, $\omega_\nu' = 3k_{2\nu}/\omega_\nu^0 k_{3\nu}$, and μ_ν is the reduced mass associated with this pole. The linear behavior of the pole frequencies around a_0 can be seen in the PDOS of **Figure 7**, from which the ω_ν^0 and ω_ν' parameters can be obtained. The poles weights w_L and w_H are taken at $\Delta a = 0$. With these approximations the Helmholtz free energy from Equation (2) can be written as:

$$A(a,T) = \frac{1}{2}K_U(\Delta a)^2 + \sum_{\nu\,=\,L,H} F_0^\nu(a) + F_T^L(a,T), \qquad (11)$$

where $F_0^\nu(a)$ and $F_T^\nu(a,T)$ are, respectively, the zero-point and temperature components of $F(a,T)$ for $\nu = \{L,H\}$. We can now find $a(T)$ by applying the minimum condition in Equation (1) to the above $A(a,T)$:

$$0 = \frac{\partial A(a,T)}{\partial a}\Big|_{a(T)} = \qquad (12)$$

$$= K_U\Delta a + \frac{\hbar}{2}\sum_{\nu=L,H} w_\nu\omega_\nu' + \frac{\partial F_T^L(a,T)}{\partial a}\Big|_{a(T)}, \qquad (13)$$

The last term in this expression can be further simplified by noticing in **Figure 4** (bottom) the nearly linear behavior of

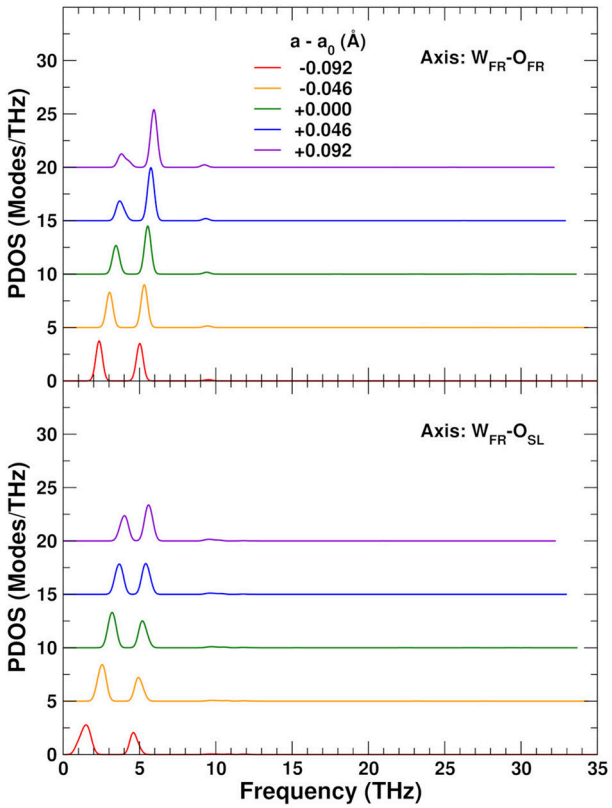

FIGURE 10 | Variation of the ZrW_2O_8 phonon density of states (PDOS) projected onto rotational coordinates around the W_{FR}–O_{FR} and W_{FR}–O_{SL} axes, as a function of lattice constant. The curves for different lattice constants have been vertically shifted for clarity.

$F(a,T)$ around a_0, and expanding $F_T^L(a,T)$ to first order in a. After this, we can calculate $a(T)$ simply as:

$$a(T) \simeq a_0 - \frac{\hbar}{K_U} \sum_{\nu=L,H} w_\nu \omega'_\nu + \frac{\hbar w_L \omega'_L}{K_U[1 - e^{\hbar\omega_L^0/k_B T}]}, \qquad (14)$$

using the internal energy minimum and constant $a_0 = 9.246$ Å and $K_U = 85.82$ eV/Å^2, respectively, weights $w_L = 21.1$ and $w_H = 30.0$, harmonic frequency $\omega_L^0 = 20.31$ THz, and effective anharmonic constants $\omega'_L = 81.90$ THz/Å and $\omega'_H = -104.39$ THz/Å. Our results are presented in **Figure 5**; they clearly show that this simplified two-pole Einstein model yields a quantitative description of the observed NTE. Of these contributions the L pole dominates but overestimates the NTE, while the H pole provides a 30% correction.

4. CONCLUSIONS

We have performed calculations of the thermal expansion of ZrW_2O_8 using an efficient approach for obtaining the variation of the dynamical matrix as a function of the lattice constant. The anomalous NTE arises almost exclusively from the transverse contributions of the O-atoms, as demonstrated by a partition of the vibrational free energy over the O, W, and Zr sites. This behavior results from the interplay between the normal positive Grüneisen parameter and hence PTE of the O-projected high frequency modes, and the anomalous negative-Grüneisen parameter driving the NTE from the low frequency modes. The low-frequency modes overestimate the effect of NTE, while the high-frequency modes provide a 30% correction. These low frequency modes are associated with distortions at the O sites transverse to the W–O or W–O–Zr bonds. More precisely, the rotational linear combination of these transverse distortions results in nearly rigid rotations of the WO_4 tetrahedra and internal distortions of the ZrO_6 octahedra. The mixed character of the low frequency modes is consistent with the variety of models previously proposed to account for the NTE. We have simplified this complex behavior by proposing a two-frequency anharmonic Einstein model of the O-PDOS which captures both the dominant negative- and weak positive-contributions to thermal expansion.

AUTHOR CONTRIBUTIONS

FV co-developed the theory, was the main developer of the specialized software used in the analysis, and performed most of the simulations. SH contributed to the simulations and helped in verifying the soundness of the software. JR co-developed the theory presented here.

ACKNOWLEDGMENTS

This work was supported by U.S. Department of Energy, Office of Science CSGBD Grant No. DE-FG02-03ER15476, with computational support from NERSC, a DOE Office of Science User Facility, under Contract No. DE-AC02-05CH11231. We thank Frank Bridges and Joshua Kas for many helpful discussions.

SUPPLEMENTARY MATERIAL

The Supplementary Material for this article can be found online at: https://www.frontiersin.org/articles/10.3389/fchem.2018.00296/full#supplementary-material

Supplementary Data Sheet 1 | Numerical data for all plots in this work.

REFERENCES

Allen, R. E., and De Wette, F. W. (1969). Calculation of dynamical surface properties of noble-gas crystals. I. The quasiharmonic approximation. *Phys. Rev.* 179, 873–886. doi: 10.1103/PhysRev.179.873

Auray, M., Quarton, M., and Leblanc, M. (1995). Zirconium tungstate. *Acta Crystallogr. Sect. C* 51, 2210–2213. doi: 10.1107/S0108270195001545

Baroni, S., de Gironcoli, S., Dal Corso, A., and Giannozzi, P. (2001). Phonons and related crystal properties from density-functional perturbation theory. *Rev. Mod. Phys.* 73, 515–562. doi: 10.1103/RevModPhys.73.515

Baroni, S., Giannozzi, P., and Isaev, E. (2010). Density-functional perturbation theory for quasi-harmonic calculations. *Rev. Mineral. Geochem.* 71:39. doi: 10.2138/rmg.2010.71.3

Boyer, L. L. (1979). Calculation of thermal expansion, compressiblity, an melting in alkali halides: NaCl and KCl. *Phys. Rev. Lett.* 42, 584–587. doi: 10.1103/PhysRevLett.42.584

Brandenburg, J. G., Potticary, J., Sparkes, H. A., Price, S. L., and Hall, S. R. (2017). Thermal expansion of carbamazepine: systematic crystallographic measurements challenge quantum chemical calculations. *J. Phys. Chem. Lett.* 8, 4319–4324. doi: 10.1021/acs.jpclett.7b01944

Bridges, F., Keiber, T., Juhas, P., Billinge, S. J. L., Sutton, L., Wilde, J., et al. (2014). Local vibrations and negative thermal expansion in ZrW_2O_8. *Phys. Rev. Lett.* 112:045505. doi: 10.1103/PhysRevLett.112.045505

Cao, D., Bridges, F., Kowach, G. R., and Ramirez, A. P. (2002). Frustrated soft modes and negative thermal expansion in ZrW_2O_8. *Phys. Rev. Lett.* 89:215902. doi: 10.1103/PhysRevLett.89.215902

Cao, D., Bridges, F., Kowach, G. R., and Ramirez, A. P. (2003). Correlated atomic motions in the negative thermal expansion material ZrW_2O_8 : a local structure study. *Phys. Rev. B* 68:014303. doi: 10.1103/PhysRevB.68.014303

Chaplot, S. L. (2005). Negative thermal expansion in ZrW_2O_8 : do we give up the concept of normal mode? *Curr. Sci.* 88, 347–349.

Deuflhard, P., and Hohmann, A. (1995). *Numerical Analysis*. Berlin: de Gruyter.

Dimakis, N., and Bunker, G. (1998). Ab initio single- and multiple-scattering EXAFS Debye-Waller factors: Raman and infrared data *Phys. Rev. B* 58:2467. doi: 10.1103/PhysRevB.58.2467

Erba, A. (2014). On combining temperature and pressure effects on structural properties of crystals with standard ab initio techniques. *J. Chem. Phys.* 141:124115. doi: 10.1063/1.4896228

Erba, A., Maul, J., and Civalleri, B. (2016). Thermal properties of molecular crystals through dispersion-corrected quasi-harmonic ab initio calculations: the case of urea. *Chem. Commun.* 52, 1820–1823. doi: 10.1039/C5CC08982D

Erba, A., Shahrokhi, M., Moradian, R., and Dovesi, R. (2015). On how differently the quasi-harmonic approximation works for two isostructural crystals: thermal properties of periclase and lime. *J. Chem. Phys.* 142:044114. doi: 10.1063/1.4906422

Ernst, G., Broholm, C., Kowach, G., and Ramirez, A. (1998). Phonon density of states and negative thermal expansion in ZrW_2O_8. *Nature* 396, 147–149. doi: 10.1038/24115

Evans, J. S. O., David, W. I. F., and Sleight, A. W. (1999). Structural investigation of the negative-thermal-expansion material ZrW_2O_8. *Acta Crystallogr. Sect. B* 55, 333–340. doi: 10.1107/S0108768198016966

Evans, J. S. O., Mary, T. A., Vogt, T., Subramanian, M. A., and Sleight, A. W. (1996). Negative thermal expansion in ZrW_2O_8 and HFW_2O_8. *Chem. Mater.* 8, 2809–2823. doi: 10.1021/cm9602959

Frenkel, A. I., and Rehr, J. J. (1993). Thermal expansion and x-ray-absorption fine-structure cumulants. *Phys. Rev. B* 48, 585–588. doi: 10.1103/PhysRevB.48.585

Gonze, X., Beuken, J.-M., Caracas, R., Detraux, F., Fuchs, M., Rignanese, G.-M., et al. (2002). First-principles computation of material properties: the ABINIT software project *Comput. Mater. Sci.* 25:478. doi: 10.1016/S0927-0256(02)00325-7

Gonze, X., and Lee, C. (1997). Dynamical matrices, Born effective charges, dielectric permittivity tensors, and interatomic force constants from density-functional perturbation theory. *Phys. Rev. B* 55:10355. doi: 10.1103/PhysRevB.55.10355

Gupta, M. K., Mittal, R., and Chaplot, S. L. (2013). Negative thermal expansion in cubic ZrW_2O_8: role of phonons in the entire Brilloiun zone from ab initio calculations. *Phys. Rev. B* 88:014303. doi: 10.1103/PhysRevB.88.014303

Hammonds, K. D., Dove, M. T., Giddy, A. P., Heine, V., and Winkler, B. (1996). Rigid-unit phonon modes and structural phase transitions in framework silicates. *Amer. Mineral.* 81, 1057–1079. doi: 10.2138/am-1996-9-1003

Hancock, J. N., Turpen, C., Schlesinger, Z., Kowach, G. R., and Ramirez, A. P. (2004). Unusual low-energy phonon dynamics in the negative thermal expansion compound ZrW_2O_8. *Phys. Rev. Lett.* 93:225501. doi: 10.1103/PhysRevLett.93.225501

Haydock, R. (1980). "The recursive solution of the schrodinger equation," in *Solid State Physics*, Vol. 35, eds H. Ehrenreich, F. Seitz, and D. D. Turnbull (New York, NY: Academic), 215.

Jain, A., Ong, S. P., Hautier, G., Chen, W., Richards, W. D., Dacek, S., et al. (2013). The materials project: a materials genome approach to accelerating materials innovation. *APL Mater.* 1:011002. doi: 10.1063/1.4812323

Krappe, H. J., and Rossner, H. H. (2002). Bayes-Turchin approach to x-ray absorption fine structure data analysis. *Phys. Rev. B* 66:184303. doi: 10.1103/PhysRevB.66.184303

Kresse, G., and Furthmüller, J. (1996a). Efficiency of ab-initio total energy calculations for metals and semiconductors using a plane-wave basis set. *Comput. Mater. Sci.* 6, 15–50. doi: 10.1016/0927-0256(96)00008-0

Kresse, G., and Furthmüller, J. (1996b). Efficient iterative schemes for ab initio total-energy calculations using a plane-wave basis set. *Phys. Rev. B* 54, 11169–11186. doi: 10.1103/PhysRevB.54.11169

Kresse, G., and Hafner, J. (1993). Ab initio. *Phys. Rev. B* 47, 558–561. doi: 10.1103/PhysRevB.47.558

Kresse, G., and Hafner, J. (1994). Ab initio. *Phys. Rev. B* 49, 14251–14269. doi: 10.1103/PhysRevB.49.14251

Kresse, G., and Joubert, J. (1999). From ultrasoft pseudopotentials to the projector augmented-wave method. *Phys. Rev. B* 59:1758. doi: 10.1103/PhysRevB.59.1758

Lee, C., and Gonze, X. (1995). Ab initio calculation of the thermodynamic properties and atomic temperature factors of SIO_2 $\alpha-$quartz and stishovite. *Phys. Rev. B* 51, 8610–8613. doi: 10.1103/PhysRevB.51.8610

Liu, K. Y., Jie, L., and Herbert, J. M. (2017). Accuracy of finite? Difference harmonic frequencies in density functional theory. *J. Comput. Chem.* 38, 1678–1684. doi: 10.1002/jcc.24811

Mary, T. A., Evans, J. S. O., Vogt, T., and Sleight, A. W. (1996). Negative thermal expansion from 0.3 to 1050 Kelvin in ZrW_2O_8. *Science* 272, 90–92. doi: 10.1126/science.272.5258.90

Perdew, J., Ruzsinszky, A., Csonka, G., Vydrov, O., Scuseria, G., Constantin, L., et al. (2008). Restoring the density-gradient expansion for exchange in solids and surfaces. *Phys. Rev. Lett.* 100:136406. doi: 10.1103/PhysRevLett.100.136406

Poiarkova, A., and Rehr, J. J. (1999). Multiple-scattering x-ray-absorption fine-structure Debye-Waller factor calculations. *Phys. Rev. B* 59:948. doi: 10.1103/PhysRevB.59.948

Poiarkova, A., and Rehr, J. J. (2001). Recursion method for multiple-scattering XAFS Debye-Waller factors *J. Synchrotron Radiat.* 8:313. doi: 10.1107/S0909049599001685

Pryde, A. K., Hammonds, K. D., Dove, M. T., Heine, V., Gale, J. D., and Warren, M. C. (1997). Rigid unit modes and the negative thermal expansion in ZrW_2O_8. *Phase Transit.* 61, 141–153. doi: 10.1080/01411599708223734

Pryde, A. K. A., Hammonds, K. D., Dove, M. T., Heine, V., Gale, J. D., and Warren, M. C. (1996). *J. Phys.* 8:10973.

Rignanese, G., Michenaud, J., and Gonze, X. (1996). Ab initio study of the volume dependence of dynamical and thermodynamical properties of silicon. *Phys. Rev. B* 53, 4488–4497. doi: 10.1103/PhysRevB.53.4488

Sanson, A. (2014). Toward an understanding of the local origin of negative thermal expansion in ZrW_2O_8 : limits and inconsistencies of the tent and rigid unit mode models. *Chem. Mater.* 26, 3716–3720. doi: 10.1021/cm501107w

Tucker, M. G., Goodwin, A. L., Dove, M. T., Keen, D. A., Wells, S. A., and Evans, J. S. O. (2005). Negative thermal expansion in ZrW_2O_8: mechanisms, rigid unit modes, and neutron total scattering. *Phys. Rev. Lett.* 95:255501. doi: 10.1103/PhysRevLett.95.255501

Tucker, M. G., Keen, D. A., Evans, J. S. O., and Dove, M. T. (2007). Local structure in ZrW_2O_8 from neutron total scattering. *J. Phys. Condens. Matt.* 19:335215. doi: 10.1088/0953-8984/19/33/335215

Vila, F. D., Rehr, J. J., Rossner, H. H., and Krappe, H. J. (2007). Theoretical x-ray absorption Debye-Waller factors. *Phys. Rev. B* 76:014301. doi: 10.1103/PhysRevB.76.014301

Conflict of Interest Statement: The authors declare that the research was conducted in the absence of any commercial or financial relationships that could be construed as a potential conflict of interest.

frontiers in Chemistry

ORIGINAL RESEARCH
published: 23 August 2018
doi: 10.3389/fchem.2018.00356

Extended X-Ray Absorption Fine Structure of ZrW_2O_8: Theory vs. Experiment

*Fernando D. Vila[1], John W. Spencer[1], Joshua J. Kas[1], John J. Rehr[1] and Frank Bridges[2]**

[1] Department of Physics, University of Washington, Seattle, WA, United States, [2] Department of Physics, University of California, Santa Cruz, Santa Cruz, CA, United States

Extended x-ray absorption fine structure (EXAFS) is well-suited for investigations of structure and disorder of complex materials. Recently, experimental measurements and analysis of EXAFS have been carried out to elucidate the mechanisms responsible for the negative thermal expansion (NTE) in zirconium tungstate (ZrW_2O_8). In contrast to previous work suggesting that transverse O-displacements are largely responsible, the EXAFS analysis suggested that correlated rotations and translations of octahedra and tetrahedra within the structure are a major source. In an effort to resolve this controversy, we have carried out *ab initio* calculations of the structure, lattice vibrations, and EXAFS of ZrW_2O_8 based on real-space multiple-scattering calculations using the FEFF9 code and auxiliary calculations of structure and Debye-Waller factors. We find that the theoretical simulations are consistent with observed EXAFS, and show that both of the above mechanisms contribute to the dynamical structure of ZrW_2O_8.

Keywords: zirconium tungstate, EXAFS, DFT, FEFF9, Debye-Waller factors

OPEN ACCESS

Edited by:
Andrea Sanson,
Università degli Studi di Padova, Italy

Reviewed by:
Andrew Goodwin,
University of Oxford, United Kingdom
Alexei Kuzmin,
University of Latvia, Latvia

****Correspondence:***
Frank Bridges
bridges@ucsc.edu

Specialty section:
This article was submitted to Physical Chemistry and Chemical Physics, a section of the journal Frontiers in Chemistry

Received: *31 May 2018*
Accepted: *30 July 2018*
Published: *23 August 2018*

Citation:
Vila FD, Spencer JW, Kas JJ, Rehr JJ and Bridges F (2018) Extended X-Ray Absorption Fine Structure of ZrW_2O_8: Theory vs. Experiment. Front. Chem. 6:356. doi: 10.3389/fchem.2018.00356

1. INTRODUCTION

Zirconium tungstate (ZrW_2O_8) is remarkable for its large negative thermal expansion (NTE). Unlike other such materials, ZrW_2O_8 exhibits NTE over a wide range of temperatures from about 10 to 1,050 K. However, the microscopic mechanism(s) underlying its NTE is controversial. In several studies this has been associated primarily with the transverse motion of the central O atom in the Zr-O-W linkages (**Figure 1**).

Recently, however, an alternative mechanism based on correlated translations of the W-centered oxygen tetrahedra and rotations of Zr-centered oxygen octahedra has been proposed (Cao et al., 2002, 2003; Bridges et al., 2014). This interpretation is based on experimental investigations of ZrW_2O_8 using extended x-ray absorption fine structure (EXAFS), a technique well suited for eludicating the structure and disorder in complex materials. X-ray total scattering results are consistent with this interpretation (Bridges et al., 2014). In particular these analyses suggest that the Zr-O2-W2 linkages are quite stiff, with the implication of limited transverse O motion. In an effort to resolve the controversy, we have carried out *ab initio* simulations of EXAFS of ZrW_2O_8 using the real-space multiple-scattering (RSMS) code FEFF9 (Rehr et al., 2009) and associated Debye-Waller factors (Vila et al., 2007). We find that these calculations are consistent with the observed EXAFS, and show that both of the above mechanisms contribute to the dynamical structure of ZrW_2O_8.

In the remainder of this work we first summarize the lattice structure of ZrW_2O_8, the multiple-scattering theory of EXAFS, and the theory of the multiple-scattering Debye-Waller factors. Subsequently we describe the results of our simulations, followed by a summary and conclusions.

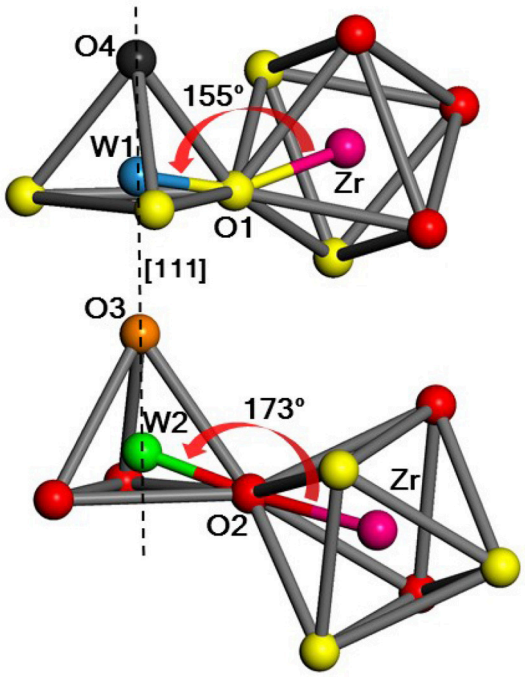

FIGURE 1 | Portion of the unit cell showing the two possible WO_4–ZrO_6 linkages in ZrW_2O_8, with Zr (magenta), W1 (blue) and W2 (green), O1 (yellow), O2 (red), O3 (orange), O4 (black). W1, O1, and W2, O2 are the atoms that form Zr-O-W linkages with bridging angles of 155° and 173°, respectively, while the O3 and O4 atoms are only weakly linked (**Table 1**). [111] denotes the body diagonal direction of the unit cell.

TABLE 1 | Experimental and theoretical structural parameters for the 44-atom ZrW_2O_8 cell used in this work.

		Expt.	DFT
Lattice parameter		9.155	9.246
Bonds	W1–O1	1.799	1.826
	W1–O4	1.712	1.728
	W2–O2	1.785	1.797
	W2–O3	1.736	1.751
	Zr–O1	2.051	2.062
	Zr–O2	2.092	2.119
	Zr–W1	3.751	3.795
	Zr–W2	3.867	3.909
Angles	Zr–O1–W1	153.9	155.0
	Zr–O2–W2	171.5	173.2

All distances are in Å and angles in degrees; experimental values are taken from Auray et al. (1995), while the DFT calculations are done using VASP with a PBEsol exchange-correlation functional.

2. THEORETICAL CONSIDERATIONS

2.1. Structure of ZrW_2O_8

The first step in our approach is a detailed treatment of the ground state equilibrium structure of ZrW_2O_8. Our calculations assume a periodic equilibrium structure with a 44-atom unit cell enclosing four equivalent Zr, 8 W, and 32 O atoms. The metal atoms are centered in polyhedra with O vertices: octahedra for Zr, and tetrahedra for W. The O atoms shared between the Zr-octahedra and W-tetrahedra form Zr–O–W "linkages." This detailed structure was refined with *ab initio* DFT calculations using the VASP plane-wave pseudopotential code (Kresse and Hafner, 1993, 1994; Kresse and Furthmüller, 1996a,b; Kresse and Joubert, 1999). These calculations show that the structure has a large degree of asymmetry; the octahedra are slightly irregular, and the unit cell contains Zr-O-W bond linkages with equally populated bond angles of about 155 and 173° respectively (see **Figure 1** and **Table 1**).

2.2. Multiple-Scattering EXAFS Theory

Formally, the normalized EXAFS at a given photon energy E is defined as $\chi = (\mu - \mu_0)/\mu_0$, where μ is the x-ray absorption coefficient and μ_0 the smooth atomic background. Theoretically χ can be represented by a sum over all possible single- (SS) and multiple-scattering (MS) paths p taken by the photoelectron following photo-absorption (Rehr et al., 2009). Assuming the thermal and structural disorder is sufficiently small, $\chi(k)$ is given by the full path expansion

$$\chi(k) = \sum_p N_p \chi_p(k) e^{-2\sigma_p^2 k^2}, \tag{1a}$$

$$\chi_p(k) = S_0^2 \frac{|f_{\rm eff}^p(k)|}{kR_p^2} \sin(2kR_p + \Phi_p) e^{-2R/\lambda_k}. \tag{1b}$$

Here $k = \sqrt{2(E - E_0)}$ is the wave-number of the photoelectron defined relative to threshold energy E_0, $f_{\rm eff}^p(k)$ the effective scattering amplitude of path p, Φ_p the net scattering phase-shift, N_p the degeneracy of the path, R_p the effective- (or half-)path length, S_0^2 is the many-body amplitude factor, typically close to unity and path independent, λ_k is the mean free path, and σ_p^2 is the mean-square relative displacement (MSRD) of path p, which characterizes the path length fluctuations. Unless otherwise specified we use atomic units for the electron, $e = \hbar = m = 1$.

In this paper we are primarily interested in the EXAFS from the Zr K and W L_3 edges, which are relevant to previous EXAFS studies of NTE in ZrW_2O_8. In particular our study focuses on the contributions to EXAFS from the SS and MS paths linking a given Zr atom to a nearby W atom or vice versa. These paths are denoted by the scattering atoms in the path. For example, the paths Zr-W-Zr, Zr-W-O-Zr, and Zr-O-W-O-Zr also have the highest *amplitude importance ratios*, which are defined relative to the amplitudes for the shortest Zr-O or W-O paths. As discussed in our companion study (Vila et al., 2018), the NTE in ZrW_2O_8 can be linked to anharmonic low frequency modes with negative Grüneisen parameters. This effect is strongest for modes with transverse O-displacements, which can also involve correlated rotations and translations. Thus we also discuss the effects of such transverse motion. Details of the dominant paths including averages of effective path lengths weighted by path degeneracy are listed in **Table 2**, where (W1, O1) and (W2, O2) denote the

TABLE 2 | Properties of some selected Zr and W paths.

					DW Factors σ_p^2 (10^{-3}Å^2)		
Path	**Length (Å)**	**Amp. Ratio**	**Degeneracy**	**Legs**	**20 K**	**160 K**	**315 K**
Zr–O1–Zr	2.041	100.00	3	2	2.18	2.38	2.94
Zr–O2–Zr	2.098	92.56	3	2	2.23	2.60	3.41
Zr–W1–Zr	3.758	25.63	3	2	1.30	2.24	3.63
Zr–W2–Zr	3.871	23.67	3	2	1.18	1.65	2.53
Zr–O1–W1–Zr	3.803	44.45	6	3	1.15	1.54	2.30
Zr–O2–W2–Zr	3.874	63.22	6	3	1.18	1.62	2.48
Zr–O1–W1–O1–Zr	3.849	25.46	3	4	1.34	1.82	2.71
Zr–O2–W2–O2–Zr	3.878	42.28	3	4	1.20	1.64	2.52
W1–O4–W1	1.711	39.64	1	2	1.22	1.22	1.25
W2–O3–W2	1.733	36.04	1	2	1.27	1.27	1.32
W2–O2–W2	1.780	99.90	3	2	1.35	1.37	1.44
W1–O1–W1	1.807	100.00	3	2	1.45	1.48	1.60
W1–O3–W1	2.315	16.03	1	2	2.85	5.61	9.03
W1–Zr–W1	3.759	14.88	3	2	1.28	2.17	3.49
W1–W2–W1	4.049	4.45	1	2	1.69	4.34	7.57
W1–W2–W1	4.652	9.45	3	2	1.77	5.27	9.27
W1–O3–W2–W1	4.049	13.46	2	3	1.69	4.33	7.57
W1–O3–W2–O3–W1	4.049	8.60	1	4	1.69	4.33	7.57

The theory used the experimental lattice constant with optimized MSRDs to avoid small phase shifts due to the 1% error in the optimized PBEsol structure.

W and O atoms in the Zr-O-W bond angles of 155 and 173°, respectively.

2.3. EXAFS Debye-Waller Factors

The EXAFS Debye-Waller (DW) factors $W_p = \exp(-2\sigma_p^2 k^2)$ provide a useful measure of damping from the correlated structural and thermal disorder in a given path. These Debye-Waller factors are essential, because they govern the exponential decay of the fine structure with increasing temperature and photoelectron energy. Our explicit calculations of σ_p^2 only include bond-length fluctuations (i.e., stretching contributions) in a given MS path, and neglect the usually negligible contributions from motion perpendicular to each bond (Poiarkova and Rehr, 1999a; Fornasini et al., 2004). Thus the MSRD for a given path is calculated in terms of averages over displacement-displacement correlation functions,

$$\sigma_p^2 = \frac{1}{4}\Big\langle \sum_{i=1}^{n_p} [(\vec{u}_i - \vec{u}_{i+1}) \cdot \hat{R}_{i,i+1}]^2 \Big\rangle, \tag{2}$$

where n_p is the number of legs in the path and $\langle \cdots \rangle$ denotes a thermal average. However, this MSRD neglects bond-angle fluctuations, which depend on a thermal average over the effective scattering amplitude $\langle |f_{\rm eff}^p(\theta)| \rangle$ for a given path. This effect is largest for paths with forward scattering contributions, such as the Zr-O-W linkages. Expanding to 2nd order in the bond-bending angle θ and keeping only the lowest order contributions to the average, yields a damping term that can be represented as an angular Debye-Waller factor

$$W_p(\theta) = e^{-a\sigma_\theta^2}, \tag{3}$$

$$\sigma_\theta^2 = \langle (\theta - \langle \theta \rangle)^2 \rangle,$$

where $a = -(1/2) f''_{\rm eff}(\theta)/f_{\rm eff}(\theta)$.

We have shown that these vibrational properties can be efficiently computed by combining DFT calculations of the dynamical matrix (DM) of lattice force constants, with a Lanczos algorithm (Vila et al., 2007). An efficient implementation based on parallelized calculations of the DMs is described in a separate paper in this collection (Vila et al., 2018), and briefly summarized below. Thermal averages such as the EXAFS mean square relative displacements σ_p^2 of a single or multiple scattering path p are calculated in terms of Debye integrals over the phonon projected density of states (PDOS)

$$\sigma_p^2(T) = \frac{\hbar}{2\mu_p} \int_0^\infty \frac{1}{\omega} \coth\Big(\frac{\beta\hbar\omega}{2}\Big) \rho_p(\omega)\, d\omega, \tag{4}$$

where μ_p is the reduced mass associated with the path, $\beta = 1/k_B T$, and $\rho_p(\omega)$ is the PDOS for that path (Poiarkova and Rehr, 1999a,b). Higher order cumulants such as $\sigma_p^{(3)}$ due to anharmonic effects are neglected, which is generally a good approximation for the relatively stiff bonds considered here. In the reminder of this work the path index subscript p is ignored unless needed for clarity.

The key system-dependent ingredient for σ_p^2 in Equation (4) is the PDOS $\rho_p(\omega)$. Following Poiarkova and Rehr (1999a,b) the unit-normalized PDOS is obtained from the imaginary part of path specific matrix elements of the lattice dynamical Green's function

$$\rho_p(\omega) = -\frac{2\omega}{\pi} \mathrm{Im}\Big\langle p \Big| \frac{1}{\omega^2 - \mathbf{D} + i\epsilon} \Big| p \Big\rangle. \tag{5}$$

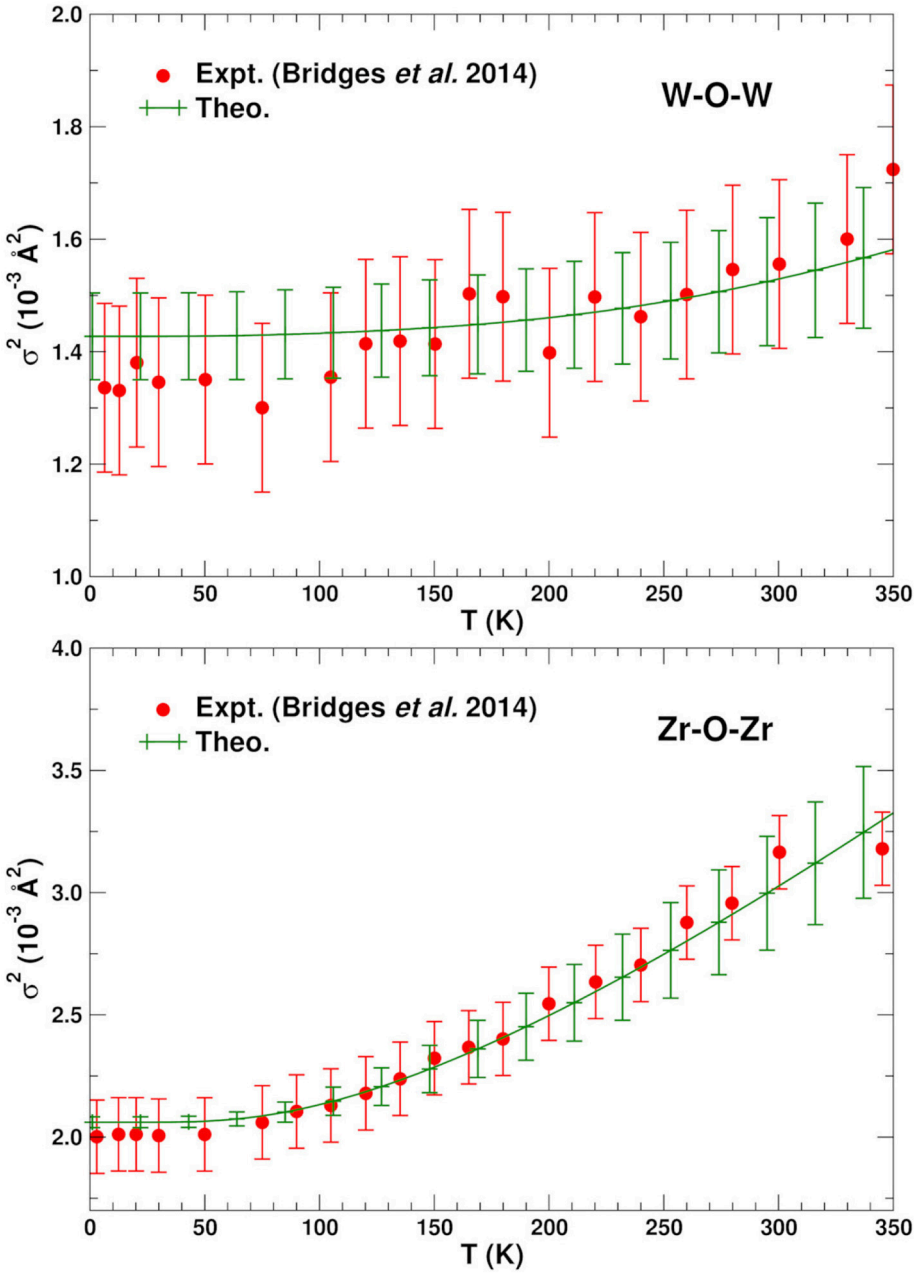

FIGURE 2 | Comparison of the experimental (Bridges et al., 2014) and average theoretical single scattering MSRD σ_p^2 for the W–O–W and Zr–O–Zr in ZrW_2O_8. The theoretical values have been shifted vertically to account for experimental static disorder.

Here $|p\rangle$ is a Lanczos seed vector representing an initial normalized, mass-weighted displacement along path p, and $\mathbf{D}$ is the dynamical matrix

$$D_{jl\alpha,j'l'\beta} = \left(M_j M_{j'}\right)^{-1/2} \frac{\partial^2 U[\{u_{jl\alpha}\}]}{\partial u_{jl\alpha}\partial u_{j'l'\beta}}, \tag{6}$$

where U is the total internal energy of the system as a function of lattice coordinates, $u_{jl\alpha}$ is a displacement of atom j in unit cell l along the direction α, and M_j is the mass of atom j. The phonon Green's function is obtained from a continued fraction representation with parameters derived from the Lanczos algorithm (Haydock, 1980; Deuflhard and Hohmann, 1995). This yields a many-pole representation of the PDOS

$$\rho_p(\omega) = \sum_{\nu=1}^{N_\nu} w_\nu \, \delta(\omega - \omega_\nu). \tag{7}$$

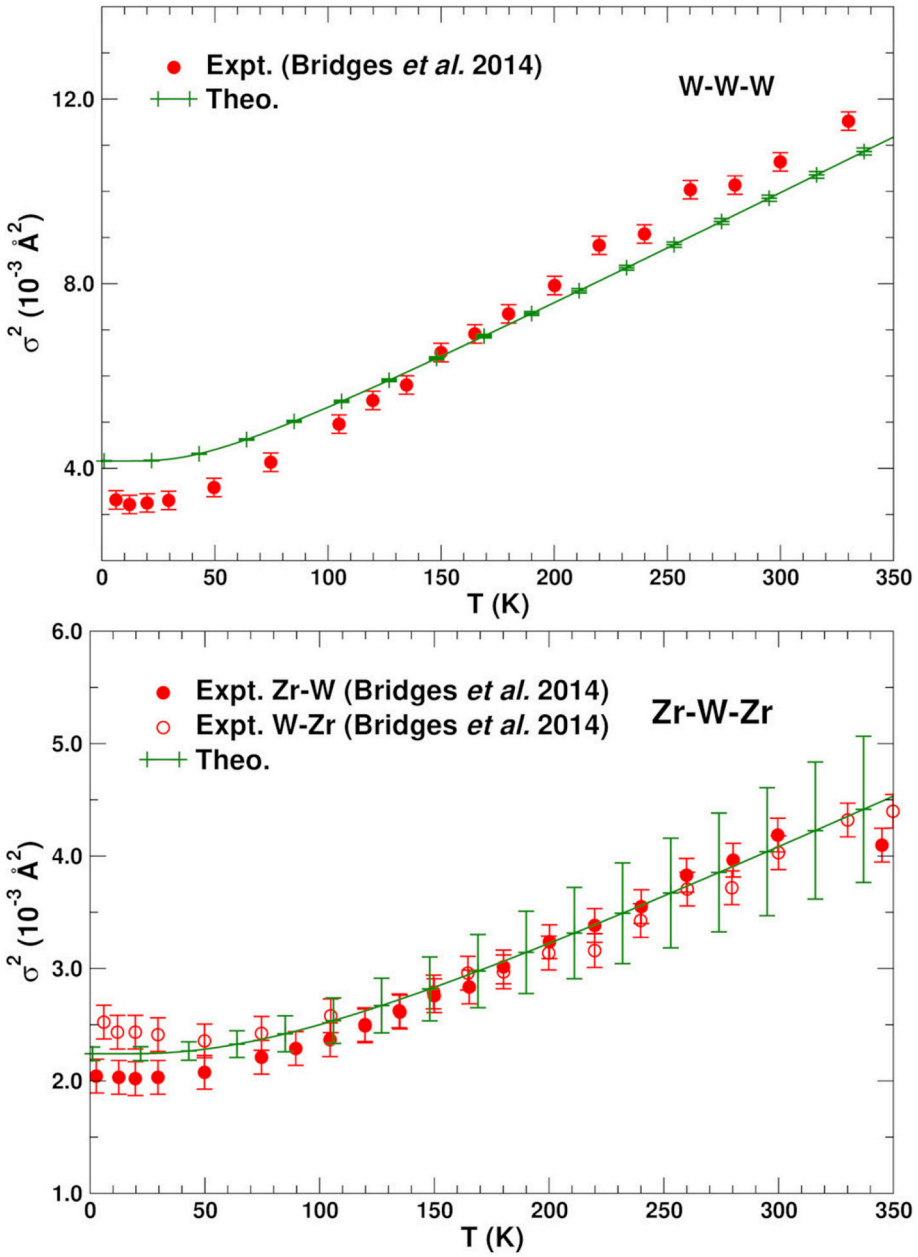

FIGURE 3 | Comparison of the experimental (Bridges et al., 2014) and theoretical mean single scattering MSRD σ_p^2 for the W–W–W and Zr–W–Zr bonds in ZrW_2O_8. The theoretical values have been shifted vertically to account for experimental static disorder.

where w_ν and ω_ν are the weights and frequencies of the N_ν poles, respectively. Typically only a few tens of poles are needed to converge calculations of σ_p^2.

3. CALCULATIONS

3.1. Debye-Waller Factors

The computational details of the Debye-Waller factor calculations are similar to those in Vila et al. (2018). Briefly, structural optimizations and DM calculations were performed with VASP (Kresse and Hafner, 1993, 1994; Kresse and Furthmüller, 1996a,b; Kresse and Joubert, 1999) using PAW pseudopotentials (Kresse and Joubert, 1999) with the PBEsol exchange-correlation functional (Perdew et al., 2008), and an energy cutoff of 350 eV; a k-point grid of $8 \times 8 \times 8$ was used to achieve converged results. The lattice constant of the cell and internal reduced coordinates of the atoms in it were optimized while preserving initial lattice symmetry for computational efficiency. This DFT optimization yields a unit cell expanded by about 1% from the experimental value (see **Table 1**) with internal

reduced coordinates that are in good agreement with experiment. Given that the internal reduced coordinates do not change with volume until the phase transition at about 430 K (Evans et al., 1999), and that the change of force constants with temperature is small in the range studied, we use the 0 K optimized structure to compute the DM. The DM is obtained using a parallelized finite difference approach with a three point centered stencil with 0.015 Å atomic displacements. The structure of the unit cell as well as the dynamical matrix are available as **Supplementary Material**.

Figures 2, **3** show the average calculated MSRDs for the various SS paths (W–O–W, Zr–O–Zr, W–W–W, and Zr–W–Zr), together with comparisons to experiment. Since only bond-stretching contributions are included σ_p^2 these results have been shifted to account for the measured structural disorder σ^2_{static} which contributes additively, i.e., $\sigma^2 = \sigma^2_{\text{static}} + \sigma^2_{\text{stretch}}$. The required shift was estimated by computing the mean absolute deviation between the theoretical and experimental MSRDs over the available temperature range. The static disorder has both physical and methodological origins. The physical static disorder arises mostly from the presence of defects and distortions which are intrinsic in materials like ZrW_2O_8, while the EXAFS analysis method introduces apparent disorder by collecting paths of closely similar lengths into a single contribution with a Debye-Waller factor that reflects the length variations. Thus, for the W–O–W and Zr–O–Zr paths, which correspond to strong, well-defined bonds, the static component is very small. For the W–W–W and Zr–W–Zr paths, on the other hand, the static disorder is significant since these paths connect different WO_4 and ZrO_6 units through a variety of soft bonds. Note that the bond stretching contributions to σ_p^2 for these paths only involve planar fluctuations of the atoms $\vec{u}_i$ in the path, and that contributions to $\sigma^2_{stretch}$ from transverse displacements are generally negligible, even for substantial transverse O-displacements. Nevertheless, angular damping $W_p(\theta)$ may be important for paths like Zr-O-W involving forward focusing (see below). Clearly the shifted MSRDs agree well with experiment (Bridges et al., 2014). Their associated Einstein temperatures $\Theta_E = \hbar\omega_E/k_B$, where ω_E is the mean vibrational frequency of the PDOS for a given path, are given in **Table 3**. Again the agreement with experiment is satisfactory, with the largest deviations occurring for the W–W–W paths. These paths are the longest ones and thus fall in the upper range of paths lengths that can be adequately described with the present simulation cell. The slight underestimation of the MSRD for these paths would likely be reduced with a larger simulation cell which would improve the representation of the low frequency- long spatial wavelength region of the phonon density of states. The computed MSRDs are consistent

TABLE 3 | Comparison of the theoretical and experimental (Bridges et al., 2014).

	Θ_E		κ_E	
Path	**Theory**	**Expt.**	**Theory**	**Expt.**
W–O–W	1,033	878 ± 68	447	323 ± 2
W–W–W	146	129 ± 4	56	44 ± 1
Zr–O–Zr	588	608 ± 36	134	143 ± 1
W–Zr–W	281	299 ± 12	137	155 ± 1
Zr–W–Zr	281	274 ± 16	137	130 ± 1

Einstein temperatures $\Theta_E = \hbar\omega_E/k_B$ (in K) and effective force constants $\kappa_E = \mu\omega_E{}^2$ associated with the dominant single scattering paths.

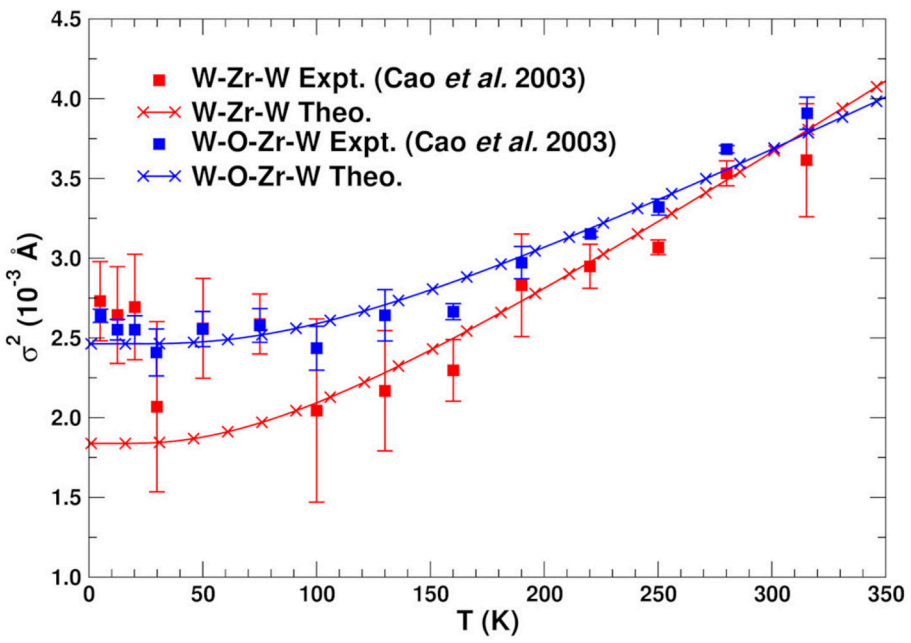

FIGURE 4 | Comparison of the experimental (Cao et al., 2003) and theoretical MSRD σ^2 for the SS and MS paths associated with the Zr–W linkage in ZrW_2O_8. The theoretical values are shifted vertically to account for experimental static disorder.

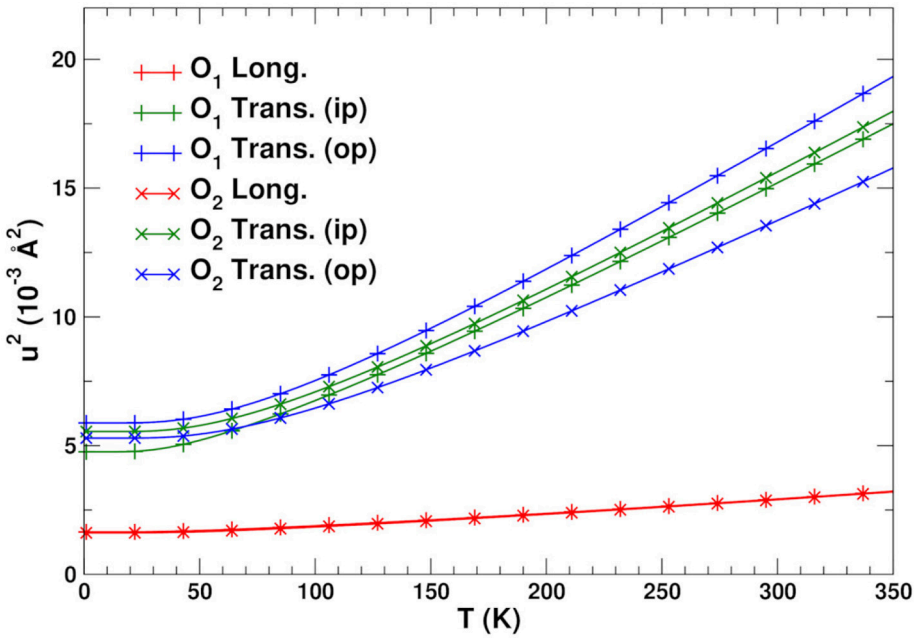

FIGURE 5 | Longitudinal and transverse MSDs u^2 for the O1 and O2 bridging atoms.

with physically expected interaction strengths. For example, the W–O and Zr–O bonds are the strongest, followed by the weak, long-range interactions between the Zr–W and W1–W2 pairs.

As noted above the most relevant paths for EXAFS studies of NTE are those involving the Zr and W atoms. **Table 2** summarizes the structural properties of these paths, as well as their MSRDs (without static disorder corrections) at three temperatures. Note that the MSRDs for the SS and MS 173° paths are nearly identical, since they are nearly collinear and the push-pull distortions of the Zr–O and W–O bonds essentially cancel. For the 155° linkage paths, the MS MSRDs are also similar again because they involve near-neighbor bond distortions. The only exception is the Zr–W1–Zr path that is slightly softer. This path involves the nearly-independent coupling between the Zr and W atoms, which is dominated by the distortion of 2 Zr–O bonds and all 4 of the W–O bonds. This suggests that the MSRD of Zr–W1–Zr paths is larger because the W1–O1 bonds are longer, and thus weaker, than the W2–O2 ones. **Figure 4** shows a comparison of the average theoretical DW factors for the Zr–W–Zr and Zr–O–W–Zr paths with experiment (Cao et al., 2003). Clearly our results match closely except at low temperature, where the experimental data also has significant errors. It is interesting to note that the larger slope for the Zr–W–Zr path arises from the Zr–W1–Zr contribution. Overall, the results in **Figure 4** and **Table 2** show that the length-fluctuations σ_p^2 of these paths are only weakly temperature dependent, and thus are "stiff," consistent with the interpretation of Bridges et al. (2014). The stiffness of a given SS or MS path linkage is characterized by the effective spring constant κ_p for the DW factor of a given path p. It is reflected by its temperature dependence which varies as $k_B T/\kappa_p$ at high T. More precisely, $\kappa_p = \mu_p \bar{\omega}_p^2$ where $1/\bar{\omega}_p^2 = \langle 1/\omega^2 \rangle$ is the inverse 2nd moment of the PDOS. Thus the Zr–O–W linkage is considered stiff because for a large κ_p, the associated path DW factor varies weakly with temperature with a small slope $1/\kappa_p$. Note however, that this weak temperature dependence does not preclude the existence of large transverse fluctuations of the O atoms in the linkages. Our calculations of the DM show that the transverse fluctuations perpendicular to the Zr–O–W plane have much smaller spring constants (Vila et al., 2018) and, hence, substantial larger values of u^2 for the O atom in the linkage (see **Figure 5**).

3.2. Atomic Displacements

Figure 5 shows the longitudinal and transverse mean square displacements (MSD) u^2 for the O1 and O2 linkage atoms. The in-plane transverse direction here is defined as the bisector of the Zr–O–W angle. The longitudinal and transverse out-of-plane directions are defined as the in- and out-of-plane perpendicular directions to this bisector, respectively. Although the 155° linkage is more asymmetric and therefore might be expected to be anisotropic, both types of linkages have similar transverse MSDs. In contrast the longitudinal motion has a relatively small, high-frequency amplitude with a large associated Einstein temperature of 600 K, as expected from the distortion along the stiff W–O and Zr–O bonds. Due to the weaker force constants associated with the bond bending (Vila et al., 2018), however, the transverse motion has an Einstein temperature of about 250 K. At T = 300 K this results in *rms* amplitudes $u \approx 0.12$ Å. This corresponds roughly to linkage angle distortions of about $\delta\theta \approx 6°$, which are more than twice the longitudinal fluctuations at the same temperature. Although these transverse distortions are substantial, they have little effect on the bond stretching MSRDs

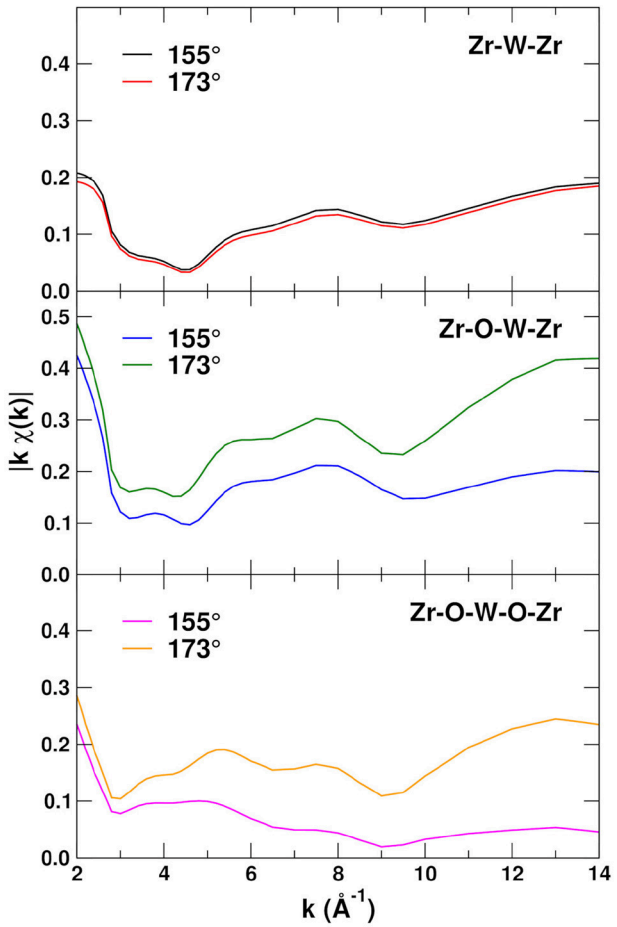

FIGURE 6 | EXAFS path amplitudes $|k\tilde{\chi}_p(k)|$ for the Zr-W-Zr single-scattering and Zr-W-O-Zr and Zr-O-W-O-Zr MS paths with linkage angles 155 and 173°.

(Poiarkova and Rehr, 1999a; Fornasini et al., 2004). For the SS paths, this is easy to see, since for a bond of length R, the perpendicular contribution from each atom is $\sigma_\perp^2 \sim (u^2/2R)^2$. For the linkage bonds with $R \sim 2$ Å and $u \sim 0.12$ Å, we estimate that $\sigma_\perp^2 \sim 0.02\times10^{-3}$ Å^2, which is an order of magnitude smaller than the typical error margins for the experimental MSRDs. A similar approach can be used for the multiple scattering paths, where the contributions of all atoms in the path need to be added. On the other hand the angular DW factors $W_p(\theta)$ may still contribute to the damping of the EXAFS from these paths.

In the amplitude-phase representation of EXAFS the magnitude of each path contribution is given by $|\tilde{\chi}_p(k)| = |f_{\rm eff}^p/kR^2|$, which eliminates the oscillations and thus emphasizes the amplitudes of the various paths. **Figure 6** shows the amplitudes $|k\tilde{\chi}_p(k)|$ for the 155 and 173° Zr–O–W linkages, including the Zr–W–Zr SS and Zr–W–O–Zr and Zr–O–W–O–Zr MS paths. Note that the amplitudes $|\tilde{\chi}_p(k)|$ do not include the Debye-Waller factors and thus have no temperature dependence. The Zr–W–Zr paths are not affected by the angle of the linkage for the Zr–W–O–Zr and Zr–O–W–O–Zr paths, also the amplitudes for the 173° linkage paths, are on average about twice as large as for the 155° paths. These differences are due to the angular dependence and forward scattering enhancement in $f_{\rm eff}^p$ and are particularly strong for bond angles close to 180° and at high k.

3.3. EXAFS Spectra

To assess the overall quality of our EXAFS calculations, **Figure 7** shows comparisons of the experimental (Bridges et al., 2014) fine structure $k\chi(k)$ at 20, 165, and 300 K for the Zr K- and W-L_3 edges to those obtained with FEFF. The theoretical results used optimized MSRDs with bond distances reduced by 1% to correct the overestimate of the lattice constant by DFT/PBEsol calculations. Our EXAFS calculations were obtained by including all SS and MS paths of up to 5.5 Å and $n_p = 4$ scattering legs, and by removing all path screening filters from FEFF. The experimental results (Bridges et al., 2014) find that the many-body amplitude factor S_0^2 in Equation (1) is very close to 1, thus we use $S_0^2 = 1$ in the EXAFS simulations. Clearly the agreement is quite satisfactory for the EXAFS range $k \gtrsim 5$ Å^{-1}, below which the path expansion approach is less appropriate and atomic background substraction artifacts are possible. The small, high frequency contribution noticeable in the Zr K-edge signal at 20 K corresponds to $\sim$ 6.5 Å Zr–Zr–Zr paths which are not included in our simulation cell.

Finally **Figure 8** shows the *phase-corrected* Fourier transforms (FTs) of the $k\chi(k)$. For these transforms the central atom theoretical phase-shift $2\delta_l$ common to all paths is subtracted before being transformed (Rehr et al., 2009), resulting in peak positions closer to their geometrical locations. Again, the overall agreement is good, except for differences in the heights of some of the peaks, due probably to static and angular disorder in the DW factors. For the Zr absorber, the FTs clearly show the Zr–O peak at about 2 Å, and the different linkage paths between 3.5 and 4.2 Å.

A potentially important issue is the effect of the Zr–O–W bond angle fluctuations during the complex low energy vibrations of the system, particularly for the Zr–O2–W2 linkage. The amplitudes of the MS peaks for the Zr–O–W linkages vary significantly with bond angle due to forward scattering through the O atom. While $f_{\rm eff}(\theta)$ is strongly peaked in the forward direction and varies substantially with θ, the angular Debye-Waller factor in Equation (3) depends on the fluctuations $\sigma_\theta^2 \approx 0.01$ rad^2. To estimate these effects we computed the average $\chi(k)$ for the Zr–O1–W1 and Zr–O2–W2 linkages over the distribution of angular distortions induced by mean u amplitues of about 0.12 Å. We find that with distortions of this amplitude the absolute change in $\chi(k)$ is only about 3 and −6% for the Zr–O1–W1 and Zr–O2–W2 linkages, respectively. This explains the good agreement between the calculations without including such averaging, and the data for the Zr edge in **Figure 8**. The actual situation can be more complicated, however, since the polyhedra can rotate as well as translate and a full treatment that takes this correlated motion into account would be desirable.

4. SUMMARY AND CONCLUSIONS

We have shown that theoretical calculations of structure, vibrational properties and the EXAFS of ZrW_2O_8 agree well

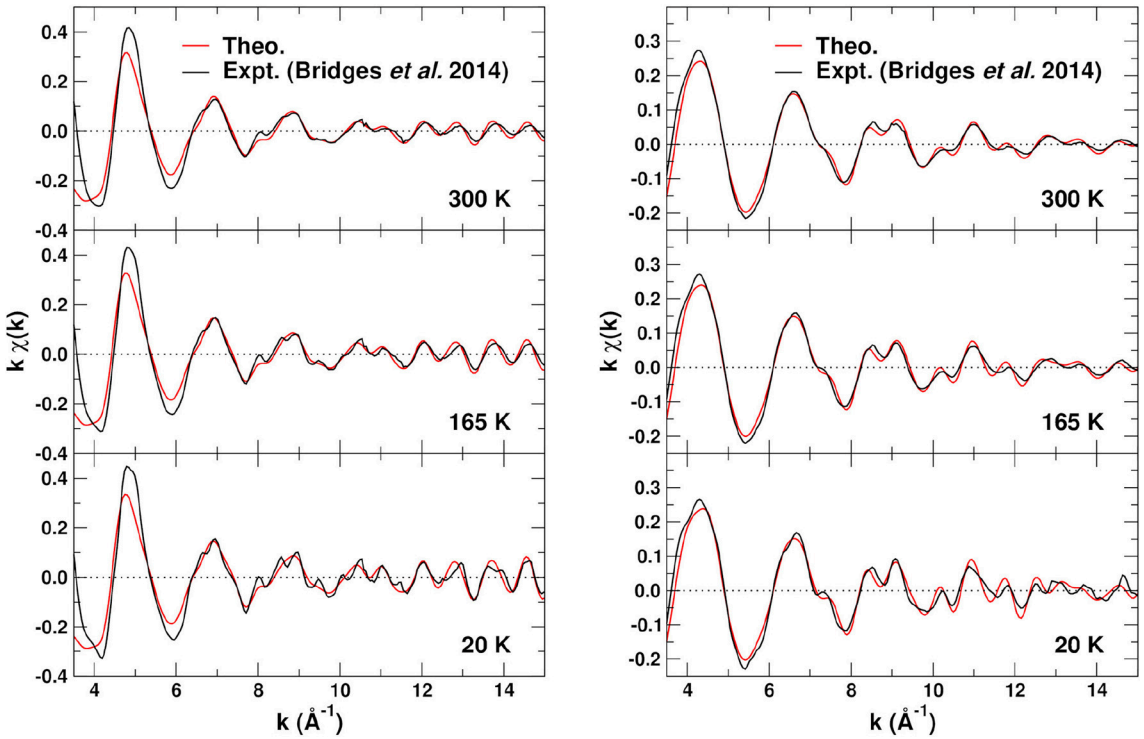

FIGURE 7 | Comparison of the experimental (Bridges et al., 2014) and theoretical EXAFS fine structure $k\chi(k)$ at 20, 165, and 300 K for the Zr K edge (left) and the W L_3 edge (right). The theory used the experimental lattice constant with optimized MSRDs to avoid small phase shifts due to the 1% error in the optimized PBEsol structure.

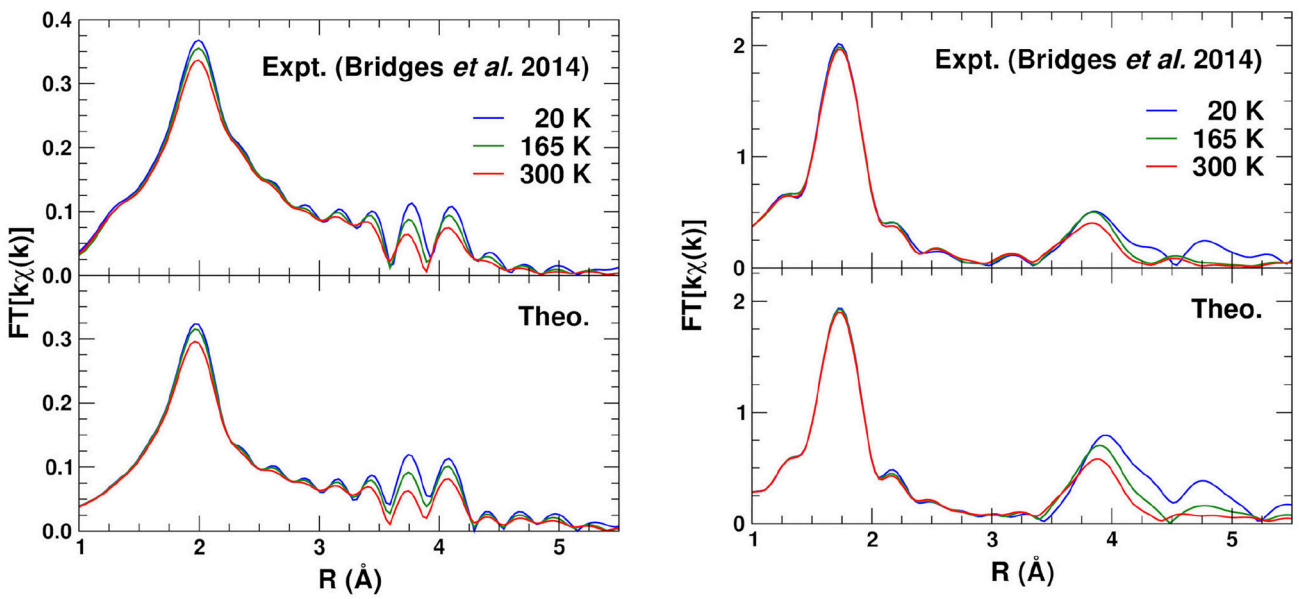

FIGURE 8 | Comparison of the Fourier transforms of the experimental (Bridges et al., 2014) and theoretical $k\chi(k)$ (**Figure 7**) at 20, 165, and 300 K for the Zr K edge (left) and the W L_3 edge (right).

with experiment (Bridges et al., 2014). The structural parameters are calculated using the DFT plane-wave pseudopotential VASP code with DFT/PBEsol while vibrational properties are obtained using a Lanczos algorithm and the phonon Green's function approach. The EXAFS calculations depend sensitively on these structural and vibrational properties. The fact that the calculations of the MSRDs for the most important SS and MS paths agree well show that an accurate treatment of correlated atomic motion is essential to understand the dynamic disorder. The small differences can likely be accounted for by static disorder and angular DW factors. For example, forward focusing effects in the Zr-O-W linkages are particularly important in these calculations. For example, the nearly collinear 173° paths contribute more to the amplitudes, due to enhanced forward scattering. Our calculations also show that transverse O fluctuations are substantial, consistent with results of our companion study (Vila et al., 2018), which imply that NTE is driven in part from the negative Grüneisen parameters of the low-frequency O modes. Thus while the effect of transverse fluctuations on the MSRDs is negligible, they may contribute to the angular DW factors. Our calculations also ignore anharmonic effects; although such effects are generally associated with thermal expansion (Frenkel and Rehr, 1993), this is a reasonable approximation for the dominant SS and MS paths with relatively stiff bonds. Overall our theoretical calculations yield results consistent with experiment for ZrW_2O_8 for a broad range of properties. In particular they show that both transverse motion and correlated atomic displacements are crucially important to understand the dynamic structure of this material.

AUTHOR CONTRIBUTIONS

FV co-developed the theory, was the main developer of the specialized software used in the analysis, and performed most of the simulations. JS contributed to the initial simulations. JK performed part of the analysis (Fourier Transforms). JR co-developed the theory and contributed to the analysis. FB provided EXAFS data and contributed to the analysis.

ACKNOWLEDGMENTS

This work was supported by U.S. Department of Energy, Office of Science CSGBD Grant No. DE-FG02-03ER15476, with computational support from NERSC, a DOE Office of Science User Facility, under Contract No. DE-AC02-05CH11231. The EXAFS experiments were performed at the Stanford Synchrotron Radiation Lightsource (SSRL), which is supported by the U.S. Department of Energy, Office of Science, Office of Basic Energy Sciences under Contract No. DE-AC02-76SF00515.

SUPPLEMENTARY MATERIAL

The Supplementary Material for this article can be found online at: https://www.frontiersin.org/articles/10.3389/fchem.2018.00356/full#supplementary-material

REFERENCES

Auray, M., Quarton, M., and Leblanc, M. (1995). Zirconium tungstate. *Acta Crystallogr. Sect. C* 51, 2210–2213.

Bridges, F., Keiber, T., Juhas, P., Billinge, S. J. L., Sutton, L., Wilde, J., et al. (2014). Local vibrations and negative thermal expansion in ZrW_2O_8. *Phys. Rev. Lett.* 112:045505. doi: 10.1103/PhysRevLett.112.045505

Cao, D., Bridges, F., Kowach, G. R., and Ramirez, A. P. (2002). Frustrated soft modes and negative thermal expansion in ZrW_2O_8. *Phys. Rev. Lett.* 89:215902. doi: 10.1103/PhysRevLett.89.215902

Cao, D., Bridges, F., Kowach, G. R., and Ramirez, A. P. (2003). Correlated atomic motions in the negative thermal expansion material ZrW_2O_8: a local structure study. *Phys. Rev. B* 68:014303. doi: 10.1103/PhysRevB.68.014303

Deuflhard, P., and Hohmann, A. (1995). *Numerical Analysis*. Berlin: de Gruyter.

Evans, J. S. O., David, W. I. F., and Sleight, A. W. (1999). Structural investigation of the negative-thermal-expansion material ZrW_2O_8. *Acta Crystallogr. Sect. B* 55, 333–340.

Fornasini, P., a Beccara, S., Dalba, G., Grisenti, R., Sanson, A., Vaccari, M., and Rocca, F. (2004). Extended x-ray-absorption fine-structure measurements of copper: local dynamics, anharmonicity, and thermal expansion. *Phys. Rev. B* 70:174301. doi: 10.1103/PhysRevB.70.174301

Frenkel, A. I., and Rehr, J. J. (1993). Thermal expansion and x-ray-absorption fine-structure cumulants. *Phys. Rev. B* 48, 585–588.

Haydock, R. (1980). "The recursive solution of the schrodinger equation," in *Solid State Physics*, Vol. 35, eds H. Ehrenreich, F. Seitz, and D. D. Turnbull (New York, NY: Academic), 215.

Kresse, G., and Furthmüller, J. (1996a). Efficiency of ab-initio total energy calculations for metals and semiconductors using a plane-wave basis set. *Comput. Mater. Sci.* 6, 15–50.

Kresse, G., and Furthmüller, J. (1996b). Efficient iterative schemes for *ab initio* total-energy calculations using a plane-wave basis set. *Phys. Rev. B* 54, 11169–11186.

Kresse, G., and Hafner, J. (1993). *Ab initio* molecular dynamics for liquid metals. *Phys. Rev. B* 47, 558–561.

Kresse, G., and Hafner, J. (1994). *Ab initio* molecular-dynamics simulation of the liquid-metal–amorphous-semiconductor transition in germanium. *Phys. Rev. B* 49, 14251–14269.

Kresse, G., and Joubert, D. (1999). From ultrasoft pseudopotentials to the projector augmented-wave method. *Phys. Rev. B* 59, 1758–1775.

Perdew, J. P., Ruzsinszky, A., Csonka, G. I., Vydrov, O. A., Scuseria, G. E., Constantin, L. A., et al. (2008). Restoring the density-gradient expansion for exchange in solids and surfaces. *Phys. Rev. Lett.* 100:136406. doi: 10.1103/PhysRevLett.100.136406

Poiarkova, A. V., and Rehr, J. J. (1999a). Multiple-scattering x-ray-absorption fine-structure debye-waller factor calculations. *Phys. Rev. B* 59, 948–957.

Poiarkova, A. V. and Rehr, J. J. (1999b). Recursion method for multiple-scattering XAFS Debye–Waller factors. *J. Synchrot. Radiat.* 6, 313–314.

Rehr, J. J., Kas, J. J., Prange, M. P., Sorini, A. P., Takimoto, Y., and Vila, F. (2009). Ab initio theory and calculations of X-ray spectra. *Comptes Rendus Phys.* 10:548-559. doi: 10.1016/j.crhy.2008.08.004

Vila, F. D., Hayashi, S. T., and Rehr, J. J. (2018). Efficient calculation of the negative thermal expansion in ZrW2O8. *Front. Chem.* 6:296. doi: 10.3389/fchem.2018.00296

Vila, F. D., Rehr, J. J., Rossner, H. H., and Krappe, H. J. (2007). Theoretical x-ray absorption debye-waller factors. *Phys. Rev. B* 76:014301. doi: 10.1103/PhysRevB.76.014301

Conflict of Interest Statement: The authors declare that the research was conducted in the absence of any commercial or financial relationships that could be construed as a potential conflict of interest.

frontiers in Chemistry

ORIGINAL RESEARCH
published: 12 November 2018
doi: 10.3389/fchem.2018.00544

Anomalous Lattice Dynamics in AgC_4N_3: Insights From Inelastic Neutron Scattering and Density Functional Calculations

Baltej Singh[1,2], *Mayanak K. Gupta*[1], *Ranjan Mittal*[1,2]*, *Mohamed Zbiri*[3], *Sarah A. Hodgson*[4], *Andrew L. Goodwin*[4], *Helmut Schober*[3] *and Samrath L. Chaplot*[1,2]

[1] Solid State Physics Division, Bhabha Atomic Research Centre, Mumbai, India, [2] Homi Bhabha National Institute, Mumbai, India, [3] Institut Laue-Langevin, Grenoble, France, [4] Department of Chemistry, University of Oxford, Oxford, United Kingdom

We have performed temperature dependent inelastic neutron scattering measurements to study the anharmonicity of phonon spectra of AgC_4N_3. The analysis and interpretation of the experimental spectra is done using *ab-initio* lattice dynamics calculations. The calculated phonon spectrum over the entire Brillouin zone is used to derive linear thermal expansion coefficients. The effect of van der Waals interaction on structure stability has been investigated using advanced density functional methods. The calculated isothermal equation of states implies a negative linear compressibility along the c-axis of the crystal, which also leads to a negative thermal expansion along this direction. The role of elastic properties inducing the observed anomalous lattice behavior is discussed.

Keywords: negative thermal expansion, linear compressibility, ab-initio, density functional theory, lattice dynamics, phonon, inelastic neutron scattering
PACS numbers: 78.70.Nx, 63.20.-e, 65.40.-b

OPEN ACCESS

Edited by:
Andrea Sanson,
Dipartimento di Fisica e Astronomia,
Università degli Studi di Padova, Italy

Reviewed by:
Engin Deligoz,
Aksaray University, Turkey
Cora Lind,
University of Toledo, United States
Giancarlo Ruocco,
Istituto italiano di Tecnologia (IIT), Italy

***Correspondence:**
Ranjan Mittal
rmittal@barc.gov.in

Specialty section:
This article was submitted to Physical Chemistry and Chemical Physics, a section of the journal Frontiers in Chemistry

Received: *01 June 2018*
Accepted: *19 October 2018*
Published: *12 November 2018*

Citation:
Singh B, Gupta MK, Mittal R, Zbiri M, Hodgson SA, Goodwin AL, Schober H and Chaplot SL (2018) Anomalous Lattice Dynamics in AgC_4N_3: Insights From Inelastic Neutron Scattering and Density Functional Calculations. Front. Chem. 6:544. doi: 10.3389/fchem.2018.00544

INTRODUCTION

In recent years, a few crystalline materials are found to exhibit expansion along certain crystallographic axes on application of static pressure (Goodwin et al., 2008a; Cairns et al., 2012, 2013; Cairns and Goodwin, 2015; Gupta et al., 2017; Yeung et al., 2017). This type of abnormal behavior is known as negative linear or area compressibility (NLC or NAC). The behavior is basically observed in materials with highly anisotropic bonding and open framework type structures (Goodwin et al., 2008a; Weng et al., 2008; Cairns et al., 2012, 2013; Cairns and Goodwin, 2015; Wang et al., 2016, 2017; Gupta et al., 2017; Zeng et al., 2017a,b; Yan et al., 2018). The anisotropic character of elastic properties is a measure of the magnitude of NLC (or NAC) in a material. The anisotropy in elastic properties of a material together with mode Grüneisen parameters give rise to the anisotropic thermal expansion (Gupta et al., 2016, 2017; Singh et al., 2017a; Mittal et al., 2018). Therefore, there is a close relation between the nature and magnitude of anisotropic thermal expansion and compressibility. Compounds which exhibit negative linear or area compressibilities are also found to show negative linear or area thermal expansion behavior along that particular directions (Conterio et al., 2008; Goodwin et al., 2008a,b, 2009; Gupta et al., 2017; Sapnik et al., 2018). However, the opposite is not true. Materials exhibiting the above properties are useful for pressure/temperature sensors, artificial muscles and can be used in piezoelectric applications (Burtch et al., 2017; Mirvakili and Hunter, 2017).

Many cyanide based metal organic flexible framework structures (Conterio et al., 2008; Goodwin et al., 2008a; David et al., 2010; Mittal et al., 2012; Cairns et al., 2013; Gupta et al., 2017; Ovens and Leznoff, 2017; Sapnik et al., 2018) like $ZnAu_2(CN)_4$, $M_3Co(CN)_6$ and $MAuX_2(CN)_2$ where M=H, Au, Ag, Cu, Fe and X=CN, Cl, Br etc., show large NLC and NTE behaviors. These stem from their special structure and bonding. In case of $ZnAu_2(CN)_4$, the NLC, and NTE along hexagonal c-axis arise from the anharmonic nature of the low energy optic phonon modes involving bending of the –Zn–NC–Au–CN–Zn– linkage, mimicking the effect of a spring in terms of compression upon heating and elongation (Gupta et al., 2017; Wang et al., 2017) under a hydrostatic pressure. The mechanism of the deformation of a wine rack structure produces NLC and NTE behavior in many compounds (Goodwin et al., 2008a; David et al., 2010; Cairns et al., 2012; Zeng et al., 2017a; Sapnik et al., 2018). Negative area compressibility and negative area thermal expansion are found to arise from the sliding of atomic layers as a function of pressure or temperature (Zeng et al., 2017b).

Experimental tools like x-ray diffraction and neutron diffraction are generally used to obtain temperature and pressure dependent lattice parameters (Goodwin et al., 2008a,b, 2009; Cairns et al., 2012, 2013; Hodgson et al., 2014; Cairns and Goodwin, 2015). However, the mechanism at the origin of this type of abnormal behavior can only be understood by studying the microscopic dynamics at the atomic level. *Ab-initio* density functional theory provides the pressure dependent phase diagram of these compounds and can be used to obtain the movements of atoms at different pressures, giving rise to negative linear or area compressibilities (Gupta et al., 2013, 2016, 2017; Singh et al., 2017a,b; Mittal et al., 2018). On the other hand, phonons in the entire Brillouin zone calculated using the *ab-initio* lattice dynamics in combination with the elastic properties have successfully been used to reproduce the experimental values of anisotropic linear thermal expansion coefficients (Gupta et al., 2013, 2016, 2017; Singh et al., 2017a,b; Mittal et al., 2018). This methodology enables us to identify specific phonon modes responsible for the negative thermal expansion behavior. Moreover, *ab-initio* techniques, being highly accurate as compared to empirical potentials based techniques, have now been used to identify and model new materials exhibiting anomalous lattice behavior (Lazar et al., 2015; Singh et al., 2018).

Recently, a combination of experimental phonon density of states coupled with *ab-initio* calculations are used for understanding the anomalous lattice response in a few metal organic framework compounds (Duyker et al., 2013; Hermet et al., 2013; Kamali et al., 2013; Gupta et al., 2016, 2017). These calculations are found to provide fair agreement of calculated and experimental phonon spectra. The structure of metal organic framework compounds has highly anisotropic bonding. The van der Waals interactions are found to play a very important role in stabilizing the structure and dynamics of these compounds (Conterio et al., 2008; Kamali et al., 2013; Gupta et al., 2017). However, the calculated temperature dependence of lattice parameters is not in satisfactory agreement with the measurements. The unavailability of accurate van der Waals dispersion interactions in the density functional theory may be responsible for this disagreement. However, the calculations are useful to qualitatively understand the mechanism responsible for anomalous lattice response of these compounds which are directly related to the low energy phonon modes in these compounds.

Silver (I) tricyanomethanide (**Figure 1**), AgC_4N_3, exhibits negative area compressibility and negative area thermal expansion in the a-c plane (Hodgson et al., 2014). The experimental temperature dependent lattice parameters were obtained from the single crystal X-ray diffraction experiments (Hodgson et al., 2014) while the pressure dependence of lattice parameter were obtained from the powder neutron diffraction experiments (Hodgson et al., 2014). The experimental X-ray and neutron diffraction techniques show large values of linear thermal expansion coefficients, $\alpha_a = -48 \times 10^{-6}\ K^{-1}$, $\alpha_b = 200 \times 10^{-6}\ K^{-1}$ $\alpha_c = -54 \times 10^{-6}\ K^{-1}$. We have used the *ab-initio* calculated equation of states to obtain the pressure dependence of the lattice parameters. The anisotropic pressure dependence of phonon spectra over the entire Brillouin zone is used to extract the anisotropic Grüneisen parameters within the quasiharmonic approximation framework. The temperature dependent phonon spectra are obtained from inelastic neutron scattering (INS) measurements. The calculated Grüneisen parameters and elastic constants are used to estimate linear thermal expansion coefficients. We find that the calculations reproduce the NLC and NTE behavior along the c-axis; however, the same along the a-axis are not reproduced. We have performed the analysis of specific phonon modes to gain insights into the atomic level mechanisms at the origin of the observed negative thermal expansion behavior along the c-axis.

EXPERIMENTAL AND COMPUTATIONAL DETAILS

INS measurements on about 2 cc of polycrystalline sample of AgC_4N_3 were carried out on the direct-geometry cold-neutron time-of-flight time-focusing spectrometer IN6 at the Institut Laue Langevin (ILL, Grenoble, France). The spectrometer is equipped with a large detector bank covering a wide range of about 13–114° of scattering angle. Data were collected at 150, 225, 300, and 400 K, in the neutron energy gain setup and high-resolution mode, using an incident wavelength of 5.12 Å (3.12 meV). In the incoherent one-phonon approximation (Carpenter and Price, 1985; Price and Skold, 1986), the measured scattering function $S(Q,E)$, as observed in the neutron experiments, is related to the phonon density of states $g^{(n)}(E)$ as follows:

$$g^{(n)}(E) = A < \frac{e^{2W(Q)}}{Q^2} \frac{E}{n(E,T) + \frac{1}{2} \pm \frac{1}{2}} S(Q,E) > \quad (1)$$

$$g^{n}(E) = B \sum_k \{\frac{4\pi b_k^2}{m_k}\} g_k(E) \quad (2)$$

where the + or − signs correspond to energy loss or gain of the neutrons, respectively and $n(E,T) = \left[\exp(E/k_BT) - 1\right]^{-1}$. A and

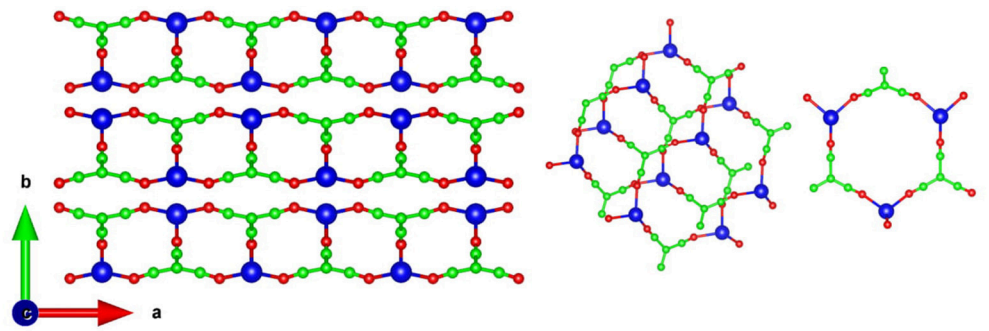

FIGURE 1 | (Left) The crystal structure of AgC_4N_3 projected in the ab plane. **(Right)** The building block consisting of 18 interpenetrating membered rings, and forming the ab plane of the structure. Key: C-Green, N-Red, and Ag-Blue.

TABLE 1 | The comparison of experimental (Single crystal X-ray diffraction Hodgson et al., 2014 at 100 K and ambient pressure) and calculated structural parameters, using various pseudopotentail corrections for the dispersion interactions.

Lattice parameters/ Optimization scheme	Expt. (100 K)	GGA	GGA + optB88	GGA + optB86b	GGA + optPBE	GGA + revPBE	GGA + DFT-D2, Grimme
a (Å)	8.0636	8.1317	7.9007	7.8991	7.8961	7.9435	8.421
b(Å)	9.7766	12.0189	9.6641	9.6466	10.0359	10.5742	9.418
c(Å)	6.2791	6.0829	6.4314	6.4110	6.4808	6.5248	6.020
V($Å^3$)	495.01	594.5	491.1	488.5	513.6	548.1	477.5
(x, y, z)							
C1	0.25	0.25	0.25	0.25	0.25	0.25	0.25
	0.4525	0.4622	0.4449	0.4456	0.4454	0.4463	0.4577
	0.9888	0.9113	0.9100	0.9103	0.9118	0.9133	0.9088
C2	0.5973	0.6005	0.5960	0.5958	0.5956	0.5963	0.6048
	0.6570	0.6368	0.6580	0.6582	0.6570	0.6545	0.6530
	0.2735	0.1962	0.1964	0.1970	0.1944	0.1921	0.2081
C3	0.75	0.75	0.75	0.75	0.75	0.75	0.75
	0.6219	0.6058	0.6251	0.6247	0.6240	0.6220	0.6171
	0.1798	0.0987	0.1007	0.1017	0.1001	0.0987	0.1100
N1	0.25	0.25	0.25	0.25	0.25	0.25	0.25
	0.5139	0.5210	0.5020	0.5027	0.5019	0.5024	0.5207
	0.8313	0.7578	0.7499	0.7493	0.7539	0.7586	0.7413
N2	0.4718	0.4751	0.4660	0.4651	0.4654	0.4674	0.4806
	0.6835	0.6622	0.6857	0.6868	0.6853	0.6824	0.6819
	0.3470	0.2771	0.2732	0.2725	0.2699	0.2676	0.2827
Ag	0.25	0.25	0.25	0.25	0.25	0.25	0.25
	0.64736	0.6244	0.6301	0.6314	0.6303	0.6295	0.6544
	0.5546	0.4678	0.4819	0.4816	0.4876	0.4919	0.4402

Various van der Waals dispersion interaction schemes (Dion et al., 2004; Jirí et al., 2010; Klimeš et al., 2011) are used in the structure optimization.

B are normalization constants. b_k, m_k, and $g_k(E)$ are, respectively, the neutron scattering length, mass, and partial density of states of the kth atom in the unit cell. The quantity between <> represents suitable average over all Q values at a given energy. $2W(Q)$ is the Debye-Waller factor averaged over all the atoms. The weighting factors $\frac{4\pi b_k^2}{m_k}$ in the units of barns/amu for C, N, and Ag are: 0.4625, 0.8221, and 0.0462, respectively. The values of neutron scattering lengths for various atoms can be found from Sears (1992).

The Vienna based *ab-initio* simulation package (VASP) (Kresse and Furthmüller, 1996; Kresse and Joubert, 1999) is used to carry out the total energy calculation based on plane-wave pseudo potential methods. The calculations are performed using projected augmented wave (PAW) formalism of Kohn- Sham density functional theory with generalized gradient approximation (GGA) for exchange correlation as given by Perdew, Becke and Ernzerhof (Perdew et al., 1996, 1997). K-point sampling was performed using 4 × 4 × 4 mesh Monkhorst-pack

scheme (Monkhorst and Pack, 1976) with a plane wave energy cutoff of 900 eV. Different schemes allowing incorporating the effect of van der Walls (vdW) interaction are available in VASP, using different approximations. The phonon frequencies in the entire Brillouin zone are estimated using finite displacement method, within the direct method approach, as implemented in PHONON5.2 (Parlinksi, 2003). Hellman-Feynman forces are calculated by the finite displacement of 0.03 Å.

Thermal expansion calculation is done using pressure dependence of phonon frequencies in the entire Brillouin zone within the quasi-harmonic approximation. Each phonon mode of energy E_{qj} (*jth* phonon mode at point q in the Brillouin zone) contributes to the thermal expansion coefficient, which is given by the following relation for an orthorhombic system (Grimvall, 1999):

$$\alpha_l(T) = \frac{1}{V_0}\sum_{q,j} C_{l'}(q,j,T)\left[s_{l1}\Gamma_a + s_{l2}\Gamma_b + s_{l3}\Gamma_c\right], \quad l, l' = a, b, c \,\&\, l \neq l'$$

Where s_{ij} are elements of elastic compliances matrix, $s = C^{-1}$ at constant temperature $T = 0$ K, V_0 is volume at 0 K and $C_{l'}(q,j,T)$ is the specific heat at constant strain due to *jth* phonon mode at point ***q*** in the Brillouin zone. The mode Grüneisen parameter of phonon energy $E_{q,j}$ is given as Grüneisen and Goens (1924),

$$\Gamma_l(E_{q,j}) = -\left(\frac{\partial lnE_{q,j}}{\partial lnl}\right)_{l'}; \; l, l' = a, b, c \,\&\, l \neq l'$$

The volume thermal expansion coefficient for an orthorhombic system is given by:

$$\alpha_V = (\alpha_a + \alpha_b + \alpha_c)$$

RESULTS AND DISCUSSION

The structure of AgC_4N_3 is a layered-like network topology along the b-axis (Hodgson et al., 2014). Ag^+ cation is coordinated to three N atoms to form trigonal arrangements. In the a–c plane it forms a crossing network made up of 18-member ($Ag_3C_9N_6$) rings (**Figure 1**). The layers in the a–c planes interact along the b-axis through a weak vdW interaction, acting between and N atoms. We have performed the relaxation of the crystal structure with and without including vdW interactions. These calculations without vdW interactions overestimated the b lattice parameter by 22% in comparison to the experimental value (**Table 1**). As shown in **Table 1**, we have initially optimized the structure including various available van der Waals schemes. We found that including vdW interaction describes better the structure whose calculated lattice parameters agree with the experimental

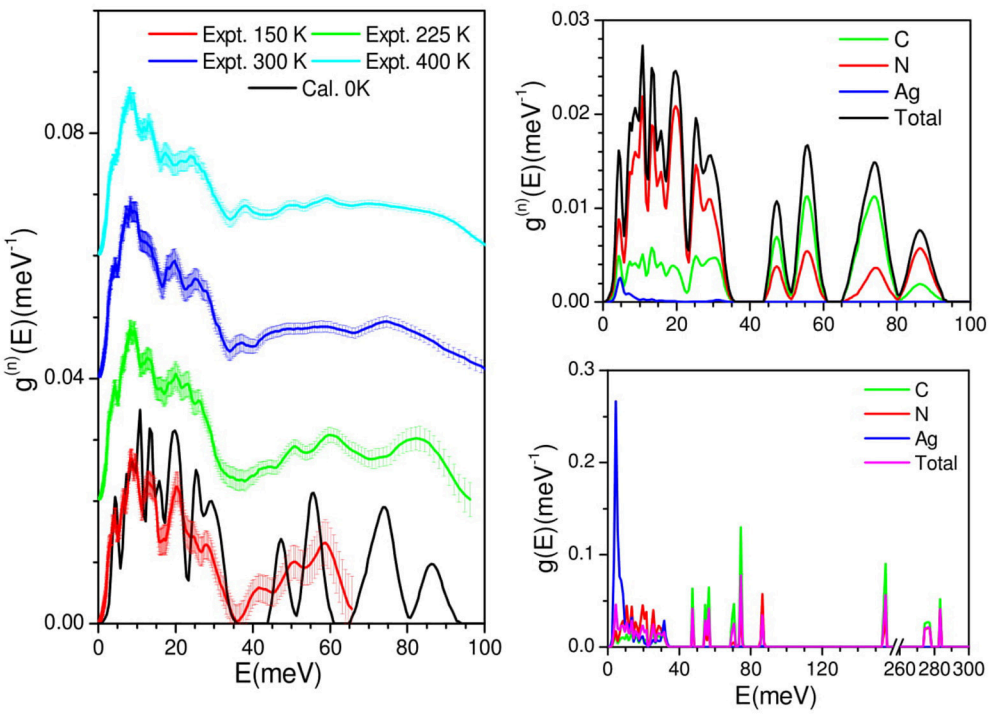

FIGURE 2 | (Left) Comparison of DFT calculation, and experimental phonon density of states of AgC_4N_3. For clarity, the experimental spectra are shift vertically. **(Right: Top)** The calculated neutron-weighted total density of states and the partial contributions from various atoms of AgC_4N_3. The calculated neutron spectra have been broadened corresponding to the experimental resolution. **(Right: Bottom)** The calculated partial density of states from various atoms of AgC_4N_3, showing the full energy range to account for the C-N modes bending and stretch.

(Cairns et al., 2013) values (**Table 1**). The vdW interaction has been considered using the optB88-vdW functional scheme of the vdw-DFT method (Dion et al., 2004; Jirí et al., 2010; Klimeš et al., 2011). The calculations produce the calculated volume within 1% of the experimental (Hodgson et al., 2014) value. The ambient condition structure is well-reproduced by the calculations.

Phonon Spectra

The measured phonon spectra at 150, 225, 300, and 400 K are shown in **Figure 2**. The INS measurements are performed in the neutorn energy gain mode. At 150 K, due to the population factorthe maximum energy transfer islimited to 65 meV. As temperature increases, modes at higher frequencies are populated, extending the energy range upto 100 meV. All the peaks in the phonon spectra show broadening with increase in temperature. However, peaks above 40 meV are found to show large temperature dependence. The broadening in the spectra reflects the explicit anharmonicity of phonons, which is expected with increase of temperature due to the increase of phonon-phonon interactions.

We have calculated the phonon spectra of this compound over the entire Brillouin zone. The calculated (0 K) phonon density of state is compared with the experimentally measured inelastic neutron scattering spectra at 150 K. The calculated neutron weighted phonon density of statesa grees very well with the experimental data (**Figure 2**). The level of agreement between the calculated and experimental phonon density of states of AgC_4N_3 is similar to that in many previous studies on metal cyanides framework compounds (Gupta et al., 2016, 2017), which is quite good considering the use of incoherent approximation (Carpenter and Price, 1985; Price and Skold, 1986) in the calculation of neutron weighted phonon spectrum. Therefore, the calculations can be further used for the microscopic understanding and interpretation of the peaks in the phonon spectra. The calculated partial phonon density of states show that Ag atoms contribute only tothe low energy part of the spectra, while C and N atomic vibrations contribute to the entire energy range. The low energy peak in the spectra around 5 meV arises from the vibrational motion of all the atomic species. The vibrations below 35 meV are dominated by the contribution from N atoms, while above 45 meV, the contributions upto 80 meV are mainly duetoC atoms. The calculated spectra in the 40–60 meV energy range shows a deviation from the observation. There could be two reasons for this deviation: (i) small mismatch between the calculated and experimental bond lengths due to limitation of density functional used for exchange correlations and dispersion interactions and (ii) this region is very sensitive to temperature so the mismatch may be due to the comparison of 0 K calculations with the meaurements performed at 150 K. As the vibrations of C≡N bond occur with very high energy of order 270 meV, they do not undergo any significant changes, but they are well-captured by our calculations. The peak in the calculated spectrumaround 165 meV corresponds to the bending vibrations of –C≡N units.

The calculated phonon dispersion curves along the high symmetry directions in the Brillouin zone are shown in **Figure 3**. The phonon dispersionss are almost flat around 48, 55, 70, and 88 meV, which give rise to intense peaks in the calculated phonon density of states (**Figure 2**). This implies a very strong short range interactions among the atoms contributing to these vibrational modes.

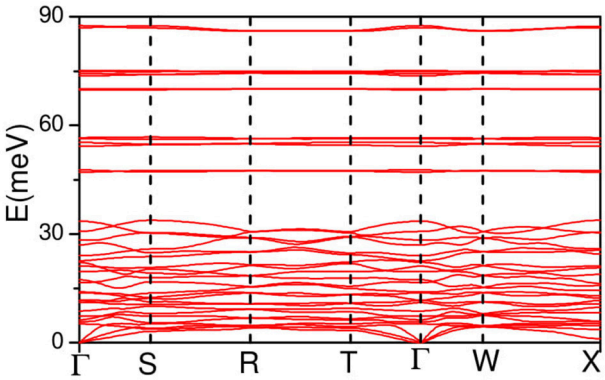

FIGURE 3 | The calculated phonon dispersion curves along the high symmetry directions in the Brillouin zone AgC_4N_3. The Bradley-Cracknell notation is used for the high-symmetry points; Γ(0, 0, 0), S(1/2, 0, 0), R(0, 1/2, 0), T(1/2 0 0), W(1/4, 1/4, 1/4), and X(1/2, −1/2, 1/2).

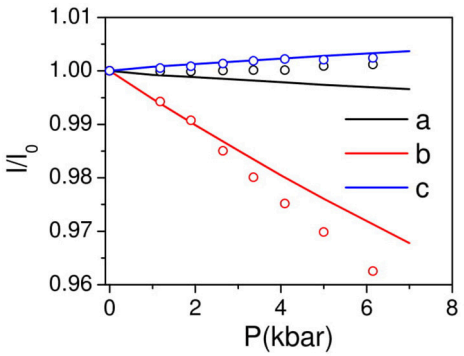

FIGURE 4 | The calculated (solid lines) pressure dependence of unit cell lattice parameters of AgC_4N_3 compared with the experimental data (circles). The experimental data is available from 1 to 6 kbar. The data was extrapolated to 0 kbar and used for estimation of l/l_0.

Anisotropic Compressibility Behavior

The pressure dependent equation of state of AgC_4N_3 has been calculated (**Figure 4**) by applying a uniform hydrostatic pressure to look at the resulting change in the lattice parameters. The *a* and *b* lattice parameters are found to show a usual, but anisotropic positive linear compressibility, while the c lattice parameter shows a negative linear compressibility. Further the elastic constants are calculated using the symmetry-general least square method (Le Page and Saxe, 2002) as implemented in VASP-5.4. The values are derived from the strain–stress relationships obtained from finite distortions of the equilibrium lattice. For small deformations the elastic domain of the solid is conserved and a quadratic dependence of the total energy with respect to the strain is expected (Hooke's law). The number of components (Mouhat and Coudert, 2014)

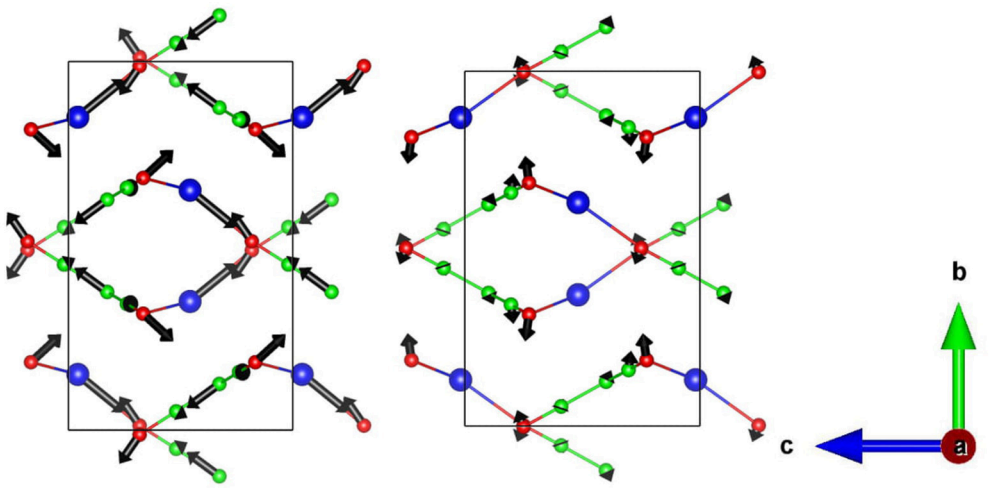

FIGURE 5 | The displacement vectors corresponding to the difference (×35) in atomic coordinates of **(Left)** experimental structures at 1.18 and 6.15 kbar, and **(Right)** calculated structures at 0.0 and 5.0 kbar. The ambient pressure experimental data is not available in the high pressure setup of the experiment. So we have used experimental structures at 1.18 and 6.15 kbar for plotting the displacement vectors. Key: C-Green, N-Red, and Ag-Blue.

of the elastic constant tensor is related to the symmetry of the crystal symmetry. The calculated elastic constant, C_{ij} (in kbar) and compliance, s_{ij} (10^{-4} kbar^{-1}) matrices are:

$$C_{ij} = \begin{pmatrix} 588 & 186 & 508 & 0 & 0 & 0 \\ 186 & 195 & 214 & 0 & 0 & 0 \\ 508 & 214 & 645 & 0 & 0 & 0 \\ 0 & 0 & 0 & 100 & 0 & 0 \\ 0 & 0 & 0 & 0 & 20 & 0 \\ 0 & 0 & 0 & 0 & 0 & 42 \end{pmatrix},$$

$$s_{ij} = \begin{pmatrix} 54.0 & -7.3 & -40.1 & 0 & 0 & 0 \\ -7.3 & 81.7 & -21.4 & 0 & 0 & 0 \\ -40.1 & -21.4 & 54.2 & 0 & 0 & 0 \\ 0 & 0 & 0 & 99.9 & 0 & 0 \\ 0 & 0 & 0 & 0 & 502.4 & 0 \\ 0 & 0 & 0 & 0 & 0 & 238.9 \end{pmatrix}$$

It can be seen that the value of longitudinal elastic constants C_{11} and C_{33} are about three times in comparison to that of C_{22}, indicating that b-axis is highly compressible in comparison to a- and c- axis. Qualitatively, this agrees quite well with the experimental (Hodgson et al., 2014) pressure dependence of unit cell lattice parameters of AgC_4N_3 which show that the response to the pressure along b-axis is very large in comparison to that along a- and c-axes. It should be noted that the a–c plane of the crystal consists of layers containing 18-membered ($Ag_3C_9N_6$) interpenetrating rings. The layers in the a–c plane are stacked along b-axis which indicates that the compound may have highly anisotropic elastic response. The calculations confirm that at ambient pressure there is large anisotropy in bonding along various crystal axes which gives rise to highly anisotropic elastic properties in this compound.

Further in order to understand the compressibility behavior along the orthorhombic axes of AgC_4N_3 we have calculated

$$X_a = S_{11} + S_{12} + S_{13}, X_b = S_{12} + S_{22} + S_{23} \ \& \\ X_c = S_{13} + S_{23} + S_{33}$$

Where X_i ($i = a, b, c$) are the compressibilities of crystal along various crystallographic axes. For negative compressibility, the values of X_a, X_b, *and* X_c should be negative along the respective axis (Weng et al., 2008). We found that $X_a = 6.4 \times 10^{-4}$ kbar^{-1}, $X_b = 53.0 \times 10^{-4}$ kbar^{-1}, $X_c = -7.3 \times 10^{-4}$ kbar^{-1}. These calculations imply negative linear compressibility along c-axis. However, the experimentally observed compressibility behavior along the *a*-axis is not obtained (**Figure 4**) from the calculations. This could be due to limitation of vdW DFT to account properly for the pressure dependent dispersion interactions in this particular structure geometry. It should be noted that a similar vdW density functional has been successfully used to obtain the experimentally observed thermal expansion behavior in many cyanide framework compounds (Kamali et al., 2013; Gupta et al., 2017).

To explore the possible origin of the above-mentioned behavior, the atomic displacement vectors (**Figure 5**) corresponding to the difference in the experimentally observed structure (Hodgson et al., 2014) at 1 and 6 kbar is compared with calculated structures at 0 and 5 kbar. It is found that experimentally the major difference comes from the displacement vector of Ag atoms, while computationally it is almost zero, i.e., no difference. There is also a significant difference in displacement patterns of the other atoms in the unit cell. Moreover, the experimentally observed atomic displacements are larger in magnitude compared to the calculated ones.

Linear Thermal Expansion

The linear thermal expansion behavior of AgC_4N_3 is calculated using the anisotropic pressure dependence of phonon spectra over the entire Brillouin zone within the framework of the quasiharmonic approximation. This methodology requires the complete elastic compliance tensor (section Anisotropic Compressibility Behavior) which is the inverse of the elastic constant tensor. The calculated anisotropic Grüneisen parameters are shown in **Figure 6**. The calculated low-energy mode Grüneisen parameters below 10 meV show negative values for the anisotropic stress along the *a* and *c*-axes, and possibly contributing to the negative thermal expansion in the ac plane. These also serve to explore thermal expansion behavior as discussed above. The calculated temperature dependence of the lattice parameters is compared with the experimental data. The calculated thermal expansion behavior (**Figure 7**) along the *b*- and *c*-axes agrees reasonably with the observation. The *c*-axis shows a negative linear thermal expansion while the b-axis shows a large positive expansion over the whole studied temperature range. However, the calculated *a*-lattice parameter shows a positive thermal expansion in contrast with the experiment. The calculated linear thermal expansion coefficients saturate above 200 K, with the values of $\alpha_a = 20\times10^{-6}$ K^{-1}, $\alpha_b = 125\times10^{-6}$ K^{-1} $\alpha_c = -75\times10^{-6}$ K^{-1}. The calculated bulk volume thermal expansion agrees well with the experimental data.

The eigenvector pattern of specific phonon modes giving rise to the large negative thermal expansion along the *c*-axis is analyzed. The zone center mode with an energy of 13.7 meV (**Figure 8**) has $\Gamma_a = 2.39$, $\Gamma_b = 0.10$, $\Gamma_c = -2.99$. Assuming it corresponds to an Einstein mode with one degree of freedom, the contribution from this mode to the thermal expansion

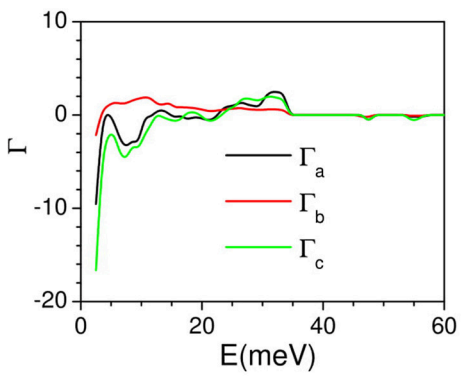

FIGURE 6 | The calculated anisotropic mode Grüneisen parameters Γ_a, Γ_b, and Γ_c, averaged over phonon modes in the entire Brillouin zone, as a function of phonon energy, on application of anisotropic pressure along a-, b-, and c-axes, respectively.

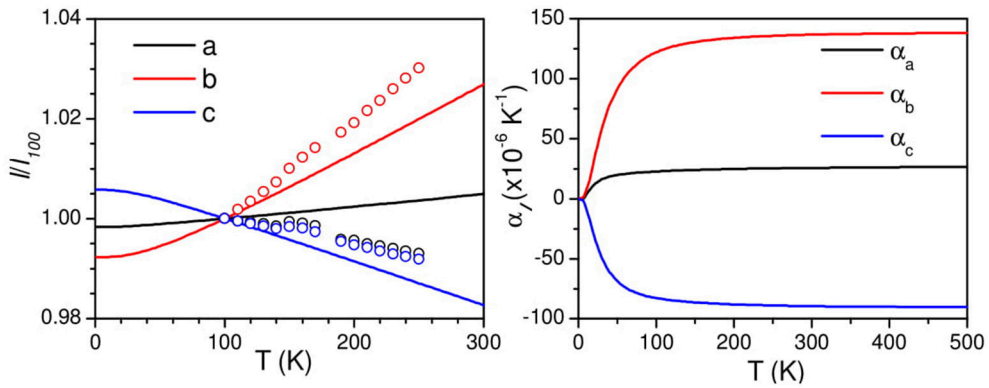

FIGURE 7 | (Left) The calculated and experimental temperature dependence of unit cell parameters of AgC_4N_3. **(Right)** The calculated temperature dependence of linear thermal expansion coefficients of AgC_4N_3.

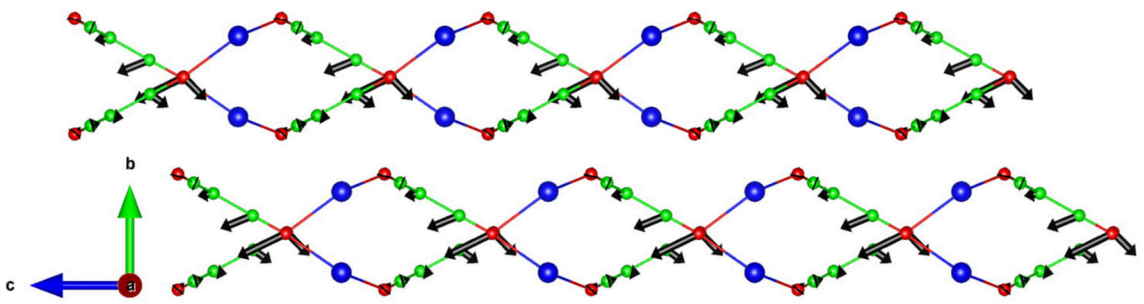

FIGURE 8 | The calculated eigenvectors of the zone center phonon at 13.7 meV, giving rise to a negative thermal expansion behavior along the *c*-axis in AgC_4N_3. The corresponding mode Grüneisen values are $\Gamma_a = 2.39$, $\Gamma_b = 0.10$, $\Gamma_c = -2.99$. Key: C-Green, N-Red, and Ag-Blue.

coefficients $\alpha_a = 11.34\times 10^{-6}$ K^{-1}, $\alpha_b = 2.50\times 10^{-6}$ K^{-1}, $\alpha_c = -11.89 \times 10^{-6}$ K^{-1}. As shown in **Figure 8**, only the atoms connected to C–N bonds have a larger amplitude and give rise to ripples in the layers along the *c*-axis, and is responsible for NTE along the *c*-axis.

In many metal organic frameworks, the experimentally observed anisotropic behavior in compressibility along a given crystallographic axis is found to lead to a fairly similar behavior in linear thermal expansion. The possible limitation of DFT to fully reproduce the compressibility behavior along the *a*-axis could be responsible for the difference in the thermal expansion behavior between the experiment and calculation. However, as far as the calculated phonon energies are concerned, these are correctly predicted by our *ab-initio* calculations at ambient pressure conditions.

CONCLUSIONS

We have performed temperature dependent inelastic neutron scattering (INS) measurements to collect the temperature evolution (softening/hardening) of phonon spectra in the metal organic framework compound AgC_4N_3. *Ab-initio* lattice dynamical calculations are used to underpin the INS phonon data, over the entire Brillouin zone. The calculated partial density of states of various atoms is used to analyse the experimental spectra. The calculated anisotropic pressure dependent phonon spectra along with the estimated elastic constants are used to derive linear thermal expansion quantities of the compound. *Ab-initio* calculations performed at various uniform hydrostatic pressures are used to obtain the compressibility of the compound. Due to the structural peculiarity of AgC_4N_3, the *ab-initio* calculations including the van der Waals interaction could not reproduce the experimentally observed temperature/pressure dependence of "a" lattice parameter. However, the behavior of "b" and "*c*" lattice parameters is well-reproduced and calculations provide the microscopic mechanism of NTE and NLC along *c*-lattice parameter which arises from the rippling of structural sheets perpendicular to b-axis. It is clear that there is need for improvements in the van der Waals functions to accurately account for the structure and dynamics of metal organic framework compounds. Moreover, the experimentally measured phonon density of states will be very helpful for verification of any new van der Waals potentials in the coming future.

AUTHOR CONTRIBUTIONS

RM formulated the problem, contributed in inelastic neutron scattering experiment, interpretation of experiment and *ab-initio* calculation, and writing of the manuscript. SC formulated the problem, contributed in interpretation of experiment and *ab-initio* calculation, and writing of the manuscript. BS and MG contributed in inelastic neutron scattering experiment, *ab-initio* calculations, interpretation of experiment and *ab-initio* calculation, and writing of the manuscript. MZ and HS participated in inelastic neutron scattering experiment and data analysis. SH and AG synthesized and characterized the AgC_4N_3 samples.

ACKNOWLEDGMENTS

SC would like to thank the Department of Atomic Energy, India for the award of Raja Ramanna Fellowship. The use of ANUPAM super-computing facility at BARC is acknowledged. The Institut Laue-Langevin (ILL) facility, Grenoble, France, is acknowledged for beam time allocation on the IN6 time-of-flight spectrometer. AG and SH gratefully acknowledge financial support from the ERC (Grant 279705).

REFERENCES

Burtch, N. C., Heinen, J., Bennett, T. D., Dubbeldam, D., and Allendorf, M. D. (2017). Mechanical properties in metal-organic frameworks: emerging opportunities and challenges for device functionality and technological applications. *Adv. Mater.* 30:1704124, 1–18. doi: 10.1002/adma.201704124

Cairns, A. B., Catafesta, J., Levelut, C., Rouquette, J., van der Lee, A., Peters, L., et al. (2013). Giant negative linear compressibility in zinc dicyanoaurate. *Nat. Mater.* 12, 212–216. doi: 10.1038/nmat3551

Cairns, A. B., and Goodwin, A. L. (2015). Negative linear compressibility. *Phys. Chem. Chem. Phys.* 17, 20449–20465. doi: 10.1039/C5CP00442J

Cairns, A. B., Thompson, A. L., Tucker, M. G., Haines, J., and Goodwin, A. L. (2012). Rational design of materials with extreme negative compressibility: selective soft-mode frustration in $Kmn[Ag(CN)_2]_3$. *J. Am. Chem. Soc.* 134, 4454–4456. doi: 10.1021/ja204908m

Carpenter, J. M., and Price, D. L. (1985). Correlated motions in glasses studied by coherent inelastic neutron scattering. *Phys. Rev. Lett.* 54, 441–443. doi: 10.1103/PhysRevLett.54.441

Conterio, M. J., Goodwin A. L., Tucker, M. G., Keen, D. A., Dove, M. T., Peters, L., et al. (2008). Local structure in $Ag_3[Co(CN)_6]$: colossal thermal expansion, rigid unit modes and argentophilic interactions. *J. Phys. Condens. Matter* 20:255225. doi: 10.1088/0953-8984/20/25/255225

David, A. K., Martin, T. D., John, S. O. E., Andrew, L. G., Lars, P., and Matthew, G. T. (2010). The hydrogen-bonding transition and isotope-dependent negative thermal expansion in $H_3Co(CN)_6$. *J. Phys. Condens. Matter* 22:404202. doi: 10.1088/0953-8984/22/40/404202

Dion, M., Rydberg, H., Schröder, E., Langreth, D. C., and Lundqvist, B. I. (2004). Van Der Waals density functional for general geometries. *Phys. Rev. Lett.* 92:246401. doi: 10.1103/PhysRevLett.92.246401

Duyker, S. G., Peterson, V. K., Kearley, G. J., Ramirez-Cuesta, A. J., and Kepert, C. J. (2013). Negative thermal expansion in $LnCo(CN)_6$ (Ln=La, Pr, Sm, Ho, Lu, Y): mechanisms and compositional trends. *Angew. Chem. Int. Ed.* 125, 5374–5378. doi: 10.1002/ange.201300619

Goodwin, A. L., Keen, D. A., and Tucker, M. G. (2008a). Large negative linear compressibility of $Ag_3[Co(CN)_6]$. *Proc. Natl. Acad. Sci. U.S.A.* 105, 18708–18713. doi: 10.1073/pnas.0804789105

Goodwin, A. L., Keen, D. A., Tucker, M. G., Dove, M. T., Peters, L., and Evans, J. S. O. (2008b). Argentophilicity-dependent colossal thermal expansion in extended prussian blue analogues. *J. Am. Chem. Soc.* 130, 9660–9661. doi: 10.1021/ja803623u

Goodwin, A. L., Kennedy, B. J., and Kepert, C. J. (2009). Thermal expansion matching via framework flexibility in zinc dicyanometallates. *J. Am. Chem. Soc.* 131, 6334–6335. doi: 10.1021/ja901355b

Grimvall, G. (1999). *Thermophysical Properties of Materials*. North-Holland: Elsevier.

Grüneisen, E., and Goens, E. (1924). Thermische Ausdehnung von Zink und Cadmium. *Z. Phys.* 29:141. doi: 10.1007/BF03184834

Gupta, M. K., Mittal, R., and Chaplot, S. L. (2013). Negative thermal expansion in cubic ZrW_2O_8: role of phonons in the entire brillouin zone from *ab-initio* calculations. *Phys. Rev. B* 88:014303. doi: 10.1103/PhysRevB.88.014303

Gupta, M. K., Singh, B., Mittal, R., Rols, S., and Chaplot, S. L. (2016). Lattice dynamics and thermal expansion behavior in the metal cyanides MCN (M= Cu, Ag, Au): neutron inelastic scattering and first-principles calculations. *Phys. Rev. B* 93:134307. doi: 10.1103/PhysRevB.93.134307

Gupta, M. K., Singh, B., Mittal, R., Zbiri, M., Cairns, A. B., Goodwin, A. L., et al. (2017). Anomalous thermal expansion, negative linear compressibility, and high-pressure phase transition in $ZnAu_2(CN)_4$: neutron inelastic scattering and lattice dynamics studies. *Phys. Rev. B* 96:214303. doi: 10.1103/PhysRevB.96.214303

Hermet, P., Catafesta, J., Bantignies, J-L., Levelut, C., Maurin, D., Cairns, A., et al. (2013). Vibrational and thermal properties of $Ag_3[Co(CN)_6]$ from first-principles calculations and infrared spectroscopy. *J. Phys. Chem. C* 117, 12848–12857. doi: 10.1021/jp402081r

Hodgson, S. A., Adamson, J., Hunt, S. J., Cliffe, M. J., Cairns, A. B., Thompson, A. L., et al. (2014). Negative area compressibility in silver(I) tricyanomethanide. *Chem. Commun.* 50, 5264–5266. doi: 10.1039/C3CC47032F

Jirí, K., David, R. B., and Angelos, M. (2010). Chemical accuracy for the Van Der Waals density functional. *J. Phys. Condens. Matter* 22:022201. doi: 10.1088/0953-8984/22/2/022201

Kamali, K., Ravi, C., Ravindran, T., Sarguna, R., Sairam, T., and Kaur, G. (2013). Linear compressibility and thermal expansion of $KMn[Ag(CN)_2]_3$ studied by Raman spectroscopy and first-principles calculations. *J. Phys. Chem. C* 117, 25704–25713. doi: 10.1021/jp410214y

Klimeš, J., Bowler, D. R., and Michaelides, A. (2011). Van Der Waals density functionals applied to solids. *Phys. Rev. B* 83:195131. doi: 10.1103/PhysRevB.83.195131

Kresse, G., and Furthmüller, J. (1996). Efficiency of *ab-initio* total energy calculations for metals and semiconductors using a plane-wave basis set. *Comput. Mater. Sci.* 6, 15–50. doi: 10.1016/0927-0256(96)00008-0

Kresse, G., and Joubert, D. (1999). From ultrasoft pseudopotentials to the projector augmented-wave method. *Phys. Rev. B* 59, 1758–1775. doi: 10.1103/PhysRevB.59.1758

Lazar, P., Bučko, T., and Hafner, J. (2015). Negative thermal expansion of ScF_3: insights from density-functional molecular dynamics in the isothermal-isobaric ensemble. *Phys. Rev. B* 92:224302. doi: 10.1103/PhysRevB.92.224302

Le Page, Y., and Saxe, P. (2002). Symmetry-general least-squares extraction of elastic data for strained materials from *ab initio* calculations of stress. *Phys. Rev. B* 65:104104. doi: 10.1103/PhysRevB.65.104104

Mirvakili, S. M., and Hunter, I. W. (2017). Multidirectional artificial muscles from nylon. *Adv. Mater.* 29:1604734. doi: 10.1002/adma.201604734

Mittal, R., Gupta, M. K., and Chaplot, S. L. (2018). Phonons and anomalous thermal expansion behaviour in crystalline solids. *Prog. Mater. Sci.* 92, 360–445. doi: 10.1016/j.pmatsci.2017.10.002

Mittal, R., Zbiri, M., Schober, H., Achary, S., Tyagi, A., and Chaplot, S. (2012). Phonons and colossal thermal expansion behavior of $Ag_3Co(CN)_6$ and $Ag_3Fe(CN)_6$. *J. Phys. Condens. Matter* 24:505404. doi: 10.1088/0953-8984/24/50/505404

Monkhorst, H. J., and Pack, J. D. (1976). Special points for brillouin-zone integrations. *Phys. Rev. B* 13, 5188–5192. doi: 10.1103/PhysRevB.13.5188

Mouhat, F., and Coudert, F-X. (2014). Necessary and sufficient elastic stability conditions in various crystal systems. *Phys. Rev. B* 90:224104. doi: 10.1103/PhysRevB.90.224104

Ovens, J. S., and Leznoff, D. B. (2017). Thermal expansion behavior of $M[AuX_2(CN)_2]$-based coordination polymers (M=Ag, Cu; X=Cn, Cl, Br). *Inorg. Chem.* 56, 7332–7343. doi: 10.1021/acs.inorgchem.6b03153

Parlinksi, K. (2003). *Phonon Software*. Krakow: Krzysztof Parlinski Computing for Materials.

Perdew, J. P., Burke, K., and Ernzerhof, M. (1996). Generalized gradient approximation made simple. *Phys. Rev. Lett.* 77, 3865–3868. doi: 10.1103/PhysRevLett.77.3865

Perdew, J. P., Burke, K., and Ernzerhof, M. (1997). Generalized gradient approximation made simple. *Phys. Rev. Lett.* 78, 1396–1396. doi: 10.1103/PhysRevLett.78.1396

Price, D. L., and Skold, K. (1986). *Neutron Scattering*. Vol. A. Orlando, FL: Academic Press.

Sapnik, A. F., Liu, X., Boström, H. L. B., Coates, C. S., Overy, A. R., Reynolds, E. M., et al. (2018). Uniaxial negative thermal expansion and metallophilicity in $Cu_3[Co(CN)_6]$. *J. Solid State Chem.* 258, 298–306. doi: 10.1016/j.jssc.2017.10.009

Sears, V. F. (1992). Neutron scattering lengths and cross sections. *Neutron News* 3, 26–37. doi: 10.1080/10448639208218770

Singh, B., Gupta, M. K., Mishra, S. K., Mittal, R., Sastry, P. U., Rols, S., et al. (2017b). Anomalous lattice behavior of vanadium pentaoxide (V_2O_5): X-ray diffraction, inelastic neutron scattering and *ab-initio* lattice dynamics. *Phys. Chem. Chem. Phys.* 19, 17967–17984. doi: 10.1039/C7CP01904A

Singh, B., Gupta, M. K., Mittal, R., and Chaplot, S. L. (2018). *Ab-initio* molecular dynamics study of 1-D superionic conduction and phase transition in β-eucryptite. *J. Mater. Chem. A* 6, 5052–5064. doi: 10.1039/C7TA08541A

Singh, B., Gupta, M. K., Mittal, R., Zbiri, M., Rols, S., Patwe, S. J., et al. (2017a). Role of phonons in negative thermal expansion and high pressure phase transitions in β-eucryptite: an *ab-initio* lattice dynamics and inelastic neutron scattering study. *J. Appl. Phys.* 121:085106. doi: 10.1063/1.4977244

Wang, L., Luo, H., Deng, S., Sun, Y., and Wang, C. (2017). Uniaxial negative thermal expansion, negative linear compressibility, and negative Poisson's ratio induced by specific topology in $Zn[Au(CN)_2]_2$. *Inorg. Chem.* 56, 15101–15109. doi: 10.1021/acs.inorgchem.7b02416

Wang, L., Wang, C., Luo, H., and Sun, Y. (2016). Correlation between uniaxial negative thermal expansion and negative linear compressibility in $Ag_3[Co(CN)_6]$. *J. Phys. Chem. C* 121, 333–341. doi: 10.1021/acs.jpcc.6b09944

Weng, C. N., Wang, K. T., and Chen, T. (2008). Design of microstructures and structures with negative linear compressibility in certain directions. *Adv. Mater. Res.* 33–37, 807–814. doi: 10.4028/www.scientific.net/AMR.33-37.807

Yan, Y., O'Connor, A. E., Kanthasamy, G., Atkinson, G., Allan, D. R., Blake, A. J., et al. (2018). Unusual and tunable negative linear compressibility in the metal-organic framework MFM-133(M)(M=Zr, Hf). *J. Am. Chem. Soc.* 140, 3952–3958. doi: 10.1021/jacs.7b11747

Yeung, H. H-M., Kilmurray, R., Hobday, C. L., McKellar, S. C., Cheetham, A. K., Allan, D. R., et al. (2017). Hidden negative linear compressibility in lithium L-tartrate. *Phys. Chem. Chem. Phys.* 19, 3544–3549. doi: 10.1039/C6CP08690J

Zeng, Q., Wang, K., Qiao, Y., Li, X., and Zou, B. (2017b). Negative linear compressibility due to layer sliding in a layered metal-organic framework. *J. Phys. Chem. Lett.* 8, 1436–1441. doi: 10.1021/acs.jpclett.7b00121

Zeng, Q., Wang, K., and Zou, B. (2017a). Large negative linear compressibility in $InH(BDC)_2$ from framework hinging. *J. Am. Chem. Soc.* 139, 15648–15651. doi: 10.1021/jacs.7b10292

Conflict of Interest Statement: The authors declare that the research was conducted in the absence of any commercial or financial relationships that could be construed as a potential conflict of interest.

frontiers in Chemistry

ORIGINAL RESEARCH
published: 18 October 2018
doi: 10.3389/fchem.2018.00455

Control of Uniaxial Negative Thermal Expansion in Layered Perovskites by Tuning Layer Thickness

Chris Ablitt[1], *Arash A. Mostofi*[1,2], *Nicholas C. Bristowe*[3] *and Mark S. Senn*[4]*

[1] Department of Materials and The Thomas Young Centre, Imperial College London, London, United Kingdom, [2] Department of Physics, Imperial College London, London, United Kingdom, [3] School of Physical Sciences, University of Kent, Canterbury, United Kingdom, [4] Department of Chemistry, University of Warwick, Coventry, United Kingdom

Uniaxial negative thermal expansion (NTE) is known to occur in low n members of the $A_{n+1}B_nO_{3n+1}$ Ruddlesden–Popper (RP) layered perovskite series with a frozen rotation of BO_6 octahedra about the layering axis. Previous work has shown that this NTE arises due to the combined effects of a close proximity to a transition to a competing phase, so called "symmetry trapping", and highly anisotropic elastic compliance specific to the symmetry of the NTE phase. We extend this analysis to the broader RP family ($n = 1, 2, 3, 4, \ldots, \infty$), demonstrating that by changing the fraction of layer interface in the structure (i.e., the value of $1/n$) one may control the anisotropic compliance that is necessary for the pronounced uniaxial NTE observed in these systems. More detailed analysis of how the components of the compliance matrix develop with $1/n$ allows us to identify different regimes, linking enhancements in compliance between these regimes to the crystallographic degrees of freedom in the structure. We further discuss how the perovskite layer thickness affects the frequencies of soft zone boundary modes with large negative Grüneisen parameters, associated with the aforementioned phase transition, that constitute the thermodynamic driving force for NTE. This new insight complements our previous work—showing that chemical control may be used to switch from positive to negative thermal expansion in these systems—since it makes the layer thickness, n, an additional design parameter that may be used to engineer layered perovskites with tuneable thermal expansion. In these respects, we predict that, with appropriate chemical substitution, the $n = 1$ phase will be the system in which the most pronounced NTE could be achieved.

Keywords: NTE, perovskite, Ruddlesden-Popper, anisotropy, compliance, corkscrew, thermal expansion

OPEN ACCESS

Edited by:
Andrea Sanson,
Università degli Studi di Padova, Italy

Reviewed by:
Qiang Sun,
Zhengzhou University, China
Lei Hu,
University of Science and Technology Beijing, China

***Correspondence:**
Mark S. Senn
m.senn@warwick.ac.uk

Specialty section:
This article was submitted to Physical Chemistry and Chemical Physics, a section of the journal Frontiers in Chemistry

Received: *03 July 2018*
Accepted: *13 September 2018*
Published: *18 October 2018*

Citation:
Ablitt C, Mostofi AA, Bristowe NC and Senn MS (2018) Control of Uniaxial Negative Thermal Expansion in Layered Perovskites by Tuning Layer Thickness. Front. Chem. 6:455. doi: 10.3389/fchem.2018.00455

1. INTRODUCTION

Ruddlesden–Popper (RP) oxides are an intriguing class of ceramic materials. They have the basic formula $A_{n+1}B_nO_{3n+1}$ and consist of a perovskite block of n corner sharing BO_6 octahedra separated by an AO rock salt layer. Blocks of octahedra are stacked perpendicular to the long crystallographic axis making this layering axis structurally distinct from the two in-plane axes. Neighboring blocks are de-phased from each other by a lattice translation of (0.5, 0.5, 0.5), and the aristotypical symmetry for any value of n is $I4/mmm$ (**Figure 1**). As with the perovskites, the A-site chemistry is dominated by larger alkali, alkali-earth, and rare earth metals, and the B-site by

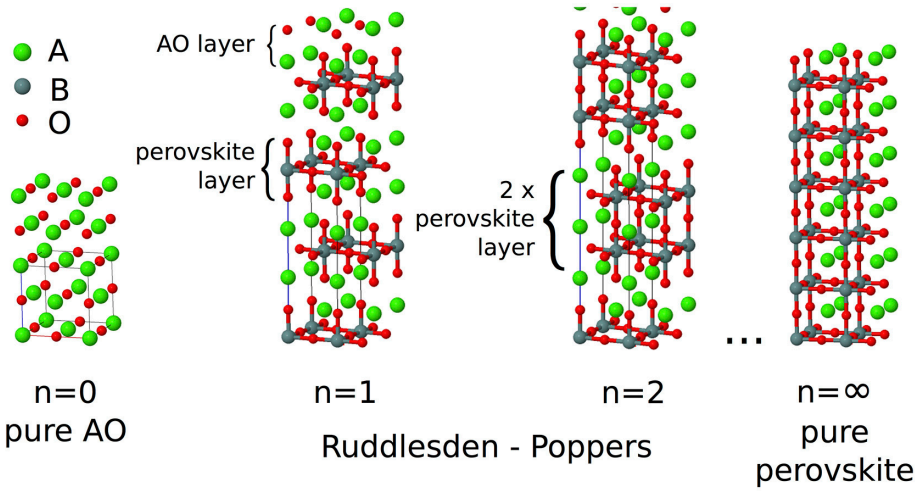

FIGURE 1 | In the $A_{n+1}B_nO_{3n+1}$ Ruddlesden–Popper series, blocks consisting of n layers of ABO_3 perovskite structure are separated by a single layer of AO rock salt structure, with BO_6 octahedra in the next block displaced by a (0.5, 0.5, 0.5) lattice translation. In the $n = \infty$ limit the pure ABO_3 perovskite structure is recovered.

transition metals. In the limit $n = \infty$, the perovskite structure is recovered. While in practice most chemistries are found to predominantly exhibit the $n = 1, 2$ phases only (Palgrave et al., 2012), in principle any value of n between 1 and ∞ is possible; $n = 3$ structures have been synthesized by careful compositional control (Battle et al., 1998) and although $n > 3$ phases are often predicted to be unstable to decomposition (McCoy et al., 1997), epitaxial growth techniques have allowed the synthesis of $n = 2-5$ (Haeni et al., 2001), $n = 6$ (Yan et al., 2011), and $n = 10$ (Lee et al., 2013) structures.

One of the most explored systems is the $n = 1$ A_2CuO_4 on account of its high-temperature superconductivity, where doping of divalent A = Ba and Sr with trivalent rare earth cations has been extensively investigated (Dwivedi and Cormack, 1991). Superconductivity in these systems is not limited to the cuprates, and there has been substantial interest in Sr_2RuO_4 (Mackenzie and Maeno, 2003) on account of its superconducting phase transition below 0.8 K, and in $Sr_3Ru_2O_7$ for its nematic orbitally-ordered phase (Borzi et al., 2007). The doped nickelates have also been much studied due to their believed proximity to a superconducting phase transition, and their charge ordering physics (Yoshizawa et al., 2000). More recently, the $n = 2$ member of the RP family has received much attention on the account of a new form of improper ferroelectricity predicated in $Ca_3Mn_2O_7$ and $Ca_3Ti_2O_7$, termed hybrid improper ferroelectricity (Benedek and Fennie, 2011). This mechanism circumvents the so-called d^0 criterion for ferroelectricity, as it does not require an off-centring of cations to drive the phase transition. Instead, this off-centring (P) may occur as a slave process driven by an octahedral tilt (R_1) and rotation mode (R_2) of the parent structure that are inherently unstable in some of these systems. This leads to a so-called trilinear term $\beta R_1 R_2 P$ in the free energy expansion about the parent structure (Benedek et al., 2015) which, regardless of the sign of the coefficient β, as R_1 and R_2 are inherently unstable, leads to a non-zero value of the polarization P (either positive or negative depending on the sign of β).

Our contribution to this field of hybrid improper ferroelectricity was to provide experimental confirmation of this mechanism for the case of $Ca_3Ti_2O_7$ (Senn et al., 2015). However, our high-resolution powder diffraction data for $Ca_3Mn_2O_7$ revealed an added complexity. What was believed to be a single phase at room temperature, having the polar symmetry $A2_1am$, was in fact a mixture of this and a phase that we identified as having $Acaa$ symmetry. Crucially, this phase only has a single octahedral rotation that is out-of-phase rather than in-phase, and the octahedra remain untilted along the c-axis. No hybrid improper ferroelectric mechanism is therefore possible. However, over the large phase coexistence region, which spans a temperature range of 120 K, we did observe pronounced uniaxial negative thermal expansion (NTE) along the c-axis in the $Acaa$ phase. This had not been observed previously in the $n = 2$ system and, although reported in the literature in an analogous $n = 1$ system (Takahashi and Kamegashira, 1993), its significance had not been noted. We were able to explain this NTE phenomenon as being driven by a leftover degree of freedom, the octahedral tilt in the $Acaa$ phase, which remains dynamic.

NTE is a rare property, that when it does occur is known to be caused by a diverse range of mechanisms in different materials. Even within inorganic perovskite-based systems, NTE has been found to originate due to coupling of the lattice parameters to: charge ordering (Azuma et al., 2011), ferroelectric ordering (Chen et al., 2013), and magnetic and orbital ordering via an invar-like mechanism (Yoshida et al., 2005, Qi et al., 2010). In framework structures, formed from connected strongly-bonded polyhedral units, NTE has been explained by transverse vibrations of these units, known as rigid-unit modes (RUMs) (Dove et al., 1995, Heine et al., 1999). We argued in $Acaa$ $Ca_3Mn_2O_7$ that certain vibrational modes with RUM character

would have negative Grüneisen parameters and be soft on account of the proximity of the system to the symmetry-forbidden phase transition to $A2_1am$ (Senn et al., 2015). Using this idea of "trapping" a soft mode in the *Acaa* phase of $Ca_3Mn_2O_7$ to systematically control and tune the uniaxial thermal expansion properties of the solid solution $Ca_{3-x}Sr_xMn_2O_7$ (Senn et al., 2016), we were able to demonstrate that this is a property exclusively of the *Acaa* phase in these materials, and that NTE is enhanced as the system approaches the $A2_1am$ phase boundary as a function of chemical composition x. Although other effects operate in related materials, in this study we restrict our discussion to NTE driven by the coupling of the cell parameters to soft lattice modes since it is the most appropriate mechanism to describe our system.

The presence of dynamic octahedral tilts in this $Ca_{3-x}Sr_xMn_2O_7$ system explained the thermodynamic driving force for NTE along the layering axis. However, the question remained open of why NTE was only observed in this *Acaa* phase with a frozen in-plane rotation and not in the high-symmetry $I4/mmm$ phase or related ABO_3 perovskite phases, where dynamic octahedral tilts would still operate. We were able to answer this question in a recent computational study using density functional theory (DFT) and working within the quasi-harmonic approximation (QHA) to reproduce experimentally measured uniaxial NTE in the $I4_1/acd$ phase of $n = 1$ Ca_2MnO_4 (Ablitt et al., 2017).

Equation (1) (Grüneisen and Goens, 1924) describes the thermal expansion, $\alpha_\eta(T)$, at temperature, T, of the three cell axes of a tetragonal crystal ($\eta = 1, 2, 3$ where $\alpha_1 = \alpha_2$ by symmetry). Equation (1) is explained in detail in **Appendix 1** and the concept of a Φ vector driving bulk PTE being transformed by a highly anisotropic $\boldsymbol{s}$ into uniaxial NTE (Barron and Munn, 1967) is depicted pictorially in **Figure 2**. In this picture, the anisotropic thermal expansion is separated into a thermodynamic driving force vector, Φ—arising from the lattice dynamics—that is transformed by the anisotropic elastic compliance matrix, $\boldsymbol{s}$. By computing the compliance matrix for our NTE phase, we were able to extract the thermodynamic driving force vector from our QHA simulation and found that the effect from dynamic tilts alone would not predict NTE over the wide temperature range observed in experiment. It is only when this thermodynamic driving force is transformed by the highly anisotropic elastic compliance of the layered RP phase that our simulations demonstrated uniaxial NTE of a magnitude and over a temperature range comparable to experiment. Comparing the compliance matrices computed for different phases, we found that particularly high anisotropic compliance is unique to the NTE phase of the RP structure and we linked this anisotropy to combined in-plane (frozen rotations) and out-of-plane (the AO layer) symmetry breaking in the NTE phase.

$$\begin{pmatrix} \alpha_1(T) \\ \alpha_1(T) \\ \alpha_3(T) \end{pmatrix} = \begin{pmatrix} s_{11} & s_{12} & s_{13} \\ s_{12} & s_{22} & s_{13} \\ s_{13} & s_{13} & s_{33} \end{pmatrix} \begin{pmatrix} \Phi_1(T) \\ \Phi_1(T) \\ \Phi_3(T) \end{pmatrix} \quad (1)$$

Until now, our research has focused on understanding uniaxial NTE in the low n RP compounds. In the present paper, we focus on extending these concepts to predict how the material properties that we have linked to NTE develop as a function of n. Studying the $Ca_{n+1}Ge_nO_{3n+1}$ system within the framework of DFT, we find that the magnitude of anisotropic elastic compliance is dependent upon the proportion of $CaGeO_3$:CaO interface in the structure—which may be conveniently expressed by the fraction $1/n$. This high compliance is then maximized with the highest proportion of interface ($n = 1$). To provide an explanation for this key result, we analyze how the components of the compliance matrix vary with $1/n$. We identify a series of regimes in which groups of structures display similar elastic behavior based on the atomic degrees of freedom allowed by symmetry, and propose mechanisms by which these internal degrees of freedom couple to cell strains. The most important of these is the atomic "corkscrew" mechanism that operates at this interface in the NTE phase. We go on to investigate how the frequencies of the softest (lowest frequency) octahedral tilt modes, which provide the thermodynamic driving force for NTE, vary as a function of n in the high-symmetry and NTE phases. We find that a higher proportion of interface causes these phonons to stiffen (increase in frequency) and we infer that within a given chemical composition, the layer thickness n provides a structural constraint on an approximate temperature window for which the NTE phase will be stable—where increasing n drives this window to higher temperatures. One may thus use this insight, combined with our previous discovery that chemical substitution

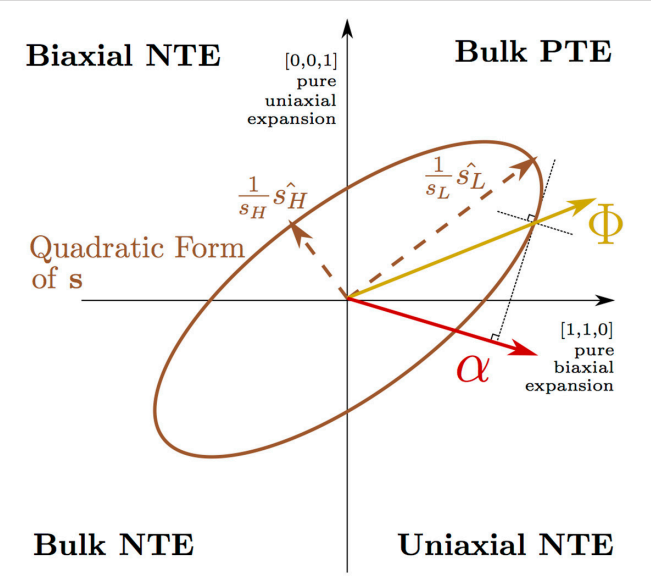

FIGURE 2 | Equation (1) is illustrated on axes describing normal cell deformations using Voigt notation (e.g., where the vector $[\epsilon, \epsilon, 0]$ corresponds to normal strains of ϵ of the *a* and *b* axes with the *c* axis unstrained). A 3 × 3 elastic compliance matrix $\boldsymbol{s}$ is shown here in its quadratic form as an ellipsoid projected onto the $(\bar{1}, 1, 0)$ plane. $\boldsymbol{s}$ may transform a vector describing the thermodynamic driving force for thermal expansion, $\boldsymbol{\Phi}$, in the positive quadrant (corresponding to bulk positive thermal expansion), into a thermal expansion vector, $\boldsymbol{\alpha}$, in the quadrant corresponding to uniaxial negative thermal expansion of the *c* axis. The direction of $\boldsymbol{\alpha}$ is given in the figure by utilizing the radius normal property of the representation ellipsoid of the matrix $\boldsymbol{s}$.

within a given structure may be used to tune the thermodynamic driving force for NTE, to use layer thickness n and composition as design parameters to engineer RP phases with optimal thermal expansion properties.

The layout of the paper is as follows: section 2 gives details of simulation parameters used in this work; section 3 is then split into four subsections: section 3.1 presents the key result of the paper, showing how the magnitude of anisotropic compliance, linked with uniaxial NTE, varies with $1/n$; for the more interested reader, sections 3.2 and 3.3 then take a step back and analyze the origin of the result in section 3.1 in more detail, in section 3.2 by analyzing how the different elements of the compliance matrix evolve with $1/n$ and in section 3.3 by identifying different compliance regimes linked to crystallographic degrees of freedom in the structure that couple to strain; finally in section 3.4 we consider how the thermodynamic driving force for NTE varies with $1/n$ by presenting lattice dynamics calculations investigating phonons corresponding to tilts of GeO_6 octahedra in $Ca_{n+1}Ge_nO_{3n+1}$, and compare these results against experimental phase diagrams constructed with data taken from the literature of the analogous $Ca_{n+1}Mn_nO_{3n+1}$ system. Additionally, in the associated Appendices file, **Appendix 1** gives a brief overview of the mathematical concepts relevant for the study of thermal expansion in an anisotropic material and **Appendix 2** outlines the symmetry of the phases simulated throughout this study.

2. METHODS

Calculations were performed using CASTEP, a plane-wave DFT code, version 7.0.3 (Clark et al., 2005). A plane wave cut-off energy of 1,400 eV was employed for all calculations with electron density stored on a grid twice as dense. A $7 \times 7 \times 2$ Monkhorst–Pack grid of kpoints shifted away from the Γ-point was used for calculations of the 14 atom $I4/mmm$ phase of ($n = 1$) Ca_2GeO_4, with grids of equivalent reciprocal space density used for all other structures (high-symmetry and rotation phases for $n = 1, 2, 3, 4, \infty$—see **Appendix 2**). Norm-conserving pseudopotentials, generated on-the-fly using CASTEP version 16.0, were used for all calculations and the associated pseudopotential strings may be found **Table S1** in the Supplementary Information. All calculations used the PBEsol exchange-correlation functional (Perdew et al., 2008). Absolute energies were converged to an accuracy of 0.5 meV/atom with respect to k-point grid density and plane wave cut-off energy. Geometric relaxations were performed with a force tolerance of 10^{-4} eV/Å and a stress tolerance of 10 MPa.

We expect our $Ca_{n+1}Ge_nO_{3n+1}$ system to be well-described by conventional GGA density functionals. There are other members of the chemical space that might require more careful consideration in terms of the appropriate methodology, such as hybrid functionals, DFT+U, or potentially even DMFT in order to accurately describe the physics associated with localized d and f-electrons.

Elastic constants were computed by fitting second order polynomials to the energies of cells with applied strains of ± 0.2, 0.4% from the fully relaxed cell, where the internal degrees of freedom (the atomic positions) were free to relax. The quadratic terms to these fits were used to construct terms within the elastic constant matrix, $\boldsymbol{c}$, and this matrix inverted to compute the elastic compliance matrix, $\boldsymbol{s}$ (see **Appendix 1** for the definition of $\boldsymbol{s}$ studied).

Bulk moduli, K, were computed by allowing the cell and all internal degrees of freedom to relax in response to hydrostatic pressures in the range -2 to $+2$ GPa. The bulk modulus was then found by fitting the computed relaxed volume, V, as a function of the external pressure, P, to the equation: $K = -\frac{d(ln[V])}{dP}$. The bulk compressibility, β, is then given by $\beta = K^{-1}$.

Density functional perturbation theory (DFPT) was used within CASTEP (Refson et al., 2006) to perform phonon calculations. In the present study, only phonon frequencies computed at single, high symmetry q-points are reported. In $n = 1, 3, \infty$ phases, these are at the X (½, ½, 0) and P (½, ½, ½) points in the $I4/mmm$ high-symmetry phase (labeled M and R, respectively, in $n = \infty$ $Pm\bar{3}m$ ABO_3) and for $n = 2, 4$ phases at the X-point in $I4/mmm$. Phonons in child rotation phases were always computed at the Γ-point. In every compound studied, the initial structure was the highest symmetry phase that was fully relaxed. All child phases were found by freezing unstable phonons (modes with imaginary frequencies) into the structure with small amplitudes and allowing this child structure to relax. The lattice parameters and cell energies relative to the high-symmetry parent of all relaxed structures may be found in **Table S2**.

3. RESULTS AND DISCUSSION

3.1. Anisotropy of the Compliance Matrix

It was previously shown in first-principles calculations performed on the NTE phase of Ca_2GeO_4 (i.e., the $I4_1/acd$ rotation phase) that a highly anisotropic $\boldsymbol{s}$ is an essential ingredient for uniaxial NTE in this system (Ablitt et al., 2017). κ, as defined in Equation (2), is the ratio of the highest (s_H) and lowest (s_L) eigenvalues of $\boldsymbol{s}$ and gives a measure of the anisotropy of $\boldsymbol{s}$; where higher κ indicates that $\boldsymbol{s}$ is more conducive to uniaxial NTE. **Figure 3** therefore shows how s_H, s_L, and κ evolve with varying n for high-symmetry and rotation phases in the $Ca_{n+1}Ge_nO_{3n+1}$ series.

$$\kappa = \frac{s_H}{s_L} \tag{2}$$

In the composite mechanics community, the elastic properties of laminates are typically described by the properties of the constituent phases, weighted by the relative fraction of that phase (Sarlosi and Bocko, 2016). However, in the functional oxides community, it is well known that the local structure of atomic interfaces within a crystal often dictate the physical properties of the entire material 2012. There are therefore two ways to conceive the layered RP structure shown in **Figure 1**: (i) as being comprised of constituent $CaGeO_3$ and CaO phases or (ii) as being comprised of $CaGeO_3$ and the $CaGeO_3$:CaO interface.

$$\begin{aligned} Ca_{n+1}Ge_nO_{3n+1} &= [CaGeO_3]_n\,[CaO] \\ &= [CaGeO_3]_{n-1}\,[CaGeO_3 : CaO] \end{aligned} \tag{3}$$

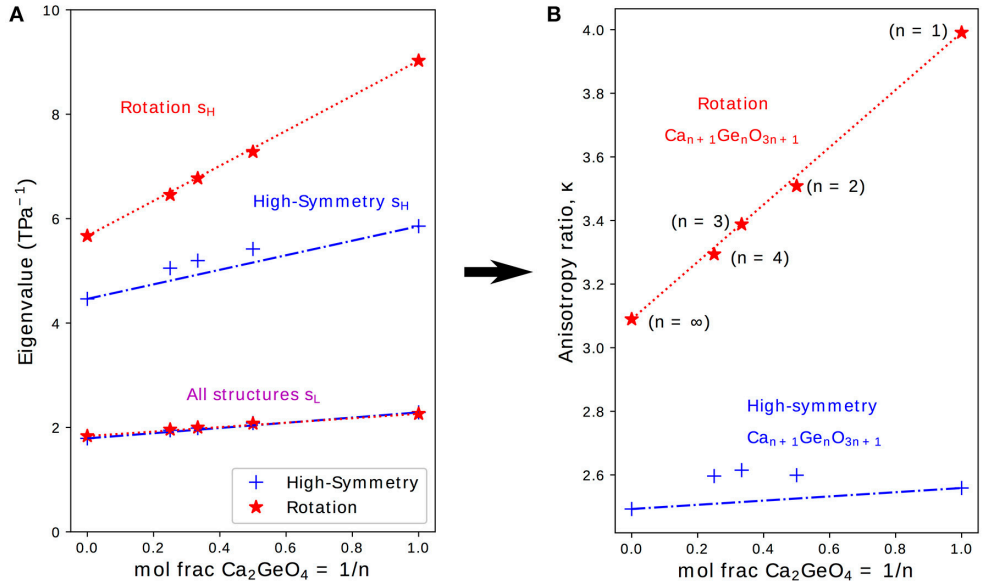

FIGURE 3 | (A) Lowest, s_L and highest, s_H, eigenvalues to the compliance matrix, $\boldsymbol{s}$, and **(B)** the anisotropy ratio κ plotted for high-symmetry and rotation phases in the $Ca_{n+1}Ge_nO_{3n+1}$ series against the mole fraction of $CaGeO_3$:CaO interface ($1/n$). Interpolations between values in the $CaGeO_3$ ($1/n = 0$) and Ca_2GeO_4 ($1/n = 1$) structures are plotted for both high-symmetry and rotation phases (blue dot-dashed and red dotted lines, respectively).

From Equation (3), it is clear that (i) the mole fraction of CaO in $Ca_{n+1}Ge_nO_{3n+1}$ is given by the ratio $1/(n+1)$ and (ii) the mole fraction of Ca_2GeO_4, which represents the fraction of $CaGeO_3$:CaO interface in the structure, is given by the ratio $1/n$. Therefore, to reflect the importance of the interface, s_H, s_L, and κ are plotted as a function of $1/n$ in the subplots on **Figure 3**. Straight lines have also been plotted interpolating between values for the $CaGeO_3$ ($1/n = 0$) and Ca_2GeO_4 ($1/n = 1$) end members to show how well the structure may be considered as a mixture of these two constituents in the high-symmetry (blue dot-dashed) and rotation (red dotted) phase series.

The least compliant eigenvector, s_L, corresponds to isotropic expansion/contraction for all structures investigated (see **Table S3**) and thus is closely linked to the bulk compressibility, β. **Figure 3** shows that s_L increases linearly with higher Ca_2GeO_4 mole fraction but is invariant to changes in symmetry for a given n. All values for s_L lie on the line interpolating between $CaGeO_3$ and Ca_2GeO_4 high-symmetry end members regardless of phase symmetry implying that s_L is determined mainly by the composition.

s_H also increases in magnitude with Ca_2GeO_4 content for all RP phases. However, unlike s_L, s_H is greatly enhanced in the phase with a frozen rotation compared to the high-symmetry phase, and the rate of increase in s_H for rotation phases with $1/n$ is also greater in the rotation phase than in the high-symmetry parent. For all the tetragonal phases studied, the eigenvector s_H lies in a strain direction corresponding to a cooperative increase in in-plane lattice parameters, *ab*, and decrease in the lattice parameter along the layering axis, *c*, or visa versa. In a previous work, we proposed an atomic mechanism to facilitate a large compliance eigenvector in RP phases with a frozen octahedral rotation that relies on combined in-plane and out-of-plane symmetry breaking at the $CaGeO_3$:CaO layer interface to closely couple the *ab* and *c* axes (Ablitt et al., 2017). Since this mechanism operates at the $CaGeO_3$:CaO interface, it is interesting to note that s_H in the rotation phase is linearly dependent upon the mole fraction of this interface in the structure, increasing as this interface fraction becomes greater, and thus s_H for intermediate values of $1/n$ may be easily predicted by interpolating between the s_H values for $CaGeO_3$ (with no interface) and Ca_2GeO_4 (maximum interface) rotation phases.

This steeper increase in s_H for rotation phases than high-symmetry phases with interface mole fraction ($1/n$) thus manifests as a large enhancement in κ between the child structure and parent, where the magnitude of this enhancement increases greatly with $1/n$, reaching a maximum in the $n = 1$ structure. The key result of this analysis of the compliances is hence that this $n = 1$ structure is the best in the Ruddelsden-Popper series for facilitating uniaxial NTE.

3.2. Elastic Compliances

Figure 3 showed how the eigenvalues of $\boldsymbol{s}$ vary with the $CaGeO_3$:CaO interface fraction ($1/n$). In this section we take a step back and analyse how the individual components of the compliance matrix, s_{ij}, vary with $1/n$. In the second half of the section, we assess the quality of the two interpolations, (i) between $CaGeO_3$ and CaO constituents and (ii) between $CaGeO_3$ and $CaGeO_3$:CaO interface constituents, to predict the compliance components of intermediate values of $1/n$.

Figure 4 shows the elastic compressibility, β, and components of the elastic compliance matrix, $\boldsymbol{s}$, computed for fully relaxed high-symmetry and rotation phases in the $Ca_{n+1}Ge_nO_{3n+1}$

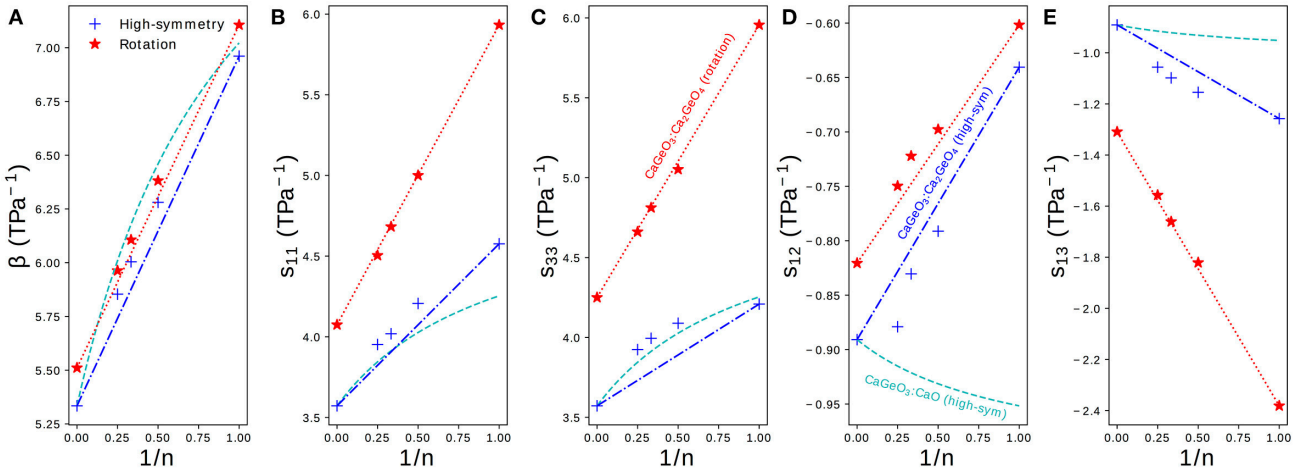

FIGURE 4 | (A) The bulk compressibility, β and **(B–E)** components s_{ij} of the elastic compliance matrix for a tetragonal material plotted for high-symmetry and rotation phases in the $Ca_{n+1}Ge_nO_{3n+1}$ series against the mole fraction of $CaGeO_3$:CaO interface ($1/n$). Interpolations between values in the $CaGeO_3$ ($1/n = 0$) and Ca_2GeO_4 ($1/n = 1$) structures are plotted for both high-symmetry and rotation phases (blue dot-dashed and red dotted lines, respectively). A third curve shows the interpolation between values in the $Pm\bar{3}m$ $CaGeO_3$ phase and CaO rock salt structure computed as a function of CaO mole fraction $1/(n+1)$ (cyan dashed).

series. Since all phases are (pseudo-)tetragonal, only the four symmetrically distinct s_{ij} components identified in Equation (1) are plotted. The full $\boldsymbol{s}$ matrix, associated eigenvalues and eigenvectors and β may be found for all structures in **Table S3**.

The bulk elastic compressibility, β, increases linearly with $1/n$ but only very slight enhancement in compressibility is seen between the high-symmetry and rotation phases for a given n. Differences in β can therefore not be used to explain why uniaxial NTE is common in low n RP rotation phases but not in parent $I4/mmm$ phases.

The normal compliance components, s_{11} and s_{33}, also increase with $1/n$ but unlike in β there is a significant enhancement in the rotation phase compared to the high-symmetry parent, with both the magnitude and gradient with respect to $1/n$ greater in the rotation phase.

The sign of the off-diagonal compliance components, s_{12} and s_{13}, that couple normal stresses to normal strains between axes, are negative for all compounds. This indicates that all materials have all positive Poisson ratios, ν_{ij}, where ν_{ij} describes the normal strain of axis j in response to a strain of axis i ($\nu_{ij} = -\frac{\varepsilon_j}{\varepsilon_i}$). Most materials have $\nu_{ij} > 0$, so these NTE RP phases are not auxetic ($\nu_{ij} < 0$), even though auxetic materials have been linked with materials that exhibit anisotropic NTE (Wang et al., 2017).

Despite the negative sign, the behavior of s_{13} is similar to that of s_{11} and s_{33}: compliance increases with $1/n$ and there is a large enhancement in both the magnitude and the gradient increase with $1/n$ in the NTE phase compared with the high-symmetry parent. s_{12}, on the other hand, displays the opposite trend since the magnitude of coupling decreases with $1/n$ and going from the high-symmetry to rotation phases.

As in **Figure 3**, straight lines have been plotted on the subplots in **Figure 4** interpolating between values for the $CaGeO_3$ ($1/n = 0$) and Ca_2GeO_4 ($1/n = 1$) end members. A third dashed cyan line has been added to interpolate between the pure high-symmetry $CaGeO_3$ and CaO rock salt constituent phases. Because the mole fraction of CaO is actually expressed as $1/(n+1)$ (Equation 3) these lines appear curved when plotted against the $1/n$ x-axis.

The trend in β follows that that would be predicted by modeling the RP series as a laminate of $CaGeO_3$ and CaO, suggesting that β is determined predominantly by the composition. Since bulk volume thermal expansion, α, is proportional to the bulk compressibility, β, this implies that the magnitude of α is heavily dependent on chemistry. This result echoes recent work showing that experimental measurements of many thermodynamic properties of RP structures may be predicted by interpolating between values of their chemical constituents (Glasser, 2017).

Whereas, β could be approximated well as a function of CaO content for RP phases, s_{11} of high-symmetry phases increases above that predicted by the cyan curve. This indicates that even in the high-symmetry phase, the $CaGeO_3$ and CaO layers do not behave independently and are affected by the interface between them. The prediction for s_{33} based on the CaO content is quite good, which may be because s_{33} corresponds to deformations along the layering axis (with the a and b lattice parameters fixed) and therefore the different constituent layers are being stretched in series[1]. For both s_{11} and s_{33}, the rotation phases follow a linear relationship with $1/n$ and therefore may be considered dependent upon the fraction of $CaGeO_3$:CaO interface in the structure (red dotted line). However, in the high-symmetry phase the $n > 1$ values for both normal compliance components increase slightly beyond that predicted by interpolating between

[1]However, we note that under these conditions one should use a Voigt average to interpolate s_{33}, whereas by drawing a straight line of compliance vs mole fraction we have actually performed a Reuss interpolation. In **Figure S1** in the SI we show that a Voigt fit against CaO mole fraction is actually less close.

the extreme $CaGeO_3$ and Ca_2GeO_4 values (blue dot-dashed line). This is surprising since it is not immediately obvious how the structure of higher n compounds is different to local regions of $CaGeO_3$ and Ca_2GeO_4 and therefore what additional compliance mechanisms could operate.

For both s_{12} and s_{13}, modeling the compliance according to the mole fraction of CaO is a poor approximation, so much so that this prediction actually gives the wrong sign of the change in s_{12} with $1/n$.

3.3. Compliance Enhancement Mechanisms

In section 3.2 we showed that certain elastic properties, such as the bulk compressibility, β, are insensitive to small changes in crystal symmetry and may be accurately predicted by interpolating between the value of β in $CaGeO_3$ and CaO end member structures based on the mole fraction of CaO. However, components of the anisotropic compliance matrix, s_{ij}, typically differ in magnitude between high and low symmetry phases and are generally more compliant than a $CaGeO_3$:CaO interpolation predicts. **Figure 5** shows the same plot as in **Figure 4E** (s_{13} vs. $1/n$) but with annotations decomposing the s_{13} behavior of different structures into regimes of increasingly enhanced compliance. By separating the compliance regimes in this way, in this section we discuss the atomic displacements allowed in each regime by the phase symmetry and thus propose atomic mechanisms that may explain these enhancements in the s_{13} axis coupling parameter. In many cases (although not discussed here) this analysis may be used to explain the different regimes of the s_{11}, s_{33}, and s_{12} components in **Figure 4**.

Taking the value of s_{13} that would be predicted by interpolating between values in the $CaGeO_3$ and CaO constituent structures as a base (the dashed cyan curve in **Figure 5**), arrow (1) represents an increase in the coupling between in-plane (a and b) axes and the layering axis (c) in the $n = 1$ Ca_2GeO_4 $I4/mmm$ phase. In a pure cubic ABO_3 perovskite, the A cations by symmetry have the same z position as the apical O anions. However, the inclusion of the AO layer in high-symmetry RP phases causes symmetry breaking along c at the ABO_3:AO interface such that the apical O and interfacial A ions are no longer restricted to the same z coordinate, leading to a so-called "rumpling" of the AO layer. We propose that this rumpling facilitates a mechanism for enhanced s_{13} coupling illustrated in **Figure 6A**: As the in-plane, ab, axes are strained, the interstitial void between BO_6 octahedra below the interfacial A cation changes in size, but the rumpling adds a degree of freedom to the z coordinate of the A cation which may thus move further into/out of the void in response to the in-plane strain. This thus couples the in-plane, ab, axes to internal displacements along the layering axis c and therefore to the layering axis itself.

It was commented in the preceding section that the enhancement in compliance from the interpolation between $CaGeO_3$ and Ca_2GeO_4 values to $n > 1$ high-symmetry RP structures (shown by arrow (2) in **Figure 5**) is surprising since all structures consist of a $CaGeO_3$:CaO interface (with rumpling of the CaO z positions) and blocks of $CaGeO_3$ (that one might expect to behave as bulk cubic $CaGeO_3$). Close inspection of the $n = 1$ and $n = 2$ $I4/mmm$ phases in **Figure 1** allows us to see that in A_2BO_4 structures, the length of all apical B–O bonds are equal due to the mirror symmetry plane lying in each BO_6 layer. Similarly the angle between epitaxial B–O and apical B–O bonds must be 90° by the same reasoning. However, in $A_3B_2O_7$ $I4/mmm$ phases, this restriction that the perovskite blocks must contain a mirror plane at the centre only means that the two outer apical B–O bond lengths and BO_6 internal angles must be equal and the apical B–O bond lengths between the two inner BO_6 layers must be equal. There is no restriction by symmetry that all apical B–O bond lengths must be equal or in fact that all BO_6 internal angles must be 90°. These weaker restrictions create internal degrees of structural freedom that may facilitate greater compliance, since there is greater freedom for the atoms to move in response to external strains. In structures relaxed using DFT, we find that there are slight differences in these two bondlengths: 1.87 and 1.90 Å for the outer and inner apical B–O bonds, respectively, and the angle between outer apical B–O and epitaxial B–O bonds is 91.2°. This same argument may be applied to all $n > 1$ $I4/mmm$ phases. However, in the special case of the $n = \infty$ series end member, there is no AO layer to break any symmetry along c and thus all B–O bond lengths are equal and all O–B–O angles are 90°. That this difference between s_{13} of $n = 2, 3, 4$

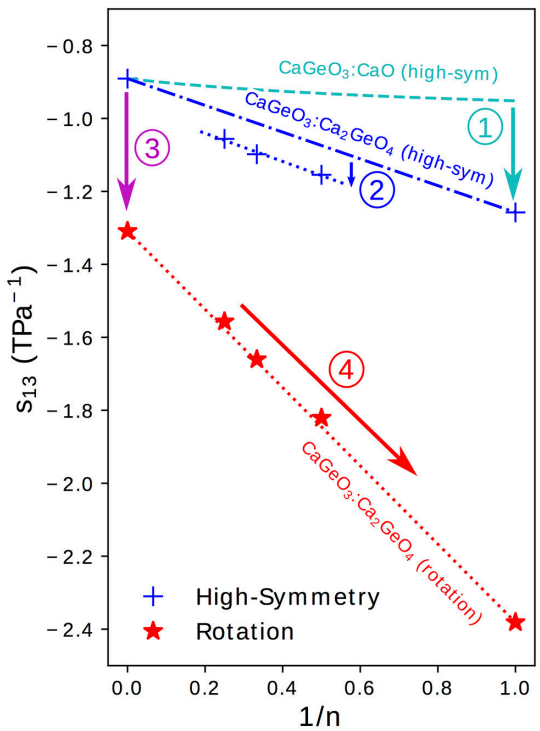

FIGURE 5 | The s_{13} term of the elastic compliance matrix (corresponding to coupling between an in-plane axis, *a* or *b*, and the layering axis, *c*) for a tetragonal material plotted for high-symmetry and rotation phases in the $Ca_{n+1}Ge_nO_{3n+1}$ series against the mole fraction of $CaGeO_3$:CaO interface ($1/n$). Numbered arrows show the enhancement in compliance between different regimes represented by lines.

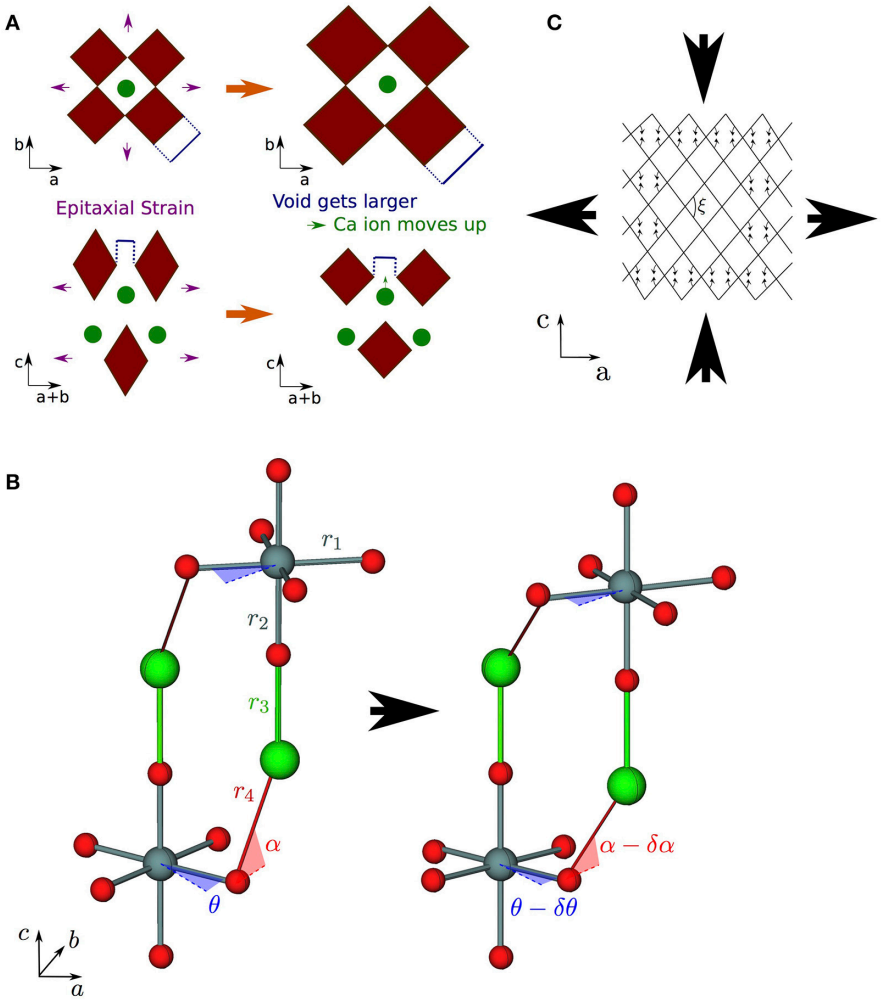

FIGURE 6 | Strain coupling mechanisms that make structures particularly compliant to cooperative strains. Since these mechanisms couple the *a* (and/or *b*) and *c* axes, they are typified by large s_{13} off-diagonal components of the compliance matrix. **(A)** Mechanism for increased compliance in *I*4/*mmm* RP structures where the rumpling between the interfacial A and apical O ions means that A is free to displace independently of O in response to in-plane strains; **(B)** corkscrew mechanism in RP rotation phases—the structure is able to couple in-plane tensile strains to compressive strains along *c* via internal displacements assuming all nearest neighbor B–O bonds and the two shortest A–O bonds do not deform (shown as rigid struts labeled r_1–r_4) by changing the angle of in-plane and out-of-plane hinges (described by the angles θ and α as shown); **(C)** wine rack structure where tensile strains along *a* may couple to compressive strains along *c* in a system of rigid struts in a trellis structure by only changing the angle ξ.

high-symmetry phases and the $CaGeO_3$:Ca_2GeO_4 interpolation is not also seen in the significantly more compliant rotation phases may be because in these rotation phases, additional compliance mechanisms operate that dwarf the effect described by arrow (2).

Arrow (3) in **Figure 5** represents the increase in coupling between the *a*/*b* and *c* axes from the cubic $CaGeO_3$ phase to an *I*4/*mcm* phase with anti-phase octahedral rotation about the *c* axis. From a structural symmetry point of view, this may again come as a surprise since the *I*4/*mcm* phase only has an internal degree of freedom in the *ab* plane and not along the *c* axis that this plane couples to. Therefore, one might expect large changes in in-plane strain in response to biaxial stress from rigid BO_6 octahedra rotating, but not also large changes in *c*. However, DFT studies on $LaAlO_3$ (Hatt and Spaldin, 2010) and $LaNiO_3$ (Weber et al., 2016) show that while the application of compressive biaxial strain to *I*4/*mcm* phases causes the rotation angle to increase, it also leads to a large tetragonal distortion of the BO_6 units with compression of the epitaxial B–O bonds and extension of the apical B–O bonds.

Finally, arrow (4) in **Figure 5** represents the increase in s_{13} coupling between rotation phases of $CaGeO_3$ perovskite and RP phases with a frozen octahedral rotation. In these phases, the rumpling of the interfacial AO layer identified in the high-symmetry structure is still present. However, whereas in the high-symmetry structure, in-plane strains necessarily involved deformations of stiff epitaxial B–O bonds, in this lower-symmetry phase, the frozen in-plane octahedral rotation adds an internal

degree of freedom in the in-plane epitaxial O positions. There are thus internal degrees of freedom in both in-plane and layering axes in RP rotation phases. In our previous paper (Ablitt et al., 2017) we proposed a "corkscrew" mechanism to explain high s_{13} coupling in RP1 rotation phases but not in $I4/mcm$ ABO_3 phases. This coupling mechanism in theory allows a and c to deform cooperatively without extending the four most stiff cation-anion bonds identified in the $I4_1/acd$ Ca_2GeO_4 structure, by only changing two bond angles, labeled θ and α in **Figure 6B**. We call this mechanism corkscrew since an in-plane rotation leads to an extension along the rotation axis: **Figure 6B** shows how the in-plane rotation angle θ may decrease in response to a biaxial expansion, such that this in turn pulls the stiff O-A bond (shown as a rigid rod), decreasing the angle α and thus increasing the rumpling of the rock salt layer and forcing contraction along the c-axis.

The net result of these interfacial strain coupling mechanisms in RP phases, yielding an enhanced off-diagonal s_{13} compliance term, is rather reminiscent of the "wine-rack" mechanism such as that which operates in methanol monohydrate (Fortes et al., 2011). In the wine-rack trellis structure, shown schematically in **Figure 6C** with rigid struts but flexible hinges, a couples strongly to c, mediated by the hinge angle, ξ, in the ac plane. Following the method used to analyse the wine-rack (Grima and Evans, 2000) and other idealized geometries (Smith et al., 2000, Grima et al., 2012), we were able to derive the mechanical properties that our pure corkscrew mechanism would exhibit under the conditions that the four *stiff* bonds shown in **Figure 6B** indeed remained rigid and all resistance to strain came from a harmonic potential in the θ and α-hinges (Ablitt et al., 2018). Under these restrictions, a corkscrew model would have an s_{13} compliance parameter as a function of RP layer thickness, n, given by

$$s_{13} = -\frac{\mathrm{f}(\theta,\alpha)\ r_1^3}{\left[n\,k_\theta + k_\alpha\left(\frac{d\alpha}{d\theta}\right)^2\right]}, \tag{4}$$

where k_θ and k_α represent the harmonic stiffness of the θ and α-hinges, respectively, and $\mathrm{f}(\theta,\alpha)$ is an expression of trigonometric functions of θ and α

$$\mathrm{f}(\theta,\alpha) = \frac{\sin(2\theta)\,[\sin(\theta)+\cos(\theta)]}{4\tan(\alpha)}. \tag{5}$$

Under the constraints of this model, α is explicitly dependent on θ by the equation

$$r_4\cos(\alpha) = r_1\,[\cos(\theta)-\sin(\theta)]\,, \tag{6}$$

and therefore given the bond lengths r_1-r_4 (as defined in **Figure 6B**), the value of θ fully determines the structure.

In the limit that $k_\alpha >> k_\theta$, the AO interface is stiffer than the ABO_3 perovskite blocks and s_{13} loses dependence on n. However, in the opposing limit that $k_\theta >> k_\alpha$ and changing the in-plane rotation angle is the main obstacle to strain, $s_{13} \propto 1/n$. The real system is closer to the $k_\theta >> k_\alpha$ limit as we observe linear behavior of s_{13} with $1/n$. Although this model has been derived assuming that all equatorial B–O bond lengths (r_1) and all apical B–O bond lengths (r_2) are equal, the bond lengths r_2 and r_3 do not feature in Equation (4) and r_1 and θ only need refer to the in-plane bond lengths and rotation angle in the outer layer of the perovskite block. Therefore, this mechanism is compatible with a distribution of possible bond lengths and rotation angles in different layers of a perovskite block if $n > 1$.

We accept the limitations of such simple models but developing the study of how symmetry-allowed local distortions can give rise to new compliance mechanisms in different crystallographic phases, such as those identified using arrows (1)–(4) in **Figure 5**, may allow for the prediction of phases with high cross compliances by symmetry alone, before needing to explicitly compute the elastic constants. Calculations of elastic constants are, in turn, frequently less expensive than performing lattice dynamics calculations across the full Brillouin zone to compute the thermodynamic driving force for anisotropic thermal expansion, Φ.

Therefore, looking for other materials with such high cross compliances, using symmetry analysis as a guide to narrow the pool of structures, may prove a more general method for searching for novel NTE materials. Indeed, by considering this analysis and our thermodynamic criteria requiring a proximity to a competing phase transition to provide Φ, we have already been able to identify (Ablitt et al., 2017) the layered double perovskites Sr_2MgWO_6 (Achary et al., 2006) and (110)-cut perovskite $LaTaO_4$ (Cordrey et al., 2015) which fall within this general paradigm. Substantial research opportunities exist in this area to more fully explore the NTE behavior of these classes of materials.

3.4. Dynamic Driving Force for NTE

So far we have not addressed the thermodynamic driving force for thermal expansion $\Phi(T)$, and it is rather more computationally expensive to calculate than κ as it requires the full phonon density of states to be computed for different strained structures within the QHA. Furthermore, this procedure is only possible if all phonons within the NTE structure simulated using DFT have real frequencies—suggesting that the phase must be stable at 0 K. For $n > 1$ structures in the $Ca_{n+1}Ge_nO_{3n+1}$ series, this latter condition is not met, and therefore full computation of $\Phi(T)$ as we performed previously (Ablitt et al., 2017) would not be possible. However, we also previously identified that the most important modes driving NTE are octahedral tilts about an in-plane axis. Thus in **Figure 7** we have plotted the frequency of the lowest frequency tilt mode to occur at a high-symmetry q-point in high-symmetry phases and phases with a frozen in-plane rotation. We note that these tilts are not the same as the vibrations of ions along the z direction predicted using a QHA-inspired method to cause NTE in a $A2_1am$ $Ca_3Ti_2O_7$ phase after 30 GPa hydrostatic pressure has been applied and in which these octahedral tilts are already frozen (Huang et al., 2016). As in previous studies (Senn et al., 2016, Ablitt et al., 2017) the $Ca_{n+1}Ge_nO_{3n+1}$ series is being treated as an analog to $Ca_{n+1}Mn_nO_{3n+1}$ for comparison against experimental data to avoid expensive magnetic calculations since Ge^{4+} and Mn^{4+} are

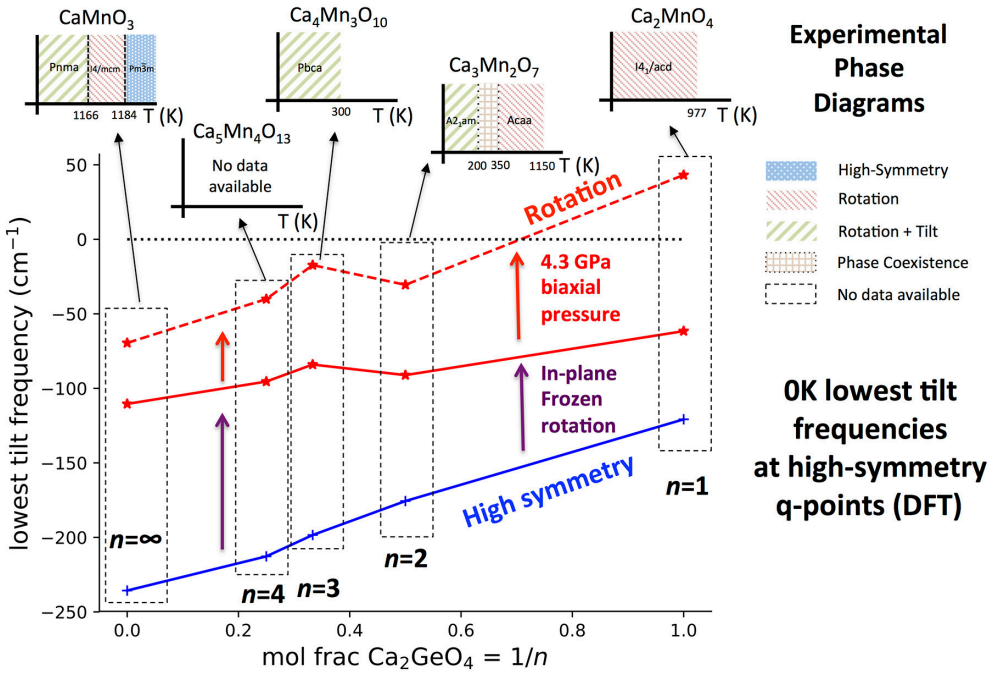

FIGURE 7 | The lowest frequency harmonic phonon mode with octahedral tilt character found in DFT simulations at high-symmetry q-points in the $Ca_{n+1}Ge_nO_{3n+1}$ series against interface fraction, $1/n$. Tilt frequencies have been plotted in the high-symmetry and rotation phases with 0 GPa external pressure, and also for the rotation phase with a 4.3 GPa biaxial pressure applied to give better agreement of the $Ca_{n+1}Ge_nO_{3n+1}$ structure to $Ca_{n+1}Mn_nO_{3n+1}$. DFT only simulates the system at 0 K whereas phonon frequencies may harden with increased temperature. This means that many octahedral tilts are predicted with imaginary frequencies (shown as negative) even if the mode has a real frequency and the structure is stable at some higher temperature. To give an idea of how the equilibrium phase changes with temperature, the inset graphs plot the experimentally observed phase diagram for each n in the $Ca_{n+1}Mn_nO_{3n+1}$ system. The data to make these illustrations was taken from: Ca_2MnO_4 (Takahashi and Kamegashira, 1993); $Ca_3Mn_2O_7$ (Senn et al., 2015); $Ca_4Mn_3O_{10}$ (Battle et al., 1998); $CaMnO_3$ (Taguchi et al., 1989).

known to have equal ionic radii (Shannon, 1976). The authors have previously shown that this substitution has little bearing on the properties (phonon frequencies, elastic constants) relevant to modeling thermal expansion within the QHA.

It can be seen from **Figure 7** that in all phases, the frequency of the softest tilt mode stiffens with increased Ca_2GeO_4 content, indicating that the inclusion of the $CaGeO_3$:CaO interface reduces the propensity of octahedra to tilt. The tilt mode is unstable (has an imaginary frequency) in all high-symmetry parent phases, which is unsurprising since these phases are not observed experimentally at low temperatures at any n for the $Ca_{n+1}Mn_nO_{3n+1}$ series. The tilt stiffens between the parent and child phases for all n, showing that the dynamic tilt couples competitively with the frozen in-plane rotation. In both the high- and low-symmetry phases, the (imaginary) octahedral tilt frequency varies approximately linearly with Ca_2GeO_4 mole fraction, although the stiffening effect going between the high- and low- symmetry phases becomes greater at higher n (lower Ca_2GeO_4 fraction). The CaO rock salt layer also stiffens octahedral rotations and thus the angle of the frozen rotation increases with n in rotation phases from 10.55° in $I4_1/acd$ Ca_2GeO_4 ($n = 1$) up to the limit of 12.7° in $I4/mcm$ $CaGeO_3$ ($n = \infty$; see **Figure S2**). Hence, the greater amplitude of frozen rotation observed in $CaGeO_3$ means that the competitive coupling between the frozen rotation and dynamic tilt is greatest for this largest n member, and leads to further hardening of the dynamic tilt frequency.

In the 0 GPa relaxed $Ca_{n+1}Ge_nO_{3n+1}$ structures, the tilt is still unstable for all n. However, it was found previously (Ablitt et al., 2017) that a discrepancy arises between the Ca_2GeO_4 and Ca_2MnO_4 in-plane lattice parameters in the $I4_1/acd$ phase—due to in-plane magneto-strictive coupling—but that applying a biaxial 4.3 GPa pressure corrects for this small difference, yielding very close agreement in the frequencies of the softest phonon modes. After applying this biaxial pressure, the $n = 1$ $I4_1/acd$ Ca_2GeO_4 rotation phase has all real mode frequencies, but the softest tilt in all structures with $n > 1$ is still unstable. This agrees with experimental observation of the low temperature stable phases, shown as inset figures for each composition on **Figure 7**.

$Ca_3Mn_2O_7$ is found at low temperature in the improper ferroelectric $A2_1am$ phase, but undergoes a wide temperature region of phase coexistence with the uniaxial NTE $Acaa$ phase between 150 and 280 K on cooling and 300 and 360 K on heating (Senn et al., 2015). The strong first order nature of the phase transition arises because frozen octahedral rotations in the $A2_1am$ and $Acaa$ phases have opposite sense (in-phase vs. out-of-phase about c within each perovskite layer—see **Figure A1** in Appendix 2) but the approximate transformation temperature gives an indication of the temperature at which octahedral tilts

in a rotation phase develop real frequencies. Furthermore, the $n = \infty$ perovskite, $CaMnO_3$, transforms around 1166 K from a *Pnma* ground state with frozen octahedral tilts, to an $I4/mcm$ phase with only an out-of-phase octahedral rotation—the $n = \infty$ analog of the $n = 2$ *Acaa*—remaining in this phase for only a brief temperature window before transforming again to the cubic parent structure at 1,184 K (Taguchi et al., 1989). For $n = 3$, the reported symmetry for $Ca_4Mn_3O_{10}$ from 5 K up until room temperature is *Pbca* (Battle et al., 1998), in which a static rotation and tilt of the octahedra are present, and, although to the best of our knowledge a transformation to a higher-symmetry phase with only a frozen octahedral rotation has not yet been reported[2], interpolating the experimental observations in **Figure 7** predicts a transformation temperature in the 250–1,100 K window. The magnitude of the imaginary tilt frequency computed in **Figure 7** may therefore by interpreted as a crude indicator of the stability of the structure with condensed rotation and tilt and thus of the temperature required to transform to the higher-symmetry rotation phase.

As well as having optimal elastic anisotropy to facilitate uniaxial NTE, the $n = 1$ Ca_2MnO_4 $I4_1/acd$ phase has soft tilt modes at low temperatures providing a thermodynamic driving force for cooperative in-plane positive and out-of-plane NTE. This feature is not unique to the $n = 1$ structure however, since at some higher temperature all $Ca_{n+1}Mn_nO_{3n+1}$ compounds should transform to a phase in which the tilt frequencies are real and soft, at least over some temperature range. Furthermore, we have demonstrated previously in the $Ca_{3-x}Sr_xMn_2O_7$ system, that for a given layer thickness n, chemical substitution (changing x) may be used to alter the Goldschmidt tolerance factor and thus the frequencies of these octahedral tilts, switching between positive and negative uniaxial thermal expansion (Senn et al., 2016). Therefore, **Figure 7** shows that the RP structure, through the layer thickness n, determines a ballpark value for the 0 K tilt frequency in the uniaxial NTE phase, and thus a ballpark temperature window in which the NTE phase will be stable. Hence, given this structural constraint we may use chemical control to optimize the proximity of the structure to the phase transition and so enhance the NTE. In this respect, the $n = 1$ family member, since one may presume that it may be tuned chemically to arbitrary proximity to the competing phase transition, is the most promising candidate for exhibiting the largest NTE on account of the anisotropy with respect to its most and least compliant directions which we have shown is maximized for this system.

4. CONCLUSIONS

We have shown that the elastic anisotropy ratio, κ, found previously to be an essential ingredient for uniaxial NTE, increases linearly in the RP $Ca_{n+1}Ge_nO_{3n+1}$ series ($n = 1$, 2, 3, 4 $\ldots\infty$) with the $CaGeO_3$:CaO content (expressed by the ratio $1/n$), reaching a maximum in the structure with maximal interface ($n = 1$). By decomposing the components of the elastic compliance matrix for high-symmetry and NTE phases (with a frozen octahedral rotation about the layering axis) into different regimes that show similar trends with $1/n$, we have been able to link these regimes with internal degrees of freedom in the structure that allow atomic mechanisms to operate that couple to cell strains. The most important of these is the "corkscrew" mechanism that operates locally at the $CaGeO_3$:CaO interface in phases with a frozen octahedral rotation about the layering axis and therefore explains the trend that anisotropic compliance correlates with the fraction of interface in these phases. This local atomic compliance mechanism is analogous in certain ways to the wine-rack mechanism that operates in many much softer framework materials. The compliance matrices can be rapidly calculated by DFT methods and diagonalized to assess them for cross coupling terms that promote pronounced uni or biaxial NTE. This makes them suitable descriptors for high throughput computational searching for novel NTE materials, especially when symmetry constraints may be employed to narrow the space of candidate phases.

We further investigated the trend in frequency of octahedral tilts with RP layer thickness and found that the 0 K tilt frequencies in NTE or analogous structures become softer with increasing n. This implies that a window of stability of the NTE phase with soft active tilt modes exists at increasingly higher temperatures with higher n. We had previously shown that the thermodynamic driver for NTE for a given n might be tuned with chemical substitution, and we now show that the anisotropic compliance necessary for NTE in these systems is maximized for a high fraction of $CaGeO_3$:CaO interface layers in the structure. On the basis of this analysis, we thus predict that the $n = 1$ systems, such as Ca_2MnO_4, will be the RP systems in which the maximum NTE can be achieved via chemical substitution.

DATA AVAILABILITY STATEMENT

Data underlying this article can be accessed on figshare at DOI:10.6084/m9.figshare.6729287, and used under the Creative Commons Attribution licence.

AUTHOR CONTRIBUTIONS

CA performed the calculations and data analysis. All authors contributed to the design of the study and the analysis and interpretation of the results. The paper was drafted by CA and MS, and all authors contributed to its development into final form.

FUNDING

CA is supported by a studentship in the Centre for Doctoral Training on Theory and Simulation of Materials at Imperial College London funded by the EPSRC (EP/L015579/1). Calculations were performed on the Imperial College London high-performance computing facility. This work was supported

[2]Although we do note that the high-symmetry $I4/mmm$ parent structure has been stabilized at room temperature from solid state synthesis at high temperatures and pressures (Yu et al., 2001).

by the Thomas Young Centre under grant TYC-101. We are grateful to the UK Materials and Molecular Modelling Hub for computational resources, which is partially funded by EPSRC (EP/P020194/1). MS acknowledges the Royal Society for a fellowship.

REFERENCES

(2012). The interface is still the device. *Nat. Mater.* 11:91. doi: 10.1038/nmat3244

Ablitt, C., Craddock, S., Senn, M. S., Mostofi, A. A., and Bristowe, N. C. (2017). The origin of uniaxial negative thermal expansion in layered perovskites. *NPJ Comput. Mater.* 3:44. doi: 10.1038/s41524-017-0040-0

Ablitt, C., Senn, M. S., Bristowe, N. C., and Mostofi, A. A. (2018). A corkscrew model for highly coupled anisotropic compliance in Ruddlesden-Popper oxides with frozen octahedral rotations. *arXiv:1810.02697*.

Achary, S. N., Chakraborty, K. R., Patwe, S. J., Shinde, A. B., Krishna, P. S. R., and Tyagi, A. K. (2006). Anisotropic thermal expansion behavior in tetragonal Sr_2MgWO_6. *Mater. Res. Bull.* 41, 674–682. doi: 10.1016/j.materresbull.2005.07.025

Azuma, M., Chen, W. T., Seki, H., Czapski, M., Olga, S., Olga, K., et al. (2011). Colossal negative thermal expansion in $BiNiO_3$ induced by intermetallic charge transfer. *Nat. Commun.* 2:347. doi: 10.1038/ncomms1361.

Barron, T. H. K. and Munn, R. W. (1967). Analysis of the thermal expansion of anisotropic solids: application to zinc. *Philos. Magaz.* 15:85

Battle, P. D., Green, M. A., Lago, J., Millburn, J. E., Rosseinsky, M. J., and Vente, J. F. (1998). Crystal and magnetic structures of $Ca_4Mn_3O_{10}$, an $n = 3$ Ruddlesden-Popper compound. *Chem. Mater.* 10, 658–664. doi: 10.1021/cm970647r

Benedek, N. A., and Fennie, C. J. (2011). Hybrid improper ferroelectricity: a mechanism for controllable polarization-magnetization coupling. *Phys. Rev. Lett.* 106:107204. doi: 10.1103/PhysRevLett.106.107204

Benedek, N. A., Rondinelli, J. M., Djani, H., Ghosez, P., and Lightfoot, P. (2015). Understanding ferroelectricity in layered perovskites: new ideas and insights from theory and experiments. *Dalton Trans.* 44, 10543–10558. doi: 10.1039/C5DT00010F

Borzi, R. A., Grigera, S. A., Farrell, J., Perry, R. S., Lister, S. J. S., Lee, S. L., et al. (2007). Formation of a nematic fluid at high fields in $Sr_3Ru_2O_7$. *Science* 315, 214–217. doi: 10.1126/science.1134796

Chen, J., Wang, F., Huang, Q., Hu, L., Song, X., Deng, J., et al. (2013). Effectively control negative thermal expansion of single-phase ferroelectrics of $PbTiO_3$-(Bi,La)FeO_3 over a giant range. *Sci. Rep.* 3: 2458. doi: 10.1038/srep02458

Clark, S. J., Segall, M. D., Pickard, C. J., Hasnip, P. J., Probert, M. J., Refson, K., et al. (2005). First principles methods using CASTEP. *Z. Kristall.* 220, 567–570. doi: 10.1524/zkri.220.5.567.65075

Cordrey, K. J., Stanczk, M., Dixon, C. A. L., Knight, K. S., Gardner, J., Morrison, F. D., et al. (2015). Structural and dielectric studies of the phase behaviour of the topological ferroelectric $La_{1-x}Nd_xTaO_4$. *Dalton Trans.* 44, 10673–10680. doi: 10.1039/C4DT03721A

Dove, M. T., Heine, V., and Hammond, K. D. (1995). Rigid unit modes in framework silicates. *Min. Mag.* 59, 629–639.

Dwivedi, A., and Cormack, A. N. (1991). Crystal chemistry of ruddlesden-popper type structures in high Tc ceramic superconductors. *Bull. Mater. Sci.* 14, 575–584. doi: 10.1007/BF02744688

Fortes, A. D., Suard, E., and Knight, K. S. (2011). Negative linear compressibility and massive anisotropic thermal expansion in methanol monohydrate. *Science* 331, 742–746. doi: 10.1126/science.1198640

Glasser, L. (2017). Systematic thermodynamics of layered perovskites: Ruddlesden–Popper phases. *Inorgan. Chem.* 56, 8920–8925. doi: 10.1021/acs.inorgchem.7b00884

Grima, J. N., Caruana-Gauci, R., Attard, D., and Gatt, R. (2012). Three-dimensional cellular structures with negative Poisson's ratio and negative compressibility properties. *Proc. R. Soc. Lond. A* 468, 3121–3138. doi: 10.1098/rspa.2011.0667

Grima, J. N. and Evans, K. E. (2000). Auxetic behavior from rotating squares. *J. Mater. Sci. Lett.* 19, 1563–1565. doi: 10.1023/A:1006781224002

Grüneisen, E. and Goens, E. (1924). Thermal expansion of zinc and cadmium. *Z. Phys.* 29:141

Haeni, J. H., Theis, C. D., Schlom, D. G., Tian, W., Pan, X. Q., Chang, H., et al. (2001). Epitaxial growth of the first five members of the Srn+1TinO3n+1 Ruddlesden-Popper homologous series. *Appl. Phys. Lett.* 78, 3292–3294. doi: 10.1063/1.1371788

Hatt, A. J. and Spaldin, N. A. (2010). Structural phases of strained $LaAlO_3$ driven by octahedral tilt instabilities. *Phys. Rev. B.* 82:195402. doi: 10.1103/PhysRevB.82.195402

Heine, V., Welche, P. R. L., and Dove, M. T. (1999). Geometrical origin and theory of negative thermal expansion in framework structures. *J. Am. Ceramic Soc.* 82, 1793–1802. doi: 10.1111/j.1151-2916.1999.tb02001.x

Huang, L.-F., Lu, X.-Z., and Rondinelli, J. M. (2016). Tunable negative thermal expansion in layered perovskites from quasi-two-dimensional vibrations. *Phys. Rev. Lett.* 117:115901. doi: 10.1103/PhysRevLett.117.115901

Lee, C.-H., Podraza, N. J., Zhu, Y., Berger, R. F., Shen, S., Sestak, M., et al. (2013). Effect of reduced dimensionality on the optical band gap of $SrTiO_3$. *Appl. Phys. Lett.* 102:122901. doi: 10.1063/1.4798241

Mackenzie, A. P., and Maeno, Y. (2003). The superconductivity of Sr_2RuO_4 and the physics of spin-triplet pairing. *Rev. Mod. Phys.* 75, 657–712. doi: 10.1103/RevModPhys.75.657

McCoy, M. A., Grimes, R. W., and Lee, W. E. (1997). Phase stability and interfacial structures in the SrO–$SrTiO_3$ system. *Philos. Magaz. A* 75, 833–846. doi: 10.1080/01418619708207205

Palgrave, R. G., Borisov, P., Dyer, M. S., McMitchell, S. R. C., Darling, G. R., Claridge, J. B., et al. (2012). Artificial construction of the layered Ruddlesden-Popper manganite $La_2Sr_2Mn_3O_10$ by reflection high energy electron diffraction monitored pulsed laser deposition. *J. Am. Chem. Soc.* 134, 7700–7714. doi: 10.1021/ja211138x

Perdew, J. P., Ruzsinszky, A., Csonka, G. I., Vydrov, O. A., Scuseria, G. E., Constantin, L. A., et al. (2008). Restoring the density-gradient expansion for exchange in solids and surfaces. *Phys. Rev. Lett.* 100:136406. doi: 10.1103/PhysRevLett.100.136406

Qi, T. F., Korneta, O. B., Parkin, S., De Long, L. E., Schlottmann, P., and Cao, G. (2010). Negative volume thermal expansion via orbital and magnetic orders in $Ca_2Ru_{1-x}Cr_xO_4$ ($0 < x < 0.13$). *Phys. Rev. Lett.* 105:177203. doi: 10.1103/PhysRevLett.105.177203

Refson, K., Tulip, P. R., and Clark, S. J. (2006). Variational density-functional perturbation theory for dielectrics and lattice dynamics. *Phys. Rev. B* 73:155114. doi: 10.1103/PhysRevB.73.155114

Sarlosi, J., and Bocko, J. (2016). Effective material moduli for composites. *Am. J. Mech. Eng.* 4, 289–292. doi: 10.12691/ajme-4-7-11

Senn, M. S., Bombardi, A., Murray, C. A., Vecchini, C., Scherillo, A., Lui, X., et al. (2015). Negative thermal expansion in hybrid improper ferroelectric Ruddlesden-Popper perovskites by symmetry trapping. *Phys. Rev. Lett.* 114:035701. doi: 10.1103/PhysRevLett.114.035701

Senn, M. S., Murray, C. A., Luo, X., Wang, L., Huang, F.-T., Cheong, S.-W., et al. (2016). Symmetry switching of negative thermal expansion by chemical control. *J. Am. Chem. Soc.* 138, 5479–5482. doi: 10.1021/jacs.5b13192

Shannon, R. D. (1976). Revised effective ionic radii and systematic studies of interatomic distances in halides and chalcogenides. *Acta Crystallogr.* A32, 751–767. doi: 10.1107/S0567739476001551

Smith, C., Grima, J., and Evans, K. (2000). A novel mechanism for generating auxetic behaviour in reticulated foams: missing rib foam model. *Acta Mater.* 48, 4349–4356. doi: 10.1016/S1359-6454(00)l00269-X

Taguchi, H., Nagao, M., Sato, T., and Shimada, M. (1989). High-temperature phase transition of $CaMnO_3$-δ. *J. Solid State Chem.* 78, 312–315. doi: 10.1016/0022-4596(89)90113-8

Takahashi, J., and Kamegashira, N. (1993). X-ray structural study of calcium manganese oxide by rietveld analysis at high temperatures. *MRS Bull.* 28, 565–573.

SUPPLEMENTARY MATERIAL

The Supplementary Material for this article can be found online at: https://www.frontiersin.org/articles/10.3389/fchem.2018.00455/full#supplementary-material

Wang, L., Luo, H., Deng, S., Sun, Y., and Wang, C. (2017). Uniaxial negative thermal expansion, negative linear compressibility, and negative Poisson's ratio induced by specific topology in $Zn[Au(Cn)_2]_2$. *Inorgan. Chem.* 56, 15101–15109. doi: 10.1021/acs.inorgchem.7b02416

Weber, M. C., Guennou, M., Dix, N., Pesquera, D., Sánchez, F., Herranz, G., et al. (2016). Multiple strain-induced phase transitions in $LaNiO_3$ thin films. *Phys. Rev. B.* 94:014118. doi: 10.1103/PhysRevB.94.014118

Yan, L., Niu, H. J., Duong, G. V., Suchomel, M. R., Bacsa, J., Chalker, P. R., et al. (2011). Cation ordering within the perovskite block of a six-layer ruddlesden-popper oxide from layer-by-layer growth - artificial interfaces in complex unit cells. *Chem. Sci.* 2, 261–272. doi: 10.1039/C0SC00482K

Yoshida, Y., Ikeda, S.-I., Matsuhata, H., Shirakawa, N., Lee, C. H., and Katano, S. (2005). Crystal and magnetic structure of $Ca_3Ru_2O_7$. *Phys. Rev. B* 72:054412. doi: 10.1103/PhysRevB.72.054412

Yoshizawa, H., Kakeshita, T., Kajimoto, R., Tanabe, T., Katsufuji, T., and Tokura, Y. (2000). Stripe order at low temperatures in $La_{2-x}Sr_xNiO_4$ with $0.289 \lesssim x \lesssim 0.5$. *Phys. Rev. B* 61, R854–R857. doi: 10.1103/PhysRevB.61.R854

Yu, R. C., Li, S. Y., Zhu, J. L., Li, F. Y., Zhang, Z., Jin, C. Q., et al. (2001). Ideal n=3 phase $Ca_4Mn_3O_{10}$ of Ruddlesden–Popper series obtained using high pressure and high temperature. *J. Appl. Phys.* 90, 6302–6306. doi: 10.1063/1.1419205

Conflict of Interest Statement: The authors declare that the research was conducted in the absence of any commercial or financial relationships that could be construed as a potential conflict of interest.

frontiers in Chemistry

ORIGINAL RESEARCH
published: 20 November 2018
doi: 10.3389/fchem.2018.00545

Negative Thermal Expansion Near the Precipice of Structural Stability in Open Perovskites

Connor A. Occhialini[1,2†], *Gian G. Guzmán-Verri*[3,4*], *Sahan U. Handunkanda*[1,2] *and Jason N. Hancock*[1,2*]

[1] Department of Physics, University of Connecticut, Storrs, CT, United States, [2] Institute of Materials Science, University of Connecticut, Storrs, CT, United States, [3] Centro de Investigación en Ciencia e Ingeniería de Materiales, Universidad de Costa Rica, San José, Costa Rica, [4] Materials Science Division, Argonne National Laboratory, Argonne, IL, United States

OPEN ACCESS

Edited by:
Andrea Sanson,
Università degli Studi di Padova, Italy

Reviewed by:
Fengxia Hu,
Institute of Physics (CAS), China
Ranjan Mittal,
Bhabha Atomic Research Centre, India

***Correspondence:**
Gian G. Guzmán-Verri
gian.guzman@ucr.ac.cr
Jason N. Hancock
jason.hancock@uconn.edu

†Present Address:
Connor A. Occhialini,
Department of Physics, Massachusetts Institute of Technology, Cambridge, MA, United States

Specialty section:
This article was submitted to Physical Chemistry and Chemical Physics, a section of the journal Frontiers in Chemistry

Received: 14 July 2018
Accepted: 19 October 2018
Published: 20 November 2018

Citation:
Occhialini CA, Guzmán-Verri GG, Handunkanda SU and Hancock JN (2018) Negative Thermal Expansion Near the Precipice of Structural Stability in Open Perovskites. Front. Chem. 6:545. doi: 10.3389/fchem.2018.00545

Negative thermal expansion (NTE) describes the anomalous propensity of materials to shrink when heated. Since its discovery, the NTE effect has been found in a wide variety of materials with an array of magnetic, electronic and structural properties. In some cases, the NTE originates from phase competition arising from the electronic or magnetic degrees of freedom but we here focus on a particular class of NTE which originates from intrinsic dynamical origins related to the lattice degrees of freedom, a property we term *structural* negative thermal expansion (SNTE). Here we review some select cases of NTE which strictly arise from anharmonic phonon dynamics, with a focus on open perovskite lattices. We find that NTE is often present close in proximity to competing structural phases, with structural phase transition lines terminating near T=0 K yielding the most prominent displays of the SNTE effect. We further provide a theoretical model to make precise the proposed relationship among the signature behavior of SNTE, the proximity of these systems to structural quantum phase transitions and the effects of phase fluctuations near these unique regions of the structural phase diagram. The effects of compositional disorder on NTE and structural phase stability in perovskites are discussed.

Keywords: negative thermal expansion, structural negative thermal expansion, quantum phase transition, structural phase transition, perovskite, antiferrodistortive phase transition, scandium trifluoride

1. INTRODUCTION

Thermal expansion is among the most widely recognized thermodynamic properties of materials. From a textbook perspective (Ashcroft and Mermin, 1976), thermal expansion occurs through anharmonic free energy terms arising from nuclear lattice degrees of freedom. The dominant appearance of the positive thermal expansion (PTE) found in both research-grade and industrial materials is heuristically ascribed (Barrera et al., 2005; Miller et al., 2009; Takenaka et al., 2012) to the expected anharmonic behavior of a generic interatomic potential, which is hard at short distance and soft at large distance (**Figure 1A**). As temperature is raised, higher energy excitations are populated which have an ever increasing mean separation, dilating the bond and presumably lattice dimensions. Of course this is not a theorem any more than crystals are molecules and collective motion of lattices permit various potential landscapes, such as a librational coordinate of tetrahedral molecular solids (Prager and Heidemann, 1997), which possess clear qualitative differences (**Figure 1B**).

Mention of negative thermal expansion (NTE), a material's tendency to shrink when heated, often evokes discussion of liquid water-ice expansion responsible for icebergs and the 4K temperature window above the ice-water phase boundary where phase fluctuations occur. This is an example of a route to achieving NTE which relies on broadened phase transitions between a low-temperature high-volume phase fluctuating into a high-temperature low-volume phase, other examples of which include the industrial alloy InVar (Guillaume, 1920) ($Fe_{64}Ni_{36}$) and more recently discovered NTE materials (Takenaka and Takagi, 2005; Azuma et al., 2011; Qu et al., 2012; Chen et al., 2013a,b) (for more details on this approach, see Takenaka's review in this volume Takenaka, 2018). While this route to realizing NTE is promising for many applications requiring only dimensional concerns, NTE at these broadened transitions occurs only in heavily restricted regions of the magnetic and electronic phase diagrams, constraining a thermodynamic number of degrees of freedom to achieve a single mechanical characteristic. Thus, these types of NTE materials will be severely restricted in their potential for multifunctional applications.

Remarkably, there exists a growing class of materials with strong, isotropic, robust, and thermally persistent NTE that arises from structural motifs (Martinek and Hummel, 1968; Mary et al., 1996; Evans et al., 1997a,b; Pryde et al., 1997; Ernst et al., 1998; Perottoni and Jornada, 1998; Ramirez and Kowach, 1998; Ramirez et al., 2000; Mittal et al., 2001, 2004, 2018; Cao et al., 2002, 2003; Ouyang et al., 2002; Drymiotis et al., 2004; Hancock et al., 2004b; Kennedy and White, 2005; Lee et al., 2005; Tucker et al., 2005, 2007; Pantea et al., 2006; Figueirêdo and Perottoni, 2007; Han and Goddard, 2007; Keen et al., 2007, 2011; Schlesinger et al., 2008; Zhou et al., 2008; Greve et al., 2010; Gallington et al., 2013, 2014; Gupta et al., 2013; Morelock et al., 2013b; Bridges et al., 2014; Sanson, 2014). NTE in these systems is often discussed in connection with transverse fluctuations of a linkage between volume-defining vertices, which may accompany the librational, or hindered rotational motion of polyhedral subunits. The energy landscape for such motion tends to be much softer (0–2 THz) than bond-stretching motion (10–30 THz in oxides) which is often the implicated culprit of PTE. Here, NTE arises from the cooperative fluctuations of the bond network on THz time scales under very strong anharmonic influences and appears without necessarily constraining the magnetic or electronic phase diagram, permitting one to envisage new multifunctional materials with diverse mechanical, spin, orbital, thermal, electronic, superconducting, and more exotic order coexisting with NTE. Study of the unusual physics behind this type of NTE informs discovery efforts to find new contexts for this remarkable phenomenon. In addition, NTE materials hold promising application potential in stabilizing fiber Bragg gratings for high-speed telecommunication (Fleming et al., 1997; Kowach and Ramirez, 2002), substrates for devices which benefit from thermally controlled stresses and the formation of rigid composite structural materials with engineered thermal characteristics through combinations of PTE and NTE components (Balch and Dunand, 2004; De Buysser et al., 2004; Lommens et al., 2005; Sullivan and Lukehart, 2005; Lind et al., 2011).

This second circumstance for NTE, which we term *structural* NTE (SNTE), is the focus of the present article. The field of SNTE has been met with sustained interest from the physics, chemistry, and materials science communities since the rediscovery of the strong SNTE in ZrW_2O_8 in 1996 (Martinek and Hummel, 1968; Mary et al., 1996). The SNTE effect here persists over the temperature range 4-1050 K and has a sizable linear coefficient of thermal expansion (CTE) of $\alpha_\ell \simeq -9$ ppm/K near room temperature, which is isotropic due to the cubic symmetry maintained at all observed temperatures under ambient pressure. The low-symmetry α-phase structure of ZrW_2O_8 (**Figure 1C**) consists of ZrO_6 octahedra and WO_4 tetrahedra in the $P2_13$ space group, which has a screw axis along [111]. An order-disorder structural transition to a (cubic) $Pm\bar{3}$ γ-phase occurs at zero pressure and $T_c \simeq 450$K. The NTE effect survives the structural transition, with a small discontinuity and reduction in the CTE to $\alpha_\ell \simeq -6$ ppm/K. Furthermore, application of hydrostatic pressure at $T = 300$K first induces an orthorhombic transition at $P_c = 0.3$ GPa, followed by pressure-induced amorphization realized between $P = 1.5-3.5$ GPa (Evans et al., 1997b; Perottoni and Jornada, 1998; Ravindran et al., 2001). Both the α- and γ-phases contain four formula units, $N = 44$ atoms, in each unit cell, leading to a complex phononic structure with 3 acoustic and $3N - 3 = 129$ optical branches.

Despite decades of intense research, the complex structure and associated dynamics of the ZrW_2O_8 lattice and the related MA_2O_8 compounds complicates the interpretation of both theoretical and experimental investigations into the mechanisms of SNTE. For instance, a commonly identified feature in the low-temperature α-phase is the two WO_4 tetrahedra with unshared "terminal" oxygen atoms aligned along the screw axis. The under-constrained freedom of these tetrahedra along this axis is often cited as being responsible for the softness of the crucial NTE modes, but there is much debate as to the precise nature of the mode and its contributions to NTE (Ramirez et al., 2000; Hancock et al., 2004b). Several attempts at describing the soft mode as either a translation or rotation of the WO_4 tetrahedron were addressed via the space group symmetry—both rotational and translational motion are permitted and necessarily coupled due to the lost inversion symmetry. Another level of controversy in ZrW_2O_8 is the extent to which the molecular subunits may be regarded as rigid (Cao et al., 2002; Tucker et al., 2007; Bridges et al., 2014; Sanson, 2014; Dove and Fang, 2016). Although ZrW_2O_8 presents clear scientific challenges, its discovery is significant in that it ignited a flurry of research into the microscopic origins of the SNTE, both theoretical and experimental, employing both thermodynamic (Ramirez et al., 2000) and spectroscopic (Ernst et al., 1998; Drymiotis et al., 2004; Hancock et al., 2004b; Pantea et al., 2006) probes of the low-energy lattice behavior. Some essential, guiding observations were revealed during the ensuing years: (i) ZrW_2O_8 has unusually low-energy lattice modes near 2-3meV (Ramirez et al., 2000; Hancock et al., 2004b), (ii) structural phase transitions are readily induced via light hydrostatic pressure (Evans et al., 1997b; Perottoni and Jornada, 1998; Ravindran et al., 2001) and (iii) the SNTE arises from a delicate balance of the degrees of freedom and constraint in the host lattice framework (Cao et al.,

2002; Tucker et al., 2007; Bridges et al., 2014; Sanson, 2014; Dove and Fang, 2016).

One central question motivating SNTE research is why some materials show SNTE and others do not? To address this question will open avenues to discovery of new NTE materials and advancing technology born from its unique properties. While the precise mechanisms behind the dramatic SNTE in ZrW_2O_8 are still under contention, a variety of other simpler systems with equally impressive SNTE have been discovered in recent years (Rodriguez et al., 2009; Greve et al., 2010; Hancock et al., 2015). In moving toward the goal of a deeper understanding of SNTE mechanisms, we sharpen our focus on the growing class of perovskite materials exhibiting NTE, including ScF_3, ReO_3 and related structural family members. We consider the rich structural phase diagrams of the perovskite structure and their description in terms of octahedral tilts and the corresponding slow lattice dynamics associated with the structural transitions. Although numerous, the hierarchy of phases is well understood and documented, making perovskites a particularly simple framework on which to study the interplay of lattice dynamics and macroscopic phenomena like NTE. In particular, we note how the corresponding dynamic modes of the perovskite lattice relate to soft-mode instabilities that accompany the approach to realized and incipient structural phase transitions and how these are coupled to mechanisms resulting in SNTE. Most importantly, we further develop the apparent connection between the emergence of SNTE alongside phase fluctuations that occur near T=0K structural quantum phase transitions (SQPTs), for which we present the available experimental evidence and develop a systematic modeling scheme to explain the coupling between phase fluctuations and thermal expansion anomalies in perovskite materials.

2. PEROVSKITES, STRUCTURAL PHASES AND SOFT-MODE INDUCED TRANSITIONS

The perovskite lattice structure may well be identified as the double-helix of the solid state–a framework which is highly functionalizable, tunable, robust, and underpins perhaps every known category of physical behavior. This includes high-temperature superconducting, itinerant ferromagnetic, local ferromagnetic, ferroelectric, insulating, metallic, glassy, as well as a plethora of antiferromagnetic and other poorly understood phases which appear to compete, coexist, and cooperate within typically rich and complex phase diagrams (Kimura et al., 2002; Maekawa et al., 2004; Takagi et al., 2010; Ngai et al., 2014). The cubic perovskites are lattice structures with formula unit ABX_3, where the A-site is typically an alkali or alkaline earth metal ion, B is a transition metal and X is the anion, most commonly forming an oxide or a halide. The highest-symmetry solid phase is shown below in **Figures 2A**, **3A**, with a cubic space group symmetry $Pm\bar{3}m$ and the B-site ions in an $n = 6$ octahedral coordination environment of X-site anions. A hierarchy of structural phases in the perovskites are achieved through various concerted rotations of the BX_6 coordination octahedra. These phases have been cataloged and a relationship between octahedral tilts and the lower-symmetry space groups due to these structural distortions have been developed (Glazer, 1972; Glazer and IUCr, 1975) and are well-known in the ferroelectric community (Benedek and Fennie, 2013).

The scheme for indexing the possible octahedral tilts begins with a 2 × 2 × 2 unit cell of the cubic $Pm\bar{3}m$ perovskite and considers rotations of the octahedra about each of the 3 fourfold (C_4) axes of the cubic phase. In the plane normal to a given rotation axis, neighboring octahedra are constrained to rotate at equal angles (θ) of opposite sign, since neighboring B-sites are

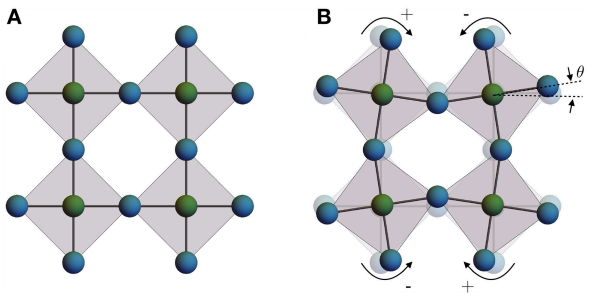

FIGURE 2 | (A) A single 2D layer of perovskite octahedra in the high-symmetry cubic phase, viewed along one of the 3 fourfold axes and **(B)** the same layer with a non-zero tilt angle θ, showing the constrained motion of neighboring octahedra due to shared inter-octahedral X-sites.

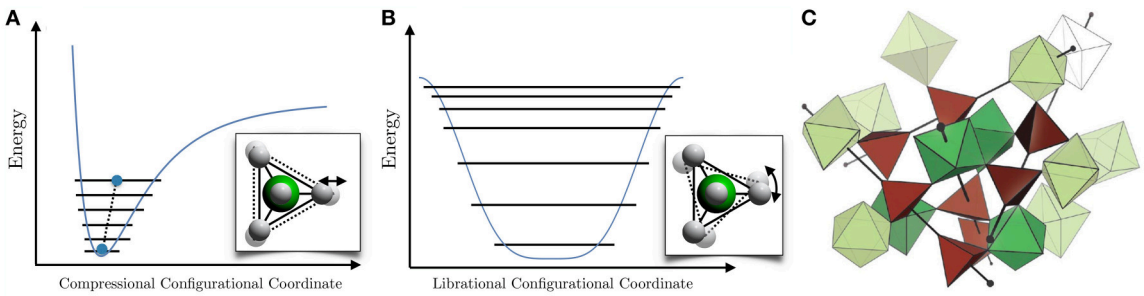

FIGURE 1 | Intermolecular potentials provide a heuristic explanation for the common occurrence of **(A)** PTE and **(B)** NTE. **(C)** The complex structure of the low-symmetry α-phase of ZrW_2O_8, from Hancock et al. (2004a).

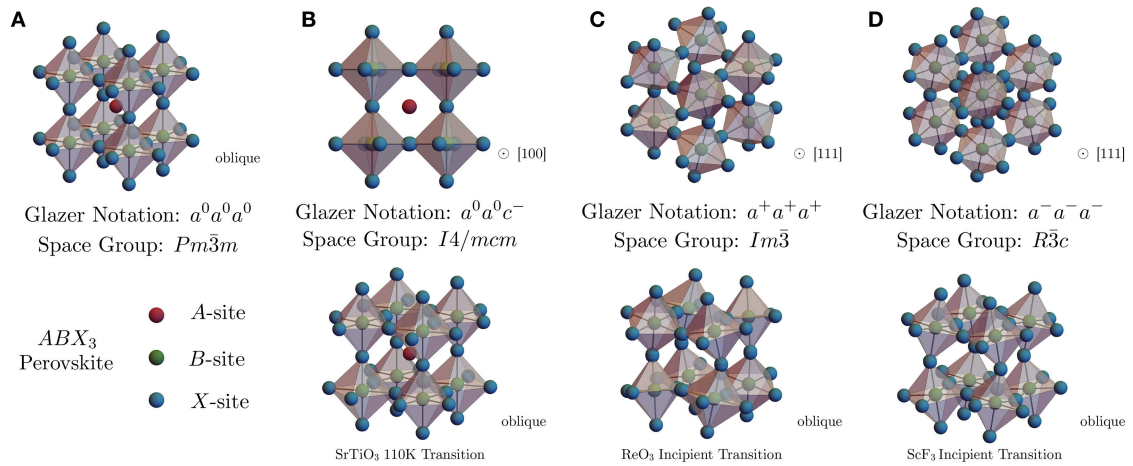

FIGURE 3 | Shown here is **(A)** the general perovskite structure of formula unit ABX_3 (see text), in the highest symmetry cubic space group $Pm\bar{3}m$ corresponding to a Glazer tilt notation $a^0a^0a^0$. Also shown are common octahedral tilt lower-symmetry perovskites found in **(B)** the $SrTiO_3$ $T_C = 110$K $Pm\bar{3}m$ to $I4/mcm$ tetragonal structural transition **(C)** the triply degenerate M_3^+ phonon condensation in the low-T, high-P ReO_3 structural transition (see text) and **(D)** the triply degenerate R_4^+ phonon condensation responsible for the rhombohedral transition is BF_3 open perovskite 3d-transition metal trifluorides which also acts as the dynamic soft-mode rotations in ScF_3, corresponding to Glazer tilts of $a^0a^0c^-$, $a^+a^+a^+$, and $a^-a^-a^-$, respectively.

bonded to a common X-site anion (**Figure 2B**); there is, however, a choice in the phase of rotations for columns of octahedra along the rotation axis. Which phase pattern is realized is denoted by a superscript of + or − for in- and out-of-phase stacking, respectively, or a superscript of 0 indicating a null rotation. The equality of rotation angles around each axis is given by using repeated characters. For instance, in Glazer notation $a^+b^+c^+$ represents three unequal rotations about [100], [010] and [001], with all rotations in phase along each respective axis. Overall, there are 23 distinct possibilities of perovskite space groups and octahedral tilting patterns, which can be cubic to triclinic and anything in between. Several relevant examples of perovskite distortions and the Glazer notation are given in **Figure 3**.

One of the best-studied structural instabilities in a perovskite structure is the transition at $T_c \simeq 110$K in $SrTiO_3$, first identified with electron spin resonance (ESR) spectra by Unoki and Sakudo (Unoki and Sakudo, 1967) and later confirmed by many others (Cowley, 1964; Fleury et al., 1968; Cowley et al., 1969; Shirane and Yamada, 1969) via inelastic neutron scattering (INS), X-ray diffraction and Raman spectroscopy (RS). The room-temperature structure of $SrTiO_3$ is that of the common $Pm\bar{3}m$ space group depicted in **Figure 3A**, but signatures of tetragonal symmetry in the ESR and Raman (Fleury et al., 1968) spectra are observed below $T \simeq 110$K, along with anomalies in the elasticity (Bell and Rupprecht, 1963). Details of the atomic displacements reveal the lower-symmetry structure is the tetragonal $I4/mcm$ space group, which corresponds to a [001]-phase-staggered rotation of the TiO_6 octahedra about a [001] rotation axis, that is an octahedral tilting pattern of $a^0a^0c^-$ (**Figure 3B**). The displacements are related to the polarization of a zone-boundary optical phonon (irrep. R_{25}) existing at the R-point of cubic Brillouin zone (BZ) (**Figure 4A**). In real space, the lowered-symmetry results in an effective doubling of the unit cell dimensions along one axis. In reciprocal space, however, the symmetry lowering occurs through a halving of the Brillouin zone and results in formation of new Bragg peaks as seen in an elastic scattering pattern (X-ray, neutron, electron). Dynamically, one can associate the transition to a slowing down of an optical phonon near the R $(\pi\pi\pi)$ point at the corner of the cubic Brillouin zone, corresponding to a "freezing" or "condensation" of one component of the triply degenerate R-point "soft" mode.

$SrTiO_3$ is the first material in which soft modes were measured using inelastic scattering, and their concomitance with structural phase transitions was subsequently established through their observation in many other perovskites, e.g., $LaAlO_3$, $KMnF_3$, $PbTiO_3$, and $BaTiO_3$ (Shirane, 1974). A *soft-mode* can generally be defined as any normal mode of the dynamic lattice whose energy or, equivalently, frequency of vibration decreases anomalously. When such a vibrational frequency reaches $\hbar\omega = 0$, the lattice becomes structurally unstable with respect to the displacements of this normal mode, and a subsequent symmetry-lowering, static deformation occurs to restore stability. For the simplest case of Landau-Ginsburg-Devonshire theory treated at the mean-field level, one expects a temperature dependence for the soft mode frequency (Scott, 1974; Shirane, 1974; Cowley, 1980):

$$\omega_s(T) \propto \sqrt{|T - T_c|} \tag{1}$$

This dependence for the R-point soft-mode in $SrTiO_3$ is shown in **Figure 4B**. This transition can be described by an order parameter, a quantity that is zero above and develops non-zero average values below T_c, which follows the angle of rotation of the TiO_6 octahedra about the principal axis in the low-symmetry tetragonal structure. The transition in $SrTiO_3$ is, by all experimental accounts, second-order (continuous) in

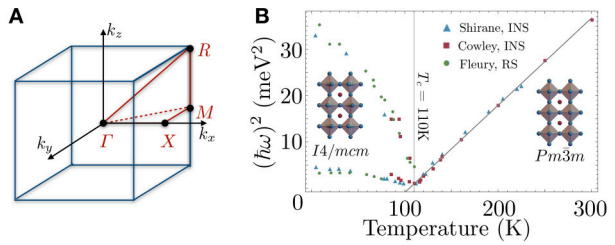

FIGURE 4 | (A) The cubic Brillouin zone indicating the high-symmetry reciprocal lattice points Γ, *X*, *M* and *R*. **(B)** *R*-point mode softening on the approach to the $T_C \simeq 110$K structural transition in $SrTiO_3$, measured from neutron (Cowley et al., 1969; Shirane and Yamada, 1969) and Raman (Fleury et al., 1968) scattering. Black line for $T \geq T_C$ shows agreement with the predicted soft-mode frequency for a dynamically driven second-order phase transition as given in Equation (1).

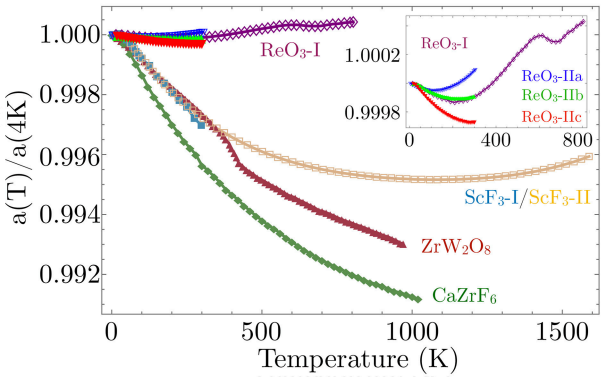

FIGURE 5 | Shown here is the normalized cubic lattice parameter temperature dependence $a(T)/a(4K)$ for ReO_3, ScF_3, and $CaZrF_6$ NTE perovskites with strong SNTE material ZrW_2O_8 for comparison. Inset focuses on available data for ReO_3 on 4 different samples, one (ReO_3-I) over an extended temperature range (Chatterji et al., 2009b) and the other 3 (ReO_3-II a-c) over a smaller temperature range, investigating the effects of compositional disorder (Rodriguez et al., 2009) (see section 5). Data taken from: ZrW_2O_8 (Mary et al., 1996), $CaZrF_6$ (Hancock et al., 2015), ScF_3-I (Handunkanda et al., 2015), ScF_3-II (Greve et al., 2010), ReO_3-I (Chatterji et al., 2009b), and ReO_3-II (Rodriguez et al., 2009).

nature, but for many structural phase transitions signatures of the more common first-order (discontinuous) behavior renders the soft-mode approach invalid *a priori*. Nonetheless, soft modes can be used to interpret weakly first-order transitions and their frequency can be indicative of an incipient transition due to soft-mode coupling to other, primary order parameters. The 110K transition in $SrTiO_3$ is also a prototypical example of critical behavior that can emerge in the vicinity of a structural transition, most notably the "central-peak" phenomenon discovered through an anomalous quasi-elastic peak in INS energy-transfer spectra, which can be explored elsewhere (Halperin and Varma, 1976; Topler et al., 1977; Riste et al., 1993).

In extreme cases, a material can approach dynamic instability with lowering temperature to near-zero soft mode energy, yet no temperature-induced transition is observed. In this situation, subsequent application of pressure, introduction of compositional disorder (doping) or other non-thermal parameters can perturb the ground-state of the system to drive the transition at $T = 0$K, realizing a quantum phase transition (QPT) (Sachdev and Keimer, 2011). Research surrounding the breakdown of canonical physical behavior near these quantum critical points (QCPs) is interesting in its own right (Coleman and Schofield, 2005; Gegenwart et al., 2008) but we below focus on QCPs within the structural phase diagrams and their relationship to the development of SNTE in a subset of the perovskites.

3. NTE IN PEROVSKITE FRAMEWORKS

Most oxide perovskites ABO_3 form with an *A*-site, otherwise requiring a rare hexavalent electronic configuration for charge balance. One prominent exception is ReO_3, which forms with no *A*-site and maintains its cubic $Pm\bar{3}m$ space group symmetry down to the lowest measured temperatures. In addition, ReO_3 has been known to exhibit SNTE for many years, which is often attributed to soft modes permitted by the open-perovskite (*A*-site-free) structure. The lack of the *A*-site puts fewer dynamical constraints on the motion of the ReO_6 octahedra in comparison to the constraints imposed by the *A*-site in other perovskites. This permits large anisotropic thermal displacements of the linking oxygen atoms perpendicular to the Re-O-Re bond direction, making ReO_3 more susceptible to lattice instabilities corresponding to these octahedral tilt patterns. This openness to the structure has also been noted as a key feature in many other SNTE materials, including ZrW_2O_8, leading to a larger set of soft, low-energy phonons that have mainly been identified as the cause of SNTE. Reports on the size of the SNTE effect in ReO_3 vary, but in one report, SNTE was observed in two separated temperature windows of 2–220 K and 600–680 K (Chatterji et al., 2009b) with a maximum measured linear thermal CTE of $\alpha_\ell = -2.56$ ppm/K (Dapiaggi and Fitch, 2009) (**Figure 5**).

ReO_3 undergoes several structural phase transitions under hydrostatic pressure and is most studied at room temperature. Early INS investigations at ambient temperature established that ReO_3 undergoes a pressure-induced second-order phase transition at $P_c = 0.52$ GPa (Axe et al., 1985). Further studies of transport at $T = 2$ K showed that the lowest structural phase boundary terminates at a light hydrostatic pressure of only $P_c = 0.25$ GPa, observed through a change of Fermi surface cross section (Schirber and Morosin, 1979); however, few reports are available in this difficult *P*-*T* region. Based on early high-temperature data, the pressure-induced phase is likely the tetragonal $P4/mbm$, although recent indications of a direct transition to a cubic $Im\bar{3}$ phase have also been reported (Axe et al., 1985; Jørgensen et al., 1986). Neutron diffraction at elevated hydrostatic pressures revealed that the $Im\bar{3}$ phase is stable in the pressure range 0.5 to 13.2 GPa, above which the phase changes to the rhombohedral $R\bar{3}c$ space group (Jørgensen et al., 2004). The soft mode driving the pressure and temperature induced structural transition between the $Pm\bar{3}m$ and $Im\bar{3}$ cubic phases was shown to be three-component M_3^+ phonon mode involving anti-phase rotation of the neighboring ReO_3 octahedra in an

$a^+a^+a^+$ tilt pattern (**Figure 3C**). The temperature-dependence of the M_3^+ mode frequency as a function of temperature at ambient pressure is shown in **Figure 6B**, along with a fit to the mean-field result (Equation 1). This mode is significant in that it is used to understand NTE behavior of open-perovskite systems but is also identified as an order parameter of the phase transition (Chatterji et al., 2009a).

Unlike oxides, fluorides commonly form stable *A*-site-free perovskite structures BF_3 due to the wider array of available B^{3+} ion valence configurations among the transition metals. Prominent among these open-perovskite fluorides is ScF_3, which was discovered in 2010 by Greve et al. (2010) to exhibit a robust NTE effect, which has significant maximal magnitude of the linear CTE $\alpha_\ell \simeq -15$ ppm/K, persisting over the broad temperature range of 4–1050 K (**Figure 5**). At room temperature, ScF_3 crystallizes isostructurally to ReO_3 with space group symmetry $Pm\bar{3}m$ and has been found to possess related structural instabilitiies corresponding to zone-boundary optical phonons. In ReO_3, the condensing soft mode responsible for the low-T high-P structural phase transition is the M_3^+ distortion, while ScF_3 and other 3*d*-transition metal trifluorides fall into the lower-symmetry rhombohedral $R\bar{3}c$ space group symmetry, attributed to the condensation of the R_4^+ optical phonon.

Although the cubic phase of ScF_3 is stable at ambient pressure over the entire temperature of the solid phase down to $T = 0.4$K (Romao et al., 2015), X-ray diffraction (Aleksandrov et al., 2009; Greve et al., 2010) and Raman spectroscopy (Aleksandrov et al., 2009) results have revealed that ScF_3 undergoes several pressure-induced phase transitions. The first is from cubic to rhombohedral (*c-r*) after $P_c = 0.6$ GPa at T=300K, with a subsequent rhombohedral to orthorhombic transition occurring above $P_c = 3.0$ GPa. The *c-r* transition has an observed pressure dependence of $dT_c/dP \simeq 525$ K/GPa (Aleksandrov et al., 2009, 2011; Greve et al., 2010). Measurement of the lattice dynamics and the soft R_4^+ mode responsible for the rhombohedral transition were performed using inelastic x-ray scattering (IXS), which revealed a 1D manifold of soft optical phonons that circumscribe the entire cubic Brillouin zone-edge. At room temperature, this manifold of modes along *M-R* have energy $\hbar\omega \simeq 3$ meV, softening nearly uniformly to < 1 meV at cryogenic temperatures (see **Figure 6B**) (Handunkanda et al., 2015). The IXS results combined with structural data permit an estimation that pressures as small as $P_c \simeq 0.074$ GPa would be sufficient to drive the transition to 0 K. The sensitivity of the phase boundary suggests that the nature of the cubic phase is delicate at low temperature and has been shown to be susceptible to even mild perturbations (Morelock et al., 2013a, 2014, 2015), implying that the ground state of this ionic insulator lie in close proximity to a SQPT.

Phase stability and thermal expansion effects in the open-perovskite trifluoride structure have also been investigated thoroughly through chemical substitution. Chemical substitutions of Sc by Ti (Morelock et al., 2014), Al (Morelock et al., 2015), and Y (Morelock et al., 2013a) have been reported and the effects of this compositional disorder will be discussed in detail in sections 4, 5. Other investigations of changing the stoichiometry have resulted in a related class of hexafluoride compounds, one of which is $CaZrF_6$. This material has $Fm\bar{3}m$ space group symmetry and is related to the $Pm\bar{3}m$ structure of ReO_3 but with a staggered *B*-site ion; that is, alternating CaF_6 and ZrF_6 octahedra tiling a simple cubic point-group structure. The resultant $(\pi\pi\pi)$ pattern is likely a key feature when attempting to relate these materials, and is in particular likely to impact the (simple cubic) *M-R* BZ edge mode dispersion and dimensional reduction observed in ScF_3 (Handunkanda et al., 2015). Compared to ScF_3, this system has isotropic NTE of larger magnitude $\alpha_\ell \simeq -18$ ppm/K over a temperature range $> 1050K$ (**Figure 5**). At $P = 0$ the system also remains cubic at all temperatures above 10 K but a pressure-induced transition to a disordered state occurs near $P_c = 0.45$ GPa (Hancock et al., 2015), closer in the *P-T* diagram than the *c-r* transition in ScF_3 (~ 0.65 GPa) (Aleksandrov et al., 2003, 2009; Greve et al., 2010). Early computational work suggests the $\Gamma - X$ manifold in the cubic BZ for this compound contribute most strongly to NTE (Gupta et al., 2018), but inelastic scattering measurements of the phonon dynamics are needed to assess the influence of the staggered substitution on the critical SNTE dynamics.

The open-perovskites presented above demonstrate this frameworks' favorable environment for harboring SNTE, but

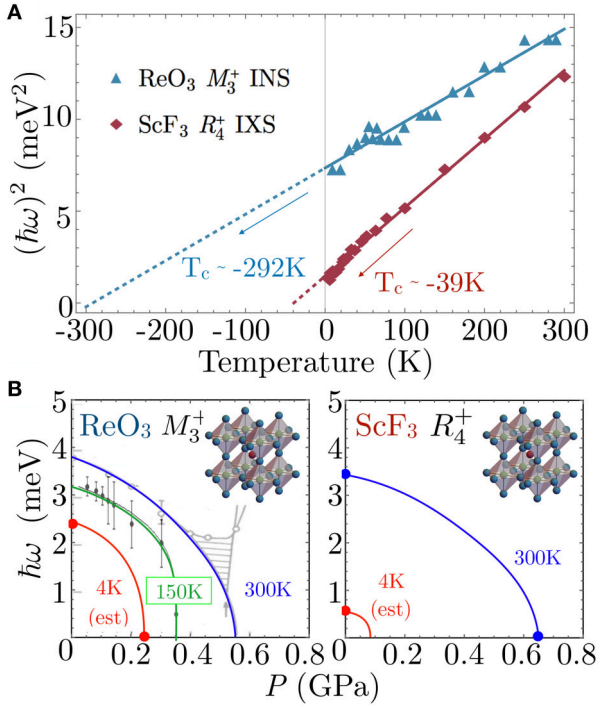

FIGURE 6 | (A) Shows the squared energy $(\hbar\omega)^2$ of the M_3^+ and R_4^+ soft modes vs. temperature at ambient pressure in ReO_3 and ScF_3, respectively. As indicated, extrapolation by mean-field approximation (Equation 1) indicates structural transition temperatures at ambient pressure of $T_C \simeq -292$K for ReO_3 and $T_C \simeq -39$K for ScF_3. **(B)** Shows the soft mode energy vs. pressure at various temperatures for (left) the M_3^+ mode in ReO_3 and (right) the R_4^+ mode in ScF_3. Solid lines are guide to the eye and symbols in both **(A,B)** are taken from references (Axe et al., 1985; Chatterji et al., 2009a; Handunkanda et al., 2015). Comparison supports our assignment that ScF_3 is closer to a SQPT than ReO_3.

begs the question of why most other purely stoichiometric transition metal trifluorides and perovskites show more conventional thermal expansion. The lattice parameters of each of these SNTE perovskites are plotted in comparison to the prototypical SNTE material ZrW_2O_8 in **Figure 5**, which gives a clear ranking of SNTE perovskites by the magnitude of the NTE effect ((1) $CaZrF_6$, (2) ScF_3, (3) ReO_3). This ranking is the opposite ordering one gets in terms of pressure required to induce the structural phase transition nearest ambient conditions, a correlation suggestive that proximity to a SQPT and strength of NTE are interrelated. We demonstrate this point for ReO_3 and ScF_3 in **Figure 6**. These plots consider the soft-mode in each system, the M_3^+ phonon in ReO_3 and the R_4^+ in ScF_3 and the available data for the energy of these modes as a function of pressure and temperature. First considering the T-dependent data at $P = 0$ in **Figure 6A**, extrapolation of the squared mode energies by Equation (1) provides a quantitative measure of the proximity to a dynamically-driven SPT, yielding $T_c \simeq -292$K in ReO_3 (Chatterji et al., 2009a) and $T_c \simeq -39$K in ScF_3 (Handunkanda et al., 2015). Furthermore, isothermal measurements of the soft-mode energy vs. hydrostatic pressure are provided in **Figure 6B**, showing that decreasing temperature and increasing pressure in both systems trend toward a QCP.

Together, the results of these data clearly show in all respects that ScF_3 is closer to a SQPT than ReO_3. Although data at this level in unavailable for $CaZrF_6$, the amorphization boundary at $P_c \leq 0.45$ GPa and $T = 300$K is a lower pressure threshold for the pressure-induced transitions at 300K in both ReO_3 (~ 0.55 GPa) and ScF_3 (~ 0.65 GPa). It is thus likely that ground-state of this compound is the closest to a structural instability at cryogenic temperature, while also exhibiting the most superlative SNTE effect in this class. Our central hypothesis in the context of the materials described is that the $T = 0$K termination of a structural phase boundary defines a structural quantum critical point (SQCP) where strong geometrical fluctuations associated with octahedral tilts drives NTE. In our view, the significance of the SQCP is a flattening of the energy landscape with respect to transverse fluctuation of the linkage unit: O in ReO_3, and F in ScF_3 and $CaZrF_6$. It is worth noting that NTE arising from phase fluctuations and the displacements of a low-T soft-mode is not unique to the antiferrodistortive (zone-boundary) phonons in perovskites, but has also predicted SNTE in materials with broadly distinct structures and geometrical motifs, e.g., the Hg dimer in Hg_2I_2 (Occhialini et al., 2017), the CN molecule in Prussian blue analogs and related compounds (Goodwin et al., 2008; Mittal et al., 2009; Fairbank et al., 2012).

NTE is often understood through the response of the phonon spectrum to the application of hydrostatic pressure, which has been formalized in the quasi-harmonic approximation (QHA) known as the Grüneisen approach (Ashcroft and Mermin, 1976). Each phonon in the Brillouin zone of frequency and wavevector $(\omega_i, \boldsymbol{k}_i)$ is assigned a mode Grüneisen parameter γ_i, defined as,

$$\gamma_i \equiv -\frac{\partial \ln \omega_i}{\partial \ln V} \equiv \frac{1}{\kappa}\frac{\partial \ln \omega_i}{\partial P} \tag{2}$$

where κ is the isothermal compressibility. Performing an average over all wavevectors $\mathbf{k}$ in the first Brillouin zone, weighted by the mode contribution to the heat capacity $c_{V,i}$, gives the overall lattice Grüneisen constant γ which is thermodynamically proportional to the volumetric thermal expansion α_V for isotropic materials. At low-temperatures, the thermodynamic properties are dominated by contributions from the lowest energy excitations. If the low-energy phonon spectrum has large magnitude, negative mode Grüneisen parameters (negative contributions to CTE), then the $\mathbf{k}$-averaged CTE will decrease as temperature is lowered. If strong enough to overcome the many high-energy excitations commonly attributed to conventional PTE, the overall expansion may turn negative in sign, strengthening at lower temperature, which is the typical functional form among the SNTE perovskites (**Figure 5**), before relaxing and limiting to a thermodynamically-required $\alpha_V = 0$ as $T \to 0$K. From this viewpoint, soft-modes with NTE contributions are natural candidates for inducing overall NTE, since their energy softens with lowering temperature, enhancing the mode occupation and weighted contributions to the thermodynamics at low-T in comparison to thermally-stable low energy excitations.

In the SNTE perovskites and other SNTE materials like ZrW_2O_8, these lowest energy lattice excitations are commonly attributed to quasi-rigid dynamics of polyhedral subunits (Dove and Fang, 2016; Schlesinger et al., 2008), i.e., the geometrically rigid octahedra as shown in **Figure 2** which could correspond to BX_6 octahedra in ScF_3, ReO_3 or $CaZrF_6$. These rigid unit mode (RUM) analyses model rigidity by freezing out portions of the phonon spectrum, such as high-energy bond-stretch and internal polyhedral bond-bend modes that are commonly attributed to causing PTE. For ScF_3 and ReO_3, the antiferrodistortive, zone-edge soft modes have an interpretation as RUMs. Moving beyond the commonly employed QHA and Landau mean-field approaches, we make the hypothesized relationship among soft RUMs, phase fluctuations and the development of SNTE precise within a systematic model in section 4 below.

4. THEORY OF SNTE FROM RUM FLUCTUATIONS

The purpose of this section is to present a microscopic description of NTE arising from soft modes in ReO_3-type lattice structures. Such modes break the symmetry of the lattice and lead to displacive structural phase transitions (Giddy et al., 1993). Typical examples are the R_4^+ mode at the point $(1, 1, 1)$ (π/a) of the Brillouin zone of the cubic (c) $Pm\bar{3}m$ phase in MF_3 (M=Sc, Al, Cr, V, Fe, Ti) metal fluorides which upon condensation gives rise to a rhombohedral (r) $R\bar{3}c$ lattice structure and the M_3^+ mode at $(1, 1, 0)$ (π/a) in ReO_3 which generates a tetragonal ($P4/mbm$) phase.

The structural transitions observed in these materials are generally described by Landau theories (Axe et al., 1985; Corrales-Salazar et al., 2017). Typically, they include an order parameter (OP) associated with cooperative tilts of a rigid unit (e.g., the MF_6 octahedron in the metal fluorides) coupled to long-wavelength acoustic phonons that generate volume, deviatoric and shear strains. While such mean field theories provide a fair

description of the structural transitions, they fail to describe NTE, e.g., they predict zero thermal expansion in their high-T cubic $Pm\bar{3}m$ phase (Corrales-Salazar et al., 2017).

Here, we present a microscopic phenomenology that describes NTE in these open perovskite frameworks. The model includes the usual rigid tilts coupled to long-wavelength strain-generating acoustic modes as well as a cooperative interaction between tilts that drives the structural transition, e.g., dipolar interactions in the metal trifluorides (Chaudhuri et al., 2004; Chen et al., 2004; Allen et al., 2006). Our main result is that any solution of the model must include fluctuations of the OP to generate NTE. We illustrate this within a so-called self-consistent phonon approximation (SCPA) in which single site fluctuations are considered while inter-site fluctuations are neglected. This point has been appreciated before (Volker et al., 2004; Simon and Varma, 2000; He et al., 2010), however, no systematic approach has been constructed so far. In addition, our model allow us to parametrize measured macroscopic quantities in terms of microscopic parameters, which provides guidance for materials design. Our model closely follows those of the well-known antiferrodistortive transitions of $SrTiO_3$ and $LaAlO_3$ (Feder and Pytte, 1970), with the important distinction that we include hydrostatic pressure and account for compositional disorder. The latter is aimed at describing compounds with tunable NTE through composition such as mixed solid solutions of metal triflurides (Morelock et al., 2013b, 2014, 2015). For concreteness, we will consider a *c-r* transition similar to that in $Sc_xTi_{1-x}F_3$ in which the threefold zone-boundary R_4^+ phonon splits into a low-energy E_g doublet and a high energy A_{1g} singlet at a transition temperature T_c (Daniel et al., 1990).

Our model analysis is by no means exhaustive. More elaborate descriptions that go beyond the picture of rigid tilts involving, for instance, distortions and translations of such building units are usually needed to describe the observed thermal expansion (Li et al., 2011). Also the observed structural transitions are frequently of first-order, which we do not consider here for the sake of simplicity. Nonetheless, our semi-analytic approach accounts for microscopic aspects of the phonon dynamics and its relation to NTE, and helps identify general trends of the solution. Moreover, it provides the basis to build other frameworks that capture atomistic details such as first-principles-based effective model Hamiltonians (Rabe et al., 2007).

4.1. Model Hamiltonian

We consider a cubic lattice with N sites and choose normal mode coordinates $\boldsymbol{Q}_i = (Q_{ix}, Q_{iy}, Q_{iz})$ in the unit cell i ($i = 1, 2, ..., N$) associated with the R_4^+ mode, the condensation of which leads to the $R\bar{3}c$ rhombohedral phase. $\boldsymbol{Q}_i$ is proportional to the local displacements generated by the cooperative tilts of the MF_6 octahedra. In addition, we introduce the strain tensor in Voigt notation $\epsilon_{i\alpha}$, $\alpha = 1, ..., 6$ in unit cell i, which is induced by displacements $\boldsymbol{u}_i = (u_{ix}, u_{iy}, u_{iz})$ of the centers of mass of the unit cells with respect to the acoustic-branch phonons. In order to determine the optical phonon contribution to the thermal expansion, we must couple the displacements $\boldsymbol{Q}_i$ with strains $\epsilon_{i\alpha}$, leading to a 3-term Hamiltonian of the form,

$$H = H_Q + H_\epsilon + H_{Q\epsilon}. \tag{3}$$

Here, H_Q accounts for harmonic and anharmonic energy contributions from the soft optical phonon up to quartic order in $\boldsymbol{Q}_i$; H_ϵ is the strain-induced energy depending on the elasticity through the bulk modulus C_a, shear moduli and hydrostatic pressure P; and $H_{Q\epsilon}$ models the coupling between these displacements and strain degrees of freedom with g_a the coupling constant between the displacements and the volume strain. The explicit form of these terms is given in the **Supplementary Material**. To solve the statistical mechanical problem posed by the Hamiltonian in Equation (3), we use a variational formulation of a SCPA, in which the temperature and pressure dependence of the phonon energies Ω_ν, ($\nu = R_4^+, A_{1g}, E_g$), displacements, strain order parameters and phase fluctuations are determined self-consistently from the minimization of the free energy (Pytte, 1972). We here focus on the main results. The details of the model Hamiltonian and its approximate solution are given in the SM.

4.2. Thermal Expansion, CTE, and Grüneisen Parameters

We first focus on the volume strain $\langle \epsilon_V \rangle = \langle \epsilon_1 + \epsilon_2 + \epsilon_3 \rangle$, which gives the change in volume with temperature and pressure with respect to a reference volume V_0. We use the notation $\langle .... \rangle$ to denote the thermal and compositional disorder average, taken in that order. By minimizing the free energy associated with the Hamiltonian in Equation (3), we find that the volume strain is given as follows,

$$\langle \epsilon_V \rangle = \frac{\Delta V}{V_0} = -\frac{g_a}{C_a} \left\langle |\boldsymbol{Q}|^2 \right\rangle - \frac{P}{C_a}, \tag{4}$$

where $\left\langle |\boldsymbol{Q}|^2 \right\rangle$ is the thermal and compositional average of the squared magnitude of the MF_6 tilt. Equation (4) already illustrates one of the main points of our work: in a mean-field theory and in the absence of pressure, $\left\langle |\boldsymbol{Q}|^2 \right\rangle = 0$ above T_c; thus fluctuations around the OP must be included to describe NTE. For instance, within the SCPA and for temperatures much greater than the phonon energy, we find that $\left\langle |\boldsymbol{Q}|^2 \right\rangle \propto T$ in the cubic phase and Equation (4) gives,

$$\frac{\Delta V}{V_0} \simeq \alpha_V T - \frac{P}{C_a}, \quad \alpha_V = -\frac{3 g_a k_B}{C_a \nu_R}, \tag{5}$$

where α_V is the CTE at high temperatures and ν_R is the strength of the cooperative interaction. **Figures 7A,B** show, respectively, our results for the volume change obtained from Equation (4) and its CTE ($\alpha_V = d \langle \epsilon_V \rangle / dT$) in the full temperature range. Model parameters were obtained by fitting to experiments (Morelock et al., 2014; Handunkanda et al., 2015) and are given in the SM. Despite its simplicity, our model produces the observed trends (Morelock et al., 2014; Handunkanda et al., 2015): NTE with a nearly linear T dependence in the *c*-phase, except near 0 K; PTE in the *r*-phase; and a discontinuity in α_V at the phase transition. Quantitatively, the model is in good agreement in the *c*-phase, but α_V is about an order of magnitude less than the observed one in the *r*-phase. We attribute this to having neglected the first-order character of the transition and additional phonons

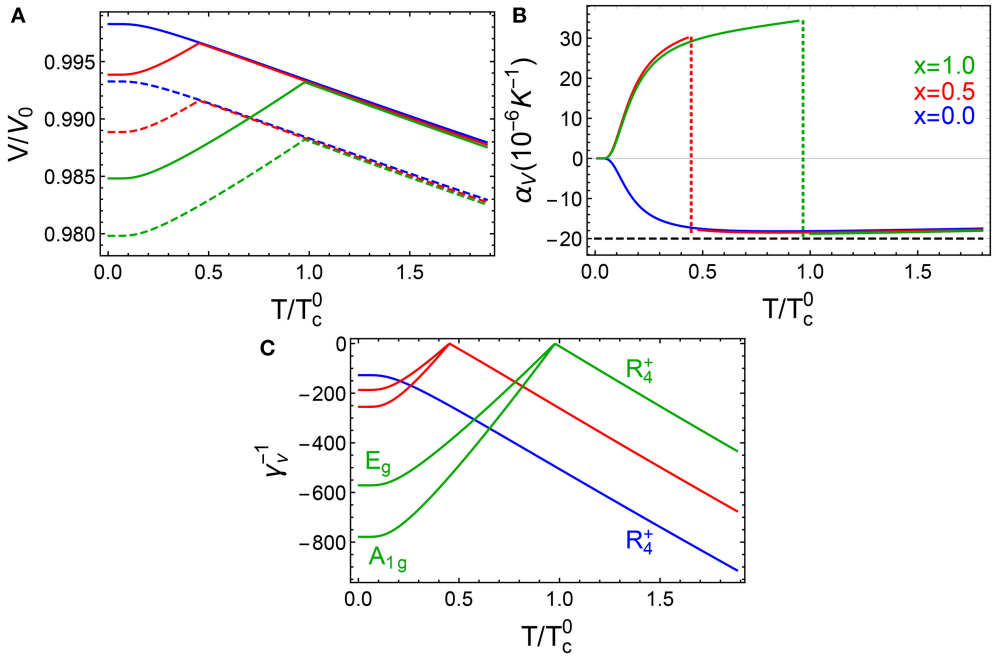

FIGURE 7 | Calculated temperature dependence of **(A)** volume change, **(B)** CTE, and **(C)** Grüneisen parameters for $P/P_0 = 0$ (solid lines) and 9.0×10^{-5} (dashed lines) for $Sc_{1-x}Ti_xF_3$. P_0 is the pressure needed to induce the c-r transition in ScF_3 ($x = 0$) at 0 K; $T_c^0 = 340$ K is the transition temperature of TiF_3 ($x = 1$) at ambient pressure. Black dashed line in **(B)** is the predicted CTE in the classical limit according to Equation (5). The phonon symmetry labels for $x = 0.5$ in **(C)** are the same as those for $x = 1$ and are not shown for clarity.

along the M-R line of the BZ which are known to contribute to the NTE (van Roekeghem et al., 2016).

We note that Equation (5) gives α_V in terms of the microscopic model parameters. It shows that mechanically compliant materials with low bulk moduli (C_a) and strong strain-phonon couplings (g_a) favor thermal expansion. α_V also increases by weakening the strength of the cooperative interaction v_R at the expense of decreasing the transition temperatures since $T_c \propto v_R$, as it is shown in the SM. It also shows that the sign of this coupling plays an essential role in the thermal expansion: $g_a > 0$ for NTE while $g_a < 0$ for PTE.

Another physically relevant quantity is the Grüneisen parameter γ_ν associated with each lattice mode $\nu = R_4^+, A_{1g}, E_g$. We find that the temperature and pressure dependence of γ_ν is entirely determined by the phonon energy Ω_ν,

$$\gamma_\nu = -\frac{g_a}{\Omega_\nu^2}, \tag{6}$$

and thus diverges near the *c-r* transition as $\Omega_\nu \to 0$. This is in agreement with previous analytic work (Volker et al., 2004) and ab-initio calculations, where large, negative values for $\gamma_{R_4^+}$ have been found for ScF_3 (Li et al., 2011; Liu et al., 2015; van Roekeghem et al., 2016). **Figure 7B** shows that $\gamma_\nu^{-1} \propto -|T - T_c|$ at the onset of the phase transition for $x = 0.5, 1.0$ and thus matches the result from Landau theory. For $x = 0$, there is no transition and the deviations from linear behavior are due to zero-point fluctuations.

5. THE ROLE OF DISORDER IN PEROVSKITE SNTE MATERIALS

Disorder is an inevitable part of any real material system. Here we discuss and develop the role of disorder in on the SNTE effect within the open perovskite structural class.

ReO_3 has been known as a SNTE material for many years, but there are varying reports of the strength and also extent in temperature over which the effect occurs, which is summarized for recent data by Chatterji (Chatterji and McIntyre, 2006; Chatterji et al., 2009b) and Rodriguez (Rodriguez et al., 2009) in **Figure 5** inset. Generally, "open" perovskite oxides are rare due to the requirement of a hexavalent *B*-site and controlled substitutional studies have not been reported to our knowledge. However, the controlled disorder study by Rodriguez (Rodriguez et al., 2009) compared crystals synthesized using different growth techniques and clearly showed that the highest quality crystals grown by chemical vapor transport method exhibited the largest and most thermally persistent SNTE effect. As with the physical properties of many perovskite oxides, controlled post-growth annealing procedure studies may be need to be developed to ensure the optimal NTE effect even in studies of its fundamental causes.

ScF_3 is an unusually clean material - single crystals have been synthesized with 0.002 degree mosaic (Handunkanda et al., 2016), free of color centers, with high chemical and isotopic purity with readily available components. The flexibility afforded by the trivalent *B*-site in the trifluorides permits wide chemical

tunability and provides new opportunities to observe disorder effects on SNTE. So far, the most thorough and complete studies of the substitutional series $Sc_{1-x}L_xF_3$ have been performed with high inorganic synthesis and high quality structural synchrotron and neutron scattering efforts of the Wilkinson group at Georgia Tech. In a series of papers (Morelock et al., 2013b, 2014, 2015), substitutions of L=Al,Y,Ti have been reported, particularly the behavior of the cubic-to-rhombohedral phase boundary in this system upon these isovalent substitutions (**Figures 8**, **9A**). Here we develop a combined analysis of these data which permits conclusions regarding the interaction of disorder and the SNTE effect.

Following the spirit of Attfield, who has studied compositional disorder effects on the A-site of transition metal oxide phase

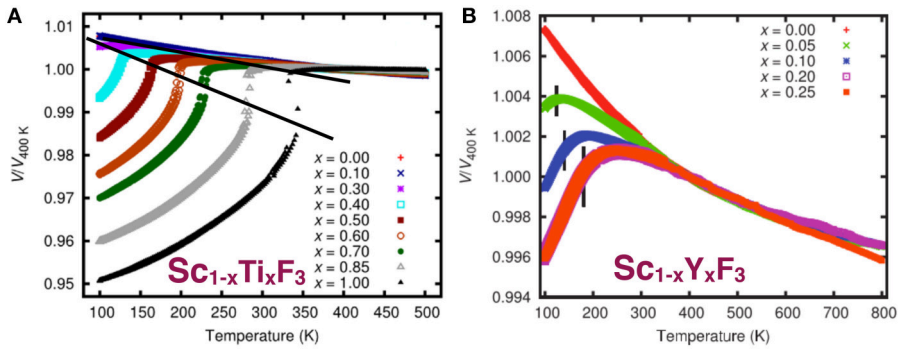

FIGURE 8 | Compositional dependence of the SNTE effect in $Sc_{1-x}(L = Ti,Y)_xF_3$ for L = Ti (Morelock et al., 2014) and L =Y (Morelock et al., 2013b). **(A)** Reprinted with permission from Morelock et al. (2014). Copyright (2018) American Chemical Society. **(B)** Reprinted from Morelock et al. (2013), with permission of AIP publishing.

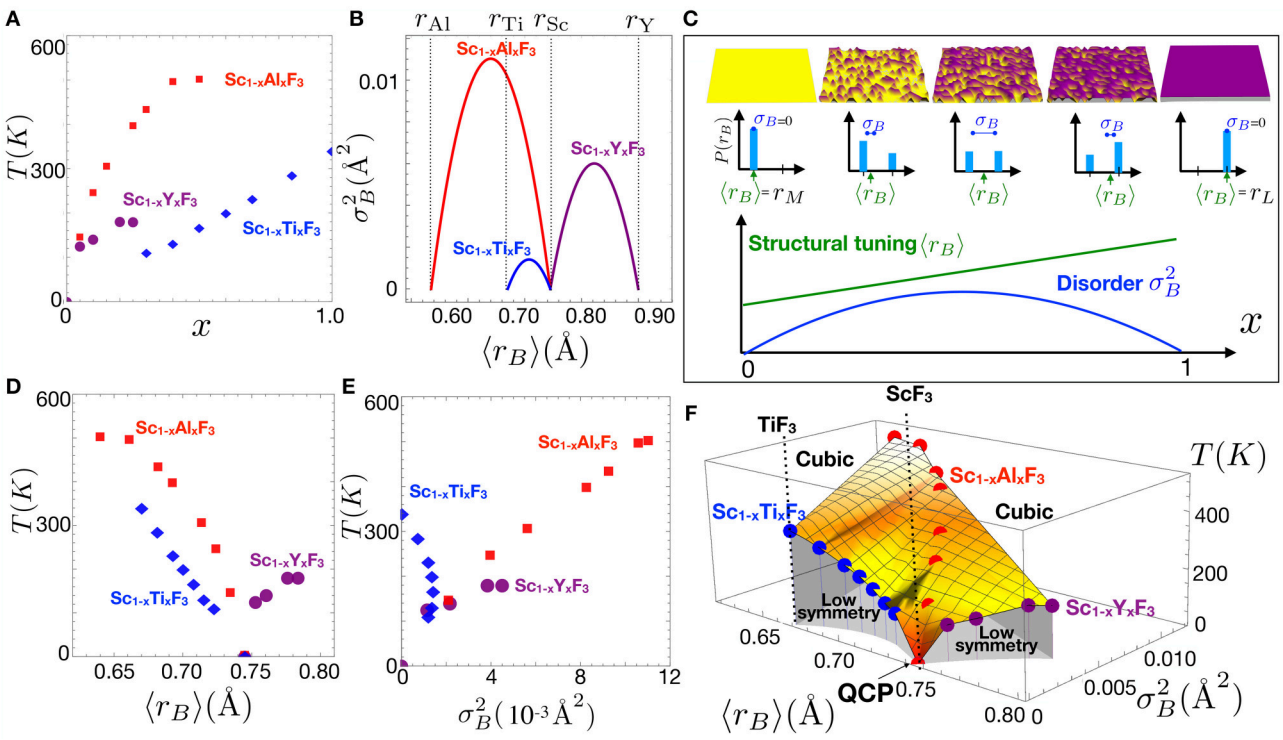

FIGURE 9 | (A) Cubic-to-rhombohedral transition temperatures T_C(x) in a isovalent substitutional series $Sc_{1-x}L_xF_3$. **(B)** The dependence of the mean and variance using Equation (8) and the Shannon ionic radii of the Ti, Y, and Al. (**C**, top row) Illustration of the effect of substitution on the potential energy landscape in a solid solution as the composition x is varied. (**C**, middle row) The binary probability distributions $P(r_B)$ for the five composition levels with the mean and standard deviation σ_B of the distributions indicated by arrows and dumbbells, respectively. (**C**, bottom) plot of the composition dependence of the first two moments of the distribution according to Equation (8). Plot showing the dependence of the transition temperatures as a function of **(D)** $\langle r_B \rangle$ and **(E)** σ_B^2, respectively, which show no obvious universal trend. **(F)** Combined plot of the transition temperatures vs. the structural tuning parameter $\langle r_B \rangle$ and the disorder parameter σ_B^2.

transitions (Attfield, 1998, 2001, 2002), we borrow the hypothesis that the ionic radius of the substituted ions represents a local energetic influence on the stability of the ordered phase and discuss in our case the probability distribution $P(r_B)$ of finding a B-site ion of radius r_B in the series $Sc_{1-x}L_xF_3$. We calculate the first two moments of this distribution and associate the mean ionic radius (1st moment) $\langle r_B \rangle$ to an energetic effect on the transition and the variance (2nd moment) σ_B^2 of the distribution as representative of disorder. For the simple binary distributions shown in **Figure 9C**, these quantities are simply calculated from the nominal composition $M_{1-x}L_xF_3$:

$$\langle r_B \rangle = r_M(1-x) + r_L x \quad (7)$$

$$\sigma_B^2 = x(1-x)(r_L - r_M)^2 \quad (8)$$

$$= (r_M - \langle r_B \rangle)(\langle r_B \rangle - r_L). \quad (9)$$

These relations are general for any binary mixture, and are applied for M=Sc and L=Y,Al,Ti in **Figure 9B** using the Shannon ionic radius for these trivalent ions. Appropriately, σ_B^2 is zero for the endpoints of the compositional series and is maximum at the 50-50 composition as expected in all cases. Note that for L=Ti, the ion best size matched to Sc, this maximum is small and the effects of disorder are expected to be weaker than for other substitutions, whereas for the much larger Y and much smaller Al ions, disorder increases substantially throughout these series. Further, substitutions of Y have opposite effects on $\langle r_B \rangle$ than substitutions of Ti and Al, therefore the three substitutional series cover well the transition in terms of both energetics and disorder.

Figures 9D,E show the transition temperatures plotted as a function of $\langle r_B \rangle$ and σ_B^2. There is not a clear common trend in either plot, except that the Y and Al substitution series are linear in σ_B^2, implying that quenched disorder is the dominant contribution toward driving the transition, as we have pointed out previously (Handunkanda et al., 2015). For the substitution L=Ti, the transition temperature is linear in x, suggesting a dominantly energetic effect, as hypothesized based on its similar size and treated theoretically in the weak-disorder limit of the last section. **Figure 9F** shows a combined plot of all three series L=Ti,Al,Y as a function of the structural tuning parameter $\langle r_B \rangle$ and the disorder parameter σ_B^2. This generalized disorder-energy analysis unifies the compositional dependencies of three different series with important implications, showing that disorder is deleterious to SNTE and that ScF_3 is situated in a very special place which is difficult to reach in the presence of any disorder. These conclusions and the known variation in the SNTE effect of ReO_3 indicate that disorder generally suppresses the SNTE effect and that careful work optimizing this property with respect to sample history may be necessary in some cases.

ScF_3 has the most dramatic SNTE effect of all members of these series and also appears at a QCP in the diagram of **Figure 9F**. **Figure 8** reproduces the figure panels for thermal expansion in each series and shows that strong SNTE persists above the transition for light substitutional levels, but weakens in all cases. We point out that no known materials exist in the large $\langle r_B \rangle$, small σ_B^2 limit, but if such a composition could be produced, would be of high interest toward exploring the robustness of SNTE to disorder. Furthermore, routine structural refinement experiments performed at liquid helium temperatures would help immensely toward refining the QCP in these systems where SNTE seems to arise near the T=0 termination of a structural phase boundary.

6. SUMMARY

We have discussed the broad issue of SNTE with particular focus on perovskite-structured SNTE materials. We have identified the presence of several competing octahedral tilt instabilities occurring near the zero-temperature state of these materials and their associated fluctuations in the high-symmetry phase as key to the SNTE effect in these materials. We have provided a model treatment beyond mean field theory to account for these fluctuations and identified key elements that move toward control of negative thermal expansion and may be invoked for rational design and discovery of future SNTE systems. We also find that quantum mechanical effects are non-negligible and play an important role in SNTE. Finally, we have described existing data in a new analysis which attempts to isolate the influences of energetics and disorder and presented a holistic and generalizable approach leading to the conclusion that disorder disrupts the balance which drives the SNTE effect in ScF_3, ReO_3, and other SNTE materials. Our thorough combined analysis of the physical properties and special circumstances in this simple structural class has identified trends and influences that we hope will guide discovery of new SNTE materials.

AUTHOR CONTRIBUTIONS

CO, SH, and JH wrote sections 1–3 and 5. GG-V developed the modeling in section 4 and the Supplementary Material. All authors contributed to writing and revising the manuscript and figures.

FUNDING

Work at the University of Connecticut was provided by National Science Foundation Award No. DMR-1506825 with additional support from the US Department of Energy, Office of Science, Office of Basic Energy Sciences, under Award No. DE-SC0016481. Work at the University of Costa Rica is supported by the Vice-rectory for Research under project no. 816-B7-601, and work at Argonne National Laboratory is supported by the U.S. Department of Energy, Office of Basic Energy Sciences, Material Sciences and Engineering Division under contract no. DE-AC02-06CH11357.

ACKNOWLEDGMENTS

The authors would like to acknowledge valuable conversations with Peter Littlewood, Richard Brierley, Premala

Chandra, and Alexander Balatsky. GG-V acknowledges Churchill College, the Department of Materials Science and Metallurgy and the Cavendish Laboratory at the University of Cambridge where part of this work was done.

SUPPLEMENTARY MATERIAL

The Supplementary Material for this article can be found online at: https://www.frontiersin.org/articles/10.3389/fchem.2018.00545/full#supplementary-material

REFERENCES

Aleksandrov, K. S., Voronov, N. V., Vtyurin, A. N., Krylov, A. S., Molokeev, M. S., Oreshonkov, A. S., et al. (2011). Structure and lattice dynamics of the high-pressure phase in the ScF_3 crystal. *Phys. Solid State* 53, 564–569. doi: 10.1134/S1063783411030036

Aleksandrov, K. S., Voronov, V. N., Vtyurin, A. N., Goryainov, S. A., Zamkova, N. G., Zinenko, V. I., et al. (2003). Pressure-induced phase transitions in ScF_3 crystal–raman spectra and lattice dynamics. *Ferroelectrics* 284, 31–45. doi: 10.1080/00150190390204691

Aleksandrov, K. S., Voronov, V. N., Vtyurin, A. N., Krylov, A. S., Molokeev, M. S., Pavlovskĭ–, M. S., et al. (2009). Pressure-induced phase transition in the cubic ScF_3 crystal. *Phys. Solid State* 51, 810–816. doi: 10.1134/S1063783409040295

Allen, P., Chen, Y.-R., Chaudhuri, S., and Grey, C. (2006). Octahedral tilt instability of ReO_3-type crystals. *Phys. Rev. B* 73:172102. doi: 10.1103/PhysRevB.73.172102

Ashcroft, N. W., and Mermin, N. D. (1976). *Solid State Physics*. Holt: Rinehart and Winston.

Attfield, J. (2001). Structure–property relations in doped perovskite oxides. *Int. J. Inorg. Mater.* 3, 1147–1152. doi: 10.1016/S1466-6049(01)00110-6

Attfield, J. (2002). 'A' cation control of perovskite properties. *Cryst. Eng.* 5, 427–438. doi: 10.1016/S1463-0184(02)00054-0

Attfield, J. P. (1998). A simple approach to lattice effects in conducting perovskite-type oxides. *Chem. Mater.* 10, 3239–3248. doi: 10.1021/cm980221s

Axe, J. D., Fujii, Y., Batlogg, B., Greenblatt, M., and Di Gregorio, S. (1985). Neutron scattering study of the pressure-induced phase transformation in ReO_3. *Phys. Rev. B* 31, 663–667. doi: 10.1103/PhysRevB.31.663

Azuma, M., Chen, W.-T., Seki, H., Czapski, M., Olga, S., Oka, K., et al. (2011). Colossal negative thermal expansion in $BiNiO_3$ induced by intermetallic charge transfer. *Nat. Commun.* 2:347. doi: 10.1038/ncomms1361

Balch, D. K., and Dunand, D. C. (2004). Copper-zirconium tungstate composites exhibiting low and negative thermal expansion influenced by reinforcement phase transformations. *Metallur. Mater. Trans. A* 35, 1159–1165. doi: 10.1007/s11661-004-1019-2

Barrera, G. D., Bruno, J. A. O., Barron, T. H. K., and Allan, N. L. (2005). Negative thermal expansion. *J. Phys.* 17, R217–R252. doi: 10.1088/0953-8984/17/4/R03

Bell, R. O., and Rupprecht, G. (1963). Elastic constants of strontium titanate. *Phys. Rev.* 129, 90–94. doi: 10.1103/PhysRev.129.90

Benedek, N. A., and Fennie, C. J. (2013). Why are there so few perovskite ferroelectrics? *J. Phys. Chem. C* 117, 13339–13349. doi: 10.1021/jp402046t

Bridges, F., Keiber, T., Juhas, P., Billinge, S. J. L., Sutton, L., Wilde, J., et al. (2014). Local vibrations and negative thermal expansion in ZrW_2O_8. *Phys. Rev. Lett.* 112:045505. doi: 10.1103/PhysRevLett.112.045505

Cao, D., Bridges, F., Kowach, G., and Ramirez, A. (2002). Frustrated soft modes and negative thermal expansion in ZrW_2O_8. *Phys. Rev. Lett.* 89:215902. doi: 10.1103/PhysRevLett.89.215902

Cao, D., Bridges, F., Kowach, G., and Ramirez, A. (2003). Correlated atomic motions in the negative thermal expansion material ZrW_2O_8: a local structure study. *Phys. Rev. B* 79:184302. doi: 10.1103/PhysRevB.68.014303

Chatterji, T., Freeman, P., Jimenez-Ruiz, M., Mittal, R., and Chaplot, S. (2009a). Pressure- and temperature-induced M_3 phonon softening in ReO_3. *Phys. Rev. B* 79:184302. doi: 10.1103/PhysRevB.79.184302

Chatterji, T., Hansen, T. C., Brunelli, M., and Henry, P. F. (2009b). Negative thermal expansion of ReO_3 in the extended temperature range. *Appl. Phys. Lett.* 94:241902. doi: 10.1063/1.3155191

Chatterji, T., and McIntyre, G. (2006). Pressure-induced structural phase transition in ReO3. *Solid State Commun.* 139, 12–15. doi: 10.1016/j.ssc.2006.05.007

Chaudhuri, S., Chupas, P. J., Wilson, M., Madden, P., and Grey, C. P. (2004). Study of the nature and mechanism of the rhombohedral-to-cubic phase transition in α-AlF_3 with molecular dynamics simulations. *J. Phys. Chem. B* 108:3437. doi: 10.1021/jp034533g

Chen, J., Fan, L., Ren, Y., Pan, Z., Deng, J., Yu, R., and Xing, X. (2013a). Unusual transformation from strong negative to positive thermal expansion in $PbTiO_3$-$BiFeO_3$ perovskite. *Phys. Rev. Lett.* 110:115901. doi: 10.1103/PhysRevLett.110.115901

Chen, J., Wang, F., Huang, Q., Hu, L., Song, X., Deng, J., et al. (2013b). Effectively control negative thermal expansion of single-phase ferroelectrics of $PbTiO_3$-(Bi,La)FeO_3 over a giant range. *Sci. Rep.* 3:2458. doi: 10.1038/srep02458

Chen, Y.-R., Perebeinos, V., and Allen, P. B. (2004). Density-functional study of the cubic-to-rhombohedral transition in α-AlF_3. *Phys. Rev. B* 69:054109. doi: 10.1103/PhysRevB.69.054109

Coleman, P., and Schofield, A. J. (2005). Quantum criticality. *Nature* 433, 226–229. doi: 10.1038/nature03279

Corrales-Salazar, A., Brierley, R. T., Littlewood, P. B., and Guzmán-Verri, G. G. (2017). Landau theory and giant room-temperature barocaloric effect in MF_3 metal trifluorides. *Phys. Rev. Mater.* 1:053601. doi: 10.1103/PhysRevMaterials.1.053601

Cowley, R. (1980). Structural phase transitions I. Landau theory. *Adv. Phys.* 29, 1–110. doi: 10.1080/00018738000101346

Cowley, R. A. (1964). Lattice dynamics and phase transitions of strontium titanate. *Phys. Rev.* 134, A981–A997. doi: 10.1103/PhysRev.134.A981

Cowley, R. A., Buyers, W. J., and Dolling, G. (1969). Relationship of normal modes of vibration of strontium titanate and its antiferroelectric phase transition at 110K. *Solid State Commun.* 7, 181–184. doi: 10.1016/0038-1098(69)90720-0

Daniel, P., Bulou, A., Rousseau, M., Nouet, J., Fourquet, J. L., Leblanc, M., et al. (1990). A study of the structural phase transitions in AlF_3: x-ray powder diffraction, differential scanning calorimetry (DSC) and Raman scattering investigations of the lattice dynamics and phonon spectrum. *J. Phys. Condens. Matter* 2:5663. doi: 10.1088/0953-8984/2/26/003

Dapiaggi, M., and Fitch, A. N. (2009). Negative (and very low) thermal expansion in ReO_3 from 5 to 300 K. *J. Appl. Crystallogr.* 42, 253–258. doi: 10.1107/S002188980804332X

De Buysser, K., Lommens, P., De Meyer, C., Bruneel, E., Hoste, S., and Van Driessche, I. (2004). ZrO_2-ZrW_2O_8 composites with tailor-made thermal expansion. *Ceramics-Silikaty* 48, 139–144.

Dove, M. T., and Fang, H. (2016). Negative thermal expansion and associated anomalous physical properties: review of the lattice dynamics theoretical foundation. *Rep. Prog. Phys.* 79:066503. doi: 10.1088/0034-4885/79/6/066503

Drymiotis, F., Ledbetter, H., Betts, J., Kimura, T., Lashley, J., Migliori, A., et al. (2004). Monocrystal elastic constants of the negative-thermal-expansion compound zirconium tungstate (ZrW_2O_8). *Phys. Rev. Lett.* 93:025502. doi: 10.1103/PhysRevLett.93.025502

Ernst, G., Broholm, C., Kowach, G., and Ramirez, A. (1998). Phonon density of states and negative thermal expansion in ZrW_2O_8. *Nature* 583, 580–583. doi: 10.1038/24115

Evans, J., Hu, Z., Jorgensen, J., and Argyriou, D. (1997a). Compressibility, phase transitions, and oxygen migration in zirconium tungstate, ZrW_2O_8. *Science* 132, 15496–15498. doi: 10.1126/science.275.5296.61

Evans, J., Mary, T., and Sleight, A. (1997b). Negative thermal expansion in a large molybdate and tungstate family. *J. Solid State Chem.* 275, 61–65. doi: 10.1006/jssc.1997.7605

Fairbank, V. E., Thompson, A. L., Cooper, R. I., and Goodwin, A. L. (2012). Charge-ice dynamics in the negative thermal expansion material $Cd(CN)_2$. *Phys. Rev. B* 86:104113. doi: 10.1103/PhysRevB.86.104113

Feder, J., and Pytte, E. (1970). Theory of a structural phase transition in perovskite-type crystals. II. Interaction with elastic strain. *Phys. Rev. B* 1, 4803–4810. doi: 10.1103/PhysRevB.1.4803

Figueirêdo, C., and Perottoni, C. (2007). B3LYP density functional calculations on the ground-state structure, elastic properties, and compression mechanism of α-ZrW_2O_8. *Phys. Rev. B* 75:184110. doi: 10.1103/PhysRevB.75.184110

Fleming, D., Johnson, D., and Lemaire, P. (1997). *A temperature compensated optical fiber refractive index grating*. Available online at: https://patents.google.com/patent/US5694503A/en

Fleury, P. A., Scott, J. F., and Worlock, J. M. (1968). Soft phonon modes and the 110K phase transition in $SrTiO_3$. *Phys. Rev. Lett.* 21, 16–19. doi: 10.1103/PhysRevLett.21.16

Gallington, L. C., Chapman, K. W., Morelock, C. R., Chupas, P. J., and Wilkinson, A. P. (2013). Orientational order-dependent thermal expansion and compressibility of ZrW_2O_8 and $ZrMo_2O_8$. *Phys. Chem. Chem. Phys.* 15, 19665–19672. doi: 10.1039/c3cp52876f

Gallington, L. C., Chapman, K. W., Morelock, C. R., Chupas, P. J., and Wilkinson, A. P. (2014). Dramatic softening of the negative thermal expansion material HfW_2O_8 upon heating through its WO_4 orientational order-disorder phase transition. *J. Appl. Phys.* 115:053512. doi: 10.1063/1.4864258

Gegenwart, P., Si, Q., and Steglich, F. (2008). Quantum criticality in heavy-fermion metals. *Nat. Phys.* 4, 186–197. doi: 10.1038/nphys892

Giddy, A., Dove, M., Pawley, G., and Heine, V. (1993). The determination of rigid-unit modes as potential soft modes for displacive phase transitions in framework crystal structures. *Acta Crystallogr. Sect. A* 49, 697–703. doi: 10.1107/S0108767393002545

Glazer, A. M. (1972). The classification of tilted octahedra in perovskites. *Acta Crystallogr. Sect. B Struct. Crystallogr. Cryst. Chem.* 28, 3384–3392. doi: 10.1107/S0567740872007976

Glazer, A. M., and IUCr (1975). Simple ways of determining perovskite structures. *Acta Crystallogr. Sect. A* 31, 756–762. doi: 10.1107/S0567739475001635

Goodwin, A. L., Calleja, M., Conterio, M. J., Dove, M. T., Evans, J. S. O., Keen, D. A., et al. (2008). Colossal positive and negative thermal expansion in the framework material $Ag_3[Co(CN)_6]$. *Science* 319, 794–797. doi: 10.1126/science.1151442

Greve, B. K., Martin, K. L., Lee, P. L., Chupas, P. J., Chapman, K. W., and Wilkinson, A. P. (2010). Pronounced negative thermal expansion from a simple structure: cubic ScF_3. *J. Am. Chem. Soc.* 132, 15496–15498. doi: 10.1021/ja106711v

Guillaume, C. E. (1920). *The Nobel Prize in Physics, 1920: Invar Alloys*. Stockholm: Royal Swedish Academy of Sciences.

Gupta, M. K., Mittal, R., and Chaplot, S. L. (2013). Negative thermal expansion in cubic ZrW_2O_8: role of phonons in the entire Brillouin zone from ab initio calculations. *Phys. Rev. B* 88:014303. doi: 10.1103/PhysRevB.88.014303

Gupta, M. K., Singh, B., Mittal, R., and Chaplot, S. L. (2018). Negative thermal expansion behaviour in $MZrF_6$ (M = Ca, Mg, Sr): Ab-initio lattice dynamical studies. *Phys. Rev. B.* 98:014301. doi: 10.1103/PhysRevB.98.014301

Halperin, B., and Varma, C. (1976). Defects and the central peak near structural phase transitions. *Phys. Rev. B* 14, 4030–4044. doi: 10.1103/PhysRevB.14.4030

Han, S. S., and Goddard, W. A. (2007). Metal–organic frameworks provide large negative thermal expansion behavior. *J. Phys. Chem. C* 111, 15185–15191. doi: 10.1021/jp075389s

Hancock, J., McKnew, T., Schlesinger, Z., Sarrao, J., and Fisk, Z. (2004a). Kondo scaling in the optical response of $YbIn_{1-x}Ag_xCu_4$. *Phys. Rev. Lett.* 92:186405. doi: 10.1103/PhysRevLett.92.186405

Hancock, J., Turpen, C., Schlesinger, Z., Kowach, G., and Ramirez, A. (2004b). Unusual low-energy phonon dynamics in the negative thermal expansion compound ZrW_2O_8. *Phys. Rev. Lett.* 93:225501. doi: 10.1103/PhysRevLett.93.225501

Hancock, J. C., Chapman, K. W., Halder, G. J., Morelock, C. R., Kaplan, B. S., Gallington, L. C., et al. (2015). Large negative thermal expansion and anomalous behavior on compression in cubic ReO_3 - Type $A^{II}B^{IV}F_6$: $CaZrF_6$ and $CaHfF_6$. *Chem. Mater.* 27, 3912–3918. doi: 10.1021/acs.chemmater.5b00662

Handunkanda, S. U., Curry, E. B., Voronov, V., Said, A. H., Guzmán-Verri, G. G., Brierley, R. T., et al. (2015). Large isotropic negative thermal expansion above a structural quantum phase transition. *Phys. Rev. B* 92:134101. doi: 10.1103/PhysRevB.92.134101

Handunkanda, S. U., Occhialini, C. A., Said, A. H., and Hancock, J. N. (2016). Two-dimensional nanoscale correlations in the strong negative thermal expansion material ScF_3. *Phys. Rev. B* 94:214102. doi: 10.1103/PhysRevB.94.214102

He, H., Cvetkovic, V., and Varma, C. M. (2010). Elastic properties of a class of solids with negative thermal expansion. *Phys. Rev. B* 82:014111. doi: 10.1103/PhysRevB.82.014111

Jørgensen, J.-E., Jorgensen, J., Batlogg, B., Remeika, J., and Axe, J. (1986). Order parameter and critical exponent for the pressure-induced phase transitions in ReO_3. *Phys. Rev. B* 33, 4793–4798. doi: 10.1103/PhysRevB.33.4793

Jørgensen, J.-E., Marshall, W. G., Smith, R. I., Staun Olsen, J., and Gerward, L. (2004). High-pressure neutron powder diffraction study of the $Im\bar{3}$ phase of ReO_3. *J. Appl. Crystallogr.* 37, 857–861. doi: 10.1107/S0021889804018758

Keen, D., Goodwin, A., Tucker, M., Dove, M., Evans, J., Crichton, W., et al. (2007). Structural description of pressure-induced amorphization in ZrW_2O_8. *Phys. Rev. Lett.* 98:225501. doi: 10.1103/PhysRevLett.98.225501

Keen, D. A., Goodwin, A. L., Tucker, M. G., Hriljac, J. A., Bennett, T. D., Dove, M. T., et al. (2011). Diffraction study of pressure-amorphized ZrW_2O_8 using *in situ* and recovered samples. *Phys. Rev. B* 83:064109. doi: 10.1103/PhysRevB.83.064109

Kennedy, C., and White, M. (2005). Unusual thermal conductivity of the negative thermal expansion material, ZrW_2O_8. *Solid State Commun.* 134, 271–276. doi: 10.1016/j.ssc.2005.01.031

Kimura, T., Ishihara, S., Shintani, H., Arima, T., Takahashi, K. T., Ishizaka, K., et al. (2002). Distorted perovskite with e_g^1 configuration as a frustrated spin system. *Phys. Rev. B* 68:060403. doi: 10.1103/PhysRevB.68.060403

Kowach, G. R., and Ramirez, A. P. (2002). *Handbook of Materials Selection*. New York, NY: John Wiley & Sons, Inc.

Lee, K., Menon, R., Yoon, C., and Heeger, A. (2005). Direct observation of a transverse vibrational mechanism for negative thermal expansion in $Zn(CN)_2$: an atomic pair distribution function analysis. *J. Am. Chem. Soc.* 127, 15630–15636. doi: 10.1021/ja055197f

Li, C. W., Tang, X., Muñoz, J. A., Keith, J. B., Tracy, S. J., Abernathy, D. L., et al. (2011). Structural relationship between negative thermal expansion and quartic anharmonicity of cubic ScF_3. *Phys. Rev. Lett.* 107:195504. doi: 10.1103/PhysRevLett.107.195504

Lind, C., Coleman, M. R., Kozy, L. C., and Sharma, G. R. (2011). Zirconium tungstate/polymer nanocomposites: challenges and opportunities. *Phys. Status Solidi B* 248, 123–129. doi: 10.1002/pssb.201083967

Liu, Y., Wang, Z., Wu, M., Sun, Q., Chao, M., and Jia, Y. (2015). Negative thermal expansion in isostructural cubic ReO_3 and ScF_3: a comparative study. *Comput. Mater. Sci.* 107, 157–162. doi: 10.1016/j.commatsci.2015.05.019

Lommens, P., De Meyer, C., Bruneel, E., De Buysser, K., Van Driessche, I., and Hoste, S. (2005). Synthesis and thermal expansion of ZrO_2/ZrW_2O_8 composites. *J. Eur. Ceramic Soc.* 25, 3605–3610. doi: 10.1016/j.jeurceramsoc.2004.09.015

Maekawa, S., Tohyama, T., Barnes, S., Ishihara, S., Koshibae, W., and Khaliullin, G., (eds.). (2004). *Physics of Transition Metal Oxides*. Berlin: Springer-Verlag.

Martinek, C., and Hummel, F. A. (1968). Linear thermal expansion of three tungstates. *J. Am. Ceramic Soc.* 51, 227–228. doi: 10.1111/j.1151-2916.1968.tb11881.x

Mary, T. A., Evans, J. S. O., Vogt, T., and Sleight, A. W. (1996). Negative thermal expansion from 0.3 to 1050 Kelvin in ZrW_2O_8. *Science* 272, 90–92. doi: 10.1126/science.272.5258.90

Miller, W., Smith, C. W., Mackenzie, D. S., and Evans, K. E. (2009). Negative thermal expansion: a review. *J. Mater. Sci.* 44, 5441–5451. doi: 10.1007/s10853-009-3692-4

Mittal, R., Chaplot, S., Schober, H., and Mary, T. (2001). Origin of negative thermal expansion in cubic ZrW_2O_8 revealed by high pressure inelastic neutron scattering. *Phys. Rev. Lett.* 86, 4692–4695. doi: 10.1103/PhysRevLett.86.4692

Mittal, R., Chaplot, S. L., and Schober, H. (2009). Measurement of anharmonicity of phonons in the negative thermal expansion compound $Zn(CN)_2$ by high pressure inelastic neutron scattering. *Appl. Phys. Lett.* 95:201901.

Mittal, R., Chaplot, S. L., Schober, H., Kolesnikov, A. I., Loong, C.-K., Lind, C., et al. (2004). Negative thermal expansion in cubic $ZrMo_2O_8$: inelastic neutron scattering and lattice dynamical studies. *Phys. Rev. B* 70:214303. doi: 10.1103/PhysRevB.70.214303

Mittal, R., Gupta, M., and Chaplot, S. (2018). Phonons and anomalous thermal expansion behaviour in crystalline solids. *Prog. Mater. Sci.* 92, 360–445. doi: 10.1016/j.pmatsci.2017.10.002

Morelock, C. R., Gallington, L. C., and Wilkinson, A. P. (2014). Evolution of negative thermal expansion and phase transitions in $Sc_{1-x}Ti_xF_3$. *Chem. Mater.* 26:1936. doi: 10.1021/cm5002048

Morelock, C. R., Gallington, L. C., and Wilkinson, A. P. (2015). Solid solubility, phase transitions, thermal expansion, and compressibility in $Sc_{1-x}Al_xF_3$. *J. Solid State Chem.* 222:96. doi: 10.1016/j.jssc.2014.11.007

Morelock, C. R., Greve, B. K., Cetinkol, M., Chapman, K. W., Chupas, P. J., and Wilkinson, A. P. (2013a). Role of anion Site disorder in the near zero thermal expansion of tantalum oxyfluoride. *Chem. Mater.* 25, 1900–1904. doi: 10.1021/cm400536n

Morelock, C. R., Greve, B. K., Gallington, L. C., Chapman, K. W., and Wilkinson, A. P. (2013b). Negative thermal expansion and compressibility of $Sc_{1-x}Y_xF_3$ ($x \leq 0.25$). *J. Appl. Phys.* 114:213501. doi: 10.1063/1.4836855

Ngai, J., Walker, F., and Ahn, C. (2014). Correlated oxide physics and electronics. *Annu. Rev. Mater. Res.* 44, 1–17. doi: 10.1146/annurev-matsci-070813-113248

Occhialini, C. A., Handunkanda, S. U., Said, A., Trivedi, S., Guzmán-Verri, G. G., and Hancock, J. N. (2017). Negative thermal expansion near two structural quantum phase transitions. *Phys. Rev. Mater.* 1:070603(R). doi: 10.1103/PhysRevMaterials.1.070603

Ouyang, L., Xu, Y.-N., and Ching, W. (2002). Electronic structure of cubic and orthorhombic phases of ZrW_2O_8. *Phys. Rev. B* 65:113110. doi: 10.1103/PhysRevB.65.113110

Pantea, C., Migliori, A., Littlewood, P., Zhao, Y., Ledbetter, H., Lashley, J., et al. (2006). Pressure-induced elastic softening of monocrystalline zirconium tungstate at 300K. *Phys. Rev. B* 73:214118. doi: 10.1103/PhysRevB.73.214118

Perottoni, C., and Jornada, J. D. (1998). Pressure-induced amorphization and negative thermal expansion in ZrW_2O_8. *Science* 280, 886–889. doi: 10.1126/science.280.5365.886

Prager, M., and Heidemann, A. (1997). Rotational tunneling and neutron spectroscopy: A a compilation. *Chem. Rev.* 97, 2933–2966. doi: 10.1021/cr9500848

Pryde, A. K., Hammonds, K. D., Dove, M. T., Heine, V., Gale, J. D., and Warren, M. C. (1997). Rigid unit modes and the negative thermal expansion in ZrW_2O_8. *Phase Transit.* 61, 141–153. doi: 10.1080/01411599708223734

Pytte, E. (1972). Theory of perovskite ferroelectrics. *Phys. Rev. B* 5, 3758–3769. doi: 10.1103/PhysRevB.5.3758

Qu, B., He, H., and Pan, B. (2012). Origin of the giant negative thermal expansion in $Mn_3(Cu_{0.5}Ge_{0.5})N$. *Adv. Condens. Matt. Phys.* 2012, 4903–4906.

Rabe, K., Ahn, C., and Triscone, J.-M., editors (2007). *Physics of Ferroelectrics: A Modern Perspective*. Berlin: Springer-Verlag.

Ramirez, A., Broholm, C., Cava, R., and Kowach, G. (2000). Geometrical frustration, spin ice and negative thermal expansion – the physics of underconstraint. *Physica B* 280, 290–295. doi: 10.1016/S0921-4526(99)01695-6

Ramirez, A., and Kowach, G. (1998). Large low temperature specific heat in the negative thermal expansion compound ZrW_2O_8. *Phys. Rev. Lett.* 80, 4903–4906. doi: 10.1103/PhysRevLett.80.4903

Ravindran, T. R., Arora, A. K., and Mary, T. A. (2001). High-pressure Raman spectroscopic study of zirconium tungstate. *J. Phys. Condens. Matt.* 13, 11573–11588. doi: 10.1088/0953-8984/13/50/316

Riste, T., Samuelsen, E. J., Otnes, K., and Feder, J. (1993). Critical behaviour of $SrTiO_3$ near the 105K phase transition. *Solid State Commun.* 88, 901–904. doi: 10.1016/0038-1098(93)90266-P

Rodriguez, E. E., Llobet, A., Proffen, T., Melot, B. C., Seshadri, R., Littlewood, P. B., et al. (2009). The role of static disorder in negative thermal expansion in ReO_3. *J. Appl. Phys.* 105:114901. doi: 10.1063/1.3120783

Romao, C. P., Morelock, C. R., Johnson, M. B., Zwanziger, J. W., Wilkinson, A. P., and White, M. A. (2015). The heat capacities of thermomiotic ScF_3 and ScF_3–YF_3 solid solutions. *J. Mater. Sci.* 50, 3409–3415. doi: 10.1007/s10853-015-8899-y

Sachdev, S., and Keimer, B. (2011). Quantum criticality. *Phys. Today* 64, 29–35. doi: 10.1063/1.3554314

Sanson, A. (2014). Toward an understanding of the local origin of negative thermal expansion in ZrW_2O_8: limits and inconsistencies of the tent and rigid unit mode models. *Chem. Mater.* 26, 3716–3720. doi: 10.1021/cm501107w

Schirber, J. E., and Morosin, B. (1979). "Compressibility Collapse" Transition in ReO_3. *Phys. Rev. Lett.* 42, 1485–1487. doi: 10.1103/PhysRevLett.42.1485

Schlesinger, Z., Rosen, J., A., Hancock, J., N., and Ramirez, A., P. (2008). Soft manifold dynamics behind negative thermal expansion. *Phys. Rev. Lett.* 101:015501.

Schlesinger, Z., Rosen, J. A., Hancock, J. N., and Ramirez, A. P. (2008). Soft manifold dynamics behind negative thermal expansion. *Phys. Rev. Lett.* 101:015501. doi: 10.1103/PhysRevLett.101.015501

Scott, J. F. (1974). Soft-mode spectroscopy: experimental studies of structural phase transitions. *Rev. Mod. Phys.* 46, 83–128. doi: 10.1103/RevModPhys.46.83

Shirane, G. (1974). Neutron scattering studies of structural phase transitions at Brookhaven. *Rev. Mod. Phys.* 46, 437–449. doi: 10.1103/RevModPhys.46.437

Shirane, G., and Yamada, Y. (1969). Lattice-dynamical study of the 110K phase transition in $SrTiO_3$. *Phys. Rev.* 177, 858–863. doi: 10.1103/PhysRev.177.858

Simon, M. E., and Varma, C. M. (2000). Dynamics of some constrained solids. *Phys. Rev. Lett.* 86:1781. doi: 10.1103/PhysRevLett.86.1781

Sullivan, L. M., and Lukehart, C. M. (2005). Zirconium tungstate (ZrW_2O_8)/polyimide nanocomposites exhibiting reduced coefficient of thermal expansion. *Chem. Mater.* 17, 2136–2141. doi: 10.1021/cm0482737

Takagi, S., Subedi, A., Singh, D. J., and Cooper, V. R. (2010). Polar behavior of the double perovskites BiMZnNbO_6 (M = Pb and Sr) from density-functional calculations. *Phys. Rev. B* 81:134106. doi: 10.1103/PhysRevB.81.134106

Takenaka, K. (2018). Progress of research in negative thermal expansion materials: paradigm shift in the control of thermal expansion. *Front. Chem.* 6:267. doi: 10.3389/fchem.2018.00267

Takenaka, K., Hamada, T., Kasugai, D., and Sugimoto, N. (2012). Tailoring thermal expansion in metal matrix composites blended by antiperovskite manganese nitrides exhibiting giant negative thermal expansion. *J. Appl. Phys.* 112:083517. doi: 10.1063/1.4759121

Takenaka, K., and Takagi, H. (2005). Giant negative thermal expansion in Ge-doped anti-perovskite manganese nitrides. *Appl. Phys. Lett.* 87:261902. doi: 10.1063/1.2147726

Topler, J., Alefeld, B., and Heidemann, A. (1977). Study of the central peak of $SrTiO_3$ by neutron spectroscopy with high energy resolution. *J. Phys. C* 10, 635–643. doi: 10.1088/0022-3719/10/5/007

Tucker, M., Goodwin, A., Dove, M., Keen, D., Wells, S., and Evans, J. (2005). Negative thermal expansion in ZrW_2O_8: mechanisms, rigid unit modes, and neutron total scattering. *Phys. Rev. Lett.* 95:255501. doi: 10.1103/PhysRevLett.95.255501

Tucker, M. G., Keen, D. A., Evans, J. S., and Dove, M. T. (2007). Local structure in ZrW_2O_8 from neutron total scattering. *J. Phys.* 19:335215.

Unoki, H., and Sakudo, T. (1967). Electron spin resonance of Fe^{3+} in $SrTiO_3$ with special reference to the 110K phase transition. *J. Phys. Soc. Jpn.* 23, 546–552. doi: 10.1143/JPSJ.23.546

van Roekeghem, A., Carrete, J., and Mingo, N. (2016). Anomalous thermal conductivity and suppression of negative thermal expansion in ScF_3. *Phys. Rev. B* 94:020303. doi: 10.1103/PhysRevB.94.020303

Volker, H., Welche, P. R. L., and Dove, M. T. (2004). Geometrical origin and theory of negative thermal expansion in framework structures. *J. Am. Ceramic Soc.* 82:1793. doi: 10.1111/j.1151-2916.1999.tb02001.x

Zhou, W., Wu, H., Yildirim, T., Simpson, J., and Walker, A. (2008). Origin of the exceptional negative thermal expansion in metal-organic framework-5 Zn_4O(1,4-benzenedicarboxylate)$_3$. *Phys. Rev. B* 78:054114. doi: 10.1103/PhysRevB.78.054114

Conflict of Interest Statement: The authors declare that the research was conducted in the absence of any commercial or financial relationships that could be construed as a potential conflict of interest.

frontiers in Chemistry

ORIGINAL RESEARCH
published: 14 August 2018
doi: 10.3389/fchem.2018.00331

Phonons and Thermal Expansion Behavior of NiSi and NiGe

Prabhatasree Goel[1], *Mayanak K. Gupta*[1], *Sanjay K. Mishra*[1], *Baltej Singh*[1,2], *Ranjan Mittal*[1,2]* *and Samrath L. Chaplot*[1,2]

[1] *Solid State Physics Division, Bhabha Atomic Research Centre, Mumbai, India,* [2] *Homi Bhabha National Institute, Mumbai, India*

We have carried out first principles calculations of the vibrational and thermodynamic behavior in NiSi and isostructural compound NiGe. Phonon density of states has also been measured in NiSi using inelastic neutron scattering techniques. We find that the vibrational spectra of the two compounds are very different, due to the difference in the size and mass of Si and Ge. Interesting anomalous thermal behavior of NiSi due to anharmonic phonons is brought out well in our calculations, particularly the negative thermal expansion (NTE) along the b-axis of the orthorhombic unit cell. Large difference in thermal expansion behavior of NiSi and NiGe is very well reproduced by the calculations. Additionally, calculations enable to identify the phonon modes which lend major contribution to the negative thermal expansion behavior in NiSi, and reasons for negligible NTE in NiGe. Such typical representative modes at the zone-boundary along b-axis involve transverse vibrations of Si/Ge along c-axis.

PACS numbers: 78.70.Nx, 63.20.-e, 65.40.–b.

Keywords: inelastic, neutron, phonons, ab-initio, negative thermal expansion, grunesien parameter

OPEN ACCESS

Edited by:
Jun Chen,
University of Science and Technology Beijing, China

Reviewed by:
Qiang Sun,
Zhengzhou University, China
Lei Wang,
University of Science and Technology Beijing, China

***Correspondence:**
Ranjan Mittal
rmittal@barc.gov.in

Specialty section:
This article was submitted to Physical Chemistry and Chemical Physics, a section of the journal Frontiers in Chemistry

Received: *05 June 2018*
Accepted: *16 July 2018*
Published: *14 August 2018*

Citation:
Goel P, Gupta MK, Mishra SK, Singh B, Mittal R and Chaplot SL (2018) Phonons and Thermal Expansion Behavior of NiSi and NiGe. Front. Chem. 6:331. doi: 10.3389/fchem.2018.00331

INTRODUCTION

Transition metal silicides are considered important in microelectronics industry. These materials are used to reduce contact resistance at source, drain and gate terminals in standard complementary metal oxide semiconductor (CMOS) devices and very-large-scale integration (VLSI) technology. There are significant experimental and theoretical studies (Wu et al., 2005; Kim, 2015; Lin et al., 2015; Parshin et al., 2016; Stern and Madsen, 2016; Tang et al., 2017; Sidorova et al., 2018; Zhang et al., 2018a,b) on silicides to investigate their electronic and transport properties. Si-Ge alloys are the backbone of the metal-oxide semiconductor industry (Von Känel et al., 1992; Dahal et al., 2016; Lee et al., 2017; Simon et al., 2017; Kim et al., 2018). Lower resistivity, lower silicon consumption and higher stability make them better alternative to conventional silicides, like $TiSi_2$ and $CoSi_2$, for CMOS devices. Apart from its electronic industry applications, the compounds are reported to be good candidates for infrared sensor and ultraviolet photo detector applications. Detailed studies on the thermal behavior has been carried out on NiSiGe (Perrin et al., 2007) and FeNiSi (Simon et al., 2017) non-stoichiometric compositions, for fruitful integration of these derived compounds in the field of microelectronics.

NiSi (Franciosi et al., 1982; Lee et al., 2000; Detavernier et al., 2003; Jin et al., 2013), FeSi (Damascelli et al., 1997a,b), CoSi (Acun and Soyalp, 2012), and similar compounds (Kim, 2015) have been extensively studied with above applications in mind, and also for their various unusual physical and chemical properties (Weber et al., 2006; Lin et al., 2015; Geenen et al., 2018). NiSi (Connétable and Thomas, 2009) is structurally similar to NiGe. FeSi, a fascinating material,

has been studied for its unusual magnetic and thermodynamic properties like thermal expansion, elastic behavior, heat capacity, Seebeck coefficients, magnetic susceptibility, insulator-metal transition with increasing temperature (Mandrus et al., 1995; Caracas and Wentzcovitch, 2004; Delaire et al., 2011; Parshin et al., 2016; Stern and Madsen, 2016). It is also described as a strongly correlated system, a possible Kondo insulator. Several electronic structure calculations have been reported on FeSi to understand its anomalous thermal expansion and to elucidate a link between its electronic density of states with the thermal disorder (Vočadlo et al., 2002). Phonon density of states have been studied in FeSi (Damascelli et al., 1997a,b; Racu et al., 2008), both experimentally and using *ab initio* molecular dynamics, to investigate softening of phonons (Delaire et al., 2013) and coupling between phonons and electronic structure in order to explain anomalous thermal expansion. Equation of state (Sarrao et al., 1994; Dobson et al., 2002) and elasticity of FeSi (Vočadlo et al., 2012) have been studied extensively to gain better understanding of the earth's core, which is mainly comprised of an alloy of iron and nickel, with a few light alloying elements like Si, C, S, H, and O.

Although NiSi and FeSi are not structurally similar at ambient conditions, their thermal expansion behavior is comparable. A cumulative study of the phonon density of states in NiSi using neutrons and first principles lattice dynamics calculations of thermal expansion would fill the gaps in complete understanding of these monosilicides and monogermanides. NiSi exhibits unusual thermal anisotropy (Donthu et al., 2004) with an expansion along the **a**- and **c**- direction while along **b**- direction there is significant contraction with increasing temperature. Although the overall thermal expansion coefficient has a positive value, yet the behavior along **b** direction makes it an interesting study. This behavior is consistent in both bulk and in thin films. In case of NiGe, there is a contraction along b- axis but it is not as large as in NiSi and FeSi. It would be very interesting to understand the differences in the behavior of NiSi, FeSi, and NiGe. The calculation of the elastic properties of NiSi and NiGe in comparison to the reported studies on FeSi would be useful to know the strength of these materials. High pressure theoretical studies on NiSi up to 500 GPa have already been reported (Lord et al., 2012; Vočadlo et al., 2012) for unraveling the mysteries surrounding the composition and behavior of earth's core. $NiSi_xGe_{(1-x)}$ compounds are found to be promising in future microelectronics industry.

The crystal structure of NiSi and NiGe at ambient temperature is found to be orthorhombic (Pauling and Soldate, 1948), with space group Pnma. There are four Ni and four Si/Ge atoms in a unit cell. Although Ni is ferromagnetic, NiSi shows no magnetic ordering even up to lowest temperature around 0 K (Dahal et al., 2016). First principle studies to understand its high pressure behavior have been extensively reported (Jin et al., 2013). Anisotropy of thermal expansion in NiSi thin films have been studied (Perrin et al., 2007). Molar specific heat up to 400 K has been measured (Acker et al., 1999). Transport properties and neutron scattering to probe its magnetic ordering at 0.48 K have been reported. FeSi has a cubic $P2_13$ (B20) structure at ambient conditions. It transforms to the CsCl structure (Pm3m) at around 24 GPa and beyond 1950 K. NiSi adopts a B20 structure above 10 GPa and at around 900 K. It finally adopts a CsCl structure above 46 GPa and 1900 K.

This paper is a combined study of the vibrational properties of ambient phase of NiSi using neutron inelastic scattering experiments and theoretical calculations to understand the anomalous behavior of the thermal contraction along b-axis. First principles calculations have been carried out to derive the phonon density of states and thermal expansion behavior is obtained using *ab initio* lattice dynamics simulations. We also performed the calculation in NiGe. These studies will throw light on the specific phonon modes which are responsible for the anisotropic thermal behavior in NiSi, and the changes which come into play as we move from NiSi to NiGe. This is particularly interesting as the anisotropic thermal behavior is much less pronounced in NiGe.

EXPERIMENTAL AND COMPUTATIONAL DETAILS

Inelastic neutron scattering to study the phonon density of states in polycrystalline NiSi sample has been carried out using the Triple Axis Spectrometer at Dhruva reactor, Trombay. A sample of about 20 g of NiSi polycrystalline powder was used. All the measurements are carried out in the energy loss mode with constant momentum transfer (***Q***) geometry over a range of *Q*-values. The energy of the analyzer in various scans was kept fixed at 25 and 34.4 meV. In the incoherent one-phonon approximation (Carpenter and Price, 1985; Price and Skold, 1986), the measured scattering function $S(Q,E)$, as observed in the neutron experiments, is related to the phonon density of states $g^{(n)}(E)$ as follows:

$$g^{(n)}(E) = A < \frac{e^{2W(Q)}}{Q^2} \frac{E}{n(E,T) + \frac{1}{2} \pm \frac{1}{2}} S(Q,E) > \qquad (1)$$

Where the + or – signs correspond to energy loss or gain of the neutrons respectively and $n(E,T) = \left[\exp(E/k_BT) - 1\right]^{-1}$. A and B are normalization constants.

The observed neutron-weighted phonon density of states is a sum of the partial components of the density of states due to the various atoms, weighted by their scattering length squares.

$$g^n(E) = B \sum_k \{\frac{4\pi b_k^2}{m_k}\} g_k(E) \qquad (2)$$

Here b_k, m_k, and $g_k(E)$ are, respectively, the neutron scattering length, mass, and partial density of states of the k^{th} atom in the unit cell. The quantity between <> represents suitable average over all Q values at a given energy. $2W(Q)$ is the Debye-Waller factor averaged over all the atoms. The weighting factors $\frac{4\pi b_k^2}{m_k}$ for the various atoms in the units of barns/amu are: Ni: 0.331, and Si: 0.077.

The density functional theory calculations using VASP (Kresse and Furthmüller, 1996; Kresse and Joubert, 1999) along with PHONON software (Parlinksi, PHONON Software, 2003) is

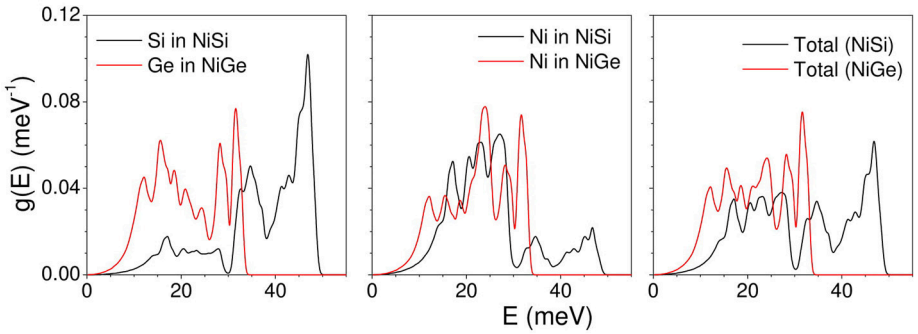

FIGURE 1 | (Color online) The calculated total and partial density of states in NiSi (black line) and NiGe (red line).

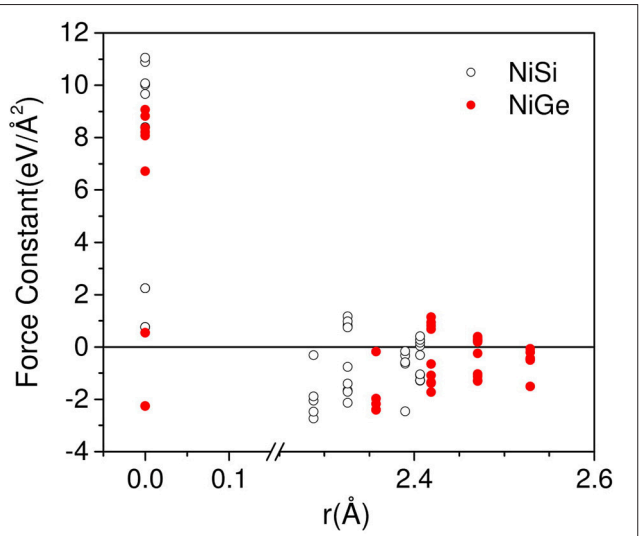

FIGURE 2 | (Color online) The calculated force constant matrix components as a function of the interatomic distance in NiSi(open circle) and NiGe (solid circle).

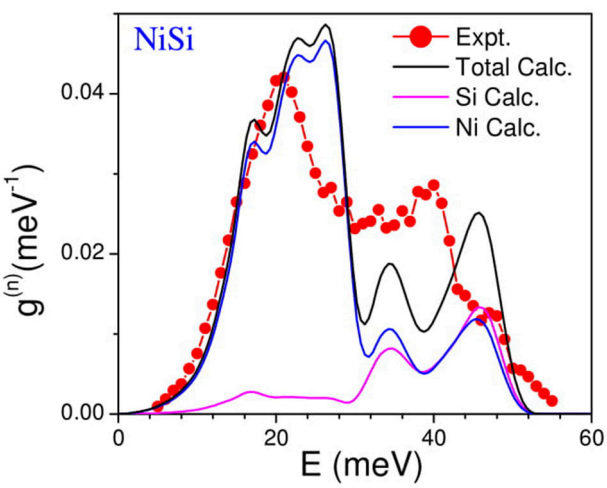

FIGURE 3 | (Color online) Experimental and computed neutron weighted phonon density of states of NiSi. The calculated neutron cross-section weighted partial phonon density of states of various atoms is also shown. The calculated spectrum has been broadened by the energy resolution in the experiment.

used to calculate the phonon frequencies of NiSi and NiGe in entire Brillouin zone. The software requires the forces on various atoms after displacement along various directions. These are obtained by computing the Hellman-Feynman forces on various atom in various configuration in a supercell with various (±x, ±y, ±z) atomic displacement patterns. The Hellman-Feynman forces on the atoms in the super cell have been calculated using density functional theory as implemented in the VASP software (Kresse and Furthmüller, 1996; Kresse and Joubert, 1999). NiSi and NiGe in orthorhombic phase (space group 62-Pnma) have 2 symmetrically inequivalent atoms in the unit cell, and total number of atoms in the primitive unit cell is 8. The force calculations is performed by displacing the symmetrically inequivalent atoms along (±x, ±y, ±z) directions. The energy cutoff is 1,000 eV and a 16 ×24 × 16 k point mess has been used to obtain energy convergence in total energy of the order of meV, which is sufficient to obtain the required accuracy in phonon energies. The Monkhorst Pack method is used for k point sampling (Monkhorst and Pack, 1976). The exchange-correlation contributions were included within PBE generalized gradient approximation (GGA) (Perdew et al., 1996). The structure is optimized with atomic pseudopotential with $d^8s^2p^2$, s^2p^2 and s^2p^2 valence electrons in Ni, Si, and Ge atom respectively. The convergence criteria for the total energy and ionic forces were set to 10^{-8} eV and 10^{-3} eV Å^{-1}, respectively.

RESULTS AND DISCUSSION

Phonon Spectra

The calculated total density of states in NiSi and NiGe along with respective partial contributions of various atoms is given in **Figure 1**. Replacing lighter Si in NiSi with Ge brings about a change in the lattice parameters and in the bond lengths. The lattice parameter as well as volume of NiGe is larger in

comparison to that of NiSi. This is reflected in the phonon density of states in the two compounds. In case of NiSi, the phonon spectra extend to 50 meV, while for NiGe it extends only up to 34 meV. The spectral range of the partial contribution of Ni is different in both the compounds. Ge (72.63 amu) is heavier in comparison to Si (28.095 amu). The low energy peak in the partial density of states of Ge in NiGe is at 8 meV in comparison to that at 16 meV in Si spectrum of NiSi. The shift in the peak position may be mainly due to the mass difference of both the atoms in respective compounds. Further, Ni-Ge bond lengths are longer in comparison to that of Ni-Si and hence the phonon frequencies are lower. As a result, the span of the vibrational spectrum of NiGe is up to 34 meV is lower in comparison to that of 50 meV in NiSi.

In order to explain the difference in the range of phonon spectrum in NiSi and NiGe, we have plotted the force constant matrix components (**Figure 2**) as a function of the interatomic distance. Typically, the force constant $\Phi(k, k')$ between a pair of atoms (k, k′) is determined from the force on the atom k' due to a small displacement of the atom k. On the other hand, the self force constant $\Phi(k, k)$ occurs due the force on the atom k when the same atom is displaced. The values at the zero distance (**Figure 2**) refer to the self force constants. The self force constants for NiGe are about 70% of the values for NiSi. The first nearest neighbor distances occur in the range of 2.2–2.6 Å in NiSi and NiGe, which correspond to Ni-Si and Ni-Ge bond lengths. We can see that the magnitude of force constant matrix elements in NiSi is larger than that in NiGe, which reflects in the phonon spectrum of these compounds. The phonon spectrum of NiSi extends up to 50 meV, while in NiGe the range is only up to 34 meV.

The measured neutron weighted phonon density of states using inelastic neutron scattering in NiSi has been shown in **Figure 3**. The experimental spectra compare very well with the calculations. The phonon spectra extend up to about 50 meV. The calculated neutron cross-section weighted partial phonon density of states of various atoms (**Figure 3**) clearly shows that the first peak in the phonon spectrum at 20 meV has mainly contribution from the Ni atom, while above 30 meV both the Ni and Si atoms contribute equally. The general characteristics of the experimental features are very well reproduced by the calculations. We may note that the peak heights in the calculated spectrum do not match very well with the measured inelastic spectrum. This may be due to the known inherent limitations both in experiment (e.g., incoherent approximation) and theory.

Phonon dispersion relation in NiSi and NiGe has been calculated (**Figure 4**). In accordance to the calculated phonon density of states, the spectral range of phonons in NiSi extends up to 50 meV, while the highest mode in NiGe is at around 34 meV. Comparison of the dispersion curve shows that the acoustic modes in NiSi extend up to 20 meV while the energy range in NiGe is up to 12 meV. These will give rise to difference in the elastic properties which arises from the slope of acoustic phonon branches along various high symmetry directions in the Brillion zone of both the compounds. The optic modes in NiSi are well separated and give rise to a three peak structure in the phonon spectrum (**Figure 1**), while in NiGe the modes are not separated and they give rise to a nearly broad peak (**Figure 1**).

The group theoretical decomposition of phonons at the zone center is given as:

$$4A_g + 2B_{1g} + 4B_{2g} + 2B_{3g} + 2A_u + 4B_{1u} + 2B_{2u} + 4B_{3u}$$

One each of the B_{1u}, B_{2u}, and B_{3u} modes are zero energy acoustic modes. The calculated Raman and infrared modes in NiSi and NiGe is given in **Table 1**. The comparison of zone center modes also shows that energies of various modes in NiSi extend up to about 50 meV while the maximum range in NiGe is up to 31 meV.

The calculated elastic constants for both the compounds are given in **Table 2**. It can be seen that all the elastic constants in NiSi have larger values in comparison to that in NiGe. This compares very well with the observed slopes of the dispersion curves in both the compounds. Similarly the bulk modulus value of NiSi (162.6 GPa) is found to be larger in comparison to that of NiGe (119.5 GPa). The bulk modulus of NiSi has been measured using synchrotron-based X-ray powder diffraction method (Lord et al., 2012) and found to be 165 ± 3 GPa, which is in very good agreement with our calculation.

Thermal Expansion Behavior

Both NiSi and NiGe are reported to show negative thermal expansion along the **b**-direction, while expansion coefficient is positive along **a**- and **c**-axis. The overall volume thermal expansion coefficient is positive. The anisotropic thermal expansion behavior can be computed under the quasiharmonic approximation. Each phonon mode of energy E_{qj} (j^{th} phonon mode at point q in the Brillouin zone) contributes to the thermal expansion coefficient, which is given by following relations for an orthorhombic (Mittal et al., 2018) system:

$$\alpha_a(T) = \frac{1}{V_0}\sum_{q,j} C_v(q,j,T)\left[s_{11}\Gamma_a + s_{12}\Gamma_b + s_{13}\Gamma_c\right] \quad (3)$$

$$\alpha_b(T) = \frac{1}{V_0}\sum_{q,j} C_v(q,j,T)\left[s_{21}\Gamma_a + s_{22}\Gamma_b + s_{23}\Gamma_c\right] \quad (4)$$

$$\alpha_c(T) = \frac{1}{V_0}\sum_{q,j} C_v\left(q,j,T\right)\left[s_{31}\Gamma_a + s_{32}\Gamma_b + s_{33}\Gamma_c\right] \quad (5)$$

Where V_0 is the unit cell volume, and s_{ij} are elements of elastic compliances matrix $s = C^{-1}$. C_v (q, j, T) is the specific-heat contribution from the phonon of energy $E_{q,j}$. Γ_a, Γ_b and Γ_c are the anisotropic mode Grüneisen parameters of phonon of energy $E_{q,j}$ as given by (Grüneisen and and Goens, 1924),

$$\Gamma_l\left(E_{q,j}\right) = -\left(\frac{\partial ln E_{q,j}}{\partial ln l}\right)_{l'};\ l, l' = a, b, c \quad (6)$$

The volume thermal expansion coefficient for a orthorhombic system is given by:

$$\alpha_V = (\alpha_a + \alpha_b + \alpha_c)$$

The calculation of anisotropic thermal expansion requires calculation of anisotropic Grüneisen parameters. The calculations of $\Gamma_l(E)$ are performed by applying an anisotropic

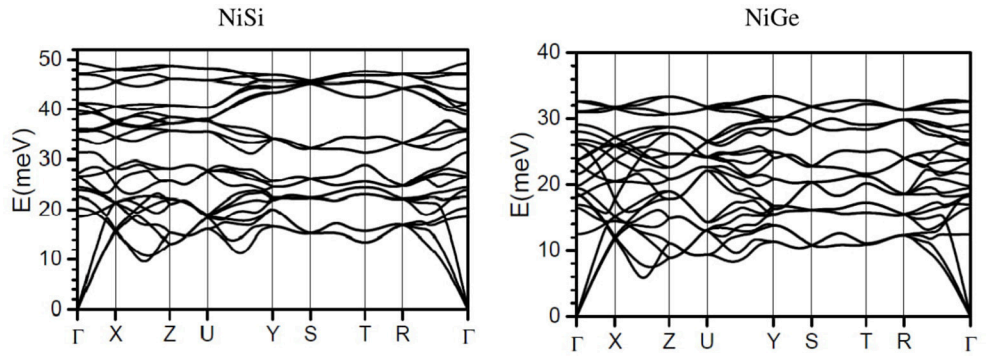

FIGURE 4 | The calculated phonon dispersion curves in NiSi and NiGe along the high symmetry points in the Brillioun zone.

TABLE 1 | The calculated Raman and infra red modes of NiSi and NiGe in meV units.

Representation	NiSi	NiGe
A_g	24	17
	27	19
	36	23
	44	31
B_{1g}	19	12
	41	29
B_{2g}	27	18
	31	26
	49	33
	41	27
B_{3g}	24	19
B_{3g}	39	24
A_u	20	18
	36	22
B_{1u}	27	16
	34	26
	47	33
B_{2u}	40	28
B_{3u}	22	20
	36	23
	47	31

TABLE 2 | The calculated elastic constants of NiSi and NiGe in GPa units.

Elastic Constants	NiSi	NiGe
C_{11}	265	194
C_{12}	160	121
C_{13}	87	84
C_{22}	215	156
C_{23}	143	91
C_{33}	227	157
C_{44}	108	102
C_{55}	131	71
C_{66}	127	104
B	163	119

stress by changing the lattice constant "a" and keeping the "b" and "c" parameters constant; and vice versa following eq.(6). **Figure 5** gives the calculated variation of anisotropic Grüneisen parameters with energy averaged over all the phonon modes in the Brillouin zone in NiSi and NiGe along a, b, and c directions.

As shown in **Figure 5**, for NiSi, the acoustic modes up to about 2.5 meV have negative values of $\Gamma_l(E)$ ($l = a, b.c$) of about -12, while in NiGe the $\Gamma_l(E)$ have relatively smaller negative values of -6 along b- and c- axis and positive values of $+8$ along a- axis. Further for NiSi, the modes in the energy range of 12–16 meV show small negative values of -0.2 along b-axis. The $\Gamma_l(E)$ ($l = a, b.c$) in the remaining part of the phonon spectrum have positive values. In case of NiGe, the Γ_b shows a dip in the energy range of 12–16 meV with positive values of $+0.5$. Above 2.5 meV, $\Gamma_l(E)$ in NiGe along the three axes have positive values.

The calculated thermal expansion coefficients as obtained from equations (3)–(5) are shown in **Figure 6**. We find that for NiSi, the thermal expansion coefficients are calculated to be positive along a and c-axes, while it is negative along b-axis. Similarly for NiGe, the α_b has small negative values up to about 100 K and it is positive above 100 K. The α_l (l = a, c) along a and c-axis are found to be positive in the whole temperature range. The experimental thermal expansion coefficient α_b has large negative value of -16.1×10^{-6} K^{-1} for NiSi, while in NiGe α_b has small negative values of $\sim -0.4 \times 10^{-6}$ K^{-1}. Our calculations are not able to quantitatively reproduce the negative values along b-axis in both the compounds, while qualitatively they agree very well with the experimental observations of a large difference in α_b in both the compounds.

The comparison between the experimental (Perrin et al., 2007) and calculated change in the lattice parameters with increasing temperature is given in **Figure 7**, along with change in unit cell volume of the two compounds. The change in a- and c- lattice parameters as computed in this work is in good agreement with reported experimental data (Perrin et al., 2007). However,

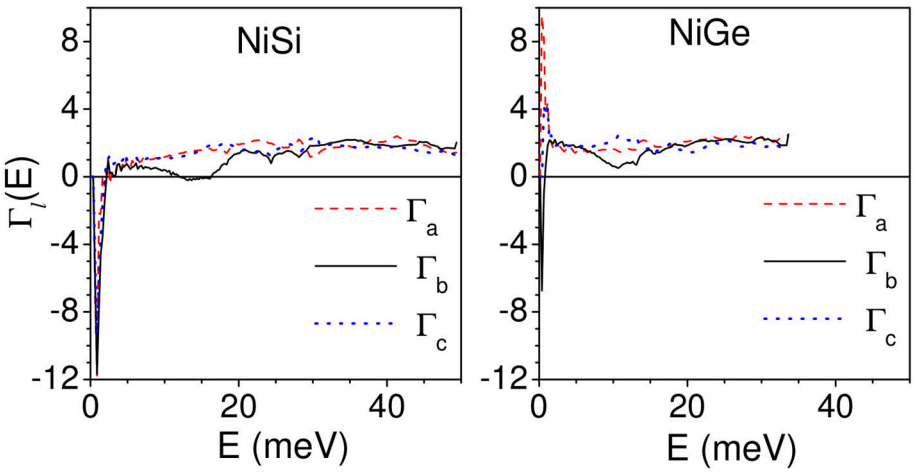

FIGURE 5 | (Color online) Calculated variation of anisotropic Grüneisen parameters with energy averaged over all the phonon modes in the Brillouin zone in NiSi and NiGe along a, b, and c directions.

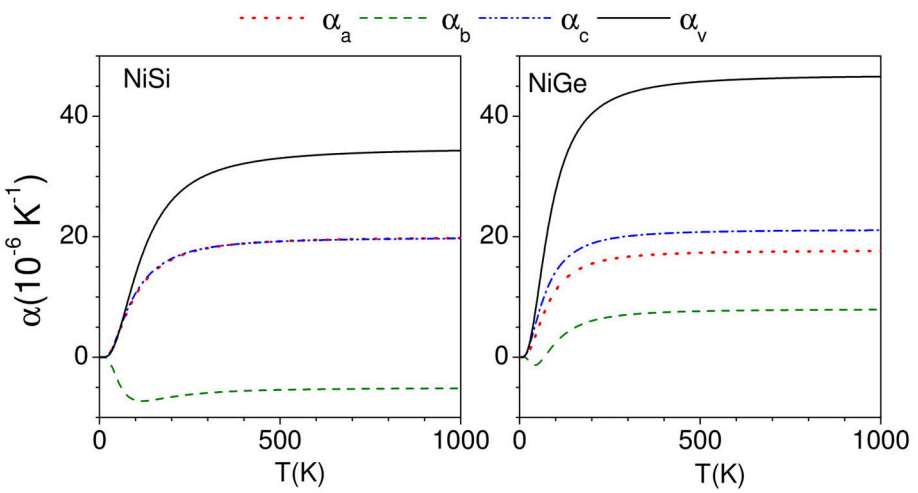

FIGURE 6 | (Color online) Calculated anisotropic behavior of the linear thermal expansion coefficients along a, b, and c directions as a function of temperature in NiSi and NiGe.

along the b- axis the contraction with increasing temperature is found to be underestimated in our calculations than from the experiments (Perrin et al., 2007). The change in b- lattice parameter is found to be more abrupt in the experimental observations for NiSi than that in our calculated values. The calculations are found to underestimate the contraction along the b-axis in NiSi, while for NiGe the comparison between the experiments and calculations seems to show good agreement with the reported data. Further, we find that the change in the volume of NiSi (**Figure 7**) from our calculations is found to be underestimated in comparison to the experimental data. The calculated volume is found to be slightly overestimated in NiGe (**Figure 7**).

As described above, the thermal expansion coefficient at a given temperature is an outcome of contribution of phonon modes of different energies in entire Brillouin zone. To get a better insight, we have calculated (**Figure 8**) the contribution of phonons of energy E, averaged over Brillouin zone, to the linear thermal expansion coefficient at 300 K. In case of NiSi, phonons from entire Brillouin zone contribute to positive expansion along both a- and c- axis. Interestingly, phonons below 30 meV contribute to negative expansion coefficient along b- axis. We find that phonon modes below 30 meV contribute in different ways along the a-, c-, and b- axis. Further, in case of NiGe, we find similar behavior of phonon contribution along a- and c- axis i.e., positive contribution to thermal expansion coefficient. However, along the b- axis, phonons up to 15 meV contribute to negative expansion coefficient. We find that the range of phonon energies contributing to NTE along b- axis is significantly different for NiSi and NiGe; and this leads to significant difference in the

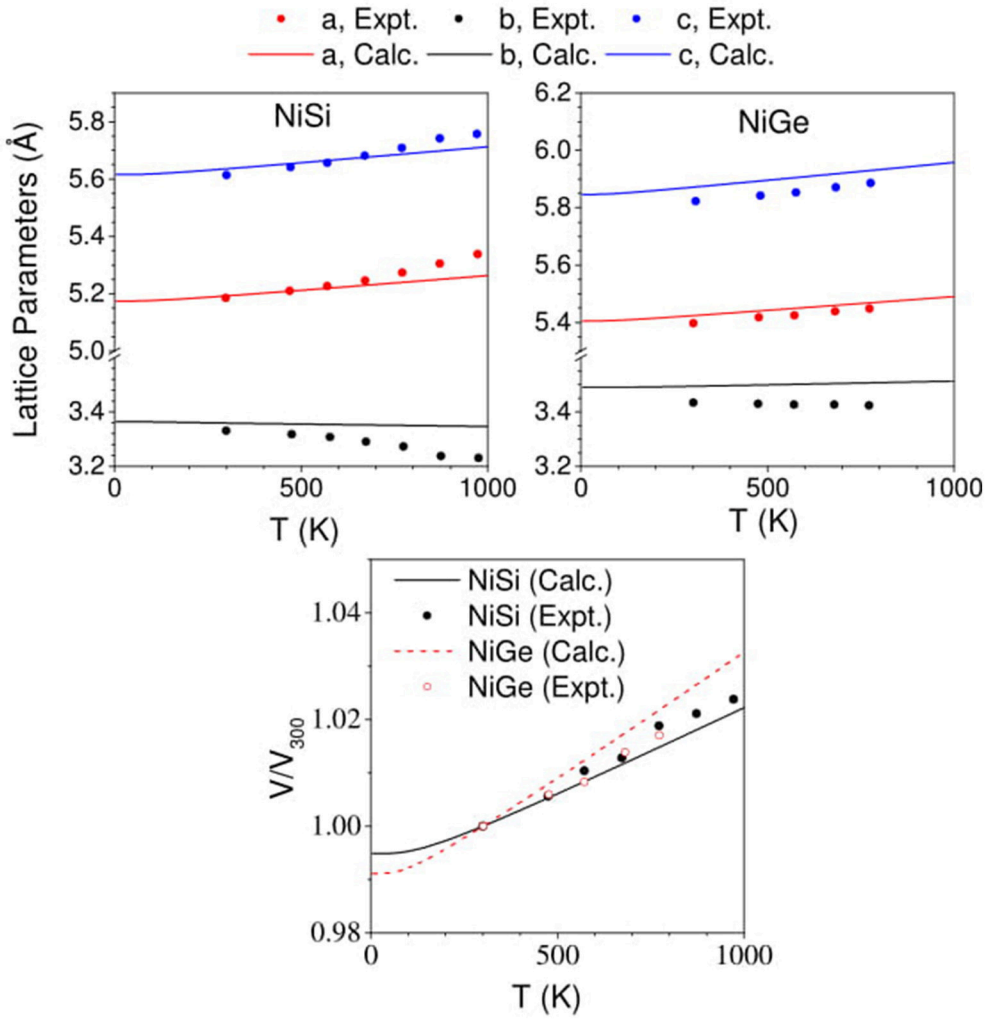

FIGURE 7 | (Color online) Change in lattice parameters and volume of NiSi and NiGe with increasing temperature. Our computed values (solid lines) in comparison with experimental data (Perrin et al., 2007) (solid symbols).

magnitude of negative thermal expansion along b- axis in these compounds. The important inference of the above analysis is that the modes below 15 meV strongly contribute to NTE along b- axis in both the compounds.

As mentioned in the computation details above, the thermal expansion coefficient along different axes is given by the sum of the products of anisotropic Γ and the elastic compliance components relevant to the given direction. These values have been calculated and given in **Table 3**. For NiSi and NiGe, thermal expansion $\alpha_b(T)$ is given by including the values of the individual compliance values from **Table 3**:

$$For\ NiSi\quad \alpha_b(T) = \frac{1}{V_0}\sum_{q,j} C_v(q,j,T)\,[-0.059\Gamma_a + 0.129\Gamma_b + 0.059\Gamma_c]$$

$$For\ NiGe\quad \alpha_b(T) = \frac{1}{V_0}\sum_{q,j} C_v(q,j,T)\,[-0.072\Gamma_a + 0.146\Gamma_b - 0.046\Gamma_c]$$

In case of NiSi, the values of Γ_a and Γ_c are comparable for both the compounds, and they cancel out: so only $0.129\Gamma_b$ term contributes. As Γ_b values are negative, the net value of α_b becomes negative. In case of NiGe, sum of the first and the third term is less than the second term, and since Γ_b values are positive, the net value of α_b is positive. The Γ_b values for different modes in the range of 12–18 meV (NiSi) are almost zero or negligibly small negative, while in case of NiGe they are small positive. As a result, the value of the thermal expansion coefficient in case of NiSi becomes more negative as compared to NiGe. Hence negative thermal expansion is more pronounced in NiSi.

In case of NiSi, the specific modes exhibiting negative values in α_b and the vibrational amplitude of the atoms in these low

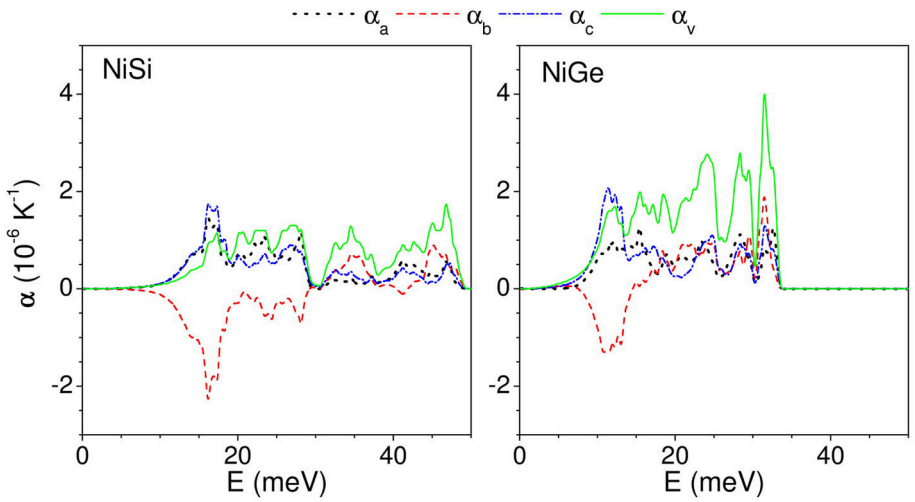

FIGURE 8 | (Color online) The contribution to anisotropic linear and volume thermal expansion coefficients at 300 K, from phonon mode of energy E averaged over the Brillouin zone.

TABLE 3 | The calculated elastic compliance of NiSi and NiGe in (10^{-3} GPa^{-1}) units.

Elastic Constants	NiSi	NiGe
S_{11}	70	103
S_{12}	−59	−72
S_{13}	10	−14
S_{22}	129	146
S_{23}	59	−46
S_{33}	77	98
S_{44}	93	98
S_{55}	77	142
S_{66}	78	96

energy modes would throw light on the physical mechanism involved in NTE. This in turn would eventually lead us to better understanding of the observed negative thermal expansion along b-direction in NiSi. The substitution of Ge in place of Si, brings about changes in the lattice which cancels out the possibility of similar behavior in NiGe. We have calculated the mean square amplitudes of various atom in NiSi and NiGe along a-, b-, and c- axis as a function of phonon energy to understand the mechanism of NTE along b- axis in both the compound (**Figure 9**). In **Figure 8**, we have observed that the NTE along b- axis in NiSi (NiGe) is mainly contributed by phonon modes of energy 8–20 meV. However, along a- and c- axis all the phonon modes contribute to positive expansion behavior (**Figure 8**). The density of states around 8–20 meV energy is very large, hence these modes play the dominating role in thermal expansion behavior of NiSi(NiGe). In **Figure 9**, the mean square displacements of Ni and Si below 20 meV show similar amplitude along a- and c- axis. However, along b- axis the magnitude of Ni is about 4 times than that of Si. In NiGe compound, the mean square displacements of Ge along b-axis are large in comparison to that of Si in NiSi. The ratio of u^2 values, along b-axis, for Ni to Ge is only about 1.5. These results of mean-square amplitudes clearly bring out the similarity between the dynamics along the **a**- and **c**- axes and a different behavior along the b-axis, particularly for the modes in the 8–20 meV range. This dynamical behavior is also reflected in the nature of the anisotropic thermal expansion behavior along the b-axis.

The NiSi structure consists of hexagonal sheets formed by Ni and Si atoms stacked along the **a**- axis. In **Figure 10**, we have given two of such representative modes at Y(0 1/2 0) point of 16.5 and 20.9 meV, which lead to negative expansion along **b**-axis. From Eq. (4), the 16.5/20.9 meV mode gives significant contraction along b- axis ($\alpha_b = -6.0 \times 10^{-6}$ K^{-1}/-3.69×10^{-6} K^{-1}, $\Gamma_a = 1.19/1.73$, $\Gamma_b = -1.31/0.00$, $\Gamma_c = 3.53/2.90$) and expansion in the a–c plane. The same representative modes in NiGe appear at an energy of 11.3/13.8 meV and contribute to NTE along b- axis ($\alpha_b = -5.5/-3.02 \times 10^{-6}$ K^{-1}, $\Gamma_a = 1.68/1.03$, $\Gamma_b = -0.59/-0.24$, $\Gamma_c = 5.12/2.98$). The displacement pattern of 16.5 meV mode shows that, two of the three neighboring Ni atoms in a given hexagon move anti parallel to each other along b- axis, while the third Ni is almost at rest; and similarly two of the Si atoms vibrate along the c-axis. In case of 20.9 meV mode, all the three Ni atoms and the Si atoms in the hexagon have significant displacements. Both of these modes propagate along the b-axis, and involve transverse Si vibrations largely along the c-axis. It may be noted that transverse vibrations may contribute to NTE since it causes a negative stress in the longitudinal direction.

The displacement patterns of these modes at 16.5/20.9 meV in NiSi are very similar to the modes at 11.3/13.8 meV for NiGe. However, in NiGe, other higher energy modes which give contribution to positive expansion are well below 30 meV and significantly contribute at ambient temperature, thus

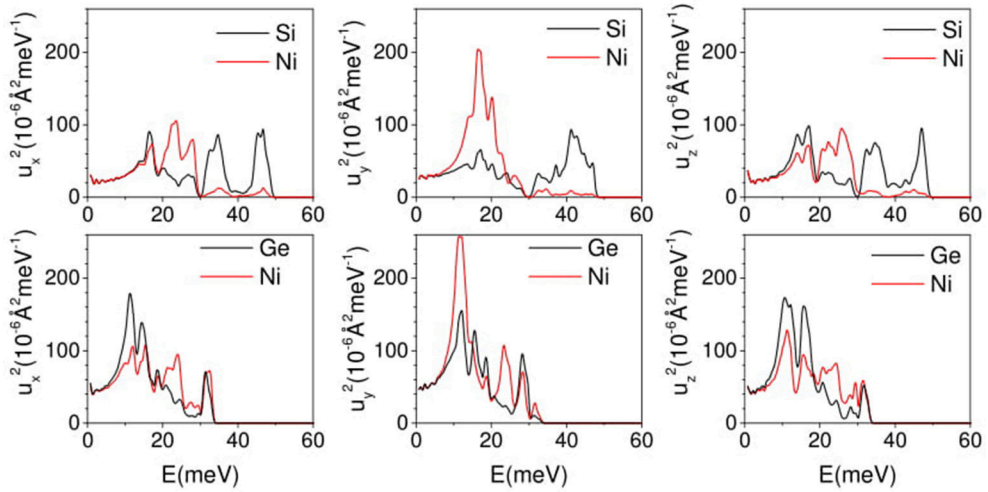

FIGURE 9 | (Color online) The calculated anisotropic mean square displacement of various atom in NiSi and NiGe as a function of phonon energy E averaged over Brillouin zone at 300 K.

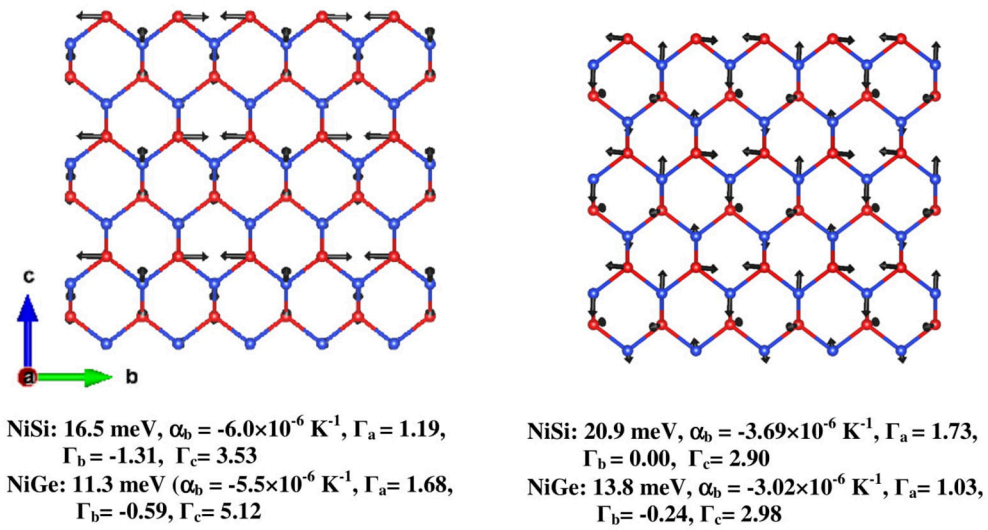

FIGURE 10 | (Color online) The displacement pattern of two representative modes at the Brillouin zone boundary (0 1/2 0) responsible for negative thermal expansion in NiSi and NiGe. The numbers below the figures give the phonon energy, α_b at 300 K, Γ_a, Γ_b, and Γ_c, respectively. Key: Ni–Red and Si/Ge–Blue.

nullifying the NTE along b- axis from the above phonon mode, while in NiSi the high-energy modes are distributed up to 50 meV, hence positive contributions from these modes are less significant.

CONCLUSIONS

Inelastic neutron scattering study of the phonon density of states in NiSi is reported. The measured data are in very good agreement with our calculations. We also report calculations on isostructural compound NiGe. Due to the heavier and bigger Ge atom, the phonon density of states of the two compounds differs in their total span. The contribution of Ni to the phonon density of states in both the compounds differs. NiSi shows large NTE along b-axis, while NiGe compound has very small NTE behavior. The difference in the negative thermal expansion along b-axis in both compounds is brought out very well in our calculations. The different thermal expansion along the b-axis for the two compounds could be understood in terms of the respective values of the Grüneisen parameters as well as the elastic compliances. We have identified representative phonon modes involving transverse vibration of Si/Ge atoms, which contribute significantly to the phenomenon of NTE along b-axis.

AUTHOR CONTRIBUTIONS

PG contributed in inelastic neutron scattering experiment, analysis and interpretation of experiment and ab-initio calculation, and writing of the manuscript. MG and BS contributed in inelastic neutron scattering experiment, ab-initio calculations, interpretation of experiment and ab-initio calculation, and writing of the manuscript. SM contributed in inelastic neutron scattering experiment, analysis and interpretation of experiment and ab-initio calculation and writing of the manuscript. RM formulated the problem, contributed in inelastic neutron scattering experiment, interpretation of experiment and ab-initio calculation, and writing of the manuscript. SC formulated the problem, contributed in interpretation of experiment and ab-initio calculation, and writing of the manuscript.

ACKNOWLEDGMENTS

SC would like to thank the Department of Atomic Energy, India for the award of Raja Ramanna Fellowship. The use of ANUPAM super-computing facility at BARC is acknowledged.

REFERENCES

Acker, J., Van Den Berg, G., Bohmhammel, K., Kloc, C., and Van Miltenburg, J. (1999). Thermodynamic properties of the nickel silicide NiSi between 8 and 400 K. *Thermochim. Acta* 339, 29–33. doi: 10.1016/S0040-6031(99)00293-2

Acun, A. D., and Soyalp, F. (2012). Elastic and phonon properties of FeSi and CoSi in the B2 structure. *Philos. Mag.* 92, 635–646. doi: 10.1080/14786435.2011.617323

Caracas, R., and Wentzcovitch, R. (2004). Equation of state and elasticity of FeSi. *Geophys. Res. Lett.* 31:L20603. doi: 10.1029/2004GL020601

Carpenter, J. M., and Price, D. L. (1985). Correlated motions in glasses studied by coherent inelastic neutron scattering. *Phys. Rev. Lett.* 54, 441–443. doi: 10.1103/PhysRevLett.54.441

Connétable, D., and Thomas, O. (2009). First-principles study of the structural, electronic, vibrational, and elastic properties of orthorhombic NiSi. *Phys. Rev. B* 79:094101. doi: 10.1103/PhysRevB.79.094101

Dahal, A., Gunasekera, J., Harringer, L., Singh, D. K., and Singh, D. J. (2016). Metallic nickel silicides: experiments and theory for NiSi and first principles calculations for other phases. *J. Alloys Compd.* 672, 110–116. doi: 10.1016/j.jallcom.2016.02.133

Damascelli, A., Schulte, K., Van Der Marel, D., Fäth, M., and Menovsky, A. (1997a). Optical phonons in the reflectivity spectrum of FeSi. *Physica B: Condensed Matter* 230, 787–789.

Damascelli, A., Schulte, K., Van der Marel, D., and Menovsky, A. (1997b). Infrared spectroscopic study of phonons coupled to charge excitations in FeSi. *Phys. Rev. B* 55:R4863.

Delaire, O., Al-Qasir, I. I., Ma, J., dos Santos, A. M., Sales, B. C., Mauger, L., et al. (2013). Effects of temperature and pressure on phonons in FeSi${}_{1{-}x}$Al${}_{x}$. *Phys. Rev. B* 87:184304. doi: 10.1103/PhysRevB.87.184304

Delaire, O., Marty, K., Stone, M. B., Kent, P. R., Lucas, M. S., Abernathy, D. L., et al. (2011). Phonon softening and metallization of a narrow-gap semiconductor by thermal disorder. *Proc. Natl. Acad. Sci. U.S.A.* 108, 4725–4730. doi: 10.1073/pnas.1014869108

Detavernier, C., Lavoie, C., and d'Heurle, F. (2003). Thermal expansion of the isostructural PtSi and NiSi: negative expansion coefficient in NiSi and stress effects in thin films. *J. Appl. Phys.* 93, 2510–2515. doi: 10.1063/1.1545156

Dobson, D. P., Vocadlo, L., and Wood, I. G. (2002). A new high-pressure phase of FeSi. *Am. Mineral.* 87, 784–787. doi: 10.2138/am-2002-5-623

Donthu, S., Tripathy, S., Chi, D., and Chua, S. (2004). Raman scattering probe of anharmonic effects in NiSi. *J. Raman Spectr.* 35, 536–540. doi: 10.1002/jrs.1164

Franciosi, A., Weaver, J., and Schmidt, F. (1982). Electronic structure of nickel silicides Ni 2 Si, NiSi, and Ni Si 2. *Phys. Rev. B* 26:546. doi: 10.1103/PhysRevB.26.546

Geenen, F., Solano, E., Jordan-Sweet, J., Lavoie, C., Mocuta, C., and Detavernier, C. (2018). The influence of alloying on the phase formation sequence of ultra-thin nickel silicide films and on the inheritance of texture. *J. Appl. Phys.* 123:185302. doi: 10.1063/1.5022070

Grüneisen, E., and Goens, E. (1924). Untersuchungen an Metallkristallen. *I. Z. Phys.* 26, 235–249.

Jin, Y.-Y., Kuang, X.-Y., Wang, Z.-H., and Huang, X.-F. (2013). Effect of pressure on structural phase transition and elastic properties in NiSi. *High Press. Res.* 33, 15–26. doi: 10.1080/08957959.2012.761213

Kim, A., Choi, E., Kwon, S. H., Zheng, L., Kang, K., Nam, M., et al. (2018). Nickel silicide phase distribution of electroless deposited contacts on silicon P+ junction substrate using nano-indented atomic force microscopy. *Sci. Adv. Materials* 10, 542–546. doi: 10.1166/sam.2018.3059

Kim, H. (2015). First-principles calculations of the lattice instability and the symmetry-lowering modulation of PtSi. *J. Korean Phys. Soc.* 66, 612–616. doi: 10.3938/jkps.66.612

Kresse, G., and Furthmüller, J. (1996). Efficient iterative schemes for {ab initio} total-energy calculations using a plane-wave basis set. *Phys. Rev. B* 54, 11169–11186. doi: 10.1103/PhysRevB.54.11169

Kresse, G., and Joubert, D. (1999). From ultrasoft pseudopotentials to the projector augmented-wave method. *Phys. Rev. B* 59, 1758–1775. doi: 10.1103/PhysRevB.59.1758

Lee, P. S., Mangelinck, D., Pey, K. L., Shen, Z., Ding, J., Osipowicz, T., et al. (2000). Micro-Raman spectroscopy investigation of nickel silicides and nickel (platinum) silicides. *Electrochem. Solid-State Lett.* 3, 153–155. doi: 10.1149/1.1390986

Lee, S. K., Seok, K. H., Chae, H. J., Lee, Y. H., Han, J. S., Jo, H. A., et al. (2017). Bottom-gate poly-Si thin-film transistors by nickel silicide seed-induced lateral crystallization with self-aligned lightly doped layer. *Solid State Electron.* 129, 6–9. doi: 10.1016/j.sse.2016.11.019

Lin, J.-Y., Hsu, H.-M., and Lu, K.-C. (2015). Growth of single-crystalline nickel silicide nanowires with excellent physical properties. *CrystEngComm* 17, 1911–1916. doi: 10.1039/C4CE02513J

Lord, O. T., Vočadlo, L., Wood, I. G., Dobson, D. P., Clark, S. M., and Walter, M. J. (2012). High-pressure phase transitions and equations of state in NiSi. II. Experimental results. *J. Appl. Crystallogr.* 45, 726–737. doi: 10.1107/S0021889812016809

Mandrus, D., Sarrao, J., Migliori, A., Thompson, J., and Fisk, Z. (1995). Thermodynamics of FeSi. *Phys. Rev. B* 51, 4763–4767. doi: 10.1103/PhysRevB.51.4763

Mittal, R., Gupta, M. K., and Chaplot, S. L. (2018). Phonons and anomalous thermal expansion behaviour in crystalline solids. *Prog. Mater. Sci.* 92, 360–445. doi: 10.1016/j.pmatsci.2017.10.002

Monkhorst, H. J., and Pack, J. D. (1976). Special points for Brillouin-zone integrations. *Phys. Rev. B* 13, 5188–5192. doi: 10.1103/PhysRevB.13.5188

Parshin, P., Chumakov, A., Alekseev, P., Nemkovski, K., Perßon, J., Dubrovinsky, L., et al. (2016). Experimental observation of phonons as spectators in FeSi electronic gap formation. *Phys. Rev. B* 93:081102. doi: 10.1103/PhysRevB.93.081102

Pauling, L., and Soldate, A. (1948). The nature of the bonds in the iron silicide, FeSi, and related crystals. *Acta Crystallogr.* 1, 212–216. doi: 10.1107/S0365110X48000570

Perdew, J. P., Burke, K., and Ernzerhof, M. (1996). Generalized gradient approximation made simple. *Phys. Rev. Lett.* 77, 3865–3868. doi: 10.1103/PhysRevLett.77.3865

Perrin, C., Nemouchi, F., Clugnet, G., and Mangelinck, D. (2007). Anisotropy of the thermal expansion of the Ni(Si1–xGex) phases investigated by high-temperature x-ray diffraction. *J. Appl. Phys.* 101:073512. doi: 10.1063/1.2713992

Price, D. L., and Skold, K. (1986). *Neutron Scattering*. Orlando, FL: Academic Press.

Racu, A.-M., Menzel, D., Schoenes, J., Marutzky, M., Johnsen, S., and Iversen, B. B. (2008). Phonon properties in narrow gap FeSi and FeSb2 single crystals. *J. Appl. Phys.* 103:07C912. doi: 10.1063/1.2885067

Sarrao, J., Mandrus, D., Migliori, A., Fisk, Z., and Bucher, E. (1994). Elastic properties of FeSi. *Physica B: Condensed Matter* 199, 478–479. doi: 10.1016/0921-4526(94)91875-9

Sidorova, M. V., Kozorezov, A. G., Semenov, A. V., Korneeva, Y. P., Mikhailov, M. Y., Devizenko, A. Y., et al. (2018). Nonbolometric bottleneck in electron-phonon relaxation in ultrathin WSi films. *Phys. Rev. B* 97:184512. doi: 10.1103/PhysRevB.97.184512

Simon, A. H., Elizabeth, T. H. W., David, P. D., Lindunka, V., and Ian, G. W. (2017). The thermal expansion of (Fe 1– y Ni y)Si. *J. Phys. Condensed Matter* 29:335701. doi: 10.1088/1361-648X/aa797d

Stern, R., and Madsen, G. K. (2016). *Ab initio* investigation of the anomalous phonon softening in FeSi. *Phys. Rev. B* 94:144304. doi: 10.1103/PhysRevB.94.144304

Tang, P., Zhou, Q., and Zhang, S.-C. (2017). Multiple types of topological fermions in transition metal silicides. *Phys. Rev. Lett.* 119:206402. doi: 10.1103/PhysRevLett.119.206402

Vočadlo, L., Knight, K., Price, G., and Wood, I. (2002). Thermal expansion and crystal structure of FeSi between 4 and 1173 K determined by time-of-flight neutron powder diffraction. *Phys. Chem. Minerals* 29, 132–139. doi: 10.1007/s002690100202

Vočadlo, L., Wood, I. G., and Dobson, D. P. (2012). High-pressure phase transitions and equations of state in NiSi. I. *Ab initio* simulations. *J. Appl. Crystallogr.* 45, 186–196. doi: 10.1107/S0021889812000337

Von Känel, H., Mäder, K., Müller, E., Onda, N., and Sirringhaus, H. (1992). Structural and electronic properties of metastable epitaxial FeSi 1+ x films on Si (111). *Phys. Rev. B* 45:13807.

Weber, W. M., Geelhaar, L., Graham, A. P., Unger, E., Duesberg, G. S., Liebau, M., et al. (2006). Silicon-nanowire transistors with intruded nickel-silicide contacts. *Nano Lett.* 6, 2660–2666. doi: 10.1021/nl0613858

Wu, H., Kratzer, P., and Scheffler, M. (2005). First-principles study of thin magnetic transition-metal silicide films on Si(001). *Phys. Rev. B* 72:144425. doi: 10.1103/PhysRevB.72.144425

Zhang, T., Song, Z., Alexandradinata, A., Weng, H., Fang, C., Lu, L., et al. (2018a). Double-Weyl phonons in transition-metal monosilicides. *Phys. Rev. Lett.* 120:016401. doi: 10.1103/PhysRevLett.120.016401

Zhang, X., Lita, A. E., Sidorova, M., Verma, V. B., Wang, Q., Nam, S. W., et al. (2018b). Superconducting fluctuations and characteristic time scales in amorphous WSi. *Phys. Rev. B* 97:174502. doi: 10.1103/PhysRevB.97.174502

Conflict of Interest Statement: The authors declare that the research was conducted in the absence of any commercial or financial relationships that could be construed as a potential conflict of interest.

The reviewer LW and handling Editor declared their shared affiliation.

frontiers in Chemistry

ORIGINAL RESEARCH
published: 11 October 2018
doi: 10.3389/fchem.2018.00478

High Pressure Behavior of Chromium and Yttrium Molybdate ($Cr_2Mo_3O_{12}$, $Y_2Mo_3O_{12}$)

*Lindsay Young, Jennifer Gadient and Cora Lind**

Department of Chemistry and Biochemistry, The University of Toledo, Toledo, OH, United States

The high pressure behavior of negative thermal expansion materials continues to be of interest, as their potential use in controlled thermal expansion composites can be affected by irreversible pressure-induced phase transitions. To date, it is not possible to predict the high pressure behavior of these compounds, necessitating measurements on each composition. In this work, high pressure synchrotron powder X-ray diffraction studies of $Cr_2Mo_3O_{12}$ and $Y_2Mo_3O_{12}$ were conducted in a diamond anvil cell. Chromium molybdate, which adopts the monoclinic $P2_1/a$ structure under ambient conditions, was found to not undergo any crystalline-crystalline transitions up to 8.9 GPa. The orthorhombic ambient pressure polymorph of yttrium molybdate was found to undergo a phase transition to the monoclinic $P2_1/a$ scandium tungstate structure below 0.13 GPa. This structure is frequently observed for related materials at low temperatures, but has never been reported for $Y_2Mo_3O_{12}$. No additional changes in this material were observed up to 4.9 GPa. The fact that the monoclinic polymorphs of these materials do not undergo phase transitions within the studied pressure range makes them unique among $A_2M_3O_{12}$ materials, as most isostructural compositions undergo at least one phase transition to crystalline high pressure phases.

Keywords: negative thermal expansion, high pressure, synchrotron radiation, *in-situ* studies, scandium tungstate family

OPEN ACCESS

Edited by:
Andrea Sanson,
Università degli Studi di Padova, Italy

Reviewed by:
Valerio Cerantola,
European Synchrotron Radiation Facility, France
Koshi Takenaka,
Nagoya University, Japan

****Correspondence:***
Cora Lind
cora.lind@utoledo.edu

Specialty section:
This article was submitted to Physical Chemistry and Chemical Physics, a section of the journal Frontiers in Chemistry

Received: *30 May 2018*
Accepted: *20 September 2018*
Published: *11 October 2018*

Citation:
Young L, Gadient J and Lind C (2018) High Pressure Behavior of Chromium and Yttrium Molybdate ($Cr_2Mo_3O_{12}$, $Y_2Mo_3O_{12}$) Front. Chem. 6:478. doi: 10.3389/fchem.2018.00478

INTRODUCTION

Thermal expansion describes the tendency of materials to change dimensions with increasing temperature. Due to longitudinal vibrations of atoms along atomic bonds as thermal energy is introduced, most materials expand. The thermal expansion coefficient α quantifies the magnitude of dimensional change over a specific temperature range. Mismatches in thermal expansion are a major concern in many engineering fields for any devices that combine two or more materials (Roy et al., 1989; Lommens et al., 2005; Takenaka, 2012). The differences in the magnitude of thermal expansion between two adhered materials can lead to degradation of devices with thermal cycling due to delamination at the interface. In addition, any optical or electronic applications where absolute dimensions are crucial for optimal performance require materials that display negligible expansion to ensure dimensional stability. These challenges have led to significant interest in materials that display negative thermal expansion (NTE) (Korthuis et al., 1995; Evans et al., 1996; Attfield and Sleight, 1998a,b; Lind et al., 1998, 2011; Sleight, 1998; Reisner et al., 2000; Li et al., 2002; Phillips et al., 2008; Chapman and Chupas, 2009; Kozy et al., 2009; Greve et al., 2010). It has been proposed that NTE materials when incorporated as fillers in composites would allow the overall

expansion of the material to be reduced or tailored to a specific value (Verdon and Dunand, 1997; Holzer and Dunand, 1999; Matsumoto et al., 2003; Sullivan and Lukehart, 2005; Tani et al., 2007, 2010; Lind et al., 2011). This has been accomplished previously with zirconium tungstate as a filler in a ceramic zirconia optical fiber coating (Fleming et al., 1997). However, other attempts to prepare composites with tailored expansion coefficients have failed due to irreversible phase transitions of the NTE filler under the temperature and pressure conditions encountered during manufacturing or use. For example, a Cu/ZrW_2O_8 composite showed highly irreproducible expansion behavior due to formation of the orthorhombic high pressure phase of ZrW_2O_8, which displays positive volume expansion (Holzer and Dunand, 1999).

There are several classes of materials that display NTE properties. One of these is the scandium tungstate family. These materials are often referred to as the $A_2M_3O_{12}$ family, which includes a wide range of compositions, as A can be any trivalent cation ranging in size from Al^{3+} to the smaller lanthanides, and M can be molybdenum or tungsten. These materials crystallize in corner-sharing networks of AO_6 octahedra and MO_4 tetrahedra, and many compositions form closely related monoclinic ($P2_1/a$-$A_2M_3O_{12}$) and orthorhombic (Pbcn-$A_2M_3O_{12}$) structures. NTE is only observed in the orthorhombic phase, and arises from concerted tilting motions of the polyhedra. The formation of the monoclinic and orthorhombic phases depends heavily on composition, and many compounds show a reversible transition between the monoclinic polymorph at low temperatures and the orthorhombic structure at high temperatures. The temperature at which this transition occurs varies widely with composition, and in extreme cases, materials can adopt the monoclinic or orthorhombic structures over their entire stability range. For instance, scandium tungstate, yttrium tungstate and yttrium molybdate (Nassau et al., 1971; Evans et al., 1998; Forster and Sleight, 1999; Marinkovic et al., 2005; Zhou et al., 2008) retain the orthorhombic structure to at least −263 to −258 °C, the lowest temperatures studied to date, while gallium molybdate remains monoclinic up to its decomposition temperature of 600 °C (Gates et al., 2006).

In addition to the corner-sharing orthorhombic and monoclinic polymorphs described above, denser structures with higher A-site coordination numbers, resulting in a combination of both corner- and edge-shared polyhedra, are known for compositions that contain the larger lanthanides lanthanum through terbium (Nassau et al., 1965, 1971). Yttrium's ionic radius falls between the ionic radii of the trivalent lanthanides that form the Pbcn structure and polymorphs with 7- or 8-coordinated A^{3+} cations, respectively (Shannon, 1976). As a result, yttrium molybdate can adopt two orthorhombic structures in space groups Pba2 and Pbcn under ambient conditions (Marinkovic et al., 2005; Gates and Lind, 2007). Pbcn-$Y_2Mo_3O_{12}$ is thermodynamically stable above 550 °C but can be retained as a metastable phase by quenching to room temperature (Gates and Lind, 2007). This structure readily absorbs water from the atmosphere, leading to formation of a trihydrate, $Y_2Mo_3O_{12}{\cdot}3H_2O$ (Kol'tsova, 2001). The denser Pba2-phase is isostructural to $Tb_2Mo_3O_{12}$, with a higher coordination number for Y and edge sharing YO_7 polyhedra. The denser Pba2-$Y_2Mo_3O_{12}$ polymorph is thermodynamically stable below 550 °C, but is kinetically disfavored, thus requiring long periods of annealing at 530 °C to prepare it. This structure does not hydrate (Gates and Lind, 2007).

Because NTE materials may need to withstand high pressures and temperatures during production and regular use of composites, it is important to characterize their behavior under non-ambient conditions for effective application. The open framework structure of these materials that gives rise to NTE is highly susceptible to pressure-induced changes. High pressure studies of a number of NTE materials have shown that they undergo phase transitions to high pressure polymorphs or amorphize (see **Table 1** and references therein). These denser structures are not expected to exhibit NTE (Hu et al., 1997; Paraguassu et al., 2004; Garg et al., 2005b; Maczka et al., 2012), as the phonon modes that cause NTE require corner-sharing open frameworks. Irreversible phase transitions to high pressure polymorphs are thus detrimental for potential applications, while reversible phase transitions may be acceptable if they occur at pressures that are not encountered during use of composites.

While a number of high pressure studies of $A_2M_3O_{12}$ materials have been conducted, the knowledge of their high pressure behavior is not comprehensive. Some compositions are well characterized, but many are only partially characterized (e.g., $In_2Mo_3O_{12}$, $In_{1.5}Y_{0.5}Mo_3O_{12}$, $Lu_2W_3O_{12}$, $Y_2Mo_3O_{12}$, see **Table 1**) or have not yet been studied (e.g., many $Ln_2M_3O_{12}$, $Cr_2Mo_2O_{12}$). Variations in data quality and experimental parameters have also led to conflicting results for the same materials (e.g., $Al_2W_3O_{12}$, $Sc_2W_3O_{12}$, **Table 1**). As such, the high pressure behavior of $A_2M_3O_{12}$ materials remains unpredictable. One exception to this has been the observation that compositions adopting the orthorhombic structure at room temperature undergo a phase transition to the slightly denser $P2_1/a$-structure below 0.5 GPa (Paraguassu et al., 2004; Garg et al., 2005a; Varga et al., 2005a,b, 2006; Cetinkol et al., 2008; Varga, 2011; Lind, 2012; Maczka et al., 2012). Generally, at least one additional phase transition occurs at higher pressures between 1 and 4 GPa. Amorphization is commonly reported, which can be reversible or irreversible and shows onsets as low as 2.3 GPa or higher than 10 GPa (Garg et al., 2001, 2005a,b; Secco et al., 2001, 2002a,b; Liu et al., 2002; Arora et al., 2004, 2005; Karmakar et al., 2004; Mukherjee et al., 2004; Paraguassu et al., 2004; Varga et al., 2005a; Gates et al., 2006; Baiz et al., 2012; Torres Dias et al., 2013). **Table 1** summarizes the current literature on high pressure behavior of $A_2Mo_3O_{12}$compounds.

This paper reports the high pressure behavior of $Cr_2Mo_3O_{12}$ and Pbcn-$Y_2Mo_3O_{12}$. $Cr_2Mo_3O_{12}$ is monoclinic at room temperature and displays positive expansion with $\alpha_l = 9.8 \times 10^{-6}\,^{\circ}C^{-1}$ up to 380 °C, where it undergoes a transition to the orthorhombic Pbcn polymorph. Above this temperature, NTE with $\alpha_l = -9.4 \times 10^{-6}\,^{\circ}C^{-1}$ is observed (Tyagi et al., 2002). $Y_2Mo_3O_{12}$ adopts the orthorhombic structure at all temperatures, and shows NTE with $\alpha_l = -9.0 \times 10^{-6}\,^{\circ}C^{-1}$ from −253 to 177 °C (Marinkovic et al., 2009). No previous high pressure studies on chromium molybdate exist, while yttrium molybdate has been investigated by low resolution

TABLE 1 | Current high pressure research on scandium tungstate family materials.

Material	Method	PTF	Transition (GPa)	Study findings/Cell	R†
$AlFeMo_3O_{12}$	PXRD (Young et al., 2016)	M:E	1.7	α' transition from isotropic to anisotropic compression	R
			3.2	$P2_1/a$ γ-phase a = 14.94 Å, b = 8.71 Å, c = 17.48 Å, β = 124.4°	R
			3.9-4.2	Monoclinic δ-phase, a = 14.20 Å, b = 8.36 Å, c = 13.57 Å, β = 102.0°	R, H
$AlGaMo_3O_{12}$	PXRD (Young et al., 2016)	M:E	2.0, 2.9	α' and α" transition from isotropic to anisotropic compression	R
			4.1–4.4	$P2_1/a$ γ-phase a = 14.76 Å, b = 8.59 Å, c = 17.21 Å, β = 124.6°	R
			5.0–5.3	Monoclinic δ-phase a = 14.16 Å, b = 8.32 Å, c = 13.62 Å, β = 102.2°	R, H
$Al_2Mo_3O_{12}$	PXRD (Young et al., 2016)	M:E	3.0	α' transition from isotropic to anisotropic compression	R
			4.6–4.9	$P2_1/a$ γ-phase a = 14.65 Å, b = 8.53 Å, c = 17.08 Å, β = 124.5°	R
			5.7–6.1	Monoclinic δ phase a = 14.04 Å, b = 8.28 Å, c = 13.47 Å, β = 101.9°	R, H
$Al_2W_3O_{12}$	Raman (Garg et al., 2001)	M:E	0.05	Unindexed phase	R < 2
			7	Amorphization	I
	PXRD (Achary et al., 2002)	None	8, 48 h	ambient phase recovered	
	PXRD/900°C (Achary et al., 2002)	None	3	Decomposes to $AlWO_4 + WO_{3-x}$	
	AC resistivity (Mukherjee et al., 2003)	None	0.5	Phase transition	I
	Raman (Maczka et al., 2004)	M:E	0.28	Potentially monoclinic	R
			2.8	Unindexed	
	PXRD/ dielectric measurement (Mukherjee et al., 2004)	M:E	0.5	P 2_1 a = 8.95 Å, b = 9.07 Å, c = 12.59 Å, β = 90.51°	ND
			3.4	P 2_1 a = 9.59 Å, b = 12.52 Å, c = 7.84 Å, β = 91.99°	ND
			6–18	Amorphization	I
	Raman (Garg et al., 2005b)	M:E	0.4–3	Unindexed phase	R
			5.3–6	Unindexed phase	ND
			14	Amorphization	I
	PXRD (Varga et al., 2005a)	iPrOH	0.1	$P2_1/a$ a = 15.41 Å, b = 9.05 Å, c = 19.91 Å, β = 125.4°	R
			7	Amorphization	I
$Fe_2Mo_3O_{12}$	PXRD (Young et al., 2016)	M:E	1.5	α' transition from isotropic to anisotropic compression	R
			2.7–2.9	$P2_1/a$ γ-phase a = 15.06 Å, b = 8.79 Å, c = 17.63 Å, β = 124.6°	R
			3.5–3.7	Monoclinic δ phase a = 14.46 Å, b = 8.48 Å, c = 13.77 Å, β = 102.0°	R, H
	Raman (Moura et al., 2016)	Mineral oil	4.8	Amorpization	R
$Ga_2Mo_3O_{12}$	PXRD (Gates et al., 2006)	M:E	3.2	Monoclinic phase a = 13.7 Å, b = 7.3 Å, c = 12.3 Å, β = 115.9°	R
			4.2	a = 14.4 Å, b = 8.3 Å, c = 13.8 Å, β = 103.1°	R
			8	Amorphization	I
	PXRD (Young et al., 2016)	M:E	<3.3	$P2_1/a$ γ-phase a = 15.24 Å, b = 8.68 Å, c = 17.44 Å, β = 126.1°	
			<4.2	Monoclinic δ-phase a = 14.45 Å, b = 8.34 Å, c = 13.71 Å, β = 101.3°	
$In_2Mo_3O_{12}$	Raman (Mendonça et al., 2016)	M:E	1.5	Denser structure	ND
			5–>7	Gradual amorphization	I

(Continued)

TABLE 1 | Continued

Material	Method	PTF	Transition (GPa)	Study findings/Cell	R†
$In_{1.5}Y_{0.5}Mo_3O_{12}$	Raman (Mendonça et al., 2016)	M:E	1.0	Denser structure	ND
			3.4–5	Two stage amorphization	ND
$In_2W_3O_{12}$	PXRD (Baiz, 2010; Baiz et al., 2012)	M:E	1.9–2.7	a = 19.68 Å, b = 4.49 Å, c = 17.34 Å, b = 99.21°	ND
			>2.7	Progressive amorphization	I
$Lu_2W_3O_{12}$	PXRD (Liu et al., 2002)	None	5–8	Progressive amorphization	I
$Sc_2Mo_3O_{12}$	PXRD and Raman (Arora et al., 2004)	M:E	4–12	Two stage amorphization; distortions and disordering at 4 GPa, complete at 12 GPa	I
	PXRD and Raman (Paraguassu et al., 2004)	M:E Raman	0.29	Unknown potentially monoclinic phase (C_{2h}^5)	R
			2.7	Unknown phase	R
			3.7–5.1	Amorphization	R < 5
		16:3:1 M:E:H(PXRD)	4–20	Amorphization	I after compression to 20
	PXRD and Raman (Arora et al., 2005)	M:E	12	Amorphization	I
	PXRD (Varga et al., 2005a)	iPrOH	0.25	$P2_1/a$ a = 16.51 Å, b = 9.54 Å, c = 18.84 Å, β = 125.35°	ND
			2.5–3.0	Unknown phase	ND
			8	Amorphization	Mostly I
$Sc_2W_3O_{12}$	Raman (Garg et al., 2001)	M:E	0.45	Unindexed	R
			7	Amorphous	I
	PXRD (Secco et al., 2001)	None	8	Amorphous	I
	PXRD/400°C (Secco et al., 2002a,b)	None	3.2	Unindexed	ND
			4	Amorphous	I
	PXRD/Raman (Garg et al., 2005a)	M:E	0.6	a = 16.0 Å, b = 9.4 Å, c = 18.6 Å, β = 124.9°	R
			1.6	a = 13.81 Å, b=9.6 Å, c=18.26 Å, β =123.91°	I
			6.5–14	Amorphous	I
	PXRD (Varga et al., 2005b)	iPrOH, N_2	0.3	a = 16.25 Å, b = 9.58 Å, c = 18.94 Å, β = 125.4°	R
			2.8	Unindexed	I
	ND (Varga et al., 2006)	He	0.25–0.3	a = 16.25 Å, b = 9.58 Å, c = 18.93 Å, β = 125.37°	H
	PXRD (Cetinkol et al., 2008)	M:E	0.3	a = 16.25 Å, b = 9.58 Å, c = 18.93 Å, β = 125.38°	
		M:E	2.7	a = 8.45 Å, b = 11.31 Å, c = 9.15 Å, α = 96.6°	I
Pbcn -$Y_2Mo_3O_{12}$	Raman (Torres Dias et al., 2013)	Mineral Oil	0.3	Potentially monoclinic, 0.3 GPa	ND
			2.4	Amorphization, 2.4 GPa	I
$Y_2W_3O_{12}$	PXRD, Raman (Karmakar et al., 2004)	M:E	>3	Progressive amorphization	I > 4
$Zr_2W_2PO_{12}$	PXRD (Cetinkol et al., 2009)	M:E	1.37	a = 9.30 Å, b = 12.10 Å, c = 9.05 Å, β = 89.60°, $P2_1/n11$	R
			>3	a = 9.34 Å, b = 11.40 Å, c = 8.21 Å, β = 97.37° $P2_1/n11$	R
			>6.3	a = 11.15 Å, b = 9.38 Å, c = 12.52 Å, α = 88.87°, β = 141.65°, γ = 90.93°	R
			>14	Partial amorphization	I

M:E, 4:1 Methanol:Ethanol; M:E:H, 16:3:1 Methanol:Ethanol:Water.

† *In the final column, I, irreversible, R, reversible, H, hysteresis, and ND, not determined.*

diffraction studies by our group and Raman spectroscopy by Torres Dias (Gates, 2008; Torres Dias et al., 2013). Our previous low resolution diffraction data showed no evidence of phase transitions until irreversible amorphization occurred at 2.3 GPa. It was surprising that no transition to the monoclinic polymorph was detected. However, the *in situ* Raman study conducted by Torres Dias et al. reported a phase transition at 0.3 GPa, followed by irreversible amorphization at 2.4 GPa. The Raman data suggested a change in symmetry from orthorhombic to monoclinic. In this work, higher resolution synchrotron diffraction data revealed that Pbcn-$Y_2Mo_3O_{12}$ indeed undergoes a transition to the monoclinic $P2_1/a$ structure at low pressure. The atomic coordinates were extracted by Rietveld analysis. Interestingly, $P2_1/a$-$Y_2Mo_3O_{12}$ and $Cr_2Mo_3O_{12}$ do not undergo any further crystalline-crystalline phase transitions before amorphization occurs. To our knowledge, this is the first report of relatively low density corner sharing polyhedral frameworks that remain stable under pressure.

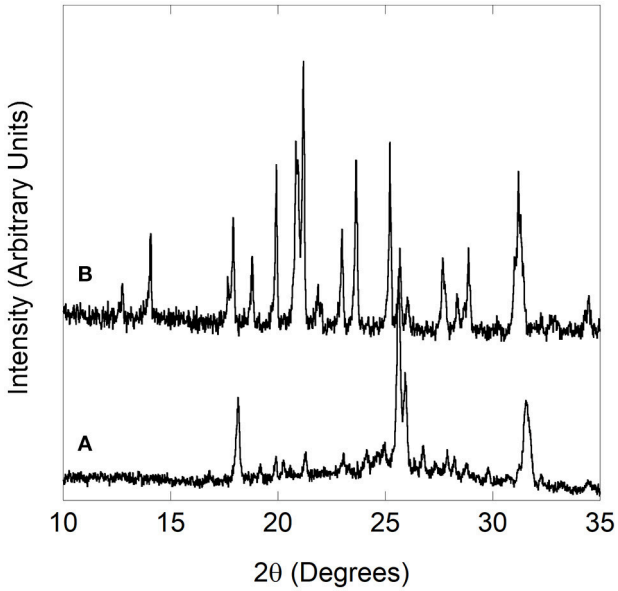

FIGURE 1 | Yttrium molybdate **(A)** trihydrate formed upon exposure to atmospheric moisture, **(B)** Pbcn polymorph reformed after drying.

EXPERIMENTAL

$Cr_2Mo_3O_{12}$ and Pbcn-$Y_2Mo_3O_{12}$ powders were synthesized using a non-hydrolytic sol-gel (NHSG) method as described previously (Gates et al., 2006; Gates and Lind, 2007; Gindhart, 2007; Baiz et al., 2008; Gates, 2008; Gindhart et al., 2008; Baiz, 2010). Well crystallized $Cr_2Mo_3O_{12}$ was obtained after heat treatment to 500 °C, while $Y_2Mo_3O_{12}$ required heating between 800 and 1,000 °C to achieve sharp peaks. Sample quality was confirmed by powder X-ray diffraction on a PANalytical X'Pert Pro Multipurpose Diffractometer. Phase pure samples with good crystallinity were chosen for the high pressure studies. Pbcn-$Y_2Mo_3O_{12}$ has a strong tendency to absorb ambient moisture and form a trihydrate (**Figure 1A**), thus the material was freshly dried (**Figure 1B**), immediately transferred to a vial while hot and sealed with Parafilm.

In situ high pressure powder diffraction studies were carried out at beamline 17-BM at the Advanced Photon Source at Argonne National Laboratory in an EasyLab "Diacell Bragg-(G)" diamond anvil cell (DAC). Data were collected with a 2-D Perkin Elmer a-Si C-window CCD detector during two separate trips. $Cr_2Mo_3O_{12}$ was measured at a wavelength of 0.72808 Å and a detector distance of 400 mm. $Y_2Mo_3O_{12}$ was investigated during a subsequent trip at a wavelength of 0.72959 Å with a larger detector distance of 600 mm to allow collection of data to smaller d-spacings. Both setups allowed even subtle changes in the PXRD patterns to be seen. Data were collected by averaging six individual 5 s exposures. Anhydrous isopropanol was chosen as a pressure transmitting fluid (PTF) with a hydrostatic limit of 4.2 GPa (Angel et al., 2007). While higher hydrostatic limits can be achieved (Klotz et al., 2009) with alcohol or alcohol/water mixtures (10.5 GPa) or some liquefied inert gases (N_2: 10 GPa, Ne: 15 GPa, He: 40 GPa), these PTFs are not suitable for the study of many NTE materials. Water is known to penetrate the open frameworks of several NTE compounds, and may lead to formation of crystalline hydrates as observed for $ZrW_2O_8{\cdot}H_2O$ (Duan et al., 1999; Banek et al., 2010) or $Y_2Mo_3O_{12}{\cdot}3H_2O$ (Kol'tsova, 2001; Marinkovic et al., 2005). While no crystalline methanol adducts have been reported, it is plausible that this molecule may also penetrate into open frameworks and impact the high pressure behavior. Similarly, atomic or diatomic gases may insert into the NTE frameworks, as has been demonstrated for $CaZrF_6$ (Hester et al., 2017a).

The powders were finely ground using a mortar and pestle in an approximately 3:1 ratio with sodium chloride as an internal pressure calibrant. An EasyLab "Diacell Bragg-(G)" membrane diamond anvil cell with diamond culet faces measuring 500 microns was fitted to a 300 micron thick steel gasket pre-indented to 100 microns with a 250 micron hole. The sample was packed into the sample chamber, flooded with anhydrous isopropanol as a PTF, and the DAC was quickly sealed. To avoid hydration of Pbcn-$Y_2Mo_3O_{12}$, this sample was packed in a glovebag under argon. An "asclosed" pattern was collected before attaching a stainless steel diaphragm to the cell, and a programmable methanol pump was used to gradually increase the pressure to 4.9 GPa ($Y_2Mo_3O_{12}$) and 8.9 GPa ($Cr_2Mo_3O_{12}$) while collecting data at pressure increments of approximately 0.02 to 0.2 GPa. After the highest pressure was reached, files were collected during decompression in approximately 1.0 GPa steps. Final pressures of 2.2 and 1.9 GPa were observed at the end of the runs for $Cr_2Mo_3O_{12}$ and $Y_2Mo_3O_{12}$, respectively. A "decompressed" pattern was collected after opening the cell to release any residual pressure. The pressure for each scan was determined from the refined NaCl lattice parameters using the equation of state published by Birch (Birch, 1986). This approach requires calculation of Eulerian strain using equation (1):

$$f = \frac{(v/v_o{}^{-2/3}) - 1}{2} \quad (1)$$

where f is the Eulerian strain, v is the cell volume at pressure P, and v_o is the ambient pressure volume. The value for v_o was determined to be 179.5864 Å^3. The calculated values for f can then be used to determine pressure using equation (2):

$$P = 3K_o f(1+2f)^{5/2}(1+af) \quad (2)$$

where K_o is the bulk modulus at ambient temperature and a is a constant that depends on temperature. Literature values for K_o (239.9 kbar at 25 °C) and a (1.796 at 25 °C) were used (Birch, 1986).

The pressures reported in this manuscript are estimated to have errors of ± 0.1 GPa due to the continuous pressure increase during data collection, which results in each pattern being collected over a small range of pressures. The only exception are scans collected in the "asclosed" cell before attaching the diaphragm, for which we estimate an error of ± 0.02 GPa based on the uncertainty of the extracted lattice parameter of the standard.

Bulk moduli of all phases were estimated using the program PASCal using a 3rd order Birch–Murnaghan equation of state (Cliffe and Goodwin, 2012). For high pressure phases, the first pressure point at which a polymorph was observed was used as critical pressure.

Data Integration and Analysis

The 2-D data were integrated using GSAS-II (Toby and Von Dreele, 2013). A pattern of NIST LaB_6 collected in the DAC was used to calibrate the detector distance and determine the penetration correction, which was necessary to correct a slight non-linear distortion of the data due to penetration of X-rays into the detector. The patterns were refined using Topas Academic (Bruker, 2006; Coelho, 2018), and consecutive refinements were conducted in command line mode by copying each output file to the input file for the next dataset. Rietveld refinements were carried out for all phases, as the atomic coordinates were either known or determined in the course of this work.

RESULTS AND DISCUSSION

The high pressure behavior of $Cr_2Mo_3O_{12}$ and $Y_2Mo_3O_{12}$ was investigated *in situ* using synchrotron powder diffraction inside a DAC. During each experiment, the pressure was continuously increased. Different pressure programs were used during the two experiments, resulting in a pressure increase that was approximately twice as fast for $Cr_2Mo_3O_{12}$ compared to $Y_2Mo_3O_{12}$. Stack plots of all high pressure datasets and selected 1D diffraction patterns are displayed in **Figures 2**, **3**.

The scans collected upon sealing the DAC showed that the materials were under a small amount of pressure at the beginning of data collection, as the diamond anvil cell must be tightened enough to avoid evaporation of the PTF. The pressure of the first dataset was 0.05 GPa for $Cr_2Mo_3O_{12}$ and 0.13 GPa for Pbcn-$Y_2Mo_3O_{12}$, respectively. Data were collected up to 8.9 GPa for $Cr_2Mo_3O_{12}$ with 0.05 to 0.2 GPa increments, and up to 4.9 GPa for Pbcn-$Y_2Mo_3O_{12}$ with 0.02 to 0.1 GPa increments between patterns. Inspection of the PXRD overlays showed that the peaks steadily shifted to higher angles with increasing pressure (**Figures 2**, **3**). Visual inspection of the data did not show any obvious signs of reconstructive phase transitions to distinct crystalline high pressure polymorphs, such as peak splitting, coalescence, or abrupt changes in the pattern. At sufficiently high pressures, the peaks became progressively broader in both materials.

Diffraction data for chromium molybdate were collected up to 8.9 GPa (scan 126, **Figure 2A**), although the conditions became non-hydrostatic above 4.2 GPa (scan 44) due to the hydrostatic limit of isopropanol. The patterns collected at lower pressures showed comparable shifts to higher angles for all peaks, suggesting relatively isotropic compressibility of $Cr_2Mo_3O_{12}$ along all three unit cell axes. Close inspection of the stacked data overlay revealed some subtle changes in the 3 to 4 GPa pressure range (see arrows in **Figure 2B**). Scan 38 (3.6 GPa) shows noticeable broadening of several peaks (e.g., 9.5, 12.3, and 13.2°), while other peaks coalesce with neighboring peaks (e.g., 12–12.2°). As these changes were not observed at lower pressures, this suggests that a subtle phase transition to a closely related structure occurred.

The data range displayed in **Figure 2A** contains two peaks that belong to the pressure standard NaCl, which are found at 12.8 and 14.8° 2θ at the beginning of the experiment (scan 0) and persist as well-defined peaks in all scans. In contrast, the $Cr_2Mo_3O_{12}$ peaks start to become progressively diffuse above 5.5 GPa (scan 54), indicating the onset of disorder or amorphization. Many NTE materials have been reported to amorphize under pressure (Huang, 1998; Perottoni and da Jornada, 1998; Garg et al., 2001, 2005b; Liu et al., 2001, 2002; Secco et al., 2001, 2002a,b; Arora et al., 2004, 2005; Karmakar et al., 2004; Mukherjee et al., 2004; Paraguassu et al., 2004; Varga et al., 2005b; Gates et al., 2006; Keen et al., 2007; Catafesta et al., 2008; Cetinkol et al., 2009; Baiz et al., 2012; Torres Dias et al., 2013; Salke et al., 2018), especially under non-hydrostatic conditions, as their open frameworks allow for volume-reducing rotations of the constituent polyhedra. Under non-hydrostatic pressure, such random reorientations can become "frozen in" at relatively low pressures, resulting in progressive loss of long range order. In most materials, amorphization is irreversible upon decompression. In this work, data were also collected during decompression (scans 127-144). The final dataset during the $Cr_2Mo_3O_{12}$ high pressure experiment was collected at a residual pressure of 2.2 GPa, and showed only NaCl peaks and very broad features resembling an amorphous material (**Figure 2C**). However, complete release of the pressure by opening the cell resulted in recovery of crystallinity, suggesting that the material does not completely disorder (**Figure 2C**).

Lattice constants as a function of pressure were extracted by Rietveld refinement. The pattern collected after closing the cell gave a good match to the PDF view cards of monoclinic $Cr_2Mo_3O_{12}$ (01-078-1654) and cubic NaCl (01-077-2064), and these phases were used as starting models for refinements. The patterns contained intensity spikes due to sample graininess, indicating that data quality was not optimal. Throughout the data set, several unidentified peaks at 6.6, 16.9, 19.4, 25.2, and 29.5° persisted. These peaks were of low intensity (see arrow in

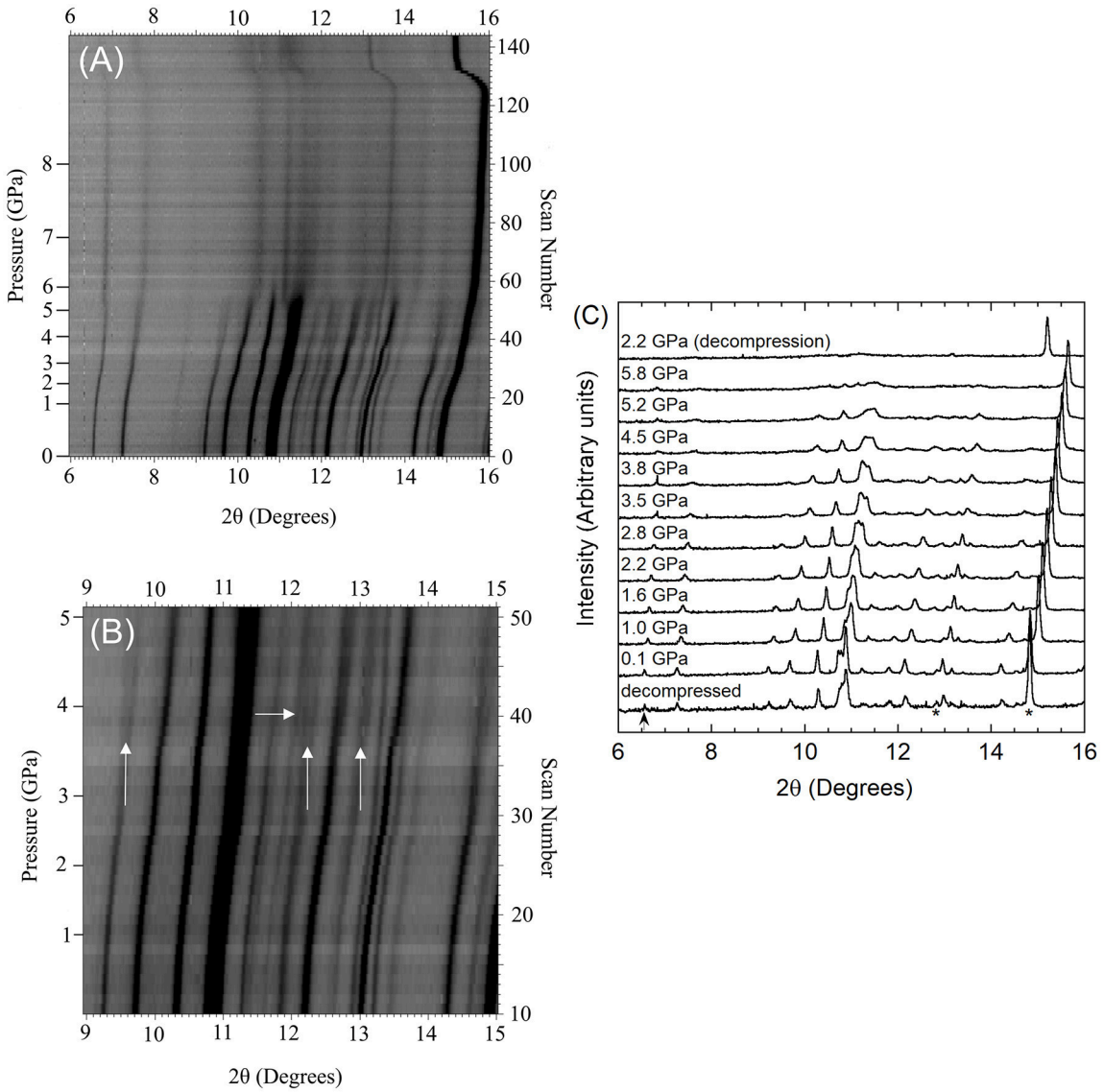

FIGURE 2 | (A,B) Stacked 2D overlays of all high pressure data and **(C)** selected patterns for $Cr_2Mo_3O_{12}$ collected during compression unless stated otherwise. In **(C)**, NaCl peaks are indicated by * in the pattern collected after decompression, and the strongest peak of the unidentified impurity phase is marked with an arrow. Vertical arrows in **(B)** mark peaks that broaden significantly compared to other $Cr_2Mo_3O_{12}$ peaks, while the horizontal arrow indicates an area of peak coalescence.

Figure 2C for most intense peak) and could not be identified as belonging to any known impurity phases, nor any known parts of the instrumental setup such as the diamond, mounting clay, or steel. It was evident that these features shifted significantly less than the chromium molybdate peaks, and persisted as sharper peaks even above the hydrostatic limit. This behavior suggests that these peaks are either due to diffraction from a material not experiencing the same pressure as the sample, or from a very hard impurity phase. Although they could not be identified, the peaks were of such low intensity that they did not interfere with Rietveld analysis.

At the lowest pressure, the data were refined using the monoclinic α-$Cr_2Mo_3O_{12}$ phase (**Figure 4A**). Bond distance restraints were necessary to vary atomic positions without losing polyhedral connectivity. Refinements with restraints resulted in slightly distorted polyhedra, but preserved the overall connectivity. After initial optimization, atom positions were fixed before running consecutive refinements to avoid potentially disastrous changes. All scans with discernible peaks could be fitted using the α-phase model. Refinement quality decreased at higher pressures as peaks began to broaden above 4.0 GPa, with only very broad features remaining above 5.0 GPa (**Figure 2C**). This pressure range extends above the hydrostatic limit of isopropanol, which is 4.2 GPa. The changes in lattice parameters and volume (**Figure 5**) were extracted up to 5.0 GPa. Linear behavior was observed up to ∼3.5 GPa, at which point

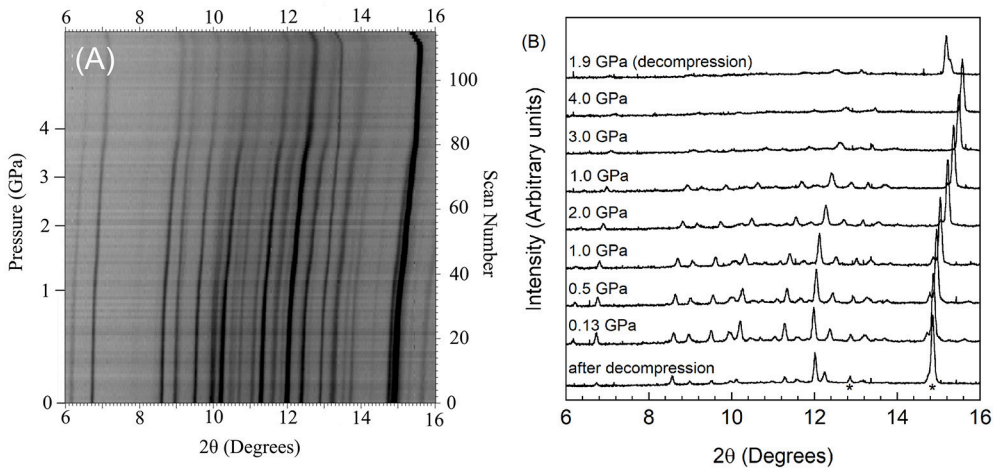

FIGURE 3 | (A) Stacked 2D overlay of all high pressure data and **(B)** selected patterns for Pbcn-$Y_2Mo_3O_{12}$ collected during compression and after decompression. In **(B)**, NaCl peaks are indicated by * in the pattern collected after decompression.

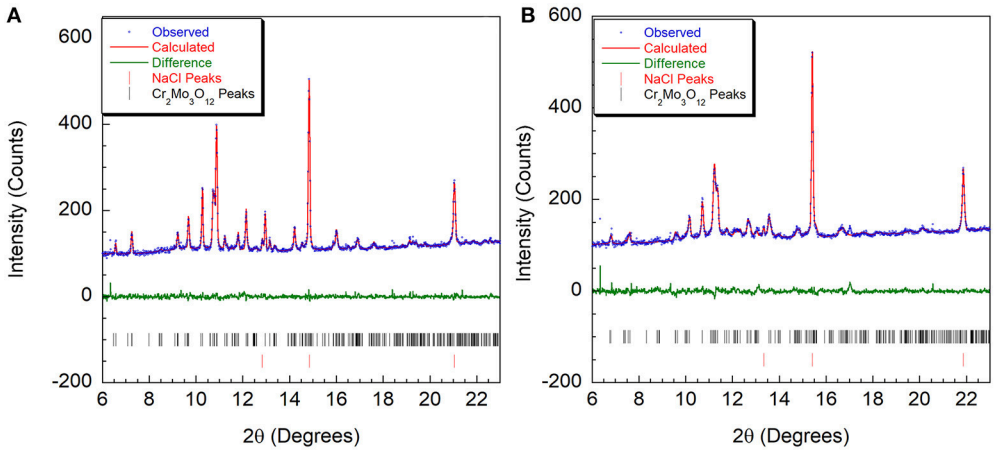

FIGURE 4 | Rietveld plots of $Cr_2Mo_3O_{12}$ data collected at **(A)** 0.05 GPa and **(B)** 3.7 GPa refined using the $P2_1/a$ structure.

a discontinuity or a change in slope occurred for all lattice parameters. A small but distinct increase in the a parameter was observed, followed by a continued decrease at a slightly lower rate. In contrast, a small stepwise decrease of the b-parameter preceded a steepening of the compressibility slope. The evolution of the c-parameter was almost continuous. This suggested a subtle structural distortion, which is supported by the observed anisotropic peak shifts in the data (**Figure 2B**). A full structural refinement of a selected dataset was carried out above this subtle phase transition using the ambient monoclinic structure of $Cr_2Mo_3O_{12}$ as a starting point. Only the metal positions could be varied despite using bond distance restraints due to the lower data quality. A good fit was achieved (**Figure 4B**), corroborating that a closely related structure was formed. Similar transitions have been observed in $Al_2Mo_3O_{12}$, $AlGaMo_3O_{12}$, $Fe_2Mo_3O_{12}$, and $FeAlMo_3O_{12}$ (Young et al., 2016), where the compressibility of the unit cell axes changed at pressures between 1.5 and 3 GPa, but structural refinements using the original α-phase model remained stable. In addition, these four compounds underwent a second transition to a γ-phase at pressures between 2.7 and 4.9 GPa, which involved a small discontinuity in several lattice parameters as well as the cell volume. All three phases could be described with the ambient pressure $P2_1/a$ monoclinic structure model. The pressure for the α- to α'- and α'- to γ-transitions correlated well with the average ionic radius of the A^{3+} cation in the previous study, with larger cations resulting in a lower transition pressure. The α- to α'- transition was in all cases accompanied by significant stiffening of the c-axis, while the a- and b axes softened, stiffened or remained largely unaffected depending on composition. In contrast, c-axis compressibility remained similar in the α'- and γ-phases, while the b-axis softened by about 30%.

The small discontinuity observed in the lattice constants of $Cr_2Mo_3O_{12}$ suggests that the transition observed should

be compared to the formation of the γ-phase in $Al_2Mo_3O_{12}$, $AlGaMo_3O_{12}$, $Fe_2Mo_3O_{12}$ and $FeAlMo_3O_{12}$, even though no stepwise decrease in cell volume is observed due to the combination of significant a-axis stiffening, b-axis softening and unaffected c-axis compressibility. The change in compressibility of the b- and c-axes between α-$Cr_2Mo_3O_{12}$ and γ-$Cr_2Mo_3O_{12}$ is comparable to what was observed in the previously studied compositions, while the significant stiffening of the a-axis is much more pronounced than the changes in $Al_2Mo_3O_{12}$, $AlGaMo_3O_{12}$, $Fe_2Mo_3O_{12}$, and $FeAlMo_3O_{12}$. The transition pressure of ∼3.5 GPa is similar to the 3.2 GPa transition pressure reported for the formation of γ-$FeAlMo_3O_{12}$ (Young et al., 2016). The ionic radius of Cr^{3+} in octahedral coordination is 61 pm, which is comparable to the average ionic radius of an equimolar mixture of Fe^{3+} and Al^{3+} in octahedral coordination (59.5 pm).

Separate compressibility constants were extracted for the pressure ranges corresponding to the α- and γ-phases of $Cr_2Mo_3O_{12}$ to avoid contributions from the phase transition. Compressibility constants for α-$Cr_2Mo_3O_{12}$ were extracted from 0.05 to 3.4 GPa, and were found to be $\beta_{\alpha,a} = 0.93 \pm 0.01 \times 10^{-2}$ GPa^{-1}, $\beta_{\alpha,b} = 1.19 \pm 0.01 \times 10^{-2}$ GPa^{-1}, $\beta_{\alpha,c} = 1.01 \pm 0.01 \times 10^{-2}$ GPa^{-1}, and $\beta_{\alpha,v} = 3.13 \pm 0.02 \times 10^{-2}$ GPa^{-1}. For $\gamma - Cr_2Mo_3O_{12}$, these values changed to $\beta_{\gamma,a} = 0.64 \pm 0.02 \times 10^{-2}$ GPa^{-1}, $\beta_{\gamma,b} = 1.51 \pm 0.04 \times 10^{-2}$ GPa^{-1}, $\beta_{\gamma,c} = 0.99 \pm 0.02 \times 10^{-2}$ GPa^{-1}, and $\beta_{\gamma,v} = 3.08 \pm 0.04 \times 10^{-2}$ GPa^{-1} for the 3.6 to 4.5 GPa pressure range, indicating that the overall volume compressibility decreased slightly. Above 4.5 GPa, stiffening of all lattice constants was observed. The compressibility of α-$Cr_2Mo_3O_{12}$ is close to isotropic, with b slightly softer than the other axes. This is similar to other scandium tungstate materials (Liu et al., 2003; Varga et al., 2006; Young et al., 2016). Above the subtle phase transition, the compressibility becomes considerably more anisotropic. The bulk moduli of the α- and γ-phases were found to be 28.7 ± 0.4 GPa and 26.3 ± 1.2 GPa, respectively, indicating almost negligible stiffening at high pressure.

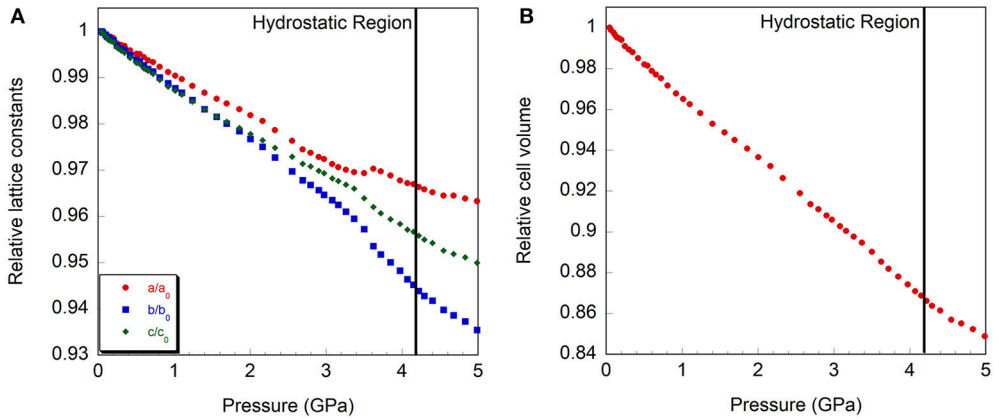

FIGURE 5 | Relative compressibility of $Cr_2Mo_3O_{12}$, **(A)** cell axes and **(B)** volume. The hydrostatic limit is indicated by a vertical line.

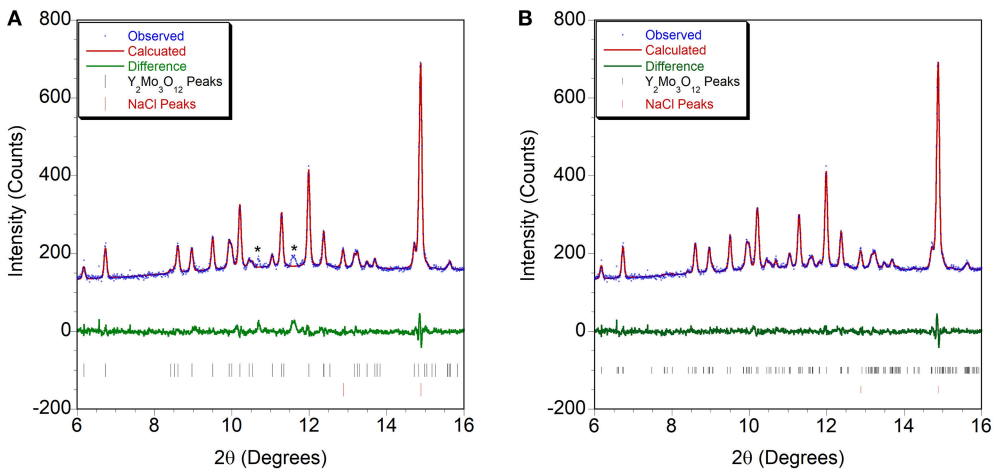

FIGURE 6 | Rietveld plots of PXRD data collected at 0.13 GPa refined using structural models in space groups **(A)** Pbcn and **(B)** $P2_1/a$. * indicates peaks that cannot be accounted for by the orthorhombic cell.

TABLE 2 | Atomic coordinates for monoclinic $Y_2Mo_3O_{12}$ at 0.13 GPa (space group $P2_1/a$).

Name	X	Y	Z
Y1	0.37 (5)	0.96 (5)	0.32 (2)
Y2	0.38 (5)	0.46 (5)	0.05 (3)
Y3	0.13 (3)	0.48 (5)	0.18 (2)
Y4	0.11 (5)	0.97 (5)	0.43 (4)
Mo1	−0.01 (3)	0.25 (4)	0.49 (3)
Mo2	0.37 (4)	0.13 (3)	0.14 (2)
Mo3	0.13 (3)	0.14 (5)	0.26 (2)
Mo4	0.14 (3)	0.61 (4)	0.37 (2)
Mo5	0.35 (3)	0.64 (4)	0.20 (2)
Mo6	−0.02 (3)	0.72 (5)	0.01 (2)
O1	0.58 (19)	0.40 (20)	0.00 (11)
O2	0.00 (20)	0.43 (18)	0.16 (9)
O3	0.90 (13)	0.20 (20)	0.10 (12)
O4	0.74 (18)	0.43 (13)	0.06 (12)
O5	0.52 (16)	0.37 (17)	0.14 (12)
O6	0.70 (20)	0.46 (16)	0.29 (10)
O7	0.46 (14)	0.12 (17)	0.40 (13)
O8	0.18 (15)	0.30 (20)	0.26 (11)
O9	0.57 (16)	0.40 (20)	0.47 (10)
O10	0.42 (12)	0.30 (20)	0.98 (13)
O11	0.12 (11)	0.38 (17)	0.08 (12)
O12	0.40 (20)	0.38 (16)	0.49 (11)
O13	0.87 (14)	0.39 (16)	0.23 (13)
O14	0.25 (17)	0.01 (19)	0.54 (12)
O15	0.15 (13)	0.04 (16)	0.35 (12)
O16	0.50 (20)	0.95 (17)	0.34 (10)
O17	0.70 (20)	0.97 (19)	0.16 (12)
O18	0.65 (15)	0.89 (14)	0.28 (9)
O19	0.97 (12)	0.93 (14)	0.30 (9)
O20	0.04 (12)	0.32 (18)	0.60 (10)
O21	0.11 (14)	0.80 (20)	0.36 (12)
O22	0.06 (17)	0.66 (19)	0.13 (13)
O23	0.37 (15)	0.61 (17)	0.12 (9)
O24	0.31 (12)	0.80 (20)	0.22 (9)

Yttrium molybdate patterns were collected at pressures up to 4.9 GPa (scan 110), which is slightly higher than the hydrostatic limit of isopropanol. No distinct phase transitions were observed in the scan overlay (**Figure 3A**), and all peaks shifted uniformly to higher angles with increasing pressure, indicating isotropic compressibility of all lattice constants. Peaks belonging to the NaCl pressure standard remained sharp throughout the experiment, while the $Y_2Mo_3O_{12}$ peaks became broader and less intense above 3.8 GPa (scan 80), which is close to the hydrostatic limit for isopropanol. Peaks remained broad throughout decompression (scans 111-115) to 1.9 GPa. Integrated patterns showed broader and weaker features as pressure was increased, and the scan collected at the end of the high pressure run [1.9 GPa (decompression)] remained largely featureless except for NaCl peaks (**Figure 3B**). Upon complete release of pressure by opening the cell, crystallinity was recovered, but peaks remained broader and weaker, indicating that some irreversible structural damage occurred.

Initially, a Rietveld refinement starting from the Pbcn structure was attempted for the as-closed dataset collected at 0.13 GPa. A reasonable fit could only be achieved after varying the atomic positions. This resulted in a cell with lattice constants of a = 13.53 Å, b = 9.81 Å, and c = 9.94 Å. However, two peaks remained unaccounted for (**Figure 6A**), and inspection of the refined structure revealed that the atoms had moved far enough to no longer form recognizable polyhedra. This held true even when constraints were applied. Additionally, the unit cell parameters indicated that a 4.4% reduction in unit cell volume had occurred when compared to the ambient pressure cell constants. This reduction in unit cell volume was much higher than expected based on the compressibility of other orthorhombic $A_2Mo_3O_{12}$ compounds, and suggested that a transition to the structurally related higher density $P2_1/a$ polymorph may have occurred below 0.13 GPa. This agrees with a previous Raman study by Torres Dias et al. (2013), which suggested that Pbcn-$Y_2Mo_3O_{12}$ underwent a transition to a lower symmetry phase below 0.3 GPa. It is not surprising that this transition would occur at such a low pressure, as previous studies have shown that $Sc_2W_3O_{12}$ (Garg et al., 2005a; Varga et al., 2005b, 2006; Cetinkol et al., 2008), $Sc_2Mo_3O_{12}$ (Varga et al., 2005a) and $Al_2W_3O_{12}$ (Varga et al., 2005a) behave similarly and undergo this transition at 0.3 GPa, 0.25 GPa and 0.1 GPa, respectively. Initial unit cell parameters for the corresponding monoclinic unit cell were estimated based on the known transformation matrix (Evans and Mary, 2000), and combined with the atomic coordinates of α−$Fe_2Mo_3O_{12}$ as a starting model for a Rietveld refinement. Soft distance restraints were applied to stabilize the refinement, which resulted in an excellent fit with final unit cell parameters of a = 16.726 Å, b = 9.943 Å, c = 19.643 Å, and β = 125.77°. Reasonable bond distances that preserved the polyhedral connectivity were obtained, confirming that a phase transition to monoclinic ε-$Y_2Mo_3O_{12}$[1] had occurred (**Figure 6B**). Some distortion of the polyhedra was evident, although this could also be a result of the limited data quality. The final atomic coordinates obtained for the 0.13 GPa dataset are provided in **Table 2**. As no evidence of further phase transitions was observed, consecutive Rietveld refinements of all scans up to the highest pressure were carried out using the monoclinic ε-$Y_2Mo_3O_{12}$ cell. Atomic positions were fixed for these consecutive refinements. Linear compressibility was observed up to 3.7 GPa (**Figure 7**). Above this pressure, peak broadening and the resulting deteriorating refinement quality made extraction of lattice constants unreliable, which was evident from significant increases in their statistical errors. While quantitative analysis at pressures above 3.7 GPa is not feasible, the evolution of lattice parameters suggests that the material softens in this pressure range. Most materials get

[1]Under ambient conditions, $Y_2Mo_3O_{12}$ may form Pba2 α−$Y_2Mo_3O_{12}$ or Pbcn β−$Y_2Mo_3O_{12}$, depending on synthetic conditions. High pressure studies of both materials have been published. Two high pressure phases were observed to evolve from the Pba2 phase, γ and δ. The Pbcn phase was shown to undergo a transition to the monoclinic $P2_1/a$ structure, designated the ε-phase.

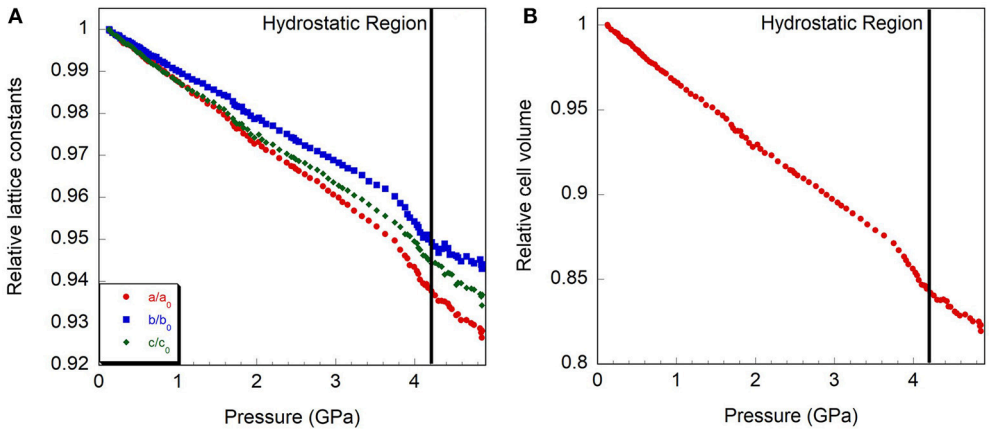

FIGURE 7 | Relative compressibility of monoclinic $Y_2Mo_3O_{12}$, **(A)** cell axes and **(B)** volume. The hydrostatic limit is indicated by a vertical line.

stiffer at high pressures due to reduction of empty space upon compression. However, pressure induced softening has been observed in a number of NTE material (Pantea et al., 2006; Fang and Dove, 2013, 2014; Fang et al., 2013; Morelock et al., 2013; Gallington et al., 2014; Hancock et al., 2015; Alabarse et al., 2017; Hester et al., 2017b; Ticknor et al., 2018), and has been linked to the facile polyhedral rotations that give rise to their expansion behavior. In many cases, amorphization is preceded by pressure induced softening as well. To avoid contributions from this region, the relative compressibilities were extracted for the 0.13 to 3.7 GPa pressure range, giving values of $\beta_{\varepsilon,a} = 1.39 \pm 0.004 \times 10^{-2}$ GPa^{-1}, $\beta_{\varepsilon,b} = 1.09 \pm 0.003 \times 10^{-2}$ GPa^{-1}, $\beta_{\varepsilon,c} = 1.26 \pm 0.01 \times 10^{-2}$ GPa^{-1}, and $\beta_{\varepsilon,v} = 3.57 \pm 0.01 \times 10^{-2}$ GPa^{-1}. In contrast to other materials in the scandium tungstate family that are most compressible along the b-axis, the $P2_1/a$-$Y_2Mo_3O_{12}$ phase is stiffest along the b-axis. The bulk modulus was estimated to be 24.8 ± 0.2 GPa, which is similar to other $A_2M_3O_{12}$ compositions studied.

The fact that the monoclinic phases of $Cr_2Mo_3O_{12}$ and $Y_2Mo_3O_{12}$ remain stable up to high pressures has interesting implications for potential uses of these materials in controlled thermal expansion applications. While the monoclinic phases observed throughout the high pressure experiment display positive expansion under ambient pressure, it is known that heating can induce the monoclinic-to-orthorhombic transition in almost all monoclinic $A_2M_3O_{12}$ compositions. This suggests that applications at increased temperatures may see a reversion to the orthorhombic structure under moderate pressures. Such temperature/pressure dependent phase transitions were observed for ZrV_2O_7 (Gallington et al., 2017), which shows positive expansion in a 3 × 3 × 3 superstructure below 100 °C and NTE in a simple cubic cell at higher temperatures. Chapman and Chupas have estimated that NTE materials are likely to be subjected to pressures of ∼1 GPa when used in composites (Chapman and Chupas, 2007). At this pressure, the majority of $A_2M_3O_{12}$ compositions studied adopt the monoclinic $P2_1/a$ phase (**Table 1**). However, heating under pressure can also provide the necessary energy to overcome kinetic barriers to the formation of denser polymorphs, the existence of which has been reported for many compositions (**Table 1**). Such transformations may affect potential uses of $Y_2Mo_3O_{12}$, as the thermodynamically stable polymorph (Pba2) below 550 °C is denser than the Pbcn- and $P2_1/a$-phases (Gates and Lind, 2007). In contrast, no denser phases are known for $Cr_2Mo_3O_{12}$. It would be interesting to study the behavior of this material in pressure-temperature space to determine the orthorhombic-monoclinic phase boundary.

CONCLUSIONS

High pressure studies of Pbcn-yttrium molybdate and chromium molybdate were conducted up to 4.9 and 8.9 GPa, respectively. Pbcn-yttrium molybdate underwent a phase transition to a monoclinic $P2_1/a$ phase below 0.13 GPa. This is the first time that this polymorph has been structurally characterized. The monoclinic $P2_1/a$ structures of both compounds are remarkably stable and do not undergo abrupt structural phase transitions upon compression. This is unexpected, as most previously investigated isostructural $A_2M_3O_{12}$ materials underwent at least one distinct pressure induced phase transition. Changes in the evolution of lattice constants and compressibility as a function of pressure suggest that $Cr_2Mo_2O_{12}$ may undergo a subtle structural distortion similar to what is observed for $Al_2Mo_3O_{12}$, $AlGaMo_3O_{12}$, $Fe_2Mo_3O_{12}$, and $FeAlMo_3O_{12}$, while no such changes were observed for $P2_1/a$-$Y_2Mo_3O_{12}$.

It is currently unclear what property of the A-site cation causes the remarkable stability of the $P2_1/a$ polymorph in these compounds and thus whether other compositions may exhibit this behavior as well. While the monoclinic phases are not expected to exhibit NTE, their stability under pressure has important implications for composite fabrication, as the facile back-conversion to the orthorhombic phase during decompression or heating would reverse any detrimental changes that could occur during composite formation. These materials could find applications in controlled thermal expansion applications at slightly elevated temperatures, which is expected

to favor the orthorhombic NTE phase even under pressure. While $Y_2Mo_3O_{12}$ may convert to the denser Pba2-structure at moderate temperatures and pressures, the exceptional stability of $Cr_2Mo_3O_{12}$ upon compression with respect to both formation of denser crystalline polymorphs and amorphization makes this material an attractive target.

AUTHOR CONTRIBUTIONS

CL devised the experiments, trained students on synthesis and characterization, participated in high pressure experiments, data collection and analysis as well as writing of paper. LY selected samples for high pressure experiments, participated in high pressure experiments, data collection and analysis as well as writing of paper. JG participated in high pressure experiments, data collection and analysis.

ACKNOWLEDGMENTS

This work is based upon research conducted at the Argonne National Laboratory Advanced Photon Source, which is supported by the U.S. Department of Energy, Office of Science, Office of Basic Energy Sciences, under Contract No. DE-AC02-06CH11357. The authors acknowledge NSF Grants DMR-0545517 and CRIF-0840474 for providing funds for this research.

REFERENCES

Achary, S. N., Mukherjee, G. D., Tyagi, A. K., and Vaidya, S. N. (2002). Preparation, thermal expansion, high pressure and high temperature behavior of $Al_2(WO_4)_3$. *J. Mater. Sci.* 37, 2501–2509. doi: 10.1023/A:1015487406446

Alabarse, F. G., Silly, G., Brubach, J. B., Roy, P., Haidoux, A., Levelut, C., et al. (2017). Anomalous compressibility and amorphization in $AlPO_4$-17, the oxide with the highest negative thermal expansion. *J. Phys. Chem. C* 121, 6852–6863. doi: 10.1021/acs.jpcc.7b00974

Angel, R. J., Bujak, M., Zhao, J., Gatta, G. D., and Jacobsen, S. D. (2007). Effective hydrostatic limits of pressure media for high-pressure crystallographic studies. *J. Appl. Crystallogr.* 40, 26–32. doi: 10.1107/S0021889806045523

Arora, A. K., Nithya, R., Yagi, T., Miyajima, N., and Mary, T. A. (2004). Two-stage amorphization of scandium molybdate at high pressure. *Solid State Commun.* 129, 9–13. doi: 10.1016/j.ssc.2003.08.032

Arora, A. K., Yagi, T., Miyajima, N., and Mary, T. A. (2005). Amorphization and decomposition of scandium molybdate at high pressure. *J. Appl. Phys.* 97:013508. doi: 10.1063/1.1819975

Attfield, M. P., and Sleight, A. W. (1998a). Exceptional negative thermal expansion in $AlPO_4$-17. *Chem. Mater.* 10, 2013–2019. doi: 10.1021/cm9801587

Attfield, M. P., and Sleight, A. W. (1998b). Strong negative thermal expansion in siliceous faujasite. *Chem. Commun.* 601–602. doi: 10.1039/a707141h

Baiz, T. I. (2010). *Non-Hydrolytic Sol-Gel Synthesis and Characterization of Materials of the Type AA'M3O12*. Doctor of Philosophy Ph. D. The University of Toledo.

Baiz, T. I., Gindhart, A. M., Kraemer, S. K., and Lind, C. (2008). Synthesis of $MgHf(WO_4)_3$ and $MgZr(WO_4)_3$ using a non-hydrolytic sol-gel method. *J Sol-Gel Sci Technol.* 47, 128–130. doi: 10.1007/s10971-008-1765-5

Baiz, T. I., Heinrich, C. P., Banek, N. A., Vivekens, B. L., and Lind, C. (2012). *In Situ* non-ambient x-ray diffraction studies of indium tungstate. *J. Solid State Chem.* 187, 195–199. doi: 10.1016/j.jssc.2012.01.019

Banek, N. A., Baiz, H. I., Latigo, A., and Lind, C. (2010). Autohydration of nanosized cubic zirconium tungstate. J *Am Chem Soc*. 132, 8278–8279. doi: 10.1021/ja101475f

Birch, F. (1986). Equation of state and thermodynamic parameters of NaCl to 300-kbar in the high-temperature domain. *J. Geophys. Res. Solid* 91, 4949–4954. doi: 10.1029/JB091iB05p04949

Bruker (2006). *"TOPAS". Ver. 5 Edn*. Karlsrule: Bruker AXS.

Catafesta, J., Haines, J., Zorzi, J. E., Pereira, A. S., and Perottoni, C. A. (2008). Pressure-induced amorphization and decomposition of $FeCo(CN)_{(6)}$. *Phys. Rev. B* 77:064104. doi: 10.1103/PhysRevB.77.064104

Cetinkol, M., Wilkinson, A. P., and Chapman, K. W. (2008). Scandium tungstate above 2.5 GPa. *Solid State Commun.* 148, 511–515. doi: 10.1016/j.ssc.2008.10.002

Cetinkol, M., Wilkinson, A. P., and Lind, C. (2009). *In Situ* high-pressure synchrotron X-ray diffraction study of $Zr_2(WO_4)(PO_4)_2$ Up To 16 GPa. *Phys. Rev. B* 79:224118. doi: 10.1103/PhysRevB.79.224118

Chapman, K. W., and Chupas, P. J. (2007). Pressure enhancement of negative thermal expansion behavior and induced framework softening in zinc cyanide. *J. Amer. Chem. Soc.* 129, 10090–10091. doi: 10.1021/ja073791e

Chapman, K. W., and Chupas, P. J. (2009). Anomalous thermal expansion of cuprites: a combined high resolution pair distribution function and geometric analysis. *Chem. Mater.* 21, 425–431. doi: 10.1021/cm802900t

Cliffe, M. J., and Goodwin, A. L. (2012). PASCal: a principal axis strain calculator for thermal expansion and compressibility determination. *arXiv:1204.3007* 45, 1321–1329.

Coelho, A. (2018). *TOPAS* and *TOPAS-Academic*: an optimization program integrating computer algebra and crystallographic objects written in *C++ J. Appl. Crystallograp*. 51, 210–218. doi: 10.1107/S1600576718000183

Duan, N., Kameswari, U., and Sleight, A. W. (1999). Further contraction of ZrW_2O_8. *JACS* 121, 10432–10433.

Evans, J. S. O., and Mary, T. A. (2000). Structural phase transitions and negative thermal expansion in $Sc_2(MoO_4)_3$. *Int. J. Inorg. Mater.* 2, 143–151. doi: 10.1016/S1466-6049(00)00012-X

Evans, J. S. O., Mary, T. A., and Sleight, A. W. (1998). Negative thermal expansion in $Sc_2(WO_4)_3$. *J. Solid State Chem.* 137, 148–160. doi: 10.1006/jssc.1998.7744

Evans, J. S. O., Mary, T. A., Vogt, T., Subramanian, M. A., and Sleight, A. W. (1996). Negative thermal expansion in ZrW_2O_8 and HfW_2O_8. *Chem. Mater.* 8, 2809–2823. doi: 10.1021/cm9602959

Fang, H., and Dove, M. T. (2013). Pressure-induced softening as a common feature of framework structures with negative thermal expansion. *Phys. Rev. B* 87:214109. doi: 10.1103/PhysRevB.87.214109

Fang, H., and Dove, M. T. (2014). A phenomenological expression to describe the temperature dependence of pressure-induced softening in negative thermal expansion materials. *J Phys Condens Matter* 26:115402. doi: 10.1088/0953-8984/26/11/115402

Fang, H., Phillips, A. E., Dove, M. T., Tucker, M. G., and Goodwin, A. L. (2013). Temperature-dependent pressure-induced softening in $Zn(CN)_{(2)}$. *Phys. Rev. B* 88:144103. doi: 10.1103/PhysRevB.88.144103

Fleming, D. A., Johnson, D. W., and Lemaire, P. J. (1997). *Article Comprising a Temperature Compensated Optical Fiber Refractive Index Grating*. USA 5,694,503 patent application.

Forster, P. M., and Sleight, A. W. (1999). Negative thermal expansion in $Y_2W_3O_{12}$. *Int. J. Inorg. Mater.* 1, 123–127. doi: 10.1016/S1466-6049(99)00021-5

Gallington, L. C., Chapman, K. W., Morelock, C. R., Chupas, P. J., and Wilkinson, A. P. (2014). Dramatic softening of the negative thermal expansion material HfW_2O_8 upon heating through its WO_4 orientational order-disorder phase transition. *J. Appl. Phys.* 115:053512. doi: 10.1063/1.4864258

Gallington, L. C., Hester, B. R., Kaplan, B. S., and Wilkinson, A. P. (2017). Pressure-dependence of the phase transitions and thermal expansion in zirconium and hafnium pyrovanadate. *J. Solid State Chem.* 249, 46–50. doi: 10.1016/j.jssc.2017.02.014

Garg, N., Murli, C., Taru, B., Karmakar, S., Tyagi, A. K., and Sharma, S. M. (2001). Pressure induced phase transitions in $Sc_2(WO_4)_3$ and $Al_2(WO_4)_3$. *Solid State Phys.* 44, 39–40.

Garg, N., Murli, C., Tyagi, A. K., and Sharma, S. M. (2005a). Phase Transitions In $Sc_2(WO_4)_3$ Under High Pressure. *Phys. Rev. B* 72, 064106. doi: 10.1103/PhysRevB.72.064106

Garg, N., Panchal, V., Tyagi, A. K., and Sharma, S. M. (2005b). Pressure-induced phase transitions in $Al_2(WO_4)_3$. *J. Solid State Chem.* 178, 998–1002. doi: 10.1016/j.jssc.2004.11.024

Gates, S. D. (2008). *Cation Influence of Negative Thermal Expansion In the A2M3O12 Family*. Doctor of Philosophy in Chemistry Ph.D. The University of Toledo.

Gates, S. D., Colin, J. A., and Lind, C. (2006). Non-hydrolytic sol-gel synthesis, properties, and high-pressure behavior of gallium molybdate. *J. Mater. Chem.* 16, 4214–4219. doi: 10.1039/B608864C

Gates, S. D., and Lind, C. (2007). Polymorphism in yttrium molybdate $Y_2Mo_3O_{12}$. *J. Solid State Chem.* 180, 3510–3514. doi: 10.1016/j.jssc.2007.10.011

Gindhart, A. M. (2007). *Synthesis and Characterization of AA'W3O12 Compounds*. Masters of Science in Chemistry Masters, The University of Toledo.

Gindhart, A. M., Lind, C., and Green, M. (2008). Polymorphism in the negative thermal expansion material magnesium hafnium tungstate. *J. Mater. Res.* 23, 210–213. doi: 10.1557/JMR.2008.0013

Greve, B. K., Martin, K. L., Lee, P. L., Chupas, P. J., Chapman, K. W., and Wilkinson, A. P. (2010). Pronounced negative thermal expansion from a simple structure: cubic ScF_3. *J. Am. Chem. Soc.* 132, 15496–15498. doi: 10.1021/ja106711v

Hancock, J. C., Chapman, K. W., Halder, G. J., Morelock, C. R., Karlan, B. S., Gallington, L. C., et al. (2015). Large negative thermal expansion and anomalous behavior on compression in cubic ReO_3-type $A(II)B(IV)F_{(6)}$: $CaZrF_6$ and $CaHfF_6$. *Chem. Mater.* 27, 3912–3918. doi: 10.1021/acs.chemmater.5b00662

Hester, B. R., Dos Santos, A. M., Molaison, J. J., Hancock, J. C., and Wilkinson, A. P. (2017a). Synthesis of defect perovskites $(He_{2-x}\square_{(x)})(CaZr)F_6$ by inserting helium into the negative thermal expansion material $CaZrF_6$. *J. Am. Chem. Soc.* 139, 13284–13287. doi: 10.1021/jacs.7b07860

Hester, B. R., Hancock, J. C., Lapidus, S. H., and Wilkinson, A. P. (2017b). Composition, response to pressure, and negative thermal expansion in (MBF_6)-B-II-F-IV (M = Ca, Mg; B = Zr, Nb). *Chem. Mater.* 29, 823–831. doi: 10.1021/acs.chemmater.6b04809

Holzer, H., and Dunand, D. C. (1999). Phase transformation and thermal expansion of Cu/ZrW_2O_8 metal matrix composites. *J. Mater. Res.* 14, 780–789. doi: 10.1557/JMR.1999.0104

Hu, Z., Jorgensen, J. D., Teslic, S., Short, S., Argyriou, D. N., Evans, J. S. O., et al. (1997). Pressure-induced phase transformation in ZrW_2O_8 - Compressibility and thermal expansion of the orthorhombic phase. *Physica B* 241, 370–372. doi: 10.1016/S0921-4526(97)00591-7

Huang, Y. M. (1998). IR spectroscopic study of the effects of high pressure on zeolites Y, A and sodalite. *J. Mater. Chem.* 8, 1067–1071. doi: 10.1039/a707631b

Karmakar, S., Deb, S. K., Tyagi, A. K., and Sharma, S. M. (2004). Pressure-induced amorphization in $Y_2(WO_4)_3$: *In Situ* X-ray diffraction and raman studies. *J. Solid State Chem.* 177, 4087–4092. doi: 10.1016/j.jssc.2004.08.020

Keen, D. A., Goodwin, A. L., Tucker, M. G., Dove, M. T., Evans, J. S. O., Crichton, W. A., et al. (2007). Structural description of pressure-induced amorphization in ZrW_2O_8. *Phys. Rev. Lett.* 98:225501. doi: 10.1103/PhysRevLett.98.225501

Klotz, S., Chervin, J. C., Munsch, P., and Le Marchand, G. (2009). Hydrostatic limits of 11 pressure transmitting media. *J. Phys. D Appl. Phys.* 42:075413. doi: 10.1088/0022-3727/42/7/075413

Kol'tsova, T. N. (2001). X-ray diffraction study of $Y_2W_3O_{12} \bullet 3H_2O$. *Inorg. Mater.* 37, 1175–1177. doi: 10.1023/A:1012557411736

Korthuis, V., Khosrovani, N., Sleight, A. W., Roberts, N., Dupree, R., and Warren, W. W. (1995). Negative Thermal Expansion and Phase Transitions In the $ZrV_{2-x}P_xO_7$ Series. *Chem. Mater.* 7, 412–417. doi: 10.1021/cm00050a028

Kozy, L. C., Tahir, M. N., Lind, C., and Tremel, W. (2009). Particle size and morphology control of the negative thermal expansion material cubic zirconium tungstate. *J. Mater Chem.* 19, 2760–2765. doi: 10.1039/b820014a

Li, J., Yokochi, A., Amos, T. G., and Sleight, A. W. (2002). Strong negative thermal expansion along the O-Cu-O linkage in $CuScO_2$. *Chem. Mater.* 14, 2602–2606. doi: 10.1021/cm011633v

Lind, C. (2012). Two decades of negative thermal expansion research: where do we stand? *Materials* 5, 1125–1154. doi: 10.3390/ma5061125

Lind, C., Coleman, M. R., Kozy, L. C., and Sharma, G. R. (2011). Zirconium tungstate/polymer nanocomposites: challenges and opportunities. *Phys. Stat. Sol. B* 248, 123–129. doi: 10.1002/pssb.201083967

Lind, C., Wilkinson, A. P., Hu, Z. B., Short, S., and Jorgensen, J. D. (1998). Synthesis and properties of the negative thermal expansion material cubic $ZrMo_2O_8$. *Chem. Mater.* 10, 2335–2337. doi: 10.1021/cm980438m

Liu, H., Secco, R. A., Imanaka, N., and Adachi, G. (2002). X-ray diffraction study of pressure-induced amorphization in $Lu_2(WO_4)_3$. *Solid State Commun.* 121, 177–180. doi: 10.1016/S0038-1098(01)00458-6

Liu, H., Secco, R. A., Imanaka, N., Rutter, M. D., Adachi, G., and Uchida, T. (2003). Ionic to electronic dominant conductivity in $Al_2(WO_4)_3$ at high pressure and high temperature. *J. Phys. Chem. Solids* 64, 287–294. doi: 10.1016/S0022-3697(02)00297-4

Liu, H. J., Secco, R. A., and Huang, Y. N. (2001). Pressure-induced amorphization of hydrated Na-X zeolite. *PhysChemComm* 4, 37–39. doi: 10.1039/b102080n

Lommens, P., De Meyer, C., Bruneel, E., De Buysser, K., Van Driessche, I., and Hoste, S. (2005). Synthesis and thermal expansion of ZrO_2/ZrW_2O_8 composites. *J. Eur. Ceram. Soc.* 25, 3605–3610. doi: 10.1016/j.jeurceramsoc.2004.09.015

Maczka, M., Paraguassu, W., Souza, A. G., Freire, P. T. C., Mendes, J., Melo, F. E. A., et al. (2004). High-pressure raman study of $Al_2(WO_4)_3$. *J. Solid State Chem.* 177, 2002–2006. doi: 10.1016/j.jssc.2004.01.021

Maczka, M., Souza, A. G., Paraguassu, W., Freire, P. T. C., Mendes, J., and Hanuza, J. (2012). Pressure-induced structural phase transitions and amorphization in selected molybdates and tungstates. *Prog. Mater. Sci.* 57, 1335–1381. doi: 10.1016/j.pmatsci.2012.01.001

Marinkovic, B. A., Ari, M., De Avillez, R. R., Rizzo, F., Ferreira, F. F., Miller, K. J., et al. (2009). Correlation between AO_6 polyhedral distortion and negative thermal expansion on orthorhombic $Y_2Mo_3O_{12}$ and related materials. *Chem. Mater.* 21, 2886–2894. doi: 10.1021/cm900650c

Marinkovic, B. A., Jardim, P. M., De Avillez, R. R., and Rizzo, F. (2005). Negative thermal expansion in $Y_2Mo_3O_{12}$. *Solid State Sci.* 7, 1377–1383. doi: 10.1016/j.solidstatesciences.2005.08.012

Matsumoto, A., Kobayashi, K., Nishio, T., and Ozaki, K. (2003). "Fabrication and thermal expansion of Al-ZrW_2O_8 composites by pulse current sintering process," in *Thermec'2003, Pts 1-5*, eds. T. Chandra, J. M. Torralba and T. Sakai. (Zurich-Uetikon: Trans Tech Publications Ltd), 2279–2283.

Mendonça, R., Paraguassu, W., Filho, J. M., Marinkovic, B. A., Filho, A. G. S., Maczka, M., et al. (2016). Pressure-induced structural transformations in $In_{2-x}Y_x(MoO_4)_3$ systems. *J. Raman. Spectrosc.* 47, 350–356. doi: 10.1002/jrs.4814

Morelock, C. R., Greve, B. K., Gallington, L. C., Chapman, K. W., and Wilkinson, A. P. (2013). Negative thermal expansion and compressibility of $Sc_{1-x}Y_xF_3$ (x <= 0.25). *J. Appl. Phys.* 114:213501. doi: 10.1063/1.4836855

Moura, J. V. B., Pinheiro, G. S., Freire, P. T. C., Filho, J. M., Saraiva, G. D., Viana, B. C., et al. (2016). High-pressure Raman scattering on $Fe_2(MOo_4)3$ microcrystals obtained by a hydrothermal method. *Vibration. Spectroscop.* 87, 88–93. doi: 10.1016/j.vibspec.2016.09.011

Mukherjee, G. D., Achary, S. N., Tyagi, A. K., and Vaidya, S. N. (2003). High pressure AC resistivity and compressibility study on $Al_2(WO_4)_3$. *J. Phys. Chem. Solids* 64, 611–614. doi: 10.1016/S0022-3697(02)00361-X

Mukherjee, G. D., Vijaykumar, V., Achary, S. N., Tyagi, A. K., and Godwal, B. K. (2004). Phase transitions in $Al_2(WO_4)_3$: high pressure investigations of low frequency dielectric constant and crystal structure. *J. Phys. Condens. Mat.* 16, 7321–7330. doi: 10.1088/0953-8984/16/41/013

Nassau, K., Levinstein, H. J., and Loiacono, G. M. (1965). A comprehensive study of trivalent tungstates and molybdates of the type $L_2(MO_4)_3$. *Phys. Chem. Solids* 26, 1815–1816. doi: 10.1016/0022-3697(65)90213-1

Nassau, K., Shiever, J. W., and Keve, E. T. (1971). Structural and phase relationships among trivalent tungstates and molybdates. *J. Solid State Chem.* 3, 411–419. doi: 10.1016/0022-4596(71)90078-8

Pantea, C., Migliori, A., Littlewood, P. B., Zhao, Y., Ledbetter, H., Lashley, J. C., et al. (2006). Pressure-induced elastic softening of monocrystalline zirconium tungstate at 300 K. *Phys. Rev. B* 73:214118. doi: 10.1103/PhysRevB.73.214118

Paraguassu, W., Maczka, M., Souza, A. G., Freire, P. T. C., Mendes, J., Melo, F. E. A., et al. (2004). Pressure-induced structural transformations in the molybdate $Sc_2(MoO_4)_3$. *Phys. Rev. B* 69:094111. doi: 10.1103/PhysRevB.69.094111

Perottoni, C. A., and da Jornada, J. A. H. (1998). Pressure-induced amorphization and negative thermal expansion in ZrW_2O_8. *Science* 280, 886–889. doi: 10.1126/science.280.5365.886

Phillips, A. E., Goodwin, A. L., Halder, G. J., Southon, P. D., and Kepert, C. J. (2008). Nanoporosity and exceptional negative thermal expansion in single-network cadmium cyanide. *Angew. Chem. Int. Ed.* 47, 1396–1399. doi: 10.1002/anie.200704421

Reisner, B. A., Lee, Y., Hanson, J. C., Jones, G. A., Parise, J. B., Corbin, D. R., et al. (2000). Understanding negative thermal expansion and 'trap door' cation relocations in zeolite rho. *Chem. Comm.* 2000, 2221–2222. doi: 10.1039/b006929i

Roy, R., Agrawal, D. K., and Mckinstry, H. A. (1989). Very low thermal expansion coefficient materials. *Annu. Rev. Mater. Sci.* 19, 59–81. doi: 10.1146/annurev.ms.19.080189.000423

Salke, N. P., Rao, R., Achary, S. N., Nayak, C., Garg, A. B., Krishna, P. S. R., et al. (2018). High pressure phases and amorphization of a negative thermal expansion compound $TaVO_5$. *Inorg. Chem.* 57, 6973–6980. doi: 10.1021/acs.inorgchem.8b00590

Secco, R. A., Liu, H., Imanaka, N., and Adachi, G. (2001). Pressure-induced amorphization in negative thermal expansion $Sc_2(WO_4)_3$. *J. Mater. Sci. Lett.* 20, 1339–1340. doi: 10.1023/A:1010967021588

Secco, R. A., Liu, H., Imanaka, N., and Adachi, G. (2002a). Anomalous ionic conductivity of $Sc_2(WO_4)_3$ mediated by structural changes at high pressures and temperatures. *J. Phys. Condens. Mat.* 14, 11285–11289. doi: 10.1088/0953-8984/14/44/468

Secco, R. A., Liu, H., Imanaka, N., Adachi, G., and Rutter, M. D. (2002b). Electrical conductivity and amorphization of $Sc_2(WO_4)_3$ at high pressures and temperatures. *J. Phys. Chem. Solids* 63, 425–431. doi: 10.1016/S0022-3697(01)00156-1

Shannon, R. D. (1976). Revised effective ionic-radii and systematic studies of interatomic distances in halides and chalcogenides. *Acta Crystallogr. A* 32, 751–767. doi: 10.1107/S0567739476001551

Sleight, A. W. (1998). Isotropic negative thermal expansion. *Ann. Rev. Mater. Sci.* 28, 29–43. doi: 10.1146/annurev.matsci.28.1.29

Sullivan, L. M., and Lukehart, C. M. (2005). Zirconium tungstate (ZrW_2O_8)/polyimide nanocomposites exhibiting reduced coefficient of thermal expansion. *Chem. Mater.* 17, 2136–2141. doi: 10.1021/cm0482737

Takenaka, K. (2012). Negative thermal expansion materials: technological key for control of thermal expansion. *Sci. Technol. Adv. Mater.* 13:013001. doi: 10.1088/1468-6996/13/1/013001

Tani, J.-I., Kimura, H., Hirota, K., and Kido, H. (2007). Thermal expansion and mechanical properties of phenolic resin/ZrW_2O_8 composites. *J. Appl. Polym. Sci.* 106, 3343–3347. doi: 10.1002/app.27025

Tani, J.-I., Takahashi, M., and Kido, H. (2010). Fabrication and thermal expansion properties of ZrW_2O_8/$Zr_2WP_2O_{12}$ composites. *J. Eur. Ceram. Soc.* 30, 1483–1488. doi: 10.1016/j.jeurceramsoc.2009.11.010

Ticknor, J. O., Hester, B. R., Adkins, J. W., Xu, W. Q., Yakovenko, A. A., and Wilkinson, A. P. (2018). Zero thermal expansion and abrupt amorphization on compression in anion excess ReO_3-type cubic $YbZrF_7$. *Chem. Mater.* 30, 3071–3077. doi: 10.1021/acs.chemmater.8b00845

Toby, B. H., and Von Dreele, R. B. (2013). GSAS-II: the genesis of a modern open-source all purpose crystallography software package. *J. Appl. Crystallogr.* 46, 544–549. doi: 10.1107/S0021889813003531

Torres Dias, A. C., Luz Lima, C., Paraguassu, W., Pereira Da Silva, K., Freire, P. T. C., Mendes Filho, J., et al. (2013). Pressure-induced crystal-amorphous transformation in $Y_2Mo_3O_{12}$. *Vib. Spectrosc.* 68, 251–256. doi: 10.1016/j.vibspec.2013.08.004

Tyagi, A. K., Achary, S. N., and Mathews, M. D. (2002). Phase transition and negative thermal expansion in $A_2(MoO_4)_3$ system (A=Fe^{3+}, Cr^{3+} and Al^{3+}). *J. Alloy. Compd.* 339, 207–210. doi: 10.1016/S0925-8388(01)02003-5

Varga, T. (2011). "Materials that shrink on heating: pressure-induced phase transitions in negative thermal expansion materials, and their energetics," in Advances in Chemistry Research, ed. J. C. Taylor (Nova Publishers), 1–54.

Varga, T., Wilkinson, A. P., Jorgensen, J. D., and Short, S. (2006). Neutron powder diffraction study of the orthorhombic to monoclinic transition in $Sc_2W_3O_{12}$ on compression. *Solid State Sci.* 8, 289–295. doi: 10.1016/j.solidstatesciences.2006.02.022

Varga, T., Wilkinson, A. P., Lind, C., Bassett, W. A., and Zha, C. S. (2005a). High pressure synchrotron X-ray powder diffraction study of $Sc_2Mo_3O_{12}$ and $Al_2W_3O_{12}$. *J. Phys.-Condens. Mat.* 17, 4271–4283. doi: 10.1088/0953-8984/17/27/004

Varga, T., Wilkinson, A. P., Lind, C., Bassett, W. A., and Zha, C. S. (2005b). *In Situ* high-pressure synchrotron X-ray diffraction study of $Sc_2W_3O_{12}$ At Up To 10 GPa. *Phys. Rev. B* 71:214106. doi: 10.1103/PhysRevB.71.214106

Verdon, C., and Dunand, D. C. (1997). High-temperature reactivity in the ZrW_2O_8-Cu system. *Scripta Mater.* 36, 1075–1080. doi: 10.1016/S1359-6462(96)00481-2

Young, L., Gadient, J., Xiaodong, G., and Lind, C. (2016). High pressure studies of $A_2Mo_3O_{12}$ negative thermal expansion materials (A_2 = Al_2, Fe_2, FeAl, AlGa). *J. Solid State Chem.* 237, 121–128. doi: 10.1016/j.jssc.2016.02.004

Zhou, Y., Adams, S., Rao, R. P., Edwards, D. D., Neiman, A., and Pestereva, N. (2008). Charge transport by polyatomic anion diffusion in $Sc_2(WO_4)_3$. *Chem. Mater.* 20, 6335–6345. doi: 10.1021/cm800466y

Conflict of Interest Statement: The authors declare that the research was conducted in the absence of any commercial or financial relationships that could be construed as a potential conflict of interest.

frontiers in Chemistry

ORIGINAL RESEARCH
published: 28 June 2018
doi: 10.3389/fchem.2018.00252

The Anisotropic Thermal Expansion of Non-linear Optical Crystal $BaAlBO_3F_2$ Below Room Temperature

Xingxing Jiang[1], Naizheng Wang[1,2], Maxim S. Molokeev[3,4,5], Wei Wang[6], Shibin Guo[6], Rongjin Huang[6], Laifeng Li[6], Zhanggui Hu[7] and Zheshuai Lin[1,2]**

[1] Technical Institute of Physics and Chemistry, Chinese Academy of Sciences, Beijing, China, [2] University of the Chinese Academy of Sciences, Beijing, China, [3] Laboratory of Crystal Physics, Kirensky Institute of Physics, Federal Research Center KSC SB RAS, Krasnoyarsk, Russia, [4] Department of Physics, Far Eastern State Transport University, Khabarovsk, Russia, [5] Department of Engineering Physics and Radioelectronic, Siberian Federal University, Krasnoyarsk, Russia, [6] Key Laboratory of Cryogenics, Technical Institute of Physics and Chemistry, Chinese Academy of Sciences, Beijing, China, [7] Institute of Functional Crystals, Tianjin University of Technology, Tianjin, China

OPEN ACCESS

Edited by:
Jun Chen,
University of Science and Technology Beijing, China

Reviewed by:
Ranjan Mittal,
Bhabha Atomic Research Centre, India
Qiang Sun,
Zhengzhou University, China

***Correspondence:**
Zheshuai Lin
zslin@mail.ipc.ac.cn
Zhanggui Hu
hu@mail.ipc.ac.cn

Specialty section:
This article was submitted to Physical Chemistry and Chemical Physics, a section of the journal Frontiers in Chemistry

Received: 26 April 2018
Accepted: 08 June 2018
Published: 28 June 2018

Citation:
Jiang X, Wang N, Molokeev MS, Wang W, Guo S, Huang R, Li L, Hu Z and Lin Z (2018) The Anisotropic Thermal Expansion of Non-linear Optical Crystal $BaAlBO_3F_2$ Below Room Temperature. Front. Chem. 6:252. doi: 10.3389/fchem.2018.00252

Thermal expansion is a crucial factor for the performance of laser devices, since the induced thermal stress by laser irradiation would strongly affect the optical beam quality. For $BaAlBO_3F_2$ (BABF), a good non-linear optical (NLO) crystal, due to the highly anisotropic thermal expansion its practical applications are strongly affected by the "tearing" stress with the presence of local overheating area around the laser spot. Recently, the strategy to place the optical crystals in low-temperature environment to alleviate the influence of the thermal effect has been proposed. In order to understand the prospect of BABF for this application, in this work, we investigated its thermal expansion behavior below room temperature. The variable-temperature XRD showed that the ratio of thermal expansion coefficient between along *c*- and along *a(b)*- axis is high as 4.5:1 in BABF. The Raman spectrum combined with first-principles phonon analysis revealed that this high thermal expansion anisotropy mainly ascribe to progressive stimulation of the respective vibration phonon modes related with the thermal expansion along *a(b)*- and *c*-axis. The good NLO performance in BABF can be kept below room temperature. The work presented in this paper provides an in-depth sight into the thermal expansion behavior in BABF, which, we believe, would has significant implication to the manipulation in atomic scale on the thermal expansion of the materials adopted in strong-field optical facility.

Keywords: BABF, anisotropic thermal expansion, phonon stimulation, NLO optical property, low temperature

INTRODUCTION

Thermal expansion behavior is a crucial performance factor for materials used in lasers, due to its affinity with the ability of the optical outputting (Wynne et al., 1999; Wang et al., 2007; Mangin et al., 2011; Ito et al., 2017; Fang et al., 2018). Non-linear optical (NLO) crystal, a type of crystals for laser frequency conversion, has played a key role in the broadening of laser spectrum and become one of the most prevailing branch of optical materials (Chen et al., 1999, 2012; Cyranoski, 2009; Meng et al., 2009; Lin et al., 2014). Among the commercial NLO crystals, $BaAlBO_3F_2$(BABF) crystal, is a very excellent member, and exhibit many superiority over its congeners in the output of laser in

532 and 355 nm (Zhou et al., 2009; Hu et al., 2011; Yue et al., 2011; Yang et al., 2016). As for the practical application of BABF, the optical spot with high-power is usually focused on one point of the crystal, and thus "tearing" stress resulted from anisotropic thermal expansion would severely affect the beam quality and outputting power. The previous study about the thermal property of BABF revealed that above room temperature, its thermal expansion coefficient along *c*-axis is about eight times of that along *a(b)-axis*, and the strongly anisotropic thermal expansion has been the major disadvantage to restrict its practical application (Yue et al., 2011). However, the microscopic mechanism of the thermal expansion anisotropy in BABF has not been investigated. Recently, it is proposed that the thermal effect on the performance of some optical crystal used in laser can be eliminated to some extent below room temperature (Marrazzo et al., 2016; Veselov et al., 2016; Roitero et al., 2018), which provide a feasible method to overcome the problem about the thermal effect. However, the thermal expansion behavior of BABF under low temperature has not been investigated yet, and its performance index below room temperature remain unclear. Therefore, it is desirable to perform a study about the thermal expansion to give a comprehensive evaluation on the application prospect below room temperature and elaborate the structure-property relationship of the anisotropic thermal expansion of BABF.

In this work, using variable-temperature X-ray diffraction, the thermal expansion behavior of BABF below room temperature is studied, and the mechanism of the thermal expansion behavior is elaborated by Raman spectrum and first-principles phonon analysis. The optical property below room temperature is also investigated by first-principles calculation. It is elucidated that BABF still exhibit a relatively strong anisotropic thermal expansion below room temperature, but its anisotropy is less prominent than that above room temperature. The optical performance is also slightly improved under low temperature. These result indicates that the performance below room temperature for the laser generation is superior than that above room temperature, and BABF is a potential NLO crystals in cryogenic system.

EXPERIMENTAL AND COMPUTATIONAL METHOD

Sample Preparation

Polycrystalline BABF was synthesized through solid-state reaction. Analytically pure BaF_2, Al_2O_3, and B_2O_3 in stoichiometric ratio as the starting materials were mixed homogeneously by agate mortar. The well-grinded reactant then was placed into muffle furnace and was heated gradually up to 800°C at the rate of 0.5°C/min with several intermediate careful grinding at 300, 600, and 800K. After cooling to room temperature, the white powder of target compound was obtained.

Variable Temperature X-Ray Diffraction

Variable temperature X-ray diffraction patterns were recorded from 13 to 300K with the internal of 20K. Each pattern was recorded with Bruker D8 advanced X-ray diffractometer Cu Kα radiation (Kα1 = 1.5406Å and Kα2 = 1.5443Å) on the finely grounded powder samples. The angular scanning range were set to 10–90° with a step of 0.01° and scanning rate 0.5 s/step. The crystal structures under different temperature were refined by Rietveld method (Rietveld, 1969) using TOPAS 4.2 program (BAXS, 2008). Based on the refined cell parameters. The thermal expansion coefficient was fitted by the PASCal software (Cliffe and Goodwin, 2012).

Raman Spectrum

The Raman pattern was recorded from 100 to 1,500 cm^{-1} at room temperature, using in Via-Reflex, equipped with a solid state laser with a wavelength of 532 nm. In order to improve the signal to noise ratio of the spectra, 10 integrations were carried out with an integration time of 10 s at a nominal resolution of 1 cm^{-1} and a precision of 1 cm^{-1}.

First-Principles Calculation

The first-principles calculation were performed by CASTEP (Clark et al., 2005), a plane-wave pseudopotential total energy package based on density functional theory (DFT) (Kohn and Sham, 1965; Payne et al., 1992). The functionals developed by Perdew, Burke, and Ernzerhof (PBE) (Perdew et al., 1996) in generalized gradient approximation (GGA) (Perdew and Wang, 1992) form were adopted to describe the exchange-correlation energy. The optimized norm-conserving pseudopential (Hamann et al., 1979) in (Kleinman and Bylander, 1982) form were used to model the effective interaction between the valcence electrons and atom cores, which allow us to use a small plane basis set without compromising the accuracy required by the calculation. High kinetic energy cutoff of 900 eV and Monkhorst-pack (Monkhorst and Pack, 1976) *k*-point mesh spanning less than 0.04 $Å^{-1}$ in the Brillouin zone were chosen. The vibrational property was calculated by linear response formalism (Baroni et al., 2001), in which the phonon frequencies were obtained by the second derivative of the total energy with respect to a given perturbation. The band gaps at variable temperature were predicted by hybridized functionals PBE0 based on the refined structure at respective temperature, and the refractive index and SHG coefficients were calculated by Kramers–Kronig transform based on the electronic transition matrix (PED, 1985) and the software developed by our group based on length-gauge formalism (Lin et al., 1999, 2014).

RESULT AND DISCUSSION

The crystal structure of BABF was determined by Hu et al. (2011). BABF possesses a hexagonal lattice with layered-tendency structure, as displayed in **Figure 1**. One boron atom is bonded with three oxygen atoms to form a planar BO_3 triangles, and one aluminum atom coordinates with three oxygen and two fluorine atoms to generate the AlO_3F_2 trigonal bipyramid. The BO_3 triangles and AlO_3F_2 trigonal bipyramids are aligned alternatively in the ratio 1:1 by sharing the vertical oxygen atoms, giving rise to the infinite two-dimensional $[AlBO_3F_2]_\infty$ layer, in which the BO_3 triangle and the AlO_3 base of AlO_3F_2 trigonal bipyramids are aligned absolutely parallel to *(a, b)* plane.

$[AlBO_3F_2]_\infty$ layer are further connected with each other via the Coulomb interaction between the dangling fluorine atoms and interstitial barium atoms to generate the layered-tendency structure.

The variable-temperature X-ray diffraction (VT-XRD) patterns are plotted in **Figure 2A**. It is observed that no new peaks appear as temperature elevate from 13 to 300K, indicating the absence of structural phase-transition and manifesting its high thermodynamical stability. The temperature-deduced diffraction peak-shifting of the lattice plane corresponding to *c*-axis is much more prominent than that of *a(b)-axis* (**Figure 2B**), suggesting the high anisotropic thermal expansion in BABF. According to the cell parameters extracted from the VT-XRD by Rietveld refinement (Figure S1, **Figure 2C** and Table S1), the average thermal expansion coefficient are 4.42(39)/MK and 20.08(71)/MK along *a(b)-axis* and *c*-axis respectively, which confirmed that the thermal expansion along *c*-axis is much more prominent than that along *a(b)*-axis. More importantly, the ratio (4.5:1) between the thermal expansion coefficients along *c*- and *a(b)-axis* below room temperature is much lower than that above room temperature (7.6:1), and the low anisotropy of the thermal expansion below room temperature is more favorable

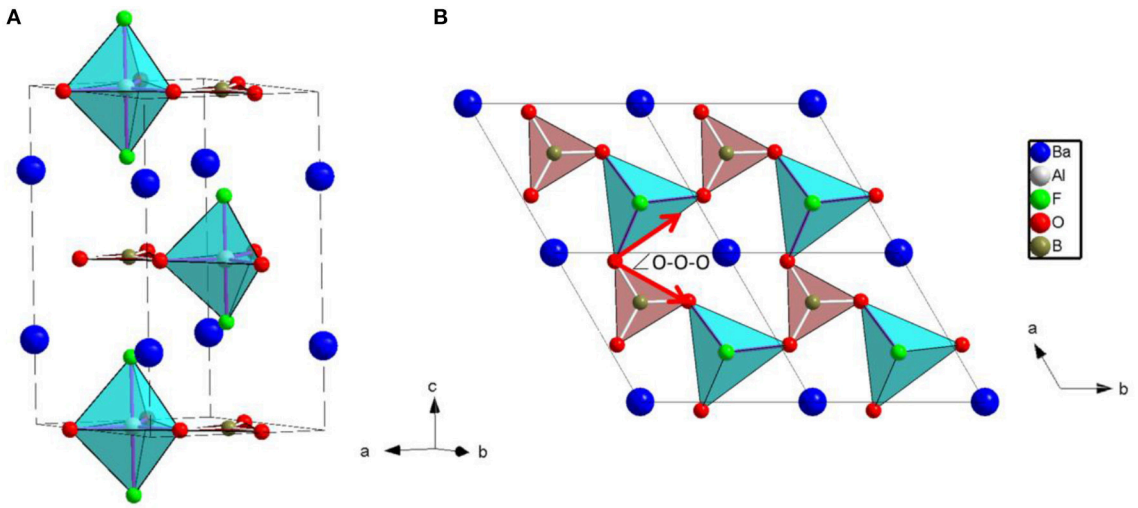

FIGURE 1 | Crystal structure of $BaAlBO_3F_2$ viewed along **(A)** *(a,b)* plane and **(B)** *c*-axis. The BO_3 and AlO_3F_2 groups are represented by pink triangles and light blue trigonal bipyramids, respectively.

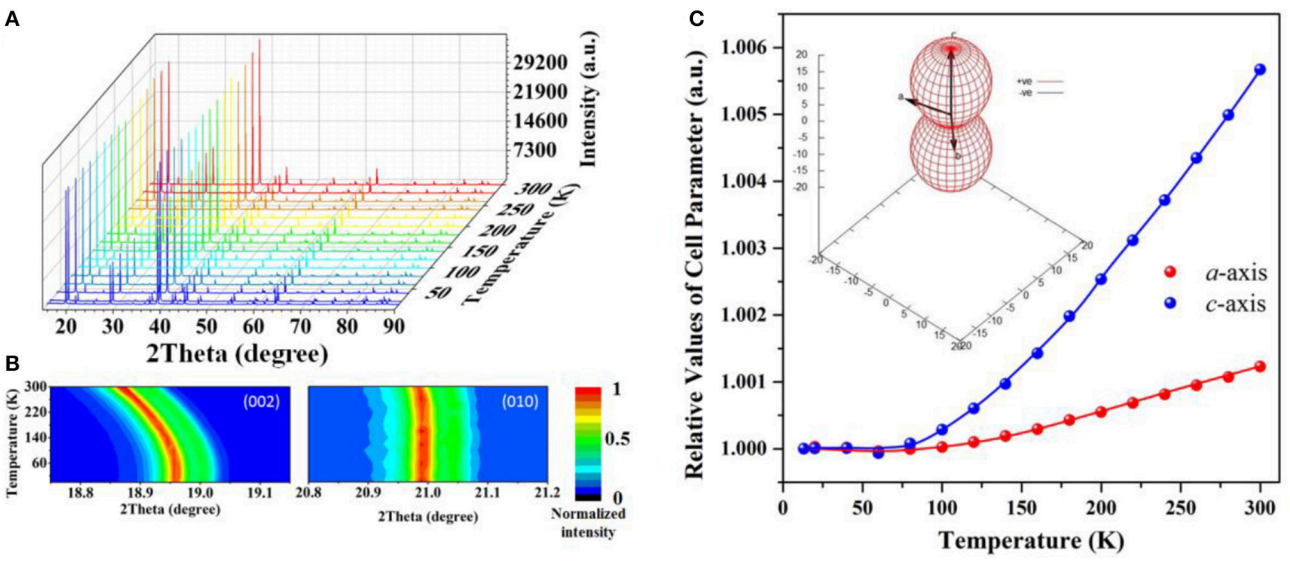

FIGURE 2 | Result of VT-XRD on BABF: **(A)** the VT-XRD patterns, **(B)** 2θ-temperature contour map of the diffraction peak of (002) and (010) plane and **(C)** evolution of cell parameters with respect to temperature. The insert in **(C)** displays the special distribution of thermal expansion coefficient plotted by PASCal software (Cliffe and Goodwin, 2012).

for elimination of the stress induced by temperature gradient when irradiated by laser. Additionally, It should be emphasized that at low temperature (13–100K) the *a(b)*-axis exhibit very low thermal expansion with the fitted linear thermal expansion coefficient 0.11(25)/MK, which is lower than that of *c*-axis [2.44(98)/MK] by one order and can be categorized to typical zero thermal expansion.

The most intuitive way to investigate the mechanism of the thermal expansion is to trace the modification of bond length and angles with respect to temperature. The *a(b)*-axis is exclusively determined by B-O, Al-O bonds, and ∠ O-O-O angle, while *c*-axis is dominantly determined by the Ba-F and Al-F bond. According to the temperature-dependent bond length and angles (**Figure 3** and Table S2), despite the clutter of the point due to the difficulty to exactly determine the position of the constituted light atoms in BABF, a roughly changing tendency can be observed. Below 140K the bond length and angles accounting for the change of *a(b)*-axis almost keep constant, resulting in the rigidity of *a(b)*-axis under low temperature. And dramatic modification only occur above 140K: B-O bond, and ∠ O-O-O angle increase from 1.301 to 1.340Å (by 3%) and 60.892–62.437° (by 2.5%) respectively as temperature increase from 140K to 300K, which both positively contribute to the thermotropic expansion. Extruded by the increase of ∠ O-O-O angle, Al-O bond decrease from 1.919 to 1.865Å (by 2.8%), which slightly cancel out the expansion effect originated from the increase of B-O bond and ∠ O-O-O angle, leading to the relative low thermal expansion along *a(b)*-axis. On the contrary, both Al-F and Ba-F bond increase as temperature increase, and thus *c*-axis exhibit a normal thermal expansion ∼10/MK of inorganic crystals.

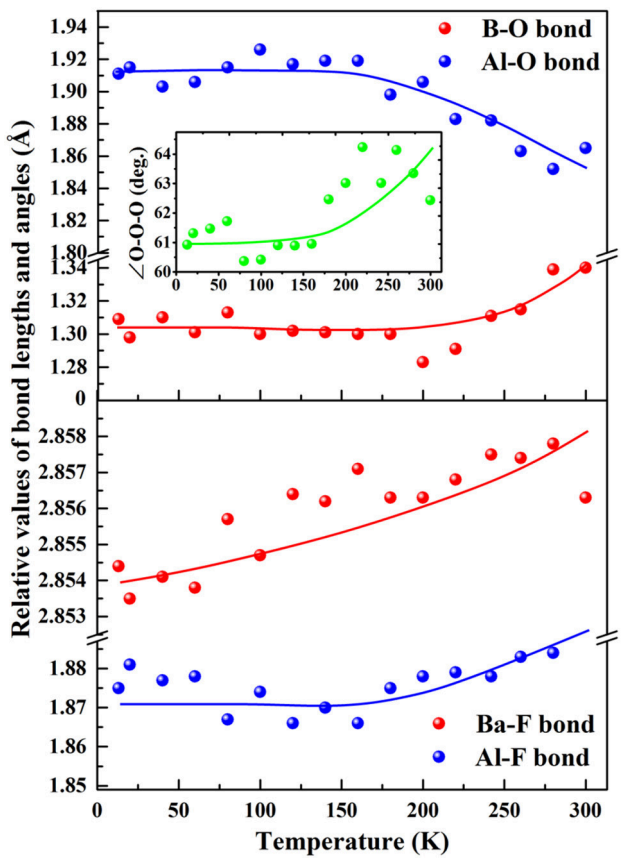

FIGURE 3 | Function of refined bond length and angles with respect to temperature in BABF.

The thermal expansion of materials is closely related with the temperature-induced stimulation of lattice vibration, and it is anticipated that first-principles phonon mode assignment would compensate the disadvantage of the littery temperature-dependent bond length and angles and make the mechanism of the thermal expansion in BABF more clear. The irreducible representation of P-62c space group at Γ-point yields a sum of 30E+7A1+8A2 phonon modes (see Table S3). According to the calculated Raman spectrum (**Figure 4**), six principal peaks are observed at around 87, 266, 338, 473, 1,030, and 1,331cm^{-1} respectively. The calculated Raman spectrum is in rather agreement with the measured ones, verifying the accuracy of the computational method. According to the vibrational vector projected onto the real space of respective phonon modes, it is revealed that as frequency increase the phonon roughly experience a evolution from the type-I (mode 1–7), -II (mode 8–29) to -III (mode 30–45). In type-I, the configuration of 2D $[AlBO_3F_2]_\infty$ layer keep constant and it vibrate as a rigid unit along *c*-axis with the reverse phase with that of interstitial barium atoms. This indicates that at low temperature the vibration modes related with the stretch between $[AlBO_3F_2]_\infty$ and barium would be firstly stimulated, in which the size of $[AlBO_3F_2]_\infty$ layer along *a(b)*-axis remain constant. Therefore, below 100K, BABF exhibit slight thermal expansion along *c*-axis and rigidity along *a(b)*-axis. In type-II, the oxygen atoms within $[AlBO_3F_2]_\infty$ layer vibrate along the direction almost vertical to B-O bonds. This implies that in these modes, the BO_3 triangles rotate within *(a,b)* plane as the rigid units. This effect corresponds to the slight contraction of Al-O bond in AlO_3F_2 trigonal bipyramids and also would lead to the expansion of the interspace within $[AlBO_3F_2]_\infty$ layer, which eventually lead to the weak thermal expansion along *a(b)*-axis. Meanwhile, the stretch vibration of Al-F bonds also partially account for the modes of type-II, which enhanced the thermal expansion along *c*-axis. In type-III modes, the phonon vibration mainly originate from the stretch of B-O bonds, which is related with the elongation of B-O bonds. It should be emphasized that high temperature is required to stimulate these vibration modes (such as ∼ 1300K for the mode at 1030 cm^{-1}), and these modes can only afford the thermal expansion at high temperature and almost contribute nothing to that below 300K. Moreover, as temperature increase, all the Raman peaks are red-shifted, affording the normal general thermal expansion. Besides, it should be emphasized that the weight of modes related with the thermal expansion along *a(b)*-axis at 300K is much more prominent than that at 13K, which also result in the enhanced thermal expansion along *a-(b)* axis as temperature increase. Therefore, the anisotropic thermal expansion behavior in BABF is mainly attributed to the progressive stimulation of the respective vibration modes related with the expansion of *c*-axis to that of *a(b)*-axis. Moreover,

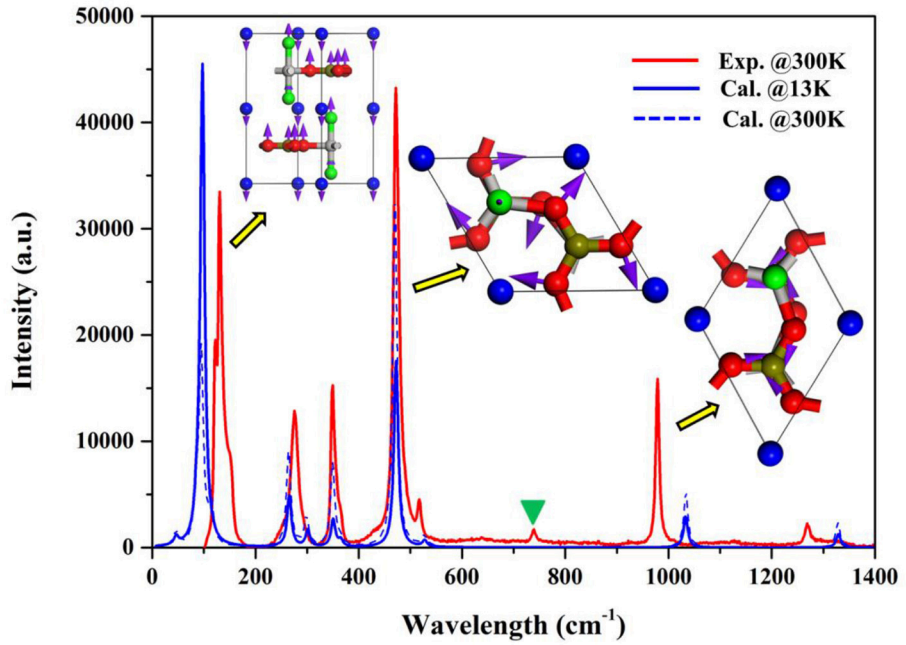

FIGURE 4 | Measured and calculated Raman spectrum of BABF. The modes with the highest peaks at 87, 473, and 1,030 cm^{-1} are used to schematically describe the atomic vibration of type-I, II, and III phonon modes respectively. The peaks at around 720cm^{-1} labeled by green triangle in the experimental spectrum is attributed to the impurity.

it should be emphasized that as temperature increase, the amplitude of atomic vibration would increase, and the phonon anharmonicity would be enhanced. Since the thermal expansion is originated from phonon anharmonicity, the thermal expansion of both *a*-axis [4.42(39)/MK] and *c*-axis [20.08(71)/MK] between 13 and 300 are less prominent than that those between 303 and 1,073K [6.3 and 48.1/MK, respectively (Yue et al., 2011)].

Additionally, considering that the optical performance is also crucial to the usage in apparatus operated at low temperature, the temperature-dependent optical property was also studied based on the refined structure by first-principles calculation (**Figure 5** and Table S4). Accordingly, both the SHG coefficient and birefringence present ultra-stability under temperature fluctuation, and the band gaps are broadened as temperature decrease, which guarantee the optical transmittance of BABF below room temperature. All these observation elucidated that the good optical performance of BABF can be well-kept, which is favorable to its practical application in the apparatus operated below room temperature.

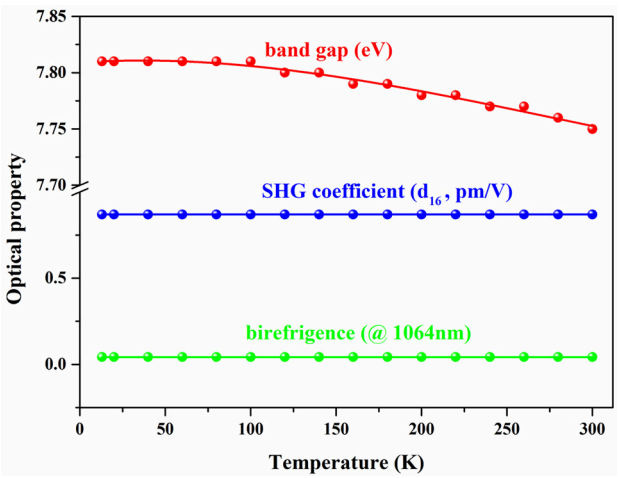

FIGURE 5 | Function of the calculated band gap, SHG coefficient and birefringence (@1,064 nm) of BABF with respect to temperature.

CONCLUSION

The thermal expansion behavior below room temperature of BABF, an important ultraviolet NLO crystal, is investigated. It is revealed that the BABF exhibit relatively high anisotropic thermal expansion, and the near-zero thermal expansion behavior along *a(b)*-axis below 100K was observed. Based on the refined temperature-dependent crystal structure, Raman spectrum and first-principles vibration phonon analysis, it is elucidated that the anisotropic thermal expansion behavior in BABF mainly stem from the progressive stimulation of the phonon modes related with the thermal expansion along *a(b)*- and *c*-axis. Moreover, it is revealed that the optical performance of BABF can also be well-kept under low temperature, which is very

favorable for its practical application. Our study exhibit a comprehensive investigation about the thermal and optical property below room temperature and shed light on the structural origin of the thermal expansion of BABF. We believed that the conclusion deduced from our study further deepens the understanding about the performance of BABF and would be beneficial for its practical application under complex environment.

AUTHOR CONTRIBUTIONS

XJ, NW, and MM performed the experiment. XJ performed the first-principles simulation. WW, SG, RH, and LL help in the variable X-ray diffraction. ZL, ZH, and XJ written the manuscript.

ACKNOWLEDGMENTS

This work was supported by the National Scientific Foundations of China (Grants 11474292, 51702330, 11611530680, 91622118, and 91622124), Russian Foundation for Basic Research (Grant 17-52-53031), the Special Foundation of the Director of Technical Institute of Physics and Chemistry (TIPC) and the Youth Innovation Promotion Association, CAS (outstanding member for ZL and Grant 2017035 for XJ).

SUPPLEMENTARY MATERIAL

The Supplementary Material for this article can be found online at: https://www.frontiersin.org/articles/10.3389/fchem.2018.00252/full#supplementary-material

REFERENCES

Baroni, S., de Gironcoli, S., Dal Corso, A., and Giannozzi, P. (2001). Phonons and related crystal properties from density-functional perturbation theory. *Rev. Mod. Phys.* 73, 515–562. doi: 10.1103/RevModPhys73.515

BAXS, (2008). *Bruker AXS TOPAS V4: General Profile and Structure Analysis Software for Powder Diffraction Data*. Karlsruhe: User's Manual.

Chen, C. T., Sasaki, T., Li, R. K., Wu, Y. C., Lin, Z. S., Yoshimura, M., et al. (2012). *Nonlinear Optical Borate Crystals-Principles and Applications*. Germany: Wiley-VCH.

Chen, C. T., Ye, N., Lin, J., Jiang, J., Zeng, W. R., and Wu, B. C. (1999). Computer-assisted search for nonlinear optical crystals. *Adv. Mater.* 11, 1071–1078. doi: 10.1002/(SICI)1521-4095(199909)11:13<1071::AID-ADMA1071>3.0.CO;2-G

Clark, S. J., Segall, M. D., Pickard, C. J., Hasnip, P. J., Probert, M. J., and Payne, M. C. (2005). First principles methods using CASTEP. *Z. Kristallogr.* 220, 567–570. doi: 10.1524/zkri.220.5.567.65075

Cliffe, M. J., and Goodwin, A. L. (2012). PASCal: a Principal axis strain calculator for thermal expansion and compressibility determination. *J. Appl. Crystallogr.* 45, 1321–1329. doi: 10.1107/S0021889812043026

Cyranoski, D. (2009). Materials science: china's crystal cache. *Nature* 457, 953–955. doi: 10.1038/457953a

Fang, Z., Liu, L., Wang, X., and Chen, C. (2018). Thermo-physical properties of a new UV nonlinear optical crystal: NaSr3Be3B3O9FF4. *Appl. J. Crystallogr.* 51, 357–360. doi: 10.1107/S1600576718001218

Hamann, D. R., Schluter, M., and Chiang, C. (1979). Norm-conserving pseudopotentials. *Phys. Rev. Lett.* 43, 1494–1497. doi: 10.1103/PhysRevLett.43.1494

Hu, Z., Yue, Y., Chen, X., Yao, J., Wang, J., and Lin, Z. (2011). Growth and structure redetermination of a nonlinear BaAlBO3F2 crystal. *Solid State Sci.* 13, 875–878. doi: 10.1016/j.solidstatesciences.2011.03.002

Ito, I., Silva, A., Nakamura, T., and Kobayashi, Y. (2017). Laser based on low thermal expansion ceramic cavity with 4.9 MHz/s frequency drift. *Opt. Express* 25, 26020–26028. doi: 10.1364/OE.25.026020

Kleinman, L., and Bylander, D. M. (1982). Efficacious form for model pseudopotentials. *Phys. Rev. Lett.* 48, 1425–1428. doi: 10.1103/PhysRevLett.48.1425

Kohn, W., and Sham, L. J. (1965). Self-consistent equations including exchange and correlation effects. *Phys. Rev.* 140:1133. doi: 10.1103/PhysRev.140.A1133

Lin, J., Lee, M. H., Liu, Z. P., Chen, C. T., and C. J. Pickard (1999). Mechanism for linear and nonlinear optical effects in beta-BaB2O4 crystals. *Phys. Rev. B* 60, 13380–13389. doi: 10.1103/PhysRevB.60.13380

Lin, Z., Jiang, X., Kang, L., Gong, P., Luo, S., and, Lee, M.-H. (2014). First-principles materials applications and design of nonlinear optical crystals. *J. Phys. D* 47:253001. doi: 10.1088/0022-3727/47/25/253001

Mangin, J., Mennerat, G., and Villeval, P. (2011). Thermal expansion, normalized thermo-optic coefficients, and condition for second harmonic generation of a Nd:YAG laser with wide temperature bandwidth in RbTiOPO4. *J. Opt. Soc. Am. B Opt. Phys.* 28, 873–881. doi: 10.1364/JOSAB.28.000873

Marrazzo, S., Goncalves-Novo, T., Millet, F., and Chanteloup, J.-C. (2016). Low temperature diode pumped active mirror Yb^{3+}: YAG disk laser amplifier studies. *Opt. Express* 24, 12651–12660. doi: 10.1364/OE.24.012651

Meng, J., Liu, G., Zhang, W., Zhao, L., Liu, H., Jia, X., et al. (2009). Coexistence of fermi arcs and fermi pockets in a high-Tc copper oxide superconductor *Nature* 462, 335–338. doi: 10.1038/nature08521

Monkhorst, H. J., and Pack, J. D. (1976). Special points for brillouin zone integrations. *Phys. Rev. B* 13, 5188–5192. doi: 10.1103/PhysRevB.13.5188

Payne, M. C., Teter, M. P., Allan, D. C., Arias, T. A., and Joannopoulos, J. D. (1992). Iterative minimization techniques for abinitio total energy calculations molecular dynamics and conjugate gradients. *Rev. Mod. Phys.* 64, 1045–1097. doi: 10.1103/RevModPhys.64.1045

PED (1985). *Handbook of Optical Constants of Solids*. New York, NY: Academic Press.

Perdew, J. P., and Wang, Y. (1992). Pair-distribution function and its coupling-constant average for the spin-polarized electron-gas. *Phys. Rev. B* 46, 12947–12954. doi: 10.1103/PhysRevB.46.12947

Perdew, J. P., Burke, K., and Ernzerhof, M. (1996). Generalized gradient approximation made simple. *Phys. Rev. Lett.* 77, 3865–3868. doi: 10.1103/PhysRevLett.77.3865

Rietveld, H. M. (1969). A profile refinement method for nuclear and magnetic structures. *J. Appl. Crystallogr.* 2, 65–71. doi: 10.1107/S0021889869006558

Roitero, E., Ochoa, M., Anglada, M., Muecklich, F., and Jimenez-Pique, E. (2018). Low temperature degradation of laser patterned 3y-tzp: enhancement of resistance after thermal treatment. *J. Eur. Ceram. Soc.* 38, 1742–1749. doi: 10.1016/j.jeurceramsoc.2017.10.044

Veselov, D. A., Shashkin, I. S., Bobretsova, Y. K., Bakhvalov, K. V., Lutetskiy, A. V., and Tarasov, I. S. (2016). Study of the pulse characteristics of semiconductor lasers with a broadened waveguide at low temperatures (110-120 K). *Semiconductors* 50, 1396–1402. doi: 10.1134/S1063782616100249

Wang, Z., Zhang, Q., Sun, D., and Yin, S. (2007). Study on thermal expansion of Nd3+:Gd3Ga5O12 laser crystal. *J. Rare Earths* 25, 244–246. doi: 10.1016/S1002-0721(07)60480-3

Wynne, R., Daneu, J. L., and Fan, T. Y. (1999). Thermal coefficients of the expansion and refractive index in YAG. *Appl. Opt.* 38, 3282–3284. doi: 10.1364/AO.38.003282

Yang, L., Yue, Y., Yang, F., Hu, Z., and Xu, Z. (2016). 266 nm ultraviolet light generation in Ga-doped BaAlBO3F2 crystals. *Opt. Lett*. 41, 1598–1600. doi: 10.1364/OL.41.001598

Yue, Y., Hu, Z., Zhou, Y., Wang, J., Zhang, X., Chen, C., et al. (2011). Growth and nonlinear optical properties of BaAlBO3F2 crystal. *J. Opt. Soc. Am. B: Opt. Phys*. 28, 861–866. doi: 10.1364/JOSAB.28.000861

Zhou, Y., Wang, G., Yue, Y., Li, C., Lu, Y., Cui, D., et al. (2009). High-efficiency 355 nm generation in barium aluminum borate diflouride BaAlBO3FF2. *Opt. Lett*. 34, 746–748. doi: 10.1364/OL.34.000746

Conflict of Interest Statement: The authors declare that the research was conducted in the absence of any commercial or financial relationships that could be construed as a potential conflict of interest.

frontiers in Chemistry

ORIGINAL RESEARCH
published: 20 March 2018
doi: 10.3389/fchem.2018.00072

Thermal Expansion and Magnetostriction Measurements at Cryogenic Temperature Using the Strain Gauge Method

Wei Wang[1,2], *Huiming Liu*[2], *Rongjin Huang*[2,3]*, *Yuqiang Zhao*[2], *Chuangjun Huang*[2], *Shibin Guo*[2], *Yi Shan*[2] *and Laifeng Li*[1,2,3]*

[1] *Institute of Advanced Metal Materials, School of Materials Science and Engineering, Tianjin University, Tianjin, China,* [2] *State Key Laboratory of Technologies in Space Cryogenic Propellants, Technical Institute of Physics and Chemistry, Chinese Academy of Sciences, Beijing, China,* [3] *Department of Science and Technology of Liquid Metal Material, School of Future Technology, University of Chinese Academy of Sciences, Beijing, China*

OPEN ACCESS

Edited by:
Jun Chen,
University of Science and Technology Beijing, China

Reviewed by:
Jun Yan,
Beijing Jiaotong University, China
Kun Lin,
University of Science and Technology Beijing, China
Ranjan Mittal,
Bhabha Atomic Research Centre, India

***Correspondence:**
Rongjin Huang
huangrongjin@mail.ipc.ac.cn
Laifeng Li
laifengli@mail.ipc.ac.cn

Specialty section:
This article was submitted to Physical Chemistry and Chemical Physics, a section of the journal Frontiers in Chemistry

Received: *30 January 2018*
Accepted: *06 March 2018*
Published: *20 March 2018*

Citation:
Wang W, Liu H, Huang R, Zhao Y, Huang C, Guo S, Shan Y and Li L (2018) Thermal Expansion and Magnetostriction Measurements at Cryogenic Temperature Using the Strain Gauge Method. Front. Chem. 6:72. doi: 10.3389/fchem.2018.00072

Thermal expansion and magnetostriction, the strain responses of a material to temperature and a magnetic field, especially properties at low temperature, are extremely useful to study electronic and phononic properties, phase transitions, quantum criticality, and other interesting phenomena in cryogenic engineering and materials science. However, traditional dilatometers cannot provide magnetic field and ultra-low temperature (<77 K) environment easily. This paper describes the design and test results of thermal expansion and magnetostriction at cryogenic temperature using the strain gauge method based on a Physical Properties Measurements System (PPMS). The interfacing software and automation were developed using LabVIEW. The sample temperature range can be tuned continuously between 1.8 and 400 K. With this PPMS-aided measuring system, we can observe temperature and magnetic field dependence of the linear thermal expansion of different solid materials easily and accurately.

Keywords: thermal expansion, magnetostriction, strain gauge method, cryogenic temperature, PPMS

INTRODUCTION

Cryogenic engineering has been extensively used in the fields of aerospace industry, superconducting technology, and large scientific instruments, etc. The physical performances of materials directly affect the safety and service time of the cryogenic system, among of which thermal expansion and magnetostriction, the strain responses of a material to temperature and a magnetic field, are the key thermodynamic properties closely related to specific heat and magnetization. Thus, accurate measurement of thermal expansion at low temperatures is necessary to ensure the security and reliability of the cryogenic systems. Also, these properties are very useful to investigate electronic and phononic properties, phase transitions, quantum criticality, and other interesting physical phenomena in cryogenic engineering and materials science (Ventura and Risegari, 2008; Inoue et al., 2014; Iwakami et al., 2014).

The approaches to estimate the thermal expansion of solid material can be classified, according to an extensometer, into quartz dilatometer, interferometer, optical lever, mechanical lever, magnetic meter, pointer meter, and capacitance micrometer methods, strain gauges, etc. (Clark, 1968; James et al., 2001; Kanagaraj and Pattanayak, 2003). The quartz dilatometer

method is frequently used at low temperatures, because of its high accuracy (Corruccini and Gniewck, 1961; Deng and Xu, 2003; ASTM, 2006).However, it is expensive and complex to operate, and the sample size requirements are quite high (Tang et al., 2014). For a test specimen of large length, the accuracy may be affected by the potential temperature gradient along it, which then requires a cryostat to have high temperature uniformity.

The strain gauge method is also widely used to measure the thermal expansion of material at low temperatures (Liu et al., 2012, 2014). Compared with the quartz dilatometer method, the strain gauge method can measure multiple samples at the same time and has lower requirements of the test specimen size. However, traditional dilatometers cannot provide magnetic field environment easily and only been used in relative higher temperature range (>77 K) (Kaufman, 1963; Hannah and Reed, 1992).

Fortunately, Quantum Design Physical Properties Measurements System has been widely used for measurements of thermodynamic properties, such as specific heat, magnetization, electrical resistance, and thermal conductivity. In this report, we present the thermal expansion and magnetostriction measurements using the strain gauge method installed in a PPMS in the temperature range of 1.8–400 K and magnetic fields up to 14 T. The interfacing software and automation were developed using LabVIEW. Since the variation of the sensitivity coefficient of strain gauges at low temperatures is a key factor affecting the measurement accuracy, it was verified in the temperature range of 2–300 K by comparing the measured thermal expansion data of oxygen-free copper with the source data from National Institute of Standards and Technology (NIST), USA.

Also, using this PPMS-aided measuring system, we observed temperature and magnetic field dependence of the linear thermal expansion of $NaZn_{13}$-type $LaFe_{13-x}Al_x$ compounds, which absolutely expands the practical application scope of this Multi-function testing system.

STRAIN GAUGE METHOD

It is well known that a strain gauge can measure the thermal strain on the surface of a test specimen to reflect the linear thermal expansion of material because it can transform the strain into the electric signal with a high precision. The strain caused by temperature fluctuation is defined as thermal output. Without a mechanical force imposed on the test specimen, the temperature change can bring about a length variation both in the test sample and in the strain gauge, which then cause the resistivity variation of the strain gauge correspondingly. And the strain variation induced by the net temperature can be expressed as follows (Poore and Kesterson, 1978; Walsh, 1997; Micro-Measurements, 2007):

$$\varepsilon = \frac{\beta_g}{F_g}\Delta T + (\alpha_s - \alpha_g)\,\Delta T \tag{1}$$

where ε is the apparent strain of strain gauge, β_g is the thermal coefficient of resistivity of the grid material, F_g is the gauge factor of strain gauge, $\alpha_s - \alpha_g$ is the difference in coefficient of thermal expansion (CTE) between the tested sample and gauge, respectively, and ΔT is the temperature change from arbitrary initial reference temperature. For two same types of strain gauges installed on test sample (α_s) and reference sample (α_r), respectively, the apparent strains can be expressed as:

$$\varepsilon_s = \frac{\beta_g}{F_g}\Delta T + (\alpha_s - \alpha_g)\,\Delta T \tag{2a}$$

$$\varepsilon_r = \frac{\beta_g}{F_g}\Delta T + (\alpha_r - \alpha_g)\,\Delta T \tag{2b}$$

Subtracting Equation (2b) from (2a), and rearranging:

$$\alpha_s = \frac{\varepsilon_S - \varepsilon_r}{\Delta T} + \alpha_r \tag{3}$$

Thus, the CTE of test sample can be obtained with the accurately measured $\varepsilon_S - \varepsilon_r$ and ΔT, as well as the known CTE of reference sample α_r. In this paper, we use fused silica of high purity (>99.99%) as the reference sample in the measurement of thermal expansion due to its very low and almost temperature-independent mean linear CTE (5.5×10^{-7}/K) (Kirby and Hahn, 1971).

EXPERIMENTAL PROCEDURES AND METHODS

The schematic view of the measurement system is shown in **Figure 1**, which consists of a PPMS, nanovoltmeters, and a LabVIEW PC.

With the help of LabVIEW, we can design experiments using our own measurement electronics when working on the general purpose platforms of the PPMS (Quantum Design Inc., 2002, 2013). Firstly, nanovoltmeters (KEITHLEY 2182A, USA) can monitor the electrical signals of samples in PPMS via a GPIB interface simultaneously. And then a LabVIEW computer attached to nanovoltmeters also via a GPIB interface. The QDInstrument VIs and QDInstrument.dll are installed on this computer and communicate over .NET. In brief, the QDInstrument program is a translator with a .NET interface for communication with the LabVIEW VI and an OLE interface for communication with MultiVu. The DLL is configured to address the QDInstrument_server.exe program running on the MultiVu computer. This is done via connecting an Ethernet cable directly between the two computers in the absence of a LAN. The server program in turn communicates over OLE with the MultiVu application. Finally, by controlling both external devices as well as PPMS's state (temperature and magnetic field) on a separate LabVIEW computer from MultiVu, we can observe the temperature and magnetic field dependence of the linear thermal expansion of different solid materials easily and accurately.

The sample puck, as demonstrated in **Figure 2**, is redesigned to meet the special requirement of thermal expansion measurement. The whole sample puck is emerged into sample chamber of PPMS to cool the test sample. The temperature and

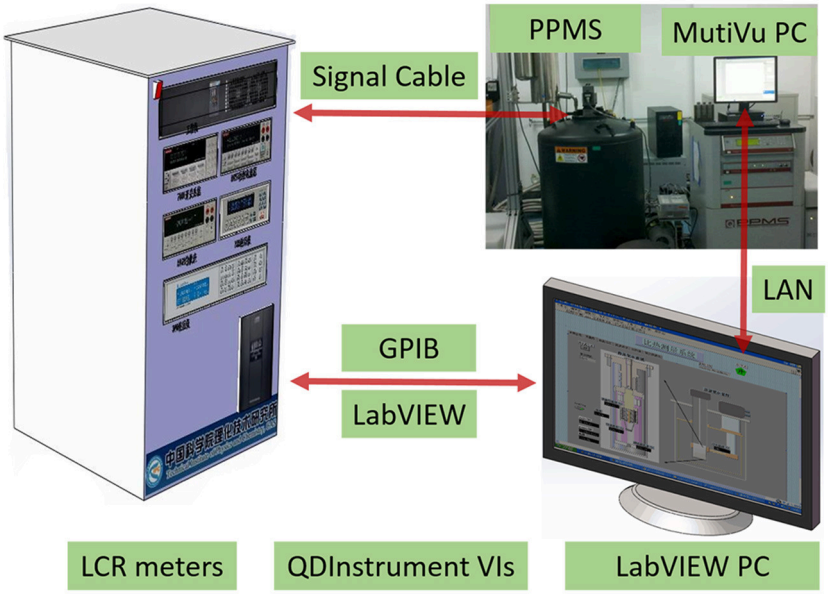

FIGURE 1 | Schematic of measurement system for thermal expansion of solid materials.

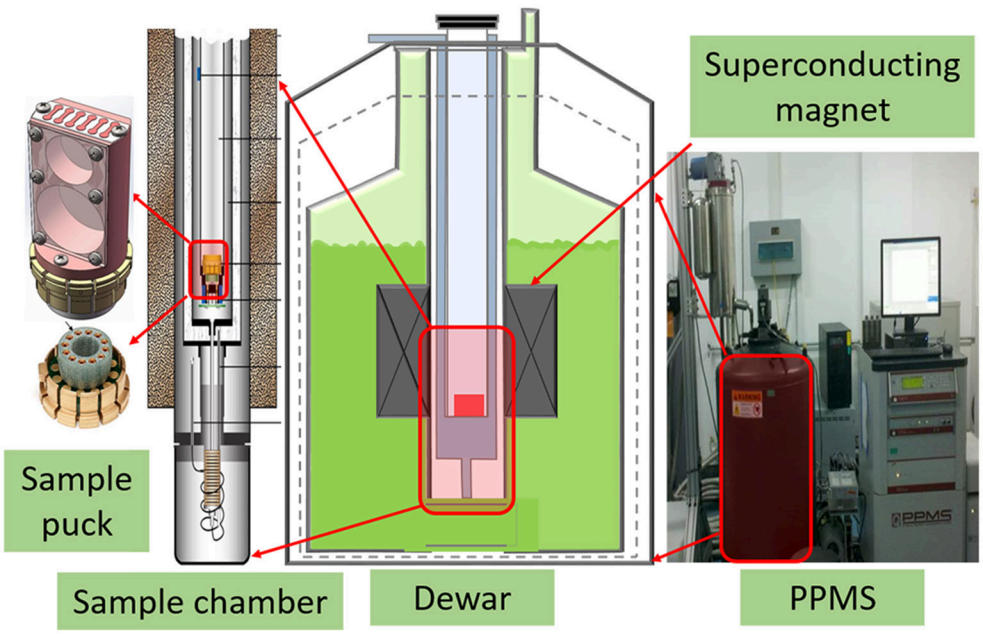

FIGURE 2 | Schematic of the sample chamber.

magnetic field can be adjusted by the PPMS in the range of 1.8–400 K and ±14 T. The dimensions of the test sample can be tuned from 3 × 3 × 3 to 8 × 8 × 8 mm. Its relatively small dimensions can reduce the difficulty in machining and the influence of the non-uniform temperature field on the measurement accuracy. The reference sample with the same dimensions is made from fused silica of 99.99% purity. To measure the thermal expansion, test sample and reference sample are placed on the sample puck stress-free. Two identical strain gauges are bonded on the center of the test sample surface and the reference sample surface, respectively, using a high performance adhesive M-Bond 610. This adhesive is capable of forming thin, hard gluelines for maximum fidelity in transferring strains from the sample surface to the gauge.

The Ni-Cr resistive elements BB120-2AA250 (11) Karma foil strain gauges (Zhonghang Electronic Measuring Instruments Co. Ltd., China) were used. The nominal resistance is (119.9 ± 0.1) Ω, and the nominal sensitivity coefficient is 1.74 ± 0.01. When the measurement starts, the automated program controls the temperatures and magnetic field of the PPMS at the different rates. And the thermal output of the strain gauges and the temperature are recorded by nanovoltmeters. Then the LabVIEW computer can save the temperature and magnetic field dependence of the linear thermal expansion of tested sample.

RESULTS AND DISCUSSION

The accuracy of the CTE measurement mainly depends on the accuracy of the strain gauges, the nanovoltmeters and the procedure of the gauges installation. To verify the accuracy of this test apparatus and method, the thermal expansion of oxygen-free copper are measured in the temperature range of 2–300 K on this apparatus and quartz dilatometer (Linseis L75), respectively. Also, the Comparisons between experimental and published values of thermal expansion of copper are displayed in **Figure 3** (Kirby and Hahn, 1969). The results of thermal expansion of copper matched closely with reference data, and the maximum error for instantaneous coefficients is 1.1 × 10^{-6} K^{-1}, which is smaller than that testing using quartz dilatometer. At the same time, to validate the reliability of the measurement, experiments are repeated from 2 – 300 K. We can see that there is no significant difference of the thermal expansions (<2%) between the two tests, which shows that the whole measurement system is applicable in the temperature range of 2–300 K. Also, this method is available for other special structure materials such as low symmetry samples and orientation preferred samples with relatively smooth and nonporous surfaces.

In the last several years, due to the giant magnetocaloric effect (MCE) and the intriguing negative thermal expansion (NTE), $NaZn_{13}$-type compounds $LaFe_{13-x}Al_x$ have aroused extensive attention (Fujieda et al., 2002; Shen et al., 2009; Li et al., 2014; Wang et al., 2015). The MCE of this materials is chiefly due to the itinerant-electron metamagnetic (IEM) transition, i.e., a magnetic-field-induced phase transition from the paramagnetic state to the ferromagnetic state. The NTE effect is a thermo-physical property and attributed to the magnetovolume effect (MVE). Nevertheless, very few report explores the relationship between the change of volume expansion and external magnetic field, i.e., magnetostriction, in $LaFe_{13-x}Al_x$ compounds.

Generally, the large magnetostriction originates from the interaction between atom magnetic moments. $LaFe_{13-x}Al_x$ compounds ($1.04 < x < 7.02$) share the same $NaZn_{13}$-type crystalline structure while showing different magnetic states (antiferromagnetic state, ferromagnetic state and paramagnetic state). Specificly, $LaFe_{13-x}Al_x$ ($1.0< x <1.8$) show an antiferromagnetic state at low temperature. And the antiferromagnetic ordering is very vulnerable and can be turned into the ferromagnetic state easily when bringing an external magnetic field. Different magnetic states have different magnetic moments. So a large magnetostriction $LaFe_{13-x}Al_x$ of compounds is caused by these magnetic phase transition. In order to better understanding the magnetostrictive property, as displayed in **Figure 4**, the linear thermal expansion data ($\Delta L/L$ 300 K) of $LaFe_{13-x}Al_x$ ($x = 1.4$, 1.6, and 1.8) compounds were measured using this PPMS-aided measuring system over a temperature range of 10–300 K firstly (Zhao et al., 2017). For $LaFe_{13-x}Al_x$ ($x = 1.4$ and 1.6) below the Neel temperature, it shows that the CTE is very constant across a wide temperature range (10–200K). However, for the sample $LaFe_{11.2}Al_{1.8}$, $\Delta L/L$ rises with decreasing temperature in the whole temperature range examined. Specifically, $\Delta L/L$ grows gradually around room temperature, then increases rapidly, and again grows slowly with decreasing temperature, indicating that NTE occurs in the whole range measured

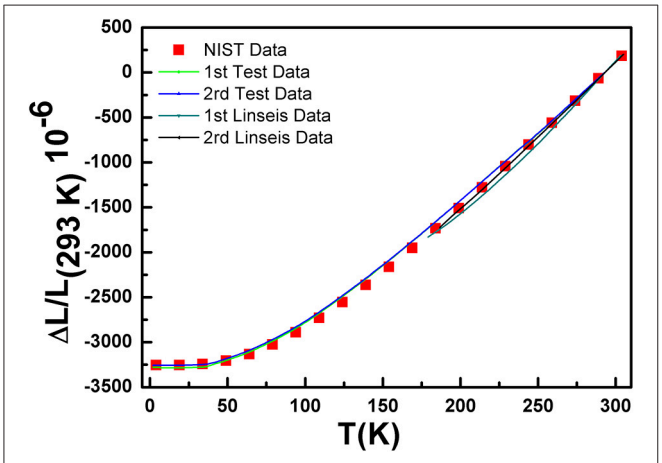

FIGURE 3 | Experimental and published values of thermal expansion of copper.

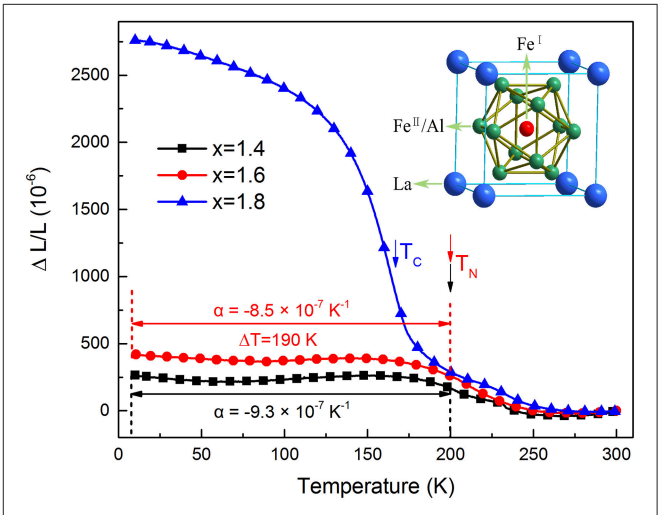

FIGURE 4 | Temperature dependence of linear thermal expansions $\Delta L/L$ (reference temperature: 300K) of $LaFe_{13-x}Al_x$.

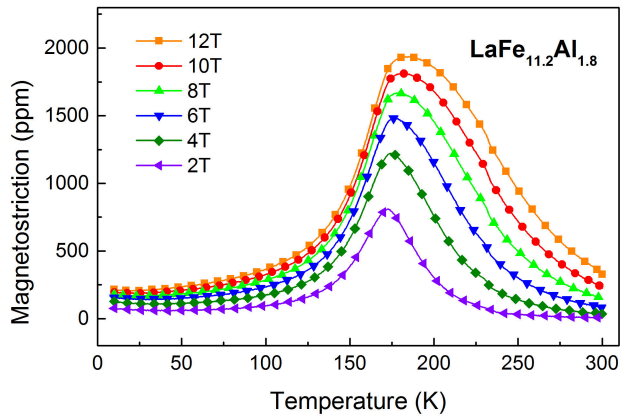

FIGURE 5 | Temperature dependence of the magnetostriction λ(T) in $LaFe_{11.2}Al_{1.8}$ at different magnetic fields.

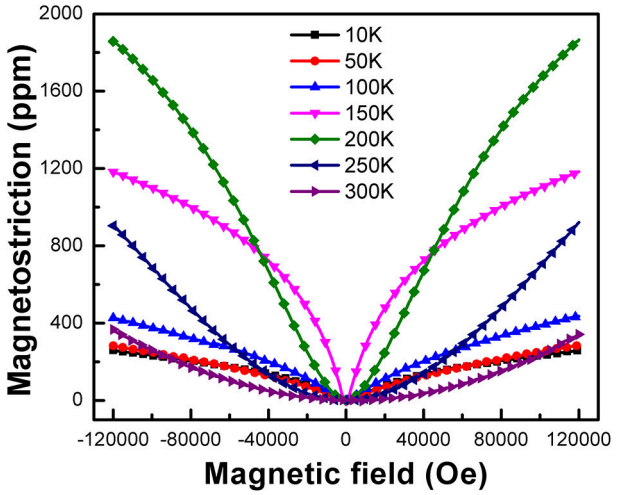

FIGURE 6 | Magnetic field dependence of the magnetostriction λ(H) of $LaFe_{11.2}Al_{1.8}$ compounds at different temperatures.

(2–300 K). It is worth noting that the ΔL/L vs. T curves are different from one another, which demonstrates that the NTE properties are affected by the partial substitution of Fe by Al sensitively.

Also it is worth mentioning that the linear magnetostriction of this material is isotropic. Because the magnetostriction measurements have been conducted along the parallel and perpendicular directions to the magnetic field separately and the anisotropic magnetostriction is negligible. **Figure 5** gives the temperature dependence of the linear magnetostriction λ(T) of $LaFe_{11.8}Al_{1.8}$ compounds between 10 and 300 K. It is noted that all the magnetostrictions of the sample in different magnetic fields exhibit a sudden increase with the decrease of the temperature and then, decrease rapidly with following temperature decline. In addition to this, it is apparent that the temperature with giant magnetostriction shifts to higher temperature as the magnetic field increases. Importantly, giant linear magnetostriction values higher than 1,000 ppm are observed when the magnetic field exceeds 4T in a relatively wide temperature range. Especially, it can reach up to 1,900ppm at 12T. Interestingly, the peak value of magnetostriction of the $LaFe_{11.2}Al_{1.8}$ compound is larger than the maximum of the typical magnetostriction material, Terfenol-D alloy (Grössinger et al., 2014).

To further explore the magnetostrictive property, the magnetic field dependence of the magnetostriction λ(H) under different temperatures for $LaFe_{11.2}Al_{1.8}$ sample have been investigated in **Figure 6**. Apparently, with the increase of the magnetic field, the λ(H) raises gently at 300 K and reaches to 340 ppm under 12T finally, suggesting the magnetostrictive effect of this material is extremely weak at room temperature. But when the temperature decreases, the λ(H) increases rapidly with increasing magnetic field. And when the temperature comes up to 200 K, the λ(H) is almost increase linearly with the increase of magnetic field. Besides, when the temperature falls below 150K, it is observed that below 4T, the magnetostriction increases quickly with the increase of the magnetic field. However, when magnetic field exceeds 4T, the magnetostriction increases slowly and becomes lower than that in 200 K. And after that, the magnetostriction is rapidly decreased with temperature decline from 100 to 10 K. The results indicate that the magnetostriction of this sample is very sensitive and the giant magnetostriction happens in a relatively narrow temperature range.

CONCLUSION

In summary, an experimental setup with a PPMS based on the strain gauge method has been developed to measure the thermal expansion and magnetostriction of solid materials at low temperatures (1.8–400 K). The relatively small dimensions of the test sample can save the liquid helium and reduce the impact of the non-uniform temperature field on measurement accuracy. The measurement accuracy was verified in the temperature range of 2–300 K by comparing the measured thermal expansion data of oxygen-free copper with the source data from NIST. Also, using this PPMS-aided measuring system, we observed temperature and magnetic field dependence of the linear thermal expansion of $NaZn_{13}$-type $LaFe_{13-x}Al_x$ compounds. Such Multi-function testing system with a broad measurement temperature range will open up an intriguing research frontier for exploring potential magnetostrictive and NTE materials.

AUTHOR CONTRIBUTIONS

WW and HL: Designed experiments; YZ, SG, and YS: Carried out experiments; HL and CH: Analyzed experimental results; WW, RH, and LL: Wrote the manuscript.

FUNDING

This work was supported by the National Natural Science Foundation of China (Grant Nos. 51577185, 51427806, 51522705, 51401224), the National Magnetic Confinement Fusion Science Program (2015GB121001), Beijing Nova program (Z161100004916114), Key Research Program of Frontier Sciences, CAS (QYZDB-SSW-JSC042), and the Fund of the State Key Laboratory of Technologies in Space Cryogenic Propellants (SKLTSCP1701, SKLTSCP1601).

REFERENCES

ASTM (2006). *E228-17 Standard Test Method for Linear Thermal Expansion of Solid Materials with a Push-rod Dilatometer*. American Society for Testing Materials, 10.

Clark, A. (1968). Low temperature thermal expansion of some metallic alloys. *Cryogenics* 8, 282–289. doi: 10.1016/S0011-2275(68)80003-7

Corruccini, R. J., and Gniewck, J. J. (1961). *Thermal Expansion of Technical Solids at Low Temperatures: a Compilation From the Literature*. Washington, DC: National Bureau of Standards.

Deng, D., and Xu, L. (2003). Measurements of thermal expansion coefficient of phenolic foam at low temperatures. *Cryogenics* 43, 465–468. doi: 10.1016/S0011-2275(03)00122-X

Fujieda, S., Fujita, A., and Fukamichi, K. (2002). Large magnetocaloric effect in $La(Fe_xSi_{1-x})_{13}$ itinerant-electron metamagnetic compounds. *Appl. Phys. Lett.* 81,1276–1278. doi: 10.1063/1.1498148

Grössinger, R., Turtelli, R. S., and Mehmood, N. (2014). "Materials with high magnetostriction," in *IOP Conference Series: Materials Science and Engineering* (Islamabad: IOP Publishing).

Hannah, R., and Reed, S. (1992). *Strain Gage Users' Handbook*. London: Elsevier Applied Science.

Inoue, D., Kaido, D., Yoshikawa, Y., Minegishi, M., Matsumoto, K., and Abe, S. (2014). Thermal expansion and magnetostriction measurements using a high sensitive capacitive dilatometer at millikelvin temperatures. *J. Phys. Conf. Ser.* 568:032001. doi: 10.1088/1742-6596/568/3/032001

Iwakami, O., Kawata, N., Takeshita, M., Yao, Y., Abe, S., and Matsumoto, K. (2014). Thermal expansion and magnetostriction measurements using a Quantum Design Physical Property Measurement System. *J. Phys.* 568:032002. doi: 10.1088/1742-6596/568/3/032002

James, J., Spittle, J., Brown, S., and Evans, R. (2001). A review of measurement techniques for the thermal expansion coefficient of metals and alloys at elevated temperatures. *Meas. Sci. Technol.* 12, R1–R15. doi: 10.1088/0957-0233/12/3/201

Kanagaraj, S., and Pattanayak, S. (2003). Measurement of the thermal expansion of metal and FRPs. *Cryogenics* 43, 399–424. doi: 10.1016/S0011-2275(03)00096-1

Kaufman, A. (1963). Investigation of strain gages for use at cryogenic temperatures. *Exp. Mech.* 3, 177–183. doi: 10.1007/BF02325791

Kirby, R., and Hahn, T. (1969). *Standard Reference Material 736. Copper Thermal Expansion.* Washington, DC: National Bureau of Standards. 10 p.

Kirby, R., and Hahn, T. (1971). *NIST Standard Reference Material 739, Fused-silica Thermal Expansion.* . Washington, DC: National Bureau of Standards.

Li, W., Huang, R., Wang, W., Tan, J., Zhao, Y., Li, S., et al. (2014). Enhanced negative thermal expansion in $La_{1-x}Pr_xFe_{10.7}Co_{0.8}Si_{1.5}$ compounds by doping the magnetic rare-earth element praseodymium. *Inorg. Chem.* 53, 5869–5873. doi: 10.1021/ic500801b

Liu, H., Gong, L., Xu, D., Huang, C., Zhang, M., Xu, P., et al. (2014). Top loading cryogen-free apparatus for low temperature thermophysical properties measurement. *Cryogenics* 62, 11–13. doi: 10.1016/j.cryogenics.2014.02.020

Liu, H., Xu, D., Xu, P., Huang, R., Xu, X., Li, L., et al. (2012). An apparatus for measurements of thermal conductivity and thermal expansion based on GM cryocooler. *J. Phys. Conf. Ser.* 400:052017. doi: 10.1088/1742-6596/400/5/052017

Micro-Measurements (2007). Measurement of thermal expansion coefficient using strain gages. *Tech. Note* TN-513-1, 119–129. Available online at: http://blhnobel.se/docs/11063/tn5131tn.pdf

Poore, M., and Kesterson, K. (1978). Measuring the thermal expansion of solids with strain gages. *J. Test. Eval.* 6, 98–102. doi: 10.1520/JTE10926J

Quantum Design Inc. (2002). *Interfacing 3rd Party Instruments to the PPMS Software Environment.* Application Note 1070-210, 4 p.

Quantum Design Inc. (2013). *Interfacing LabVIEW Programs with PPMS, DynaCool, Versalab and MPMS 3 Systems*. Application Note 1070-210, 5 p.

Shen, B., Sun, J., Hu, F., Zhang, H., and Cheng, Z. (2009). Recent progress in exploring magnetocaloric materials. *Adv. Mater.* 21, 45–64. doi: 10.1002/adma.200901072

Tang, K., Sha, L., Li, Y. J., Jin, T., and Liu, S. J. (2014). Measurement of thermal expansion at low temperatures using the strain gage method. *J. Zhejiang Univ. Sci. A.* 15, 323–330. doi: 10.1631/jzus.A1400051

Ventura, G., and Risegari, L. (2008). *The Art of Cryogenics: Low-Temperature Experimental Techniques*. Oxford: Elsevier Ltd.

Walsh, R. P. (1997). "Use of strain gages for low temperature thermal expansion measurements," in *Proceedings of the 16th ICEC/ICMC* (Kitakyushu: Elsevier Science), 661–6644.

Wang, W., Huang, R., Li, W., Tan, J., Zhao, Y., Li, S., et al. (2015). Zero thermal expansion in NaZn13-type La(Fe, Si)13 compounds. *Phys. Chem. Chem. Phys.* 17, 2352–2356. doi: 10.1039/C4CP04672B

Zhao, Y., Huang, R., Li, S., Liu, H., Wang, W., Jiang, X., et al. (2017). Giant isotropic magnetostriction in $NaZn_{13}$-type $LaFe_{13-x}Al_x$ compounds. *Appl. Phys. Lett.* 110:011906. doi: 10.1063/1.4973476

Conflict of Interest Statement: The authors declare that the research was conducted in the absence of any commercial or financial relationships that could be construed as a potential conflict of interest.

The reviewer KL and handling Editor declared their shared affiliation.

Advantages of publishing in Frontiers

OPEN ACCESS
Articles are free to read for greatest visibility and readership

FAST PUBLICATION
Around 90 days from submission to decision

HIGH QUALITY PEER-REVIEW
Rigorous, collaborative, and constructive peer-review

TRANSPARENT PEER-REVIEW
Editors and reviewers acknowledged by name on published articles

Frontiers
Avenue du Tribunal-Fédéral 34
1005 Lausanne | Switzerland

Visit us: www.frontiersin.org
Contact us: info@frontiersin.org | +41 21 510 17 00

REPRODUCIBILITY OF RESEARCH
Support open data and methods to enhance research reproducibility

DIGITAL PUBLISHING
Articles designed for optimal readership across devices

FOLLOW US
@frontiersin

IMPACT METRICS
Advanced article metrics track visibility across digital media

EXTENSIVE PROMOTION
Marketing and promotion of impactful research

LOOP RESEARCH NETWORK
Our network increases your article's readership